Transactions of the ASME®

Journal of Fluids Engineering

(Contents continued)

Technical Briefs

Announcements and Special Notices

Editorial

This issue of JFE contains a number of papers addressing the important topic of turbulence in fluid flow, especially those aspects related to modeling. Turbulence modeling has long been driven by a practical need to incorporate turbulence effects in predictions of fluid flow. This need has not diminished but has instead increased as other sources of error in predictions have been reduced, and computational power and numerical techniques have improved. The capability to compute the flow around major components and even complete vehicles has been demonstrated, but the resulting accuracy in quantities most affected by a turbulence model, such as drag and smooth surface separation has been inadequate.

Lacking a comprehensive fundamental theory of turbulence, researchers and designers have resorted to approximate methods progressing from the simple to increasingly complex as approach after approach proved limited in performance. Much of the early work demonstrated remarkable intuition but had only a modest mathematical foundation. Today there is an expanding body of formal theory upon which to build, and models are required to meet stringent criteria derived from fundamental principles, including tensor formulation, reliability, response to system rotation, and consistency with rapid deformation theory, among others. Measurement capabilities, too, have improved dramatically. Though the hot-wire anemometer has undoubtedly produced the greatest body of information on turbulence, optical techniques such as LDV and PIV have contributed substantially, especially in complex or hostile environments.

Though there have been substantial improvements, the prediction of turbulent flow is still far from satisfactory. The most complex models, full second-order closures, have not generally been found to outperform simpler models, especially in wall-bounded flow. On the other hand, the more sophisticated of the simpler eddy-viscosity models are based on equilibrium concepts which should limit their applicability. The extent of our knowledge of their usefulness has often been limited somewhat by unknown levels of error due to interaction with numerics and gridding. The continued increase in available computational power will permit closer investigation of these issues in the future.

Research efforts continue on a broad range of problems in the rich, challenging field of turbulence. In this issue, papers range from important reports on focused efforts, such as "High Freestream Turbulence Effects on Turbulent Boundary Layers" by K. Thole and D. Bogard to invaluable broad contributions, such as "Collaborative Testing of Turbulence Models" by P. Bradshaw, B. Launder, and J. Lumley and "Review: Advances in Three-Dimensional Turbulent Boundary Layers with Emphasis on the Wall-Layer Regions" by J. Johnston and K. Flack. The particularly important challenge of predictions in the wall-region is addressed in "A New Low-Reynolds-Number $k-e$ Model for Turbulent Flow Over Smooth and Rough Surfaces" by H. Zhang, M. Faghri, and F. M. White, and "Modeling Reynolds-Number Effects in Wall-Bounded Turbulent Flows" by R. M. C. So, H. Aksoy, S. P. Yuan, and T. P. Sommer.

The papers of Johnston and Flack and Bradshaw, Launder, and Lumley are also contributions to the Data Bank as is the paper "An Experimental Study of a Three-Dimensional Pressure-Driven Turbulent Boundary Layer" by M. S. Olcmen and R. L. Simpson. Two other experimental papers address important and complex internal flows: "Development of a Two-Dimensional Turbulent Wake in a Curved Channel with a Positive Streamwise Pressure Gradient" by J. John and M. T. Schobeiri, and "Turbulent Flow in Longitudinally Finned Tubes" by D. P. Edwards, A. Hirsa, and M. K. Jensen. The collection is rounded out by a thought-provoking paper on the interaction of computation and experiment in "The Experimentalist and the Problem of Turbulence in the Age of Supercomputers" by M. Gharib, and a contribution from the exciting field of large-eddy simulation, "Large-Eddy Simulation of Turbulent Flow in a Curved Pipe" by B. J. Boersma and F. T. M. Nieuwstadt. The papers cover a broad range of topics in turbulence modeling research and should serve as an encouragement for the development of new ideas to help us along the path toward reliable, accurate predictions of turbulent flow based on a firm foundation of scientific understanding.

<div align="right">

L. Patrick Purtell
Office of Naval Research

</div>

BOOK REVIEW

HANDBOOK OF FLUID DYNAMICS AND FLUID MACHINERY,

J. A. Schetz and A. E. Fuhs (Editors), John Wiley & Sons, Inc., New York, 1996.

This comprehensive work contains a very complete and extensive coverage of virtually all aspects of fluid dynamics and fluid mechinery. It has been more than three decades since a comparable work was published edited by Victor Streeter. This *Handbook* does an admirable job of bringing the newest advances in theory, experiment, computations and engineering practice up-to-date in this important area of engineering and applied science.

The various chapters and sections of the *Handbook* were written by more than 100 distinguished international authors, experts in their respective fields from industry, government and universities. The editors did a marvelous job organizing the coverage, assembling such a noteworthy team of authors and pursuing this Herculean effort through to completion.

The *Handbook* is not addressed to the experts. The level of coverage is designed such that an engineer or applied scientist with an undergraduate training in fluid dynamics will be able to gain an introduction into a new area of the general subject and also be directed to critical references with more detailed information. In addition, the *Handbook* contains important practical data on fluid properties, empirical correlations and performance of fluid machinery components and systems. It will therefore prove very useful to practicing fluids engineers.

The *Handbook* is divided into three volumes for ease of use consisting of 29 chapters with 2628 pages of text and figures. Each volume has its own Table of Contents and an Index for all three volumes. The appearance and usability of the book are excellent.

Volume One covers Fundamentals of Fluid Dynamics in 14 chapters with 919 pages. The topics are: Equations for Fluid Statics and Dynamics, Properties of Fluids, Non-Newtonian Liquids, Flow of Fluids with Viscosity and Thermal Conductivity, Internal Flows, Waves in Fluids, Thermodynamics for Fluid Flow, Fundamentals of Compressible Flows, Transonic Flow, Hypersonic Flow, Rarefied Gas Dynamics, Unsteady Flows, Complex Flows, and Multiphase Multicomponent Flows.

Volume Two treats Experimental and Computational Fluid Dynamics in 8 chapters with 670 pages. The chapter titles are: Instrumentation for Fluid Dynamics, Fluid Dynamics Ground Test Facilities, Videotapes and Movies on Fluid Dynamics, Introduction to Computational Fluid Dynamics, Methods of Solving Fluid Dynamic Equations, Computational Methods for Inviscid Flow, Computational Methods for Viscous Flow, and Computational Methods for Chemically Reacting Flow.

Volume Three provides coverage of Applications of Fluid Dynamics in 7 chapters consisting of 1037 pages. The chapters are entitled: Fluid Dynamic Related Technologies; Fluid Dynamics in Nature; Static Components of Fluid Machinery; Positive Displacement Compressors; Pumps and Motors, Turbomachinery; Hydraulic Systems; and Pneumatic Systems.

The editors and authors are to be congratulated for their selfless efforts in making the latest state-of-the-art accessible to a wide audience. This *Handbook* will find a useful place in the library of any practitioner or researcher in the field of fluid dynamics.

The Technical Editor

J. P. Johnston

Professor Emeritus,
Department of Mechanical Engineering,
Stanford University,
Stanford, CA 94305-3030, Fellow ASME

K. A. Flack

Assistant Professor,
Department of Mechanical Engineering,
U. S. Naval Academy,
Annapolis, MD 21402-5042

Review—Advances in Three-Dimensional Turbulent Boundary Layers With Emphasis on the Wall-Layer Regions

(Data Bank Contribution)*

Current information concerning three-dimensional turbulent boundary layers is discussed. Several topics are presented including (i) a detailed description of eleven experiments published since 1990. In nine cases cross flows are controlled by pressure gradients imposed from the freestream, but in two cases the cross flows are wall-shear-driven. The other topics include (ii) an examination of state of the art in measurement techniques; (iii) a look at some issues and ideas in turbulence modeling; and (iv) an introduction to new work on the visualization and description of quasi-coherent structures (high/low-speed streaks and turbulent vortices) in three-dimensional turbulent boundary layers.

Introduction

Turbulent boundary layers subject to forces which create cross-flow three-dimensionality (skewing of the mean velocity vectors) have been studied for over 60 years. Skewed turbulent boundary layers are more the rule than the exception in a multitude of engineering flows including swept airfoils, curved ducts, axial compressor end walls, rotating disks, the bow and stern regions of ships, submarine hulls and so forth. Any time a force (pressure, shear, MHD, etc.) is applied to a boundary layer in a direction perpendicular to the local streamwise direction a cross-flow may be generated or changed. All cases studied here are generally designated 'secondary flow of the first kind' after Prandtl. We are not going to consider weak cross-flow three-dimensionality produced directly by anisotropy in the turbulent Reynolds stresses seen, for example, in the corner bisector regions of straight rectangular duct flows. This class of cross-flow is often referred to as 'secondary flow of the second kind'.

About 60 years ago, Gruschwitz (1935) studied the boundary layer on the flat end-wall of a curved rectangular duct in Prandtl's laboratory at Göttingen. He was the first investigator to display the cross-flow velocity component, W, as a function of the streamwise component, U, in a hodograph or polar plot, and his data were used to help formulate an early computational model of three-dimensional turbulent boundary layer (3DTBL)[1] effects, Mager (1952). Later, Johnston (1960) proposed a simplified version of this plot and called it "triangular," a designation which has unfortunately stuck to this day in spite of the fact that real data when presented in hodograph form (W versus U) forms a triangle with a rounded apex. By 1960, only a handful of experimental studies existed and none of these contained any turbulence data. A comprehensive study on computation of 3DTBLs (Nash & Patel 1972), based models of the Reynolds shear stresses on rather limited experimental data available at the time. In the late 1960's and early 1970's hot-

wire anemometry was used routinely in a few laboratories, and some three-dimensional turbulent Reynolds stress data (about five sets) using this technique were available by 1976 when an early review of the subject was undertaken, Johnston (1976). Other reviews are available today, including Bradshaw (1987), Cousteix (1986), Humphreys and Lindhout (1988), and a recent paper of Ölcmen and Simpson (1993) which reviews and evaluates the commonly used algebraic eddy-viscosity models. Schwarz and Bradshaw (1993) clearly summarize the main stumbling points in current efforts at turbulence modeling for 3DTBLs.

The current state of turbulence modeling for computation in 3DTBLs is not satisfactory. A principal goal of this paper is to summarize and interpret experimental data sets on simple 3DTBLs which are shear or pressure driven, and thereby indicate the role such a study may play in the improvement of turbulence models. As noted in Johnston's 1976 review, and confirmed in all subsequent studies, the assumption of a single, direction-insensitive (isotropic) eddy viscosity in 3DTBLs is not an accurate model to represent the turbulent shear stresses. But perhaps more important Bradshaw and Pontikos (1985) confirmed an earlier discovery by Van den Berg and Elsenaar (1972): skewed three-dimensional layers tend to have a ratio of turbulent shear stress to turbulent kinetic energy (the a_1 parameter often named after A. Townsend) that is lower than observed in equivalent two-dimensional flows. It would seem that the presence of cross-flow (mean streamwise vorticity) in the layer, can somehow disrupt or modify the quasi-coherent turbulent "eddy" structures responsible for the generation and destruction of the principal shear stresses $-\overline{u'v'}$ along the main-flow and $-\overline{w'v'}$ in the cross-flow directions.

By the mid-1980's hot-wire technology was widespread and laser Doppler anemometry (LDA) was coming into increasing use. Recently for example, LDA measurements of turbulence have been obtained down to y^+ (distance from the wall, y, scaled on total wall shear velocity, $Q_\tau = \sqrt{\tau_w/\rho}$, and kinematic viscosity, ν) of about 7, well into the viscous sublayer, a region not easily accessible by hot-wire methods. These and other new experimental results have been augmented by use of a new approach to the study of turbulence in three-dimensional flows, direct numerical simulation (DNS). Spalart (1989), Moin et al. (1990), Sendstad and Moin (1992), and Coleman et al.

(1995) studied three-dimensional flows using DNS, and obtained useful near-wall data for low Reynolds number turbulent flows.

A major objective of this paper is to discuss recent experimental results selected from sources that might shed some light on the nature of skewed wall-layers with particular emphasis on the near-wall region, below $y^+ \approx 100$. (i) Eleven cases are reviewed individually. The experiments selected for review are representative of the majority of current work which we consider useful for advancing knowledge in turbulence modeling. Commentary on experimental methods and accuracy of the current data is provided. (ii) Some issues on modeling for computation are discussed, and recent data are used to illustrate some ideas. The particular issue of effects of upstream history on turbulence in three-dimensional flows is discussed, and some problems of modeling in the wall layers are clarified using the data. Finally (iii), we discuss the limited and controversial data on the quasi-coherent structure of turbulence in 3DTBLs. In quantity and quality these data can hardly be compared to the extensive structure results for two-dimensional flows, see Robinson (1991a, b). But, we feel that the development of greater understanding of the three-dimensional effects such as the strange lowering of a_1 cannot be achieved without better knowledge of the structural details.

Summary of Recent Experiments With Skewed Layers

The purpose of this summary is to bring the reader up-to-date on recent experimental work not yet reviewed by others. Only those experiments which contain a reasonable amount of turbulent Reynolds stress data are summarized in Table 1 which also includes columns for special notations.

The review is divided according to the principal mechanism which drives the cross-flows: nine cross-stream pressure gradient cases and two tangential wall shear driven flows. In the latter cases, the distinction is not completely valid because additional pressure gradients are introduced in one case (Driver and Johnston, 1990), and in rotating disk flows, the tangential motion of the disk creates cross-flow in the radial direction because radial pressure forces are not available to balance the radial acceleration of fluid particles with tangential motion. A short section is included to discuss some new developments in the field, flows computed by direct numerical simulation (DNS) of the full Navier-Stokes equations, and finally we present comments on limitations of measurement techniques in use today.

Flows Driven by Transverse Pressure Gradients

(1) Schwarz and Bradshaw (1992, 1993) used a simple geometry, the flat end-wall of a constant area, square (762×762 mm) duct. The duct, which was approximately 4000 mm long, included a 30 degree bend (approx. 600 mm along a central arc) at its mid-point. The inlet momentum thickness Reynolds number, $Re_{\theta 1}$, was 4100, 1628 mm upstream of the bend where the reference air speed was 26.5 m/s. At the start of the bend, the boundary layer was 30 mm thick and $Re_{\theta 1} \approx 6000$. Numerous pressure probe and hot-wire anemometer (Method II, see below) profiles were obtained along, and off, the centerline of the flat wall upstream of, inside of, and downstream of the 30 degree bend. The streamwise pressure gradients are rather small along the center line compared to the cross-stream gradients in the bend region. In addition, the boundary layer was thin ($\delta \approx$ 30 mm) compared to the width of the duct. Consequently, flow from the concave, side-wall boundary layer did not enter the region of measurement until well downstream, in the rear portion of the straight duct that followed the bend. Here, the flow, which had been skewed by up to 24 degrees in the bend, was slowly "recovering" to a 2D state. The major results of this study include details of the mean flow, all six Reynolds stresses, and all triple products of the fluctuations across the outer layers of the boundary layer, from $y/\delta \approx 0.1$ to 1.2. The wall-layers

are not resolved below the log-law region. The work is well documented and looks quite suitable as a test case for computation with advanced turbulence models.

(2) Flack and Johnston (1993a, 1994) constructed an experiment very similar to the Schwarz and Bradshaw case, but for use in a water-flow channel with reference flow speed of 0.2 m/s and a lower Reynolds number, $Re_{\theta 1} \approx 1300$, upstream of the 30 degree bend. The boundary layer thickness, δ, was 55 mm at the inlet to the bend. Like Schwarz and Bradshaw they also had a straight duct downstream of the bend, but it was short and only allowed for partial recovery from three-dimensional flow conditions. Their measurement technique (a three-component laser Doppler velocimeter) was designed to penetrate deep into the viscous sublayers, down to $y^+ \approx 1$ for mean speed, Q, and $y^+ \approx 5$ to 7 for other properties. Wall shear stress was obtained directly from the slope of the mean velocity profile, $\partial Q / \partial y$, at the wall (see discussion on wall stress measurement below). A complete set of nine mean velocity and turbulence profiles was obtained along the center line of the flat, end-wall (two upstream, five in the bend and two in the recovery zone, downstream). These results complement the data of Schwarz and Bradshaw in that they include the wall layers, well below $y/\delta \approx 0.1$, of a geometrically similar flow. In comparison to Schwarz & Bradshaw, this case is not likely to be useful as a direct test case for Reynolds averaged Navier-Stokes CFD codes. For example, wall static pressure distributions could not be obtained.

(3) Flack and Johnston (1993a, b) also studied another case in their water channel, a flow which geometrically reproduced the case studied by Johnston (1970) on a separating boundary layer ahead of a sharp-edged, forward-facing, "infinite" step, swept back at 45 degrees on a flat wall. The $Re_{\theta 1} \approx 1500$ was again smaller than in the earlier air-flow study where $Re_{\theta 1} \approx 6900$. However, using the LDV instrumentation, they were again able to look at the wall layers in detail. The number of profiles measured was small, but sufficient to show the similarity to Johnston's case. In this case, and in the 30 degree bend, they also obtained flow visualization data in the wall layers.

Other recent pressure driven flows are *more complex* than the flows discussed above. The flows of Schwarz and Bradshaw and Flack and Johnston have the cross-stream pressure gradient in a single direction without reversal of sign. This leads to cross-flow mean profiles which roughly approximate a triangle when viewed in W versus U coordinates, the hodograph or polar-plot form. As soon as the cross-stream gradient reverses sign, the flows become considerably more complex with the possibility of 180 degree reversal of sign of W in the inner part with respect to the outer part of a $W(y)$ profile; the polar-plot tends to become S-shaped. Cases (4) through (9), presented below, show this additional degree of complexity, but the last two cases (10) and (11), do not.

(4) Ölcmen and Simpson (1992) present results for flow in the boundary layer on a flat wind-tunnel wall where the cross-stream pressure gradient reverses downstream. Three-dimensionality is of the wing-body junction type caused by a symmetric airfoil mounted vertically on the flat, boundary layer wall. The reference air speed was 27 m/s and $Re_{\theta 1}$ was 6000. They collected mean velocity and Reynolds stress profiles by LDA at 8 stations along a mild, s-shaped space curve in the plane of the flat wall. This curve, along which the profiles are equally spaced, starts about $\frac{1}{2}$ chord upstream of the airfoil disturbance and ends about $\frac{1}{4}$ chord downstream of the airfoil's nose. The line of profiles is off the symmetry plane by roughly $\frac{1}{2}$ to 1 times the airfoil maximum thickness, outboard of the separation region formed by the horseshoe-shaped vortex that wraps around the nose of the airfoil. The wall shear stress was obtained by oil-film laser interferometry (Asilinger 1990). In this flow the pressure gradient along the freestream was mildly favorable, and the cross-stream pressure gradient reverses direction be-

tween the third and fourth downstream station. Some data below $y^+ \approx 10$ were obtained, but its high uncertainty reduces its utility beyond indicating general trends. Even further from the wall, above y^+ of 50, substantial scatter is demonstrated in profiles of the turbulence stresses and kinetic energy. (A new, and more accurate, data set has recently been produced to replace the original data. Evaluation of the new data is still in progress).

(5) Kreplin and Stäger (1993) and Stäger (1993), describe an experiment on a 2.4 m long, 6:1 prolate spheroid mounted at 10 degrees angle of attack in a 3 m × 3 m low speed wind tunnel. The Reynolds number based on model length was 4.8 × 10^6 for tunnel reference speed of 30 m/s. A four sensor hot-wire probe was used to obtain boundary layer profiles of the mean flow and six Reynolds stress components in the outer regions from $y/\delta \approx 0.05$ to 1.0 at various azimuthal and axial locations. Data in the wall-layers were not obtained, and wall shear stress was not measured. The results confirmed the trends seen in other flows as discussed under "modeling issues" below, and the data set might be useful as a computational test case. However, a new case, (6) below, has become available which is geometrically and dynamically almost identical to this flow. Improvements in measurement technique make the newer data more attractive for future study.

(6) Chesnakas and Simpson (1994a) describe another experiment on a 6:1 prolate spheroid set at 10 degrees to the wind tunnel freestream. This paper is a sequel to earlier studies of the same flow (Ahn 1992, Barber and Simpson 1991). The model was 1.37 m long, the tunnel flow speed was 67 m/s and the model length Reynolds number was 6.0 × 10^6, a bit higher than for the nearly identical case (5) above. A special feature of this experiments is that all velocity data, up through turbulent triple products, were obtained with a unique, three-component, fiber-optic LDA probe designed for this case (Chesnakas and Simpson, 1994b). Uncertainty limitations on the data are carefully delineated. There is general agreement between results presented in this case and case (5), but here the boundary layers could be surveyed much closer to the wall, down to $y^+ \approx 7$ in the lower parts of the wall-layer. Individual profiles were obtained at 32 stations for five axial locations along the model and at a number of peripheral locations spaced equally from the windward to the leeward side. Careful attention was paid to obtaining profiles in the region of primary three-dimensional separation. Each profile contained only a limited number of radial positions (14 to 17) were measured from the edge of the boundary layer down to $y = 0.1$ mm from the wall. Wall shear stress was obtained by fitting mean velocity data in the inner, approximately collateral region to a Spalding type $y^+(U^+)$ curve over five to six points between $y^+ = 7$ and 100. Because of its relatively simple geometry this experiment looks very good for the purpose of comparison to computed results.

(7) Gleyzes et al. (1993) is a summary and status report on two experiments on scaled, finite, swept-back, three-dimensional wing models, being conducted in parallel in two different wind tunnels, the LST of NLR (Netherlands) and the F2 of ONERA (France). This cooperative effort is using many different measurement techniques, HW methods II and III, and LDA, to (i) show that the turbulent boundary layer flows in the two systems are properly similar, and (ii) to study the characteristics of the suction and pressure side boundary layers in sufficient detail to aid in turbulence modeling for Reynolds-averaged Navier-Stokes (RANS) type computation. The overall Reynolds number (based on tunnel speed and model chord length) was set at 3.3 × 10^6 in both facilities, and comparative profiles demonstrate that the flows are indeed similar. Only a small amount of the data is presented in this paper, but a comparison to Schwarz and Bradshaw's case suggests that the effects of streamwise pressure gradients may be more important to turbulence energy production than are the effects of cross-flow, even in this case where skewing angles as high as 40 degrees were

obtained on the suction side of the airfoil. Because this case represents a flow of practical interest and because of the care and attention to detail in the acquisition of data, it will almost surely be used as a computational test case, and thus fulfill the intentions of its authors and the European Community, the sponsors of the work.

(8) Truong and Brunet (1992) conducted an air flow experiment with reversal of the cross-stream pressure gradients as part of a second European Community program of computational modeling of turbulence. Using rotatable X-wire anemometry, HW method II, they measured the mean velocity and Reynolds stress profiles at 24 stations downstream and 21 closely spaced stations far upstream along one flat wall of a duct with an S-bend. Wall stress was determined by Preston tube at the downstream stations and the static pressure distribution was recorded in detail. The test region consisted of a 9 m long, horizontal, flat plate which spanned the distance between two identically shaped, vertical sidewalls of a duct. The vertical sidewalls were parallel and separated by 1 m. Downstream of the tunnel contraction, the first 3 m of each sidewall was straight; an S-shaped portion occupied the second 3 m; and the final 3 m was again straight and parallel to the upstream part of the wall. The free-stream turned monotonically a total of 19 degrees over a distance of about 4.5 m (starting at flat plate's leading edge) before reversal of the cross-stream pressure gradient reduced the total turning angle to about 9 degrees at the final measurement station, 5.5 m downstream. About 1.2 m downstream of the leading edge, the flow was two-dimensional with a freestream speed of 18 m/s and $Re_\theta \approx 6100$. Since the primary purpose of the study was to provide a test case for modeling and computations, detailed analysis of the data itself was not presented. Our preliminary examination indicates some problems in the data for the region below $y+ \approx 200$ where the X-wire probe may accrue errors due to mean velocity gradients across its measurement volume. Fourteen additional papers in the volume where the paper appears attempt to compute the flow by a wide variety of methods and turbulence models. These efforts are summarized by Ryhming et al. (1992) who provide some thoughtful conclusions for those who believe their measurements may be useful as a test case for development of turbulence models.

(9) Pompeo (1992) and Pompeo et al. (1993) present measurements in a different kind of 3DTBL. The flow is created on a flat wall with a central plane of symmetry along which there are no cross-flows, with the primary purpose of investigating effects of spanwise strain on boundary layer turbulence. A duct is used to create convergent flow in one case, and divergent flow in a second case (duct reversed). The duct decreases in vertical height as the side walls diverge so that the pressure gradient along the symmetry plane was nearly zero, except for the slow acceleration of the flow due to growth of the boundary layer displacement thickness. Reynolds stresses are measured on- and off-symmetry plane by HW method II, but near-wall data is limited because the boundary layers were quite thin. The upstream Re_θ ranged from 4000 to 4700. Off the symmetry plane, spanwise pressure gradients cause mild skewing with maximum yaw angles of -8 degrees in the converging flow and $+5$ degrees in the diverging flow. Off-symmetry profiles show some of the characteristics already seen in other cases; the shear stress vector angle, γ_t, tends to lag behind the angle of the rate of strain, γ_g, in the outer layer, above $y/\delta \approx 0.1$ to 0.2 (see later discussion). The turbulence parameter, a_1, decreases by a small amount in the region of strongest cross-flow, but reductions of the same magnitude are also evident on the symmetry plane where there is no skewing. It appears that effects of boundary layer cross-flow on turbulence structure may be small in this case compared to effects of spanwise strain.

Flows Driven by Transverse Wall Shear and Pressure Gradient

(10) Driver and Johnston (1990) modified the rig used by Driver and Hebbar (1987) so that they could apply a streamwise

adverse pressure gradient to the swirling, axially symmetric boundary layer on a stationary cylinder. The swirling flow was produced upstream by a segment of the cylinder which rotated with a surface speed equal to the upstream axial air speed, 30 m/s. The Re_θ was approximately equal to 6000 at the start of the rotating section. In this case, the instantaneous values of all three velocity components were measured with a laser Doppler anemometer down to the edge of the viscous sublayer, as low as $y^+ \approx 20$. A number of different cases were run with and without swirl and axial pressure gradient. When the pressure gradient was applied to the non-swirling, purely axial flow, separation occurred, but with swirl the separation was suppressed. This flow was qualitatively no different than other cases, the turbulent shear stress angle lagged behind the rate of strain angle, and the structure parameter, a_1, was low with respect to the range of values usually seen in 2-D layers, 0.14 to 0.16. In addition to acquiring a substantial amount of profile data, the wall shear stresses were measured by oil-film laser interferometry. Driver and Johnston analyzed their data and compared them to results obtained by various turbulence models, including a full Reynolds stress equation model.

(11) Littell and Eaton (1992) present results on a single rotating disk in stationary air which, in addition to mean velocity and Reynolds stress profiles, include profiles of velocity fluctuation triple products. Their disk was one meter in diameter and built to exacting specifications in regard to flatness. It was spun slowly to verify hot-wire probe accuracy (HW method II) in the laminar flow regime where the theoretical solution is known. Turbulent boundary layer flow was achieved over a substantial fraction of the disk at Reynolds numbers (based on disk radius and tip speed) up to 1.6×10^6. Errors in the turbulence data became large in the outer boundary layer ($y > 0.6\ \delta$) where the mean velocity was small relative to the hot-wire probe which was held stationary in laboratory coordinates. The angle γ_τ lagged behind γ_g, but only slightly, and a_1 decreased a small amount near the wall, but it was lower in the central parts of the layer compared to most other data. The structure of turbulence was investigated in some unique measurements of spatial correlations using two X-wire probes with variation of radial distance between their axes. A separate study of flow over a rotating disk in stationary water was conducted by Chiang and Eaton (1993) where they reproduced Littell's flow conditions, and provided some very interesting flow visualization on the near-wall, quasi-coherent turbulence structures. Selected results from both of these experiments will be discussed further in separate sections below.

The important characteristics of this kind of flow, the rotating disk, are that it is (i) *fully three-dimensional in the laminar, transitional and turbulent regions;* (ii) the flow is axially symmetric, like case (10); and (iii) it has a very simple "effective" freestream pressure gradient, $-\rho\Omega^2 r$, the gradient that drives the cross-flow when viewed from the rotating surface of the disk. The two flows on pitched up prolate spheroids, cases (5) and (6), and the swept, tapered wing case (7) are also fully three dimensional, but they are strongly affected by complex free-stream pressure gradients. All the other experimental cases start as two-dimensional turbulent boundary layers and only become three-dimensional downstream once they are perturbed by cross-stream pressure gradients. The evidence of upstream history is clear in the way their mean velocity profiles develop. The effects of upstream history on turbulence structure and statistical quantities, such as Reynolds stresses and turbulence energy, need to be assessed if any real progress is to be made in development of improved turbulence models. The geometric simplicity of rotating disk flow and the fact that it is fully three-dimensional makes this set of data very useful for model testing.

Other New Developments. An interesting recent development has been the introduction of the computational method called Direct Numerical Simulation (DNS). This method,

which involves numerically solving the full Navier-Stokes equations, including all of the unsteady (turbulence) terms, was first introduced in the early 1980's in order to solve a very simple case, fully-developed flow in a 2-D straight-walled channel, and has been adapted to a number of other simple turbulent flows, including 2-D boundary layers without freestream pressure gradient, Spalart (1988). The results of such DNS solutions are viewed by some workers as "experimental" turbulence data[2] which may be used to help construct turbulence models for use with the Reynolds averaged Navier-Stokes equations. To our knowledge, the DNS method has been applied to two cases where the flow contains skewed mean velocity profiles, the mean flow is 3D and turbulent.

For the *first case,* Spalart (1989) simulated the boundary layer on a flat plate with a time dependent free-stream velocity whose direction (parallel to the wall) rotates at a constant angular rate. The flow develops mild skewing due to the instantaneous cross-stream pressure gradient which rotates with the freestream. This case cannot be realized experimentally, but has some similarity to a low Reynolds number, turbulent Ekman layer. The turbulence is only weakly three-dimensional as the angle of the Reynolds shear stress was in close alignment with the rate of strain direction and, in the outer layers, a_1 was only slightly lower than expected for a 2-D flow.

The *second case,* Moin et al. (1990) and Senstad and Moin (1992), is also a transient flow which is not easily replicated experimentally. Here, a 2-D fully-developed, pressure-driven, turbulent channel flow is turned by the application of a spanwise pressure gradient. For a period of time the mean velocity profiles are skewed, but eventually flow reverts to 2-D along an axis aligned with the vector representing the sum of the original pressure gradient and the imposed spanwise gradient. They found that the changes observed in Reynolds shear stress, turbulent kinetic energy, and the parameter a_1 during the 3-D transient period must be due to "subtle effects of three-dimensionality." After the spanwise pressure gradient was imposed, the temporal changes in turbulence statistics, as the flow developed, were relatively slow compared to the turbulence time scales and thus the flow could be investigated with the objective of understanding the details of the mechanics of the structure, some of which will be discussed below in the final section.

Comments on Measurement Techniques and Accuracy. *Hot-wire anemometry* has advanced slowly in the past decade, and it is still the main method for the measurement of the properties of simple and complex turbulent shear flows. There are three principal approaches, HW Methods I, II and III. These designations, which are useful for our purposes, were used by Pompeo (1992) in a more detailed review of hot-wire methods for 3DTBLs.

HW Method I employs a single normal or slant wire probe which is rotated into enough angular positions to resolve as many components of the mean velocity vector and turbulence properties as are desired. Although conceptually simple, this method has been used very little in recent years. Probe stem flow interference causes Method I to suffer from somewhat higher measurement uncertainty than Method II because the stem is aligned perpendicular to rather than along the predominant mean flow direction.

In HW Method II, an X-probe with two wires at ± 45 degrees to the probe axis is operated with its axis along the local mean velocity vector determined a priori by independent means, a three- or a five-hole pressure probe survey for example. The X-probe is then rotated about its axis to enough different positions to produce all desired turbulence correlations. In addition to

---

[2] DNS results are now restricted to flows at lower Reynolds numbers because of severe grid resolution problems, even on current generation large scale computers. Turbulent boundary layer computations for Re_θ as high as 1400 were acheived by Spalart (1988) and these results are closely matched to experiments at the same Reynolds number (Johnson and Johnston, 1989).

providing alignment information for the subsequent X-probe survey, a pressure probe survey, when properly implemented, generally gives more accurate mean velocity profiles than obtainable by hot-wire anemometry. Schwarz and Bradshaw (1992) agreed with Anderson and Eaton (1989), and others, that uncertainties (20:1 odds) of 5 percent of measured value for normal stresses,. $\overline{u'u'}$, $\overline{v'v'}$ and $\overline{w'w'}$ are attainable. In the case of the shear stresses, uncertainties of 10 percent for $\overline{u'v'}$ and $\overline{w'u'}$ and 15 percent for $\overline{v'w'}$ are achievable. Reynolds stress profiles with scatter greater than these values should be viewed with caution. It is yet to be determined what uncertainties are likely to apply for triple and higher correlations, but results from TKE balances suggest that they are not much different than for the double correlations.

HW Method III involves the use of a probe with three or more wires set at different angles and operated simultaneously. The method is mechanically less complex than Method II, because the probe is not rotated about an axis to different positions. The idea is to obtain the complete, instantaneous velocity vector at a point, the components of which are subsequently resolved, and, with time averaging, the mean velocity and all turbulence statistics result. Despite its apparent attractiveness, Method III has not been very successful in practice for a variety of reasons. The most important is the larger size of most multi-wire probes, leading to susceptibility to large errors in regions with steep instantaneous velocity gradients. Pompeo (1992) has drawn some interesting conclusions concerning the use of Method III and why he finally had to resort to Method II. In essence, he could not reduce errors sufficiently, for small, but physically realizable probes.

Recently, Löfdahl et al. (1995) compared performance of HW Methods I, II, and III together with a new heated element probe which is based on Silicon sensor technology. They employed the S-bend facility described by Truong and Brunet (1992), Case (8) above, and measured two-dimensional profiles upstream and three-dimensional profiles at several downstream stations. In the two-dimensional case, all methods were in fairly good agreement with each other as well as with published flat plate data for similar flow conditions. This was not the case in the three-dimensional regions of the flow. Methods I and II were in good agreement at stations where the yaw angle was small, but method I, the rotatable, slant, single-wire, deviated some from the other results downstream where local yaw is larger. At all stations, the reference direction of the crossed-wire probe (II) and the triple-wire (III) were aligned with the predetermined local mean yaw angles across the profile, but the single-wire (I) was fixed in the yaw direction of the local free-stream. The results indicated that Method I loses resolution of local yaw angle as the angle changes across the profile. In general, the authors conclude that a large separation between the measuring volume and the probe body is desirable to minimize probe blockage effects, and that local alignment with the predetermined mean flow direction is required for accurate measurements.

In all 3DTBL cases seen to date no attempt has been made to use sub-miniature probes as has been the case for a few 2D boundary layer flows. If the near-wall region is to be successfully measured by hot-wire methods, such probes will have to be developed. Up to this date, full Reynolds stress profiles have not been achieved for $y^+ < 50$ by any of the hot-wire methods.

Laser-Doppler anemometry (LDA) in air, or Laser-Doppler velocimetry (LDV) in gas or liquid has been employed by several investigators: Cases 2, 3, 4, 6, 7, and 10, Table 1. There are a number of reasons for selection of LDV, two being: (i) flow-probe interference effects are nonexistent, and (ii) measurements very near the wall may be obtained. In lower Reynolds number water flows, like Flack and Johnston's cases, the boundary layers and wall layers are thick so no exotic technology is required to obtain data of low uncertainty deep in the

viscous and buffer layer regions. Here, a standard three-beam, two-color Argon ion system for u and v components was combined at the measurement volume with a red (He-Ne laser) waterproof probe on a fiber optic cable for measurement of the w component. The method developed for 3D came directly from well established results in 2D boundary layers, Johnson and Johnston (1989), who showed that it was sound by comparing measured Reynolds stress profiles to profiles computed using DNS, Spalart (1988). Both experiment and computation were at a Reynolds number, Re_θ, of approximately 1400.

The methods for employing LDA in air flows at higher Reynolds numbers are quite different between (i) Driver and Johnston (1990), and (ii) Ölcmen and Simpson (1992) and Chesnakas and Simpson (1994a, b). Method (i) is a conventional multi-beam, Bragg-shifted, three-color (blue, green, violet) system with 60 degrees between axes of the beam pairs. Three components of velocity could be obtained down to within 0.5 mm of the surface. The seeded flow was electronically gated to assure that the velocity vector of a single particle was obtained at any instant. This requirement for simultaneity reduces verified data acquisition rates to rather low values and thus increases time to obtain stable averages. This was not a problem in Flack & Johnston's water flow studies where seeding was copious, but in air flows seeding difficulties can lead to problems. We will not attempt to describe method (ii) which is unique to Professor Simpson's wind tunnels.[3] In its most recent version, method (ii) involves some special short focal length technology to create a very small measuring volume (0.055 mm on a side). This permits measurement of three orthogonal components ($u + v$, $u - v$, w) to within 0.2 mm of the surface.

The optics in Flack and Johnston's cases assured that the measurement volume's diameter was about 1 viscous wall unit in the vertical ($x - y$) plane and 7 wall units in the spanwise, z-direction. A viscous wall unit (length) equals ν/Q_τ. Coincidence timing was also used here to help assure that all three velocity components were coming from a single seed particle. For Driver and Johnston, the respective measurement volume was about 24 by 80 wall units, and this obviously limited the useful distance from the wall to about y^+ of 20 to 30. Chesnakas and Simpson obtained results down to $y^+ = 7$. The absolute uncertainty of data obtained by LDV methods is subject to errors not seen in other methods; All the methods used in air flow studies had to correct their data for bias errors, but Flack and Johnston did not. It would appear, upon examination of scatter in data profiles, that the uncertainties for Ölcmen and Simpson (1992) are a bit higher than those by the more conventional LDV methods. Also uncertainties in the other LDV results appear to be as low as measurement uncertainties in good hot-wire results. However, these informal observations should not be generalized.

Finally, in regard to the accuracy of turbulence statistics in the wall layers, note that the turbulent shear stresses drop to less than $\frac{1}{2}$ of the total shear stresses at $y^+ \approx 10$ to 12, and at $y^+ < 5$ all the Reynolds stresses become very small indeed. Consequently, accurate measurement of these small quantities in the viscous sublayers of any turbulent boundary layer is very difficult, no matter what method is being employed. Since the region of greatest rate of production and dissipation of turbulent energy and stress is just above the viscous sublayer, improved methods for turbulence measurement in the wall-layers, below $y^+ \approx 30$, would be welcome.

Wall shear stress magnitude and direction should be obtained by direct methods. They should not be deduced or inferred indirectly especially if the near-wall region of the flow is to be understood, a fact appreciated by Ölcmen and Simpson (1992). Three different methods (a, b, and c) of direct skin-friction

---

[3] Department of Aerospace and Ocean Engineering, V.P.I. & S.U., Blacksburg, VA 24016.

Table 1 Experimental flows reviewed

(Case) Authors (dates) Typical Re numbers	Flow description	Results and Techniques	Useful y^+ range	Direct wall stress data?	Useful as CFD case
(1) Schwarz and Bradshaw (1992, '93, '94a) $Re_\theta \approx 6000$	30° const. area bend over flat wall, pressure gradients ≈ 0 along freestream	Full Re stress tensor triple correlations HW method II	>100	No, fit to log-law near y^+ = 100	Yes (done by author)
(2) Flack and Johnston (1993a, '94, '95) $Re_\theta \approx 1300$	30° const. area bend over flat wall, pressure gradients ≈ 0 along freestream	Full Re stress tensor triple correlations Laser Doppler Veloc. (structure visualization)	>2 for mean vel. >10 for turbulence	Yes, mean profile slope below y^+ = 4	No (no $p(x, y)$ data)
(3) Flack and Johnston (1993a, '93b) $Re_\theta \approx 1500$	45° infinite swept foward-facing step	Full Re stress tensor triple correlations Laser Doppler Veloc. (structure visualization)	>2 for mean vel. >10 for turbulence	Yes, mean profile slope below y^+ = 4	No (no $p(x, y)$ data)
(4) Ölcmen and Simpson ('92, '95) $Re_\theta \approx 6000$	Thick, symmetric airfoil standing on a flat wall	Full Re stress tensor Laser Doppler Veloc.	>10	Yes, oil film	Maybe
(5) Kreplin and Stäger (1993) $Re_L = 4.8 \times 10^6$	6:1 prolate spheroid at 10° angle of attack	Full Re stress tensor HW method III	>100	No	No
(6) Chesnakas and Simpson (1994a, b) $Re_L = 6 \times 10^6$	6:1 prolate spheroid at 10° angle of attack	Full Re stress tensor triple correlations Laser Doppler Veloc.	>7	No, fit to $y^+(U^+)$ for 7 $< y^+ < 100$	Yes
(7) Gleyzes et al. (1993) $Re_L = 3.3 \times 10^6$	Swept back, tapered wings, pressure & suction surfaces	Full Re stress tensor triple correlations HW methods II and III and Laser Doppler Veloc.	>100	No	Yes
(8) Troung and Brunet (1992) $Re_\theta \approx 6100$	"S"-shaped channel with layer on flat end-wall	Full Re stress tensor HW methods II and III	>100	No, Preston tube	Yes (Test case I)
(9) Pompeo (1992) Pompeo et al. (1993) $Re_\theta \approx 4700$	Symmetrical converging/ diverging flows over flat wall	Full Re stress tensor HW method II	>100	Yes, direct force	Yes (done by author)
(10) Driver and Johnston (1990) $Re_\theta \approx 6000$	Axial flow over a stationary cylinder downstream of a rotating cylinder with & without adverse axial pressure grad.	Full Re stress tensor triple correlations Laser Doppler Veloc.	>20	Yes, oil film	Yes (done by author)
(11) Littell and Eaton (1991) $\Omega R^2/v \approx 1.6 \times 10^6$	Rotating, single disk flow in stationary air	Full Re stress tensor triple correlations HW method II (structure data)	>100	No, fit to log-law near y^+ = 100	Yes

Re numbers: Re_θ based on freestream speed and bl momentum thickness; Re_L based on fs speed and body length; Case (11): R = radius, Ω = rotor speed

stress measurement were employed by some of the authors reviewed here, see Table 1. All the others used indirect methods such as a surface fence, a Preston tube, a fit of the velocity profile to a law-of-the-wall (a log-law, or a relation for the buffer layer region), or a surface heat-flux meter, all of which depend on calibration in known 2D flows. Direct method (a), a mechanical, surface-force balance, was used by Pompeo et al. (1992, 1993) to measure the surface-force vector directly. Method (b) the oil-flow method, where the rate of change of thickness of a very thin film of oil is measured by laser interferometry, was used by Ölcmen and Simpson (1992). Driver and Johnston (1990) used this method for the stress magnitude, but determined the direction of the surface flow by measurement of angles of oil drop traces after the drops ran and dried on absorbing paper. The wall stress angles from both of these experiments seemed to be relatively inaccurate with an uncertainty as large as ± 2 degrees in some regions of the flow. Method (c), the measurement of velocity profile slope at $y \approx 0$ (actually in a thin region out to $y^+ \leq 4$) provided reasonably accurate data on the magnitude of the wall shear in Flack's studies (uncertainty of ± 5 percent), but estimates of the wall flow angle had relatively high errors, again on the order of ± 2 degrees. Ultimately, a new or improved method which obtains

more precise (± 0.5 degrees) wall flow angles would be welcome in 3DTBL experimental research.

Modeling For Computation

Equations and Notation. For reference, it is useful to introduce the Reynolds-averaged equations of motion appropriate for a steady (in the mean), thin turbulent boundary layer on a smooth flat surface.[4] In addition to these assumptions, the effects of heat transfer and compressibility are neglected, and rectangular coordinates (x, y, z) will be used. For convenience in interpretation of data, the x-coordinate and the U-component of velocity are usually assumed to be directed along the local freestream velocity, U_e, the main-flow at the outer edge of the layer. The axis y and velocity V are normal to the wall, so that z and W point in the cross-flow direction. The mean velocity profiles are often depicted as shown in Fig. 1 which also shows the wall shear stress.

With these conventions and assumptions, the continuity equation of the mean flow is:

---

[4] Almost all experimental data corresponds to these conditions and the condition of constant density flow, so it is of little value to expand our equations further.
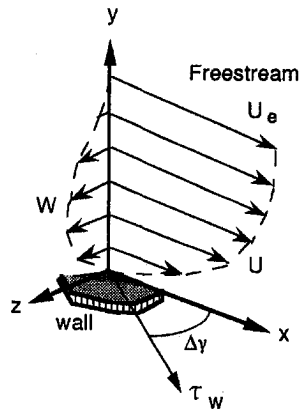
Fig. 1 Main flow, U, and crossflow, W, mean velocity profiles in coordinates aligned with the local freestream so total skew angle between wall shear stress and freestream is $\Delta\gamma$

$$\frac{\partial U}{\partial x} + \frac{\partial V}{\partial y} + \frac{\partial W}{\partial z} = 0 \qquad (1)$$

The mean momentum equation in the mainflow direction is:

$$U\frac{\partial U}{\partial x} + V\frac{\partial U}{\partial y} + W\frac{\partial U}{\partial z}$$
$$= -\frac{1}{\rho}\frac{\partial P}{\partial x} + \frac{\partial(-\overline{u'v'} + \nu\partial U/\partial y)}{\partial y} \qquad (2a)$$

and the mean momentum equation for the cross-flow direction is:

$$U\frac{\partial W}{\partial x} + V\frac{\partial W}{\partial y} + W\frac{\partial W}{\partial z}$$
$$= -\frac{1}{\rho}\frac{\partial P}{\partial z} + \frac{\partial(-\overline{v'w'} + \nu\partial W/\partial y)}{\partial y} \qquad (2b)$$

U, V, W are the mean velocity components, and P is the mean static pressure which, according to the thin shear-layer approximation, is independent of y. Stated explicitly, this approximation requires that $|V| \ll Q$ where $Q = \sqrt{U^2 + W^2}$ is the magnitude of the velocity vector in the plane parallel to the wall.

At this level of approximation, models must be provided for only two components of the Reynolds stress tensor, $-\overline{u'v'}$ and $-\overline{w'v'}$, the turbulent shear stress components parallel to the wall which appear in Eqs. (2a,b). In the plane of the wall the total shear stress t is a vector with components $t_x = -\overline{u'v'} + \nu\partial U/\partial y$ and $t_z = -\overline{w'v'} + \nu\partial W/\partial y$. The viscous parts of the stresses are negligible outside of the viscous sublayer, $y^+ > 30$. In addition to two Reynolds shear stresses, the four other components of this stress tensor ($-\overline{u'u'}$, $-\overline{v'v'}$, $-\overline{w'w'}$, and $-\overline{u'w'}$), the third order correlations ($-\overline{u'u'u'}$, etc.) and some forth order terms (e.g. $-\overline{u'u'u'u'}$, etc.) should be measured and presented in experimental results. They are frequently used in equations for modeling the Reynolds stresses. In the simplest models, only $-\overline{u'v'}$ and $-\overline{w'v'}$ are considered. This level of modeling is representative of current practice even though more advanced modeling may utilize model equations for all six Reynolds stresses.

Modeling Issues

Isotropy of Eddy Viscosity. At the present time, the only models generally used by industry for computation of practical flows (e.g. over swept back wings) assume that the turbulent eddy viscosity is a simple scalar despite experimental evidence to the contrary. In general, the eddy viscosity should be represented by a fourth order tensor, but as noted, in the thin shear

layer limit, there are only two significant turbulent shear stresses, consequently a two-component vector eddy viscosity suffices, namely:

$$\nu_{tx} = -\overline{u'v'}/(\partial U/\partial y) \qquad (3a)$$

and

$$\nu_{tz} = -\overline{w'v'}/(\partial W/\partial y) \qquad (3b)$$

The eddy-viscosity ratio, $N_e = \nu_{tz}/\nu_{tx}$, is often used to show the deviation of the stresses from isotropy, the condition where $N_e = 1$. Unfortunately, N_e, is not invariant with respect to rotation of the coordinate axes about the y-axis, and thus it cannot be generally useful in modeling (see comment below re Rotta-T model). Nevertheless, many experiments are available where this ratio has been presented in local freestream coordinates so that the results from various sources may be compared to each other. The experiments show that N_e values are widely scattered, but most of the cases indicate that $N_e < 1$ for flows which develop cross-flows, starting from a two-dimensional, turbulent condition. N_e values as low as 0.2 have been observed although it is much more common to see N_e in the range from 0.6 to 0.8 after a sustained region of cross-flow development. There are a few exceptional cases which have $N_e > 1$, for reasons that are not currently understood.

Another method for examination of anisotropy of the eddy viscosity is to compare the directions of the shear-stress vector,

$$\gamma_\tau = a\tan\left(\frac{-\overline{w'v'}}{-\overline{u'v'}}\right) \qquad (4a)$$

and the velocity-gradient vector,

$$\gamma_g = a\tan\left(\frac{\dfrac{\partial W}{\partial y}}{\dfrac{\partial U}{\partial y}}\right) \qquad (4b)$$

If these angles are *different*, then the eddy viscosity is anisotropic. Compared to the eddy viscosity ratio, N_e, the angle difference ($\gamma_g - \gamma_\tau$) is invariant with respect to coordinate system orientation, and thus it might be useful in modeling. In addition, we prefer this approach because when profiles of γ_g and γ_τ are compared together with the cross-flow deviation angle,

$$\gamma = a\tan\left(\frac{W}{U}\right), \qquad (4c)$$

one may easily visualize the relative magnitudes of "lead" or "lag" of the angles in many simple flows, and lead and lag may be interpreted in physical terms as noted below.

As an example, Fig. 2 is shown to illustrate the point. Here, the angles (measured relative to local free-stream direction) are plotted versus y^+ for two stations of the bend flow by Flack and Johnston (1993a). The 30° station is at the end of the bend following a prolonged region of cross-flow development, and the R2 station is located further downstream in the straight duct where the flow is starting to recover back to a two-dimensional state even though the turning angle, γ, across the boundary layer is still large. In this case, γ_τ lags behind γ_g in the outer regions but it leads γ_g near the wall, in the inner buffer layer. At the end of the bend, these lags and leads are substantial, and an isotropic state, ($\gamma_g - \gamma_\tau$) ≈ 0, occurs in a very limited zone, $20 < y^+ < 40$. Both the lag and the lead are reduced in the downstream recovery, R2, profiles and the isotropic region is larger, $20 < y^+ < 100$. Because the magnitudes of the turbulent shear stresses are small compared to the viscous stresses for $y+ < 10$, the assumption of isotropy out through the middle of the buffer layer (neglects inner region "lead") may be satisfactory for practical turbulence models. Furthermore, if $|(\gamma_g -$

$\gamma_\tau)| < 10$ deg. than the errors in assuming eddy viscosity isotropy should be less than 2 to 3 percent. Only in cases where the outer region lag exceeds 10 to 15 degrees are larger errors anticipated. Many 3DTBL's in practice probably meet these criteria, and thus the isotropic assumption may be sufficient for many practical cases.

Physically, the *lag* effect in the outer layer is believed to result from the residual effects of the 2D boundary layer upstream of the bend. Slowly decaying large eddies convected downstream carry the history of their upstream orientation and thus contaminate the effects of the more recently developed eddies from the turning region in the bend. The near-wall *lead* effect is more difficult to understand, but it is a indicator that the eddy structure in the inner layers may be substantially different from 2D boundary layer flows. Evidence for such structural changes is discussed further below.

Structure Parameter, a_1. A second important issue is how to represent and model the observation that the magnitudes of the turbulent shear stress,

$$\tau_t = \sqrt{\overline{u'v'}^2 + \overline{v'w'}^2} \qquad (5)$$

and the turbulence kinetic energy,

$$k = \tfrac{1}{2}\left(\overline{u'u'} + \overline{v'v'} + \overline{w'w'}\right) \qquad (6)$$

are different in 3DTBLs than in two-dimensional flows. The ratio, $a_1 = \tau_t/2k$, called the structure parameter or 'Townsend's structure parameter', is generally used to discuss this effect. The quantity a_1 may be thought of as an "efficiency" relating the ability of random turbulence energy to sustain the cross-correlated fluctuations responsible for turbulent shear stress and its behavior provides quantitative evidence that cross-flows disrupt the turbulent processes which generate higher levels of turbulent stress. Some ideas concerning the underlying physics of the disruption process are reviewed below in the section on quasi-coherent structure. General knowledge on the effect has been accumulating for 20 years, but it has yet to be effectively employed in a practical model. Some of our thoughts on the subject are presented below in the hope that they may inspire a new or improved model.
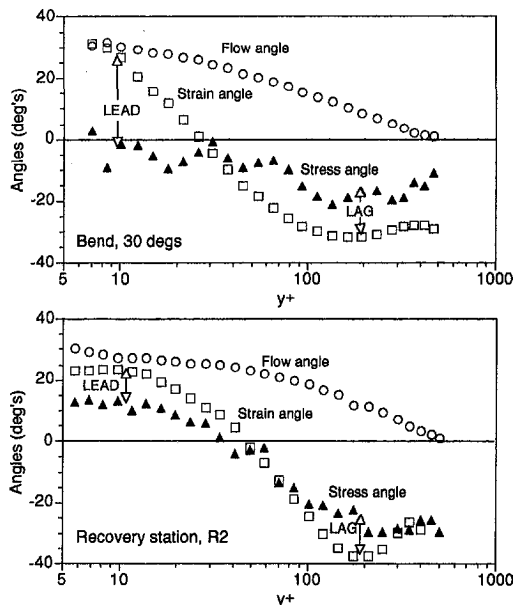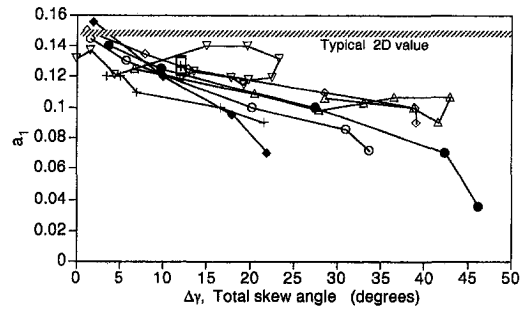

Fig. 3 Typical values of structure parameter, a_1, for the turbulent inner layers ($y/\delta \approx 0.1$) versus local value of total skew angle. Flows identified in Table 2.

In the limit, a_1 must go to zero at the wall.[5] In most two-dimensional turbulent boundary layers it increases from zero, through the buffer layer out to $y^+ \approx 30$ to 50 ($y/\delta \approx 0.1$ to 0.2) where it obtains a value of $a_1 \approx 0.15 \pm 0.01$. In the central regions, below $y/\delta \approx 0.7$ to 0.8, it stays nearly constant at 0.15. Finally, in the intermittent outer regions ($y/\delta > 0.8$) a_1 drops to low values, but experimental evaluation becomes very uncertain here. Almost all our data on a_1 were obtained for 2D boundary layers under constant freestream velocity. However, some reduction in a_1, below the nominal value of 0.15, have been observed in cases with strong adverse pressure gradients. Furthermore, substantial reductions are seen in a number of 3DTBL experiments, down to values as low as 0.03 to 0.05 at $y/\delta \approx 0.1$ in the case of the Anderson and Eaton (1989) flows.

This is illustrated in Fig. 3 where the a_1 values for the turbulent near-wall region ($y/\delta \approx 0.1$) of nine selected cases (Table 2) are plotted against cross-flow *skewing* angle, the total turning angle of the local mean velocity profile, $\Delta\gamma = \gamma_{\text{wall}} - \gamma_e$. Driver and Johnston (1990) already demonstrated that $\Delta\gamma$, or alternatively, the ratio of peak cross-flow velocity to freestream velocity, $W_{\max}/U_e$, were useful parameters for sorting 3D results in terms of strength of cross-flow. Clearly, an increase of skewing generally drives a_1 down, but other effects must be responsible for the differences between the various cases because the spread in a_1 values shown in Fig. 3 is larger than the measurement uncertainty. These effects are thought to include; (i) the cross-flow pressure gradient, $\partial p/\partial z$, a driving force that causes skewing, (ii) the streamwise pressure gradient, $\partial p/\partial x$, (iii) the boundary layer Reynolds number, $\text{Re}_\theta = \theta U_e/\nu$, based on momentum thickness, (iv) the upstream initial conditions (2D, 3D, laminar, turbulent), and (v) the "history" of the flow as conditions are affected by the parameters taken in combination, and the distribution of parameters as the flow develops downstream.

Two cases in Fig. 3 illustrate the point. The bend end-wall boundary layers of Schwarz and Bradshaw, indicated by the symbol (∇), and Flack & Johnston ($\triangle$) have similar initial conditions (2D and turbulent), and similar pressure gradient histories but quite different Reynolds numbers. Maximum skewing, before recovery begins near the end of the bend, is larger for the lower Reynolds number flow. At low Reynolds number, a_1 in the wall-layer region ($y/\delta \approx 0.1$) appears to be rather closely controlled by local skewing and less dependent on the history of flow development. As evidence, note that the hysteresis loop in the ($\triangle$) curve is small as skew angle drops back to lower values in the region where the flow relaxes ($-\partial p/\partial z$ is reduced) in the downstream end of the bend and straight

Fig. 2 Typical angle profiles in wall-layer coordinates from Flack and Johnston (1993a): $\bigcirc - \gamma$ the flow angle, $\square - \gamma_g$ the velocity gradient angle, and $\blacktriangle - \gamma_\tau$ the shear stress angle. Angles are with respect to the local freestream direction.

---

[5] Starting at the wall and expanding by Taylor's series gives: $u' = 0 + \alpha_1 y + \beta_1 y^2 + \cdots$; $v' = 0 + \alpha_2 y + \beta_2 y^2 + \cdots$; and $w' = 0 + \alpha_3 y + \beta_3 y^2 + \cdots$. The coefficient $\alpha_2 = 0$ in the expansion of v' due the constraint of continuity, see equ. (1) which also applies to the fluctuations. Considered at an instant in time $a_1 = 2 \, \overline{u'v'}/(\overline{u'u'} + \overline{v'v'} + \overline{w'w'}) \propto \overline{v'/u'} \propto y^2/y \propto y$. Thus $a_1 = 0$ at $y = 0$, the wall.

Table 2   Key to symbols in Figs. 3, 4, 5, and 6

	Reference	$\partial p/\partial z$	$\partial p/\partial x$	Remarks
●	Anderson and Eaton ('89) Case 1, at St.-5 in Figs. 4–6	>0	>0	Flat, end-wall flow driven by vertical 90 deg. wedge. Rapid development under strong pressure grads.
○	Anderson and Eaton ('89) Case 2, at St.-5 in Figs. 4–6	>0	>0	Flat, end-wall flow driven by vertical 60 deg. wedge. Rapid development under strong pressure grads.
◆	Bradshaw and Pontikos ('85) at St.-9 in Figs. 4–6	>0	>0	Flat wall flow simulating swept back, "infinite" wing. Very similar to Elsenaar & Boelsma ('74).
◇	Elsenaar and Boelsma ('74) at St.-9 in Figs. 4–6	>0	>0	Flat wall flow simulating swept back, "infinite" wing. 3D ordinary separation at station, St.-9.
▽	Schwarz and Bradshaw ('93, '93) at 30 deg station, bend exit	>0	≈0	Along centerline of end-wall of 30 deg. bend. Momentum thickness Reynolds number at inlet, $Re_\theta \approx 6000$
△	Flack and Johnston ('93a, '94) at 30 deg station, bend exit	>0	≈0	Along centerline of end-wall of 30 deg. bend. Conditions and geometry same as above, but lower Reynolds number, $Re_\theta \approx 1400$
+	Driver and Johnston ('90) Case A.S1, at x = 6″ in Figs. 4–6	=0	=0	Axially symmetric 3DTBL on cylinder relaxing back to 2D
×	Driver and Johnston ('90) Case D.S1, at x = 6″ in Figs. 4–6	=0	>0	Same as above, but with imposed axial, adverse pressure gradient
□	Littel and Eaton ('91) at radius = .421m, Re = 1.3×10^6	>0*	≈0	Boundary layer on rotating, flat disk. radius = 1 m. Re based on disk tip speed and tip radius.

Note: *Freestream pressure gradients:* $\partial p/\partial z$ in crossflow direction, $\partial p/\partial x$ along local freestream
* In disk flow $\partial p/\partial z$ is a "virtual" gradient, $\rho U_e^2/r$, caused by centrifual acceleration.

recovery region. The larger loop in the high Reynolds number case, Schwarz and Bradshaw (∇), shows only small a_1 changes as $-\partial p/\partial z$ and skewing increase along the bend's inlet region, but as the flow relaxes again downstream (bottom of the loop) the a_1 values fall and come into agreement with the data from the low Reynolds number case. The lag in the response of a_1 to changes in the force driving skewing, $-\partial p/\partial z$, is an indicator that flow development history is important in consideration of turbulence structure, and consequently any valid model must account for this fact.

The effects of flow development history are also shown in Fig. 4 where profiles of a_1 versus y/δ are plotted. For each case, the profiles are selected from downstream stations, near the location of maximum total skewing, $\Delta\gamma$, for the particular flow. Near the wall where $y/\delta \approx 0.1$ to 0.2, the effect of turning on a_1 is smallest for two cases, ($\square$) the rotating disk flow, and (∇) the higher Reynolds number bend flow. The lower Reynolds number bend flow ($\triangle$) has a lower value of a_1 in this region due to the larger skewing for this profile, as already noted above. The largest near wall reductions in a_1 are seen in the two cases (● and ◆) with strong streamwise pressure ($\partial p/\partial x$) gradients and large skewing. For the central regions, from $y/\delta \approx 0.2$ to $y/\delta \approx 0.7$, a_1 *increases* as y/δ *increases* in five of the seven profiles. For these five cases the upstream initial condition was a well developed, turbulent, 2-D flow which had almost constant values of $a_1 \approx 0.15$ from $y/\delta \approx 0.1$ to $y/\delta \approx 0.7$. The rotating disk flow by contrast is structurally fully three-dimensional from its origin, and shows the opposite trend, a_1

decreases as y/δ *increases*. These results suggest that the structural changes leading to low a_1 start in the wall-layers where the flow turning are largest and propagate away from the wall by turbulent diffusion processes. The effects of streamwise pressure gradient, $\partial p/\partial x$, and Reynolds number are also important, and may be qualitatively explained by sorting and comparing certain cases discussed below.

Four profiles of comparable Reynolds number are shown in Fig. 5. (i) Two cases of decaying skewed flow ($\partial p/\partial z = 0$) by Driver and Johnston (1990) are shown where one case (+) has constant freestream pressure and the other (×) has an adverse streamwise pressure gradient, $\partial p/\partial x$, imposed. Near the wall the effects of skew dominate and the profiles tend to overlap, but father out, above $y/\delta \approx 0.25$, where skewing is small, the curves spread apart. The profile (×) with the adverse pressure gradient shows lower a_1 values. (ii) The other two cases (●, $\partial p/\partial x > 0$) and ($\nabla$, $\partial p/\partial z = 0$), were flows with increasing skew as the flow developed downstream, have $\partial p/\partial z < 0$. Streamwise adverse pressure gradient definitely tends to reduce a_1 near the wall, in one case (●) well below the reduction caused by skewing alone. Consequently, the history of the flow in regards to distribution of streamwise pressure gradients is also of consequence.

Finally three profiles are isolated in Fig. 6 to illustrate the effects of Reynolds number on flow development history in the absence of streamwise pressure gradient effects. Downstream profiles of a_1 from the high Reynolds number (∇) and low Reynolds number ($\triangle$) bend flows show that the initial, 2D turbulence structure decays more rapidly at low Reynolds num-
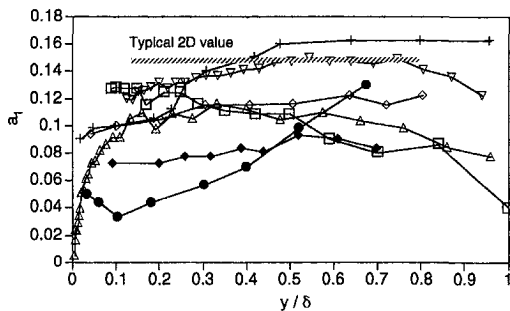

Fig. 4   Typical profiles of structure parameter, a_1, versus dimensionless distance from the wall, y/δ. Flows and profile locations identified in Table 2.
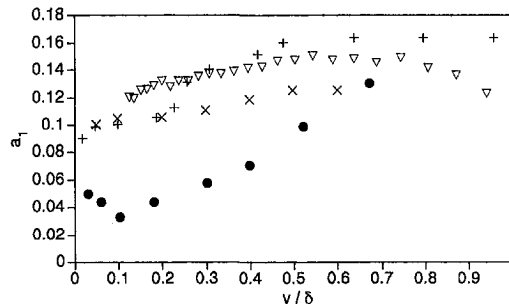

Fig. 5   Profiles of a_1 versus y/δ to illustrate effects of streamwise pressure gradients. Flows and profile locations identified in Table 2.
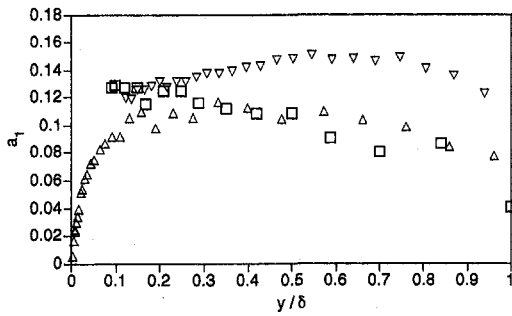
Fig. 6 Profiles of a_1 versus y/δ to illustrate effects of Reynolds number and degree of development. Flows and profile locations identified in Table 2.

ber because a_1 in the outer layers is lower everywhere, not just near the wall. This lowering may also be attributed to the more rapid outward diffusion of the skewing effect from the wall. The third curve ($\square$) is from the disk flow of Littell and Eaton where the Reynolds number is higher than the low Reynolds number bend case ($\triangle$). Except near the wall, for $y/\delta < 0.2$, the profiles nearly overlap. It is hypothesized (see below) that the disk flow profile represents conditions for a 3D 'self-preserving' state, analogous to fully-developed pipe flow, where turbulence structure is only weakly dependent on Reynolds number. Interestingly, like fully-developed pipe flow, the mean velocity profile of the Littell and Eaton disk flow show no evidence of a wake function. The log-law region extends out almost to the free-stream. The rapidly developing low Reynolds number bend flow may be approaching a 'self-preserving' condition which is independent of initial conditions, and as a consequence the a_1 profile comes close to the disk flow profile, except near the wall where differences due to Reynolds number effects should be noticed in y/δ coordinates. All the other, higher Reynolds cases, like (∇) in Fig. 6, preserve some of the upstream, 2-D turbulence structure and thus a_1 is higher in the outer parts of the boundary layer.

The disk flow is fundamentally different that the other cases shown here because it is three-dimensional from its birth as a laminar layer near the center of the disk. Transition to turbulence was three-dimensional, a process which is basically different in that the primary instability mode consists of streamwise vortical structures with a single sign of rotation. The turbulent development downstream of transition is also three-dimensional as it takes place in the presence of skewed mean velocity everywhere. It is for this reason that the high Reynolds number case of Littell and Eaton may be thought of as attaining a 'self-preserving' three-dimensional state. Turbulence models should recognize this idea, and be able to approach such a state where a_1, the efficiency of conversion of random turbulence energy to turbulent shear stress magnitude decreases across the outer boundary layer in the presence of skewing in the mean flow.

The discussion above concentrates on the fully turbulent parts of the boundary layer, but what of the details concerning the very near-wall regions, for $y/\delta < 0.1$? It is seen from the preceding that 3D effects are strongest near the wall and in many cases they diffuse outward from the wall as the flow develops downstream starting from a non-self-preserving initial state. Flack and Johnston (1993a) recently obtained useful turbulence data below $y^+ \approx 10$. The new data set by Chesnakas and Simpson (1994) and Öchmen and Simpson (1995) should also be useful.

Data from case (2), Flack and Johnston, are illustrated in Fig. 7 to show some effects of skewing on profiles of a_1 plotted versus y^+ all the way down to the viscous sublayer. Once the flow enters the bend a_1 is reduced by 5 to 20 percent relative to equivalent 2-D flows from $y^+ \approx 100$ all the way down into the viscous sublayers. The final profile at the end of the bend

($\bullet$) shows the largest reduction, particularly in the region above $y^+ \approx 50$. Also, an increase is noted for the profiles ($\times$) in the straight recovery duct where the skewing effects start of relax downstream. More results from the viscous and buffer layers are needed for substantiation and extension of these early results before firm conclusions can be drawn. However, it is interesting to speculate that application of skewing somehow disrupts the rather orderly, quasi-periodic development of structures that leads to shear-stress producing eddies, and as a consequence the "efficiency" of shear stress production is reduced as is reflected in decreased values of a_1.

Evaluation of Models. There have been a few concerted attempts to evaluate the effectiveness of models proposed for 3D boundary layers. Isotropic mixing length models and two one-equation turbulence models, one of which allows for lag in the stress angle, Bradshaw (1969), were tested against a set of four different flows in Wheeler and Johnston (1973). Some of the conclusions obtained then are not much different than those reached recently by others.

Ölcmen and Simpson (1993) analyzed eight different experimental flows (six pressure-driven and two shear-driven) in regard to the applicability of various models for the eddy viscosity, including an algebraic ("zero-equation") model (Cebeci-Smith), the Rotta-T model, a one-equation (k) model (Patel), and a 3-D implementation of the Johnson-King model. Three of these models (C-S, Patel and J-K) are isotropic, i.e., require $\gamma_\tau = \gamma_g$, and therefore can't represent stress lag or lead effects. However, the authors suggest that the J-K model can be used to compute the shear stress magnitude in pressure gradient driven flows. Only the Rotta-T method (specifies a constant value of N_e across the layer) can account for the lag or lead effects, but a wide range of values from $N_e = 0.5$ to 1.5 is needed to satisfactorily agree with the eight cases examined. The authors fail to note that Rotta-T is *not* invariant in regard to choice of coordinate direction as a proper model must be, and this is the reason (i) why one cannot expect a universal value of N_e, and (ii) why the model should not be used except in special circumstances.

Higher order models are starting to be examined for their general applicability to 3DTBLs. Recently a few workers have measured complete profiles of turbulence statistics up through triple products and flatness factors, data which is necessary to directly test full Reynolds stress equation models, term-by-term. Some interesting results are being produced, see Schwarz and Bradshaw (1992, 1994b) but it is still early to summarize results of these pioneering efforts.

Some workers are implementing existing models, and computing their results as single test cases. For example, Driver and Johnston (1990) utilized three different models: a mixing
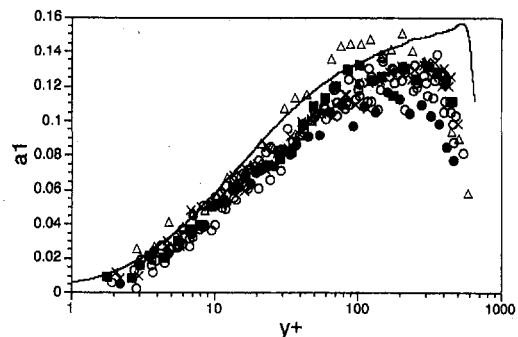
Fig. 7 Profiles of a_1 versus y^+ to illustrate wall-layer behavior. *Solid curve:* Direct numerical simulation of Spalart (1988), 2D turbulent boundary layer, $Re_\theta = 1410$. *Symbols:* Data from Case (2), Flack and Johnston (1993), $Re_\theta \approx 1400$; *Profiles:* $\triangle$–upstream 2D region, $\blacksquare$–beginning of bend, $\bigcirc$–four profiles inside bend, $\bullet$–end of 30 degree bend, $\times$–two profiles in downstream recovery region.

length model, a two-equation k-ω^2 model after Wilcox and Rubesin (similar to a k-e model), and a full Reynolds stress model after Launder, Reece and Rodi. The first two models have isotropic eddy viscosity. When tested against their own experimental results the mixing length model was clearly inferior, and the LRR model the best in representing the mean and turbulence data, but none of the models was able to predict the lowering of $-u'v'$ due to 3D effects, a failure attributed to the models' missing physics. Incidentally, both the higher order models tend to underpredict turbulence kinetic energy, k, probably due to errors in the equation for rate of dissipation of turbulence kinetic energy. This also was a conclusion from Schwarz and Bradshaw (1994b) who utilized their own experimental data as the basis for term-by-term comparisons with the most popular models for (i) the triple-product transport (diffusion) and (ii) the redistribution by pressure-strain of Reynolds stress.

Very recently Wu and Squires (1995) computed the flow studied by Spalart (1989) using DNS. They used a large eddy simulation (LES) computation together with several models for the small scale, unresolved turbulence. This low-Reynolds-number case is interesting because it is an equilibrium flow, a flow where the turbulence structure is independent of flow development history. It bears some similarity to high Reynolds number rotating disk flow, where transition is confined to the inner parts of the disk.

The problems of modeling are far from resolution, and few firm conclusions may be drawn at this time. If it is important to allow for stress angle lead and lag effects, one will have to resort to full Reynolds stress equation modeling. The leads and lags of the angle γ_t relative to γ_g should then be resolved naturally at the RSE level if good 3D physics are employed in the modeling, a situation which is yet to be demonstrated. Finally, it is important to observe that many engineering design situations may not require accuracy of modeling beyond simple isotropic eddy viscosity and mixing length theory.

The Quasi-Coherent Structure of Near-Wall Turbulence

Research on quasi-coherent structures is motivated by the changes in turbulence quantities, such as the structure parameter, a_1, for three-dimensional boundary layers compared to their two-dimensional counterparts. These changes, which have important implications for turbulence modeling, may reflect structural changes in the near-wall region due to the cross-flow which is usually strongest near the wall. The investigation of near-wall, quasi-coherent structures in two-dimensional turbulent boundary layers has been an area of active research since the early work of Corrsin (1959) and Kline et al. (1967). However, only a few researchers have studied three-dimensional near-wall quasi-coherent structure. These structure studies, which use a variety of techniques, are discussed in this section.

Three-dimensional structure studies have generally assumed that cross-flow perturbs the known two-dimensional turbulent boundary layer near-wall structure. The currently accepted picture of the two-dimensional turbulent boundary layer structure is described by Robinson (1991a, b). This study observed the simulated structures produced by the direct numerical simulation of Spalart (1988), a low Reynolds number, ($Re_\theta = 1410$) flat plate boundary layer. The near-wall picture emerging from this analysis shows that the primary quasi-coherent elements are (i) a series of low and high speed streaks in the viscous sublayer, the well known "wall-layer streaks," and (ii) the legs of quasi-streamwise vortices in the buffer and lower log-layer regions. These vortices tilt away from the wall and are often observed well out into the log-layer where their heads form asymmetric vortical arches. The near-wall streaks are formed by the quasi-streamwise vortices as they convect downstream leaving a trail of low speed fluid near the wall on the upward-rotating side and high speed fluid on the downward rotating

side of a vortex. Farther out in the buffer layer, the quasi-streamwise vortices are closely linked to the sweeps and ejections which occur along side of a single vortex. Ejections, and to a lesser extent the sweeps, are a principal source of newly produced Reynolds shear stress, $-u'v'$, in the mean-flow direction. Instantaneous cross-flow shear stresses are also produced, but symmetry causes the mean value, $-w'v'$, to be zero.

Three-dimensional mean flow may affect the strength and symmetry of quasi-coherent structures in the near-wall region and consequently influence the Reynolds stresses. Current investigations on near-wall structures have concentrated on the quasi-streamwise vortices which, because of the symmetry of two-dimensional flow, must on the average exist in equal numbers of positive and negative signed vortical structures of statistically equal strength. Several questions have been addressed. (i) Are equal numbers of each sign of vortex present in skewed boundary layers, and (ii) do the number of vortical structures decrease or increase with the presence of cross-flow? Another question relates to the strength of the vortex structures; (iii) are quasi-streamwise vortices of one sign (+ or −), on average, stronger than vortices of the opposite sign and thus able to produce stronger ejections or sweeps? Some three-dimensional structure studies also focus on the trajectory of the fluid being swept toward and ejected away from the wall; three-dimensionality may modify the path of the near-wall fluid in a way not possible for two-dimensional turbulent boundary layers.

Unfortunately the results of current studies are not easily compared. Not only are the results dependent on the method used for the structure detection, but also on the region of the boundary layer investigated (i.e., viscous sublayer, buffer region or log-layer region) with respect to the location of the maximum cross-flow mean velocity. Another limitation to the structure results is that a number of the experiments and simulations are for low Reynolds number flows. The extent to which near-wall three-dimensional structural modifications are present or important in higher Reynolds number flow is unknown. However differences in three-dimensional turbulence statistics have been observed for higher Reynolds number flows.

Several hypotheses have been proposed to explain the changes of near-wall structure with the imposition of three-dimensionality and the effects these changes may have on the production and dissipation of turbulence stresses. Eaton (1991) proposed that the mean vorticity, produced by the presence of the cross-flow gradient, $\partial W/\partial y$, near the wall overwhelms quasi-coherent vortices of the opposite sign, thus reducing the number of turbulence producing vorticies. This conclusion was based on the research of Anderson and Eaton (1989) who studied the three-dimensional boundary layer produced by flow approaching a wedge. Sublayer visualization indicated that the high and low speed streaks in the three-dimensional region were more stable than in the two-dimensional region, and this in turn suggested a reduced rate of streak bursting in three-dimensional flows. The idea that the sign of mean vorticity can modify the behavior of an individual vortex was further investigated by Shizawa and Eaton (1992) where, stationary longitudinal vortices of both signs, produced by vortex generators, were embedded in a three-dimensional boundary layer and cross-flow mean velocity profiles measured. It was found that the longitudinal vortices with the same sign as the mean streamwise vorticity, suppressed cross-flow separation, whereas longitudinal embedded vortices of the opposite sign promoted cross-flow separation.

Littell and Eaton (1991) focused on the near-wall ejections and sweeps in a three-dimensional turbulent boundary layer on a spinning disk. They conducted dual hot-wire probe measurements of spatial correlations in the spanwise direction. Their results indicate that an equal number of each sign of longitudinal quasi-coherent vortices exist in the boundary layer, however, the sweeps and ejections are more efficiently produced by vorti-

ces with different signs. The majority of the strongest sweeps are caused by vortices that rotate in the same sense as the mean streamwise vorticity in the near-wall region, whereas the strongest ejections are caused by vortices that rotate with the opposite sign as the mean streamwise vorticity near the wall.

The near-wall turbulent boundary layer structure on a disk spinning in water (same Reynolds number as Littell and Eaton's (1991) disk flow in air) was investigated by Chiang and Eaton (1993). Using hydrogen-bubble-wire flow visualization, they observed an asymmetry of near-wall ejection events and related the ejections to the strengths of the streamwise vorticies. On average, a vortex structure of one sign (opposite to the mean near-wall streamwise vorticity) produced stronger ejections than ejections from vortex structures of the other sign. The mechanism for structural changes was explained using a model of a single vortex interacting with the cross flow. The trajectory of the fluid being ejected away from the wall was modified depending on the sign of the vortex with respect to the cross-flow. Based on this visualization study, along with results from his whole collection of boundary layer structure experiments, Eaton (1995) modified his original hypothesis to explain the reduction of turbulence shear stress production in three-dimensional flows. Vortices of both sign are equally present in the boundary layer, however three-dimensionality reduces the effectiveness of longitudinal vortices at producing new ejections and sweeps by modifying the path of the near-wall fluid.

Hydrogen-bubble-wire and dye-injection flow visualization methods were used by Flack and Johnston (1993a, 1995) in their study of two separate three-dimensional turbulent boundary layers: flow approaching a 45 degree swept step and flow in a 30 degree bend. Dye seeped into the wall layer through wall slots was used to investigate the sublayer streaky structure. The nondimensional, spanwise, low-speed streak spacing decreased slightly with three-dimensionality from the value of approximately 100 viscous units reported in previous two-dimensional boundary layer studies (for example, Kline et al. (1967), Clark and Markland (1971)). The spacing of the streaks should be directly related to the spacing of the streamwise quasi-coherent vortices. Hydrogen bubbles were utilized to mark fluid in the viscous sublayer and buffer regions in order to investigate the ejections produced by the near-wall quasi-streamwise vortices. As was found in the studies of Littell and Eaton (1991), each sign of vortex ejection occurred with approximately equal frequency, indicating an equal number of each sign of streamwise vortex. The size of ejection events (wall normal extent) from each sign vortex structure was also approximately equal indicating that cross-flow does not preferentially influence the strength of near-wall vortices. Modifications to the near-wall boundary layer structure were observed when the frequency of ejection events was examined. The total number of ejection events (per unit time) decreased with increased three-dimensionality producing a more quiescent near-wall region.

Reduced near-wall activity was also observed by Fleming and Simpson (1994) using hydrogen bubble visualization to study the near-wall streaky structure in the 3DTBL on the flat wall around a simulated wing-body junction. Zones of two-dimensional flow displayed more vigorous streak oscillations than seen in regions of skewed three-dimensional flow which, compared to two-dimensional regions, appeared to be more stable with less movement in the spanwise direction. The spanwise spacing of near-wall streaks also decreased slightly (approximately 10 percent) for three-dimensional flow compared to the two-dimensional case.

Statistical methods were used by Ha and Simpson (1993) in a study of a three-dimensional turbulent boundary layer around a wing-body junction. Using multipoint velocity measurements from a hot-wire rake located in the buffer layer, they found that the length scales of the low frequency structures (low speed, near-wall fluid) decreased with increasing three-dimensionality.

This reduction occurred together with a reduction in the Reynolds shear stress. They also found that the mean motion of the near-wall quasi-coherent structures was not quite streamwise but skewed in a direction between the local turbulent shear stress and local mean velocity vectors. The turbulent shear stresses would appear to be pulling the quasi-coherent structures away from the direction of the local mean velocity vector. The preferred spanwise spacing of the near-wall structure was determined by Ha to be on the range of 85 to 100 viscous units, a result in agreement with the three-dimensional wall-streak spacing results of Flack and Johnston (1993a, 1994), and Fleming and Simpson (1994). The streak spacing studies indicate that if there is a reduction of the spanwise streak spacing with three-dimensionality, then the reduction is small. However, a small reduction may be significant considering that the wall streaks are the footprints of the streamwise vortices that occur in the buffer and log regions.

Sendstad and Moin (1992) studied the structure of the wall layer of a three-dimensional boundary layer using a numerical simulation of a two-dimensional, fully developed channel flow which is turned by a suddenly imposed spanwise pressure gradient. The statistics of this flow were reported by Moin et al. (1990). Differences in the near-wall structure of a three-dimensional boundary layer, as compared to two-dimensional boundary layers, were shown to be responsible for the reduction of shear stress. The fluid in the sweeps from vortices with the same sign as the mean near-wall vorticity does not get as close to the wall in three-dimensional boundary layers and therefore appear to generate less Reynolds shear stress. This modified trajectory also causes the velocity fluctuations from fluid being ejected away from the wall by the opposite signed vorticies to be less intense, since the fluid originated at a higher distance from the wall. Another structural difference observed was an apparent break-up of wall layer streaks due to the differential turning of streamwise vortices further from the wall. This would lead to shorter streaks in the streamwise direction.

Concluding Remarks

Measurement Techniques and Accuracy. Until very recently, most experiments have been conducted using hot-wire probes. The usual limits on hot-wire accuracy apply to three-dimensional flows. It has been found that accuracy is enhanced if probe axes are consistently aligned with the local, predetermined mean-flow vector at each point in a profile. Probe-wall interference has limited the region of measurement of the turbulence stresses to the outer regions of the boundary layer, above $y^+ \approx 50$ to 100 in most cases. Recently, a few experiments have been carried out using LDV methods, and fairly accurate data have been obtained inside the wall-layers, down into the inner buffer layers. Table 1 has comments on the useful y^+ range of the hot-wire and the LDV measurements for the 11 cases reviewed here.

The accurate measurement of wall shear stress magnitude and direction is still an art in need of further development. A variety of methods have been applied to date, (see Table 1), and all have been found lacking in one way or another. For example, the direct force method used in Case 9, is exceedingly difficult and would be very expensive, or even impossible to employ in most situations.

Modeling Issues. For years now, an isotropic (scalar) eddy viscosity model has been shown to poorly represent the *direction* of the turbulent shear stress vector especially in the outer parts of the layer. In simple flows, for example where cross-flow pressure gradients don't change sign downstream, the direction of the shear stress tends to lag behind the change of direction of the rate-of-strain angle. However recent data now indicate that this model may be a fairly good approximation in the wall-layers. There may even be a region in the viscous

sublayer and inner buffer layer where the stress angle leads the strain angle by a small amount. In the prediction of the mean flow velocity profiles, an accurate model of stress direction is most important in the wall-layers and of less importance in the outer parts of the layer where shear-stress forces are small compared to pressure forces. Consequently, an isotropic eddy viscosity model may be a useful, and practical approach where predictive accuracy need not be extreme.

However, this model, with the usual 2-D constants, doesn't properly represent the *magnitude* of the shear stress vector, an effect represented in profiles of structure parameter a_1 versus distance from the wall. For flows examined here and in earlier studies, a_1 values are lowered by three-dimensional effects near the wall. As noted by Driver and Johnston (1990), the degree of lowering is roughly a simple monotonic function of local skewing angle. Our investigation indicates that such a simple modification of the model is deficient in that the degree of lowering of a_1 also depends on (i) the initial state of the turbulence structure where cross-flow pressure gradients are first applied, (ii) the streamwise pressure gradients, (iii) the flow development history under these gradients, and (iv) the boundary layer Reynolds number. These complications are the most likely cause of inaccurate predictions using a simple isotropic eddy viscosity. It would thus appear that higher order models will be required for the best predictions.

Evaluation of Models. Models need to be evaluated by direct comparison to a range of data sets from a number of different studies. The acid test of a model is to compare measured and computed results for a wide variety of documented cases. This kind of comprehensive study has never been conducted for 3DTBLs. Eight of the eleven cases examined in this paper are identified in Table 1 as potential candidates for use in an evaluation. Further study, will force the elimination of some of the cases, but we feel that Cases 1, 6, 9, 10, and 11 are the most likely candidates. *Case 11, the rotating disk flow, is the most important for early consideration because it is the only case with simple, unidirectional cross-flow which is truly three dimensional all the way from its laminar origin.* We urge modellers to tackle this case as a prelude to the predication of more complex flows. Secondly, we recommend prediction of cases 1 and 10 in the near future as they would appear to be well qualified data sets obtained in geometrically relatively simple flows; cases 10 and 11 are axisymmetric which greatly simplifies computation.

Quasi Coherent Structures in the Wall-Layers. Recent three-dimensional boundary layer studies have identified several structural changes that could lead to modification of turbulent stresses in three-dimensional boundary layers. Changes due to the presence of cross-flow include (i) a possible asymmetry of sweep and ejection strengths from streamwise vorticies of opposite signs and (ii) modified sweep and ejection trajectories. In several studies (iii) the number of each sign of quasi-streamwise vortex was found to be approximately equal, however (iv) the number of vortex structures and (v) the spanwise spacing and streamwise extent of these vortices appeared to have been reduced.

Although all the studies indicate that changes occur, some of the results are contradictory. First, discrepancies, in part, result from use of a variety of detection techniques and concentration on different parts of the near-wall region. Secondly, the upstream origins of the layers may affect the response of the structures. Some boundary layers, those grown on rotating disks for example, are three-dimensional all the way from their laminar origins. However, most of the others were fully-developed, two-dimensional turbulent layers before they were subject to any cross-flow perturbation. Finally, the effects of Reynolds number on the various results needs to be fully taken into account. Present results are far from complete. If structure research is extended in the future, a more complete understanding of the behavior of near-wall quasi-coherent structures might result and be useful for the prediction of the effects of three-dimensionality on the turbulence quantities modeled for use in engineering flows.

JFE Data Bank Contributions

The experimental data sets obtained from the authors who produced their data at Stanford University are being added to the *Journal of Fluids Engineering* data bank. The sets include some of the cases reviewed here: Schwarz and Bradshaw (#1), Flack and Johnston (#2 & #3), Driver and Johnston (#10), and Littel and Eaton (#11). Also, it is planned to add data sets from Johnson and Johnston (1989), a two-dimensional flow at Re_θ = 1400 which compliments Flack and Johnston's Case #3, and the two-dimensional DNS data set of Spalart (1989) at Re_θ = 1410. To access the file for this paper follow the instructions in this issue.

References

Ahn, S., 1992, "An Experimental Study of Flow Over a 6 to 1 Prolate Spheroid at Incidence," Ph.D. Dissertation, Aerospace and Ocean Engineering, Virginia Polytechnic Institute and State University, Blacksburg, Virginia.

Anderson, S. C., and Eaton, J. K., 1989, "Reynolds Stress Development in a Pressure Driven Three-Dimensional Turbulent Boundary Layer," *Journal of Fluid Mechanics*, Vol. 202, pp. 263–294.

Aslinger, K., 1990, "Measurements of Surface Shear Stress Under a Three-Dimensional Turbulent Boundary Layer Using Oil-Film Laser Interferometry," M.S. thesis, Virginia Tech, Aerospace and Ocean Engineering Dept.

Barber, K. M., and Simpson, R. L., 1991, "Mean Velocity and Turbulence Measurements of Flow Around a 6:1 Prolate Spheroid," AIAA Paper 91-0255, 29th Aerospace Sciences Meeting, January 7–10, Reno, Nevada.

Bradshaw, P., and Pontikos, N. S., 1985, "Measurements in the Turbulent Boundary Layer on an Infinite Swept Wing," *Journal of Fluid Mechanics*, Vol. 159, pp. 105–130.

Bradshaw, P., and Terrell, M., 1969, "The Response of a Turbulent Boundary Layer on a 'Infinite' Swept Wing to the Sudden Removal of Pressure Gradient," National Physical Lab. Aero Rept. 1305, Teddington, England.

Bradshaw, P., 1987, "Turbulent Secondary Flows," *Annual Review of Fluid Mechanics*, Vol. 19, pp. 53–74.

Chesnakas, C. J., and Simpson, R. L., 1994a, "Three-Dimensional Turbulence Structure in the Vacinity of a 3-D Separation," *Forum on Turbulence in Complex Flows*, ASME Winter Annual Meeting, Chicago, Nov. 6–11, 1994.

Chesnakas, C. J., and Simpson, R. L., 1994b, "Full Three-Dimensional Measurements of the Cross-Flow Separation Region of a 6:1 Prolate Spheroid," *Experiments in Fluids*, Vol. 17, pp. 68–74.

Chiang, C., and Eaton, J. K., 1993, "An Experimental Investigation of Corotating Disks and Single Disk Flow Structures," Thermosciences Division Report MD-62, also available as: Chiang, C., Ph.D. dissertation, Dept. of Mechanical Engineering, Stanford University, 1992.

Clark, J. A., and Markland, E., 1971, "Flow Visualization in Turbulent Boundary Layers," *Journal of the Hydraulics Division, Proc. ASCE*, Vol. 10, pp. 1653–1663.

Coleman, G. N., Kim, J., and Le, A.-T., 1995, "A Numerical Study of Three-Dimensional Boundary Layers," *10th Symposium in Turbulent Shear Flows*, University Park, PA, Aug. 14–16, 1995.

Corrsin, S., 1959, "Some Current Problems in Turbulent Shear Flows," Naval Hydrodynamics, National Academy of Sciences, NRC Publication no. 515.

Cousteix, J., 1986, "Three-Dimensional and Unsteady Boundary Layer Computations," *Annual Review of Fluid Mechanics*, Vol. 18, pp. 173–196.

Driver, D. M., and Johnston, J. P., 1990, "Experimental Study of a Three-Dimensional Shear-Driven Turbulent Boundary Layer With Streamwise Adverse Pressure Gradients," NASA Technical Memorandum 102211, also available as: Driver, D. M., Ph.D. dissertation, Dept. of Mechanical Engineering, Stanford University, 1990.

Driver, D. M., and Hebbar, S. K., 1987, "Experimental Study of a Three-Dimensional Shear-Driven Turbulent Boundary Layer," *AIAA Journal*, Vol. 25, pp. 35–42.

Eaton, J. K., 1991, "Turbulence Structure and Heat Transfer in Three-Dimensional Boundary Layers," *Proceedings of the 9th Symposium on Energy Engineering Sciences*, Argonne Nat. Lab.

Eaton, J. K., 1995, "Effects of Mean Flow Three Dimensionality on Turbulent Boundary-Layer Structure," *AIAA Journal,* Vol. 33, pp. 2020–2025.

Elsenaar, A., and Boelsma, S. H., 1974, "Measurements of the Reynolds Stress Tensor in a Three-Dimensional Turbulent Boundary Layer Under Infinite Swept Conditions," NRL TR 74095 U.

Flack, K. A., and Johnston, J. P., 1993a, "Near-Wall Investigation of Three-Dimensional Turbulent Boundary Layers," Report MD-63, Thermosciences Div., also available as: Flack, K. A., Ph.D. dissertation, Dept. of Mechanical Engineering, Stanford University, 1993.

Flack, K. A., and Johnston, J. P., 1993b, "Experimental Study of a Detaching Three-Dimensional Turbulent Boundary Layer," Near-Wall Turbulent Flows, Proc. Int. Conf. on Near-Wall Turbulent Flows, Tempe, AZ, 15–17 Mar., pp. 977–986.

Flack, K. A., and Johnston, J. P., 1994, "Near-Wall Flow in Three-Dimensional Turbulent Boundary Layer on the End-Wall of a Rectangular Bend," AIAA paper no. 94-0405, 32nd Aerospace Sciences Meeting, Reno, NV, 10–13 Jan.

Flack, K. A., and Johnston, J. P., 1995, "Near-Wall Structure of Three-Dimensional Turbulent Boundary Layers," 10th Symposium in Turbulent Shear Flows, University Park, PA, Aug. 14–16.

Fleming, J., and Simpson, R., 1994, "Experimental Investigation of the Wall Flow Structure of a Low Reynolds Number 3-D Turbulent Boundary Layer," AIAA paper no. 94-0649, 32nd Aerospace Sciences Meeting, Reno, NV, 10–13 Jan. 1994.

Gleyzes, C., Maciel, Y., and Cousteix, J., 1993, "Three-Dimensional Turbulent Flow Around the Garteur Swept Wing. Selected Features," *9th Symposium on Turbulent Shear Flow,* Kyoto, Japan, Aug. 16–18, 1993, pp. 4-4-1-6.

Gruschwitz, E., 1935, "Turbulente Reibungsschichten mit Secondarstromung," Ingenieur-Archiv., Bd. VI, pp. 355–365. Translated version: NASA TM 77494, 1984.

Ha, S., and Simpson, R. L., 1993, "An Experimental Investigation of a Three-Dimensional Turbulent Boundary Layer Using Multiple-Sensor Probes," *9th Symposium on Turbulent Shear Flow,* Kyoto, Japan, Aug. 16–18, 1993, pp. 2-3-1-6.

Humphreys, D. A., and Lindhout, J. P. F., 1988, "Calculation Methods for Three-Dimensional Turbulent Boundary Layers," *Progress in Aerospace Sciences,* Vol. 25, pp. 107–129.

Johnson, P., and Johnston, J. P., 1989, "The Effects of Grid-Generated Turbulence on Flat and Concave Turbulent Boundary Layers," Thermosciences Report MD-53, also available as: P. Johnson, Ph.D. dissertation, Dept. of Mechanical Engineering, Stanford University, 1989.

Johnston, J. P., 1960, "On Three-Dimensional Turbulent Boundary Layers Generated by Secondary Flow," ASME *Journal of Basic Engineering,* Vol. 82, pp. 233–248.

Johnston, J. P., 1970, "Measurements in a Three-Dimensional Turbulent Boundary Layer Induced by a Swept, Forward-Facing Step," *Journal of Fluid Mechanics,* Vol. 42, Part 4, pp. 823–844.

Johnston, J. P., 1976, "Experimental Studies in Three-Dimensional Turbulent Boundary Layers," Thermosciences Division Report MD-34, Mechanical Engr., Stanford University.

Kline, S. J., Reynolds, W. C., Schraub, F. A., and Runstadler, P. W., 1967, "The Structure of Turbulent Boundary Layers," *Journal of Fluid Mechanics,* Vol. 30-4, pp. 741–773.

Kreplin, H.-P., and Stäger, R., 1993, "Measurements of the Reynolds-Stress Tensor in the Three-Dimensional Boundary Layer of an Inclined Body of Revolution," *9th Symposium on Turbulent Shear Flow,* Kyoto, Japan, Aug. 16–18, 1993, pp. 2-4-1-6.

Littell, H. S., and Eaton, J. K., 1991, "An Experimental Investigation of the Three-Dimensional Boundary Layer on a Rotating Disk," Thermosciences Report MD-60, also available as: Littell, H. S., Ph.D. dissertation, Dept. of Mechanical Engineering, Stanford University, 1991.

Littell, H. S., and Eaton, J. K., 1994, "Turbulence Characteristics of the Boundary Layer on a Rotating Disk," *Journal of Fluid Mechanics,* Vol. 266, pp. 175–207.

Löfdahl, L., Truong, T. V., Bruns, L. M., 1995, "Measurements of Turbulent Quantities in a Complex Three-Dimensional Boundary Layer Flow," *Experiments in Fluids,* Vol. 18, pp. 335–342.

Mager, A., 1952, "Generalization of Boundary Layer Momentum Integral Equations to Three-Dimensional Flows Including Those of Rotating Systems," NACA Report 1067.

Moin, P., Shih, T. H., Driver, D. M., and Mansour, N. M., 1990, "Direct Numerical Simulation of a Three-Dimensional Turbulent Boundary Layer," *Physics of Fluids A,* Vol. 2, pp. 601–639.

Nash, J. F., and Patel, V. C., 1972, "Three-Dimensional Turbulent Boundary Layers," SBC Technical Books.

Ölcmen, M. S., and Simpson, R. L., 1992, "Perspective on the Near Wall Similarity of Three-Dimensional Turbulent Boundary Layers," *Journal of Fluids Engineering,* Vol. 114, pp. 487–495.

Ölcmen, M. S., and Simpson, R. L., 1993, "Evaluation of Algebraic Eddy-Viscosity Models in Three-Dimensional Turbulent Boundary Layer Flows," *AIAA Journal,* Vol. 31, No. 9, pp. 1545–1554.

Ölcmen, M. S., and Simpson, R. L., 1995, "An Experimental Study of a Three-Dimensional Pressure-Driven Turbulent Boundary Layer," *Journal of Fluid Mechanics,* Vol. 290, pp. 225–262.

Pompeo, L., 1992, "An Experimental Study of Three-Dimensional Turbulent Boundary Layers," Doctoral dissertation-Swiss Federal Institute of Technology, Zurich.

Pompeo, L., Bettelini, M., and Thomann, H., 1993, "Laterally Strained Turbulent Boundary Layers Near a Plane of Symmetry," *Journal of Fluid Mechanics,* Vol. 257, pp. 507–532.

Robinson, S. K., 1991a, "Coherent Motions in Turbulent Boundary Layers," *Annual Review of Fluid Mechanics,* Vol. 23, pp. 601–639.

Robinson, S. K., 1991b, "The Kinematics of Turbulent Boundary Layer Structure," Ph.D. dissertation, Dept. of Mechanical Engineering, Stanford University, Stanford, CA. Available as NASA Technical Memorandum 103859.

Ryhming, I. L., Truong, T. V., and Lindberg, P-A, 1992, "Summary and Conclusions for Test-Case T1," *Numerical Simulation of Unsteady Flows and Transition to Turbulence,* Proc. ERCOFTAC Workshop at EPFL, 26–28 March 1990, Lusanne, Switzerland, Editors: O. Pironneau, W. Rodi, I. L. Ryhming, A. M. Savill, and T. V. Truong, Cambridge Univ. Press (1992), pp. 197–244.

Schwarz, W. R., and Bradshaw, P., 1992, "Three-Dimensional Turbulent Boundary Layer in a 30 Degree Bend: Experiment and Modeling," Thermosciences Division Report MD-61, also available as: Schwarz, W. R., Ph.D. dissertation, Dept. of Mechanical Engineering, Stanford University, 1992.

Schwarz, W. R., and Bradshaw, P., 1993, "Measurements in a Pressure Driven Three-Dimensional Turbulent Boundary Layer During Development and Decay." *AIAA Journal,* Vol. 31, No. 7, pp. 1207–1214.

Schwarz, W. R., and Bradshaw, P., 1994a, "Turbulence Structural Changes for a Three-Dimensional Turbulent Boundary Layer in a 30° Bend," *Journal of Fluid Mechanics,* Vol. 272, pp. 183–209.

Schwarz, W. R., and Bradshaw, P., 1994b, "Term-By-Term Tests of Stress-Transport Models in a Three-Dimensional Boundary Layer," *Physics of Fluids,* Part 2, Vol. 6, No. 2, pp. 986–998.

Sendstad, O., and Moin, P., 1992, "The Near-Wall Mechanics of Three-Dimensional Turbulent Boundary Layers," Thermosciences Division Report TF-57, also available as: Sendstad, O., Ph.D. dissertation, Dept. of Mechanical Engineering, Stanford University, 1992.

Shizawa, T., and Eaton, J. K., 1992, "Turbulence Measurements for a Longitudinal Vortex Interacting With a Three-Dimensional Turbulent Boundary Layer," *AIAA Journal,* Vol. 30-1, pp. 49–55.

Spalart, P. R., 1988, "Direct Numerical Simulation of a Turbulent Boundary Layer up to $Re_\theta = 1410$," *Journal of Fluid Mechanics,* Vol. 187, pp. 61–98.

Spalart, P. R., 1989, "Theoretical and Numerical Study of a Three-Dimensional Turbulent Boundary Layer," *Journal of Fluid Mechanics,* Vol. 205, pp. 319–340.

Stäger, R., 1993, "Turbulence Measurements in the Three-Dimensional Boundary Layer of an Inclined Prolate Spheroid," Report DLR-FB 93-37, Institute für Strömungsmechanik der DLR, and Dissertation George-August Universität, Göttingen.

Truong, T. V., and Brunet, M., 1992, "Test Case T1: Boundary Layer in a "S"-Shaped Channel, *Numerical Simulation of Unsteady Flows and Transition to Turbulence* Proc. ERCOFTAC Workshop at EPFL, 26–28 March 1990, Lusanne, Switzerland, Editors: O. Pironneau, W. Rodi, I. L. Ryhming, A. M. Savill, and T. V. Truong, Cambridge Univ. Press (1992), pp. 78–115.

Wheeler, A. J., and Johnston, J. P., 1973, "An Assessment of Three-Dimensional Turbulent Boundary Layer Prediction Methods," ASME JOURNAL OF FLUIDS ENGINEERING, Vol. 95, pp. 415–421.

Wu, X., and Squires, K. D., 1995, "Large-Eddy Simulation of a Canonical Three-Dimensional Boundary Layer," *10th Symposium in Turbulent Shear Flows,* University Park, PA, Aug. 14–16, 1995.

Perspective: The Experimentalist and the Problem of Turbulence in the Age of Supercomputers

Morteza Gharib

Professor of Aeronautics,
Center for Quantitative Visualization,
Graduate Aeronautical Laboratories,
Pasadena, CA 91125

Due to the rising capabilities of computational fluid mechanics (CFD), the role of the experimentalist in solving the problem of turbulence has come under serious question. However, after much initial excitement by the prospect of CFD, the basic understanding of non-linear fluid phenomena such as turbulence still remains a grand challenge and will remain so into the unforeseeable future. It appears that in order to accelerate the development of a comprehensive and practical understanding and modeling of turbulence, it is required that a constructive synergism between experiments and simulations be created. Moreover, the digital revolution has helped experimental fluid mechanics to acquire new capabilities in the whole-field flow mapping technique which enables it to efficiently interface with CFD. This new horizon is promising in its capabilities to guide, validate and actively interact in conducting reliable simulations of turbulent flows.

Introduction

Since the time of Galileo, progress in science has greatly depended on the experimentalist's capabilities to question nature by means of observation and experimentation, and by way of measuring magnitudes that could be analyzed and interrelated through mathematical formulation. It is an historical fact that every time experimental techniques have taken a leap forward, the "experimentalist" has made totally unexpected and unimagined discoveries. The history of natural science is filled with examples of experimental discoveries that have resulted in the formulation of new laws of physics by theorists. On the other hand, regardless of the way that a theory is born, ultimately, it has been the job of experimentalists to weed out the theories that work from those that don't. The dual role of experimentalists in exploration and discovery, on the one hand, and checking the newborn theories against the hard realities of the real world, on the other, creates an intricate interplay between observation and theory which is, above all, a unique demonstration of man's unintimidated but disciplined exercise of the imagination.

In recent decades, this balance between observation and theory has definitely been altered by advances in numerical methods and rising computational capabilities in the fields of engineering and physics. The remarkable advances in the computing powers of today's computers has opened the era of simulation; physical processes that can be recreated through existing laws of physics. The attractive prospects of accurately simulating the experimentally hard-to-realize problems of science at lower costs is the promise of the computational physicist or engineer. This promise is extremely appealing to the scientific and technical community in general and has been a hard one for the experimentalist to compete with. Indeed, in some branches of science and engineering where simulations can be conducted based on firm and well-behaved mathematical models, the role of the experimentalist has grown weaker. However, the role of experiments in weeding out the simulations that work from those that don't continues to be essential in all branches of science and technology. Nonetheless, the concept of exploration and discovery through simulation, rather than experimentation, has most threatened the role of the experimentalist as discoverer.

Among many fields of science that have faced this threat, fluid mechanics has suffered the greatest impact. In the past 100 years, from the primitive wind tunnel studies of the Wright brothers to the large scale wind tunnels of national laboratories, and from the desktop experiments of G. I. Taylor to sophisticated oceanographic laboratory platforms, experiments have been the only viable source of knowledge for basic or industrial fluid mechanics research. The rapid advances in computational fluid dynamics in the 70s and early 80s have been responsible for the creation of the narrow view that experimental facilities (for example, wind tunnels) would eventually be replaced by their digital counterparts. Such views, which were based on projections of dramatic increases in the performance of computers, reflected a lack of appreciation for the non-linear and multidimensional nature of many of today's unresolved grand scientific challenges, of which a majority happen to reside in the field of fluid mechanics. In the middle of the broad range of flow problems that challenge today's scientists stands the greatest puzzle of classical physics—turbulence.

The Grand Challenge

Fluid turbulence, in its many forms, shapes and degrees, from the grandest reaches of space to the sand and sea, is the elemental dynamic form. Its appearance in the atmosphere, in plasma, in fluid interfaces or in multi-phase flows is a manifestation of the convective and nonlinear nature of physical laws that govern the flow of fluids. The problem of understanding turbulence, in order to model and predict its mixing and transport properties or the prediction of flow around and inside geometries, is the grand challenge of this and quite possibly the next century. Turbulence has remained the last frontier of twentieth century science. For all the efforts of the great minds of science, the problem of turbulence has remained empirical.

The history of fluid mechanics would certainly credit the foundation of our current understanding of turbulence to the bold and pioneering work of scientists such as Osborn W. Reynolds, G. I. Taylor, Ludwig Prandtl, and Theodore von Kàrmàn who were products of a scientific culture that exercised the aforementioned intricate interplay between experiments and theory. Since their milestone work, many subsequent theoretical and modeling efforts to represent the physical process of turbulence have been pursued. Ultimately, these theories and models had to face the practical demands of industry where predictive capabilities were required. The rise of computational fluid dy-

namics was a natural answer to this demand for which experimentalists and theorists had not yet provided a viable solution.

After much justifiable initial excitement by the prospects of computational fluid dynamics, the basic understanding of fluid turbulence in its various forms (plasma, climatology, hydro, and aerodynamics) still remains a challenge to the theorist, experimentalist and numerical analyst alike. The colossal nature of this problem requires the development of novel approaches based on the synergism that experimentalists, numerists and theorists can create. This synergism should provide a higher level of validation for turbulence models by reaching deeper levels of understanding for the physics of turbulence. In order to construct this synergism, one needs to appreciate the nature of the problem of turbulence and identify the issues that currently slow the progress toward achieving a comprehensive understanding of this problem. In doing so, I have tried to express my opinion and understanding of these issues from the point of view of an experimentalist. In many cases, the ideas expressed in this paper are far from novel in their essence, but they reflect the means shared by many traditional and "contemporary" experimentalists. The particular examples cited in this paper only partially represent the state-of-the-art and are by no means the only ones. For the sake of brevity, I have tried to avoid combing the literature for every possible similar work, which I hope will not lessen the credibility of the ideas presented in this paper.

Some Insights

Many fluid mechanical problems of scientific and technological importance exhibit complex, unsteady and multi-dimensional dynamics. Large-scale turbulent separated flows, turbulent mixing, combustion and geostrophic flows provide a few unsteady examples. Above all, the three-dimensionality of these flows poses the greatest difficulty in the simulation or measurements of these flows. In this respect, some scaling arguments will help us to appreciate what it takes to "resolve" turbulence through experimentation and simulation.

We would like to consider turbulence as an ensemble of interacting eddies, where energy is provided by the large eddies and lost by the viscous action of the fluid on the smallest eddies. Based in this scenario and dimensional analysis, Kolmogorov's scaling arguments for turbulence (1941) suggest,

$$\frac{\delta_{max}}{\delta_{min}} \sim \mathrm{Re}^{3/4}$$

where δ_{max} is the nominal size of the large energy-containing eddies in a shear flow and δ_{min} is the size of the smallest existing eddies (known as Kolmogorov eddies) and Re is the Reynolds number (i.e., $\mathrm{Re} = \delta_{max}U/\nu$) based on the δ_{max} and the typical velocity of large eddies (i.e., U). If we assume that δ_{min} represents the minimum spatial resolution, then the above ratio will become an indication of the number of grid points that the computation or measurements will be required to have in order to describe the entire dynamic range of scales (Frisch and Orszag, 1990). In 3-D, this ratio would be proportional to $(\mathrm{Re}^{3/4})^3$.

The minimum temporal resolution can be obtained by dividing the smallest spatial scale (δ_{min}) by the convective velocity of large eddies (U)

$$\tau_{min} = \frac{\delta_{min}}{U} \sim \frac{\delta_{max}}{U} \mathrm{Re}^{-3/4}.$$

Again, the ratio of the largest to smallest temporal scales can be expressed as

$$\frac{\delta_{max}/U}{\tau_{min}} \sim \mathrm{Re}^{3/4},$$

which also indicates the number of required time steps (Karnia-

dakis and Orszag, 1990). Therefore, the minimum number of points that ultimately need to be obtained is proportional to

$$N_{total} \equiv (\mathrm{Re}^{3/4})^3 \cdot (\mathrm{Re}^{3/4}) = \mathrm{Re}^3.$$

This estimate is quite conservative since the minimum number of required grid points in time and space, in order to reliably resolve the spectral properties of turbulence, should follow the Nyquist criteria for space and time, in that it should be sixteen times higher. This requirement for the minimum number of points in measurements or computations, in order to describe the flow, is rather depressing since every order of magnitude increase in the flow Reynolds number requires a three orders of magnitude increase in the number of required computational/experimental grid points.

To scale the problem, consider the fact that, for the onset of fully developed turbulence in shear flows, a minimum Reynolds number of 10^4 is usually required (Dimotakis, 1993). At the outset, for transport airliners or atmospheric flows, the Reynolds number will be in the range of 10^8 to 10^{12}, respectively. The sobering resolution requirement for performing practical measurements or simulations of turbulent flows in this range demands computing powers and diagnostic tools beyond the capabilities of standard available technology.

Computing the Turbulence

What might have been called a supercomputer in the 1980s (to distinguish it from the standards of the industry at that time) will be hard-pressed to compete with some of the hand-held PC's of the 1990s. Therefore, the term *supercomputer* is a relative but attractive name and, therefore, should be judged based on what it achieves. This term has been passed on from sequential (von Neumann) machines to today's parallel processors with giga (10^9) and, very soon, tera (10^{12}) flops (floating-point operations per second) capabilities.

Application of paralleled codes on massively parallel computers with efficient networking and a large memory capacity are becoming the methods of choice for simulating turbulent flows. In the background of the ever-increasing power of supercomputers, there exists a whole spectrum of methodologies that can be used to compute turbulent flows—some with short term objectives and some with a look toward a comprehensive approach to the turbulence problem.

Ideally, one should be able to compute an entire flow field by solving the 3-D unsteady Navier-Stokes equations. This approach, which is known as direct numerical simulation or DNS, should (within the numerical approximation) render the full range of turbulent motions as well as transport properties of the flow. DNS is an alternative to experimental realization in the laboratory with all the attractive aspects of exploration and discovery which have been unique to experiments. However, the restriction caused by the aforementioned resolution requirements inhibits the practical application of DNS in simulating turbulent flows with a Reynolds number in excess of 10^4. In this respect, considering the current state-of-the-art in computing and the most optimistic prediction for its expansion, DNS applications will be confined to turbulent flows involving simple geometries at Reynolds numbers below 10^4 for many years to come. For example, using an efficient DNS code, a typical calculation of 100 cycles of vortex shedding from a circular cylinder at a Reynolds number of 1000 (Henderson and Karniadakis, 1995; see also Appendix) takes up to 400 hours to generate on a parallel supercomputer with a speed of 0.5 giga flops.

Despite the current limitations of direct simulations, DNS has proved that, when it is used appropriately, it is an unsurpassed method for understanding the physics of flow, interacting with experiments, or guiding modeling efforts. We will discuss the unique opportunities that DNS provides in the next section. However, the practical needs of industry demand intermediate

solutions for high Reynolds number flow problems in the form of predictive models.

At the heart of practical technological problems is the need for predicting turbulent fluxes of momentum and passive scalars such as species and temperature. Depending on the nature of properties in demand, various approximation schemes have been developed that do not involve omission of viscous or turbulent stress terms. All of these methods represent some kind of averaging or filtering operations on the N-S equations. In its simplest form, the averaging or filtering of N-S takes the following form:

$$\rho\left(\frac{\partial \bar{u}_i}{\partial t} + \bar{u}_j \frac{\partial \bar{u}_i}{\partial x_j}\right) = -\frac{\partial \bar{p}}{\partial x_i} + \frac{\partial}{\partial x_j}(\bar{\tau}_{ij} + T_{ij}), \qquad (1)$$

where

$$u_i \equiv \text{velocity vector}$$
$$p \equiv \text{pressure}$$
$$\tau_{ij}\,(\text{viscous stress}) \equiv \mu[(\partial \bar{u}_i/\partial x_j) + (\partial \bar{u}_j/\partial x_i)]$$
$$\rho \equiv \text{density (constant)}$$
$$T_{ij}\,(\text{Reynolds stress tensor}) \equiv -\rho\overline{u_i' u_j'}$$

The overbar represents the filtering or averaging process in the form of spatial, temporal or ensemble averaging. On one extreme of the filtering processes stands the Reynolds (1985) scheme which results in Reynolds averaged N-S or RANS equations where the entire time dependent parameters are averaged based on the assumption of statistically steady turbulence. In general, the averaging or filtering introduces correlations $(-\rho\overline{u_i' u_j'})$ between unresolved fluctuating velocities which act as stresses $(T_{ij} = -\rho\overline{u_i' u_j'})$ on the resolved motions. Equation (1) is not closed until a model is constructed that can relate the Reynolds stress (T_{ij}) to the mean velocities $(\bar{u}_i)$.

Through Boussinesq's hypothesis, the Reynolds stresses can be related to the gradients of averaged or filtered velocities (strain rate tensor) through the following eddy-viscosity relation for incompressible flows:

$$T_{ij} = \mu_T\left(\frac{\partial \bar{u}_i}{\partial x_j} + \frac{\partial \bar{u}_j}{\partial x_i}\right). \qquad (2)^1$$

The variation of the eddy viscosity μ_T over space and time must be obtained through turbulence modeling. The first models for closure were proposed by Prandtl (see Hinze, 1959) and is known as the mixing length theory. For two-dimensional flows, it suggests

$$v_T = l_0^2\left|\frac{du}{dy}\right| \quad \text{or} \quad v_T = l_1\Delta u.$$

l_1 is the shear layer thickness while l_0 is the mixing length. For the near wall region of turbulent boundary layers, the mixing length is related to the transverse coordinate (y) as $l_0 = Ky$ where K is the von Kàrmàn constant. This is a one-dimensional model that is mainly applicable to turbulent boundary layers. Validation studies of RANS codes of this type are mainly limited to two-dimensional flows. A particular three-dimensional version of the Prandtl model is the Baldwin-Lomax Model (Baldwin and Lomax, 1978), which has been very popular for RANS models in aerodynamics. It takes the following form:

$$v_T = l_0^2(\overline{\omega_i\omega_i})^{1/2}$$

where $\bar{\omega} = \nabla \times \bar{u}$ is the mean vorticity vector (Speziale, 1990).

The predictive power of this type of RANS model is limited since the turbulent length scale (l_o) should be independently provided for every specific application. One can avoid direct modeling of turbulent shear stresses by using a corresponding transport equation for the Reynolds stress itself, which results in the generation of additional higher order correlations to be modeled. The modeling of this higher order correlation is a central challenge to the statistical theory of turbulence. The application of RANS codes to massively 3D and transient flows has been limited to simple geometries. To obtain the drag coefficient or the pressure distribution, one needs to accurately model the separation regions where the dynamics have a profound effect on the separation points and thus on the base pressure distribution. In defining the averaging schemes, one can design filters that preserve certain dominant frequencies and average out stochastical turbulent motions altogether. This is an unsteady version of RANS codes whose application again requires explicit experimental input (Rodi, 1993).

Roshko (1992) points out that "one impact of [the original] RANS methods and the statistical theory was to tend to encourage a view of 'fully turbulent' flow as too complicated and disorganized to contain structural features that could be usefully incorporated into any model." The discovery of large vortical structures in boundary layers (Kline et al., 1967) and high Reynolds number mixing layers of Brown and Roshko (1974) has certainly changed this view. The impetus for an alternative method that stands between the two extreme approaches of DNS and RANS codes stems from these discoveries. Large eddy simulation methods tend to benefit from the fact that, for high Reynolds number flows, the large eddies are responsible for the transport of momentum and energy in recirculating regions, in free shear flows and in setting up the large scale pressure fields. In large eddy simulations, the behavior of the large scale motion of turbulence is simulated through conventional DNS codes, while modeling is used for the smaller unresolved scales. The fundamental aspect of LES is in the projection operation or filtering of the N-S equation. Similar to the RANS approach, the resulting truncated N-S equation lacks closure because of the stress-like reflection of eddies that fail to pass the filter on those that do (Ferziger, 1983; Rogallo and Moin, 1984). This stress-like reflection, which is called subgrid-scale (SGS) Reynolds stress, must be related to the large scale eddies in order for the scheme to work.

The Smagorinsky model, which is a 3D version of the eddy viscosity model, has been used to tackle the closure issue. In this model the SGS Reynolds stress tensor $\overline{u_i' u_j'}$ is assumed to be related to the corresponding components of the strain rate tensor of the large scalar field, $(\bar{S}_{ij})$, through

$$\overline{u_i' u_j'} = v_T\bar{S}_{ij} = \frac{1}{2}\,v_T\left(\frac{\partial \bar{u}_i}{\partial x_j} + \frac{\partial \bar{u}_j}{\partial x_i}\right)$$

where v_T is the SGS eddy viscosity given by

$$v_T = C_s(\bar{S}_{ij}\bar{S}_{ij})^{1/2}\bar{\Delta}$$

where $\bar{\Delta}$ is the corresponding length scale associated with the low pass filter and C_s is a constant parameter.

Many variations and modifications of the Smagorinsky model (e.g., dynamic SGS models, Germano et al., 1991) have been developed and used to attain the proper reflection of the unresolved scales on the resolved large eddies. The improper modeling of small scales results in excessive dissipation and can have catastrophic results in terms of the behavior of large scales.

The main shortcoming of the RANS and LES approaches is the fact that turbulent time and length scales are not universal and their modeling requires empirical information provided by experiments. A true modeling of the small scales in fully developed turbulent flows require experimental construction of strain rate and turbulent stress tensors. This is an exceedingly chal-

---

[1] In relation (2), we have neglected the normal stresses.

lenging task, since the current available experimental techniques can hardly render such information for three-dimensional flows.

The last method that we must mention, and what Ferziger (1993) calls the chief competition of the LES technique for the simulation of turbulent separated flows, is the discrete vortex method (Leonard, 1985; Sarpkaya, 1988). Excellent results, in terms of the flow pattern and of flow quantities at very large Reynolds numbers, can be obtained for 2-D geometries by this technique. Application of this technique to 3-D complex flows is the subject of much current research.

Probing the Turbulence

Single point measurement techniques such as hot wire and laser Doppler velocimetry (LDV) have been widely used for turbulence studies. Hot wire anemometry and LDV had been perfected and are still in use for many fluid measurements and control applications, while remaining useful for obtaining various quantities at a single point or array of points as a function of time. Still, the Eulerian nature of the information obtained by these devices yields insufficient information for an adequate description of turbulence. The discovery of large vortical structures at high Reynolds number flows through flow visualization (Brown & Roshko) proved that single point probes can miss the big picture altogether.

Naturally, flow visualization, benefiting from a remarkable function of the human brain in recognizing moving patterns, has helped the observers of nature—from Leonardo Da Vinci to modern vortex chasers—to appreciate the Lagrangian nature of turbulent flows. In science and technology, wherever adequate visualization has been part of the creative process, it has yielded new insights into complex phenomena and has provided better descriptions and predictive models. Examples range from Osborn Reynolds' description of turbulence to the observation of large vortical structures by Brown and Roshko. From the mixing of dye patterns to patterns generated by the pathlines of small suspended particles, the rendered information has been a remarkable source of knowledge. Obviously, the global nature of this information has invited many attempts to develop quantitative methods for flow visualization. A major drawback in doing so has been the lack of advanced imaging, acquisition and subsequent processing hardware and software technology. It is interesting that the same digital revolution that converted the primitive abacus machines to today's supercomputers has also helped experimenters to develop some of the most amazing means of quantitative imaging. In other words, this revolution has helped to develop the new art and science of quantitative visualization.

Quantitative Flow Visualization

Quantitative flow visualization has many roots and has taken several approaches. The advent of digital image processing has made it possible to practically extract useful information from every kind of flow image. In a direct approach, the image intensity or color (wavelength or frequency) can be used as an indication of concentration, density and temperature fields or of gradients of these scalar fields in the flow (Merzkirch, 1987). These effects can be part of the inherent dynamics of the flow (e.g., gradients of density are used in shadowgraph and Schlieren techniques) or generated through the introduction of optically passive or activate dye agents (fluorescent tracers, liquid crystals) or various molecular tagging schemes.

In general, the optical flow or the motion of intensity fields can be obtained through time sequenced images (Singh, 1991). For example, the motion of patterns generated by dye, clouds or particles can be used to obtain such a time sequence. The main problem with using a continuous-intensity pattern, generated by scalar fields (e.g., dye patterns), is that it must be fully resolved (space/time) and contain variations of intensity at all

scales before mean and turbulent velocity information can be obtained (Pearlstein, 1995). In this respect, the discrete nature of images generated by seeding particles has made particle tracking the method of choice for whole field velocimetry. The technique recovers the instantaneous two- or three-dimensional velocity vector field from multiple images of a particle field within a plane or volumetric slab of a seeded flow, which is illuminated by a laser light sheet. Various methods such as individual tracking of particles or statistical techniques can be used to obtain the displacement information and subsequently the velocity information. The spatial resolution of this method depends on the number density of the particles. A major drawback in using particle tracking techniques has been the unacceptable degree of manual work that was required to obtain the velocity field from a large number of traces or particle images. Digital imaging techniques have helped to make particle tracking less laborious (Gharib and Willert, 1989). However, because of the errors involved with identifying the particle pairs in high particle-density images, the design of automatic particle tracking methods for three-dimensional flows has been especially challenging. Therefore, applications of the automatic particle tracking methods have been limited to low particle density images.

In contrast to the tracking of individual particles, the particle image velocimetry (PIV) technique follows a group of particles through statistical correlation of sampled windows of the image field (Adrian, 1991). This scheme removes the problem of identifying individual particles which is often associated with tedious operations and large errors in the detection of particle pairs. In terms of the spatial resolution, the obtained velocity at each window represents the average velocity of the group of particles within the window. The interrogating window in PIV is the equivalent of the grid cell in CFD. Development of the video-based digital version of PIV, known as DPIV (Willert and Gharib, 1991; Westerweel 1993), resulted directly from advances in charge coupled device (CCD) technology and fast, computer-based, image processing systems. In terms of overall steps involved, DPIV is much faster than photographic PIV and particle tracking methods. The spatial resolution of the DPIV technique is decided by the resolution of the CCD array which is usually less than photographic films. However, this shortcoming is being reduced by the continuing improvement in high resolution/high speed CCD technology.

The capability of whole field measurement techniques in providing velocity vector or scalar field information in a format compatible to CFD calculations has made a major impact in defining common ground for designing new approaches toward resolving the turbulent flow problem. Figure 1 presents an example of companion DPIV (Gharib and Weigand, 1995) and DNS (Zhang and Yue, 1995) simulations of the interaction of a vortex ring (Reynolds number of 1000) with a free surface. The velocity vector fields are shown at the surface and in the symmetry plane of the vortex. The DNS simulation was carried out using non-linear free-surface boundary conditions. For DPIV, two simultaneous laser sheets and two simultaneous video-cameras were used to map the flow. Figure 1(c) shows temporal evolution of the vorticity field at the free surface and the symmetry plane. A single flow parameter such as circulation has been used to draw a quantitative comparison between the two approaches. Qualitative and quantitative agreements in the domains of time and space serve to confidently use the CFD results to explore other flow parameters that are not obtainable through experiments. Such a comparison could not be obtained by using methods such as LDV or hot wire anemometry that do not address the global Lagrangian and the temporal nature of this flow.

DPIV can be utilized to obtain three components of the velocity field (Raffel et al., 1995). However, this extension of DPIV is limited to a few planes and cannot address the full dimensionality of turbulent flows with the current video technology. Holo-
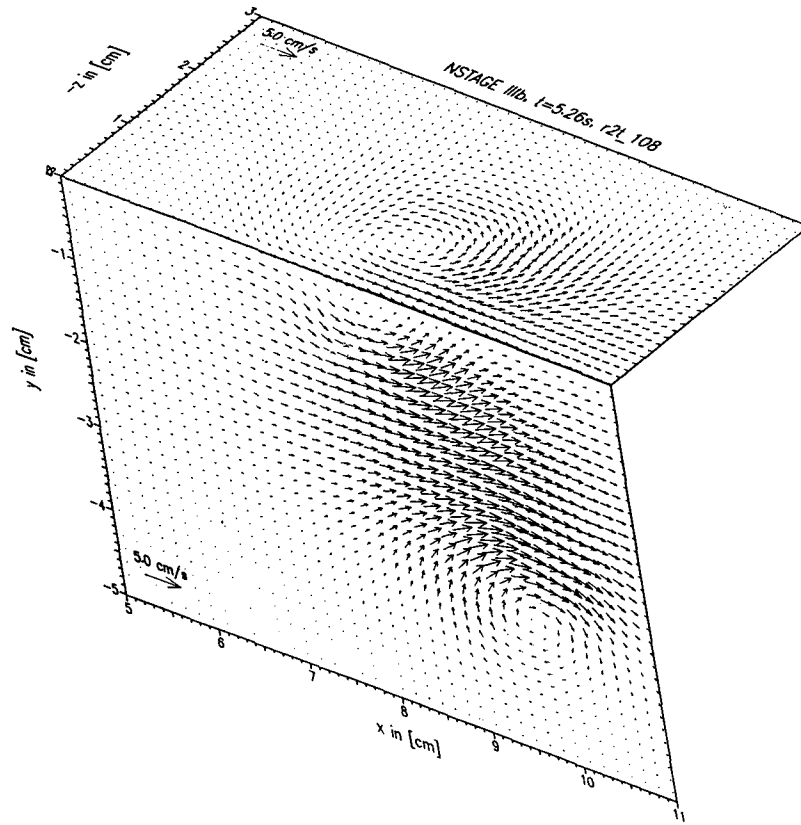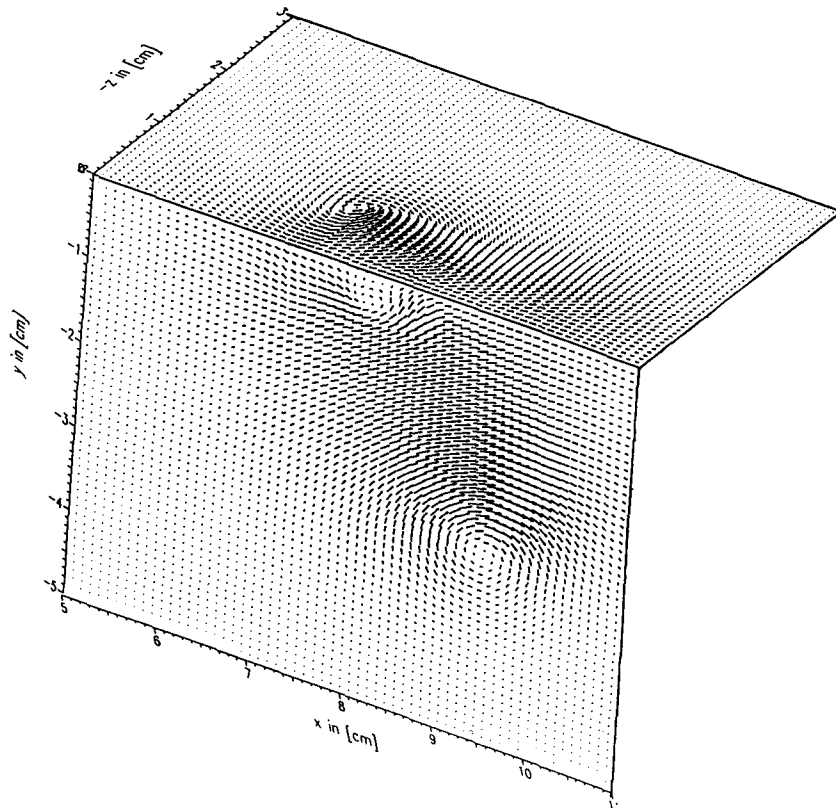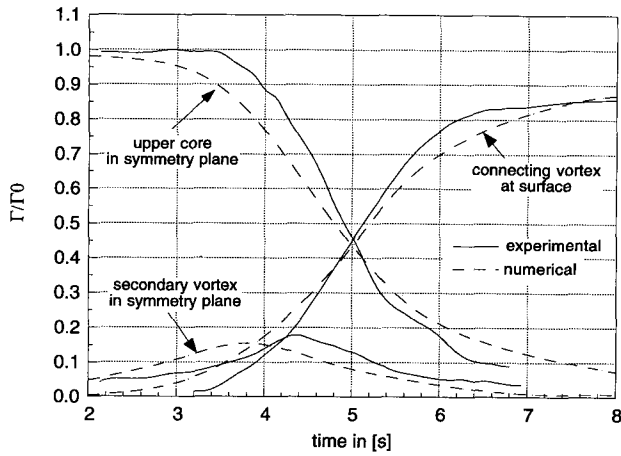
Fig. 1(*a*)

Fig. 1(*b*)

Fig. 1(c)

Fig. 1 The velocity vector field obtained by (a) DPIV (Gharib and Weigand, 1995) and (b) DNS (Zhang and Yue, 1995)

graphic PIV techniques are more suitable for obtaining three-dimensional distribution of the velocity vector field (Barnhart et al., 1994). Figure 2 depicts such a three-dimensional mapping of velocity vector field in a fully developed turbulent channel flow. The photographic nature of holographic PIV techniques limits their ability to address the temporal dynamics of turbulent flows. Recent advances in three-dimensional video-based particle tracking techniques have removed some of these shortcomings (Kasagi and Sata, 1992).
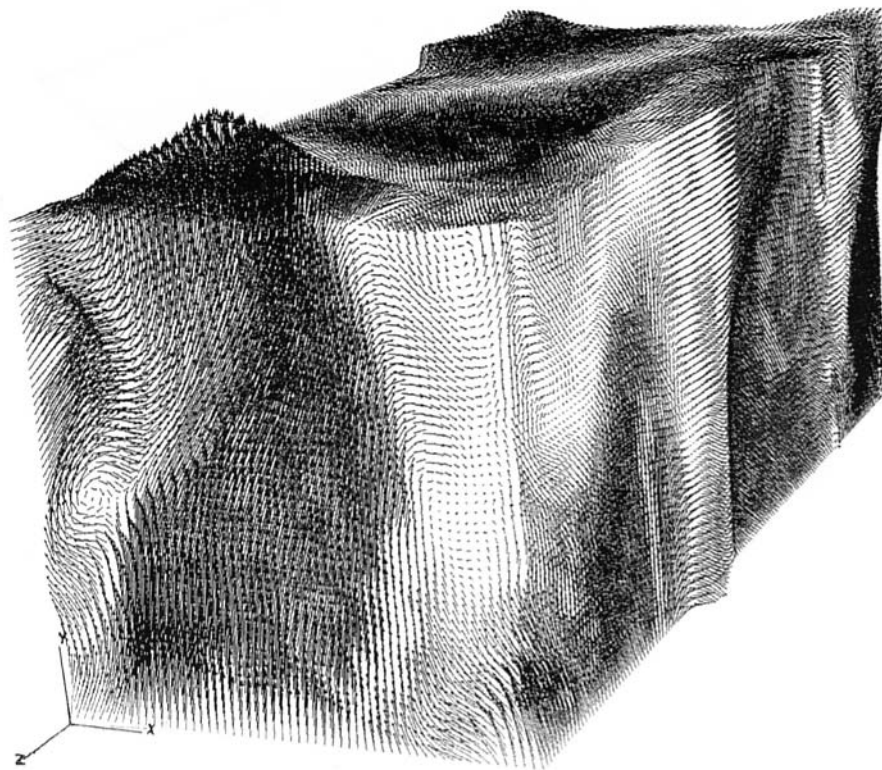
Besides DPIV, quantitative scalar imaging techniques have also been developed for concentration measurements (Koocheshfahani and Dimotakis, 1986), for temperature (Dabiri and Gharib, 1991), and for surface elevation and slope (Zhang and Cox, 1994; Zhang, 1994). In the latter, the surface slopes can be directly obtained from a novel color-coding technique; an example of its use to study free-surface turbulence generated by an underwater jet is given in Fig. 3. Each color in this picture is representative of a certain slope which can be converted to the surface elevation through a spatial integration scheme.

The aforementioned examples from the author's group and others represent various whole field quantitative flow visualization methods that hold the promise of providing new dimensions in measurements and their interaction with CFD.

Defining Common Ground

It would be greatly deceiving to attribute the shortcomings of simulations to the limitations of computational power or numerical issues (Rizzi and Engquest, 1987; Leschziner, 1993). There are many other issues that severely challenge various computational approaches to solving turbulent flow problems including:

1. Steady and unsteady boundary conditions (common to all types of CFD methods)
2. Complex 3-D geometries (common to Euler methods, RANS, LES, vortex methods)
3. Multi-phase flows (common to all types of CFD methods)
4. Coupled-fields (common to all types of CFD methods)
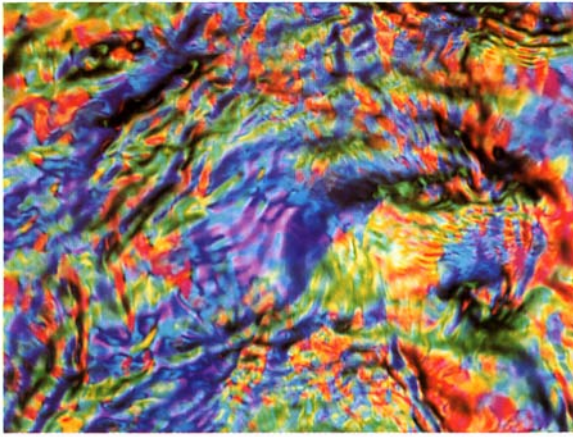5. Compressibility (common to all types of CFD methods)

HPIV

Fig. 2 Three-dimensional velocity vector field obtained by a phase-conjugated holographic PIV technique (Barnhart, 1994)

Fig. 3 Free-surface color slope mapping of a near surface turbulent jet (Zhang et al., 1994)

In this respect, the interaction between experiments and CFD can take place at two levels:

1. Low and Medium Reynolds Number. For straight validation purposes; such as checking on the two-dimensionality of the flow, geometry definition, and velocity and vorticity field comparisons; quantitative flow visualization methods offer a unique opportunity. In our second example shown in Fig. 4 simulation of vortex shedding from a circular cylinder using DNS (Henderson 1994) is compared with its DPIV counterpart.
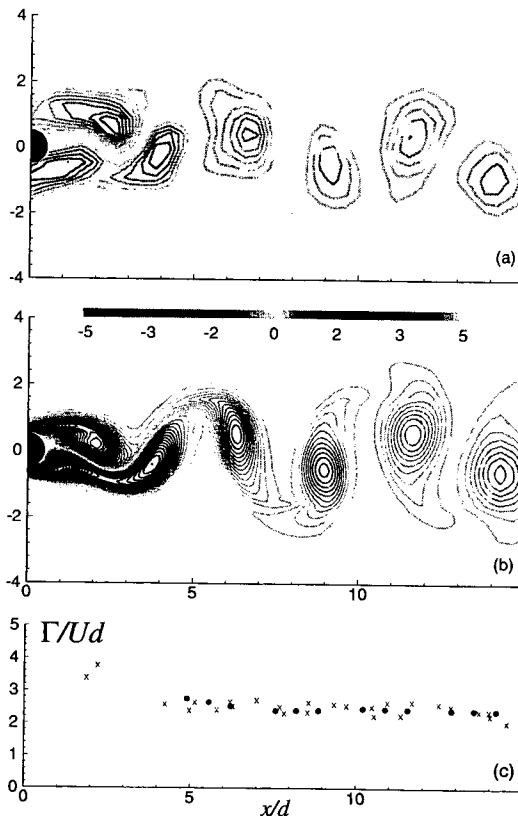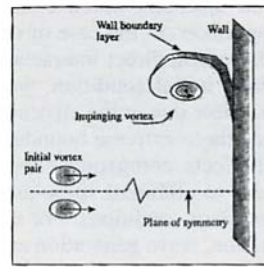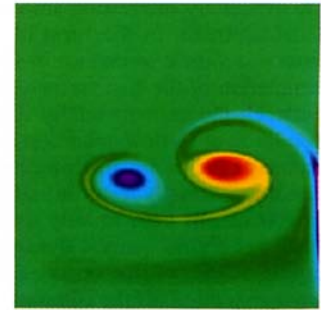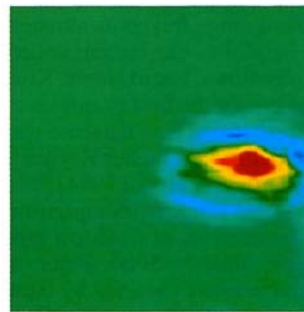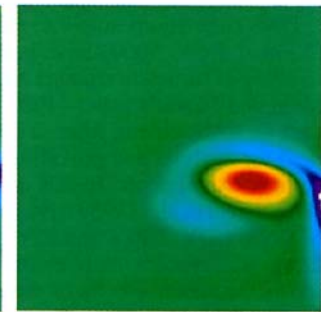

Schematics of the initial vortex pair and its interaction with the wall.

DNS simulation with Gaussian vorticity distribution for the initial vortex.

DPIV results.

DNS with vorticity distribution from DPIV for the initial vortex.

Fig. 5 A comparative study of DNS simulation based on initial conditions from a model or DPIV vorticity distribution (Liepmann and Dommermuth 1991; Fabris et al., 1995)

Experiments are essential in resolving modeling issues, such as boundary conditions, where modeling errors can produce errors in the solution of order one. The problem of defining the proper in-flow (upstream) condition and the determination of the dimensions of the computational box (blockage effect and correlation lengths) can easily benefit from appropriate laboratory simulation of the flow condition. One of the most important features of DPIV is the compatibility of its format with that of the CFD method. In-flow conditions or initial flow properties can be used directly as input to initiate DNS or LES. This approach removes unrealistic in-flow conditions which often result in dubious flow solutions. In Fig. 5(a), (b), (c), and (d), we present the interaction of a vortex pair with a solid boundary obtained by DPIV and DNS. Figure 5(b) shows the DNS simulation initiated by a Gaussian vorticity distribution for the approaching vortex. Figure 5(c) depicts the DPIV results. Figure 5(b) shows that the simulation does not generate the correct flow field if the initial experimental conditions were not used. Using initial vorticity fields from the DPIV measurement, Figure 5(d) shows a much better agreement with experiments. It is interesting to note that without such novel experiments, the whole validity of the DNS code used for this simulation might have ended in doubt for a wrong reason (Liepmann and Dommermuth, 1991; Fabris et al., 1995). Also, it has to be mentioned that such experiments open new opportunities for interactive computational/experimental methods to be developed for thermofluid flows (Humphrey et al., 1991).

There are two other types of boundary conditions that are especially troublesome; namely, boundaries that involve fluid that leaves the computational domain (out-flow condition), and unsteady moving boundaries such as flexible cables (Newman and Karniadakis, 1995) or free surfaces (Dommermuth, 1993). For simulations, these boundary conditions are part of the solution to the problem and need to be defined in transit. Proper resolutions of these problems are important for situations involving free surfaces as boundary conditions. Exit conditions

Fig. 4 Vorticity in the wake of a circular cylinder, Re = 100: (a) DPIV measurements, (b) 2-D numerical simulations, (c) computed values of the circulation of wake vorticies from (×) experiments and (●) simulations. This example is typical of the excellent qualitative (vortex size and shape) and quantitative (circulation) agreement now possible for unsteady two- and three-dimensional flows.

Journal of Fluids Engineering

JUNE 1996, Vol. 118 / **239**

are especially interesting since they can create feedback problems upstream in the form of altered upstream initial conditions—acoustic resonance or sloshing modes in the case of the simulation of the free surface. In these cases, direct interaction between the experimentally determined initial condition, wall condition or in-flow condition is impossible due to the unsteady nature of the problem. However, since these extreme boundary conditions usually result in additional effects, companion experiments can be used to tune simulations to eliminate these artifacts and obtain realistic dynamic boundary conditions. For example, studies of free surface deformation, wave generation and wave reflection off the computational boundaries can be studied under realistic experimental conditions. Techniques such as the surface mapping technique can become very valuable in resolving these types of boundary problems.

DNS simulations at low to medium range Reynolds numbers ($2000 <$ Re < 5000) have been helpful to our current understanding of turbulent channel and pipe flows. For example, Kim, Moin and Moser's paper (1987) is one of the best examples of such an achievement, where a comprehensive flow database was used for analysis and providing guidelines for higher Reynolds number experiments. In this respect, Eggels et al. (1994), and Westerweel et al. (1995) have conducted extensive comparisons of DNS, LDV, DPIV and PIV measurements of turbulent pipe flows at Reynolds number of approximately 5000. Figure 6 shows the power spectra of the axial velocity obtained by these four methods. It is interesting to note that DNS results indicate the poor resolution of the selected DPIV and PIV parameters in high wave number ranges. This problem can be solved by reducing the imaging area. On the other hand, at low wave numbers, the short period of DNS calculations results in an underestimation of the power spectra. LDV appears to reflect the flow properties correctly at high and low wave number ranges. However, the LDV information is one-dimensional (only in time) and fails to provide the spatial correlation information which is essential for RANS and LES simulations. DNS can be quite valuable in providing resolution analysis for LES and for experiments (Jimenez, 1994) or guiding experiments in resolving fine flow structures (Visbal, 1994; Lin and Rockwell, 1995).

As Reynolds number increases, a turbulent flow involves either high speed or large scale or both. The current limitation of video technology in providing high speed imaging limits the capabilities of techniques such as DPIV in providing time-resolved temporal behavior of the flow. Spatial resolution can also become an issue, but—at the expense of the dynamic range—this problem can be avoided. For this range, CCD-based whole-field measurement techniques can be used to construct reliable mean and fluctuating flow statistics. For example, length scale correlation of energy-containing eddies, obtained through PIV, can be used to truncate the DNS and computational domain (Le Penven et al., 1985). Such studies would be important in constructing SGS models for large eddy simulation of turbulent flows in medium range Reynolds numbers.

2. High Reynolds Numbers. LES, while very promising for high Reynolds number applications, can become quite expensive when, for example, the wall layers need to be resolved. Simple turbulent boundary layer flow approximations, such as "law of the wall" (Murakami et al., 1985), can be used as the boundary condition to alleviate the fine grid requirements. For more complex 3-D flows, such as junction flows or free surfaces, such approximations do not exist; therefore, SGS modeling cannot be avoided. On the other hand, the majority of SGS models, such as the Smagorinsky model, are based on the assumption of isotropic flow conditions in the wall region. While the Smagorinsky model, based on the isotropy assumption, works well for wall bounded flows (Saddoughi, 1994), its reliable application to more complex flows; such as massively separated flows, jets, wakes, or flows near free surfaces (Sarpkaya et al., 1994);

remains to be verified. Experimental techniques with multi-dimensional capabilities should be used to address the question of anisotropic turbulent viscosity for complex flows through measurements of Reynolds stresses and strain rate fields. In the meantime, methods such as DPIV and LDV can be used to measure dissipation rates which can be used directly in LES models. It is imperative to the problem of turbulence that such interfaces between simulations and scalar field measurements be developed. For example, spectral behavior of free-surface fluctuation such as the one shown in Fig. 3 will be essential in SGS modeling and also for estimating the dissipation rate in the near-surface region.

Regardless of whether a viable solution can be found for SGS modeling, the LES for high Reynolds numbers would still be expensive since it requires the computation and storage of a large quantity of data for the purpose of extracting statistics. In this regard, RANS approaches are the only available methods for obtaining detailed flow information for very high Reynolds number flows. Examples include ship hydrodynamics (Tahara and Stern, 1994) and wind engineering (Rodi 1993). Information that has been obtained by single point measurement in terms of mean quantities and correlations has been instrumental in the development and application of the RANS method to boundary layer problems. However, further development of RANS has been restricted by the lack of knowledge regarding spatial correlation functions for the cases where separated flows or free surfaces are involved. According to the statistical theory of turbulence, spatial correlations provide useful knowledge (Batchelor, 1953; Lesieur, 1986) about the structure of turbulence and can be used in RANS methods. Also, this information can be used to design mathematical models of physical vortical turbulence for RANS methods (Lundgren, 1982; Pullin and Saffman, 1993). Development of such models, based on information that can be obtained from whole field velocimetry techniques, is essential for the further development of classical modeling.

In order to give RANS models predictive capabilities, the need for empirical constants must be removed. One exciting possibility is to incorporate the underlying, driving instability of the flow, based on mean velocities, to obtain a prediction of Reynolds stresses without using any empirical constants (Liou and Morris, 1992). The future development of this method would depend on the construction of amplitude equations that can correctly represent instability characteristics of various shear flows. It is essential that the mean velocity profile and its spatial evolution be incorporated into these amplitude equations. Quantitative whole field velocimetry techniques can readily provide global mean flow information at high Reynolds numbers beneficial to this technique.

Conclusion

In the last two decades, considerable national, human and monetary resources have been redirected to the development of CFD. Despite the phenomenal increase in computing power, the promise of economical, realistic simulation of turbulent flows in practical Reynolds number ranges ($>10^5$) has not been realized. In this respect, the confluence between computational fluid dynamics and experiments, beyond its traditional validation role, becomes a mandatory requirement for progress. In order to materialize this synergism, it is imperative that we develop a common ground between simulations and physical experiments. The digital imaging technique has turned flow visualization from a qualitative tool into a powerful flow diagnostic method. This development in digital imaging technology has created a unique and novel link between the development of experimental and computational approaches that interactively help each other in order to develop a better understanding of the physics of turbulent flows which will lead to subsequent development of models for conducting realistic simulation of industrial-type

flows. For the purpose of discovering new phenomena, experiments remain the most economical tool for fluid mechanics, while simulations, once they have been verified against experiments, are more suitable for producing comprehensive flow databases. Simulations can be used for three-dimensional visualization of flow quantities that the current state-of-the-art flow diagnostic tools are unable to provide.

The computation of physical phenomena without developing a physical understanding can often produce misleading results. On the other hand, misguided experiments can equally contribute to the generation of more questions than answers. These somewhat orthogonal approaches have created two cultures of fluid mechanicians. The continuation of this two-culture mentality, namely experimentalists and numerical analysts who conduct experiments and simulations in isolation, would delay reaching the goals of understanding, modeling and predicting turbulence. To solve this problem, we need to include provisions in our university and government/industrial research policies to accommodate and encourage a new generation of scientists and engineers who understand and appreciate both simulations and experiments.

Acknowledgment

References

Adrian, R. J., 1991, "Particle-Imaging Techniques for Experimental Fluid Mechanics," *Annual Review of Fluid Mechanics,* Vol. 23, pp. 261–304.

Baldwin, W. S., and H. Lomax, 1978, "Thin-Layer Approximate and Algebraic Model for Separated Turbulent Flows," AIAA paper 78-257.

Barnhart, D. H., R. J. Adrian, and G. C. Papen, 1994, "Phase-Conjugate Holographic System for High Resolution PIV," *Applied Optics,* Vol. 3, No. 30, pp. 7159–7170, October 20.

Batchelor, G. K., 1953, *The Theory of Homogeneous Turbulence,* Cambridge UP, England.

Brown, G. L., and A. Roshko, 1974, "On Density Effects and Large Structure in Turbulent Mixing Layers," *Journal of Fluid Mechanics,* Vol. 64, pp. 775–816.

Dabiri, D., and M. Gharib, 1991, "Digital Particle Image Thermometry: The Method and Implementation," *Experiments in Fluids,* Vol. 11, pp. 77–86.

Dimotakis, P. E., 1993, "Some Issues on Turbulent Mixing and Turbulence," GALCIT Report FM 93-1.

Dommermuth, D. G., 1993, "The Laminar Interaction of a Pair Vortex Tube with a Free Surface," *Journal of Fluid Mechanics,* Vol. 246, pp. 91–115.

Eggels, J. G. M., F. Unger, M. H. Weiss, J. Westerweel, R. J. Adrian, R. Friedrich, and F. T. M. Nieuwstadt, 1994, "Fully Developed Turbulent Pipe Flow: A Comparison Between Direct Numerical Simulation and Experiment," *Journal of Fluid Mechanics,* Vol. 268, pp. 175–209.

Fabris, Drazin, D. Marcus, and D. Liepmann, 1995, "Quantitative Experimental and Numerical Investigation of a Vortex Ring Impinging on a Wall," submitted to *Physics of Fluids.*

Ferziger, J. H., 1977, "Large Eddy Numerical Simulations of Turbulent Flows," *AIAA J.,* Vol. 15, pp. 1261–1267.

Ferziger, J., 1993, "Simulation of Complex Turbulent Flows: Recent Advances and Prospects in Wind Engineering," *Journal of Wind Engineering and Industrial Aerodynamics,* Vols. 46 and 47, pp. 195–212.

Frisch, U., and S. A. Orszag, 1990, "Turbulence—Challenges for Theory and Experiment," *Physics Today,* Vol. 43, pp. 24–32.

Germano, M., U. Piomellig, P. Moin, and W. H. Cabot, 1991, "A Dynamic Sub-Grid Eddy Viscosity Model," *Physics of Fluids A,* Vol. 3, No. 7, pp. 1760–1765.

Gharib, M., and A. Weigand, 1995, "Experimental Studies of Vortex Disconnection and Connection at a Free Surface," submitted to *Journal of Fluid Mechanics.*

Gharib, M., and C. Willert, "Particle Tracing: Revisited," (A) AIAA Paper No. AIAA-88-3776-CP, 1935–1943. (B) Chapter 3, *Advances in Experimental Fluid Mechanics, Lecture Notes in Engineering,* Vol. 37, Springer-Verlag, pp. 109–126, 1989.

Henderson, R., and G. E. Karniadakis, 1995, "Unstructured Spectral Element Methods for Simulation of Turbulent Flows," to appear in *Journal of Computational Physics.*

Henderson, R., 1994, "Unstructured Spectral Element Methods: Parallel Algorithms and Simulations," Ph.D. thesis, Princeton University.

Hinze, J. O., 1959, *Turbulence: An Introduction to Its Mechanism and Theory,* McGraw-Hill, New York.

Humphrey, J. A. C., Devarakonda, R., and Queipo, N., 1991, "Interactive Computational-Experimental Methodologies (ICEME for Thermofluids Research: Application to the Optimized Packaging of Heated Electronic Components," *Computer and Computing in Heat Transfer Science and Engineering,* KT. Yang and W. Nakayama, eds., CRC Press.

Jimenez, J., 1994, "Resolution Requirements for Velocity Gradients in Turbulence," *Center for Turbulence Research Annual Brief,* Stanford Univ., AMES Research Center, NASA.

Karniadakis, G. E., and S. Orszag, 1990, "Nodes, Modes and Flow Codes," *Physics Today,* American Institute of Physics.

Kasagi, N., and Y. Sata, 1992, "Recent Development in Three-Dimensional Particle Tracking Velocimetry," *Proceedings of Flow Visualization Conference VI,* Yokohama, Japan.

Kim, J., Moin, P., and Moser, R., 1993, "Turbulence Statistics in Fully Developed Channel Flow at Low Reynolds Number," *Journal of Fluid Mechanics,* Vol. 255, pp. 65–90.

Kline, S. J., Reynolds, W. C., Schraub, F. A., and Runstadler, P. W., 1967, "The Structure of Turbulent Boundary Layers," *Journal of Fluid Mechanics,* Vol. 30, pp. 741–773.

Kolmogorov, A. N., 1941, "The Local Structure of Turbulence in Incompressible Viscous Fluids at Very Large Reynolds Numbers," *Dokl. Nauk. SSSR,* Vol. 30, pp. 301–305, (see e.g., L. D. Landau and E. M. Lifshitz, *Fluid Mechanics,* Pergamon, 116–123, 1959).

Koochesfahani, M., and P. Dimotakis, 1980, "Mixing and Chemical Reactions in a Turbulent Liquid Mixing Layer," *JFM,* Vol. 170.

Launder, B. E., D. P. Tgelepidakis, and B. A. Younis, 1987, "A Second-Moment Closure Study of Rotating Channel Flow," *Journal of Fluid Mechanics,* Vol. 183, pp. 63–75.

Le Penven, L., Gence, J. N., and Comte-Bellot, G., 1985, "On the Approach to Isotropy of Homogenous Turbulence: Effect of the Partition of Kinetic Energy Among the Velocity Components," *Frontiers in Fluid Mechanics,* Springer-Verlag: New York.

Leonard, A., 1985, "Computing Three-Dimensional Incompressible Flows with Vortex Elements," *Annual Review of Fluid Mechanics,* Vol. 17, pp. 523–59.

Leschziner, M. A., 1993, "Computational Modeling of Complex Turbulent Flow: Exceptions, Reality and Prospects," *Journal of Wind Engineering and Industrial Aerodyn.,* Vols. 46 and 47, pp. 37–51.

Lesieur, M., 1989, *Turbulence in Fluids,* Klewer Academic Publishers (2nd ed. 1991).

Liepmann, D., and D. Dommermuth, 1991, "Quantitative Experimental and Numerical Investigation of a Vortex Ring Impinging on a Wall," *Proceedings of APS/DFD,* Scottsdale, AZ.

Lin, J.-C., and Rockwell, D., 1995, "Transient Structure of Vortex Breakdown on a Delta Wing at Angle of Attachment," *AIAA Journal,* Vol. 33, No. 1, pp. 6–12.

Liou, W. W., and P. G. Morris, 1992, "Weakly Nonlinear Models for Turbulent Mixing in a Plane Mixing Layer," *Physics of Fluids A,* Vol. 4 (12), pp. 2798–2808.

Lundgren, T. S., 1982, "Strained Spiral Vortex Model for Turbulent Fine Structure," *Physics of Fluids,* Vol. 25, p. 2193.

Merzkirch, W., 1987, *Flow Visualization,* Academic Press.

Moin, P., and P. Kim, 1982, "Numerical Investigation of Turbulent Channel Flow," *Journal of Fluid Mechanics,* Vol. 118, pp. 341–371.

Murakami, S., Mochida, A., and K. Hiki, 1985, "Three-Dimensional Numerical Simulation of Air Flow Around a Cubic Model by Means of LES," *Journal of Wind Engineering and Industrial Aerodynamics,* Vol. 25, pp. 291–305.

Newman, D., and G. E. Karniadakis, 1995, "Simulations and Models of Flow over a Flexible Cable: Standing Wave Patterns," to be presented at ASME/JSME Fluids Engineering Conf., Hilton Head, SC, Aug.

Pearlstein, A. J., and B. Carpenter, 1995, "On the Determination of Solenoidal or Compressible Velocity Fields From Measurements of Passive and Reactive Scalars," *Physics of Fluids,* Vol. 7, No. 4, pp. 754–763.

Pullin, D., and P. G. Saffman, 1993, "On the Lundgren-Townsend Model of Turbulent Fine Scales," *Physics of Fluids A,* Vol. 5 (1), pp. 126–145.

Raffel, M., M. Gharib, O. Ronneberger, and J. Kompenhans, 1995, "Feasibility Study of Three-Dimensional PIV by Correlating Images of Particles Within Parallel Light Sheet Planes," accepted in *Experiments in Fluids.*

Rizzi, A., and Engquist, B., 1987, "Selected Topics in the Theory and Practice of Computational Fluid Dynamics," *Journal of Computational Physics,* Vol. 72, No. 1, Sept.

Rodi, W., 1993, "On the Simulation of Turbulent Flow Past Bluff Bodies," *Journal of Engineering and Industrial Aerodynamics,* Vols. 46 and 47, pp. 3–9.

Rogallo, and P. Moin, 1984, "Numerical Simulation of Turbulent Flows," *Annual Review of Fluid Mechanics,* Vol. 16, pp. 99–137.

Roshko, A., 1992, "Instability and Turbulence in Shear Flows," *Theoretical and Applied Mechanics.*

Saddoughi, S. G., and S. V. Veeravalli, 1994, "Local Isotropy in Turbulent Boundary Layers at High Reynolds Numbers," *Journal of Fluid Mechanics*, Vol. 268, pp. 333–372.

Sarpkaya, T., and Suthon, P., 1991, "Interaction of a Vortex Couple with a Free Surface," *Experiments in Fluids*, Vol. 11, pp. 205–217.

Sarpkaya, T., 1988, "Computational Methods with Vortices: The 1988 Freeman Scholar Lecture," ASME JOURNAL OF FLUIDS ENGINEERING, Vol. 111, pp. 5–52.

Sarpkaya, T., M. Magee, and C. Merril, 1994, "Vortices, Free Surface and Turbulence," *Proceedings of ASME Fluids Engineering Division Summer Meeting*, Lake Tahoe, Nevada, June 19–23, RED-Vol. 181.

Singh, A., 1991, "Optic Flow Computation," *IEEE*, Computer Society Press.

Speziale, C. G., 1990, "Discussion of Turbulence Modeling: Past and Future," *Lecture Notes in Physics*, ed. J. L. Lumley, Vol. 357, Springer-Verlag: New York, pp. 354–368.

Tahra, Y., and F. Stern, 1994, "Validation of an Interactive Approach for Calculating Ship Boundary Layers and Wakes for Nonzero Frouhe Numbers," *Journal of Computers and Fluids*, Vol. 23, No. 6, pp. 785–816.

Visbal, M. R., 1994, "Onset of Vortex Breakdown Above a Pitching Delta Wing," *AIAA Journal*, Vol. 32, pp. 1568–1575.

Westerweel, J., A. A. Draad, J. G. van der Hoeven, and J. van Oord, 1995, "Measurement of Fully-Developed Turbulent Pipe Flow with Digital Particle Image Velocimetry," submitted to *Exp. Fluids*.

Westerweel, J., 1993, *Digital Image Velocimetry: Theory and Application*, Delft UP, Delft, Netherlands.

Willert, C., and M. Gharib, 1991, "Digital Particle Image Velocimetry," *Experiments in Fluids*, Vol. 10, pp. 181–183.

Zhang, C., and D. Yue, 1995, private communication.

Zhang, X., and C. S. Cox, 1994, "Measuring the Two-Dimensional Structure of a Wavy Water Surface Optically: A Surface Gradient Detector," *Experiments in Fluids*, Vol. 17, pp. 225–237.

Zhang, X., D. Dabiri, and M. Gharib, 1996, "Optical Mapping of Fluid Density Interfaces: Concepts and Implementation," *Review of Scientific Instruments.*, May, Vol. 67.

APPENDIX

When one starts talking about turbulence, one gets pushed immediately into a statistical way of thinking—what is the mean velocity, what are the r.m.s. turbulence fluctuations, how large are the Reynolds stresses? Statistical quantities come from long averages relative to some fundamental time scale of the flow, so it seems like an interesting question to ask what the computational time scale is to compute a turbulent flow versus the laboratory time scale to generate one? Consider this for one of the classic problems in bluff body wakes: flow past a circular cylinder.

The wake of a circular cylinder becomes "turbulent" at a relatively low Reynolds number $Re = Ud/v$ of a few hundred. It is fully turbulent at $Re = 1000$ but still accessible to direct numerical simulations because the range from $O(d)$ to the dissipation scale is fairly narrow, say three to four decades in an energy scale based on the kinetic energy per unit volume of the mean flow. This is an ideal case for comparing simulations and experiments because both should be well within our current capabilities.

First, consider the numbers for the experiment. Assume the working fluid is air ($v = 1.5 \times 10^{-5}$ ms/s), and the tunnel velocity is a steady 5 m/s. A cylinder with diameter $d = 2.5$ mm can be made from brass and supported to prevent vibrations, giving a value for Re that is $O(1000)$. We know the dimensionless shedding frequency or Strouhal number is St ≈ 0.2, so the dimensional shedding frequency is $f = $ St $U/d = 400$ Hz. In the wind tunnel, the fundamental time scale for the cylinder wake is 0.0025 seconds.

What about a simulation of the same flow? Consider a state-of-the-art calculation with a highly accurate multi-domain spectral method. On a 64 processor Intel Paragon with a sustained rate of 0.5 Gflops, such a calculation can integrate a model with $O(10^6)$ degrees of freedom ("mesh points") as fast as 5 seconds per time step. Moving up the scale, that is 3 hours per shedding cycle (2100 time steps); 4 shedding cycles per day (this is a shared facility, so you can only count on 12 hours of dedicated time); 25 shedding cycles per week; or 100 shedding cycles in a month. Of course, that is a month of "real time" as opposed to a month of computer time, but it is an accurate picture of what might be expected at a national supercomputing center. Here is the bottom line: one month of high-performance computer-simulated flow equals 0.25 seconds of experimentation time in the wind tunnel, for this case. Even assuming we have a dedicated facility, it places the ratio of time scales at roughly 4,000,000:1. It is important to keep in mind that simulations provide comprehensive flow information (e.g., unsteady pressure field) which might not be attained through experiments.

P. Bradshaw

Thomas V. Jones Professor of Engineering,
Mechanical Engineering Department,
Stanford University,
Stanford, CA 94305

B. E. Launder

Professor,
Mechanical Engineering Department,
University of Manchester Institute of
Science and Technology,
Manchester,
England

J. L. Lumley

Willis H. Carrier Professor of Engineering,
Sibley School of Mechanical and
Aerospace Engineering,
Cornell University,
Ithaca, NY

Collaborative Testing of Turbulence Models

(Data Bank Contribution)*

This is a brief report on a special project. Data from experiments and simulations were collected and distributed to over 100 turbulence modelers and other participants in 16 different countries. The modelers mailed the results of their "predictions" back to the organizers for distribution to all the participants for comment. The data covered most types of turbulent flow, compressible and incompressible, but the emphasis was on complex (strongly nonequilibrium) flows. No model was capable of predicting the full range of flows to good engineering accuracy, but stress-transport models seemed to perform best. The exchange of views and results alone has been of real benefit to modelers.

Introduction

This international undertaking was a sequel to the Stanford 1980–81 Conference on Complex Turbulent Flows (Kline et al., 1982), in which Reynolds-averaged prediction methods were compared with selected experimental data. The present project on Collaborative Testing of Turbulence Models (hereafter "CTTM") was conducted by mail, to allow time for modest improvements to be made to prediction methods and for dialog to be established between participants. Our conclusion is, alas, much the same as that of the 1980–81 meeting: no current Reynolds-averaged turbulence model can predict the whole range of complex turbulent flows to worthwhile engineering accuracy. Stress-transport models ("second-moment" closures") did appear somewhat better than eddy-viscosity methods (two-equation models, etc.), but not enough to warrant the abandonment of eddy-viscosity models. It seems likely that the dissipation transport equation, used to provide a length (or time) scale in both two-equation and stress-transport models, is a major source of error. One of the main alternative "length scale" transport equations, the Wilcox ω equation, appears to perform better but has not been widely tested in complex flows.

The project was funded by no less than four US agencies— Air Force Office of Scientific Research, Army Research Office, NASA, and Office of Naval Research. This paper is the top layer of a stack of increasingly detailed documents, available from Stanford as specified in Appendix 1. There is no room in a journal paper for a complete presentation of the predictions or even a worthwhile number of plots, so that the justifications for our conclusions are available only in the lower layers. Also, some of the most useful results of the Collaboration were in information exchange, notably corrections of errors in models, codes or concepts, which it would be time-wasting and tactless to discuss in detail.

Turbulence Models

Full solutions of the time-dependent Navier-Stokes equations ("direct numerical simulation," or DNS), are restricted to very

low Reynolds numbers; and although large-eddy simulations (LES) are now competitive with DNS in accuracy at an order of magnitude less cost, even LES is currently too expensive for routine calculations. Therefore, current engineering prediction methods are based on Reynolds-averaged (more simply, time-averaged) equations, with models for the unknown Reynolds stresses which appear as the result of time-averaging the nonlinear Navier-Stokes equations. Note that a turbulence model is by definition semi-empirical: quantitative data from experiments or other sources of inspiration (including, of course, numerical simulations) must be fed in at some stage.

Models for Reynolds stresses fall into two classes: "eddy-viscosity" relations between the stresses and the mean velocity gradients at the same point in space; and models of the further unknowns in the exact partial-differential transport equations for the Reynolds stresses. The latter equations make it clear that the Reynolds stresses at a given point depend on the whole history of the flow: eddy viscosity is conceptually unsound.

Eddy-viscosity models have been successful enough to be widely adopted in industry: the effect of history on the local behavior of a turbulent flow is small if the mean flow changes only slowly with distance downstream. However, many real-life turbulent flows change rapidly in the streamwise direction, or are perturbed by some external effect. In such "complex" or "non-equilibrium" flows, eddy-viscosity models can give misleading results, because the turbulent stresses change much less rapidly than the mean flow. Models based directly on the Reynolds-stress transport equations ought to perform much better than eddy-viscosity models in complex flows, and one of the main objects of CTTM was to see if this was true in practice.

The models used included one or more examples of

- algebraic eddy-viscosity or mixing-length formulas
- one-equation eddy-viscosity-transport models
- two-equation eddy-viscosity models, with variable-pairs (k, ϵ), (k, kL), (k, ω), or (k, τ), where k is the turbulent kinetic energy, ϵ is its dissipation rate, and the other quantities are alternative length or time scales, all expressible as $k^m \epsilon^n$. The different choices lead to essential differences in the equations which cannot be removed by adjustment of coefficients. Wilcox (1993) suggests that ω ($m = -1$, $n = 1$) is near the optimum. There was also one Algebraic Stress Model.
- stress-equation models, solving PDEs for some or all of the Reynolds stresses. All except the Wilcox multiscale model

(which is a somewhat truncated stress-equation model) used the ϵ transport equation, nominally modeled in the same way as for two-equation methods, to provide a length scale.

• large-eddy simulation. The presence of an LES method in the Collaboration is a landmark: LES may soon become a serious rival of Reynolds-averaged models.

To compute wall-bounded flows, either the main turbulence model must be extended to low local Reynolds number (small $u_\tau y/\nu$ or small $k^2/\epsilon\nu$) or the main calculation must be matched to a function specifying the law of the wall, slightly outside the viscous wall region. The effect of the different "wall treatments" was checked, early in the Collaboration, by asking for comparisons with the standard law of the wall (see below).

Descriptions of the individual models are contained in the project newsletters (see Appendix 1: many models have matured since those descriptions were written).

Organization of the Collaboration

In the early stages, we planned a conference on the lines of the 1981 Stanford meeting, but Dr. D. M. Bushnell of NASA Langley Research Center pointed out that a collaborative effort conducted by correspondence (including mailing of tapes and disks, plus Fax and electronic mail) would allow better interaction, optimisation and discussion than a "sudden death" conference.

Development of turbulence models since 1981 has not been spectacular, and the few new types of model were not well represented in CTTM. However, significant advances have been made, partly in numerics (including generally-improved grid independence due to the availability of larger, cheaper computers), and partly in ensuring proper limiting behavior in special cases (e.g., "realizability," and the two-component limit at a solid surface). The number and quality of test cases has improved considerably, mainly because the use of microcomputers in the laboratory has greatly increased the rate of data taking and allowed more complicated flows to be studied: also, DNS results are now generally accepted as equivalent to experimental data. Thus the time was ripe for a new test of turbulence models.

We distributed experimental data and simulation results to all model developers who responded to our invitation, on microcomputer disk. The data sets were selected by the organizers after informal consulations: there was no equivalent of the 1980 part of the 1980–81 conference, a discussion of possible test cases. In the event, by no means all the available data were used, but a data library has been established (see Appendix 2).

The results of each model for the specified test cases were returned to the organizers, and the graphs were redistributed to all the modelers, plus some experimenters and other experts (the total peaked at about 120), for comments. The administrative effort was considerable. The test cases were sent out in several packages of increasing difficulty. All were for simple geometries (not excluding complex physics): we realised that the most up-to-date turbulence models would probably be the least flexible numerically (perhaps coded only for rectangular meshes). Nevertheless a number of modelers did not report results for the final set of complex flows: we have no way of knowing how many were unable to complete the calculations, and how many did not choose to report poor results.

The reaction times of modelers proved to be much longer than anticipated and, furthermore, comparatively few sets of detailed comments were received from the collaborators. One reason for slow progress or complete withdrawal, not clearly foreseen by the organizers or the agencies, is that funding of turbulence modeling in the 1990s is more closely tied to the sponsor's interests than it was ten years ago, making it difficult to divert effort to a general-interest project (although the U.S. agency sponsors all said they would be sympathetic to requests to do this). Another reason for the failure to keep deadlines

was that comparisons with data prompted many modelers to improve their models or numerics: this was the main reason for conducting a "mail order" operation, but made it very difficult to administer.

As a result of the poor response, the number of different computations of each of the final group of complex flows is too small for firm conclusions to be drawn about the performance of the different types of model: clearly there is a danger of doing injustice to a model type that is mainly represented by incompletely-developed codes.

Numerical Accuracy

We did not require explicit demonstrations of grid independence, believing that it would not be reasonable to expect this for each flow. We did, however, use the flat plate "entry" cases as a check on accurate reproduction of the law of the wall: the commonest example of inadequate resolution is too coarse a grid in the viscous wall region or improper use of a wall function. A good deal of time was taken up in sorting out the difficulties—not all strictly numerical—that did appear, and considerable improvements in some of the codes resulted.

It was suggested by others at the start of the project that we might be overwhelmed by large numbers of people using the standard k, ϵ model. In fact there were several examples of this popular model with standard coefficients but with different wall-layer treatments or numerics, and comparisons proved very useful.

Test Cases and Results

The February 1990 "Entry Cases." The first set of test cases to be sent out was simply a request for predictions of skin-friction coefficient and Stanton number in boundary layers in zero pressure gradient at a single Reynolds number of 10^4 based on momentum thickness: (i) in incompressible isothermal flow, (ii) incompressible flow with small temperature difference, (iii) flow over an adiabatic wall at a free-stream Mach number of 5.0, (iv) low-speed flow over a wall at 6 times the free-stream temperature, i.e., about the same temperature ratio as for case (iii). The results for cases (i) and (ii) immediately identified any models with severe accuracy problems, (iii) was a simple check of general ability to predict compressible flow, and (iv) allowed discrepancies in (iii) to be attributed either to high-Mach-number difficulties as such, or inability to handle large density differences at any speed.

Some of the compressible-flow methods were not used on case (i) or the later incompressible cases. This was unfortunate, because the incompressible data base is much larger, more complete and generally more reliable. Some codes will indeed not run at zero Mach number, but extrapolation back to zero Mach number is fairly straightforward and was encouraged by the organizers.

Most of the results for flat-plate c_f in (i) were fairly close to the data consensus of 0.00264 (which has an uncertainty of no more than ± 2 percent). An interesting spinoff from our checks of wall-treatment accuracy was a plot of predicted c_f against I_{100}, the predicted value of U/u_τ at $u_\tau y/\nu = 100$ (which is somewhere in the middle of the logarithmic region at $Re_\theta = 10^4$). Here u_τ is the friction velocity $\sqrt{\tau_w/\rho}$. The recommendations of Coles (Coles and Hirst, 1969) for the logarithmic-law constants ($\kappa = 0.41$, $C = 5.0$) give $I_{100} = 16.23$. The range of predicted values of I_{100} was quite large (initially between 15.2 and 17.5, a 14 percent band), indicating a wide variety of wall-treatment results. Furthermore there was little trace of negative correlation between c_f and I_{100}: that is, low/high results for c_f could not generally be attributed to high/low predictions of I_{100} by the wall treatment, but must have arisen in the outer layer. It appears that some models may have been optimised for flat-plate c_f by adjusting the wall treatment without checking confor-

mity with the universal law of the wall. We asked modelers to justify the departures from Coles' recommendations for the law of the wall, but the only specific response was from Fernholz who based his preference for $\kappa = 0.40$, $C = 5.1$ ($I_{100} = 16.61$) on the data analysis in the series of AGARDographs on compressible flow data by himself and co-authors.

The "August 1990" Test Cases. (Full details of the test cases, including references to publications, are given in the project newsletters.)

(i)   Thin shear layers and homogeneous flows.

The incompressible cases began with the Samuel and Joubert boundary layer in increasing adverse pressure gradient, which proved a hard case at the 1980–81 meeting. Results here were generally better, though the k, ϵ method overpredicted turbulent mixing in general, and skin friction in particular, as before. The stress-transport models, and also the k, ω and multiscale models, gave much better results.

Direct simulations of a constant-pressure boundary layer (Spalart, 1988) and a two-dimensional duct (Kim et al., 1987) were included, and modelers were asked to compare the highest order quantities they modeled (e.g. dissipation or triple product). This use of simulation results is another landmark in turbulence model testing. These simulations of simple flows were particularly useful in assessing wall treatments.

Homogeneous turbulence (strained and unstrained) was represented by experimental data. Some of the dissipation data proved unreliable, and most modelers adjusted the initial dissipation so as to reproduce the initial TKE decay rate from the experimental data. With this legitimate amendment, most models predicted the homogeneous turbulence cases quite accurately: bear in mind that many models have been adjusted to fit (unstrained) homogeneous turbulence data.

For the free shear layers (round jet, plane jet, and plane mixing layer) modelers were simply asked to compare their predicted spreading rate with data correlations. One object was to discover the status of the "round-jet/plane-jet anomaly," the curious fact that many codes cannot produce good predictions of both flows with a single set of coefficients. The anomaly was still present in some codes: part of the explanation is that the streamwise transport of dissipation, which would be neglected if the boundary-layer approximation was made, is in fact quite large, so that an elliptic code is needed (Baz et al., 1992). This may be an artifact of current dissipation-equation models but is certainly real according to the rules of the game. A converse difficulty is that, to calculate thin shear layers with specified pressure distributions, users of fully-elliptic codes have to adjust the normal velocity on a fictitious upper boundary by trial and error if the full experimental geometry is unavailable.

(ii)   Backward-facing steps.

These (data of Driver and Seegmiller, 1985) were the only complex flows attempted by enough modelers for different types of model to be compared. Key quantities are the distance to reattachment, and the maximum negative surface shear stress in the separated region (a measure of the strength of the recirculation). It has been pointed out by Jovic and Driver (1993) that $(-c_f)_{max}$ varies strongly with Reynolds number: evidently, predicting it is a severe test of a near-wall model. Most methods underpredicted the reattachment distance x_r in both cases: for the step with the opposite wall inclined at 6 deg, where x_r is $8.1h$, 13 out of 15 predictions were too low, the range being $4.8h$ to $8.95h$, while for the parallel-wall case ($x_r = 6.2h$) 10 out of 11 predictions were low, the range being $4.5h$ to $6.5h$. $(-c_f)_{max}$ predictions were scattered over a range of between two and three to one in both cases, most of the results for the parallel-wall case being low, while over- and underpredictions were about equal in number for the 6 deg case. A given model generally erred in the same way in both flows. Curiously there was a slight tendency for low x_r (too much mixing) to be associated with low $(-c_f)_{max}$. Modelers were asked to continue

the calculations to 32 step heights downstream of the step, to see how well the models predicted recovery, but computing costs prevented some from doing this.

It was not possible to rank the different types of model for accuracy: there were good and bad examples of each. The standard (and near-standard) k, ϵ models did badly (too much mixing), but Rodi and Scheuerer's "two-layer" model (k, ϵ with a single equation in the wall region) was much better. Leschziner's family of stress-transport models produced widely differing predictions, especially for the 6 deg. case. The best results were those of the k, ω model (computations by F. Menter of the Marvin group at NASA Ames Research Center), overpredicting x_r by about 5 percent in each case, with $(-c_f)_{max}$ overpredicted by 10 percent for the parallel-wall case and 20 percent for the inclined wall. The k, ω model overpredicted the peak shear stress at $x = 32h$ by 15 percent for the 6 deg wall case but underpredicted by 10 percent for the parallel wall case. The multiscale model was not tried on this flow: in thin shear layers it gave results close to the k, ω method and one would expect its advantages, if any, to appear in complex flows.

(iii)   Compressible flows.

These included a second set of "entry" cases, requiring prediction of skin friction and heat transfer in constant-pressure boundary layers at free-stream Mach numbers of 2, 3, 5, and 8, with temperatures down to 0.2 of the adiabatic-wall temperature. The corresponding "data" were simply the predictions of the Van Driest II skin-friction formula, which is still regarded as an acceptable data correlation. Many of the models explicitly or implicitly use the Van Driest transformation: in the inner layer, it is equivalent to the mixing-length formula. Some of the compressible flow models were evidently not intended for such high Mach numbers and/or low temperatures and performed very badly.

The requirement for compressible mixing layer computations was to plot spreading rate against convective Mach number. (Convective Mach number is not quite a unique parameter but is adequate to distinguish present-day models.) As expected, only models with empirically-adjusted compressibility terms could reproduce the observed decrease in spreading rate with Mach number. The status of compressible-flow modeling is changing rapidly at present, and warrants a full review in a few years' time.

The final compressible case was a boundary layer in adverse pressure gradient (Fernando and Smits) at $M \approx 3$. The three sets of results submitted for this case, from an "integral" model, a k, L model and a k, ϵ model, were all acceptably accurate: it seems that turbulence models calibrated for low-speed flow will deal satisfactorily with distributed pressure gradients at moderate supersonic speeds. We did not request a calculation of a shock/boundary layer interaction. Also, we were not able to find any satisfactory test case for a hypersonic ($M > 5$) boundary layer in distributed pressure gradient, and Settles and Dodson (1993) have recently confirmed this disconcerting gap in our experimental knowledge of turbulent flows.

Complex Flows—The "August 1991" Cases. Results for the August 1990 cases were slow to come in, and many model changes were made (modelers were asked to repeat the "entry" test cases if they changed the model). The final set of test cases was sent out a year later, and comprised: a "sink-flow" boundary layer simulation (Spalart), run at Reynolds numbers approaching reverse transition and therefore a severe test of near-wall models; boundary layers on convex (Alving et al.) and concave (Johnson and Johnston) surfaces; two-dimensional (Castro and Bradshaw) and axisymmetric (Cooper et al.) inpinging "jets" (better described as mixing layers); three three-dimensional flows, namely a swirling jet (Morse), an idealized swept wing (Van den Berg et al.) and a simulation of an approximation to the turbulent Ekman layer (Spalart); and a "one-dimensional" time-dependent oscillating flow (Sumer et al.).

These test cases were chosen to be computationally simple, although a full Navier-Stokes code was needed for most of them. Unfortunately the number of results reported for each test case was too small for meaningful comparisons between models. It was, however, clear that two-equation models behaved poorly in the more rapidly-changing flows. Stress-transport models gave better results but were still not good for the impinging jet flows. Results for the three-dimensional cases were too few for any conclusions to be drawn.

A clear conclusion is that none of the models could reproduce the effects of streamline curvature (curved-surface boundary layers, impinging jets) better than qualitatively. Evidently ad hoc corrections for curvature are still needed, but it is difficult to make them properly independent of the axes.

Conclusions

We have to offer the same unwelcome conclusion as that of the 1980–81 Stanford meeting: no current turbulence model gives results of good engineering accuracy for the full range of flows tested. That range was smaller than in 1980–81, but generally more demanding.

The results confirm that models using the dissipation-transport equation perform rather badly in boundary layers with pressure gradients, a comparatively simple class of flow: both here and in the backward-facing step flows, Wilcox's equation for ω (equivalent to ϵ/k) seemed to be an improvement but it was not used on the final set of complex-flow test cases.

A defect of even the highest-order (stress-transport) models is an inability to predict the effects of streamline curvature without empirical correction factors.

A major source of confusion in comparing results for complex flows was scattered predictions for simple flows; many models had simply not been adjusted to compute such flows accurately, in particular to reproduce the "law of the wall." The Collaboration certainly had a good influence here. Indeed, probably the most valuable part of the Collaboration is that the world's turbulence modelers have had the chance to exchange quantitative results and qualitative ideas, and to compare their models with independently-chosen test cases as a preliminary to applying them to predictions of real-life turbulent flows.

Acknowledgments

We wish to thank the sponsors for their moral, as well as financial, support for the project, which took far longer to complete than we had envisaged. We are grateful to the many experimenters who sent us machine-readable data, now permanently available in the Data Library. It is a pleasure to record that the collaborators, in many cases communicating in a language not their own and sometimes in the face of serious political difficulties, were without exception patient and polite. Dr. P. G. Huang, Prof. W. Rodi, and Dr. G. Scheuerer were particularly helpful in performing trial calculations and in giving advice on numerical methods.

References

Baz, A. El, Craft, T. J., Ince, N. Z., and Launder, B. E., 1992, "On the Adequacy of the Thin-Shear-Flow Equations for Computing Turbulent Jets in Stagnant Surroundings," Manchester University, England, UMIST Rept. TFD/92/1.

Coles, D., and Hirst, E. A., (eds.), 1969, *Computation of Turbulent Boundary Layers*, Vol. 2, Thermosciences Division, Mech Engg Dept, Stanford.

Jovic, S., and Driver, D. M., 1993, "Reynolds-Number Effect on Skin Friction in Separated Flows Behind a Backward-Facing Step," paper in draft.

Kline, S. J., Cantwell, B. J., and Lilley, G. M. (Eds.) 1982, *Complex Turbulent Shear Flows: Comparison of Computation and Experiment*, Thermosciences Division, Mech Engg Dept, Stanford University.

Settles, G. S., and Dodson, L., 1993, "Hypersonic Turbulent Boundary-Layer and Free Shear Database," NASA Contractor Report 177610.

Wilcox, D. C., 1993, *Turbulence Modeling for CFD*, DCW Industries, La Canada CA.

APPENDIX 1

Further information is available in several "layers":

1. A more detailed summary of the project, including a summary of the test cases, tabulated results and an address list for those participants who were still active at end of March 1992, is available as an expanded version of the December 1992 Final Report to the sponsors.

2. Newsletters numbers 1 through 7 (total about 500 pages) which contain full details of the project including selected graphs of results as submitted by the modelers. In some cases more details were submitted than actually specified by the organizers, and the extra graphs are on file at Stanford.

3. Description of the JFE Data Bank. Data distributed to the collaborators (but not all used) comprised: about 45 test cases from the 1980–81 meeting, replacements for many of these, five compressible flows selected from AGARDograph 315, and a set of nine complex-flow cases including simulation results. A further selection of 16 test cases was made in 1992: the data are mainly as supplied by the originators, without editing at Stanford. The final group of 16 cases is also unedited but available electronically.

Paper copies of *text* material (much of which was never available electronically) can be obtained from Bradshaw at Stanford University (address above): the larger items will be charged for at the cost of reproduction, handling and mailing (approx. 7.5 cents/page). Requests for information about the latest versions of the models, and for further information about the test cases, should be directed to the originators and not to Stanford, but Stanford can supply addresses if needed.

APPENDIX 2

The JFE Data Bank "Data Library"

This collection of experimental data and simulation results, totalling about 10MB of information, was originally made available on 1.2MB 5-$\frac{1}{4}$ in. MS-DOS floppy disk or 1.44MB 3-$\frac{1}{2}$ in. MS-DOS diskette and for convenience each set in the JFE Data Bank is referred to below as a "disk." All the data are in the public domain. The library falls into four parts, available separately:

(i) Hard-copy description of the library (enlarged self-contained version of this Appendix).

(ii) The data originally distributed (on six 5$\frac{1}{4}$ in. 1.2 MB disks) to modelers taking part in the Collaboration, containing edited data for many more cases than were actually used. Part (i) of the library is included as an ASCII file.

(iii) Sixteen further selected, but mainly unedited, cases from the bank of undistributed data (equivalent of five 5-$\frac{1}{4}$ in. 1.2 MB disks). This selection is not to be regarded as a definitive choice, but a set which happened to interest a particular expert (not one of the organizers).

(iv) the remainder of the data bank, "as-is": communication with the originators is advised before the data are used.

Disks 1–6 of the original distribution contain files which list the cases and contain running instructions for the more difficult cases actually used in the project; the data files for each test case contain some extra information. However the library does not contain full descriptions of the experiments: these are available either in the references quoted or from the experimenters.

We distributed the data from the 1980–81 meeting (Kline et al., 1982) unaltered (on Disk 1 for incompressible flow and Disks 2 and 3 for compressible flow) and in full except for five very long files. These exceptions are 0411 (circular cylinder), 0441 (stalled airfoil), 0511 (wing-body junction), 0512 (curved duct) and 8602 (shock/BL interaction): they can be furnished on request. All files have the same names as the

1980–81 cases, with prefix "F," e.g. F0141 for 1980–81 case 0141, Samuel/Joubert boundary layer. For the 1980–81 cases actually used in the Collaboration, we distributed unpacked and annotated data: these files are mostly on disk 4 onward, and have suffix "A": for example, unpacked and interpolated data for the 1980–81 case 0141 are on file F0141A. Some of the 1980–81 cases were ignored in favor of more recent data sets for similar configurations. These and other new cases are in the format supplied by the originators, but with some editing to produce reasonable uniformity.

Disk 5 contains selected test cases from AGARDograph 315 "A survey of measurements and measuring techniques in rapidly distorted compressible turbulent boundary layers" by H. H. Fernholz, P. J. Finley, J. P. Dussauge, and A. J. Smits. The complete data are available from NASA Sci. and Tech. Info. Ctr., phone (301) 621-0204, or from the AGARD National Centers listed on p. 1–3 of AGARDograph 315.

Disk 6 contains new complex flow data, from simulation and experiment, and some edited data from 1980–81, as used in the "August 1991" test cases.

B. J. Boersma
PhD-Student.

F. T. M. Nieuwstadt
Professor.

Laboratory for Aero and Hydrodynamics,
Rotterdamseweg 145,
2628 AL Delft,
The Netherlands

Large-Eddy Simulation of Turbulent Flow in a Curved Pipe

In this paper, we use Large-Eddy Simulation (LES) to compute a fully-developed turbulent flow in a curved pipe. The results allow us to study how the curvature influences the mean velocity profile and also various turbulent statistics. We find reasonable agreement with the few experiments that are available. Our simulation also allows a detailed study of secondary motion in the cross section of the pipe which are caused by the centrifugal acceleration due to the pipe curvature. It is known that this secondary motion may consist of one, two, or three circulation cells. In our simulation results we find one circulation cell.

1 Introduction

A study of turbulent flow in curved pipes is of great practical importance. Pipes with bends occur in almost any flow appliance or equipment and for its design or operation data on the flow parameters are required. For instance, the increase in pressure loss due to a bend must be known in order to calculate the total resistance of a pipeline. Furthermore, a bend disturbs the flow due to the generation of secondary circulations. This upsets the axial flow pattern and, consequently, the reading of a flow meter which is positioned too close to a bend.

The flow in a bend is influenced by a centrifugal force due to the curvature. This centrifugal force is, in principle, balanced by a pressure gradient in the plane of the bend. However, near the wall where the velocity is small, this pressure gradient can no longer be balanced by the flow and, consequently, the fluid is forced inward, i.e., toward the center of the bend. Due to continuity, the rapidly moving central part of the flow is forced outward. The result is a so-called "secondary" flow in the plane perpendicular to the mean flow and we already have referred to this effect above. If the curvature is significant so that the secondary circulation sufficiently strong, the axial velocity profile will be completely altered with respect to a straight pipe and a considerable increase in drag is observed. The magnitude and shape of the secondary motion depends on the Dean number of the flow which is defined as:

$$\text{De} = \kappa^{0.5} \, \text{Re} \qquad (1)$$

where κ is the inverse radius of curvature non-dimensionalised with the pipe diameter and Re is the Reynolds number based on the bulk velocity and the diameter.

An extensive amount of work has been done both on developing curved pipe flows, i.e., a flow influenced by the entrance length and on fully-developed flows where the flow is independent of the entrance length. A fairly complete review has been provided by Berger et al. (1983) and by Ito (1987). For more recent studies, we refer to Azolla et al. (1986), Anwer and So (1993), and Anwer et al. (1989). These studies are mainly experimental and they report on measurements of mean velocity profiles, turbulent statistics, and sublayer bursting. With respect to numerical modelling, we can mention Patankar et al. (1974) who solve the parabolic Navier-Stokes equations for developing flow in a curved pipe using a two-equation $k - \epsilon$ turbulence model. Recently, Lai et al. (1991) performed a similar computation however, with a Reynolds stress model. The parabolic equations used in these references are only applicable for pipes

with a very small curvature. In pipes with a dimensionless curvature κ^{-1} of, say $\kappa > 0.1$, significant elliptic effects are present (e.g., Ito, 1987) and the parabolic equations can no longer be used.

Only very few experimental investigations exist of the secondary circulation patterns in a turbulent curved pipe flow. The reason is that it is very difficult to measure the secondary flow velocities, of which the magnitude is less than 10 percent of the mean axial velocity (see Bradshaw, 1987). Based on the experimental studies carried out so far, Anwer and So (1993) conclude that there may be one, two, or three secondary cells present in the cross section of the pipe. The number of cells depends on the entrance length and also on the Dean and Reynolds number of the flow. Anwer and So (1993) characterize the secondary motions in the following way: a so-called Dean cell is found near the pipe wall at the inside of the bend. This cell is directly driven by the centrifugal force and is therefore always present. A second cell may form near the pipe center as a result of a local imbalance between the centrifugal force and the pressure gradient. Finally, a third cell can sometimes be found at the outside of the bend. Its formation is attributed to the anisotropy of the turbulent normal stresses and their gradients. The second cell is only present in developing flow and the third cell is only found in a flow with a rather high Dean number.

In the aforementioned study of Lai et al. (1991), in which a computation is performed with a Reynolds-stress model in combination with a near-wall correction and symmetry conditions at the half plane of the pipe, one finds three secondary cells. The results obtained with this model agree qualitatively with the measurements carried out by Anwer and So (1993), but no quantitative comparison has been made.

It will be clear that there are a number of interesting flow phenomena but at the same time also a lack of detailed data for the problem of a curved turbulent pipe flow. Therefore, the objective of the present paper is to present such data with the aid of a LES. Our study is restricted to a fully-developed curved pipe flow, because in that case the in- and outflow boundary conditions can be approximated as periodic. Such boundary conditions are rather straightforward to implement in a LES code, whereas the correct boundary conditions for a developing flow are still far from being solved.

As outcome from our LES computations, we will present data on the various turbulence parameters, such as the turbulence intensities and Reynolds stresses. In addition, we will discuss how these statistics are influenced by the curvature. Simulation results will be also given for the secondary flow patterns.

2 Governing Equations

The coordinate system used in the computations in a toroidal system (see Fig. 1). The metric of this system is given by Germano (1982):
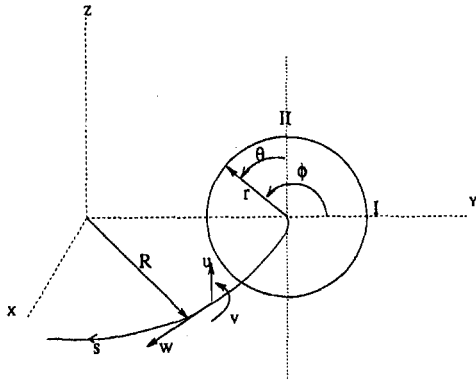
Fig. 1 The system of toroidal coordinates defined along the curve s. The I and II indicate the two planes in which we will present our simulation results.

$$\mathbf{dx} \cdot \mathbf{dx} = dr^2 + (rd\theta)^2 + (1 + \kappa r \sin \theta)^2 ds^2 \qquad (2)$$

where dr, $d\theta$, ds are the infinitesimals in the radial, tangential and axial direction, and κ stands for the inverse radius of curvature. With the metric given by Eq. (2) one can obtain the scale factors h_1, h_2, h_3 (e.g., Batchelor, 1967):

$$h_1 = 1, \quad h_2 = r, \quad h_3 = 1 + \kappa r \sin \theta \qquad (3)$$

With these scale factors it is rather straightforward to derive all the terms in the continuity equation and in the Navier-Stokes equations (e.g., Batchelor, 1967). The governing equations are non-dimensionalized with as scaling variables the pipe diameter D, the mean friction velocity U_*, and the dimensionless time D/U_*. The mean friction velocity U_* is here defined as

$$U_* = \frac{1}{2\pi} \int_0^{2\pi} u_*(\theta) d\theta \qquad (4)$$

where $u_*(\theta)$ is the square root of the wall shear stress divided by the mass density of the fluid.

3 Large Eddy Simulation

Any turbulent flow consists of a range of flow scales (eddies). In a LES, the small eddies are removed from the problem by a spatial filtering procedure and the remaining large scales are solved explicitly. The filtered variables are often called the resolved scales, and the scales (eddies) smaller than the filter the subgrid scales. This filtering technique is inspired by the fact that large eddies are geometry or flow dependent while small eddies are more or less universal, i.e., geometry independent. Therefore, a model for the small scales (the so-called subgrid model) can be formulated, which may not depend strongly on the flow geometry. Moreover, the energy in the subgrid scales is small by definition so that even a not completely correct subgrid model will have only minor influence on the large scales.

Every flow variable is subdivided in a resolved and a subgrid contribution according to $\psi = \bar{\psi} + \psi''$. The overbar denotes the filtering and the double prime the subgrid scale. To obtain an equation for the resolved variables, we apply the filter procedure to the Navier-Stokes equations with as result:

$$\rho \left(\frac{\partial \bar{\mathbf{u}}}{\partial t} + \nabla \cdot (\bar{\mathbf{u}} \bar{\mathbf{u}}) \right) = -\nabla \bar{P} + \nabla \cdot \bar{\tau} - \nabla \cdot \tau_{sgs} \qquad (5)$$

where $\mathbf{u}$ is the velocity vector with components (u, v, w). We find that the filter procedure applied to the momentum equations leads to an additional stress tensor τ_{sgs}. This stress is a new unknown in the equations and therefore needs to be modeled. This is denoted as the subgrid model. Here, we shall use the most simple subgrid model which is based on the assumption of gradient transfer. In that case the subgrid stress tensor is related to the (resolved) deformation rate tensor, $\bar{e}_{ij} = \frac{1}{2}(\partial \bar{u_i}/\partial x_j + \partial \bar{u_j}/\partial x_i)$ by

$$\tau_{sgs} = 2\nu_t \bar{e}_{ij} \qquad (6)$$

where ν_t is the turbulent viscosity. Application of Eq. (6) requires an expression for ν_t. Here we will use the well-known model of Smagorinsky for which ν_t is related to the resolved motions by:

$$\nu_t = (C_s \Delta)^2 \sqrt{\bar{e}_{ij}^2}. \qquad (7)$$

where Δ is a characteristic grid spacing, and C_s is the Smagorinsky constant. The standard Smagorinsky model does not reduce the subgrid viscosity to zero at the wall as it should be, because the Reynolds stress is exactly zero at the wall. Therefore a damping function is required near the wall. Here we apply the van Driest damping function (Piomelli et al., 1988) given by

$$C_s \Delta := C_s \Delta [1 - \exp(-y^+/26)] \qquad (8)$$

where $y^+ = u_* y/\nu$ is the dimensionless distance to the wall based on the *local* friction velocity. This distance y^+ is not known a priori because we have only fixed the mean frictional velocity (U_*), and not the local frictional velocity (u_*). Therefore, we have to calculate the local wall friction u_* at every position θ and at every time step. Recently more sophisticated models have been developed for the near-wall region. These are based on the dynamical model of Germano (see for instance Ghosal et al., 1995). However, previous simulations of fully-developed straight pipe flow with the Smagorinsky model and the van Driest damping function have shown good agreement with experiments (e.g., Eggels 1993). Besides this the Smagorinsky model (with damping) is much cheaper than the dynamic model. Therefore, we will use this simple model also in this case.

As already mentioned above, the background of the Smagorinsky subgrid model is the gradient transfer hypothesis or K-theory. From turbulence modeling we know that models based on K-theory do not perform well in flows with curved streamlines. This may perhaps lead one to expect that a Smagorinsky subgrid model is not applicable for LES of curved pipe flow. However, Eggels et al. (1995) show that a LES with the Smagorinsky subgrid model correctly predicts the large scales in a rotating pipe flow for which standard K-theory is also totally inappropriate. As we have argued above, the explanation for this success is that the details of the subgrid model, even if they are not correct, do not strongly influence the large scales because the energy of the subgrid scales is small compared to the energy of the large scales. Therefore, we are confident that in our case the Smagorinsky model can be applied to curved pipe flow without much adverse effect on the simulation of the general characteristics of the flow.

4 Numerical Model and Computation

In this section, we give an outline of the numerical method. We use a finite volume method (FVM) on a staggered grid to discretize the spatial derivatives and source terms in the continuity and momentum equations.

The advective part of the Navier-Stokes equations is integrated in time with an explicit Leap-Frog scheme in radial and axial direction. In the tangential direction we have used an implicit Crank-Nicolson scheme. The viscous terms in the Navier-Stokes equations are integrated with an Euler forward scheme.

The pressure correction method is applied to ensure the incompressibility condition. This involves the solution of a discrete 3-D Poisson equation. Due to the complexity of the geometry, a standard fast Poisson solver cannot be used. Therefore,

we use a solver which uses a Fast Fourier Transform (FFT) in the axial direction. This reduces the 3-D Poisson equation to N, 2-D discrete Helmholtz equations, where N denotes the number of gridpoints in the axial direction. The 2-D Helmholtz equations are solved with a Conjugate Gradient method. The solutions of the Helmholtz equations are then transformed back with a FFT to the physical space, which yields the pressure.

4.1 Boundary Conditions and Forcing. At the in- and outflow cross section we apply periodic boundary conditions for the velocity and pressure variables. These boundary conditions can only be justified when the computation domain in the axial direction is larger than the integral length scale of the turbulence, i.e., the streamwise correlation should become small over a distance equal to half the computational domain. In the tangential direction all variables are periodic by definition. For the velocity components at the pipe wall we do not use a wall function, which is a rather controversial issue especially in complex flows. Therefore we directly apply the no-slip boundary conditions. This can be done when the first grid point is placed sufficiently close to the wall, i.e., within the viscous sublayer, and this is accomplished by a nonuniform grid in the radial direction. At the centerline we ensure continuity of the velocity components by imposing artificial conditions which are based on interpolation across the centerline. In addition, the term $\partial u/\partial \theta$ in the $\tau_{r\theta}$-stress component is set to zero at $r = 0$. For the pressure we use, beside the periodic boundary conditions at the in- and outlet, Neumann boundaries at the pipe wall and centreline.

The flow is forced in the axial direction by means of an external pressure gradient ∇P. This pressure gradient must balance the viscous friction at the pipe wall and can be estimated from a simple force equilibrium

$$-\nabla P = -\frac{\Delta P}{\Delta s} = 4\rho \frac{U_*^2}{D} \qquad (9)$$

where Δs is a distance along the pipe centreline.

4.2 Computational Details. The length of the pipe along the axial coordinate s is taken to be 6.5 pipe diameters. The Reynolds number, based on the mean friction velocity and pipe diameter, is chosen to be 2000. The numerical grid has 40 points in radial, 114 points in tangential and 200 points in axial direction. As mentioned in the previous subsection the grid spacing in the radial direction is nonuniform. Also a run on a much coarser grid ($32 \times 80 \times 100$) has been carried out to check the effect of grid refinement and the influence of the subgrid model.

The computations are carried out on a Cray-C90 supercomputer. The simulations were started from a velocity profile for fully developed straight pipe flow with small random perturbations superimposed. The computations, in principle should be extended sufficiently long so that results are independent of the initial conditions. In our case we took four characteristic timescales D/U_*, which may seem to be somewhat short especially when compared with standard pipe flow, where the transients from the initial conditions are noticeable for a long time. In the curved pipe case the flow is strongly mixed by the secondary flow so that the transients from the initial conditions disappear faster than for the case of a straight pipe. As a result the bulk velocity becomes stationar after 2.5 timescales.[1]

After the 4 timescales 40 data-fields are collected separated in time, with equal intervals, over 4 additional timescales D/U_*. One may wander whether these forty fields generate enough independent samples to obtain stable statistics, especially because apart from time averaging there is only one homogeneous

direction available over which can be averaged. Therefore, some statistical scatter in the results should be expected. One complete run with the finest resolution mentioned above, takes approximately 60 CPU-hours (Cray-C90).

5 Results

In Table 1 several mean quantities obtained from the LES are listed for three different simulations with $\kappa = 0$, $\kappa = 0.01$, and $\kappa = 0.05$, respectively.

It is clear that the flow rate decreases with increasing curvature. This could be expected because in principle increasing curvature implies increasing secondary circulation and consequently increasing drag. However, we have fixed the external pressure gradient or the mean wall shear stress so that drag increase in this case shows up as a decreasing bulk velocity. The friction factor obtained from the standard pipe flow simulation, i.e. $\kappa = 0$ is in reasonable agreement with the value predicted by the Blasius correlation: $C_{blas} = 0.0791 \, \text{Re}_b^{-0.25}$. The small difference between computed friction factor and the Blasius equation is caused by a too large value of the subgrid eddy viscosity or a too small damping near the wall as explained by Eggels (1993). The friction factors obtained from the simulations with $\kappa > 0$ are clearly larger than the value for the straight pipe as one would expect.

In Fig. 2, we show the mean velocity profiles obtained from the simulations A, B, C, D in two different planes (plane I and II in Fig. 1). Before we discuss these velocity profiles in more detail, we will consider the effect of the grid size and the Smagorinsky coefficient on our results. Both in Table 1 and Fig. 2, we give some results obtained from run D which is computed with a much lower resolution than run C. The differences between the results of run C and D are very small and therefore we expect that the resolution of run C is high enough to obtain grid independent solutions. Moreover, a run with a somewhat lower value of the Smagorinsky coefficient ($C_s = 0.08$) has been carried out showing again only minor differences. Also a run without the subgrid model has been carried out (results not shown) for the case $\kappa = 0.05$, resulting in an oscillating solution with a much too high bulk velocity (20 percent higher than the value predict by the Blasius correlation for a straight pipe). This clearly underlines the necessity of a subgrid model.

Let us continue with a discussion of the velocity profiles of Fig. 2. We first consider the velocity profile in a plane perpendicular to the plane of curvature (plane II). This profile is symmetric with respect to the pipe centreline and has its velocity maximum near the pipe wall. For this velocity profile the difference between the straight and the curved pipe flow is on the average rather small. Next, we consider the velocity profiles in the plane of curvature (plane I). The maximum of the axial velocity is shifted in simulations B and C to the outside of the bend. The difference between the velocity profiles for a straight and curved pipe flow is very large at the inside of the bend, even for the small value $\kappa = 0.01$. This large effect of a rather small curvature is also observed by Moser and Moin (1987) in curved channel flow.

From Fig. 2, it becomes also clear that the velocity gradient $\partial w/\partial r$ at the outside wall is much larger than at the inside wall. Therefore, the viscous sublayer ($y < 5y^+$) which is proportional to $1/\tau_{rs} \approx (\partial w/\partial r)^{-1}$ must be thinner at the outside than at the inside of the bend. This nonuniform thickness of the viscous sublayer has some consequences for the accuracy of the numerical calculations. The calculations are started with a computational grid which has two gridpoints in the region $0 < y < 5\nu/U_*$, i.e., two gridpoints in the "initial" viscous sublayer, which is in general enough for LES of wall bounded flows. When the flow reaches the fully developed state, the sublayer thickness at the outside is approximately $3.5\nu/U_*$, which implies that there is only one grid point in the viscous sublayer. It will be obvious that the numerical accuracy of the simulation is some-

---

[1] A typical size of an eddy in pipe flow is $0.1D$ and the timescale of this eddy is equal to $0.1D/U_*$, two timescales correspond thus with twenty large eddy turnover times.

Table 1 Some quantities obtained from the LES. The N denotes the number of gridpoints, $Re_* = U_* D/\nu$ the Reynolds number based on the mean friction velocity, κ the dimensionless inverse radius of curvature, $\langle W \rangle$ the bulk velocity, $Re_b = \langle W \rangle D/\nu$ the bulk Reynolds number, De the Dean number, C_f/C_{blas} the friction factor normalised with the Blasius value and C_s the Smagorinsky constant

	A	B	C	D	E
N	$40 \times 114 \times 200$	$40 \times 114 \times 200$	$40 \times 114 \times 200$	$32 \times 80 \times 100$	$32 \times 80 \times 100$
$Re_* \times 10^{-3}$	2.0	2.0	2.0	2.0	2.0
κ	0	0.01	0.05	0.05	0.05
$\langle W \rangle / U_*$	19.06	18.88	18.42	18.46	18.61
$Re_b \times 10^{-3}$	38.120	37.760	36.840	36.920	37.220
De	0	3776	8240	8256	8320
C_f/C_{blas}	0.97	0.98	1.03	1.03	1.02
C_s	0.10	0.10	0.10	0.10	0.08

what affected by the low resolution in the viscous layer at the outside of the bend. It is also clear that the resolution at the inside of the bend, where the depth of the viscous sublayer measures $8\nu/U_*$, will be increased with respect to the straight pipe.

In Fig. 3, we have plotted the axial velocity profiles at several tangential positions in the upper-half plane using "law of the wall" coordinates, based on U_*. Furthermore, the logarithmic velocity profile for a fully developed flow $W = 2.5 \ln (Y^+) + 5.5$ is also shown. We should mention here that for a straight pipe Eggels (1994) has already shown that the LES results agree well with this logarithmic profile. However, for the curved pipe the differences between simulation results and the standard logarithmic law are striking. These differences occur not only in values of the velocity but also in the slope of the curves. Only the profile at the inside wall, i.e., $\theta = 180$ deg, has the same slope as the standard logarithmic profile but with a different constant. In Fig. 4 the same profiles as in Fig. 3 are plotted, but now using the local u_* as a scaling variable instead of U_*. This figure shows that all profiles are more or less linear in the viscous sublayer, i.e. $w = y^+$ holds. This means that, in view

of the points mentioned above, the numerical resolution in the viscous sublayer seems to be fine enough to resolve this layer.

In Fig. 5, a contour plot is given of the axial velocity for both $\kappa = 0.01$ and $\kappa = 0.05$. This figure illustrates clearly that the flow is symmetric about the y-axis (Fig. 1) and that the fluid velocity at the inside of the pipe is relatively low. The regions with high velocity at the top and bottom of Fig. 5 are caused by the secondary motions to be discussed in the next section.

5.1 Secondary Motion. In the introduction, we have explained that the centrifugal force causes a secondary motion in the cross-plane of the pipe. In this section we will investigate this motion. In Fig. 6 we have plotted the tangential velocity profiles in the upper-half plane of the pipe. The tangential velocity has a large positive value (counter clockwise) near the pipe wall and a rather small negative value (clockwise) near the centreline. Thus, near the wall the flow in the cross-plane is moving from the outside to inside of the bend and in the opposite direction near the centre. The tangential velocity near the wall advects the axial velocity and this explains the maxima in the axial velocity at the top and bottom of Fig. 5.

In Fig. 7, the radial velocity profile is plotted in the plane of curvature (I) for the two values of κ. This figure shows that the radial velocity has a high value at the inside of the bend and a relative low value at the outside. This decrease in the absolute value of radial velocity from the inside to the outside of the bend can be explained as follows: the centrifugal forces due to the axial velocity are partly balanced by a radial pressure gradient, i.e., the pressure is high at the outside of the bend and low at the inside. Therefore, along plane I (see Fig. 1.) the radial velocity is against the pressure gradient and consequently will decrease in strength.

In Fig. 8, we have plotted the stream function of the secondary motion for $\kappa = 0.01$ and $\kappa = 0.05$. We observe two strong vortices near the inside of the bend. These are the Dean vortices
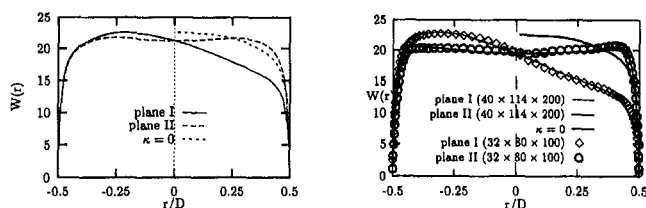
Fig. 2 The mean axial velocity profiles in two different planes (see Fig. 1). The left figure is for run B, i.e., obtained with an inverse radius of curvature $\kappa = 0.01$. The right figure is for run C (lines) and run D (symbols) with $\kappa = 0.05$.
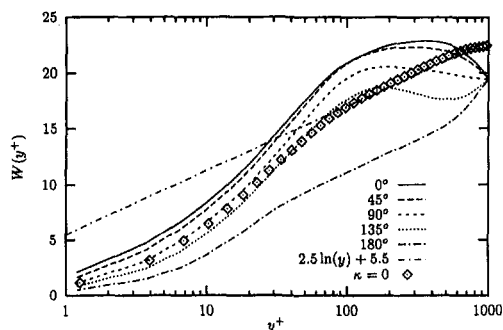
Fig. 3 The mean velocity profiles (run B) in the upper half-plane, for $\phi = 0, 45, 90, 135, 180$ deg, in wall coordinates using mean friction velocity U_* as velocity scale. The straight line is the logarithmic approximation $W = 2.5 \ln (U_*(D/2 - r)/\nu) + 5.5$, and the symbols denote the axisymmetric profile obtained from run A for $\kappa = 0$.
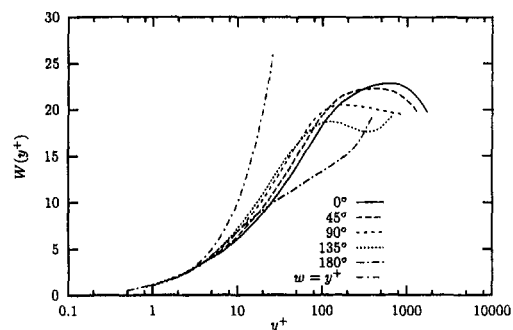
Fig. 4 The mean velocity profiles (run B) in the upper half-plane, for $\phi = 0, 45, 90, 135, 180$ deg, in wall coordinates using the local friction velocity u_* as velocity scale. The linear profile valid in the viscous sublayer is also given.
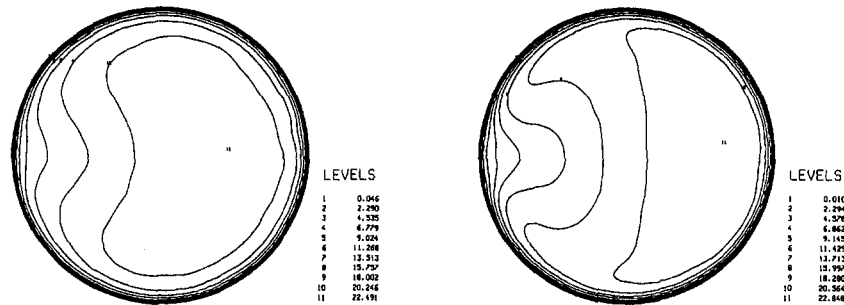
Fig. 5 Contour lines of the mean axial velocity. The left figure is for $\kappa = 0.01$ and the right figure for $\kappa = 0.05$. In both case the outside of the bend is to the right.
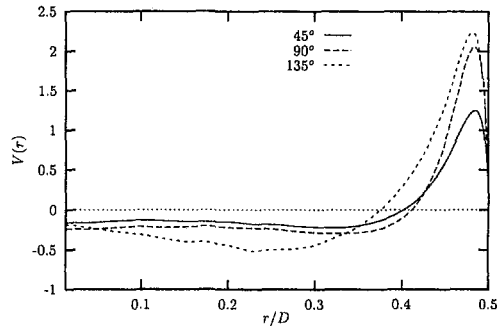

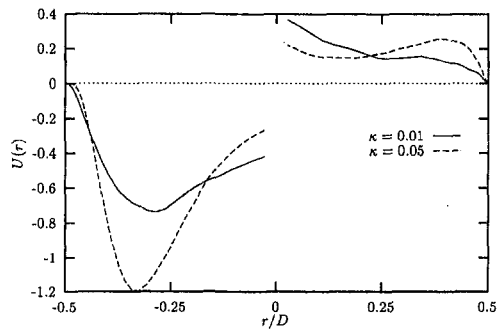**Fig. 6** The tangential velocity profiles at an angle $\phi = 45, 90,$ and 135 deg, for $\kappa = 0.05$

Fig. 7 The radial velocity in plane I. The jump in the profile at $r/D = 0$ is caused by our definition of the radial velocity (from the centre to the wall) and a net flow across the centre will thus chance sign. The flow is thus everywhere from the inner to the outer wall. The solid line is for $\kappa = 0.01$ and the dashed line for $\kappa = 0.05$ (the outside of the curvature is to the right).

that we mentioned in the introduction. The figure also shows that the secondary motion is very strong near the inner wall, i.e. at $\phi \approx 40 - 160$ deg (see Fig. 1), and at the symmetry plane near the inside of the bend. At the outside of the bend the secondary motion is rather weak.

5.2 Turbulence Statistics. In the previous section, we have presented numerical results for some mean flow quantities. In this section, we will turn to turbulence statistics. In Fig. 9, we have plotted the rms-values of the three velocity components in the plane of curvature (plane I), nondimensionalized with the mean friction velocity U_*. For comparison, we have plotted in the same figure the rms-values for a straight pipe flow. This figure shows that for the axial or streamwise component the turbulence intensity near the outside wall is slightly higher than at the inside wall. Moreover, it seems that in comparison with the results for the straight pipe, the turbulence intensity at the outside wall is also somewhat larger. The reverse holds for the inside wall. This effect becomes larger for increasing curvature. For the tangential and radial components the opposite occurs, i.e., the rms data with respect to the values for the straight pipe, are higher at the inside than at the outside of bend. The same behavior of these rms-values is also observed in curved channel flow by Moser and Moin (1987).

For completeness we have also included the axial or streamwise rms-profile obtained from run D which shows only minor differences with the results of run C. This again confirms our earlier conclusion that the results obtained at the highest resolution may be sufficiently grid-independent.

The profiles of the rms-values of the three velocity components in plane II, i.e., the plane perpendicular to the plane of curvature, are plotted in Fig. 10. For the axial component, the rms-profile for the $\kappa = 0.01$ case is almost equal to the result for the straight pipe with only a rather small difference in the core region. In contrast, the results for $\kappa = 0.05$ show a much larger difference between the straight and curved pipe. In the case of $\kappa = 0.05$ the maximum of the axial rms is decreased by 25 percent compared with the $\kappa = 0.01$ case. Figure 10 also
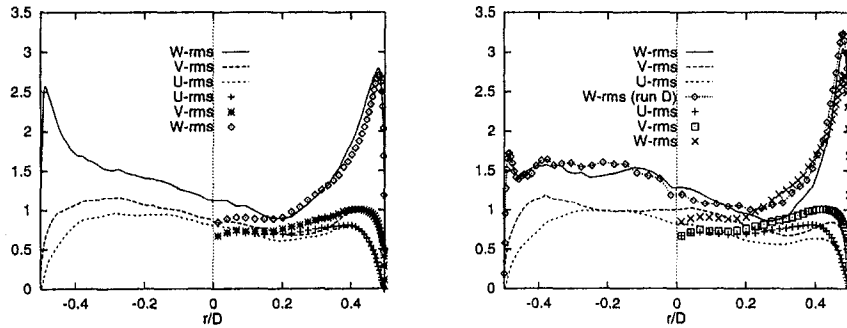

Fig. 8 Contour plot of the stream-function χ of the secondary motion. The left figure is for $\kappa = 0.01$ and the right figure for $\kappa = 0.05$ (the outside of the curvature is to the right).

Fig. 9 The rms-values of the three velocity components in plane I, scaled with U_*. The left figure is for $\kappa = 0.01$ and the right figure for $\kappa = 0.05$. The lines denote the rms values for curved pipe flow and the symbols denote the rms-values for a straight pipe (outside of curvature to the right). For $\kappa = 0.05$ we also show the streamwise fluctuations obtained for the low resolution case (D).
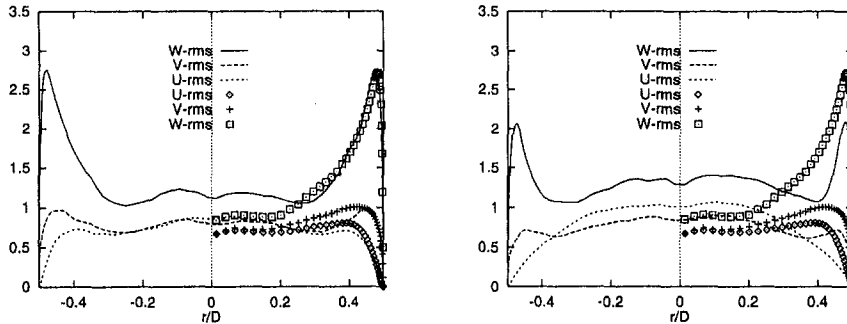

Fig. 10 The rms-values of the three velocity components in plane II, scaled with U_*. The left figure is again for $\kappa = 0.01$ and the right figure for $\kappa = 0.05$. The symbols denote the rms-values for a straight pipe.

shows that the radial velocity has a rather large rms-value in the core and near wall region compared with the result for the straight pipe flow.

Finally, in Figs. 11 and 12 we have plotted the Reynolds stresses $\langle u'v' \rangle$, $\langle u'w' \rangle$ and $\langle v'w' \rangle$ in the planes II and I, respectively. The $\langle u'w' \rangle$ and the $\langle v'w' \rangle$ are the important components of the Reynolds-stress in plane II, in contrast to straight pipe flow where only the $\langle u'w' \rangle$ stress is important. In plane I, shown in Fig. 12, the Reynolds-stress components $\langle u'v' \rangle$ and $\langle v'w' \rangle$ are small, whereas the $\langle u'w' \rangle$ term is quite large. This behavior of the Reynolds stress components can be qualitatively explained in the following way: let us consider the averaged equation for the Reynolds stresses in the axial direction which reads:

$$\frac{1}{rh_3} \left(\frac{\partial}{\partial r} [rh_3 \langle u'w' \rangle] + \frac{\partial}{\partial \theta} [h_3 \langle v'w' \rangle] \right)$$

$$= \frac{1}{rh_3} \left(\frac{\partial}{\partial r} [rh_3 \tau_{rs}] + \frac{\partial}{\partial \theta} [h_3 \tau_{\theta_s}] \right) + O(\tau_{rs}) \quad (10)$$

where we have assumed that the source terms are small compared to the other terms in the equation. In plane II both Reynolds-stress components in the equation above can balance the viscous stresses τ_{rs} and τ_{θ_s}. In the plane of curvature, i.e., the symmetry plane $\partial/\partial\theta$ is zero and therefore the Reynolds stress component $\langle u'w' \rangle$ is the only component which can balance the viscous stress τ_{rs}.
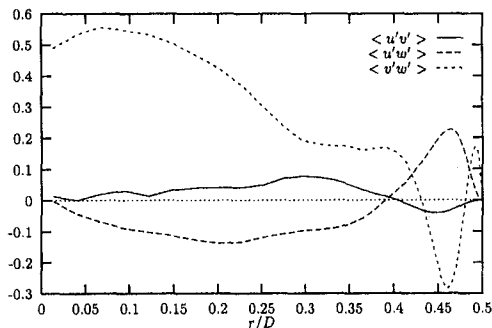

Fig. 11 The turbulent Reynolds-stresses in plane II ($\phi = 90$ deg), scaled with U_* for $\kappa = 0.05$.S
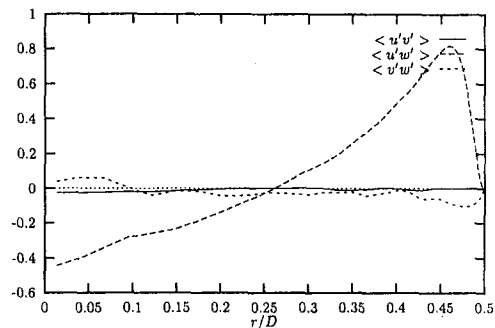

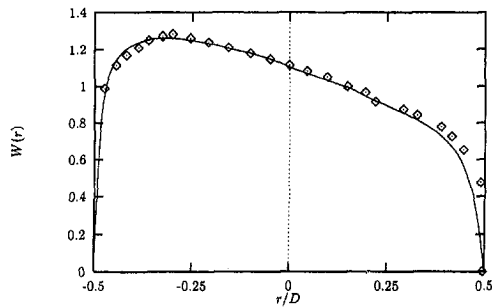**Fig. 12** The turbulent Reynolds-stresses in plane I ($\phi = 0$), scaled with U_* for $\kappa = 0.05$

Fig. 13 The axial velocity in symmetry plane I. The symbols denote the experimental values obtained by Adler for κ = 0.01 and Re = 11.77 10^3. The line has been calculated with LES for κ = 0.01 and Re$_b$ = 12.9 10^3. In both cases the results are scaled with the bulk velocity $\langle W \rangle$.

6 Comparison With Experiment

In this section we will compare the results from our simulations with the experimental data obtained by Adler (1934). Two measurements are available, one with a bulk Reynolds number of 8.5 10^3 and one with a bulk Reynolds number of 11.8 10^3. The inverse radius of curvature κ is 0.02 and 0.01, respectively. The Dean number of the high Reynolds number experiment is equal to 1170 and we may not expect good agreement with the simulations reported in the previous section because these are representative for a higher Dean number as apparent from Table 1. Therefore, we have carried out a simulation with exact the same curvature and approximately the same Reynolds number (Re$_*$ = 750) as in the experiments of Adler (1934). Furthermore, we have decreased the Smagorinsky constant to C_s = 0.07 which in view of previous studies is required in order to perform a LES at a rather low Reynolds number. In this case we have used the damping function proposed by Horiuti (1992) instead of the van Driest function, because this damping function has been found to give better results for low Reynolds number flows than the Van Driest damping function. In Fig. 13 the mean axial velocity profiles obtained from experiment and simulations are plotted.

The agreement between experiment and simulation is quite good, especially in the core region. Near the wall there are some small differences between numerical and experimental data. This difference may be caused by an improper subgrid modeling near the wall as discussed by Eggels (1993). However, we can also not rule out possible experimental errors. Although the comparison is rather limited, it is nevertheless quite satisfactory. This gives us confidence in the results presented in the previous sections for which no experimental data are available.

7 Conclusions

The main objective of this paper has been to investigate the turbulent flow in a curved pipe. In particular, we have considered the secondary flow patterns which have also been observed experimentally. From our results, it follows that these secondary circulations can indeed be predicted with a LES. We have found that the secondary flow patterns consist of two strong counter rotating vortices near the inside of the bend which are driven

by the centrifugal force. These cells are ordinary Dean cells, which are also present in a laminar curved pipe flow.

Our simulations also show that the turbulence intensities are enhanced at the outside of the bend and suppressed at the inside, which is consistent with observations in a curved channel flow. Furthermore, it is shown that the turbulent Reynolds stresses are large in the core region of the pipe, in contrast to straight pipe flow where the Reynolds stresses are small in this region.

The results of our simulations for the mean profile agree well with experimental observations. A more extensive comparison is not yet possible because there is not enough experimental data available, e.g., on the turbulent statistics. Nevertheless, this perhaps somewhat limited verification shows in our opinion the usefulness of LES to study these complicated flows.

Acknowledgments

References

Adler, M., 1934, "Strömung in gekrümmten Rohren," *Zeitschrift für angewandte Mathematik und Mechanik,* Vol. 14, pp. 257–275.

Anwer, M., and So, R. M. C., 1993, "Swirling Turbulent Flow Through a Curved Pipe," *Experiments in Fluids,* Vol. 14, pp. 85–96.

Anwer, M., So, R. M. C., and Lai, Y. G., 1989, "Perturbation by and Recovery from Bend Curvature of a Fully Developed Turbulent Pipe Flow," *Physics of Fluids A,* Vol. 1, pp. 1387–1397.

Azzola, J., Humphrey, J. A. C., Iacovides, H., and Launder, B. E., 1986, "Developing Turbulent Flow in a U-Bend of Circular Cross-Section: Measurements and Computations," ASME JOURNAL OF FLUIDS ENGINEERING, Vol. 108, pp. 214–221.

Batchelor, G. K., 1967, *An Introduction to Fluid Mechanics,* Cambridge University Press, Cambridge UK.

Berger, S. A., Talbot, L., and Yao, L. S., 1983, "Flow in Curved Pipes," *Annual Review of Fluid Mechanics,* Vol. 15, pp. 461–512.

Bradshaw, P., 1987, "Turbulent Secondary Flows," *Annual Review of Fluid Mechanics,* Vol. 19, pp. 53–74.

Eggels, J. G. M., Boersma, B. J., and Nieuwstadt, F. T. M., 1995, "Direct and Large-Eddy Simulations of Turbulent Flow in an Axially Rotating Pipe," submitted to *Journal of Fluid Mechanics.*

Eggels, J. G. M., 1993, "Direct and Large Eddy Simulation of Turbulent Flow in a Cylindrical Pipe Geometry," PhD. thesis, Delft University of Technology, Delft, The Netherlands.

Germano, M., 1982, "On the Effect of Torsion on Helical Pipe Flow," *Journal Fluid Mechanics,* Vol. 125, pp. 1–8.

Ghosal, S., Lund, T., Moin, P., and Akselvoll, K., 1995, "A Dynamic Localization Model for Large-Eddy Simulation of Turbulent Flow," *Journal of Fluid Mechanics,* Vol. 286, pp. 229–255.

Horiuti, K., 1992, "A Proper Velocity Scale for Modelling Subgrid-Scale Eddy Viscosities in Large-Eddy Simulation," *Physics of Fluids A,* Vol. 5, pp. 146–157.

Ito, H., 1987, "Flow in Curved Pipes," *JSME International Journal,* Vol. 30, pp. 543–552.

Lai, Y. G., So, R. M. C., and Zhang, H. S., 1991, "Turbulence-Driven Secondary Flows in a Curved Pipe," *Theoretical and Computational Fluid Dynamics,* Vol. 3, pp. 163–180.

Moser, R., and Moin, P., 1987, "The Effects of Curvature in Wall-Bounded Turbulent Flows," *Journal Fluid Mechanics,* Vol. 175, pp. 479–510.

Patankar, S. V., Pratab, V. S., and Spalding, D. B., 1974, "Prediction of Turbulent Flow in Curved Pipes," *Journal of Fluid Mechanics,* Vol. 67, pp. 583–595.

Piomelli, U., Ferziger, J., and Moin, P., 1988, "Model Consistency in Large Eddy Simulation of Turbulent Channel Flows," *Physics of Fluids,* Vol. 31, pp. 1884–1891.

Hanzhong Zhang
TSI Incorporated,
P.O. Box 64394,
St. Paul, MN 55164

Mohammad Faghri

Frank M. White

Department of Mechanical Engineering,
University of Rhode Island,
Kingston, RI 02881-0805

A New Low-Reynolds-Number k-ε Model for Turbulent Flow Over Smooth and Rough Surfaces

A new low-Reynolds-number k-ε model is proposed to simulate turbulent flow over smooth and rough surfaces by including the equivalent sand-grain roughness height into the model functions. The simulation of various flow experiments shows that the model can predict the log-law velocity profile and other properties such as friction factors, turbulent kinetic energy and dissipation rate for both smooth and rough surfaces.

Introduction

Low-Reynolds-number k-ε models are being used increasingly in engineering analysis for their applicability to a wider range of flows compared to their high-Reynolds-number form. However, with the exception of Tarada's model (1990), existing low-Reynolds-number k-ε models only deal with the smooth wall. The only low-Reynolds-number k-ε model accounting for roughness, the form-drag formulation of Tarada, requires detailed knowledge of the shape and distribution of the roughness elements, which is difficult to determine in engineering applications. Simpler models use a single roughness parameter based on the traditional assumption that the aerodynamic characteristics of a rough surface may be characterized by a single parameter called the equivalent sandgrain roughness height h_s (Schlichting, 1936). However, the existing equivalent sandgrain roughness models are based on the mixing-length assumption and are not suitable for complicated flows.

This paper will develop a new low-Reynolds-number k-ε model that is valid for both smooth and rough surfaces by incorporating the equivalent sandgrain roughness height into the model functions. The proposed model will then be applied to various experiments.

Existing Turbulence Models

Low-Reynolds-Number k-ε Models (Smooth Wall). The equations for the low-Reynolds-number k-ε model may be written as:

$$\frac{\partial k}{\partial t} + U_j \frac{\partial k}{\partial x_j}$$
$$= \frac{\partial}{\partial x_j}\left\{ \left(\nu + \frac{\nu_t}{\sigma_k}\right) \frac{\partial k}{\partial x_j} \right\} + \nu_t \frac{\partial U_i}{\partial x_j}\left(\frac{\partial U_i}{\partial x_j} + \frac{\partial U_j}{\partial x_i}\right) - \epsilon \quad (1)$$

$$\frac{\partial \epsilon}{\partial t} + U_j \frac{\partial \epsilon}{\partial x_j} = \frac{\partial}{\partial x_j}\left\{ \left(\nu + \frac{\nu_t}{\sigma_\epsilon}\right) \frac{\partial \epsilon}{\partial x_j} \right\}$$
$$+ C_1 f_1 \nu_t \frac{\epsilon}{k} \frac{\partial U_i}{\partial x_j}\left(\frac{\partial U_i}{\partial x_j} + \frac{\partial U_j}{\partial x_i}\right) - C_2 f_2 \frac{\epsilon^2}{k} \quad (2)$$

$$\nu_t = f_\mu C_\mu k^2 / \epsilon \quad (3)$$

The constants C_μ, C_1, C_2, σ_k, σ_ϵ and model functions f_1, f_2 and f_μ differ for different models (Patel, 1985; Nagano and Hishida, 1987; Myong and Kobayashi, 1991).

Rough Surface Turbulence Models. Existing rough surface models can be classified into equivalent sandgrain roughness models and topographic form-drag models. The earliest equivalent sandgrain roughness model was proposed by van Driest (1956):

$$\nu_t = (F\kappa y)^2 (\partial U / \partial y) \quad (4)$$

$$F = 1 - \exp\left(-\frac{y^+}{26}\right) + \exp\left(-2.3\frac{y^+}{h_s^+}\right) \quad (5)$$

The effect of damping function F for smooth wall flow is to reduce the turbulent viscosity when y^+ is very small. For a rough surface, the viscous layer is reduced since turbulent mixing is more vigorous. Van Driest suggested that this effect could be obtained by reducing the amount of damping and hence the third term was added to Eq. (5). Krogstad (1991) modified the van Driest damping function and was able to reproduce the correct log-law shift for large roughness. His formulation is:

$$F = 1 - \exp\left(-\frac{y^+}{26}\right) + \exp\left(-\frac{y^+}{26}\left(\frac{70}{h_s^+}\right)^{3/2}\right)$$
$$\times \sqrt{1 + \exp\left(-\frac{70}{h_s^+}\right)} \quad (6)$$

The existing equivalent sandgrain roughness models are usually mixing-length type and can only be used for very simple flow situations.

One topographic model is the discrete element roughness model of Taylor et al. (1985, 1988) which includes surface roughness form drag and blockage effects into the momentum equations. Another topographic model is Tarada's (1990) low-Reynolds-number k-ε model, which adds sink and source terms to the equations for momentum, k and ϵ, respectively. Those terms depend on roughness topographic parameters and another complementary roughness drag coefficient model. Because of the complexity of characterizing stochastic roughness, topographic models are difficult to use in engineering application.

Development of New Turbulence Model for Smooth and Rough Surface

Formulation of f_μ. The role of f_μ in low-Reynolds-number k-ε model is similar to van Driest's damping function. In order
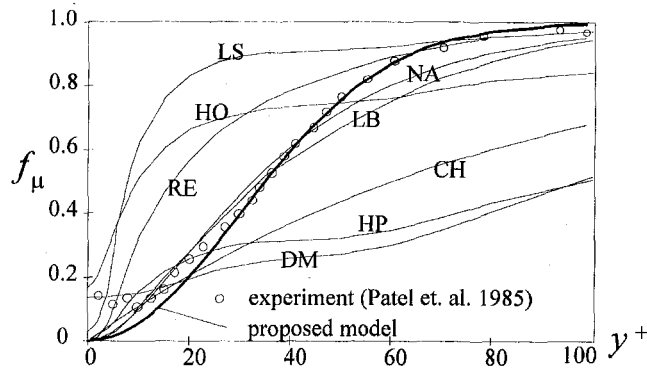
Fig. 1 Variation of function f_μ with wall distance

Fig. 2 Velocity profile in smooth pipe at Re = 41667

that ν_t vanishes near smooth wall, f_μ must approach zero when y^+ goes to zero. For a rough wall, the viscous region is reduced because of more vigorous mixing caused by roughness and the amount of damping should be less. This can be achieved by adding a roughness term to the smooth wall f_μ formula:

$$f_\mu = 1 - \exp\left(-\left(\frac{y^+}{A_1}\right)^n\right) + g_1(h_s^+) \exp\left(-A_2 \frac{y^+}{h_s^+}\right) \quad (7)$$

The function $g_1(h_s^+)$ is zero for smooth wall and positive for rough wall. Its form will be derived later. A_1 and n are determined by fitting f_μ to the smooth wall experimental data on f_μ (Patel et al. 1985):

$$A_1 = 42, \quad n = 2 \quad (8)$$

The smooth wall f_μ function is plotted in Fig. 1 against the experimental data and other model results, including LB (Lam and Bremhorst, 1981), LS (Launder and Sharma, 1974), RE (Reynolds, 1976), HO (Hoffmann, 1975), DM (Dutoya and Michard, 1981), HP (Hassid and Poreh, 1978), CH (Chien, 1982), and NA (Nagano and Hishida, 1987).

Formulation of f_1 and f_2. The function f_1 should be unity far from wall and have larger values near wall in order to increase ϵ and to decrease k and thereby to reduce turbulent viscosity ν_t. To get an idea how f_1 varies with y^+, let us look at the f_1 formulation of Lam and Bremhorst (1981)

$$f_1 = 1 + (0.05/f_\mu)^3 \quad (9)$$

For the smooth wall, from Eqs. (7) and (8)

$$f_\mu = 1 - \exp(-(y^+/42)^2) \propto (y^+)^2 \quad \text{when} \quad y^+ \to 0 \quad (10)$$

Substituting the above relation into Eq. (9), we obtain

$$f_1 = 1 + constant/(y^+)^6 \quad (11)$$

In the above equation, f_1 becomes infinity when $y^+ \to 0$. To avoid this problem, y^+ is replaced with $1 + y^+$ and the f_1 formulation becomes

$$f_1 = 1 + (A_3/(1 + y^+))^6 \quad (12)$$

The effect of surface roughness on f_1 is opposite the effect of smooth wall. Surface roughness will increase the turbulence level and reduce the dissipation rate. The increase in f_1 should be less near a rough wall compared to a smooth wall. Therefore a roughness function modifier is added to Eq. (12) and final form of f_1 is

$$f_1 = 1 + g_2(h_s^+)(A_3/(1 + y^+))^6 \quad (13)$$

The roughness modifier $g_2(h_s^+)$ should be decreased for increasing h_s^+ with the value of 1 at $h_s^+ = 0$. Its formulation will be derived later.

The f_2 formulation developed by Lam and Bremhorst (1981) is adopted in the current model without change.

$$f_2 = 1 - \exp(-R_t^2) \quad (14)$$

Model Constants and Roughness Functions. The constants C_μ, C_1, C_2, σ_k, and σ_ϵ are the same as in the standard k-ϵ model of Launder and Spalding (1974)

Nomenclature

A_1, A_2, A_3 = constants in proposed model functions
b = half height of channel (or duct)
C_1, C_2, C_μ = turbulence model constants
C_f = friction factor = $\tau_w/\frac{1}{2}\rho U_b^2$
d = hydraulic diameter
F = van Driest damping function
f_1, f_2, f_μ = turbulence model functions
g_1, g_2 = roughness function in the proposed model
h_s = equivalent sandgrain roughness height
h_s^+ = nondimensional roughness height = $h_s v^*/\nu$
k = turbulent energy
k^+ = dimensionless turbulent energy = k/v^{*2}

n = constant in the proposed f_μ function
$\bar{p}$ = cross-sectional averaged pressure in a duct
p' = pressure variation in a cross-stream direction
Re = Reynolds number = $U_b d/\nu$
R_t = turbulence Reynolds number = $k^2/\nu\epsilon$
t = time
U^+ = nondimensional velocity = U/v^*
U_b = bulk mean velocity in a duct
U_i, U_j = tensor notation for velocity components
U, V, W = mean velocity component
v^* = shear velocity = $\sqrt{\tau_w/\rho}$
x = streamwise coordinate in a duct

x_i, x_j = tensor notation for space coordinates
y = normal distance from wall
y^+ = distance from wall defined as = yv^*/ν
z = coordinate in the channel cross-section
ΔB = velocity shift for rough wall
ϵ = turbulent dissipation rate
ϵ^+ = dimensionless turbulent dissipation rate = $\epsilon\nu/v^{*4}$
κ = von Karman constant = 0.41
ν = kinematic viscosity
ν_t = turbulent viscosity
ρ = fluid density
σ_k = diffusion Prandtl number for turbulence energy
σ_ϵ = diffusion Prandtl number for dissipation rate
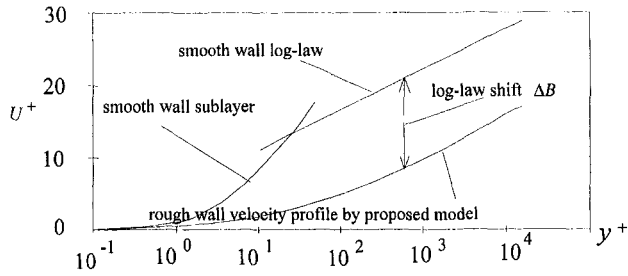τ_w = shear stress at the wall

Fig. 3 Velocity profile in rough pipe at $Re = 10^6$, $h_s^+ = 500$

Fig. 5 Friction factor for smooth pipe

$$\sigma_k = 1.0, \quad \sigma_\epsilon = 1.3,$$
$$C_1 = 1.44, \quad C_2 = 1.92, \quad C_\mu = 0.09 \qquad (15)$$

A_3 is determined by calculating smooth wall circular pipe flow. In that case, $g_1(h_s^+) = 0$ and $g_2(h_s^+) = 1$, the roughness term in Eq. (7) drops out and A_3 becomes the only unknown constant. A series of A_3 values are used and the resulted friction factors are compared with the classical Prandtl-Karman-Nikuradse's correlation (von Karman, 1934) of the experimental data for fully-developed smooth-wall circular pipe flow:

$$1/\sqrt{C_f} = 1.7372 \ln(\mathrm{Re}\sqrt{C_f}) - 0.3946 \qquad (16)$$

The best value found is $A_3 = 9.2$.

A_2 is determined by first setting $g_1 = 1$, $g_2 = 1$ and then trying to best predict the traditional rough-pipe formula of Colebrook (1939):

$$\frac{1}{\sqrt{C_f}} = 3.48 - 1.7372 \ln\left(\frac{h_s^+}{\mathrm{Re}} + \frac{9.35}{\mathrm{Re}\sqrt{C_f}}\right) \qquad (17)$$

The best selection is $A_2 = 25$.

The two roughness functions $g_1(h_s^+)$ and $g_2(h_s^+)$ are kept unity in the above process and the predicted friction factor is very poor compared to Colebrook's formula. For a better prediction, different values should be used for different h_s^+. Starting from $h_s^+ = 5$, a large number of g_1 and g_2 values are tested and the final selection is given to the one that best predicts Colebrook's formula for that roughness. This process is repeated for $h_s^+ = 10, 20, 30, \ldots 1000$ and the g_1 and g_2 values are obtained for all those roughness heights. The final results can be expressed as the following functions

$$g_1(h_s^+) = \sqrt{\frac{h_s^+}{200}} \qquad (18)$$

$$g_2(h_s^+) = \exp\left(-\frac{1}{0.1 + 1/h_s^+}\right) \qquad (19)$$

Numerical Procedure

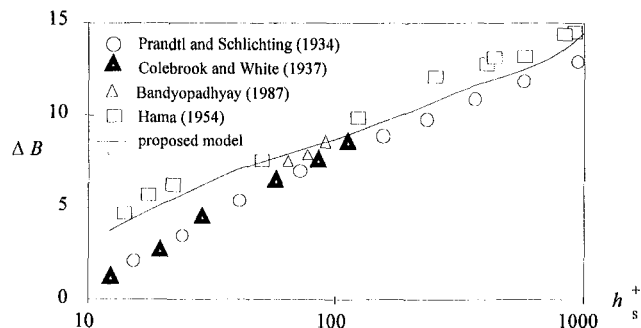The governing equations for a straight duct flow (Patankar and Spalding, 1972) are:
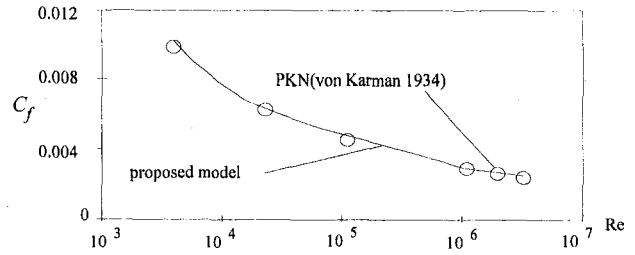
$$\frac{\partial U}{\partial x} + \frac{\partial V}{\partial y} + \frac{\partial W}{\partial z} = 0 \qquad (20)$$

$$U\frac{\partial U}{\partial x} + V\frac{\partial U}{\partial y} + W\frac{\partial U}{\partial z}$$
$$= -\frac{\partial \bar{p}}{\partial x} + \frac{\partial}{\partial y}\left((\nu + \nu_t)\frac{\partial U}{\partial y}\right) + \frac{\partial}{\partial z}\left((\nu + \nu_t)\frac{\partial U}{\partial z}\right) \qquad (21)$$

$$U\frac{\partial V}{\partial x} + V\frac{\partial V}{\partial y} + W\frac{\partial V}{\partial z} = -\frac{\partial p'}{\partial y} + \frac{\partial}{\partial y}\left((\nu + \nu_t)\frac{\partial V}{\partial y}\right)$$
$$+ \frac{\partial}{\partial z}\left((\nu + \nu_t)\frac{\partial V}{\partial z}\right) \qquad (22)$$

$$U\frac{\partial W}{\partial x} + V\frac{\partial W}{\partial y} + W\frac{\partial W}{\partial z} = -\frac{\partial p'}{\partial z} + \frac{\partial}{\partial y}\left((\nu + \nu_t)\frac{\partial W}{\partial y}\right)$$
$$+ \frac{\partial}{\partial z}\left((\nu + \nu_t)\frac{\partial W}{\partial z}\right) \qquad (23)$$

$$\frac{d}{dx}\left(\iint_{\text{cross area}} U\,dy\,dz\right) = 0 \qquad (24)$$

The boundary conditions for k and ϵ are:

$$y = 0: \quad k = 0 \quad \epsilon = \nu\frac{\partial^2 k}{\partial y^2} \qquad (25)$$

Velocities are set to zero on the wall and the distribution of variables are prescribed at the duct inlet according to the actual flow condition. The SIMPLER algorithm of Patankar (1972, 1980) is used for solving the governing equations.

Results

The proposed model is tested against experiments including: smooth and rough wall fully developed flow in circular pipe;
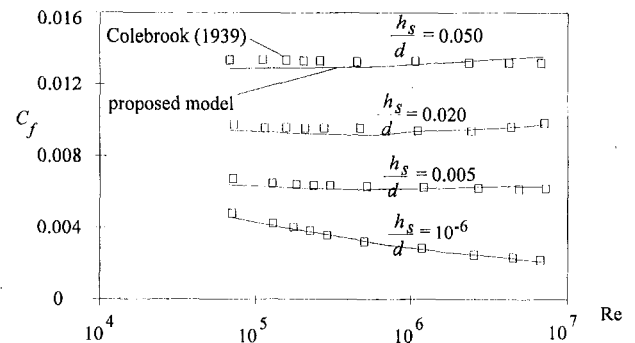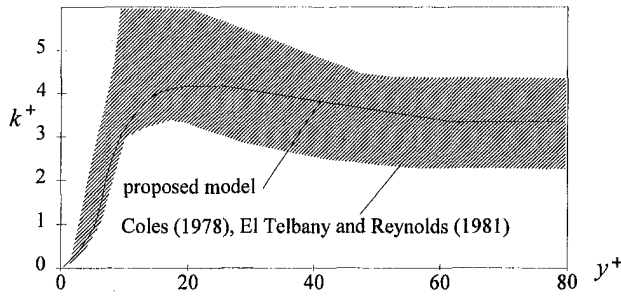

Fig. 4 Log-law velocity shift at various roughness height

Fig. 6 Friction factor for rough pipe

Fig. 7 Turbulence kinetic energy near smooth wall

Fig. 9 Friction coefficient for square duct

smooth wall developing and fully developed flow in the square duct; smooth and rough wall fully developed flow in the rectangular channel.

Figure 2 compares the predicted velocity profile in smooth pipe with the universal log-law and sublayer profiles (White, 1991). The agreement is excellent in both regions.

Figure 3 shows that the model predicts a logarithmic velocity profile at large y^+ in rough pipe. The line is parallel to the smooth wall log-law line with a shift of ΔB.

Figure 4 compares the predicted log-law velocity shift ΔB with data (Prandtl and Schlichting, 1934; Colebrook and White, 1937; Bandyopadlyay, 1987; and Hama, 1954) for various roughness. The prediction is within the data scatter.

Figure 5 compares the predicted friction factor C_f with classical Prandtl-Karman-Nikuradse correlation (von Karman, 1934) for smooth pipe. The agreement is very good for all Reynolds numbers.

Figure 6 compares the predicted C_f with classical Colebrook's (1939) formula for rough pipe at various Reynolds number and roughness height. The largest error is 10 percent with underprediction for low Reynolds numbers and overprediction for the high. The prediction is better for smaller roughness height.

Figure 7 compares the predicted near wall turbulent kinetic energy with data (Coles, 1978; El Telbany and Reynolds, 1981). The calculation is for smooth pipe at Re = 41,667. The prediction lies in the middle of the data which has large scatter.

Figure 8 compares the predicted turbulence dissipation rate with data (Coles, 1978; Laufer, 1954). The prediction lies inside the data cloud.

Figure 9 compares the predicted friction coefficient C_f with data (Hartnett et al., 1962; Lund, 1977) for fully developed flow in square duct. The error is less than 10 percent.

Figure 10 compares the predicted velocity profiles with data (Gessner et al., 1979) at three streamwise locations for developing flow in square duct entrance. It shows a good agreement at $x/d = 8$, however the agreement deteriorates at downstream locations at $x/d = 84$ because secondary flow is not considered in the current model.

Figure 11 compares the predicted friction factor with data (Zhang, 1993) in the rectangular channel of width to height
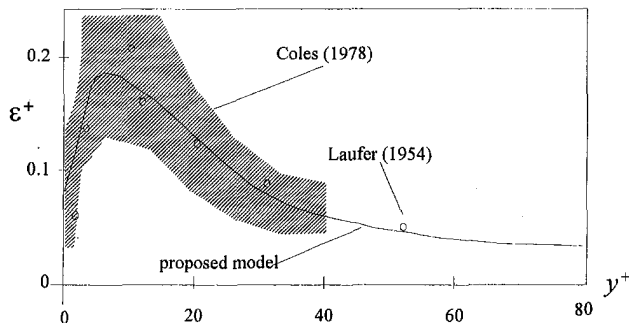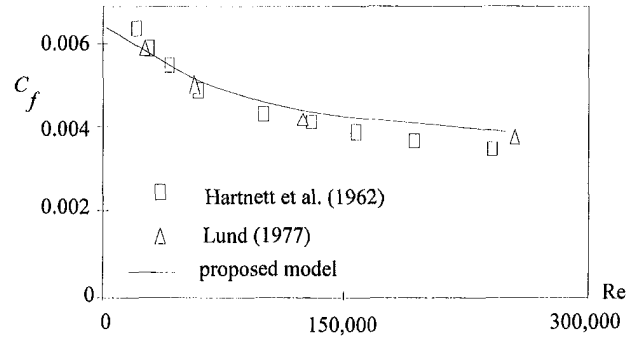
ratio 5.5. The prediction for smooth wall is very good for lower Reynolds numbers but 4 percent higher for the highest Reynolds number. The error for rough wall is 5 percent for $h_s/d = 0.0036$ and 8 percent for $h_s/d = 0.0053$.

Figures 12 shows the velocity profile along the shorter symmetrical line of a rectangular channel with y^+ representing the nondimensional distance from the wider wall of the channel. The predicted profile has the correct slope except slight overprediction in log-law shift compared to Zhang's (1993) experiment at $h_s/d = 0.0036$ and Re = 120,000.

Conclusions

A low-Reynolds-number k-ϵ turbulence model has been developed for smooth and rough wall turbulence by using new forms of model functions f_μ and f_1. The comparison with various experiment shows that:

• The equivalent sandgrain roughness height can be successfully included into low-Reynolds-number k-ϵ model to predict rough-wall flow.

• The model predicts rough-wall log-law velocity profile with correct slope and velocity shift.

• The predictions of the near smooth-wall behavior of k, ϵ, and velocity by the proposed model agree well with the available experimental data.
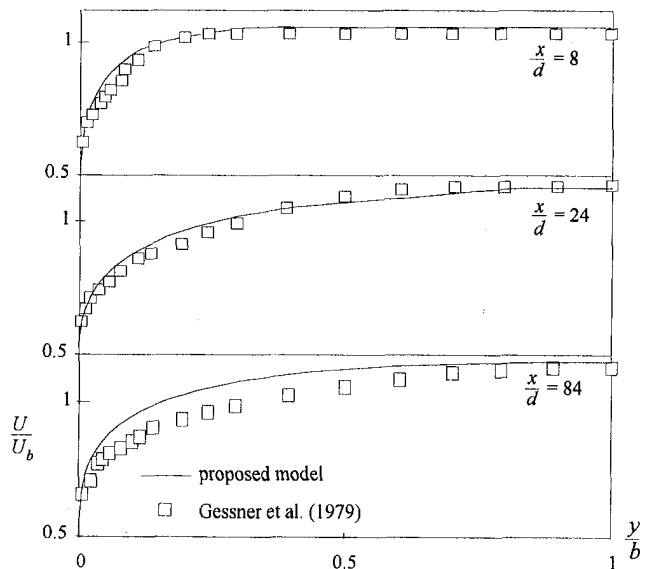

Fig. 8 Dissipation rate near smooth wall

Fig. 10 Velocity profiles at various streamwise locations in square duct entrance at Re = 250,000
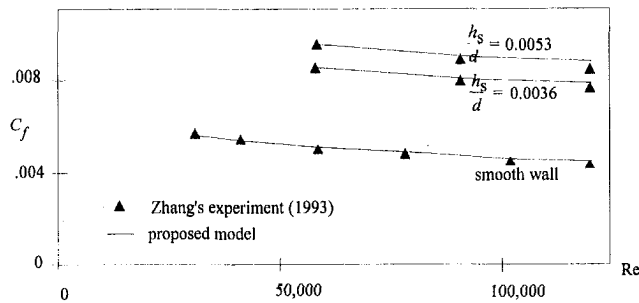
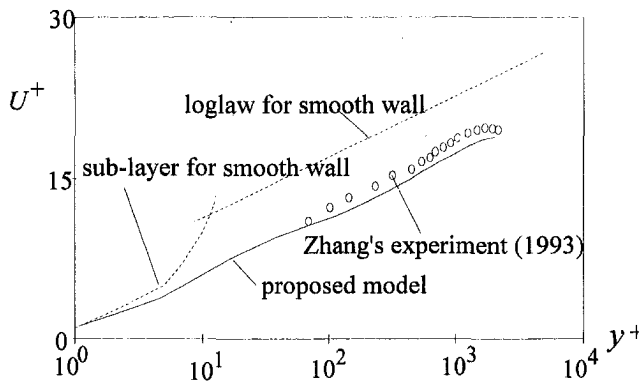**Fig. 11 Friction factor for rectangular channel**

Fig. 12 Velocity profile in rough wall rectangular channel

- The model can predict the friction factor of a smooth wall circular pipe flow within 5 percent in the Reynolds number range from 5×10^3 to 5×10^7. For a rough wall, the error is within 10 percent in the Reynolds number range from 5×10^4 to 5×10^6 and the roughness heights range h_s^+ from 0 up to 1000.
- Although the current model does not consider the secondary flow, it can still predict the friction coefficient for flows in square duct and rectangular channel within 10 percent for both smooth and rough surfaces.
- The model is applicable to developing flows.

References

Bandyopadhyay, P. R., 1987, "Rough-wall Turbulent Boundary Layers in the Transition Regime," *Journal of Fluid Mechanics,* Vol. 180, 231–266.

Chien, K.-Y., 1982, "Predictions of Channel and Boundary-Layer Flows with a Low-Reynolds-Number Turbulence Model," *AIAA Journal,* Vol. 20, pp. 33–38.

Colebrook, C. F., 1939, "Turbulent Flow in Pipes with Particular Reference to the Transition Region between the Smooth and Rough Pipes Laws," *The Journal of the Institution of Civil Engineers,* Vol. 11, pp. 133–156.

Colebrook, C. F., White, C. M., 1937, "Experiments with Fluid Motion in Roughened Pipes," *Proceedings of the Royal Society of London,* Series A, Vol. 161, 367–381.

Coles, D., 1978, "A Model for Flow in the Viscous Sublayer," *Proceedings of the Workshop on Coherent Structure of Turbulent Boundary Layers,* Lehigh University, Bethlehem, Pa.

Dutoya, D., Michard, P., 1981, "A Program for Calculating Boundary Layers along Compressor and Turbine Blades," *Numerical Methods in Heat Transfer,* R. W. Lewis, K. Morgan, and O. C. Zienkiewicz, eds., Wiley, New York.

El Telbany, M. M. M., Reynolds, A. J., 1981, "Turbulence in Plane Channel Flows," *Journal of Fluid Mechanics,* Vol. 111, pp. 283–318.

Gessner, F. B., and Emery, A. F., 1981, "The Numerical Predictions of Developing Turbulent Flow in Rectangular Ducts," ASME JOURNAL OF FLUIDS ENGINEERING, Vol. 103, pp. 445–455.

Hamm, F. R., 1954, "Boundary-layer Characteristics for Smooth and Rough Surfaces," *Transactions./The Society of Naval Architects and Marine Engineers,* Vol. 62, pp. 333–358.

Hartnett, J. P., Koh, J. C. Y., McComas, S. T., 1962, "A Comparison of Predicted and Measured Friction Factors for Turbulent Flow Through Rectangular Ducts," ASME *Journal of Heat Transfer,* Vol. 84, pp. 82–88.

Hassid, S., Poreh, M., 1978, "A Turbulent Energy Dissipation Model for Flows with Drag Reduction," ASME JOURNAL OF FLUIDS ENGINEERING, Vol. 100, pp. 107–112.

Hoffmann, G. H., 1975, "Improved Form of the Low-Reynolds Number k-ϵ Turbulence Model," *Physics of Fluids,* Vol. 18, pp. 309–312.

Krogstad, P., 1991, "Modification of the van Driest Damping Function to Include the Effects of Surface Roughness," *AIAA Journal,* Vol. 29, No. 6, pp. 888–894.

Lam, C. K. G., and Bremhorst, K., 1981, "A Modified Form of the k-ϵ Model for Predicting Wall Turbulence," ASME JOURNAL OF FLUIDS ENGINEERING, Vol. 103, pp. 456–460.

Laufer, J., 1954, "The Structure of Turbulence in Fully Developed Pipe Flow," NACA Report 1174.

Launder, B. E., and Spalding, D. B., 1974, "The Numerical Computation of Turbulent Flows," *Computer Methods in Applied Mechanics and Engineering,* Vol. 3, pp. 269–289.

Launder, B. E., and Sharma, B. I., 1974, "Application of the Energy-Dissipation Model of Turbulence to the Calculation of Flow Near a Spinning Disc," *Letters in Heat and Mass Transfer,* Vol. 1, pp. 131–138.

Lund, E. G., 1977, "Mean Flow and Turbulence Characteristics in the Near Corner Region of a Square Duct," M.S. Thesis, Department of Mechanical Engineering, University of Washington.

Myong, H. K., and Kobayashi, T., 1991, "Prediction of Three-dimensional Developing Turbulent Flow in a Square Duct With an Anisotropic Low-Reynolds-Number k-ϵ Model," ASME JOURNAL OF FLUIDS ENGINEERING, Vol. 132, pp. 608–615.

Nagano, Y., and Hishida, M., 1987, "Improved Form of the k-ϵ Model for Wall Turbulent Shear Flows," ASME JOURNAL OF FLUIDS ENGINEERING, Vol. 109, pp. 156–160.

Patankar, S. V., 1980, *Numerical Heat Transfer and Fluid Flow,* McGraw-Hill.

Patankar, S. V., and Spalding, D. B., 1972, "A Calculation Procedure for Heat, Mass and Momentum Transfer in Three-dimensional Parabolic Flows," *International Journal of Heat and Mass Transfer,* Vol. 15, pp. 1787–1806.

Patel, V. C., Rodi, W., and Scheuerer, G., 1985, "Turbulence Models for Near-Wall and Low Reynolds Number Flows: A Review," *AIAA Journal,* Vol. 23, pp. 1308–1319.

Prandtl, L., Schlichting, H., 1934, "Das Wiederstandagesetz rouher Platten," *Werft Reederere Hafen,* Vol. 15, pp. 1–4.

Reynolds, W. C., 1976, "Computation of Turbulent Flows," *Annual Review of Fluid Mechanics,* Vol. 8, pp. 183–208.

Schlichting, H., 1936, "Experimentelle Untersuchungen zum Rauhigkeits-problem," *Ingenieur-Archiv,* Vol. VII, No. 1, pp. 1–34, (Also "Experimental Investigation of the Problem of Surface Roughness," NACA TM 823).

Tarada, F., 1990, "Prediction of Rough-wall Boundary Layers Using a Low Reynolds Number k-ϵ Model," *International Journal of Heat and Fluid Flow,* Vol. 11, No. 4, pp. 331–345.

Taylor, R. P., Coleman, H. W., and Hodge, B. K., 1985, "Prediction of Turbulent Rough-wall Skin Friction Using a Discrete Element Approach," ASME JOURNAL OF FLUIDS ENGINEERING, Vol. 107, pp. 251–257.

Taylor, R. P., Scaggs, W. F., and Coleman, H. W., 1988, "Measurement and Prediction of the Effects of Nonuniform Surface Roughness on Turbulent Flow Friction Coefficients," ASME JOURNAL OF FLUIDS ENGINEERING, Vol. 110, pp. 380–384.

Van Driest, E. R., 1956, "On Turbulent Flow Near a Wall," *Journal of Aerospace Science,* Vol. 23, pp. 1007–1011.

Von Karman, 1934, "Turbulence and Skin Friction," *Journal of Aerospace Science,* Vol. 7, pp. 1–20.

White, F. M., 1991, *Viscous Fluid Flow,* 2nd Edition, McGraw-Hill, pp. 411–417.

Zhang, H., 1993, "Study of a Numerical Turbulence Model for Flow Past Smooth and Rough Surfaces," Ph.D. thesis, Department of Mechanical Engineering, University of Rhode Island.

R. M. C. So[1]
Professor.

H. Aksoy
Graduate Assistant.

S. P. Yuan
Graduate Assistant.

Mechanical and Aerospace Engineering,
Arizona State University,
Tempe, AZ 85287-6106

T. P. Sommer
ABB Power Generation Ltd.,
Gas Turbine Development,
CH-5401 Baden, Switzerland

Modeling Reynolds-Number Effects in Wall-Bounded Turbulent Flows

Recent experimental and direct numerical simulation data of two-dimensional, iso-thermal wall-bounded incompressible turbulent flows indicate that Reynolds-number effects are not only present in the outer layer but are also quite noticeable in the inner layer. The effects are most apparent when the turbulence statistics are plotted in terms of inner variables. With recent advances made in Reynolds-stress and near-wall modeling, a near-wall Reynolds-stress closure based on a recently proposed quasi-linear model for the pressure strain tensor is used to analyse wall-bounded flows over a wide range of Reynolds numbers. The Reynolds number varies from a low of 180, based on the friction velocity and pipe radius/channel half-width, to 15406, based on momentum thickness and free stream velocity. In all the flow cases examined, the model replicates the turbulence statistics, including the Reynolds-number effects observed in the inner and outer layers, quite well. Furthermore, the model reproduces the correlation proposed for the location of the peak shear stress and an appropriately defined Reynolds number, and the variations of the near-wall asymptotes with Reynolds numbers. It is conjectured that the ability of the model to replicate the asymptotic behavior of the near-wall flow is most responsible for the correct prediction of the Reynolds-number effects.

Introduction

According to Millikan (1939), the mean velocity U near a wall is influenced by the wall shear stress, τ_w, the local fluid density, ρ, the viscosity, μ, and the normal distance from the wall, y, for incompressible, isothermal turbulent flows. Application of the Buckingham Π theorem therefore results in $U^+ = U/u_\tau = F$ ($y^+ = \rho y u_\tau/\mu$) in the inner layer, where $u_\tau = (\tau_w/\rho)^{1/2}$ is the friction velocity. In the outer or defect layer, the drag generated as a result of the presence of the wall acts to slow down the fluid, thus creating a velocity defect. Therefore, the velocity defect is independent of the fluid viscosity, but instead depends on outer variables, such as the free stream velocity, U_∞, the boundary-layer thickness, δ, and the stream-wise pressure gradient, dP/dx. Here, x and y are the stream and normal coordinates, respectively, and P is the mean pressure. Again, dimensional arguments lead to $(U_\infty - U)/u_\tau = G$ ($\eta = y/\delta$, β), where $\beta = (\delta dP/dx)/\tau_w$ is a pressure gradient parameter. Millikan (1939) pointed out that if an overlap exists between the inner layer and the outer layer, the functions F and G must be logarithmic so that

$$U^+ = \kappa^{-1} \ln y^+ + B, \tag{1a}$$

$$(U_\infty - U)/u_\tau = -\kappa^{-1} \ln (\eta) + A(\beta), \tag{1b}$$

where κ is the von Karman constant, B is a constant and A is parametric in β. These arguments assume local similarity and, in the overlap region, the logarithmic law of the wall is a universal law. Here, the inner layer is defined to include the viscous sublayer, the buffer layer, and the logarithmic region of the velocity profile. On the other hand, the outer layer is taken to consist of the logarithmic and the wake regions. Therefore, Reynolds-number (hereafter denoted by Re for short) effects

are absent in the mean profiles given in (1). Later analysis by Mellor and Gibson (1966), however, reveals that A should also be parametric in the Reynolds number based on the displacement thickness, δ^*. Even then, the implication is that Re effects are only present in the outer layer and not in the inner layer. This is shown to be true also for compressible boundary layers (So et al., 1994b).

The above arguments are analogous to those used by Kolmogorov (1941) to establish the universal equilibrium theory of turbulence. According to this theory, an inertial subrange exists in the turbulence energy spectrum when Re is large enough and viscosity serves only to provide a dissipative sink for the kinetic energy at the small-scale end of the spectrum. This line of reasoning, when extended to boundary layers, implies that an inertial sublayer exists at large Re and the overall flow dynamics is independent of viscosity. The presence of viscosity is merely to provide a momentum sink at the wall. Millikan's (1939) arguments, therefore, establish that the mean flow near a wall is independent of Re and this is supported by the later work of Coles (1962) and Mellor and Gibson (1966) who showed that Re only affects the logarithmic and wake regions in a boundary-layer flow. However, as Re decreases, the logarithmic region slowly disappears while the viscous region remains unaffected by the Re decrease (Purtell et al., 1981). For fully-developed channel/pipe flows, the logarithmic region extends all the way to the centerline because the wake component of the mean velocity is much weaker than in the case of boundary layers (Wei and Willmarth, 1989).

When the local similarity arguments are applied to higher-order statistics, they imply that, at least in the inner layer, the individual second-order statistics obtained from different facilities and at different Re would collapse into a single curve if they were made dimensionless using inner-layer scalings. In reality, it is found that they do not scale with wall variables even deep inside the inner layer (Bandyopadhyay and Gad-el-Hak, 1994). The scatter between measurements is generally attributed to resolution problems associated with measuring techniques and inaccuracies related to diagnostic instruments. With the advent of miniature hot-wires and optical techniques,

careful and accurate measurements of the velocity field near a wall have been obtained by various researchers (e.g., Schild-knecht et al., 1979; Purtell et al., 1981; Andreopoulos et al., 1984; Karlsson and Johansson, 1988; Wei and Willmarth, 1989; Durst et al., 1993). These measurements show that the second-order turbulence statistics made dimensionless by inner-layer variables are influenced by Re over a very substantial portion of the boundary layer. The dependence on Re is even noticeable down to $y^+ < 15$. A most convincing demonstration of the Re effects is given by Bandyopadhyay and Gad-el-Hak (1994), who showed that the location of the peak value of the turbulent shear stress normalized by inner variables increases with Reynolds numbers.

Recently, direct numerical simulations (DNS) of turbulent flows in a plane channel (Kim et al., 1987), in a curved channel (Moser and Moin 1987), on a flat plate (Spalart 1988) and in a square duct (Huser and Biringen, 1993) and of a turbulent plane Couette flow (Kristoffersen et al., 1993) have been carried out. The Re range covered by these studies is too low and too narrow to provide sufficient evidence to indicate Re effects. However, when taken together with the experimental work quoted above, Re effects on wall-bounded turbulent flows are very evident, not only in the second-order statistics of the turbulence field but also in the mean flow profiles. Since the computational resource required varies approximately as the cube of Re, it would not be possible to simulate high-Reynolds-number turbulent flows soon (Karniadakis and Orszag, 1993). Therefore, the use of DNS experiments to study Re effects in wall-bounded turbulent flows with complex geometries is rather remote. On the other hand, very high Re experiments in wind and water tunnels are prohibitively expensive, and are not commonly carried out.

In general, most practical flows are wall-bounded and have very high Re. Since DNS and wind tunnel experiments could not be used to study these flows for a long time to come, the alternative is to resort to turbulent flow modeling. It should be noted that near-wall effects are different from low-Re effects. Even though the local Re is low near a wall, there is an additional effect due to wall blocking that is absent in the case of unbounded turbulence. This wall blocking effect gives rise to increased anisotropy of the turbulence as the wall is approached (Kim, 1989). If a model can be formulated so that it could replicate the Re effects of existing experimental and DNS data, the confidence of its extension to flows with ever higher Re could be established. Strictly speaking, most models are not valid for flows with low Re; be it wall-bounded or in an unbounded medium (Launder et al., 1975; Demuren and Sarkar, 1993). However, they are routinely validated against flows with low to moderate Re but seldom against flows with high Re. In this paper, the emphasis is placed on the modeling of low-Re effects in wall-bounded flows only. Therefore, the present objective is to seek a near-wall second-order turbulence model that could replicate Re effects fairly correctly in the calculations of two-dimensional, wall-bounded flows. Both DNS and experimental data are used to evaluate the model. The Re range chosen varies from $Re_\tau = 180$ to $Re_\tau = 8758$ for fully-developed channel/pipe flows and from $Re_\theta = 1410$ to $Re_\theta = 15406$ for flat plate boundary layers. Here, $Re_\tau = u_\tau h/\nu$ and $Re_\theta = U_\infty \theta/\nu$, ν is the fluid kinematic viscosity, h is the channel half-width or pipe radius and θ is the momentum thickness.

Near-Wall Reynolds-Stress Closure

A detailed derivation of the near-wall Reynolds-stress closure based on an asymptotic analysis of the exact and modeled Reynolds-stress equations has been given by So et al. (1994a). Therefore, only a brief summary is given here. Incompressible, isothermal turbulent flows are governed by the mean flow equations which can be written in Cartesian tensor form as

$$\frac{\partial U_i}{\partial x_i} = 0, \qquad (2)$$

$$\frac{DU_i}{Dt} = -\frac{1}{\rho}\frac{\partial P}{\partial x_i} + \nu \frac{\partial^2 U_i}{\partial x_j \partial x_j} - \frac{\partial \overline{u_i u_j}}{\partial x_j}, \qquad (3)$$

where D/Dt is the material derivative, upper case letters are used to denote Reynolds-averaged quantities and lower case letters their corresponding fluctuating part. Here, the Einstein summation convention is followed, U_i is the ith component of the mean velocity, u_i is the ith component of the fluctuating velocity and x_i is the ith component of the coordinates. These equations need closure because of the presence of the kinematic Reynolds stress terms, $\overline{u_i u_j}$. If a Reynolds-stress or second-order closure is invoked, the equations governing the transport of $\overline{u_i u_j}$ and ϵ, the dissipation rate of turbulent kinetic energy, k, are given by

$$\frac{D\overline{u_i u_j}}{Dt} = \frac{\partial}{\partial x_k}\left(\nu \frac{\partial \overline{u_i u_j}}{\partial x_k}\right) + D_{ij}^T + \left[-\overline{u_i u_k}\frac{\partial U_j}{\partial x_k} - \overline{u_j u_k}\frac{\partial U_i}{\partial x_k}\right]$$

$$+ \Pi_{ij} - \epsilon_{ij}, \qquad (4)$$

$$\frac{D\epsilon}{Dt} = \frac{\partial}{\partial x_j}\left(\nu \frac{\partial \epsilon}{\partial x_j}\right) + \frac{\partial}{\partial x_j}\left(C_\epsilon \frac{k}{\epsilon}\overline{u_i u_j}\frac{\partial \epsilon}{\partial x_i}\right)$$

$$+ C_{\epsilon 1}\frac{\epsilon}{k}\tilde{P} - C_{\epsilon 2}\frac{\epsilon \tilde{\epsilon}}{k} + \xi, \qquad (5)$$

where $\tilde{\epsilon} = \epsilon - 2\nu(\partial\sqrt{k}/\partial y)^2$, $\tilde{P}$ is the production of k and $C_\epsilon = 0.12$, $C_{\epsilon 1} = 1.50$, $C_{\epsilon 2} = 1.83$ are constants introduced in the modeled ϵ-equation. The function ξ is identically zero for flows far away from a wall and is introduced to account for near-wall effects. Its specific form depends on the near-wall models formulated for the Reynolds-stress equation. Therefore, only ξ and D_{ij}^T, Π_{ij}, ϵ_{ij}, which are the turbulent diffusion tensor, the velocity-pressure-gradient correlation tensor and the dissipation rate tensor, respectively, need modeling in (4) and (5).

It should be noted that D_{ij}^T is of higher order compared to ϵ_{ij} and Π_{ij}. Consequently, D_{ij}^T does not need near-wall corrections and the commonly used model of Launder et al. (1975) could be adopted. On the other hand, viscous dissipation is exactly balanced by viscous diffusion at the wall. This, and the fact that ϵ_{ij} should contract correctly to 2ϵ, suggests a way to correct the high-Reynolds-number, isotropic model proposed by Kolmogorov (1941) for ϵ_{ij}. Furthermore, in the near wall region, ϵ_{ij} and $\overline{u_i u_j}$ have to asymptote correctly to the kinematic constraints $\epsilon_{ij}/\overline{u_i u_j}$ given by Launder and Reynolds (1983). One such proposal is given by Lai and So (1990). Therefore, if $n_i = (0, 1, 0)$ denotes the wall unit normal and $C_s = 0.11$ introduced by Launder et al. (1975) is adopted, the models for the turbulent diffusion and viscous dissipation tensors can now be written as

$$D_{ij}^T = \frac{\partial}{\partial x_k}\left[C_s \frac{k}{\epsilon}\left(\overline{u_i u_l}\frac{\partial \overline{u_j u_k}}{\partial x_l} + \overline{u_j u_l}\frac{\partial \overline{u_k u_i}}{\partial x_l} + \overline{u_k u_l}\frac{\partial \overline{u_i u_j}}{\partial x_l}\right)\right],$$

$$(6)$$

$$\epsilon_{ij} = \frac{2}{3}\epsilon\delta_{ij} + f_{w1}\frac{\epsilon}{k}\left[-\frac{2}{3}k\delta_{ij}\right.$$

$$\left. + \frac{\overline{u_i u_j} + \overline{u_i u_k}n_k n_j + \overline{u_j u_k}n_k n_i + n_i n_j \overline{u_k u_l}n_k n_l}{1 + 3\overline{u_k u_l}n_k n_l/2k}\right]. \qquad (7)$$

The near-wall corrections for Π_{ij} are derived by including the contribution of the pressure diffusion part of the velocity-pressure-gradient correlation tensor. Far away from the wall,

pressure diffusion is negligible compared to pressure redistribution. Therefore, the high-Reynolds-number limit of Π_{ij} can be approximated by the pressure strain, or SSG, model of Speziale et al. (1991). Thus, pressure diffusion is included as part of the near-wall corrections to Π_{ij} so that the near-wall SSG model would give rise to a Reynolds-stress equation that is asymptotically correct as a wall is approached. The modeled equation is at least asymptotically correct to order y compared to the exact equation and, in some components of the equation, the balance is even correct to order y^2. A damping function based on the turbulent Reynolds number, $Re_t = k^2/\epsilon\nu$, is proposed for the near-wall correction term to diminish its influence away from the wall. Without going into details, the near-wall SSG model can be written as

$$\Pi_{ij} = -(C_1\epsilon + C_1^*\tilde{P})b_{ij} + C_2\epsilon\left(b_{ik}b_{kj} - \frac{1}{3}\Pi\delta_{ij}\right)$$

$$- \alpha_1\left(P_{ij} - \frac{2}{3}\tilde{P}\delta_{ij}\right) - \beta_1\left(D_{ij} - \frac{2}{3}\tilde{P}\delta_{ij}\right)$$

$$- 2\left(\gamma_1 + \frac{C_3^*}{2}\Pi^{1/2}\right)kS_{ij} + \Pi_{ij}^w. \quad (8)$$

The unknown second-order tensors in (8) are given by

$$b_{ij} = \frac{1}{2k}\left(\overline{u_iu_j} - \frac{2}{3}k\delta_{ij}\right), \quad (9a)$$

$$S_{ij} = \left(\frac{1}{2}\right)\left(\frac{\partial U_i}{\partial x_j} + \frac{\partial U_j}{\partial x_i}\right), \quad (9b)$$

$$P_{ij} = -\left[\overline{u_iu_k}\frac{\partial U_j}{\partial x_k} + \overline{u_ju_k}\frac{\partial U_i}{\partial x_k}\right], \quad (9c)$$

$$D_{ij} = -\left[\overline{u_iu_k}\frac{\partial U_k}{\partial x_j} + \overline{u_ju_k}\frac{\partial U_k}{\partial x_i}\right], \quad (9d)$$

where b_{ij}, S_{ij}, P_{ij}, and D_{ij} are the anisotropy tensor, the strain-rate tensor, the production tensor and its variation, respectively, $2\tilde{P} = P_{ii}$ and $\Pi = b_{ij}b_{ij}$. The model constants specified by Speziale et al. (1991) are $C_1 = 3.4$, $C_2 = 4.2$, $C_1^* = 1.8$, $C_3^* = 1.3$, $\alpha_1 = 0.4125$, $\beta_1 = 0.2125$ and $\gamma_1 = 0.01667$. Finally, Π_{ij}^w is the near-wall correction tensor, which is derived based on asymptotic analysis of the near-wall flow and is given by

$$\Pi_{ij}^w = f_{w1}[(C_1\epsilon + C_1^*\tilde{P})b_{ij} - C_2\epsilon\left(b_{ik}b_{kj} - \frac{1}{3}\Pi\delta_{ij}\right)$$

$$+ \alpha^*\left(P_{ij} - \frac{2}{3}\tilde{P}\delta_{ij}\right) + 2\gamma^*kS_{ij}] + \Pi_{ij}^P. \quad (10)$$

Here, f_{w1} is the damping function and Π_{ij}^P is the near-wall correction proposal for pressure diffusion. The final expression derived for Π_{ij}^P is given by

$$\Pi_{ij}^P = -\frac{1}{3}\left[\frac{\partial}{\partial x_l}\left(\nu\frac{\partial\overline{u_iu_k}}{\partial x_l}\right)n_kn_j + \frac{\partial}{\partial x_l}\left(\nu\frac{\partial\overline{u_ju_k}}{\partial x_l}\right)n_kn_i\right]$$

$$+ \frac{1}{3}\frac{\partial}{\partial x_m}\left(\nu\frac{\partial\overline{u_ku_l}}{\partial x_m}\right)n_kn_ln_in_j. \quad (11)$$

Two near-wall model constants, α^* and γ^*, are introduced and they are calibrated to give a correct prediction of the near-wall

asymptotes of a fully-developed channel flow. Thus, their values are determined to be $\alpha^* = -0.29$ and $\gamma^* = 0.065$.

Since the damping function f_{w1} is introduced into the model to limit the extent of the influence of the near-wall correction, it should vanish at a reasonable distance away from the wall. It is precisely for this reason that no single damping function has been found to be capable of yielding a limited extent for its influence covering a wide range of Re and different types of external and internal wall-bounded flows. In the course of validating this new near-wall Reynolds-stress closure, it is found that two damping functions are necessary if different types of flows covering a very wide range of Re are to be predicted correctly. These damping functions are found to be

$$f_{w1} = \exp\left[-\left(\frac{Re_t}{G}\right)^2\right], \quad (12a)$$

$$f_{w1} = \exp\left[-\left(\frac{A\,Re_t}{60}\right)^3\right], \quad (12b)$$

where $A = 1 - (9/2)(b_{ij}b_{ij} - 2b_{jk}b_{ki})$ and G is a constant. The choice of the damping function depends on Re and the correct one to use for each flow case is determined by monitoring the behavior of f_{w1} so that it vanishes in the range $80 < y^+ < 200$ depending on Re and the type of flow considered. The present investigation shows that, for all flow cases examined, (12a) with an appropriately determined G is applicable. The only exceptions are fully-developed channel and pipe flows with $Re_\tau \leq 250$. For these flows, the use of (12b) is more suitable.

It should be noted that three constants have been introduced in the near-wall SSG model; they are α^*, γ^*, and G. A systematic optimization procedure has not been followed to evaluate the correct values for these constants. The reason being that, depending on the number of constraints imposed (or the number of flow cases selected), a different set of optimized values could be obtained. Besides, an optimization study thus carried out would be likely to depend on the range of Re selected. Instead, $\alpha^* = -0.29$ and $\gamma^* = 0.065$ are determined by calibrating the calculation against one particular channel flow at a very low Re. Consequently, two values of G are found to be necessary in the use of (12a). For all channel and boundary-layer flows examined, $G = 200$ is found to yield the best results; while G takes on a value of 220 for all pipe flows investigated. This difference is probably due to the fact that α^* and γ^* have not been optimized properly. The higher value of G used in the pipe flow calculations does not affect the calculated κ, the location of the maximum shear stress and the behavior of the Reynolds stresses in these flows. As far as it can be ascertained, the major influence of G is in the prediction of the log law intercept at the high Re end of the pipe flow cases examined. Furthermore, the ability of the model to replicate the Re effects does not hinge on the optimized values of the model constants. Since the ability of the model to reproduce the trend is of primary importance here, it is not crucial to optimize the constants at this point. In the present investigation, again (12a), with G given by either 200 or 220 depending on the flow type, is used for all flow calculations except channel/pipe flows with $Re_\tau \leq 250$, where (12b) is assumed instead.

A similar approach, and the stipulation of the Shima (1988) compatibility condition, was used by So et al. (1994b) to derive the near-wall correcting function ξ for the ϵ-equation. Again, without going into details, the final result is given by

$$\xi = f_{w2}\left(-N\frac{\epsilon\tilde{\epsilon}}{k} + M\frac{\overline{\epsilon}^2}{k} - L\frac{\epsilon}{k}\tilde{P}\right), \quad (13)$$

where $f_{w2} = \exp[-(Re_t/40)^2]$ is a damping function introduced to insure the disappearance of the effects of ξ far away from a wall, and L, M, and N are model constants. Here, one single
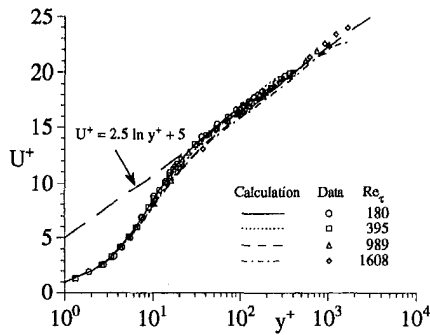
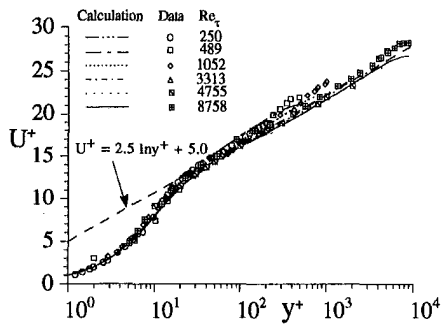**Fig. 1(a) Mean velocities plotted in inner-layer variables for channel flows**

Fig. 1(b) Mean velocities plotted in inner-layer variables for pipe flows
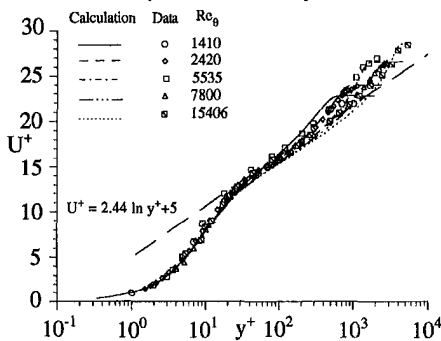

Fig. 1(c) Mean velocities plotted in inner-layer variables for boundary-layer flows

damping function is found to be applicable for all flow cases considered. Their calculations showed that these constants should take on values given by $L = 2.25$, $M = 0.5$ and $N = 0.57$. The modified ϵ, $\bar{\epsilon} = \epsilon - 2\nu k/y^2$, is introduced to ensure proper behavior of ϵ near a wall.

Thus modeled, (4) and (5) are valid as a wall is approached and are used to calculate wall-bounded flows where the boundary conditions on $-\overline{u_i u_j}$ and ϵ are given by: $-\overline{u_i u_j} = 0$ and $\epsilon_w = 2\nu(\partial\sqrt{k}/\partial y)^2$, respectively. The usual no slip condition is assumed for all mean velocities at the wall. The governing equations and their respective models are solved by specifying the proper inlet and outlet conditions for the flow under consideration. For fully-developed turbulent channel/pipe flows, the governing equations can be reduced to a set of ordinary differential equations. Standard Newton iteration or time marching numerical technique is used to solve the equations and the numerical errors incurred are well known. For these flows, a grid with 51 points is sufficient to yield grid independent solutions. On the other hand, thin shear layer approximations are invoked to simplify the governing equations to a set of boundary-layer equations. The boundary-layer code, developed by Anderson and Lewis (1971) and adopted a Crank-Nicolson type implicit finite-difference scheme to solve the equations, is used to numerically integrate the parabolic equations. The solutions are

found to be grid independent with 101 grid points. Therefore, the calculated differences between flows with a wide range of Re, if present, can be interpreted as the modeled Re effects rather than numerical errors. In the following, the Re effects on the mean flow and the turbulence statistics are discussed separately.

Reynolds-Number Effects on Mean Flow

Existing experimental and DNS data indicate that the mean velocity of channel/pipe flows and boundary layers can be scaled by inner-layer variables and they give rise to a fairly universal distribution in the inner region. In the outer layer, the wake component of the boundary layer is influenced by the Reynolds number and it will eventually disappear as the Reynolds number decreases to a certain minimum value. According to Coles (1962), this minimum value is about $\mathrm{Re}_\theta \leq 600$. At this Reynolds number, the logarithmic law of the wall would also disappear.

The test cases selected consist of four cases of channel flows, six cases of pipe flows and five cases of zero pressure gradient (zpg) boundary-layer flows (Table 1). Following Bandyopadhyay and Gad-el-Hak (1994), a reduced Reynolds number, $\mathrm{Re}_\tau^* = u_\tau\delta/\nu$, is defined for the boundary-layer flow. This would allow the pipe/channel flow and boundary-layer flow data to be compared on the same basis. The normalized mean velocities of these flow cases, U^+, plotted versus y^+, are shown in Figs. 1(a) to 1(c), separately for each type of flows. As expected, the channel/pipe flow results show very little wake component (Figs. 1(a) and 1(b)) and the data and model calculations are essentially well correlated by a single curve in the inner layer. The boundary-layer flows, on the other hand, show a substantial wake component and a gradual disappearance of the logarithmic law of the wall as the Reynolds number decreases (Fig. 1(c)). This behavior is fairly well reproduced by the near-wall model.

Within experimental and numerical errors, the calculated logarithmic region can be correlated by a single curve given by (1a) with $\kappa = 0.40$ and $B = 5.0$ for channel/pipe flows and $\kappa = 0.41$ and $B = 5.0$ for flat plate boundary layers. A more accurate determination of κ for the individual cases is obtained by following the procedure outlined in So et al. (1994b) and the results are reported in Table 1 for comparison. Contrary to the arguments of Simpson (1970), the von Karman constant is not dependent on Re. This universality of κ can be reproduced if an asymptotically correct near-wall model is used to calculate two-dimensional, wall-bounded turbulent flows. The near-wall model does a fair job of reproducing this universal inner-layer

Table 1 Comparison of the measured and calculated κ, H, and C_f

Data Source	Flow Type	Re_τ	Re_θ (Re_τ^*)	Calculation (Data) H	Calculation (Data) $C_f \times 10^3$	κ Model	κ Data
Kim et al. (1987)	Channel	180	-	-	-	0.40	0.40
Durst et al. (1993)	Pipe	250	-	-	-	0.39	0.40
Kim (1991)	Channel	395	-	-	-	0.39	0.40
Schildknecht et al. (1979)	Pipe	489	-	-	-	0.39	0.41
Wei and Willmarth (1989)	Channel	989	-	-	-	0.40	0.39
Laufer (1954)	Pipe	1052	-	-	-	0.40	0.40
Wei and Willmarth (1989)	Channel	1608	-	-	-	0.40	0.40
Perry and Abell (1975)	Pipe	3313	-	-	-	0.40	0.41
Perry and Abell (1975)	Pipe	4755	-	-	-	0.40	0.41
Laufer (1954)	Pipe	8758	-	-	-	0.40	0.40
Spalart (1988)	Boundary layer (zpg)	-	1410 (538)	1.46 (1.42)	3.84 (4.10)	0.36	0.41
Karlsson and Johansson (1988)	Boundary layer (zpg)	-	2420 (813)	1.43 (1.39)	3.44 (3.54)	0.38	0.41
Andreopoulos et al. (1984)	Boundary layer (zpg)	-	5535 (1464)	1.42 (1.30)	3.04 (2.70)	0.40	0.40
Klebanoff (1955)	Boundary layer (zpg)	-	7800 (2404)	1.37 (1.33)	2.84 (2.81)	0.40	0.43
Andreopoulos et al. (1984)	Boundary layer (zpg)	-	15406 (4029)	1.37 (1.28)	2.44 (2.36)	0.41	0.40

behavior and the prediction of κ is within the error margin of its determination from experiments. In general, a value of 0.4 is obtained and this is in excellent agreement with experimental and DNS data. The only exception is the case where $\mathrm{Re}_\theta = 1410$ (Spalart 1988). Here, the predicted κ falls outside of the error margin. One possible reason is the calculated extent of the log region which is much smaller than is indicated by the DNS data (Fig. 1(c)). In other words, the model predicts a larger Re effect than is indicated by the data. When the calculated values of κ are used to determine B, its value varies from a low of 3.4 to a high of 5.0 with most of the cases giving a value very close to 5.0. In general, the values of B determined for channel and boundary-layer flows are slightly smaller than 5. Again, the largest error in the estimate of B occurs in the case where $\mathrm{Re}_\theta = 1410$. This is associated with the much lower κ predicted by the model. Consequently, the calculated U^+ for these two flows appear below the log law. In spite of these differences, the law of the wall as given in (1) is reproduced by the near-wall SSG model. Also, the calculated κ is in agreement with data, to within measurement errors.

Another feature of boundary-layer flows is the variation of the shape factor $H = \delta^*/\theta$ with Re. The calculated H and skin friction coefficient, $C_f = 2\tau_w/\rho U_\infty^2$, are reported in Table 1 for comparison with experimental and DNS data. It can be seen that H varies from a high of 1.46 at the lowest Re_θ to about 1.37 at the highest Re_θ. This trend is consistent with the data shown (Table 1) and that reported by Bandyopadhyay and Gad-el-Hak (1994). The calculated C_f agrees to within 7 percent of the experimental and DNS values, except for the case, $\mathrm{Re}_\theta = 5535$, where the measured C_f does not agree with the measured trend (Table 1). In general, the Re effects on the mean flow are fairly well reproduced by the near-wall SSG model.

Reynolds-Number Effects on Turbulence Statistics

Evidence that Re effects penetrate deep into the viscous region can be gleaned from a plot of the near-wall asymptotes of the turbulence statistics. The leading term of these expansions near a wall are given by $k^+ = a_k y^{+2} + \ldots$, $-\overline{uv}^+ = a_{uv} y^{+3} + \ldots$, $\epsilon^+ = 2a_k + \ldots$, $u' = a_u y^+ + \ldots$, $v' = a_v y^{+2} + \ldots$, $w' = a_w y^+ + \ldots$, where the a's are time-averaged coefficients of the expansions and u', v', w' are the rms normal stresses normalized by u_τ along the axial, wall normal and transverse directions, respectively, $\overline{uv}^+ = \overline{uv}/u_\tau^2$, $k^+ = k/u_\tau^2$, and $\epsilon^+ = \epsilon\nu/u_\tau^4$. The near-wall asymptotes for u', k^+ and $-\overline{uv}^+$ are determined according to the following procedure. From the above expansions, it can be deduced that $k^+/\epsilon^+ y^{+2} = 0.5$. Also, $a_k = \epsilon_w^+/2$, where ϵ_w^+ is the wall value of ϵ^+. These two relations offer a way to determine a_k and an independent way to check its value. The value of ϵ_w^+ is known from the solution of the governing equations. At the same time, the calculated profile of k^+/ϵ^+ can be plotted against y^{+2}. A line with a slope of 0.5 is then drawn through the points closest to the wall. This way, the range of y^+ in which $k^+/\epsilon^+ y^{+2} = 0.5$ is valid can be determined. The same y^+ range is used to determine the near-wall asymptotes of the other expansions. Thus determined, a_k is found to agree to within 3 percent of that deduced from ϵ_w^+. Log-log plots of these values versus $\mathrm{Re}_\tau(\mathrm{Re}_\tau^*)$ are given in Fig. 2. A least square fit to these values is performed and the resultant straight lines are also displayed in Fig. 2. These plots clearly indicate that the near-wall asymptotes increase with Re, even though some scatter is noticed.

Momentum transport in two-dimensional turbulent wall-bounded flows is mainly carried out by the Reynolds shear stress. Therefore, it is of paramount importance to model the shear stress behavior correctly. However, the accuracy in which this quantity can be measured is not as good as that for u^2. Therefore, it is not possible to quantify with great accuracy the Re effects of the turbulent shear stress. Wei and Willmarth
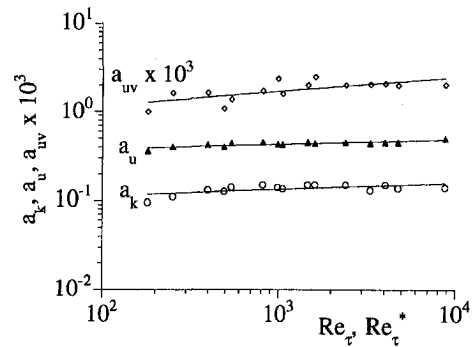

Fig. 2 Variations of the asymptotic coefficients a_k, $a_u a_{uv}$ with Re

(1989) examined channel and pipe flows where the normalized shear stress can be expressed as

$$-\overline{uv}^+ = (1 - y^+/\mathrm{Re}_\tau) - dU^+/dy^+. \qquad (14)$$

Once the mean velocity profile is known, the normalized shear stress can be calculated from (14) and used as a check on the accuracy of the measurements themselves. The agreement between the calculated profiles based on (14) and measurements is in general very good, except in a region very close to the wall. Wei and Willmarth (1989) found that the normalized shear stress at different Re does not collapse in the outer layer and the separation of the different profiles is still discernible well into the inner layer. Assuming a universal velocity profile, it can be seen from (14) that the Re dependency of the shear stress in the inner layer is particularly strong at low Re. The calculated shear stress profiles are compared with data in Figs. 3(a)-3(c) for channel, pipe and boundary-layer flows, respectively. Whenever data are available, they are also plotted in the figures for comparison. In the logarithmic and outer regions, the shear stress profiles do not collapse into a single curve. The predicted Re effects are more pronounced in channel and pipe flows; the shear stress profiles at different Re do not quite collapse in any region of the channel and pipe flows (Figs. 3(a) and 3(b)). However, they collapse into a single curve in the viscous region of boundary layers (Fig. 3(c)). The similarity for boundary layers extends to about $y^+ < 30$. According to (14), $-\overline{uv}^+ \rightarrow (1 - dU^+/dy^+)$ as $\mathrm{Re}_\tau \rightarrow \infty$. This implies that $-\overline{uv}^+$ has a broad maximum as $\mathrm{Re}_\tau \rightarrow \infty$ (Figs. 3(b) and 3(c)). In general, the agreement between data and calculations is very good.

Another test of the ability of the near-wall SSG model to reproduce the Re effects is to plot the location of the peak shear stress versus $\mathrm{Re}_\tau(\mathrm{Re}_\tau^*)$. If the location of the peak shear stress is denoted by y_p^+, its value can be determined from the shear stress profiles shown in Figs. 3(a)-3(c). A log-log plot of y_p^+ versus $\mathrm{Re}_\tau(\mathrm{Re}_\tau^*)$ is shown in Fig. 4. According to Sreenivasan (1988), a linear relation should exist between $\ln y_p^+$ and $\ln \mathrm{Re}_\tau$ or $\ln \mathrm{Re}_\tau^*$. Bandyopadhyay and Gad-el-Hak (1994) show that the straight line $y_p^+ = 2(\mathrm{Re}_\tau)^{1/2}$ correlates well with the experimental data they have examined in a log-log plot. The calculated results plotted in Fig. 4 can also be correlated by the same straight line. Strictly speaking, the coefficient 2 in $y_p^+ = 2(\mathrm{Re}_\tau)^{1/2}$ should be given by $1/\sqrt{\kappa}$ which can be deduced from (1a) and (14). At low to moderate Re_τ, the log-law does not apply at the point where the maximum shear stress occurs because the maximum shear stress occurs within the buffer region. At this point, the second derivative of the mean velocity with respect to y^+ is quite different from that calculated from the log-law. A composite mean velocity profile that predicts the buffer region correctly will lead to a higher value for the coefficient. Therefore, over a wide range of Re_τ, a larger coefficient seems to correlate better with data.
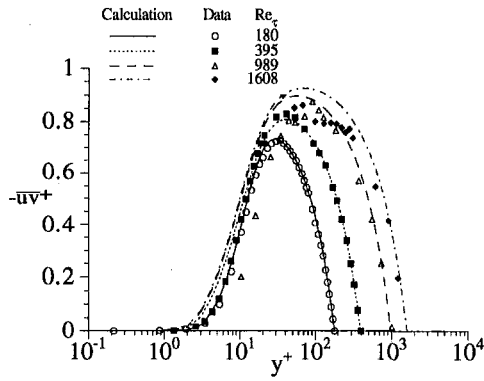
Fig. 3(a) Comparison of the calculated shear stress $\overline{uv}^+$ with data to show Re effects for channel flows
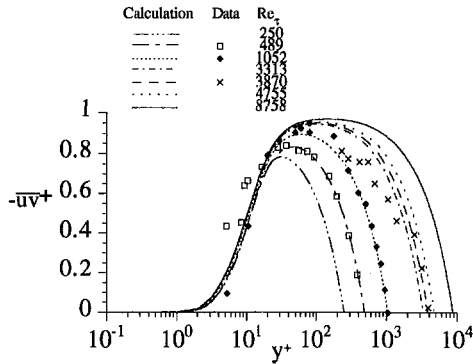

Fig. 3(b) Comparison of the calculated shear stress $\overline{uv}^+$ with data to show Re effects for pipe flows
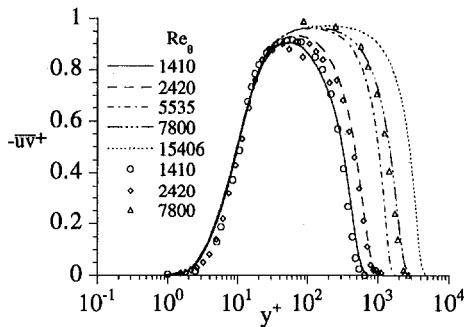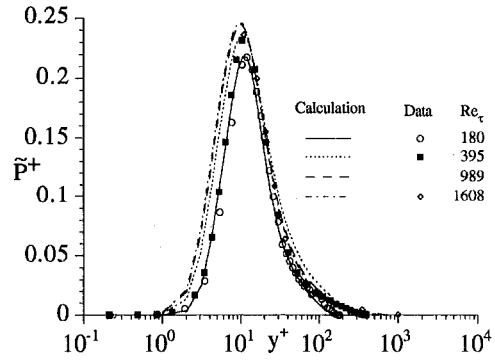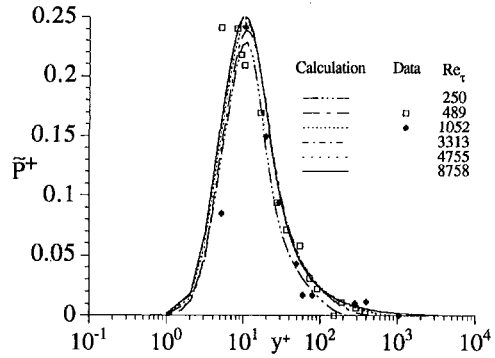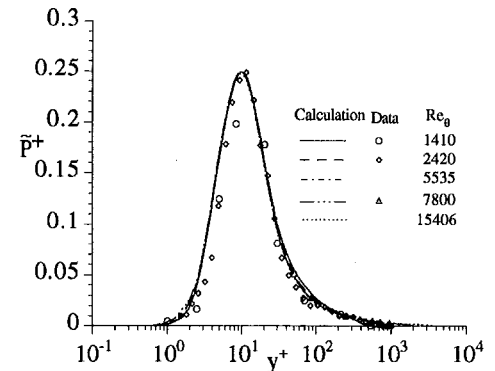

Fig. 3(c) Comparison of the calculated shear stress $\overline{uv}^+$ with data to show Re effects for boundary layers

Fig. 5(a) Comparison of the calculated k production $\tilde{P}^+$ with data to show Re effects for channel flow

Fig. 5(b) Comparison of the calculated k production $\tilde{P}^+$ with data to show Re effects for pipe flow

Fig. 5(c) Comparison of the calculated k production $\tilde{P}^+$ with data to show Re effects for flat plate boundary layers

Fig. 4 Variation of the shear stress peak location y_p^+ with Re

Wei and Willmarth (1989) showed that the normalized production of k, $\tilde{P}^+ = -\overline{uv}^+ (dU^+/dy^+)$, is relatively independent of Re in the outer region of channel flows but not so in the inner region. The Re range they investigated is bounded by

$2970 \le \text{Re} \le 39582$. Furthermore, Bandyopadhyay and Gad-el-Hak (1994) pointed out that even though the location of the peak shear stress varies with Re, the location of the peak value of $\tilde{P}^+$ is relatively independent of Re. The reason is that the scales producing the Reynolds shear stress are quite different from those responsible for the production of k. These conclusions can also be deduced from (14) and the definition of $\tilde{P}^+$. As $\text{Re}_\tau \to \infty$, $\tilde{P}^+$ reaches a maximum at $dU^+/dy^+ = \frac{1}{2}$ and this leads to a maximum $\tilde{P}^+ = \frac{1}{4}$. The calculations and measurements of $\tilde{P}^+$ plotted versus $\log y^+$ are shown in Figs. 5(a)–5(c). As expected, there are no Re effects on the calculated $\tilde{P}^+$ in the outer layer for channel/pipe flows and boundary-layer flows. In the inner layer, the behavior of $\tilde{P}^+$ is different for the different wall-bounded flows examined. For channel/pipe flows, $\tilde{P}^+$, particularly its peak value, distinctly depends on Re (Figs. 5(a) and 5(b)). This, however, is not true for boundary layers (Fig. 5(c)). Even though the calculated location of the peak value of $\overline{uv}^+$ varies with Re (Fig. 4), there is little variation in the calculated location of the peak value of $\tilde{P}^+$. Furthermore, the peak value of $\tilde{P}^+$ is less or equal to $\frac{1}{4}$; approaching the $\frac{1}{4}$ value
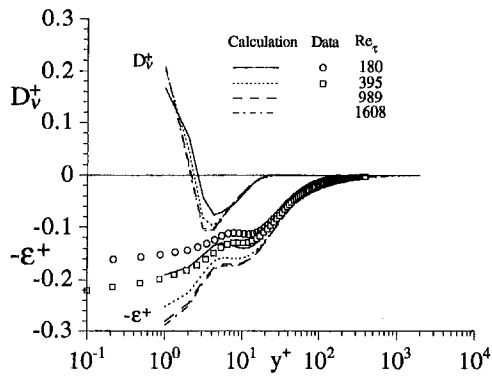
Fig. 6(a) Comparison of the calculated dissipation rate ϵ^+ and diffusion D_v^+ of k with data to show Re effects for channel flows
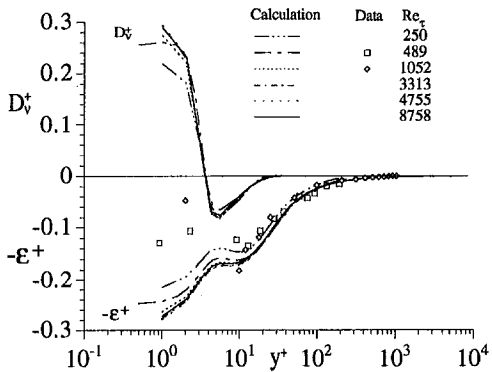

Fig. 6(b) Comparison of the calculated dissipation rate ϵ^+ and diffusion D_v^+ of k with data to show Re effects for pipe flows
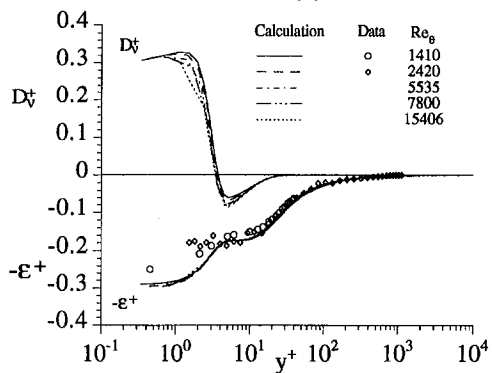

Fig. 6(c) Comparison of the calculated dissipation rate ϵ^+ and diffusion D_v^+ of k with data to show Re effects for boundary layers

only at high Re. For both channel/pipe flows and boundary layers, production of k seems to peak at about $y^+ = 10$. This is consistent with a value of about $y^+ = 12$ deduced by Bandyopadhyay and Gad-el-Hak (1994) who examined a different set of data with a different Re range. The ability of the model to predict these important features of wall-bounded flows is an indication of the validity of the model.

The corresponding profiles of ϵ^+ and the viscous diffusion of k^+, $D_v^+ = d^2 k^+/dy^{+2}$, are compared in Figs. 6(a)–6(c) with DNS data and measurements. Very near the wall, the dissipation rate is approximately balanced by viscous diffusion and pressure diffusion. The pressure diffusion term is not plotted in Figs. 6(a)–6(c); its value could be obtained by taking the difference between viscous dissipation and diffusion in the very near-wall region only. Depending on Re, the pressure diffusion contribution amounts to no more than 10% of the dissipation rate at the wall. The calculated results show that the dissipation rate behavior is essentially Re independent, except for very low Re (Fig. 6(a)). Viscous diffusion goes negative at about $y^+ =$

2 for channel flows (Fig. 6(a)) and at about $y^+ = 4$ for pipe and boundary-layer flows (Figs. 6(b) and 6(c)). In the region, $2 < y^+ < 20$, for channel flows and the region, $4 < y^+ < 20$, for pipe and boundary-layer flows, viscous diffusion remains negative and represents a major part in the balance between viscous dissipation, viscous diffusion and the production of k (Figs. 6(a)–6(c)). As Re increases, the part contributed by viscous diffusion to the balance decreases by about a factor of 2 (Figs. 6(b) and 6(c)). In all flow cases studied, equilibrium turbulence, where production approximately balances dissipation, is present only beyond $y^+ = 20$, and the calculated dissipation rate reaches a maximum at the wall; a fact well supported by DNS data. Therefore, the near-wall SSG model is replicating the Re effects of two-dimensional, wall-bounded turbulent flows quite well.

Conclusions

Among the experimental and DNS data examined, Re effects in the outer layer of the wall-bounded flows are very distinct. In the inner layer, these effects are not so distinct for boundary layers; however, they are quite discernible for channel/pipe flows. The trends as exhibited by the experimental and DNS data are essentially reproduced by the near-wall SSG model. Normalized production and dissipation of k is found to be independent of Re in the outer layer, except for very low Re channel flows. Also, at this low Re, viscous diffusion is found to be about twice that at higher Re in the region, $2 < y^+ < 20$. A most striking Re effect is the correlation of the location of the peak shear stress with Re for two-dimensional, wall-bounded flows. This relation is given by $y_p^+ = 2(\text{Re}_\tau)^{1/2}$ or $y_p^+ = 2(\text{Re}_\tau^*)^{1/2}$ in a log-log plot. Among the fifteen flow cases investigated, the calculated y_p^+ is well correlated by this relation. The experimental and DNS data show that the location of the peak shear stress varies with Re; however, the location of the peak production of k does not. The calculated location of the peak production of k occurs at about $y^+ = 10$ and compares well with $y^+ \approx 12$ reported by Bandyopadhyay and Gad-el-Hak (1994). All these results are accomplished with one set of model constants. Therefore, it can be concluded that the near-wall SSG model is capable of reproducing the Re effects in two-dimensional, wall-bounded flows.

References

Anderson, E. C., and Lewis, C. H., 1971, "Laminar or Turbulent Boundary Layer Flows of Perfect Gases or Reacting Gas Mixtures in Chemical Equilibrium," NASA Contractor Report 1893.

Andreopoulos, J., Durst, F., Jovanovic, J. and Zaric, Z., 1984, "Influence of Reynolds Number on Characteristics of Turbulent Wall Boundary Layers," Experiments in Fluids, Vol. 2, 7–16.

Bandyopadhyay, P. R. and Gad-el-Hak, M., 1994, "Reynolds Number Effects in Wall-Bounded Turbulent Flows," Applied Mechanics Review, Vol. 47, 307–365.

Coles, D. E., 1962, The Turbulent Boundary Layer in a Compressible Fluid. Report R-403-PR, Rand Corporation, Santa Monica, CA.

Demuren, A. O. and Sarkar, S., 1993, "Perspective: Systematic Study of Reynolds Stress Closure Models in the Computations of Plane Channel Flows," ASME JOURNAL OF FLUIDS ENGINEERING, Vol. 115, pp. 5–12.

Durst, F., Jovanovic, J., and Sender, J., 1993, "Detailed Measurements of the Near Wall Region of Turbulent Pipe Flows," Proceedings of the 9th Symposium on Turbulent Shear Flows, Kyoto, Japan, Paper No. 2.2.

Huser, A. and Biringen, S., 1993, "Direct Numerical Simulation of Turbulent Flow in a Square Duct," Journal of Fluid Mechanics, Vol. 257, pp. 65–95.

Karniadakis, E. G. and Orszag, S. A., 1993, "Nodes, Modes, and Flow Codes," Physics Today Vol. 46, No. 3, 34–42.

Karlsson, R. I. and Johansson, T. G., 1988, "LDV Measurements of Higher Order Moments of Velocity Fluctuations in a Turbulent Boundary Layer," Laser Anemometry in Fluid Mechanics, D. F. G. Durao et al., eds., Ladoan-Instituto Superior Tecnico, Portugal, pp. 273–289.

Kim, J., 1989, "On the Structure of Pressure Fluctuations in Simulated Turbulent Channel Flow," *Journal of Fluid Mechanics,* Vol. 205, pp. 421–451.

Kim, J., 1991, Private communication.

Kim, J., Moin, P., and Moser, R. D., 1987, "Turbulence Statistics in Fully Developed Channel Flow at Low Reynolds Number," *Journal of Fluid Mechanics,* Vol. 177, pp. 133–186.

Klebanoff, P. S., 1955, Characteristics of Turbulence in a Boundary Layer with Zero Pressure Gradient, NACA Report 1247.

Kolmogorov, A. N., 1941, "The Local Structure of Turbulence in an Incompressible Viscous Fluid for Very Large Reynolds Numbers," *Comptes Rendus Academy of Science,* U.S.S.R. 30, 301–305 (Translation, *Turbulence, Classic Papers on Statistical Theory,* S. K. Friedlander & L. Topper, Interscience, 1961).

Kristoffersen, R., Bech, K. H. and Andersson, H. I., 1993, "Numerical Study of Turbulent Plane Couette Flow at Low Reynolds Number," *Applied Scientific Research,* Vol. 51, pp. 337–343.

Lai, Y. G. and So, R. M. C., 1990, "On Near-Wall Turbulent Flow Modeling." *Journal of Fluid Mechanics,* Vol. 221, pp. 641–673.

Laufer, J., 1954, "The Structure of Turbulence in Fully-Developed Pipe Flow," NACA Report 1174.

Launder, B. E., Reece, G. J., and Rodi, W., 1975, "Progress in the Development of a Reynolds Stress Turbulence Closure," *Journal of Fluid Mechanics,* Vol. 68, pp. 537–566.

Launder, B. E. and Reynolds, W. C., 1983, "Asymptotic Near-Wall Stress Dissipation Rates in a Turbulent Flow," *Physics of Fluids,* Vol. 26, pp. 1157–1158.

Mellor, G. L. and Gibson, D. M., 1966, "Equilibrium Turbulent Boundary Layers," *Journal of Fluid Mechanics,* Vol. 24, pp. 225–253.

Millikan, C. B., 1939, "A Critical Discussion of Turbulent Flow in Channels and Circular Pipes," *Proceedings of the Fifth International Congress on Applied Mechanics,* Wiley, New York, pp. 386–392.

Moser, R. D. and Moin, P., 1987, "The Effects of Curvature in Wall-Bounded Turbulent Flows," *Journal of Fluid Mechanics,* Vol. 175, pp. 479–510.

Perry, A. E. and Abell, C. J., 1975, "Scaling Laws for Pipe-Flow Turbulence," *Journal of Fluid Mechanics,* Vol. 67, pp. 257–271.

Purtell, L. P., Klebanoff, P. S. and Buckley, F. T., 1981, "Turbulent Boundary Layer at Low Reynolds Number," *The Physics of Fluids,* Vol. 24, pp. 802–811.

Schildknecht, M., Miller, J. A. and Meier, G. E. A., 1979, "The Influence of Suction on the Structure of Turbulence in Fully-Developed Pipe Flow," *Journal of Fluid Mechanics,* Vol. 90, pp. 67–107.

Simpson, R. L., 1970, "Characteristics of Turbulent Boundary Layers at Low Reynolds Numbers With and Without Transpiration," *Journal of Fluid Mechanics,* Vol. 42, pp. 769–802.

So, R. M. C., Aksoy, H., Sommer, T. P. and Yuan, S. P., 1994a, "Development of a Near-Wall Reynolds-Stress Closure Based on the SSG Model for the Pressure Strain," NASA Contractor Report 4618.

So, R. M. C., Zhang, H. S., Gatski, T. B. and Speziale, C. G., 1994b, "On Logarithmic Laws for Compressible Turbulent Boundary Layers," *AIAA Journal,* Vol. 32, pp. 2162–2168.

Spalart, P. R., 1988, "Direct Simulation of a Turbulent Boundary Layer up to $R_\theta = 1410$," *Journal of Fluid Mechanics,* Vol. 187, pp. 61–98.

Speziale, C. G., Sarkar, S., and Gatski, T. B., 1991, "Modeling the Pressure-Strain Correlation of Turbulence: An Invariant Dynamical Systems Approach," *Journal of Fluid Mechanics,* Vol. 227, pp. 245–272.

Sreenivasan, K. R., 1988, "A Unified View of the Origin and Morphology of the Turbulent Boundary Layer Structure," *Turbulence Management and Relaminarization,* eds., H. W. Liepmann and R. Narasimha, Springer-Verlag, pp. 37–61.

Wei, T. and Willmarth, W. W., 1989, "Reynolds-Number Effects on the Structure of a Turbulent Channel Flow," *Journal of Fluid Mechanics,* Vol. 204, pp. 57–95.

Measurements of the Turbulence Structure in the Vicinity of a 3-D Separation

(Data Bank Contribution)*

C. J. Chesnakas

R. L. Simpson

Department of Aerospace
and Ocean Engineering,
Virginia Polytechnic Institute
and State University,
Blacksburg, VA 24061-0203

The flow in the cross-flow separation region of a 6:1 prolate spheroid at 10 deg angle of attack, $Re_L = 4.20 \times 10^6$, was investigated using a novel, miniature, 3-D, fiber-optic Laser Doppler Velocimeter (LDV). The probe was used to measure three simultaneous, orthogonal velocity components from within the model, from approximately $y^+ = 7$ out to the boundary layer edge. Velocity, Reynolds stress, and velocity triple product measurements are presented. These measurements are used to calculate the skin friction and to examine the convection, production, and diffusion of turbulent kinetic energy (TKE) about the three-dimensional separation. Comparisons of the measured production and diffusion of TKE in the cross-flow separation region—as well as in nonseparated regions of the flow—to the production and diffusion predicted by several models for these terms are shown.

Introduction

The phenomenon of three-dimensional separation of the flow about a body, though quite common, is both difficult to model and poorly understood. Indeed, since—unlike in two-dimensional flow separation—three-dimensional flow separation is rarely associated with the vanishing of the wall shear stress, it can often be difficult to even identify its presence or its precise location in 3-D flow.

In order to better understand three-dimensional flow separation, several groups have studied the flow about a 6 to 1 prolate spheroid at angle of attack. This flow is a well-defined, relatively simple 3-D flow which exhibits all the fundamental phenomena of three-dimensional flow, and is schematically illustrated in Fig. 1. The flow separating from the lee-side of the prolate spheroid, at the point marked S_1, rolls up into a strong vortex on each side of the body which reattaches at the point R_1. This primary separation may or may not, depending on flow conditions, be accompanied by secondary separations, S_2 and S_3, and reattachment R_2. This results in a highly skewed, and thus three-dimensional, boundary layer.

Previous works by Meier et al. (1984 and 1986), Kreplin et al. (1985) and Vollmers et al. (1985) at the DFVLR (now the DLR) have documented the surface flow, surface pressure, skin friction and mean velocity around the prolate spheroid at Re = 7.7×10^6. Previous work at VPI by Ahn (1992) has documented the Reynolds number and angle of attack effects on the boundary layer transition and separation phenomena for this flow. Barber and Simpson (1991) documented the mean and turbulent velocities in the cross-flow separation region, but due to the limitations of their instrumentation they obtained no data within the inner boundary layer.

Because of the simple geometry and the extent of the experimental data, this flowfield has made an excellent test case for three-dimensional computational models. A recent study by AGARD (1990) used the DFVLR data for comparison to three-dimensional computations utilizing integral boundary-layer, al-

gebraic mixing-length, and eddy-viscosity turbulence models. All of the computational models experienced difficulties in calculating the flowfield in the cross-flow separation region. Gee et al. (1992) obtained somewhat better results using versions of the Baldwin-Lomax and Johnson-King turbulence models modified for three dimensions, but stated that "more experimental data may be required before a better understanding of the effects of turbulence models on flow parameters can be gained."

One of the previously noted effects of boundary-layer skewing on turbulence is the inequality of the flow-gradient angle, γ_g, and the turbulent-shear-stress angle, γ_τ, which are defined as

$$\gamma_g = \tan^{-1} \frac{\partial W/\partial y}{\partial U/\partial y}, \quad \gamma_\tau = \tan^{-1} \frac{\overline{vw}}{\overline{uv}}. \tag{1}$$

The inequality of γ_g and γ_τ implies that models which use an eddy viscosity must allow the eddy viscosity to vary in the streamwise and cross-stream directions. Currently, most models do not incorporate this 3-D effect. One notable exception is the Rotta-T model, (Rotta, 1979), which assumes that the cross-stream to streamwise eddy viscosity ratio is a constant. This, unfortunately, makes the model coordinate-system dependent.

Since turbulent quantities can be very difficult to measure near the wall in a 3-D boundary layer, and since some quantities of interest—most notably the pressure-velocity correlations—are nearly impossible to accurately measure, it would seem that Direct Numerical Simulation (DNS) would be an excellent tool for "experimentally" obtaining turbulence data for 3-D boundary layers. Unfortunately, the enormous computer resources required for these calculations makes them impractical for most 3-D flows. Two simple 3-D flows which have been investigated with DNS. Spalart (1988) investigated the boundary layer on a flat plate with a freestream velocity which rotated at a constant angular rate and Moin et al. (1990) and Sendstad and Moin (1992) investigated the flow in a 2-D channel with a suddenly applied, cross-stream pressure gradient. Both these flows are highly idealized; however, these flows do reproduce the fundamental effects of three dimensionality on turbulence and can help illuminate experimental observations of 3-D turbulent flow.

The present work extends the knowledge of this 3-D separated flow with measurements of the total-velocity vector, as well as the full Reynolds-stress tensor and velocity triple prod-

---

Fig. 1 Flow lines in the separation region of the prolate spheroid, 2-D projection

Experimental Facility

Tests were performed in the Virginia Polytechnic Institute and State University Stability Wind Tunnel. This tunnel is a continuous, closed-test-section, single-return, subsonic wind tunnel with a 7 m long, 1.8 m square test section. The 9:1 contraction ratio and seven anti-turbulence screens provide for very low turbulence levels—on the order of 0.03 percent or less. Temperature stabilization is provided by an air exchange tower.

The 6 to 1 prolate spheroid model used in this experiment is 1.37 m (54 in.) in length and 0.229 m (9 in.) in diameter. The model has a fiberglass skin bonded to an aluminum frame. A circumferential trip, consisting of posts 1.2 mm in diameter, 0.7 mm high spaced 2.5 mm apart, was placed around the nose of the model at $x/L = 0.2$ in order to stabilize the location of transition, and consequently, the location of the separation. Windows 30 × 150 × 0.75 mm thick were placed in the skin for optical access to the flow. The windows were molded to the curvature of the model to minimize flow disturbances, and were mounted flush with the model surface within 0.1 mm. Wax was used to smooth any small steps between the windows and model skin. The model was supported with a rear-mounted, 0.75 m long sting connected to a vertical post coming through the wind tunnel floor.

A unique, three-component, fiber-optic LDV probe was used for these measurements. It was designed specifically to measure the complete velocity vector and full Reynolds-stress tensor from the viscous sublayer to the edge of the boundary-layer on the 6:1 prolate spheroid. The design of the probe is discussed in detail in Chesnakas and Simpson (1994).

The probe is a two-color, three-component, fiber-optic design. Light for the probe comes from the blue and green lines of an argon-ion laser with scattered light collected in off-axis backscatter. The measured velocity components are mutually orthogonal, and the probe volume is roughly spherical with a diameter of approximately 55 μm. The probe was positioned inside the model with all beams passing through the window as shown in Fig. 2. In this way the flow is undisturbed by the presence of the probe. The probe was mounted to the frame of the model on a two-component traverse which could be remotely positioned ±2.5 cm in both the axial and radial directions. Positioning in the circumferential, or ϕ, direction was accomplished by rotating the model about its primary axis. The Doppler frequency of the LDV signals was analyzed using three Macrodyne model FDP3100 frequency domain signal processors operating in coincidence mode.

Polystyrene latex (PSL) spheres 0.7 μm in diameter were used to seed the flow. The seed was suspended in ethanol and

ucts, throughout the boundary layer in the cross-flow separation region. Previous to this work, little data on the Reynolds stress tensor were available, and no data on the velocity triple products existed. The data which were available did not extend to the sublayer. The spacing of the data presented here is such that the computation of the wall shear stress and virtually all the terms of the turbulent kinetic energy equation is possible.

The present measurements were accomplished using a miniature, three-dimensional, fiber-optic LDV designed specifically for this application. The probe was placed within the model, and all beams passed through a plastic window molded to the shape of the model so that the flow was virtually undisturbed by the instrumentation. The full set of velocity measurements can be found in Chesnakas et al. (1994) and in the *Journal of Fluids Engineering* data bank.

——— Nomenclature ———

C_f = skin-friction coefficient, $\tau_w/(\rho U_\infty^2/2)$

k = turbulent kinetic energy, $(\overline{u^2} + \overline{v^2} + \overline{w^2})/2$

L = length of model, 1.37 m

Re = Reynolds number, $U_\infty L/\nu$

u^* = friction velocity, $\sqrt{\tau_w/\rho}$

U = velocity component in the plane tangent to the model surface, parallel to the wall-flow angle

U_e = total velocity at the edge of the boundary layer

U_{fs} = velocity component in the plane tangent to the model surface, parallel to the flow angle at the boundary-layer edge

U_∞ = wind tunnel freestream velocity

V = velocity component perpendicular to the model surface (+ outward)

W = velocity component in the plane tangent to the model surface, perpendicular to the wall-flow angle

x = axial distance from the nose of model

y = perpendicular distance from the model surface.

β = flow angle, in plane perpendicular to y, from the axial direction (positive in the windward direction)

γ_g = flow gradient angle

γ_τ = turbulent shear stress angle

ϵ = dissipation of turbulent kinetic energy

θ = boundary-layer streamwise-momentum thickness

ν = kinematic viscosity

ρ = density

τ_w = wall shear stress

δ = boundary-layer thickness ($U_{fs}/U_e = 0.99$)

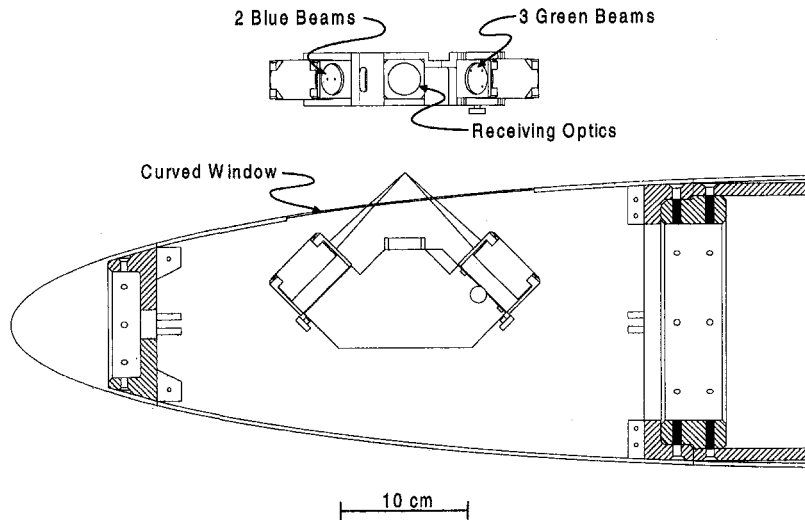ϕ = circumferential angle, from windward side

---

Fig. 2   3-D, fiber-optic, boundary-layer LDV probe placed inside the prolate spheroid

introduced into the flow using two air-atomizing paint spray nozzles placed just downstream of the turbulence-reducing screens. The arrangement of the two nozzles produced a localized region of seeded flow extending a minimum of 10 cm on all sides of the model. This arrangement causes some increase in the freestream turbulence; the increase, however, is below the measurement resolution of this instrument, and has not been quantified.

All tests were performed at a 10° angle of attack and with a Reynolds number based on the model length and free-stream velocity of 4.20×10^6. Surface oil flow visualizations by Ahn (1992) indicated that the primary separation begins approximately at $x/L = 0.600$, $\phi = 145°$. Boundary-layer profiles were therefore measured at $x/L = 0.400$ and 0.600 from $\phi = 90°$ to $\phi = 180°$ in 10° increments in order to examine the conditions leading to separation. Ahn's oil-flows also showed the separation to be well developed by $x/L = 0.762$, with the convergence of flow lines indicating the separation line at $\phi = 123$ deg. To examine the development of the flow about the primary separation, boundary-layer profiles were measured at $x/L = 0.752$ and 0.762 at $\phi = 120$, 123, and 125 deg, and at 0.772 at $\phi = 105$ to 130 deg in 5 deg increments, plus at $\phi = 123$ deg. This paper will concentrate primarily on the measurements about $x/L = 0.762$, $\phi = 123$ deg, where the measurements are sufficiently clustered to allow the evaluation of all spatial derivatives.

Each boundary-layer profile consisted of from 14–17 radial locations, from less than 0.01 cm from the model surface out to the boundary-layer edge. At each of these locations, 16,384 coincident 3-D velocity realizations were acquired.

Uncertainty Estimates

Uncertainty estimates for the measurements presented here are listed in Table 1. It should be noted that turbulence quantities

Table 1   Uncertainty estimates

Term	Uncertainty	Term	Uncertainty
U_i	$0.005\,|U|$	γ_g	$1.1°$
u_i^2	2%	γ_τ	$4°$
$u_i u_j$	$0.03\,(u_i^2 \cdot u_j^2 + (u_i u_j)^2)^{1/2}$	Convection	20%
u_i^3	$0.05\,(u_i^2)^{1.5}$	Production	20%
$u_i^2 u_j$	$0.05\,u_i^2\,(u_j^2)^{1/2}$	Diffusion	20%
β	$0.7°$	Dissipation	20%
β_w	$1.5°$	Visc. diff.	40%
C_f	4%		

Note: i and j subscripts DO NOT imply summation.

at the edge of the boundary layer are limited by a minimum measurable turbulence intensity of about 1.5 percent, and that the TKE terms at the point measured closest to the wall are of higher uncertainty due to the high uncertainty of calculating one-sided derivatives.

Motion in the radial direction was powered by a rotary-encoded servo-motor, and repeatability of the radial positioning was found to be better than ±0.008 mm. Positioning of the measurement volume in the circumferential direction was measured with a sting-mounted index and was accurate to within 0.1 deg.

Results

Measured Flow Quantities. Boundary-layer measurements are presented here in a wall-collateral coordinate system—with the V-velocity component perpendicular to the model surface and positive outward, U perpendicular to V and in the direction of the mean velocity at the wall, and W completing the right-hand rule. For this measurement set, flow with a positive W component is in the windward direction.

Plots of the mean-velocity profiles are shown in Fig. 3. The average quantities displayed in these plots are not strictly numerical averages of the approximately 16,000 velocity realizations at each measurement point, but are rather averages with two statistical corrections applied. The first of these is a correc-
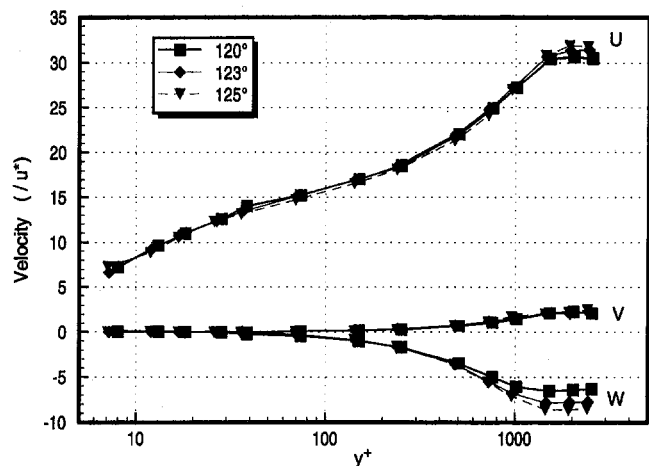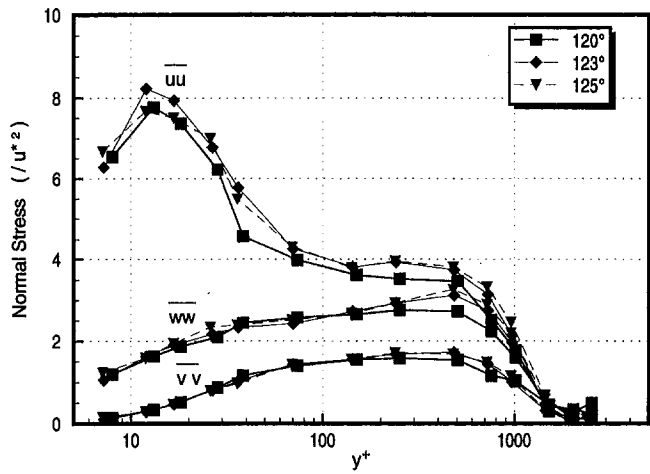

Fig. 3   Velocity profiles, $x/L = 0.762$

Fig. 4 Reynolds normal stress profiles, $x/L = 0.762$

Fig. 6 Third moments of velocity, $x/L = 0.762$, $\phi = 123$ deg

tion for velocity bias. To correct for velocity bias, individual particle velocity realizations are averaged using a weighting factor of 1 over the total measured velocity, as originally suggested by McLaughlin and Tiederman (1973). That is, an inverse-velocity weighting scheme is employed. The second statistical correction is intended to compensate for flow gradients across the measurement volume. These gradients become significant near the wall, and cause the measured turbulence intensities to be higher than what would be measured with an infinitely small probe volume. To correct for this "gradient broadening," all computed components are corrected by a scheme similar to that of Durst et al. (1992).

Also, the radial position of the measurements has been corrected for errors in setting the zero (wall) position by a scheme discussed in the section on skin-friction calculation.

The measurements at $\phi = 120$ deg are on the attached side of the primary separation line, and the measurements at $\phi = 125$ deg lie within the separated region of the flow. The measurements at $\phi = 123$ deg are, according to the work of Ahn (1992), very near the separation line. None of these profiles exhibit reverse flow as one would see in two-dimensional separated flows. This is to be expected since, as was noted above, the skin friction does not usually vanish in 3-D separated flows. The profiles at 123 and 125 deg merely exhibit more moderate gradients near the wall and greater flow turning than the profile at 120 deg.

Plots of the Reynolds normal stresses are shown in Fig. 4. From Fig. 4 it can be seen that the maximum value of the
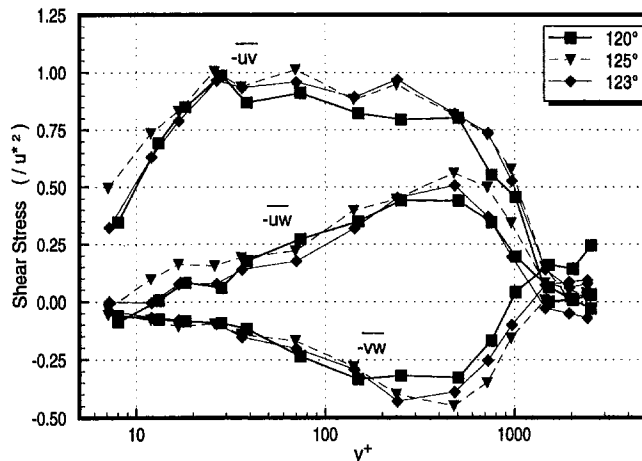
normal stress occurs quite far down in the boundary layer, at approximately $y^+ = 12$. The normal stress is dominated by $\overline{uu}$, with $\overline{vv}$ becoming negligible near the wall.

Plots of the Reynolds shear stresses are shown in Fig. 5. The dominant shear stress, $-\overline{uv}$, is near the expected value of 1 (when normalized by u^{*2}) from $30 < y^+ < 500$. The $-\overline{vw}$ shear stress is near zero near the wall—where the flow is aligned with the coordinate system—and becomes comparable in magnitude to $-\overline{uv}$ for $y^+ = 600$, where a considerable cross flow exists. The $-\overline{uw}$ shear stress behaves similarly to $-\overline{vw}$. The DNS study of Moin et al. (1990), in which a three-dimensional turbulent channel flow experiences a sudden, transverse pressure gradient, found that $-\overline{uw}$ became quite large—up to three times the magnitude of $-\overline{uv}$—as the flow became three dimensional. Clearly that is not the case here. If the boundary-layer profiles shown here are plotted in a local-freestream coordinate system, however, $-\overline{uw}$ can indeed become quite large. It seems then that the large value of $-\overline{uw}$ observed in some 3-D flows may say more about the choice of coordinate system than about the structure of the flow. Moin et al.'s choice of a coordinate system aligned with the initial, 2-D flow is one which will enhance the value of $-\overline{uw}$ near the wall compared to a wall-flow-oriented coordinate system.

Plots of all velocity triple products at $\phi = 123$ deg are shown in Figs. 6, 7, and 8. Knowledge of these terms is necessary to evaluate turbulence models utilizing equations for any of the Reynolds stresses. Here, they will be used to evaluate the turbu-
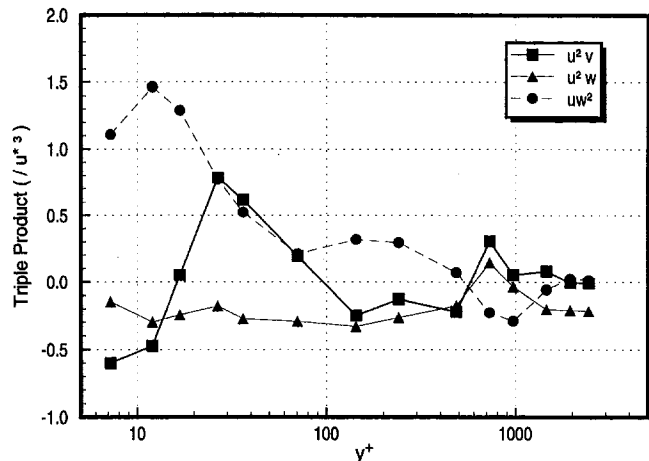

Fig. 5 Reynolds shear stress profiles, $x/L = 0.762$

Fig. 7 Triple products of velocity, $x/L = 0.762$, $\phi = 123$ deg

Fig. 8   Triple products of velocity, x/L = 0.762, ϕ = 123 deg

Fig. 10   Skin-friction coefficient
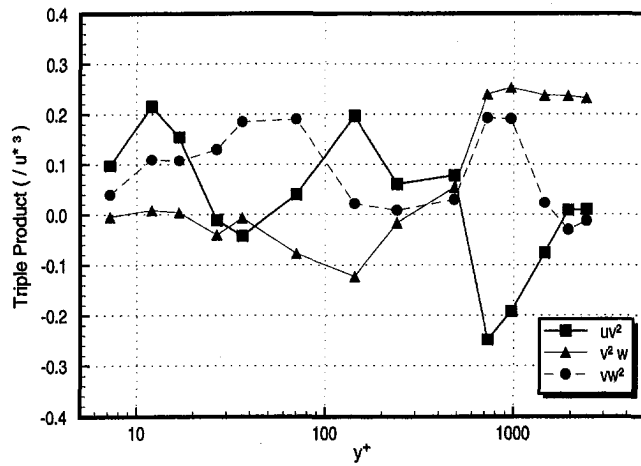
lent diffusion term of the TKE equation. As can be seen from these plots, u^3 becomes quite large and positive near the wall, apparently due to the wall's limiting influence on the magnitude of negative u events. The quantity uw^2, which appears in the turbulent transport term of the $\overline{uw}$ equation is several times larger than uv^2, which appears in the turbulent transport term of the $\overline{uv}$ equation, suggesting that the turbulent structure is changing rapidly in the third dimension near the separation line.

Calculated Flow Quantities. The measured boundary-layer profiles were integrated by

$$\theta = \int_0^\delta \frac{U_{fs}}{U_e}\left(1 - \frac{U_{fs}}{U_e}\right)dy \qquad (2)$$

where U_{fs} is the streamwise component of the velocity in the local-freestream coordinate system, to obtain the boundary-layer streamwise momentum thickness, θ. The resulting momentum-thickness Reynolds numbers, Re_θ, are presented in Fig. 9.

In order to calculate the skin friction, the velocity profiles were fitted to a Spalding-type wall law

$$y^+ = u^+ + \frac{1}{E}\left[e^{\kappa u^+} - 1 - \kappa u^+ - \frac{(\kappa u^+)^2}{2} - \frac{(\kappa u^+)^3}{6}\right] \qquad (3)$$

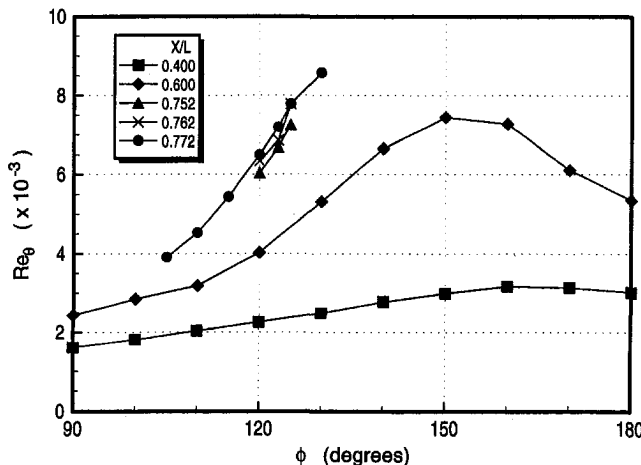with the constants E = 8.323 and κ = 0.41, and with the substitutions
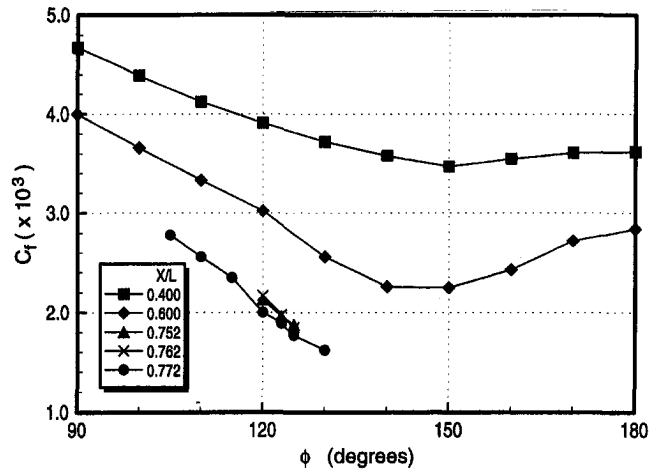
$$u^+ = \frac{U}{U_\infty}\Big/\sqrt{\frac{C_f}{2}} \qquad y^+ = \frac{y + \Delta y}{L}\,\mathrm{Re}_L\sqrt{\frac{C_f}{2}} \qquad (4)$$

This equation satisfies the continuity equation requirements (Rotta, 1962) that $u^+ - y^+$ vary as y^{+4} nearest the wall while u^+ approaches a semi-logarithmic form for large y^+. In this way, the skin-friction coefficient (and the term Δy, which is a term correcting for any error in the traverse zero point) can be calculated from a least squares fit of this equation to the measured U/U_e versus y/L pairs. This equation is, strictly, only applicable to 2-D flows, so for these 3-D profiles, only the points measured within the collateral wall region are used for the least squares fit.

The magnitude of the measured skin-friction coefficient, C_f, is plotted in Fig. 10, and the direction of the flow at the wall relative to the axial direction, β_w, is plotted in Fig. 11. C_f has been normalized by the wind tunnel velocity, U_∞, to make comparisons between different measurement locations more convenient. It can be seen in these figures that, as the flow moves downstream, the wall flow angle becomes more positive and the skin friction coefficient decreases. Over the range of circumferential angles measured at x/L = 0.752 through 0.772, there is no local minima or maxima in either of these quantities. However, at x/L = 0.772 there is a small kink in both the profiles of C_f and β_w at ϕ = 123 deg. Since this is approximately the point of the primary separation, it is believed that these kinks are due to the separation. The kinks in these profiles are
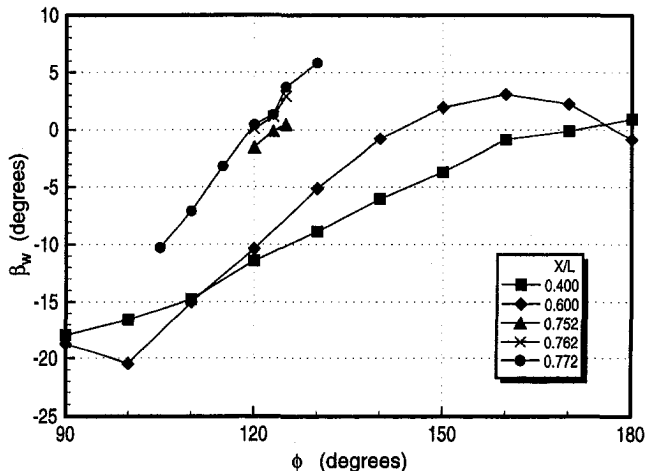

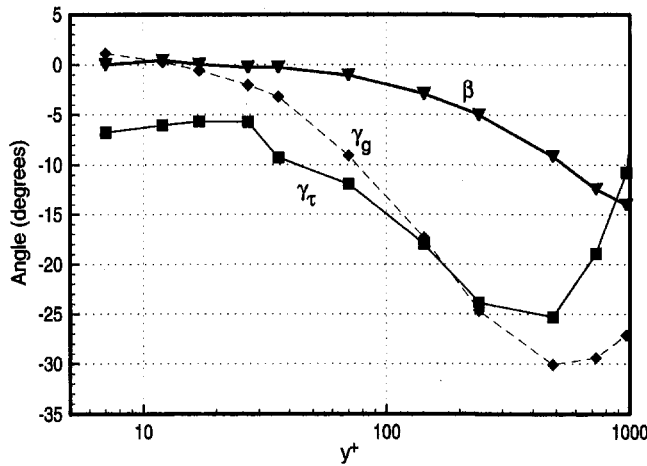Fig. 9   Momentum-thickness Reynolds number

Fig. 11   Wall flow angle
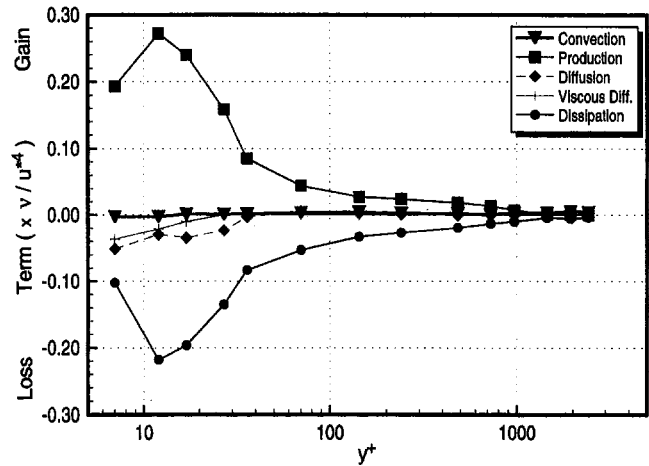
Fig. 12 Flow angles, $x/L = 0.762$, $\phi = 123$ deg

Fig. 13 TKE budget, $x/L = 0.762$, $\phi = 123$ deg

small, however, and the possibility exists that they are just artifacts of the measurement uncertainty. It should be noted that extrema in skin friction, wall flow angle, and momentum thickness should not be expected at the separation line; these extrema normally lag the 3-D separation line.

At $x/L = 0.600$ there are very clear local extrema in the wall-flow angle and skin friction, as well as in the momentum thickness. These local extrema are not, however, coincident in ϕ. The maximum wall flow angle lags (is at higher ϕ than) the minimum skin friction line by approximately 15 deg. The point of maximum momentum thickness is approximately halfway between the minimum skin friction and the maximum wall-flow angle. The location of the minimum skin friction, at approximately $\phi = 145$ deg, agrees quite well with that found by Kreplin et al. (1985).

At $x/L = 0.400$ there are local extrema in momentum thickness and in skin friction, but not in the wall flow angle. The wall flow angle increases continuously from $\phi = 90$ to 180 deg. The point of maximum momentum thickness lags the point of minimum skin friction by about 20 deg. The point of minimum skin friction, at approximately $\phi = 150°$, is slightly displaced from the value of $\phi = 160$ deg found by Kreplin et al.

Plots of the flow angle, β, the flow-gradient angle, γ_g, and the turbulent-shear-stress angle, γ_τ, at $x/L = 0.762$, $\phi = 123$ deg are shown in Fig. 12. The flow-gradient angle is different from the shear-stress angle over most of the boundary layer. As was noted in the introduction section, this implies that the eddy viscosity can not be assumed to be isotropic. The second, and perhaps more interesting feature of Fig. 12, is that though γ_g approaches β_w as the wall is approached, γ_τ does not. Even at the wall, γ_τ lags the flow angle (note that at this location the flow is turning to the windward side). Similar results have been seen in the experimental study of the boundary layer near a wing-body junction of Ölçmen and Simpson (1995), and the 3-D DNS study of Moin et al. (1990).

TKE Budget. Since the boundary-layer profiles are closely spaced about $x/L = 0.762$, $\phi = 123$ deg, it is possible to evaluate most of the terms of the TKE equation at this location. The TKE equation for steady flow can be written as

$$U_j \frac{\partial k}{\partial x_j} + \frac{\partial}{\partial x_j}\left(\frac{\overline{u_j p}}{\rho} + \overline{u_j k} \right) + \overline{u_i u_j} \frac{\partial U_i}{\partial x_j}$$

$$+ \epsilon - \nu \frac{\partial}{\partial x_j} \overline{u_i \left(\frac{\partial u_i}{\partial x_j} + \frac{\partial u_j}{\partial x_i} \right)} = 0 \quad (5)$$

In this form, the terms from left to right are convection of TKE, diffusion, production, dissipation, and viscous diffusion.

With the data available in this study, the convection and production terms can be evaluated exactly as can, with a little manipulation, the viscous-diffusion term. The diffusion term can not be fully evaluated due to the presence of the pressure-velocity term; however, if the pressure-velocity term is assumed to be small—an assumption supported by the DNS data of Spalart (1988)—then the diffusion term can be evaluated. The dissipation of turbulent kinetic energy, ϵ, was then found by summing the other terms.

The TKE budget calculated in this way is shown in Fig. 13. Clearly, the budget is dominated by the production and dissipation terms over most of the boundary layer. The diffusion and viscous diffusion terms become significant near the wall, but at the closest measured point to the wall, $y^+ = 7$, these terms are still considerably smaller than the production and dissipation. This can be seen more clearly in Fig. 14, where the terms of the TKE equation have been normalized by the value of the dissipation at each y^+ location. In this plot it can be seen that there is a balance between production and dissipation for $20 < y^+ < 1000$. The diffusion and viscous-diffusion terms both become significant below $y^+ = 30$, their sum rising to approximately 50 percent of the value of ϵ at $y^+ = 7$. Convection is small over most of the boundary layer, becoming significant only above $y^+ = 800$. These trends are quite similar to those seen in the DNS study of Spalart (1988).

One interesting item which can be calculated from these data is the relative contribution of terms normally neglected in the modeling of turbulent boundary layers. In Fig. 15, it can be
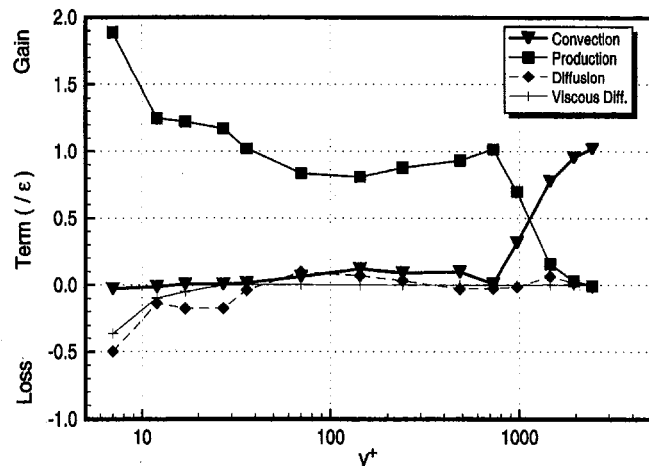

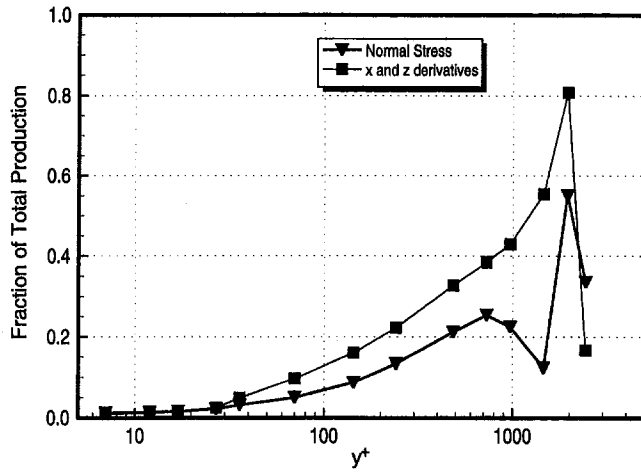Fig. 14 TKE budget, normalized by ϵ, $x/L = 0.762$, $\phi = 123$ deg

Fig. 15 Sources of TKE production, $x/L = 0.762$, $\phi = 123$ deg

Fig. 17 Dissipation of TKE, $x/L = 0.762$, $\phi = 123$ deg

seen that the terms in the turbulent kinetic energy production containing x and z derivatives become a significant portion of the total production above $y^+ = 100$, as do the terms containing Reynolds normal stresses. The terms containing x and z derivatives account for approximately 40 percent of the total production at $y^+ = 1000$, while the terms containing Reynolds normal stresses account for better than 20 percent of the total production at this same location. It is not clear, however, if the large magnitude of these terms is a result of the close proximity of these measurements to the 3-D separation, or is a general feature of turbulent boundary layers. Similar measurements at locations away from separation should help resolve this question.

Figure 16 shows the measured diffusion of TKE and the diffusion predicted by two models for this term. The first of these models is the Prandtl energy method (Schetz, 1993), in which the diffusion of TKE is calculated as

$$\text{TKE Diffusion} = -\frac{\partial}{\partial y}\left(\frac{\nu_T}{\sigma_K}\frac{\partial k}{\partial y}\right) \tag{6}$$

where ν_T is the turbulent eddy viscosity and σ_K is the turbulent Prandtl number. Equation 6 was solved for the data at $x/L = 0.762$, $\phi = 123$ deg using the generally accepted value for σ_K of 1 and an experimentally determined turbulent eddy viscosity. The second model shown in Fig. 16 is the model of East and Sawyer (1979):
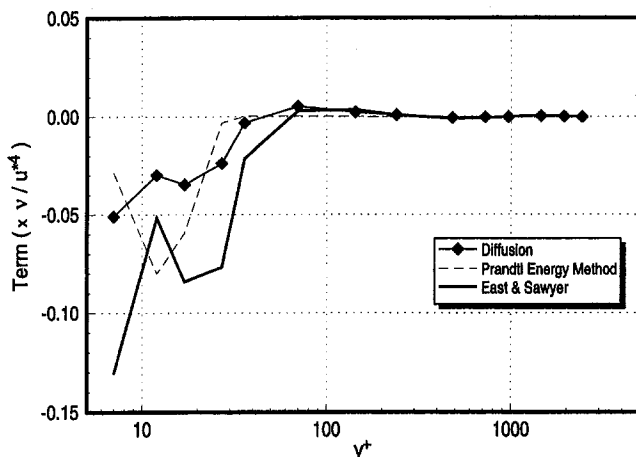
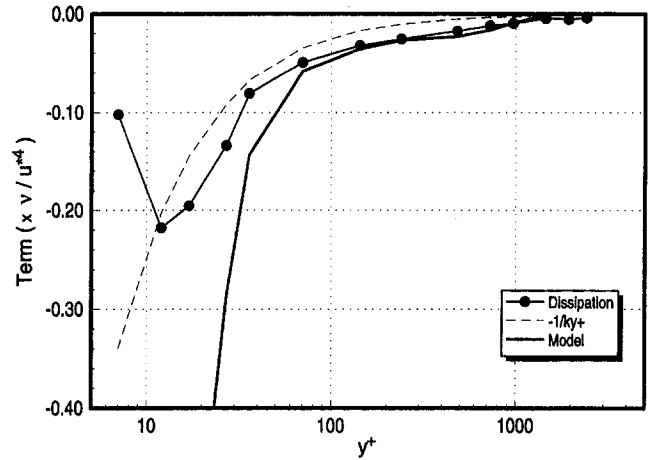

Fig. 16 Diffusion of TKE, $x/L = 0.762$, $\phi = 123$ deg

$$\text{TKE Diffusion} = -\frac{\partial}{\partial y}\left(0.8l\frac{\partial}{\partial y}k^{3/2}\right) \tag{7}$$

where l is the mixing length. Equation (7) was solved for this location using East and Sawyer's formula for the mixing length

$$l = 0.075Y\frac{Y^2 + 1}{Y^3 + 1}, \quad Y = 5\frac{y}{\delta}. \tag{8}$$

The results of these two calculations show that both models yield only a gross approximation of the turbulent diffusion in this flow. There is little to distinguish either of these models for this flow. The Prandtl energy method yields numbers closer to the measured diffusion below $y^+ = 30$, while the model of East and Sawyer better predicts the region of positive diffusion measured at $y^+ = 100$.

The behavior of the dissipation is detailed in Fig. 17. A relatively simple analysis of the TKE equation—starting with the assumptions that the shear is relatively constant through the boundary layer and equal to τ_w, that a log region in the u^+ vs. y^+ curve exists with a slope $1/\kappa$, and that the production equals the dissipation—leads to the conclusion that $\epsilon = 1/\kappa y^+$ in the log region. This line is plotted on Fig. 17 along with the measured dissipation. The measured dissipation follows the shape of this line, but exceeds the value predicted by this analysis. It is not clear, however, if this analysis applies to this flow situation, since 3-D flows do not generally follow the same wall law as 2-D boundary layers (Ölçmen and Simpson, 1992).

Also shown in Fig. 17 is the dissipation predicted from the model

$$\epsilon = C_D\frac{K^{3/2}}{l} \tag{9}$$

where C_D is a constant equal to 0.08 and l is a length scale. To calculate the line shown in Fig. 17, an experimentally determined mixing length times the factor $C_D^{1/4}$ was used for l. This model predicts the dissipation admirably well above $y^+ = 80$. Below this point, however, the dissipation is greatly overpredicted.

Summary and Conclusions

The flow about a 6:1 prolate spheroid at 10 deg angle of attack was investigated using a novel, miniature, 3-D LDV. This probe was used to obtain high-accuracy, high-spatial-resolution measurements of all three velocity components—as well as all Reynolds stresses and all velocity triple products—from closer than $y^+ = 7$ out to the boundary-layer edge.

Measurements were made of boundary-layer profiles at x/L = 0.400, 0.600, 0.752, 0.762, and 0.772. Profiles at the latter three measurement stations were in the vicinity of a three-dimensional separation. Velocity measurements were spaced close to the wall in each boundary-layer profile, and were used to calculate the skin friction on the prolate spheroid through a fit to a wall law.

Measurements of the flow angle, β, the flow-gradient angle, γ_g, and the turbulent-shear-stress angle, γ_τ show that there is a substantial lag in the direction of γ_g and γ_τ with respect to β. The lags in these quantities are not equal, implying that turbulence models which use an isotropic eddy viscosity do not adequately describe the behavior of three-dimensional boundary layers. Moreover, the measurements show that, although γ_g approaches β at the wall, there can be a significant difference between γ_τ and β at the wall.

Measurements about x/L = 0.762, ϕ = 123 deg, a point very near the three-dimensional separation, were used to calculate the balance of turbulent kinetic energy at this station. The quality of data and the close spacing of measurements allowed nearly all terms of the TKE equation to be evaluated.

With this TKE balance, it was shown that terms frequently neglected in the modeling of TKE can account for a substantial portion of the production for $y^+ > 100$. It is not presently clear, however, whether the large magnitude of these terms is a general characteristic of boundary layers or is caused by the close proximity of these measurements to the 3-D separation.

Several models for the diffusion and dissipation of turbulent kinetic energy were compared to the measured values of these terms. It was found that these models only grossly approximated the behavior of these terms near the wall.

Data Bank Contribution

Data presented here, along with additional data upon which the calculated quantities presented here were based, are being placed in the *Journal of Fluids Engineering* data bank. The data include all time-averaged velocity terms (first through third order), calculated skin friction and momentum thickness, and the calculated TKE budget terms.

Acknowledgments

References

AGARD, 1990, "Calculation of 3D Separated Turbulent Flows in Boundary Layer Limit," AGARD-AR-255, Neuilly sur Seine, France.

Ahn, S., 1992, "An Experimental Study of Flow Over a 6 to 1 Prolate Spheroid at Incidence," PhD Dissertation, Aerospace and Ocean Engineering, Virginia Polytechnic Institute and State University, Blacksburg, VA.

Barber, K. M., and Simpson, R. L., 1991, "Mean Velocity and Turbulence Measurements of Flow Around a 6:1 Prolate Spheroid." AIAA Paper 91-0255, 29th Aerospace Sciences Meeting, January 7–10, Reno, NV.

Chesnakas, C. J., and Simpson, R. L., 1994, "Full Three-Dimensional Measurements of the Cross-Flow Separation Region of a 6:1 Prolate Spheroid," *Experiments in Fluids*, Vol. 17, No. 1/2, pp. 68–74.

Chesnakas, C. J., Simpson, R. L., and Madden, M. M., 1994, "Three-Dimensional Velocity Measurements on a 6:1 Prolate Spheroid at 10° Angle of Attack," Data Report VPI-AOE-202, Department of Aerospace and Ocean Engineering, Virginia Polytechnic Institute and State University, Blacksburg, VA.

Durst, F., Martinuzzi, R., Sender, J., and Thevenin, D., 1992, "LDA Measurements of Mean Velocity, RMS-Values and Higher Order Moments of Turbulence Intensity Fluctuations in Flow Fields with Strong Velocity Gradients," *Proceedings of the Sixth International Symposium on Applications of Laser Techniques to Fluid Mechanics*, Lisbon, Portugal, 5.1.1–5.1.6.

East, L. F., and Sawyer, W. G., 1979, "An Investigation of the Structure of Equilibrium Turbulent Boundary Layers," *NATO-AGARD Fluid Dynamics Symposium Proceedings*, No. 271, pp. 6.1–6.19.

Gee, K., Cummings, R. M., and Schiff, L. B., 1992, "Turbulence Model Effects on Separated Flow About a Prolate Spheroid," *AIAA Journal*, Vol. 30, No. 3, pp. 655–664.

Kreplin, H. P., Vollmers, H., and Meier, H. U., 1985, "Wall Shear Stress Measurements on an Inclined Prolate Spheroid in the DFVLR 3m × 3m Low Speed Wind Tunnel," Data Report, DFVLR IB 222-84/A 33, Göttingen, Germany.

McLaughlin, D. K., and Tiederman, W. G., 1973, "Biasing Correction for Individual Realization of Laser Anemometer Measurements in Turbulent Flows," *Physics of Fluids*, Vol. 16, No. 12, pp. 2082–2088.

Meier, H. U., Kreplin, H. P., Landhaußer, A., and Baumgarten, D., 1984, "Mean Velocity Distributions in Three-Dimensional Boundary Layers Developing on a 1:6 Prolate Spheroid with Natural Transition," Data Report, DFVLR IB 222-4/A 10, Göttingen, Germany.

Meier, H. U., Kreplin, H. P., and Landhaußer, A., 1986, "Wall Pressure Measurements on a 1:6 Prolate Spheroid in the DFVLR 3m × 3m Low Speed Wind Tunnel (α = 10°, U_∞ = 55 m/s, Artificial Transition)," Data Report, DFVLR IB 222-86 A 04, Göttingen, Germany.

Moin, P., Shih, T. H., Driver, D. M., and Mansour, N. M., 1990, "Direct Numerical Simulation of a Three-Dimensional Turbulent Boundary Layer," *Physics of Fluids A*, Vol. 2, pp. 601–639.

Ölçmen, S. M., and Simpson, R. L., 1992, "Perspective: On the Near Wall Similarity of Three-Dimensional Turbulent Boundary Layers," ASME JOURNAL OF FLUIDS ENGINEERING, Vol. 114, pp. 487–495.

Ölçmen, S. M., and Simpson, R. L., 1995, "An Experimental Study of a Three-Dimensional Pressure-Driven Turbulent Boundary Layer," *Journal of Fluid Mechanics*, Vol. 290, pp. 225–262.

Rotta, J. C., 1962, "Turbulent Boundary Layers in Incompressible Flow," *Progress in Aeronautical Sciences*, A. Ferri, D. Küchemann, and L. H. G. Sterne, eds., The MacMillan Company, New York, Vol. 2, pp. 1–220.

Rotta, J. C., 1979, "A Family of Turbulence Models for Three-Dimensional Boundary Layers," *Turbulent Shear Flows 1*, F. Durst, B. E. Launder, F. W. Schmidt and J. H. Whitelaw, eds., Springer-Verlag, Berlin, pp. 267–278.

Schetz, J. A., 1993, *Boundary Layer Analysis*, Prentice Hall, Englewood, NJ.

Sendstad, O., and Moin, P., 1992, "The Near Wall Mechanics of Three-Dimensional Turbulent Boundary Layers," TF-57, Department of Mechanical Engineering, Stanford University, Stanford, California.

Spalart, P. R., 1988, "Direct Simulation of a Turbulent Boundary Layer up to R_θ = 1410," *Journal of Fluid Mechanics*, Vol. 187, pp. 61–98.

Vollmers, H., Kreplin, H. P., Meier, H. U., and Kühn, A., 1985, "Measured Mean Velocity Field Around a 1:6 Prolate Spheroid at Various Cross Sections," Data Report, DFVLR IB 221-85 A 08, Göttingen, Germany.

High Freestream Turbulence Effects on Turbulent Boundary Layers

K. A. Thole
Assistant Professor,
Mechanical Engineering Department,
University of Wisconsin,
Madison, WI 53706-1572

D. G. Bogard
Associate Professor,
Mechanical Engineering Department,
University of Texas,
Austin, TX 78712-1063

High freestream turbulence levels significantly alter the characteristics of turbulent boundary layers. Numerous studies have been conducted with freestreams having turbulence levels of 7 percent or less, but studies using turbulence levels greater than 10 percent have been essentially limited to the effects on wall shear stress and heat transfer. This paper presents measurements of the boundary layer statistics for the interaction between a turbulent boundary layer and a freestream with turbulence levels ranging from 10 to 20 percent. The boundary layer statistics reported in this paper include mean and rms velocities, velocity correlation coefficients, length scales, and power spectra. Although the freestream turbulent eddies penetrate into the boundary layer at high freestream turbulence levels, as shown through spectra and length scale measurements, the mean velocity profile still exhibits a log-linear region. Direct measurements of total shear stress (turbulent shear stress and viscous shear stress) confirm the validity of the log-law at high freestream turbulence levels. Velocity defects in the outer region of the boundary layer were significantly decreased resulting in negative wake parameters. Fluctuating rms velocities were only affected when the freestream turbulence levels exceeded the levels of the boundary layer generated rms velocities. Length scales and power spectra measurements showed large scale turbulent eddies penetrate to within $y^+ = 15$ of the wall.

Introduction

Highly turbulent freestream effects on boundary layer flows are relevant in such flow geometries as along gas turbine blades, in heat exchangers, and in combustors. It is well-documented that freestream turbulence levels of 7 percent and less, increase skin friction and heat transfer. More recently, studies of increases in skin friction and heat transfer due to high freestream turbulence have been extended to turbulence levels much greater than 10 percent. However, there has been little study of the detailed characteristics for a boundary layer affected by turbulence levels above 10 percent, such as mean and rms levels, correlation coefficients, power spectra, and length scales. This paper presents these detailed characteristics for high freestream turbulence levels ranging between 10 percent < Tu < 20 percent.

There have been numerous studies of freestream turbulence effects on boundary layers, dating back to Kestin (1966), in which grids were used to generate turbulence levels up to 7 percent. The primary objectives of these past studies have been from a practical standpoint of finding parameters to correlate increases of skin friction and surface heat transfer. These increases were generally correlated as a function of turbulence level (Tu) alone. Later, Hancock and Bradshaw (1983) and Blair (1983) showed that increases in skin friction best scaled using a combination of turbulence level and turbulence length scale (L_ϵ^u) in terms of a β parameter defined as,

$$\beta = \frac{Tu(\%)}{\left(\dfrac{L_\epsilon^u}{\delta} + 2\right)} \qquad (1)$$

Hancock and Bradshaw (1983) and Blair (1983) also showed

that as freestream turbulence levels start to increase, the outer regions of the velocity boundary layers exhibited a depressed wake region. At a turbulence level of Tu = 5.3 percent, the wake region was essentially nonexistent.

Both the Hancock and Bradshaw (1983) and Blair (1983) studies, as well as other grid-generated turbulence studies, have presumed that the log-law was valid for a boundary layer influenced by freestream turbulence levels of Tu = 7 percent or less. Hence, the wall shear stress for these studies were obtained from Clauser fits of the near-wall velocity profile. In a later study, Hancock and Bradshaw (1989) measured various terms in the turbulent energy transport equation to determine whether there was local equilibrium between production and dissipation in the near-wall region. Bradshaw (1978) had presented arguments that the log-law holds when there is local equilibrium in the near wall-region. For a freestream turbulence level of 4 percent, Hancock and Bradshaw found that near the wall there was a definite increased loss of turbulent energy by diffusion. Although this loss increased with freestream turbulence, it was still small relative to the production and dissipation terms. Hence, the boundary layer influenced by turbulence levels of 4 percent was found to be in local-equilibrium. Although this energy balance supports the validity of the log-law for the lower turbulence freestream turbulence levels, the question still remains whether the boundary layer stays in equilibrium at turbulence levels above 4 percent.

Conditional sampling studies were included in the Hancock and Bradshaw (1989) freestream turbulence study and were also performed by Charnay, Mathieu, and Comte-Bellot (1976). In these conditional sampling studies, the boundary layer fluid was thermally tagged through the use of a heated test plate. By thermally tagging the boundary layer fluid, a distinction could be made between the turbulence statistics associated with the boundary layer and freestream fluid elements. Hancock and Bradshaw used conditional sampling analyses to study turbulent stress statistics within the hot boundary layer fluid and the cold freestream fluid. Of particular interest was that, for low freestream turbulence, R_{uv} correlation coefficients for the freestream

fluid which penetrates well within the boundary layer are quite large. However, for higher freestream turbulence levels, the R_{uv} correlation coefficients for freestream fluid decreased substantially. Charnay et al. had a significant difference in the way that fluctuating velocity components were defined. Charnay et al. defined the fluctuating components relative to the hot or cold zone average, while Hancock and Bradshaw defined the fluctuating components relative to the total time average. With this difference, Charnay et al. found that the freestream fluid had a relatively low R_{uv} correlation coefficient with similar levels for freestream turbulence levels ranging from Tu = 0.3 to 4.7 percent. Charnay et al. also showed a significant downward zonal mean velocity for the freestream fluid relative to the boundary layer fluid. The magnitude of this relative downward mean velocity increased with increasing turbulence level. Comparing the results of Charnay et al. with those of Hancock and Bradshaw indicates that the high R_{uv} correlation coefficients found by Hancock and Bradshaw was due to a general downward velocity of the freestream fluid penetrating into the boundary layer. The R_{uv} correlation coefficient decreased with increasing turbulence levels because the increased streamwise velocity fluctuations within the freestream fluid were uncorrelated with the general downward movement. These results were important because the general downward movement of the penetrating freestream fluid is identified as a key transport mechanism.

More recently, there have been studies using devices other than grids to generate turbulence levels greater than 7 percent. Ames and Moffat (1990) used a combustor-simulator to generate turbulence levels up to 19 percent, Thole and Bogard (1994) used high-velocity cross jets to generate turbulence levels up to 20 percent, while Maciejewski and Moffat (1989) used a free jet directed over a flat plate to generate turbulence levels up to 60 percent. Both the Ames and Moffat and the Thole and Bogard studies investigated several different parameters, based on freestream turbulence level and length scale, for correlating skin friction and heat transfer.

To date, the interaction between high freestream turbulence levels and turbulent boundary layers for these higher freestream turbulence levels has not been fully investigated. An important issue to be addressed for these types of flows is the validity of the log-law. In addition, there is no data available on how the velocity correlation coefficient (R_{uv}), length scales, and power spectra are affected inside the boundary layer as a result of the highly turbulent freestream. These items are addressed in this paper for freestream turbulence levels ranging between 10 percent < Tu < 20 percent.

Experimental Facilities and Instrumentation

The facility used for the experiments in this paper included a closed-loop, boundary layer wind tunnel in the Turbulence and Turbine Cooling Research Laboratory at the University
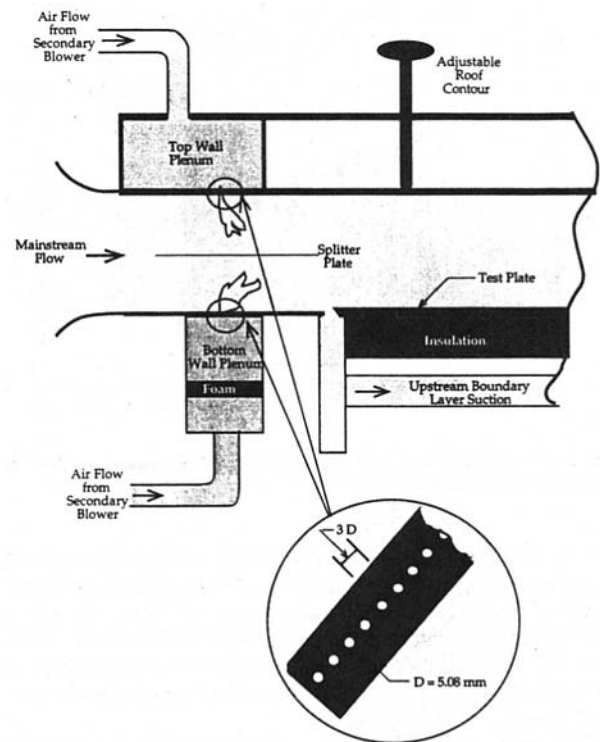

Fig. 1 Schematic of the wind tunnel test section and the turbulence generator

of Texas at Austin. This section briefly describes the facility, including the turbulence generator, as well as the instrumentation used for these studies.

Flow for the closed-loop wind tunnel was driven by a 5-hp fan and adjusted using a frequency-modulated motor controller. Flow conditioning upstream of the test section consisted of a honeycomb section followed by four fine mesh screens. Following these screens was a 9:1 area contraction which was then followed by the test section. Figure 1 is a schematic of the test section which was 244 cm in length, 61 cm in width, and 15.2 cm in height.

As indicated in Fig. 1, the initial 60 cm of the test section was occupied by the turbulence generator. Details of the turbulence generator are presented in Thole, Whan-Tong, and Bogard (1994). The design of the turbulence generator consisted of a row of small, high-velocity, normal jets injecting into the cross-flow mainstream as shown by the inset in Fig. 1. The diameter of the jet holes were 5.08 mm in diameter. The jet holes were spaced three diameters apart and had a length-to-diameter ratio

---

Nomenclature

D = jet hole diameter
E_u = streamwise velocity power spectral density
f = frequency
L_ϵ^u = dissipation length scale, $L_\epsilon^u = -[(u'^2)^{3/2}/U_\infty(du'^2/dx)]$
Re_D = Reynolds number based on hole diameter
Re_λ = turbulent Reynolds number, $\lambda_g u'/\nu$
Re_θ = Reynolds number based on momentum thickness
R_{uv} = correlation coefficient, $\overline{uv}/u'v'$

Tu = turbulence intensity (%), u'/U_∞
u' = RMS velocity in streamwise direction
u^+ = nondimensional velocity, u/u_τ
u_τ = friction velocity, $\sqrt{\tau_w/\rho}$
U = mean streamwise velocity
U_∞ = mainstream velocity in streamwise direction
$\overline{uv}$ = turbulent shear stress
v' = RMS velocity in normal direction
w' = RMS velocity in the lateral direction
x = streamwise distance

y = vertical distance
y^+ = nondimensional vertical distance, $y \cdot u_\tau/\nu$
β = correlation parameter,
δ = boundary layer thickness, 99 percent point
κ = von Kármán constant
Λ_f = streamwise integral turbulent length scale
θ = momentum thickness
τ_{total} = total shear stress, $(\mu(\partial U/\partial y) - \rho\overline{uv})$
$\tau_{\mathrm{log\text{-}law}}$ = wall shear stress determined from the log-law
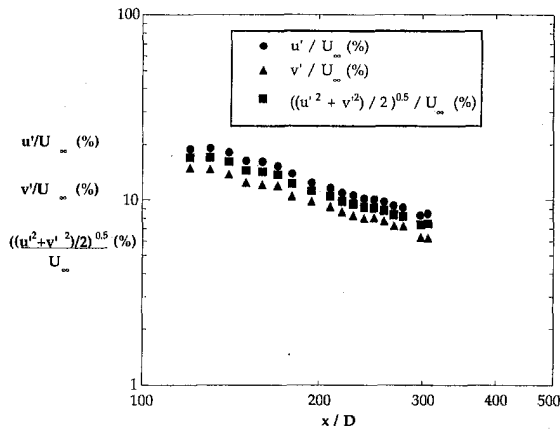
Fig. 2 Streamwise decay of turbulence for streamwise, vertical, and combined fluctuating velocities

of 2.5. The jet holes were located 57.5 hole diameters upstream of the leading edge of the test plate. To achieve the turbulence levels of interest, the jet-to-mainstream velocity ratio was 17, and the jet Reynolds number was $Re_D = 1700$. Mass addition from the normal jets into the mainstream was 20 percent, and the mainstream velocity downstream of the generator was nominally 8 m/s.

The mean and rms velocities as well as the $\overline{uv}$ correlation measurements were made using a Thermal Systems Inc. (TSI) two-component LDV system with frequency shifting. The optical axis of the two component LDV system was inclined slightly to obtain measurements close to the wall. Consequently, v-component measurements were actually inclined at an angle of 10° from the true vertical which caused a bias error of 2 to 6 percent of the v' measurement due to contamination by w' fluctuations. Measurements of simultaneous U and V components of velocity were required to be coincident within a 10 μs window. Incense smoke, filtered to remove inherent tar particles, was used to seed the flow with a particle diameter slightly smaller than 1 μm. The velocity data was corrected for velocity bias errors using residence time weighting (Edwards, 1987). Care was also taken to insure that the large frequency range of the Doppler signal for a highly turbulent flow was measured over a range of flat frequency response for the counter filters.

Integral time scales and power spectra were obtained from hot-wire measurements of the streamwise velocity fluctuations. Power spectra were obtained from a spectrum analyzer. The integral time scales were calculated directly from correlations of the digitized hot-wire measurements, or from the power spectra extrapolated to zero frequency (Hinze, 1975).

Uncertainty Estimates

Precision uncertainties for all measurements were determined statistically using a series of repeatability tests. Mean and rms velocity measurements were made using a sample time of about 60 s. This resulted in precision uncertainties for mean velocities of 1.2 percent in the freestream and 2.3 percent in the near-wall region, and for rms velocities of 1.2 percent in the freestream and 3 percent in the near-wall region. Bias errors for the LDV measurements, including residual errors after velocity bias corrections, uncertainty in fringe spacing, and frequency variations in electronic filtering, resulted in less than 3 percent bias uncertainty for the mean velocity. Uncertainty for the friction velocity, u_τ, was dominated by the uncertainty for the mean velocity measurement which caused a similar 3 percent uncertainty for u_τ. Repeatability tests indicated nominally 5 percent uncertainty for correlation coefficient, R_{uv}, measurements, and nominally 5 percent uncertainty for the integral length scales. For the highly turbulent cases, accurate measure-

ment of the boundary layer thickness δ (based on interpolating the point at which the mean velocity was 99 percent of the freestream) was difficult because of the relatively flat velocity profiles and larger uncertainties for the freestream velocity estimate. The uncertainty of the δ estimate was 2 percent for low freestream turbulence and 10 percent for high freestream turbulence.

Statistics of the Freestream Turbulence Field

Turbulence levels produced by the normal jets-in-crossflow turbulence generator are shown in Fig. 2 as a function of streamwise distance measured from the jet holes. The test plate starts 29 cm downstream from the jet injection ($x/D = 57.5$) with a sharp leading edge. At 8 cm downstream from the start of the leading edge, a 2.4 mm rod was placed to insure a turbulent boundary existed for the low and high freestream turbulence cases. The region of interest for these tests was from 66 cm to 152 cm downstream of the jet injection ($x/D = 130$ to 300). At the $x/D = 130$ location, the mean velocity field was relatively uniform. The turbulence level was Tu = 20 percent at $x/D = 130$ and decayed to a level of Tu = 9 percent at $x/D = 300$. Figure 2 shows both the streamwise and vertical rms velocity components and, as indicated, the turbulent field is slightly non-isotropic. The decay rate for the freestream turbulence compares well with the theoretical decay rate for homogeneous, isotropic turbulence (Hinze, 1975).

The streamwise turbulent integral length scales (Λ_f), the dissipation length scales (L_ϵ^u, defined by Townsend, 1956), and the power spectra for the streamwise velocity fluctuations (E_u) were also documented for this highly turbulent freestream. The integral length scales were deduced from the measured integral time scales and mean velocities invoking Taylor's hypothesis.

Figure 3 shows the streamwise growth of the integral and dissipation scales normalized by the jet hole diameter for the highly turbulent flow field. Both Blair (1983a) and Simonich and Bradshaw (1978) indicated that there was a fixed value for the ratio of dissipation to integral length scales. In these two grid-generated turbulence studies, Blair (1983) reported a ratio of $L_\epsilon^u/\Lambda_f = 1.5$, whereas Simonich and Bradshaw (1978) reported a ratio of $L_\epsilon^u/\Lambda_f = 1.1$. However, Comte-Bellot and Corrsin (1971) show results for grid-generated turbulence indicating a range for this ratio of $1.3 < L_\epsilon^u/\Lambda_f < 1.7$. Also, in the turbulent flowfield generated by a combustor simulator, Ames and Moffat (1990) reported a range of length scale ratios of $1.6 < L_\epsilon^u/\Lambda_f < 2.6$. In the study described here, the dissipation length scales and the integral length scales were similar, as shown in Fig. 3, with a length scale ratio of $1.1 < L_\epsilon^u/\Lambda_f < 1.4$ over the region of interest.
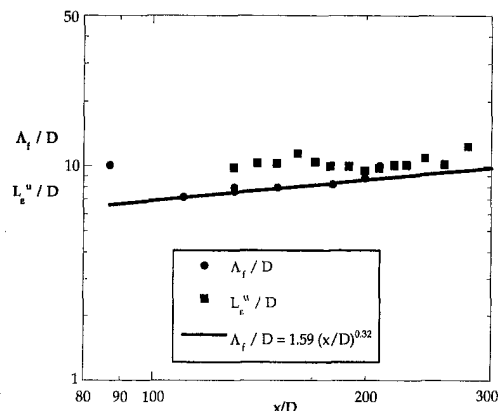

Fig. 3 Streamwise integral and dissipation turbulent length scales for the high turbulent flowfield

Fig. 4 Energy spectra of freestream turbulence as compared with the von Kármán Spectrum

$$U^+ = \frac{1}{\kappa} \ln y^+ + C \qquad (2)$$

where κ is the von Kármán constant, $\kappa = 0.41$, and C is a constant taken to be 5.0. This technique is well established for low freestream turbulence boundary layer flows, and has been assumed to be valid in previous studies with high freestream turbulence. For this study, we were particularly concerned about the applicability of the log-law since freestream turbulence levels were significantly higher than most previous studies. To evaluate the accuracy of the log-law fit for determining wall shear stress, comparisons were made with measurements of the total stress (τ_{total}), i.e. viscous plus turbulent shear stress ($\mu(\partial U/\partial y) - \rho\overline{uv}$), near the wall. The total shear stress data were normalized using wall shear stress determined from a Clauser fit to the log-law, $\tau_{log-law}$. The Clauser fit was done in the log-law region of the mean velocity profile between $y^+ = 30$ and $y/\delta = 0.2$. Results from these measurements, as shown in Fig. 5, indicate a normalized total stress of nominally $\tau_{total}/\tau_{log-law} = 1$ near the wall for all freestream turbulence levels, confirming the accuracy of the log-law fit in determining the wall shear stress. Note that a streamwise pressure gradient is expected for this flow due to the decaying freestream turbulence, but this was estimated to have less than a 5 percent effect on the total stress in the near wall region ($y^+ < 50$).

Mean velocity profiles measured in the present study and in previous studies by Johnson and Johnston (1989) and Ames and Moffat (1990) are presented in terms of inner variable scaling in Figure 6a. A distinct log-linear region following the log-law profile is evident for all freestream turbulence levels. This may be explained physically if one assumes that the mean velocity gradient near the wall (in the constant stress region) is proportional to a velocity scale of $(-\overline{uv})^{1/2}$ and the distance from the wall y, i.e., $\partial U/\partial y \sim (-\overline{uv})^{1/2}/y$ (see Gad-el-Hak and Bandyopadhyay, 1994). Integration of this equation results in the well-recognized log-law mean velocity profile. From this viewpoint it is important to recognize that the normalized turbulent shear stress, $-\overline{uv}/u_\tau^2$, is essentially unaffected by the high free-stream turbulence levels in the near wall region as is evident from Fig. 5 where $\tau_{total}/\tau_{log-law}$ is essentially equal to $-\overline{uv}/u_\tau^2$ (because the viscous stress is negligible). The turbulent shear stress profiles are relatively unaffected by the high freestream turbulence levels in the near wall region because the level of the shear stress in the constant stress layer must be balanced with the wall shear stress, i.e., $-\overline{uv} = u_\tau^2$, regardless of the freestream conditions. Consequently, the mean velocity profile remains unaffected in the log-law region even though the rms turbulence levels significantly increase.
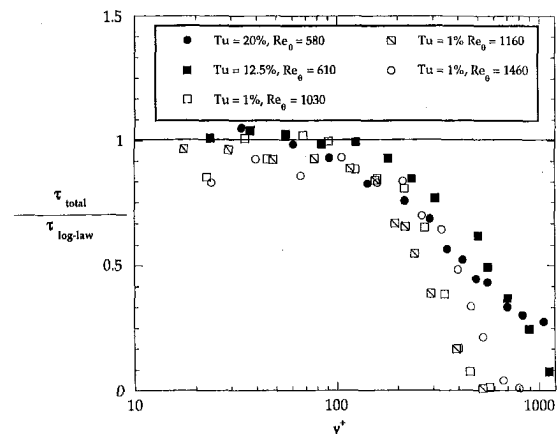
Of particular importance, in terms of the effect of the freestream turbulence on the boundary layer, was that the ratio of integral length scale to the boundary layer thickness. The integral scale of the freestream turbulence relative to the boundary layer thickness was approximately $\Lambda_f/\delta = 2$ for most of the data analyzed. This ratio of the integral scale to boundary layer thickness was significantly larger than the integral scale of turbulence self-generated in the boundary layer for negligible freestream turbulence (discussed later in this paper). For negligible freestream turbulence, the wall generated turbulence length scale to boundary layer thickness was found to be $\Lambda_f/\delta = 0.4$ through most of the boundary layer.

All high freestream turbulence positions had a nominal Reynolds number of $Re_\theta = 600$, and these data were compared to data from a low freestream turbulence boundary layer which also had $Re_\theta = 600$. For the low freestream turbulence boundary layer, the boundary layer and momentum thicknesses were $\delta = 18$ mm and $\theta = 1.8$ mm, respectively. For the high freestream turbulence conditions, the boundary layer had a constant thickness of nominally $\delta = 20$ mm, and a constant momentum thickness of nominally $\theta = 1.2$ mm along a streamwise distance of 65 cm. With the constant momentum thickness, a momentum integral analysis indicates that a significant pressure gradient exists in the flow. Although the freestream velocity was kept nominally constant, Ames and Moffat (1990) showed that for decaying freestream turbulence levels, similar to that in this study, there was a significant decay in the total pressure of the flow. In fact they found that "acknowledging a total pressure loss along the channel is important in producing a reasonable momentum balance." In a different facility, Sahm and Moffat (1992) found that in a region of decaying high freestream turbulence levels, the boundary layer thickness and momentum thickness actually decreased with streamwise distance.

Figure 4 shows the measured power spectral density in the freestream for turbulence levels of Tu = 20 percent and 13 percent as compared with the classic von Kármán spectrum. These two positions have the maximum and minimum turbulence Reynolds numbers in the flowfield, $Re_\lambda = 271$ and $Re_\lambda = 159$, respectively. The spectra are in good agreement with the von Kármán spectrum and are at a sufficiently high turbulent Reynolds number to have a large inertial subrange.

Effects of Freestream Turbulence on Boundary Layer Mean and RMS Velocities

The wall shear stress for turbulent boundary layer flows is commonly determined by fitting to the mean velocity profile measured near the wall (known as a Clauser fit). The velocity profile is assumed to follow the following log-law profile:

Fig. 5 Total shear stress distribution normalized by the friction velocity obtained from the Clauser fit
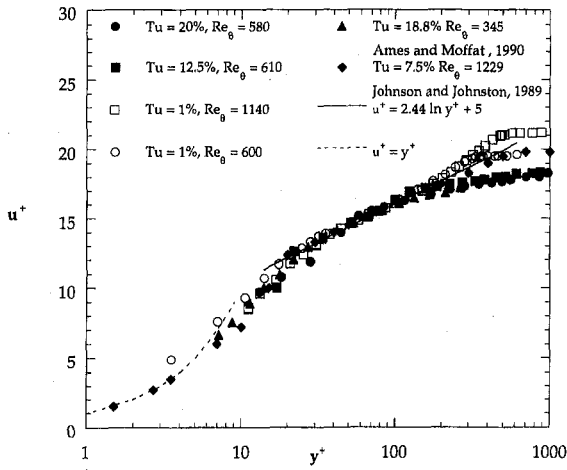
Fig. 6(a) Effect of freestream turbulence on the mean velocity in terms of inner variables
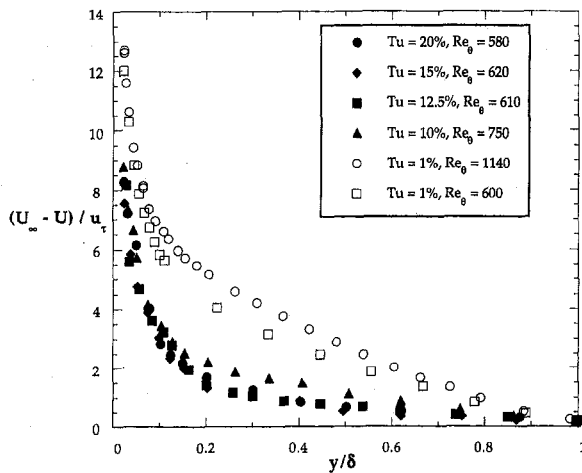

Fig. 6(b) Effect of freestream turbulence on the mean velocity in terms of inner variables

Also evident in Fig. 6(a) is a significant alteration of the outer part of the boundary layer due to high freestream turbulence. As the turbulence levels were increased, the mean velocity profiles fell below the log-law resulting in negative wake values. Another perspective of the effect of high freestream turbulence on the outer part of the mean velocity profile is evident from the defect velocity profiles presented in Figure 6(b) with outer scaling for y, i.e., y/δ. Clearly there is distinct difference between the low and high freestream turbulence cases, with much lower defect velocities in the outer region for the high freestream turbulence cases. Note there was a collapse of the defect velocity profiles for freestream turbulence levels above Tu = 12.5 percent which indicates a constant wake strength.

Figure 7 shows the wake parameter, Π, as a function of the Hancock and Bradshaw's β-parameter. The data included in Fig. 7 are results from grid-generated studies such as Johnson and Johnston (1989), Rüd (1985), and Hoffmann and Mohammadi (1991). Also included are higher freestream turbulence measurements of Ames and Moffat (1990) and the present measurements. The wake parameter, Π, was determined using the following relation,

$$\frac{U_\infty}{u_\tau} = \frac{1}{\kappa} \ln \frac{\delta u_\tau}{\nu} + C + \frac{2\Pi}{\kappa} \qquad (3)$$

Hoffmann and Mohammadi (1991) showed a systematic de-

crease in wake strength with increases in β to $\beta = 2$, resulting in a negative wake component for approximately $\beta > 1$. Although there is scatter in the data, at values greater than $\beta = 3$ the data appear to be asymptotically approaching a constant wake strength of $\Pi = -0.5$.

Figures 8(a)–8(d) show the u' and v' velocity profiles plotted in terms of inner variables and outer variables. The rms velocity profiles for the highly turbulent flows are compared with those of a low turbulence (Tu = 1 percent) boundary layer for two different Reynolds numbers. In Figs. 8(a) and 8(b), the data is supplemented with that of Johnson and Johnston (1989) for the turbulence levels of Tu = 7.5 percent (Re$_\theta$ = 1230) and Tu < 1 percent (Re$_\theta$ = 1450).

Figure 8(a) shows that for turbulence levels less than Tu = 12.5 percent, the u' velocities scale quite well with u_τ in the near-wall region ($y^+ < 40$). However, for higher turbulence levels, Tu > 15 percent, the peak values of u'/u_τ increase ($u'/u_\tau = 3.3$). These profiles indicate the penetration of the freestream turbulence into the boundary layer very close to the wall. For Tu = 15 percent, $u'/u_\tau = 2.8$ throughout most of the boundary layer until very close to the wall where there is a slight increase to $u'/u_\tau = 3.2$. However, for the highest freestream turbulence case, Tu = 20 percent, the streamwise fluctuating velocity is relatively constant across the entire boundary layer with a value of $u'/u_\tau = 3.3$. Ames and Moffat (1990) measured a similar increase in u'/u_τ at high turbulence levels with peak values of $u'/u_\tau = 2.8$ for Tu < 10.5 percent in a Reynolds number range of $875 < \text{Re}_\theta < 1179$, and an increase to $u'/u_\tau = 3.4$ for a Tu = 19 percent at a Re$_\theta$ = 345.

In Fig. 8(b) the v' profiles are shown to be substantially different from the u' profiles shown in Fig. 8(a). First, scaling of v' with u_τ very near the wall is relatively good for all the turbulence levels. The second noticeable difference is a systematic decrease in v' as the wall is approached. This difference is more clearly seen in comparing Figs. 8(c) and 8(d) where the u' and v' velocity profiles are plotted in terms of outer variables. It is evident that the v' levels are continually decreasing when approaching the wall, whereas the u' profiles are relatively flat (except very near the wall).

The attenuation of v' levels throughout the boundary layer is due to the wall limitation, which is not a restriction for the u' velocity fluctuations. Wall effects on freestream velocity fluctuations were studied analytically by Hunt and Graham (1978) and experimentally by Thomas and Hancock (1978). These studies showed that a wall, which is moving with the flow so that there is no boundary layer, will significantly attenuate the normal velocity fluctuations. Figure 8(e) shows the decrease in v' velocity fluctuations relative to the freestream level as a function of distance from the wall normalized with the integral
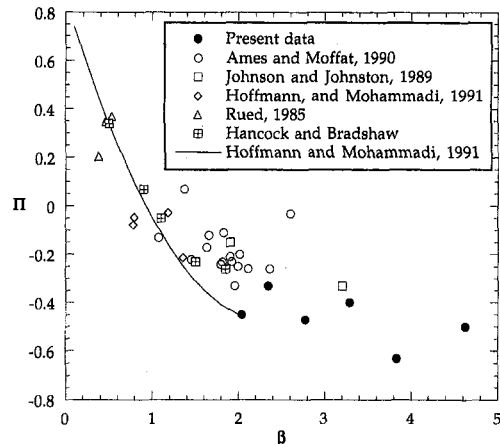

Fig. 7 Wake strengths as a function of the Hancock and Bradshaw's β-parameter
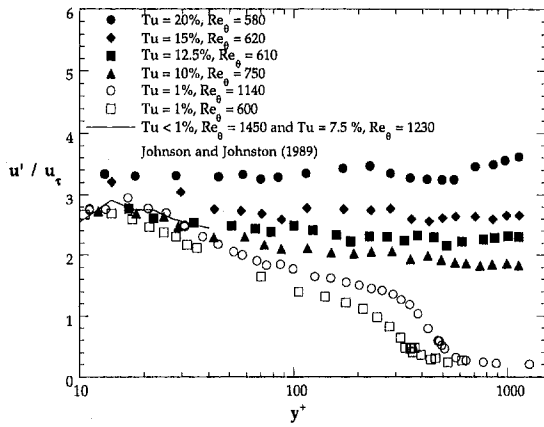
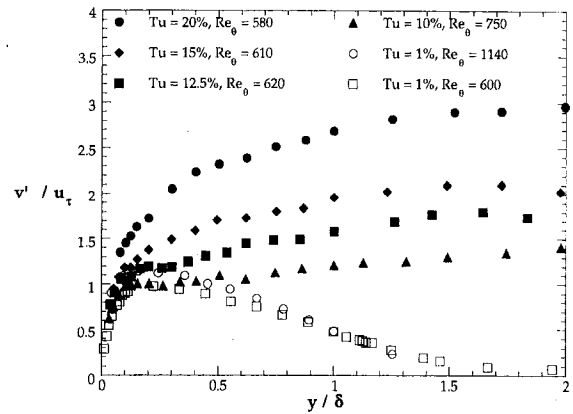**Fig. 8(a)** Streamwise rms velocity profiles for different turbulence levels plotted using inner variables

Fig. 8(b) Vertical rms velocity profiles for different turbulence levels plotted using inner variables
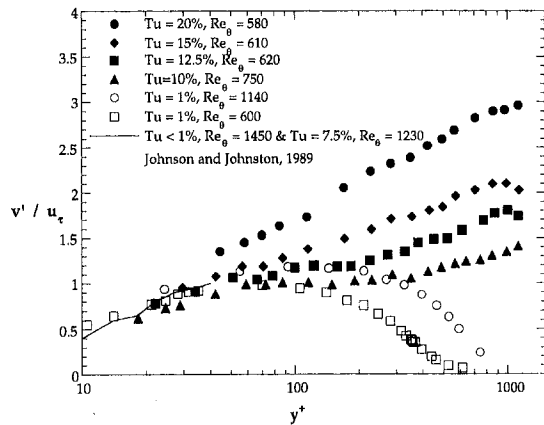

Fig. 8(c) Streamwise rms velocity profiles for different turbulence levels in terms of outer variable scaling

Fig. 8(d) Vertical rms velocity profiles for different turbulence levels plotted using outer variables
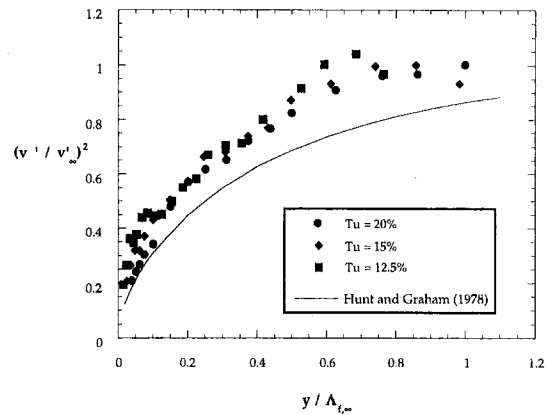

Fig. 8(e) Attenuation of the vertical velocity fluctuations as a function of vertical distance normalized by the dissipation length scale (Hunt and Graham, 1978)
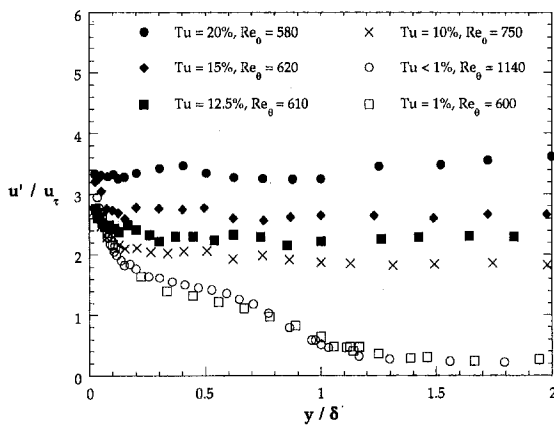
length scale of the freestream turbulence. Also shown is the trend predicted by Hunt and Graham. The attenuation of the v' velocity fluctuations was found to be similar to the prediction of Hunt and Graham (also to the measurements of Thomas and Hancock, not shown) suggesting that this attenuation is due to the wall proximity and not caused by the boundary layer flow.

Effects of Freestream Turbulence on Boundary Layer

Power Spectra and Length Scales. The integral length scales as well as the power spectra were measured at several positions throughout the boundary layer. In each case, the length scales and power spectra for boundary layers with high freestream turbulence levels, Tu = 20 percent and 12.5 percent, were contrasted with those for boundary layers with low freestream turbulence, Tu = 1 percent.

As shown in Fig. 9(a), the integral scales for velocity fluctuations were much larger for the high turbulence cases throughout the entire boundary layer than for the low freestream turbulence case. Although there was a sharp decrease in the length scales when approaching the wall for the higher turbulence cases, this decrease did not start until well within the boundary layer ($y/\delta < 0.3$).

In Fig. 9(b), which shows the variation of the integral length scales relative to y^+, it is clear that even very near the wall ($y^+ = 15$), the velocity integral length scales for the boundary layers with high freestream turbulence were several times larger than that for a boundary layer with low freestream turbulence. Note that normalizing the integral length scales with the inner length scale, ν/u_τ, or with the distance from the wall, y, still resulted in the length scales for the high freestream turbulence cases being several times larger than for the low freestream turbulence case.

Power spectra for the streamwise velocity component were measured to obtain more detail on the effect of freestream turbulence on turbulence structure near the wall. The spectra, shown in Fig. 10, were measured at the same non-dimensionalized vertical distance from the wall ($y^+ = 15$), for three different turbulence levels (Tu = 1 percent, 12.5 percent, and 20 percent) and are compared to the classical von Kármán's equation for isotropic turbulence. These spectra are normalized using the integral length scale, Λ_f, local mean velocity, U, and the rms
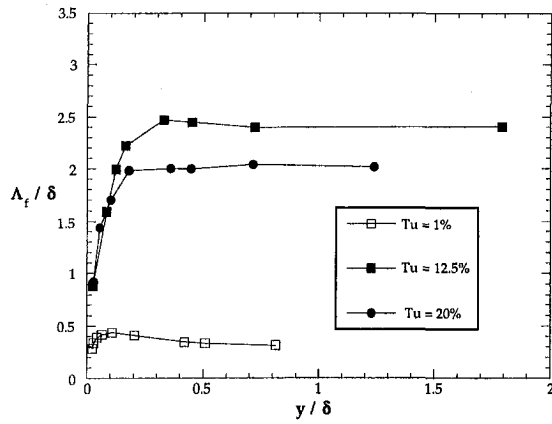
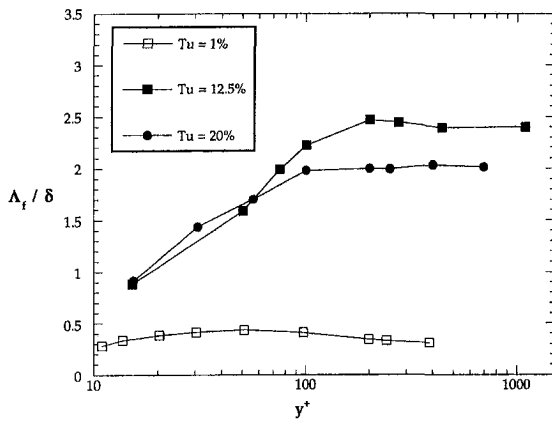Fig. 9(a) Profiles of integral length scales in the boundary layer

Fig. 9(b) Profiles of integral length scales plotted in terms of inner wall variables

velocity, u'. At low wavenumbers ($2\pi f/U$), the different spectra collapse and agree well with the von Kármán spectrum. The influence of the high freestream turbulence is evident in the larger inertial subrange as compared with the $Tu = 1$ percent case. However, for the $Tu = 12.5$ and 20 percent cases, the power spectral density is slightly above the von Kármán equation in the intermediate wavenumber range. The significance of this will be shown in the following discussion.
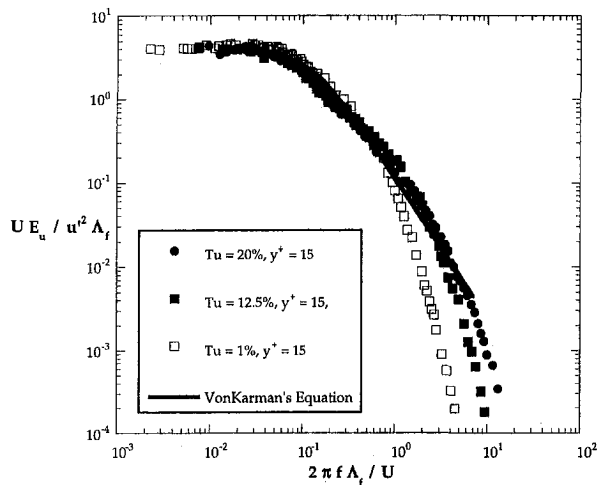

Fig. 10 Comparison of normalized energy density spectra in the boundary layer at a $y^+ = 15$ influenced by freestream turbulence
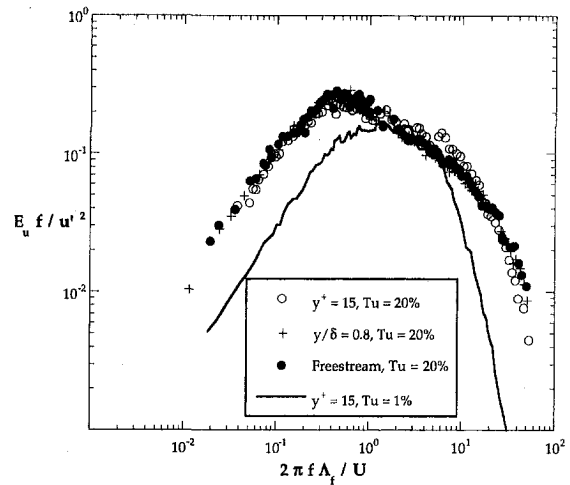

Fig. 11(a) Energy spectra as a function of wavenumber normalized by length scale measured throughout the boundary layer influenced by a turbulence level of 20 percent

Fig. 11(b) Energy spectra as a function of wavenumber normalized by boundary layer thickness measured throughout the boundary layer influenced by a turbulence level of 20 percent

The wavenumber at which the peak power occurs can more easily be seen by plotting the normalized power ($f \cdot E_u/u'^2$) rather than power density. The influence of the freestream turbulence on the turbulence within the boundary layer was evaluated by comparing freestream power spectra with the power spectra at different positions in the boundary layer, and by comparing with the spectra near the wall for a boundary layer with low freestream turbulence. Figure 11(a) shows spectra at three different vertical distances, $y^+ = 15$, $y/\delta = 0.8$ ($y^+ = 440$), and the freestream for the $Tu = 20$ percent case. Also, for comparison, the spectrum at $y^+ = 15$ for the $Tu = 1$ percent case is presented. In Fig. 11(a), the wavenumber has been normalized with the local integral scale. From this figure it is clear that there was a much broader frequency range for the highly turbulent case than for the $Tu = 1$ percent case. Moreover, throughout the entire $Tu = 20$ percent boundary layer, the power spectra were similar to the freestream power spectrum. This suggests that the freestream turbulence penetrated to $y^+ = 15$, essentially unaffected by the boundary layer turbulence. However, Fig. 11(a) shows a slight increase in the $Tu = 20$ percent power spectrum at wavenumber of about $2\pi f \Lambda_f/U = 10$. The significance of this is illustrated by normalizing the wavenumber with the boundary layer thickness δ, shown in Fig. 11(b), rather than the integral length scale, Λ_f. The rational for this is that

Fig. 12(a) Energy spectra as a function of wavenumber normalized by length scale measured throughout the boundary layer influenced by a turbulence level of 12.5 percent
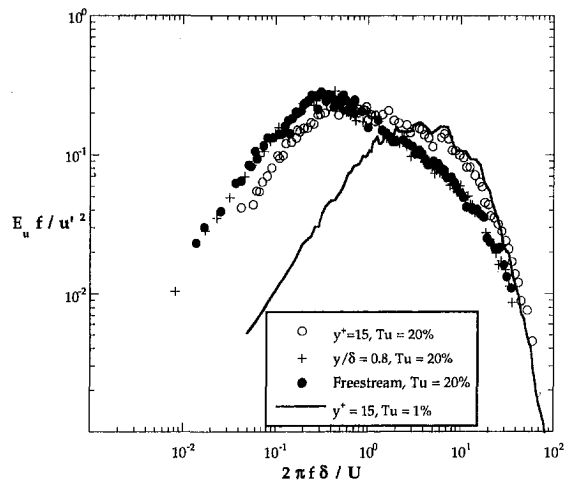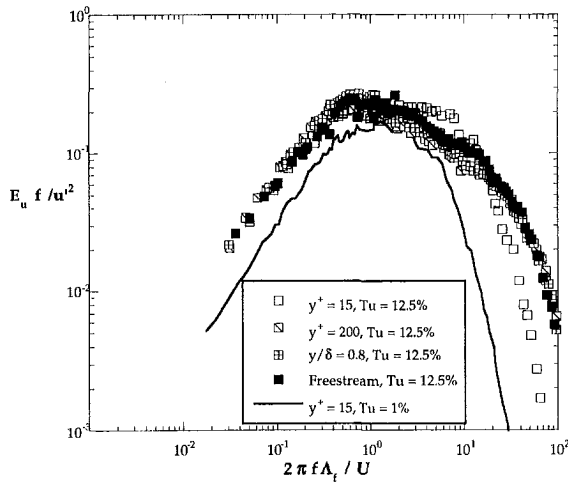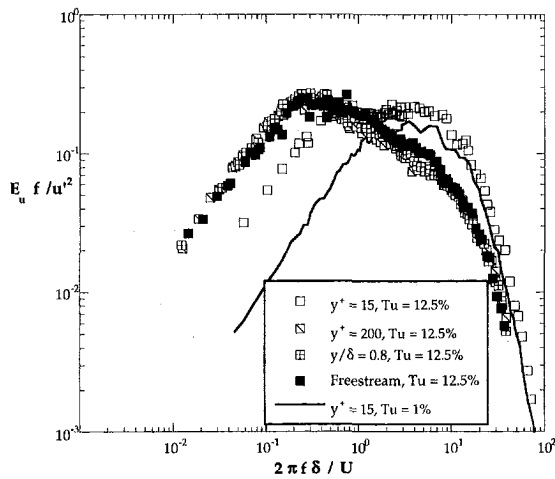

Fig. 12(b) Energy spectra as a function of wavenumber normalized by boundary layer thickness measured throughout the boundary layer influenced by a turbulence level of 12.5 percent

the boundary layer generated turbulence will scale with δ, whereas Λ_f is representative of the large scale freestream turbulence because the freestream turbulence dominates the power spectrum. Figure 11(b) shows that when normalizing the wavenumber with δ, the spectra at $y^+ = 15$ at low and high freestream turbulence levels correspond well for $2\pi f \delta/U \geq 2$. Consequently, the slight increase in turbulence energy at the higher wavenumbers may be recognized as boundary layer generated turbulence. However, the contribution of the boundary layer generated turbulence energy to the total turbulence energy is still quite small.

A similar analysis was done for turbulence spectra measured in the boundary layer at the position where the freestream turbulence level was Tu = 12.5 percent. Figures 12(a) and 12(b) show the normalized power spectra case at four different vertical distances, $y^+ = 15$, $y/\delta = 0.33$ ($y^+ = 200$), $y/\delta = 0.8$ ($y^+ = 480$), and the freestream. Also for comparison, the Tu = 1 percent case at a $y^+ = 15$ is presented. There was a similar large broadening of the spectra due to the high freestream turbulence, and at the $y/\delta = 0.33$ and 0.8 locations the power spectra were again essentially the same as the freestream spectrum. However, at a $y^+ = 15$, the power spectrum was double-peaked. Figure 12(b) shows that the deviation of the spectrum at higher wavenumbers for the high freestream turbulence case at $y^+ = 15$ corresponded to the Tu = 1 percent case when the wavenum-

ber is normalized with δ. Clearly, at $y^+ = 15$ the turbulence energy at higher wavenumbers is boundary layer generated and is a significant part of the total turbulence energy. However, the low wavenumber freestream turbulence is still a major component of the total turbulence energy.

These results show that at very high freestream turbulence levels, the freestream turbulence significantly affects the turbulence structure very near the wall. Large-scale motions are present throughout the boundary layer as a result of high freestream turbulence levels. Note that the influence of freestream turbulence in increasing the integral length scales and broadening the power spectra was particularly evident in this study because the length scales of the freestream turbulence were significantly larger than the boundary layer generated turbulence. In contrast, Johnson and Johnston (1989) found that freestream turbulence levels as high as Tu = 7.5 percent had no effect on the streamwise velocity spectrum at $y^+ = 15$. Although the lower turbulence level might have been a factor, the relatively small freestream turbulence length scale in their study (essentially equal to the integral scale expected for their boundary layer) probably resulted in spectral characteristics of the freestream turbulence which would be difficult to distinguish from the boundary layer spectra.

Effects of Freestream Turbulence on Boundary Layer Correlation Coefficients

Figure 13 shows the velocity correlation coefficients measured throughout the boundary layer for the highly turbulent flow as compared with the Tu = 1 percent case. For negligible freestream turbulence (Tu = 1 percent), the correlation coefficient measured in the near-wall region is the well-established $R_{uv} = -0.45$. The effect of increasing the freestream turbulence on R_{uv} was quite evident in Fig. 13 which shows a lower magnitude of the correlation coefficient in the outer part of the boundary layer for a Tu = 12.5 percent. However, the correlation coefficient does rise to a magnitude of $R_{uv} = -0.4$ near the wall which is close to the low freestream turbulence value. However, for the freestream turbulence level of Tu = 20 percent, the magnitude of the correlation coefficient is significantly reduced all the way to the wall.

Also shown on Fig. 13 are curves representing the results of Hancock and Bradshaw (1983). In their study, Hancock and Bradshaw concluded that the trends of R_{uv} scaled with the β parameter. Note that our data increase the range of β to $\beta = 3.7$, and that there is a consistent trend of decreasing R_{uv} magnitude with increase in β. The effect of the penetration of uncorrelated, large-scale, freestream turbulence is to reduce the velocity
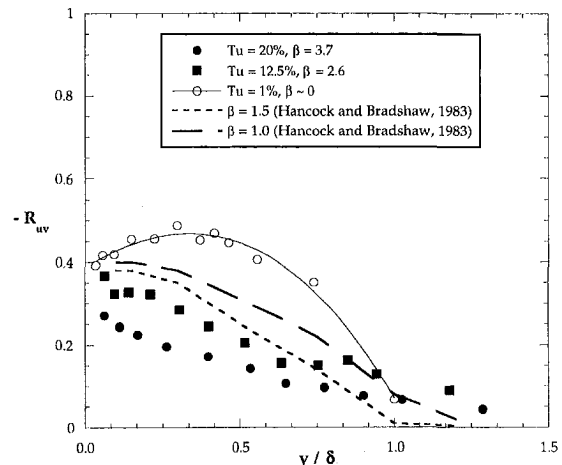

Fig. 13 Effect of freestream turbulence on velocity correlation coefficients

correlation coefficient. These uncorrelated, large-scale free-stream eddies have only a small contribution to $\overline{uv}$.

Conclusions

Using a unique freestream turbulence generator, the effect of high freestream turbulence on a two-dimensional, flat plate boundary layer has been studied with high freestream turbulence levels, 10 percent < Tu < 20 percent, significantly higher than most previous investigations. The freestream turbulence was homogeneous and approximately isotropic, and had integral length scales five to eight times larger than that in a boundary layer unaffected by freestream turbulence.

The mean velocity profile was found to retain the log-law profile near the wall for all freestream turbulence levels tested, but the outer region of the profile was significantly altered. Direct measurements of total shear stress (turbulent shear stress and viscous shear stress) verified the validity of the log-law at high freestream turbulence levels. High freestream turbulence caused the outer part of the boundary layer to become much flatter, i.e. the defect velocities in the wake region were substantially reduced, and the wake parameter asymptotically approached a constant value of $\Pi = -0.5$ for large values of the freestream turbulence parameter β.

For low freestream turbulence, the maximum streamwise rms velocity in a boundary layer is $u'/u_\tau = 2.8$. If the freestream u'_∞ level was larger than this, the u' level remained essentially constant at $u' = u'_\infty$ through the boundary layer to within $y^+ = 15$ of the wall. If the freestream u'_∞ level was less than $u'_\infty/u_\tau = 2.8$, then near the wall the u' levels matched the u' levels for a low freestream turbulence boundary layer. For the remainder of the boundary layer the u' levels were approximately constant with $u' = u'_\infty$. In contrast to the u' velocity fluctuations, the v' velocity fluctuations were found to decay significantly as the wall was approached. This decay of v', and the lack of decay for u', were found to correspond closely to predictions of the decay of isotropic turbulence due to wall effects.

Because of the much larger integral length scale of the freestream turbulence compared to the wall generated turbulence, the penetration of freestream turbulence far into the boundary layer was clearly evident from measurements of the integral length scales and the velocity power spectra. For Tu = 20 percent, the velocity power spectrum at $y^+ = 15$ was almost exactly the same as the freestream velocity power spectrum indicating that the freestream turbulence was dominating and essentially unaltered even this close to the wall. For Tu = 12.5 percent, the freestream turbulence still dominated the velocity power spectrum at $y^+ = 15$, but there was a distinct contribution from wall generated turbulence at higher wavenumbers. In all high freestream turbulence cases, the velocity power spectra were much broader than for the low freestream turbulence boundary layer because of the much larger length scales for the freestream turbulence.

Another effect of the dominance of freestream turbulence within the boundary layer was the reduction of R_{uv} correlation coefficient throughout the boundary layer. The reduced values of R_{uv} were because of the uncorrelated nature of the freestream turbulence.

As a final note, we point out that these results should not be interpreted in terms of the freestream turbulence levels alone, but rather the combination of the freestream turbulence levels and the large turbulence length scale. The decay of normal velocity fluctuation near the wall, and characteristics of the velocity power spectra were clearly dependent on the length scale of the turbulence. Furthermore, the strong penetration of the turbulence into the boundary layer, and the dominance of the freestream turbulence within the boundary layer may well not have occurred if the length scale of the freestream turbulence had been of the same order or smaller than the length scale of the wall generated turbulence.

Acknowledgments

References

Ames, F. E., and Moffat, R. J., 1990, "Heat Transfer with High Intensity, Large Scale Turbulence: The Flat Plate Turbulent Boundary Layer and the Cylindrical Stagnation Point," Stanford University Report HMT-44.

Blair, M. F., 1983, "Influence of Free-Stream Turbulence on Turbulent Boundary Layer Heat Transfer and Mean Profile Development: Part II-Analysis of Results," ASME Journal of Heat Transfer, Vol. 105, pp. 41–47.

Bradshaw, P., 1978, Topics in Applied Physics, Turbulence, P. Bradshaw, ed., Vol. 12, 2nd ed., New York, Springer-Verlag.

Charnay, G., Mathieu, J., and Comte-Bellot, G., 1976, "Response of a Turbulent Boundary Layer to Random Fluctuations in the External Stream," Physics of Fluids, Vol. 19, pp. 1261–1272.

Comte-Bellot, G., "Simple Eulerian Time Correlation of Full- and Narrow-Band Velocity Signals in Grid-Generated, 'Isotropic' Turbulence," Journal of Fluid Mechanics, Vol. 48, part 2, pp. 273–337.

Edwards, R. V., 1987, "Report on the Special Panel on Statistical Particle Bias Problems in Laser Anemometry," ASME JOURNAL OF FLUIDS ENGINEERING, Vol. 109, pp. 89–93.

Gad-el-Hak, M., and Bandyopadhyay, P. R., 1994, "Reynolds number effects in wall-bounded turbulent flows," Applied Mechanical Review Vol. 47, No. 8, pp. 307–365.

Hancock, P. E., and Bradshaw, P., 1983, "The Effect of Free-stream Turbulence on Turbulent Boundary Layers," ASME JOURNAL OF FLUIDS ENGINEERING, Vol. 105, pp. 284–289.

Hancock, P. E., and Bradshaw, P., 1989, "Turbulence Structure of a Boundary Layer Beneath a Turbulent Freestream," Journal of Fluid Mechanics, Vol. 205, pp. 45–76.

Hinze, J. O., 1975, Turbulence, 2nd Edition, New York, McGraw-Hill.

Hoffmann, J. A., and Mohammadi, K., 1991, "Velocity Profiles for Turbulent Boundary Layers Under Freestream Turbulence," ASME JOURNAL OF FLUIDS ENGINEERING, Vol. 113, pp. 399–404.

Hunt, J. C. R., and Graham, J. M. R., 1978, "Free-stream turbulence near plane boundaries," Journal of Fluid Mech. Vol. 84, pp. 209–235.

Johnson, P. L., and Johnston, J. P., 1989, "Active and Inactive Motions in a Turbulent Boundary Layer—Interactions with Free-Stream Turbulence," Proceedings 7th Symposium of Turbulent Shear Flows, Stanford University, pp. 20.2.1–20.2.6.

Kestin, J., 1966, "The Effect of Freestream Turbulence on Heat Transfer Rates," Advances in Heat Transfer, Vol. 3., New York, Academic Press.

Maciejewski, P. K., ands Moffat, R. J., 1992, "Heat Transfer with Very High Free Stream Turbulence: Part II-Analysis of Results," ASME Journal of Heat Transfer, Vol. 114, pp. 834–839.

Simonich, J. C., and Bradshaw, P., 1978, "Effect of Free-Stream Turbulence on Heat Transfer through a Turbulent Boundary Layer," ASME Journal of Heat Transfer, Vol. 100, pp. 671–677.

Thole, K. A., and Bogard, D. G., 1994, "Enhanced Heat Transfer and Shear Stress due to High Freestream Turbulence," ASME Journal of Turbomachinery, Vol. 117, no. 5, pp. 418–424.

Thole, K. A., Bogard, D. G., and Whan-Tong, J. L., 1994, "Generating High Freestream Turbulence Levels," Experiments in Fluids Vol. 17, pp. 375–380.

Thomas, N. H., and Hancock, P. E., 1977, "Grid Turbulence Near a Moving Wall," Journal of Fluid Mechanics, Vol. 82, pp. 481–496.

Townsend, A. A., 1956, The Structure of Turbulent Shear Flow, Cambridge Press.

Turbulent Flow Simulation of a Runner for Francis Hydraulic Turbines Using Pseudo-Compressibility

Chuichi Arakawa
The University of Tokyo,
Faculty of Engineering,
7-3-1 Hongo, Bunkyo-ku, Tokyo 113, Japan

Yi Qian
Fuji Electric Co. Ltd.,
Kawasaki, Japan

Takashi Kubota
Kanagawa University,
Yokohama, Japan

A three-dimensional Navier-Stokes code with pseudo-compressibility, an implicit formulation of finite difference, and a $k - \epsilon$ two-equation turbulence model has been developed for the Francis hydraulic runner. The viscous flow in the rotating field can be simulated well in the design flow operating condition as well as in the off-design conditions in which a strong vortex occurs due to the separation near the leading edge. Because the code employs an implicit algorithm and a wall function near the wall, it does not require a large CPU time. It can therefore be used on a small computer such as the desk-top workstation, and is available for use as a design tool. The same kind of algorithm that is used for compressible flows has been found to be appropriate for the simulation of complex incompressible flows in the field of turbomachinery.

1 Introduction

Because the algorithms for incompressible and compressible flows are fundamentally different from each other due to the characteristics of the governing equations, the authors were required to develop separately programs for similar flows in water and air turbines. The idea of pseudo-compressibility has already been introduced for fundamental flows (Chorin, 1967) and has the possibility to be applied to complex compressible and incompressible flows in turbomachinery using a single algorithm for compressible flows. One of the authors previously developed a calculation code for three-dimensional turbulent flows in advanced turboprops (ATP) for jet engines using a compressible flow scheme for the rotating blade. This code enables the successful prediction of the performance and the detailed flows including the location of shock (Matsuo et al., 1989). The subject of this paper is the Francis runner of hydraulic turbines, and the complex incompressible flows are analyzed in the same manner as compressible one in the rotating frame of the ATP through combination with pseudo-compressibility formulation.

For the numerical algorithm, the implicit finite difference and approximate factorization method are utilized in order to obtain a comparatively large time step for the time marching (Beam and Warming, 1976). The $k - \epsilon$ turbulence model, which requires two transport equations to derive the turbulent viscosity, is incorporated to simulate a high Reynolds number flow, and a wall function is used to decrease the number of grid points. This algorithm, which introduces the implicit algorithm as well as the wall function, enables us to utilize not only a large supercomputer, but also to use a standard desk-top computer such as a workstation to carry out the hydraulic design of turbomachinery.

The computational model of the Francis runner was provided by the organizer of the GAMM Workshop in Lausanne, 1989 (Sottas and Rhyming, 1993), which was attended by over 40 scientists and engineers. At this workshop, 11 groups presented simulations of the 3-D flow in a Francis runner. Avellan et al. (1993) described the details of their experiments for researchers of numerical simulations, and the organizers by themselves reported their numerical researchers in which they employed an explicit algorithm and paid particular attention to the difference between the mesh types (Neury and Bottaro, 1990). The authors contributed an Euler analysis for inviscid flows to the workshop, and have continued with the development to produce the turbulent flow code described in this paper. This code can accurately predict the flow pattern for the best operating point as well as for off-design points.

2 Basic Equations and the Numerical Algorithm

The unsteady, three-dimensional, incompressible flow with constant density for a runner of the Francis turbine is governed by the following equation written in the vector form associated with rotating Cartesian coordinates.

$$\frac{\partial Q}{\partial t} + \frac{\partial E}{\partial x} + \frac{\partial F}{\partial y} + \frac{\partial G}{\partial z} + H = Re^{-1}\left(\frac{\partial R}{\partial x} + \frac{\partial S}{\partial y} + \frac{\partial T}{\partial z}\right) \quad (1)$$

$$Q = \begin{bmatrix} 0 \\ u \\ v \\ w \end{bmatrix}, \quad E = \begin{bmatrix} u \\ uu + p \\ uv \\ uw \end{bmatrix}, \quad F = \begin{bmatrix} v \\ vu \\ vv + p \\ vw \end{bmatrix},$$

$$G = \begin{bmatrix} w \\ wu \\ wv \\ ww + p \end{bmatrix},$$

$$H = \begin{bmatrix} 0 \\ -\Omega^2 x - 2\Omega v \\ -\Omega^2 y + 2\Omega u \\ 0 \end{bmatrix}, \quad [R, S, T] = \begin{bmatrix} 0 & 0 & 0 \\ u_x & u_y & u_z \\ v_x & v_y & v_z \\ w_x & w_y & w_z \end{bmatrix}$$

The direction of rotation is clockwise about the positive z-direction and Ω denotes the angular velocity. The notations p, u, v and w are the pressure and relative velocity components on the rotating frame respectively, and all variables are properly normalized to produce the Reynolds number Re^{-1} as the coefficient of the viscous term. In order to introduce the pseudo-compressibility proposed by Chorin (1967) and developed by Rogers et al. (1989), the continuity equation is modified by adding a time derivative of the pressure term which allows the pressure wave to propagate at some limited speeds and

to disappear when the converged steady solution is achieved. General curvilinear coordinates (ξ, η, ζ) are introduced in order to fully accommodate three-dimensional geometry. After using the chain rule to transform the physical coordinates into curvilinear coordinates, we obtain the following form of the basic equations.

$$\frac{\partial \hat{Q}}{\partial t} + \frac{\partial \hat{E}}{\partial \xi} + \frac{\partial \hat{F}}{\partial \eta} + \frac{\partial \hat{G}}{\partial \zeta} + \hat{H} = \text{Re}^{-1}\left(\frac{\partial \hat{R}}{\partial \xi} + \frac{\partial \hat{S}}{\partial \eta} + \frac{\partial \hat{T}}{\partial \zeta}\right) \quad (2)$$

where,

$$\hat{Q} = J^{-1}\begin{bmatrix} p^* \\ u \\ v \\ w \end{bmatrix}, \quad \hat{E} = J^{-1}\begin{bmatrix} \beta U \\ uU + \xi_x p^* \\ vU + \xi_y p^* \\ wU + \xi_z p^* \end{bmatrix},$$

$$\hat{F} = J^{-1}\begin{bmatrix} \beta V \\ uV + \eta_x p^* \\ vV + \eta_y p^* \\ wV + \eta_z p^* \end{bmatrix}, \quad \hat{G} = J^{-1}\begin{bmatrix} \beta W \\ uW + \zeta_x p^* \\ vW + \zeta_y p^* \\ wW + \zeta_z p^* \end{bmatrix},$$

$$\hat{H} = J^{-1}\begin{bmatrix} 0 \\ -2\Omega v \\ 2\Omega u \\ 0 \end{bmatrix},$$

$$[\hat{R}, \hat{S}, \hat{T}] = (1 + \nu_t)J^{-1}$$

$$\times \begin{bmatrix} 0 & 0 \\ (\xi_x\xi_x + \xi_y\xi_y + \xi_z\xi_z)u_\xi & (\eta_x\xi_x + \eta_y\xi_y + \eta_z\xi_z)u_\eta \\ (\xi_x\eta_x + \xi_y\eta_y + \xi_z\eta_z)v_\xi & (\eta_x\eta_x + \eta_y\eta_y + \eta_z\eta_z)v_\eta \\ (\xi_x\zeta_x + \xi_y\zeta_y + \xi_z\zeta_z)w_\xi & (\eta_x\zeta_x + \eta_y\zeta_y + \eta_z\zeta_z)w_\eta \end{bmatrix}$$

$$p^* = p - \tfrac{1}{2}\Omega^2(x^2 + y^2) + gz$$

The notations U, V, and W are contravariant velocities, and J is the Jacobian of the transformation connecting the cartesian variables with the curvilinear variables. The parameter of pseudo-compressibility that controls the speed of the pressure wave is denoted as β in the continuity equation. A parameter survey of β carried out in an isolated aerofoil confirms the fact that there is no discrepancy in the numerical results when using a value between 0.5 and 5 as the parameter. β has been fixed as 1 for all of the runner simulations in this paper.

The numerical algorithm to advance Eq. (2) in time is an implicit, approximately factored, finite-difference scheme that was originally developed by Beam and Warming (1976). The basic equations are discretized into the conventional delta form with the use of Euler backward time differencing. The upwind-based high accuracy TVD scheme by Chakravarthy and Osher (1985) is used for the spatial differencing of the explicit terms in the delta form. TVD has been fundamentally developed to clearly capture shock waves with discontinuity in compressible flows, and plays the role of depressing the instability induced accidentally with turbulence models in order to converge the numerical iterations quickly.

The implicit terms rely on the diagonalized ADI method whereby the computational efficiency is improved for the reason that the steady state solution will be indifferent to implicit operators. The spatial difference utilizes an upwind flux-split technique. Each ADI operator is decomposed into the product of the lower and upper bi-diagonal matrices by using diagonally dominant factorization, and the operator is efficiently inverted by the forward and backward sweeps (Obayashi and Fujii, 1985). The final formulations of this implicit algorithm for the rotating blades can be referenced in papers by Matsuo et al. (1989) or Arakawa et al. (1991).

For the turbulence model, the standard $k - \epsilon$ model is employed to describe the viscous flow of a high Reynolds number including the separation region. Turbulent viscosity is derived with two transport equations of the turbulent energy k and dissipation rate ϵ. The wall function is used in the near-wall region in order to reduce the number of grid points, assuming that the production and dissipation of the turbulent energy are in equilibrium and that the other terms can be neglected in the so-called logarithmic region near the wall. The authors (Arakawa et al., 1991) have checked the reliability of the wall function against a low Reynolds number model (Jones and Launder 1972) which analyzes the flow accurately near the wall, and it was found that the difference of the pressure distribution between the two methods is very small. It was also found that the CPU time of the low Reynolds number model is about 4 times larger than that of the wall function in a two-dimensional single aerofoil having a small incidence of angle, where the grid numbers for the wall function and the low Reynolds number model are 157 × 31 and 157 × 41, respectively. Finally, the number of grid points in the Francis runner has been decreased to about 30,000 in this paper from the 300,000 points in the ATP calculations using the low-Reynolds number model which requires a finer grid near the wall.

3 Geometry and Boundary Conditions

The computational model of the Francis runner provided by the organizer of the GAMM Workshop is shown in Fig. 1 with grids pasted on all surfaces. It would be ideal to calculate the flow in the whole system of the Francis hydraulic turbine consisting of the spiral-casing, stay ring, guide vanes, runner and draft tube. However, the domain of this analysis is limited to the rotating part, that is, the water passage in the runner, and the pressure and velocity distributions at the inlet of the runner are required as the boundary conditions. These boundary conditions have also been supplied by the organizer of the GAMM Workshop and slightly modified by the authors in order to satisfy the continuity equation (Arakawa et al., 1990). The presented runner is specified by the following principal model performance test data. The power, head, mass flow rate, rotation velocity, number of blades and reference radius are 19.6 kw, 5.96 m, 0.372 m³/s, 500 rpm, 13 and 0.2 m, respectively.

The flow is assumed to be periodic around the runner and to be steady, so that the computational domain can contain only a single channel between the two blades, as shown in Fig. 2. The in- and out-flow boundaries are located at cross-sections denoted with "runner entrance" and "draft tube entrance" in Fig. 3, respectively. The crown surface is, for simplicity, smoothly extended to the rotating axis. H-mesh topology is adopted on the blade-to-blade plane in order to facilitate the periodic boundary conditions. The mesh clustering near the surfaces is imposed to enhance the numerical accuracy of the specified boundary conditions such as wall functions. Finally, the mesh for this turbulent flow calculation is 65 × 21 × 21. In order to check the grid dependency of the solutions, the grid positions near the wall were changed under the condition that the first grid point is located in the logarithmic region, and the difference of the numerical results between two grids was negligible.
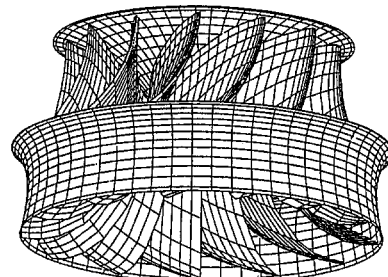

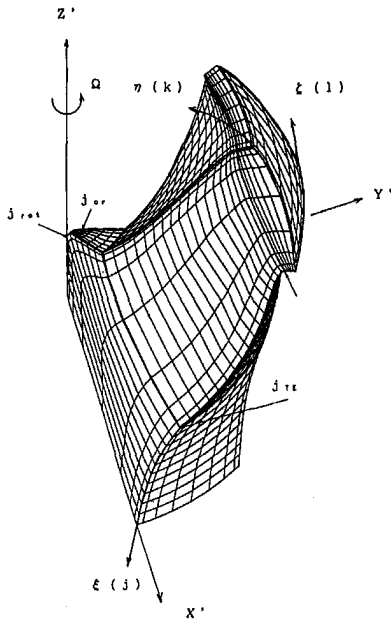Fig. 1 Computational model of GAMM Francis runner
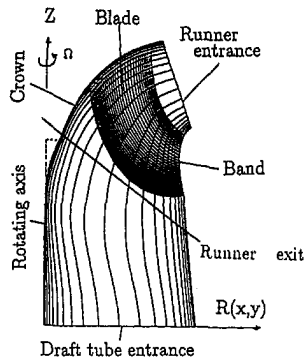
Fig. 2   Computational domain

Fig. 3   Projection of computational domain onto the meridian surface

For the boundary conditions, the pressure and all the velocity components are given by the measured values, with some modifications in the velocity field at the inflow boundary. As described previously, some modifications to the inlet values of the velocity were required to conserve the mass flow as given at the runner inlet. This was achieved by multiplying a constant value to the velocity component in the experiment. The axial symmetry requires that the velocity components u and v should be equal to zero and that the other values should be averaged from the surrounding points. On the crown, band and blade surfaces, impermeable conditions are specified as follows. The tangency condition is enforced by specifying the contravariant velocity $W = 0$ on the crown and band surfaces, and $V = 0$ on the blade surfaces. Other contravariant velocities and their pressures are obtained by linear extrapolation from interior points when required. The wall function is also applied on each surface as described previously. At the outflow boundary, the derivatives of all the velocity components in the streamwise direction are assumed to be zero, and the velocities are corrected in order to conserve the mass flow rate.

Strictly speaking, the inflow boundary conditions should be derived as a solution of the guide vanes installed in front of the runner. Another way would be to solve the whole field of guide vanes and the runner as an unsteady three-dimensional flow. However, the former method has a problem regarding the reliability of averaging the solution of the guide vanes, and the latter

Fig. 4   Comparisons of predicted and measured distributions of pressure and velocity components at the inlet (Solid line: predicted value, Symbols: measured value)

method requires a very large computational time. In this paper experimental data are employed for the boundary conditions only at the inlet in order to simulate the complex flow in the runner with a reasonable computational time to obtain information concerning the reliability of the developed algorithm.

Note that the words "crown" and "band," which are well-established classical words in hydroturbine fields, correspond to the hub and the shroud respectively for other turbo machinery.

4   Numerical Results in the Design Condition

The results of the Navier-Stokes calculations explained in the previous section are described for the designed flow condition
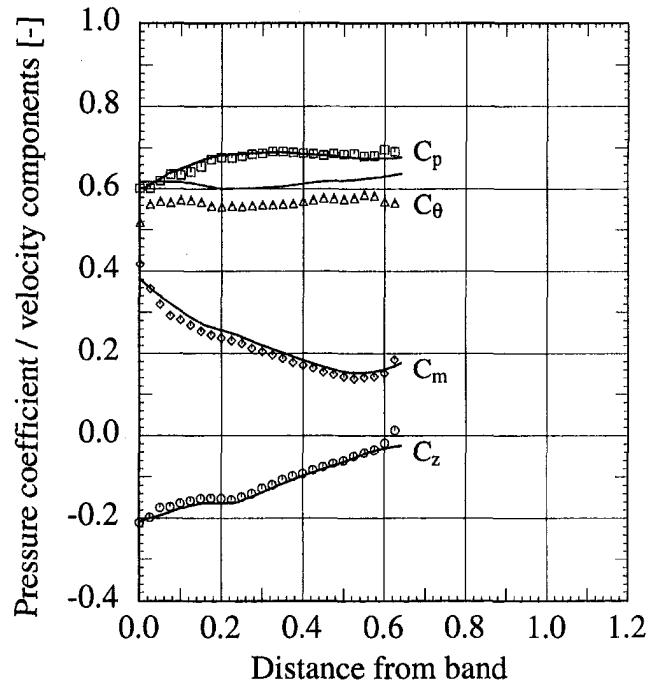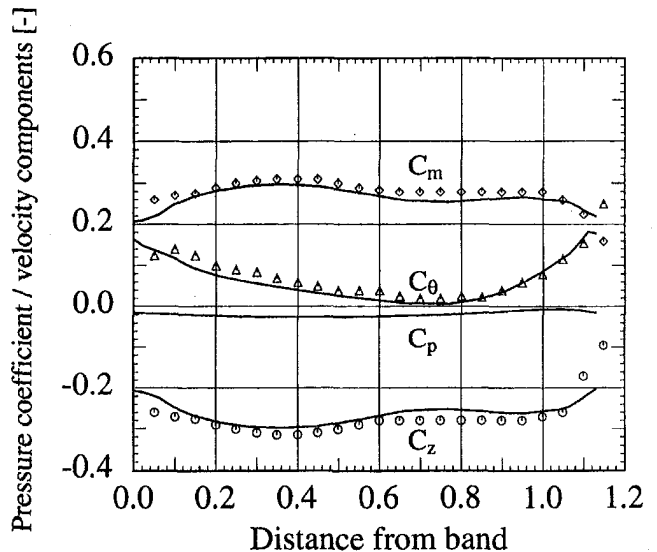

Fig. 5   Comparisons of predicted and measured distributions of pressure and velocity components at the outlet (Solid line: predicted value, Symbols: measured value)
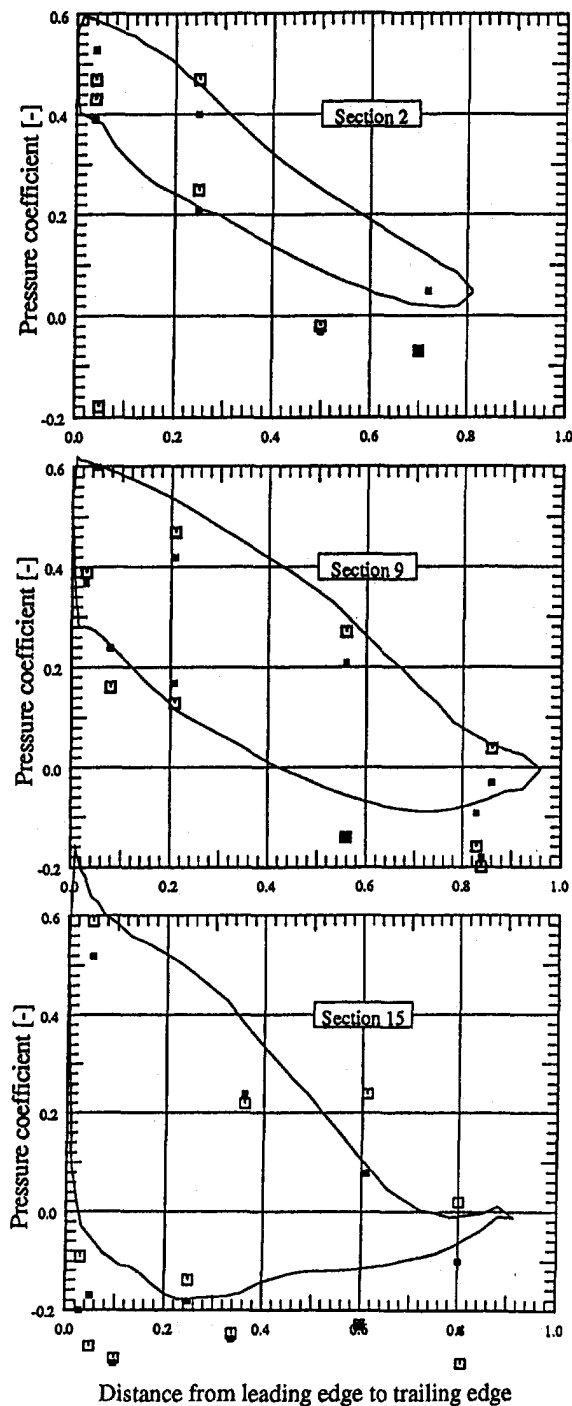
Fig. 6 Pressure distributions on the aerofoil sections of the runner (Solid line: predicted value, Symbols: measured value)

the tangential velocity. This difference is due to the corrections that were necessary to satisfy the mass conservation explained in the last section.

At the exit of the runner shown in Fig. 5, the velocity distributions of all three components are reasonably reproduced in the numerical simulation. The uniformity of the axial velocity distribution in the radial direction and the small value of the circumferential velocity component describe a typical structure of flow motion in the design condition, which appears to confirm the reliability of the program code developed in this paper. However, there is a small difference in each component between the numerical and experimental data, which may be due to the disagreement of the continuity in the experiment. The pressure distribution is predicted to be nearly constant from the band to the crown, which seems reasonable when taking the small value of the circumferential velocity into account, although there is no experimental data to be used for confirmation.

Figure 6 shows the pressure distributions along the hydrofoil section of the blade. Stations 2, 9, and 15 in the three diagrams correspond to the sections near the crown, at the center and near the band, respectively, so that the distance from the axis of rotation will be larger as the number of the station becomes greater. The predicted distributions of pressure depicted with solid lines are similar to the standard distributions in a cascade of turbines. In other words, the pressure decreases in the downstream direction, and a lower pressure appears on the suction surface of the runner. The difference of pressure between the two surfaces is larger at the outer section of Station 15 where a strong suction peak appears, and some cavitations may occur.

The comparison between the numerical and experimental data shows that there is a qualitative agreement in the pressure drop, but a small discrepancy still remains. As shown in Fig. 6, the experiments to measure the pressure on the rotating blades were carried out twice by the GAMM organizers, but a perfect reappearance could not be attained because of the difficulty in carrying out these experiments. We can at least confirm that the pressure level on the runner and its variance in the downstream and radial directions can be predicted using the proposed numerical analysis.

Figure 7 illustrates the velocity vectors at the first grid point near the surface of the blade as well as the pressure contours on the surface. These vectors are obtained using the wall function in order to decrease the grid number near the wall. The wall function assumes that the shear stress at the first grid point is as large as the wall shear stress and that the velocity has strong correlation with the wall shear stress. The assumption leads to the fact that the direction of the velocity is the same as that of the wall shear stress. Consequently both the shear stress direction and the qualitative scale of the velocity components near the wall are visible in Fig. 7.

It is found from this figure that the centrifugal forces that push the fluid in the radial direction work more strongly downstream of the suction side than at the pressure side, because the growth of the boundary layer on the runner in the downstream direction is larger on the suction side. Another radial flow appears strongly near the region of the leading edge on the pressure side, where the fluid that has a small velocity near the stagnation area is influenced strongly by the centrifugal forces. The form of the pressure contours shows that a strong peak of low pressure occurs near the leading edge beside the band on the suction side, and that pressure decreases uniformly in the downstream direction on the pressure side.

These comparisons make it clear that this numerical method, which has been developed for incompressible flows using the pseudo-compressibility and the wall function, is available for use with complex flows in the runner. The CPU time to obtain a converged solution is about 12 hours using a small work station whose maximum speed and memory size are 16 MFLOPS (Million Floating-point Operations Per Second) and 32 MB, respectively, although ATP simulations required about

and compared with the experimental data provided by the GAMM organizer.

Figure 4 shows the absolute velocity and pressure distributions at the runner inlet. The notations of C_z, C_θ, and C_m are, respectively, the axial, tangential and meridian components of velocity averaged between the rotating blades in the circumferential direction, and C_p is the pressure coefficient, all of which are made non-dimensional using the spouting velocity corresponding to the net head $\sqrt{2gH}$. The abscissa represents the distance along the straight traverse line from the band side. The figure for the inlet of the runner illustrates that the numerical data coincides with the experimental data well except for
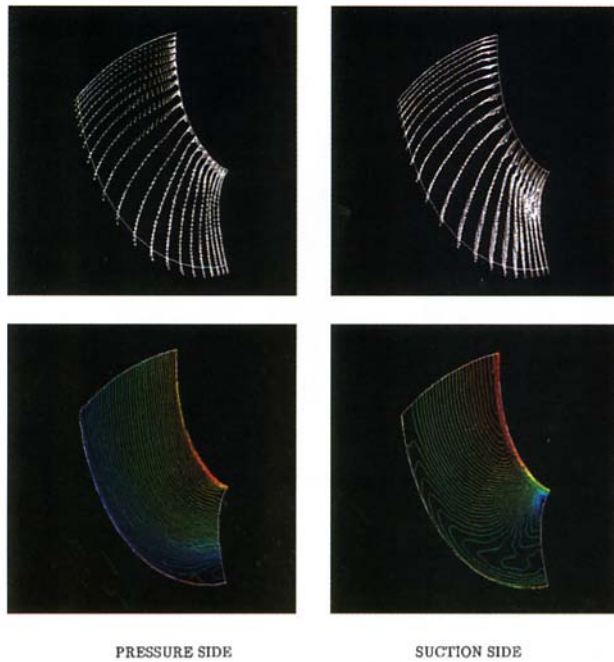
Fig. 7   Velocity vectors at the first grid point (upper figures) and pressure contours (lower figures) on the runner surface

6 hours using a supercomputer of 2000 MFLOPS even when the efficient implicit algorithm was incorporated. This computer code has great possibilities to be employed as a design tool for turbomachinery due to the short CPU time.

5   Predictions of a Channel Vortex Filament in Off-Design Conditions

More complex flow fields in off-design conditions have been simulated using the proposed numerical code in order to understand its applicability. The angle of attack for the hydrofoil section of the runner in off-design flow conditions is so large that a separation appears near the leading edge and leads to a strong vortex in the radial or downstream directions. For example, as the flow quantity is increased for a constant number of rotations, the pressure drop through the runner becomes large and the power derived from the flow increases. A similar phenomenon appears when the number of rotations decrease in the constant flow rate. In these off-design operating conditions, the angle of attack becomes larger than in the design condition, and a strong vortex induced by the separation develops when the deviation from the design value is large.

The boundary conditions of the runner for the off-design conditions at the inlet are assumed to be the same as those for the design flow in the following simulations. This assumption is available for the operation of variable rotational speed with constant mass flow rate in Francis hydraulic turbines of medium specific speed. Neumann conditions, which assume that the gradient of the velocity and pressure in the downstream direction is zero, are also used at the outflow boundary for the boundary conditions.

Figure 8 shows the pressure distributions when changing the rotational speed between 1.0 and $0.7N_d$ (N_d = designed rotation number) in the constant quantity flow. A strong peak of low pressure appears near the leading edge for all sections of the aerofoil at 0.8 and $0.7N_d$, and the pressure recovers in the downstream region. Pressure contours at seven sections between the pressure and suction surfaces of the runner are described in Fig. 9 at $0.8N_d$. The region of the strong peak of low pressure starts from the leading edge near the crown and develops in the radial and downstream directions.

Velocity vectors at four sections between the crown and the band of the runner are illustrated in Fig. 10 in order to visualize the vortex development at the operating condition of $0.8N_d$. A strong vortex is generated near the corner of the leading edge and crown on the suction surface and grows toward the band. This is thought to be the same as the vortex filament which can be observed flowing out from the runner to the draft tube in off-design operations with a large head. The operation with a large head at a constant rotation number is equivalent to an operation with a smaller rotation number such as $0.8N_d$ under the constant head simulated here.
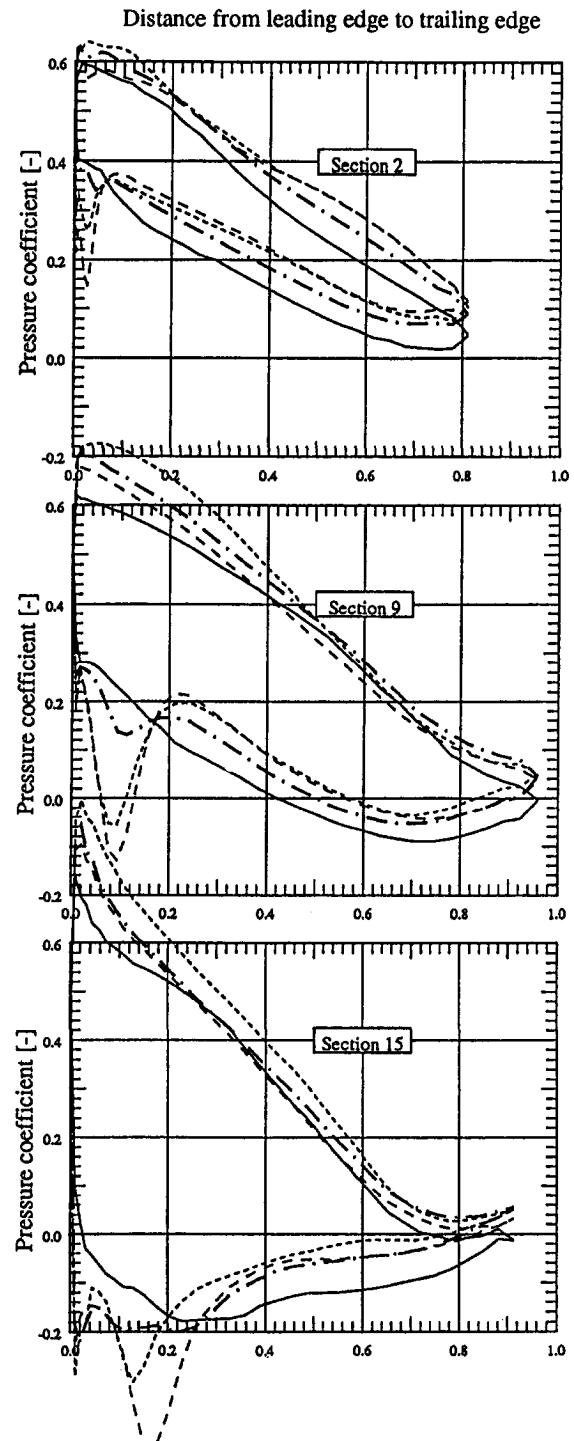

Fig. 8   Pressure distributions on the runner when changing the number of rotations (Solid line: $1.0N_d$, Alternate long and short dashed line: $0.9N_d$, Short dotted line: $0.8N_d$, Long dotted line: $0.7N_d$)
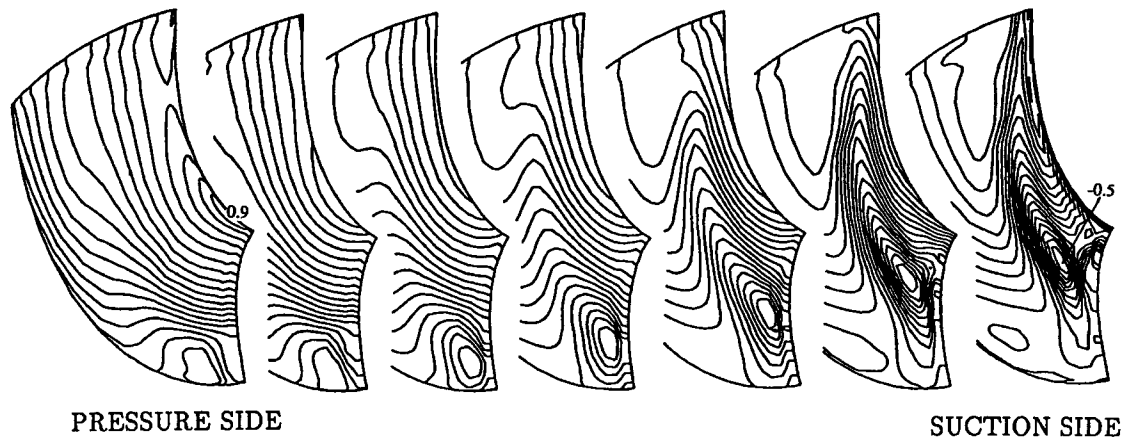
Fig. 9 Pressure contours on seven sections between the pressure and suction surfaces of the runner at $0.8N_d$ (There are fifty contours between the maximum pressure coefficient 0.9 and the minimum coefficient −0.5.)
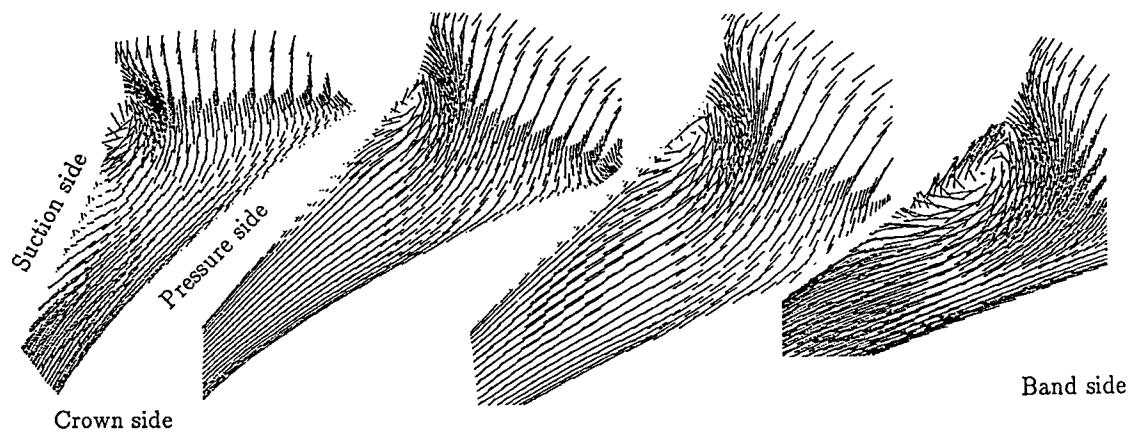
Fig. 10 Velocity vectors on four sections between the crown and band of the runner at $0.8N_d$

The color computer graphics in Fig. 11 show the pressure distribution on all the surfaces of the runner except the band, and on two cross sections parallel to the band and crown. The red and blue colors represent high and low pressures, respectively. Figure 12 illustrates the velocity vectors at four cross sections in the runner depicted in three dimensional form. Combining the informations in Figs. 9 and 10 with the color graphics

of Figs. 11 and 12, a vortex filament is observed to grow out in the direction of the band from the crown, accompanied by a region of low pressure. This vortex filament turns the band downstream and the strength diminishes. The three-dimensional form of the velocity vectors shown in Fig. 12 unfortunately

Fig. 11 Color indication of pressure for the whole runner region at $0.8N_d$

Fig. 12 Solid indication of velocity vectors on four sections between the crown and band of the runner at $0.8N_d$

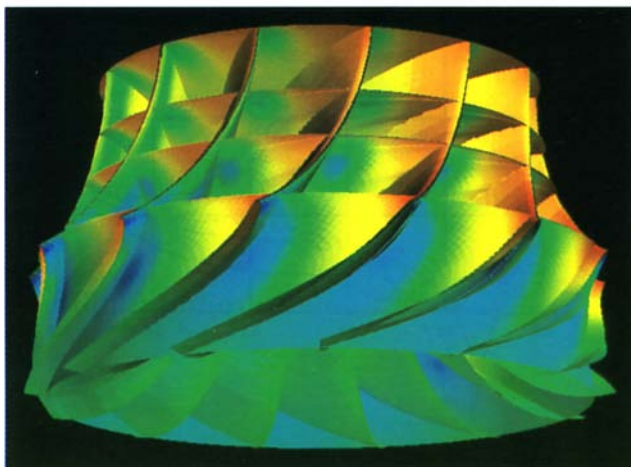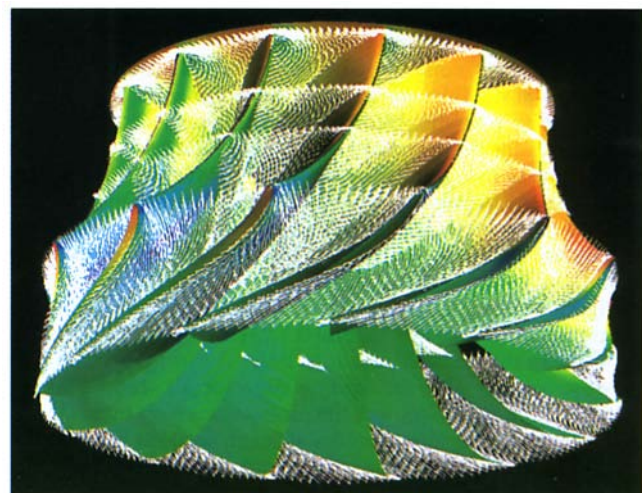obscures the development of the vortex owing to the large components in the direction of the vortex. In general, in experiments this vortex filament flows out into the draft tube while keeping its strength. However, in this simulation it disappears at the exit of the runner according to other computer graphics not referred to in this paper. This defect of the simulation is due to the shortcomings of the $k - \epsilon$ turbulent model in predicting vortex flows, which Hogg and Leschziner (1989), for example, discuss for basic confined swirling flows.

The phenomena discussed above are known as channel vortex filaments which are entrained in the main flows in the multiple channels of a rotating runner due to the flow separation at the leading edge of the blades. There is said to be a quite different vortex rope at the draft tube centerline which appears in the stationary closed conduit due to the swirl component of the main flow. The latter vortex cannot be observed in these simulations.

The experimental data for off-design conditions were not presented by the GAMM organizer, and therefore quantitative comparisons cannot be carried out in this paper. However, it is confirmed that the proposed algorithm has the ability to predict the qualitative flow pattern.

6 Conclusions

A three-dimensional incompressible Navier-Stokes code with pseudo-compressibility, implicit finite difference formulation and $k - \epsilon$ turbulence model has been developed and applied to the flow around the Francis runner. The reliability of this program can be confirmed in the design condition through comparison with experimental data. More complex flows for off-design conditions can be predicted and a vortex filament is seen to appear in the flow channel between the blades of the runner. Through incorporation of pseudo-compressibility, the same algorithm is available for use in predicting both compressible and incompressible flows in complicated flows such as in turbomachinery. This method can be easily included in the design process, because the efficient algorithm of the implicit time marching and the wall-function of $k - \epsilon$ model makes it possible to simulate these flows with small computers like workstations as well as with supercomputers.

References

Arakawa, C., Samejima, M., Matsuo, Y., and Kubota, T., 1990, "Numerical Simulation of Francis Runner Using the Pseudo-Compressibility," *Proceedings, IAHR Symposium 1990,* Belgrade Yugoslavia, Vol. 1 C1, pp. 1–10.

Arakawa, C., Samejima, M., Matsuo, Y., and Kubota, T., 1991, *Computational Simulation of Francis Water Runner with Pseudo-Compressibility,* FED-Vol. 120, ASME, pp. 119–124.

Avellan, F., et al., 1993, "Experimental Flow Study of the GAMM Turbine Model," Notes on Numerical Fluid Mechanics, Vol. 39, pp. 33–54.

Beam, R. F., and Warming, R. M., 1976, "An Implicit Finite-Difference Algorithm for Hyperbolic Systems in Conservation Laws," *Journal of Computational Physics,* Vol. 22, pp. 87–110.

Chakravarthy, S. R., and Oshers, S., 1985, "A New Class of High Accuracy TVD Schemes for Hyperbolic Conservations Laws," AIAA Paper 85-0369.

Chorin, A. J., 1967, "A Numerical Method for Solving Incompressible Viscous Flow Problems," *Journal of Computational Physics,* Vol. 2, pp. 12–26.

Jones, W. P., and Launder, B. E., 1972, "The Prediction of Laminarization with a Two-Equation Model of Turbulence," *International Journal of Heat and Mass Transfer,* Vol. 15, pp. 301–314.

Hogg, S., and Leschziner, M., 1989, "Computation of Highly Swirling Confined Flow with a Reynolds Stress Turbulence Model," Vol. 27, No. 1, pp. 57–63.

Matsuo, Y., Arakawa, C., Saito, S., and Kobayashi, H., 1989, "Navier-Stokes Simulations around a Propfan Using Higher-order Upwind Scheme," AIAA Paper 89-2699.

Neury, C., and Bottaro, A., 1990, "Influence of Mesh Type in the Simulation of Hydraulic Machines," *Proceedings, IAHR Symposium 1990,* Belgrade, Yugoslavia, Vol. 1 C4, pp. 1–13.

Obayashi, S., and Fujii, K., 1985, "Computation of Three-Dimensional Viscous Transonic Flows with the LU Factored Scheme," AIAA Paper 85-1510.

Rogers, S. E., Kwak, D., and Kiris, C., 1989, "Numerical Solutions of the Incompressible Navier-Stokes Equations for Steady-State and Time-Dependent Problems," AIAA Paper 89-0463.

Sottas, G., and Rhyming, I. L., 1993, "3D-Computation of Incompressible Internal Flows," *Notes on Numerical Fluid Mechanics,* Vol. 39.

Development of a Two-Dimensional Turbulent Wake in a Curved Channel With a Positive Streamwise Pressure Gradient

J. John
Research Assistant.

M. T. Schobeiri
Professor. Mem. ASME

Texas A&M University,
Turbomachinery Performance Laboratory,
College Station, TX, 77843-3123

The development of turbomachinery wake flows is greatly influenced by streamline curvature and streamwise pressure gradient. This paper is part of a comprehensive experimental and theoretical study on the development of the steady and periodic unsteady turbulent wakes in curved channels at different streamwise pressure gradients. This paper reports on the experimental investigation of the two-dimensional wake behind a stationary circular cylinder in a curved channel at positive streamwise pressure gradient. Measurements of mean velocity and Reynolds stress components are carried out using a X-hot-film probe. The measured quantities obtained in probe coordinates are transformed to a curvilinear coordinate system along the wake center line and are presented in similarity coordinates. The results show strong asymmetry in velocity and Reynolds stress components. The Reynolds stress components have higher values at the inner half of the wake than at the outer half of the wake. However, the mean velocity defect profiles in similarity coordinates are almost symmetric and follow the same Gaussian function for the straight wake data. A comparison with the wake development in a curved channel at zero streamwise pressure gradient suggests the decay rate of velocity defect is slower and the growth of wake width is faster for a positive streamwise pressure gradient.

1 Introduction

In turbomachinery aerodynamics and heat transfer the periodic unsteady wakes generated by the preceding row of blades influence the boundary layer development and, consequently, the heat transfer characteristics of the blades downstream of the wake. Because of its significant impact on the turbomachinery efficiency and performance, the wake development associated with the inherent unsteadiness induced by mutual interaction between stator and rotor has recently attracted the interest of the scientific and engineering community resulting in many publications in the turbomachinery performance area. As extensively discussed by Schobeiri and Pardivala (1992), the major part of the research work done in the above areas deals with the effects of the periodic unsteady wakes on various turbomachinery performance aspects mentioned previously. The wake development under turbomachinery flow conditions is subjected to pressure gradient and curvature effects. The streamline curvature significantly influences the properties of turbulent flows as shown by Wattendorf (1935) in his study of turbulent flows through curved channels and by Lumley and Margolis (1963) in their study of a curved turbulent mixing layer. The curvature and pressure gradient will significantly effect the mean velocities and turbulent properties of the wake.

Most of the research conducted on wakes deals with two-dimensional straight wakes at zero streamwise pressure gradient. The literature on zero streamwise pressure gradient straight wake includes those by Schlichting (1930), Reichardt (1950), Townsend (1947, 1949a,b), Eifler (1975), and Pfeil and Eifler (1975a,b). Hill et al. (1963) and Gartshore (1967) investigated

the effect of pressure gradients on the decay of two-dimensional symmetrical wakes.

Turbomachinery wake flow is an important case of turbulent flow with streamline curvature. Raj and Lakshminarayana (1973) investigated the near and far wake characteristics of a cascade of airfoils for three different incidence angles. The measurements of mean velocity, turbulence intensity, and Reynolds stress showed asymmetric distribution and the decay of the wake defect was strongly dependent on the downstream variation of wake edge velocity.

Koyama (1983) studied the effect of curvature on the mean velocity and turbulent stress in the initial part of a cylinder wake developing in a curved channel without a streamwise pressure gradient. When the wake generating cylinder is normal to the streamline curvature (spanwise), he observed asymmetry about the wake centerline in the mean velocity and turbulent intensity profiles owing to the destabilizing effects on the inner side of the wake and the stabilizing effects on the outer side. The effects of pressure gradient and curvature on wakes were investigated by Savill (1983) and recently by Nakayama (1987). Savill investigated a fully developed cylinder wake that is abruptly turned 90 deg by means of a back plate so that the wake is subjected to strong curvature and streamwise pressure gradient. The data for mean velocity and turbulent stress revealed the strong influence of curvature on the wake. The turbulent stress fields are complex owing to the coexistence of the stabilized and destabilized regions across the wake and strong interaction between them. Nakayama (1987) carried out a systematic study of the effect of mild pressure gradient and mild streamline curvature on a small-deficit wake. The wake was subjected to mild curvature and mild pressure gradient by deflecting it by an airfoil-like thin plate placed at small angles in the external flow. The qualitative separation between the effects due to the curvature and pressure gradient is achieved by placing

the thin plate at positive and negative angles to the freestream direction. Despite the governing mild pressure gradient and curvature, the measured data indicates a strong sensitivity of turbulence quantities, especially the Reynolds shear stress, to the curvature and pressure gradient.

The above investigations have significantly contributed to a better understanding of the wake flow under different boundary conditions. However, several fundamental questions, such as the wake decay mechanism under these conditions, are still unanswered. Further, the existing data on the direct influence of curvature and pressure gradient on the development of wake are limited. Therefore, the present study is part of a comprehensive experimental and theoretical investigation of the steady and periodic unsteady wake development through curved channels under positive, zero, and negative longitudinal (streamwise) pressure gradients. Schobeiri et al. (1994) theoretically and experimentally investigated the development of a wake flow downstream of a cylindrical rod within a curved channel at zero longitudinal pressure gradient. Their theoretical framework generally describes the wake flow through two-dimensional curvilinear channels. It also describes the wake development through a two-dimensional straight channel as a special case, for which the curvature radius approaches infinity. Schobeiri et al. (1994) presented a consistent set of comprehensive experimental data and compared it with their developed theory. This paper reports the wake development behind a stationary cylinder in a curved channel at positive longitudinal pressure gradient. Measurements of mean velocity and Reynolds stress components are carried out using a X-hot-film probe. The measured quantities obtained in probe coordinates are transformed to a curvilinear coordinate system along the wake center line and are presented in similarity coordinates.

2 Experimental Research Facility

Figure 1 shows the layout of the test section. A large centrifugal fan supplies air to the test section. The air flows through a diffuser, settling chamber, nozzle, wake generating section and to the curved channel test section. The inlet of the test section has a free-stream turbulence intensity of 1.25 percent. The paper by Schobeiri and Pardivala (1992) gives detailed information about the design description and performance tests. The wake generator is designed to simulate the unsteady inlet flow and the flow pattern downstream of a rotor row. For the investigations reported in this paper, the wake generator was kept stationary, with a single circular rod of diameter $d = 1.98$ mm fixed at the mid-height of the channel and a distance 67 mm upstream of the entrance to the curved test section in order to generate a wake. The average velocity at the inlet of the test section was about 20 m/s, corresponding to a Reynolds number, based on the diameter of the wake generating rod, of 2600. The test
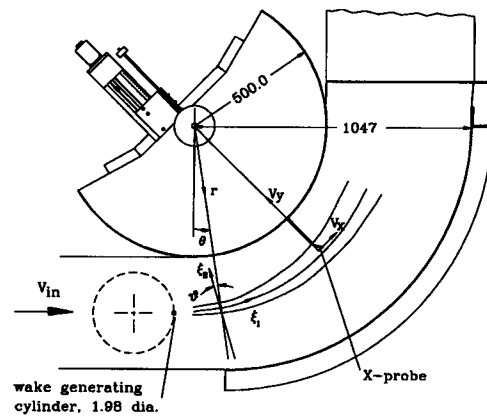

Fig. 1 Layout of test section and representation of probe coordinate and curvilinear coordinate systems. Dimensions are in mm.

section in Fig. 1 is downstream of the wake generator and consists of a convex top wall, a concave bottom wall, and two vertical plexiglass side walls. The convex wall has a radius of curvature of 500 mm and the concave wall has a radius of curvature of 920 mm. The concave bottom wall is designed to slide horizontally within two T-slots in the bottom wall of the wake generator. This allows the creation of adverse or favorable longitudinal pressure gradients within the test section. In the present investigation, the test section has an inlet area of 420 $\times$ 593 mm^2 and an outlet area of 547 $\times$ 593 mm^2, corresponding to an inlet to outlet area ratio of 0.7. Considering the channel wall boundary layer blockage effect, the above area ratio corresponds to the velocity deceleration ratio of a conventional compressor blade channel. The convex top wall of the test section was designed to allow the mounting of the probe traversing system, which provides accurate radial positioning of the probes with a resolution of 2.5 μm. Angular (longitudinal) positioning of the probes is accomplished by rotating the convex wall assembly about its center of curvature. The slider of the traversing system allows simultaneous positioning of two probes at the same longitudinal and radial location. The first probe is a hot-wire or hot-film probe (X-film) while the second probe is a total pressure probe (Kiel probe).

3 Instrumentation, Data Acquisition, Analysis

Digital data acquisition and analysis have been used for the entire measurements. The test facility was instrumented for fully automated data acquisition. A 386SX, 16 mHz personal computer controls the data acquisition system. A 12-bit A/D (analog

---

Nomenclature

b = wake width
C = resultant velocity
C_p = pressure coefficient
d = diameter of wake generating cylinder
f = frequency
H_{12} = shape factor of wake
p, p_t = static, total pressure
U, V = velocity components in ξ_1, ξ_2 direction
U_p = hypothetical potential velocity distribution of streamwise component of velocity
U_{1m} = maximum velocity defect

α = angle between resultant velocity vector and x-axis
γ = integral of the Gaussian curve γ
$\quad = \int_0^{+\infty} e^{-\zeta^2} d\zeta = \sqrt{\pi}/2$
ζ = nondimensional coordinate = ξ_2/b
θ = angular position of the probe location from the inlet
ξ_1 = streamwise direction of curvilinear coordinates
ξ_2 = lateral direction of curvilinear coordinates

ρ = density of air
ϑ = angle between probe and curvilinear coordinates
φ_1 = nondimensional velocity defect φ_1
$\quad = \bar{U}_1/\bar{U}_{1m}$

Subscripts

m = maximum
o = location of maximum velocity defect
x = x-direction
y = y-direction

Superscripts

— = time averaged value

to digital conversion) board is installed in one of the expansion slots of the computer. The board has 16 channels and a 1-mHz throughput data transfer rate. The mean velocity and turbulent stress components are obtained using a 3-channel, constant temperature anemometer (TSI, IFA 100) system. Each channel of the anemometer system has a signal conditioner with variable low and high pass filters, dc-offset, and adjustable gain. Based on numerous spectral measurements within the wake (Schobeiri et al., 1994), the low pass filter of the signal conditioner is set at 20 kHz. The hot-film probes are operated at 1.5 overheat ratios and 250°C sensor operating temperature. A simple and accurate method by John and Schobeiri (1993) is used to calibrate the X-probes. The uncertainties of the measurements for the velocity components using the X-probe are estimated to be about 1.2 percent for longitudinal velocity and 3 percent for the normal velocity.

The pressure is measured by two high precision differential pressure transducers (MKS 220 CD, Range: 0–10 mm Hg and 0–100 mm Hg) of capacitance type and having 0–10 V analog outputs. A Prandtl probe (pitot-static probe), placed upstream of the diffuser, is connected to one pressure transducer that monitors a reference velocity at a fixed location. The second pressure transducer measures the total pressure from a Kiel probe (United Sensor) positioned at the same radial and longitudinal location as the X-probe. A thermocouple placed just downstream of the test section constantly monitors the flow temperature. More details of the instrumentation and data acquisition system are given by Schobeiri et al. (1994) and John (1993).

The equations and the methods employed for the data reduction and analysis are presented in the paper by Schobeiri et al. (1994). The velocity components are measured in the probe coordinates which coincide with the radial and tangential directions to the convex wall. The measurements are made in the probe coordinates (x, y), shown in Fig. 1, giving the tangential velocity component $\bar{V}_x$ and radial velocity component $\bar{V}_y$. The results are transferred into a curvilinear coordinate system $(\xi_1 - \xi_2)$, where ξ_1 is the direction along a streamline near the center of wake and ξ_2 the direction normal to it. The maximum inclination between these two orthogonal coordinate systems was less than 7.5 deg for the data presented here. Therefore, the distance taken radially from the wake center to a measuring point was approximated as ξ_2 and for all the measuring points at an angular position θ, the ξ_1 coordinate was assumed constant. The errors due to this approximation will be even smaller considering the fact that for most longitudinal locations the inclination between the two coordinate systems was less than 4 deg.

The time averaged velocity and turbulent stresses in the (x, y)-coordinate system are transformed into the curvilinear coordinate system $(\xi_1 - \xi_2)$.

$$\bar{U} = \bar{V}_x \cos \vartheta + \bar{V}_y \sin \vartheta \tag{1}$$

$$\bar{V} = \bar{V}_y \cos \vartheta - \bar{V}_y \sin \vartheta \tag{2}$$

where ϑ is the angle between the ξ_1 and x-direction, $\bar{U}$ and $\bar{V}$ are the velocities in the ξ_1 and ξ_2 directions, respectively. To find the angle ϑ (see Fig. 1), required for the above transformation, the location of maximum velocity defect was determined at every longitudinal locations. The location of maximum velocity defect is called the wake center. The trajectory of the path of the wake center was determined by curve fitting the locations of maximum wake defect by least-squares fit. The angle ϑ was determined at each measuring station along the wake centerline. It exhibited certain sensitivity with respect to the type of curve fit used for the path of the wake centerline. For most of the longitudinal locations the angle ϑ closely agreed with the angle of velocity vector α ($\alpha = \tan^{-1} (\bar{V}_y/\bar{V}_x)$) at the location of maximum wake velocity defect. At the longitudinal locations where ϑ was different from α, the difference was less than 1 deg. In these locations getting close agreement between α and ϑ was still possible, if the degree of the polynomial of curve
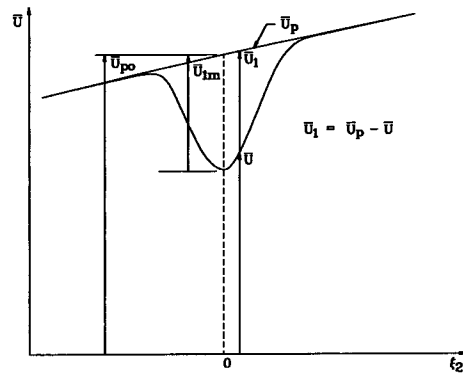

Fig. 2 Representation of longitudinal component of velocity, velocity defect, and potential velocity distribution

fit for the path of wake center was different from the one used for other locations. Considering the uncertainty in locating the wake center and calculating the velocity components using the X-film probe, it can be assumed that the flow angle α at the wake center is equal to ϑ. In other words, the velocity vector is tangent to the wake centerline at the location of maximum velocity defect. Therefore, the wake centerline is a streamline with $\xi_2 = 0$ in the curvilinear coordinate system. The mean Reynolds stress components in $(\xi_1 - \xi_2)$-coordinates are obtained by taking the product of the fluctuating velocities and time averaging, and are given by:

$$\overline{u^2} = \overline{v_x^2} \cos^2 \vartheta + \overline{v_y^2} \sin^2 \vartheta + \overline{v_x v_y} \sin 2\vartheta \tag{3}$$

$$\overline{v^2} = \overline{v_x^2} \sin^2 \vartheta + \overline{v_y^2} \cos^2 \vartheta - \overline{v_x v_y} \sin 2\vartheta \tag{4}$$

$$\overline{uv} = (\overline{v_y^2} - \overline{v_x^2}) \frac{\sin 2\vartheta}{2} + \overline{v_x v_y} \cos 2\vartheta \tag{5}$$

A schematic representation of the longitudinal component of velocity, mean velocity defect, and hypothetical potential velocity $\bar{U}_p$ are shown in Fig. 2. The mean velocity defect $\bar{U}_1$ and its maximum value at the wake center $\bar{U}_{1m}$ are calculated as follows. A hypothetical potential velocity distribution is determined in the wake by fitting the mean velocity $\bar{U}$ data outside the wake on both halves by a suitable curve. Nakayama (1987) used a straight line fit to obtain the hypothetical potential velocity distribution. For the present case, a straight line fit through the mean velocity data outside the wake was inaccurate for determining the potential velocity in the wake for all longitudinal locations. Overall, a least-squares fit by a third order polynomial was found accurate for representing the potential velocity distribution. The value of $\bar{U}_1$ is obtained from the definition ($\bar{U}_1 = \bar{U}_p - \bar{U}$). The procedure for determining the velocity defect distribution are described in detail by Schobeiri et al. (1994).

The maximum velocity defect $\bar{U}_{1m}$ is used as the velocity scale to nondimensionalize mean velocity defect, normal velocity $\bar{V}$, and Reynolds shear stress. Many researchers have used $(\bar{U}_\infty(d/(x - x_0))^{-0.5})$ as the velocity scale for plane turbulent wakes at zero streamwise pressure gradient since the decay of maximum velocity defect is proportional to it in plane turbulent wakes. The notation x stands for the downstream distance from the wake generating cylinder, x_0 for the virtual origin of the wake, and $\bar{U}_\infty$ for the freestream velocity. In the literature, values ranging from 40 to 100 cylinder diameters have been reported for x_0. The length scale to nondimensionalize the ξ_2 was the wake width b defined by

$$b = \frac{1}{\bar{U}_{1m}} \int_{-\infty}^{+\infty} \bar{U}_1 d\xi_2 \tag{6}$$

4 Presentation and Discussion of Results

All measurements were carried out for an average inlet velocity of about 20 m/s. The wake profiles were obtained at fifteen
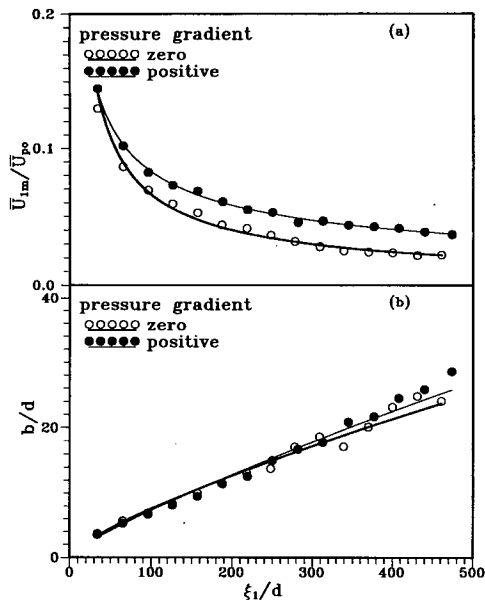
Fig. 3 Decay of maximum velocity defect (a) and growth of wake width (b) as a function of longitudinal position. The uncertainty of the longitudinal velocity measurement essential for calculating the velocity defect is 1.2 percent.

Fig. 4 Variation of potential velocity with an uncertainty of 1.2 percent and pressure coefficient at the wake center as a function of longitudinal position

angular positions from $\theta = 0$ to 70 deg in 5 deg intervals. The first measuring station $\theta = 0°$ corresponds to the inlet of the curved test section, and is at a distance of 67 mm downstream of the wake generating cylinder. Comprehensive preliminary investigations concerning the two-dimensional nature of flow were done (see Schobeiri and Pardivala, 1992) before starting with the final measurements presented in this paper. It was found that for the longitudinal locations up to $\xi_1/d = 400$, the moderate growth of boundary layer on the concave, convex, and the side walls did not affect the two-dimensionality of the wake flow under investigation. However, as shown in the following results, the two-dimensionality was influenced for longitudinal locations beyond the above value.

Wake Center, Development. The path of wake center represents the ξ_1 direction for the curvilinear coordinate system. As the wake convects through the channel, the trajectory of the wake center gradually moves toward the convex wall up to a longitudinal location $\xi_1/d = 100$, and from there onward it moves away from the convex wall. The maximum inclination between the trajectory of the wake center and the tangential direction x was less than 7.5 deg. The local curvature of the wake centerline is calculated from the first and second derivative of the polynomial fit through the wake center at different longitudinal position. The negative value of K suggests that the curvature of the wake centerline is concave in the positive ξ_2 direction.

Figure 3(a) shows the decay of maximum velocity defect normalized by the potential velocity at the wake center $\bar{U}_{po}$. The solid line represents a power law fit with $\bar{U}_{1m}/\bar{U}_{po} \sim (\xi_1/d)^{-0.51}$. For comparison, the wake development in the curved channel at zero streamwise pressure gradient followed the law $\bar{U}_{1m}/\bar{U}_p \sim (\xi_1/d)^{-0.71}$. Therefore, the decay rate of a nondimensionalized maximum velocity defect in the positive pressure gradient curved channel is slower than the zero streamwise pressure gradient curved channel. Figure 3(b) shows the wake width b nondimensionalized by the diameter of the wake generating rod as a function of ξ_1/d. The solid line is the power law fit with $b/d \sim (\xi_1/d)^{0.81}$. For the zero streamwise pressure gradient curved wake b/d is proportional to $(\xi_1/d)^{0.74}$. Therefore, the spreading rate of b in the positive pressure gradient
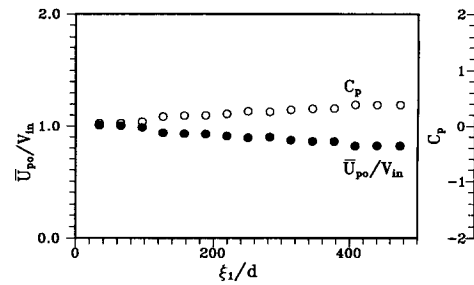
curved wake is slightly higher than the zero streamwise pressure gradient curved wake.

Figure 4 shows the distribution of the hypothetical potential velocity at wake center nondimensionalized by the freestream velocity just upstream of the wake generating rod as function of ξ_1/d. The decreasing hypothetical potential velocity distribution along the wake centerline is due to the diverging channel used to create the positive longitudinal pressure gradient. Figure 4 also shows the pressure coefficient C_p ($C_p = (p - p_{in})/\frac{1}{2}\rho V_{in}^2$) at the wake center at various longitudinal locations. Here p denotes the static pressure at the wake center and p_{in} denotes the static pressure at the straight section upstream of the wake generating cylinder. The static pressure p at the wake center is calculated from the total pressure p_t at the wake center measured with the Kiel probe and the velocity obtained with a X-film probe (i.e., $p = p_t - \frac{1}{2}\rho(\bar{U}^2 + \bar{V}^2 + \overline{u^2} + \overline{v^2})$). Figure 4 also shows the pressure coefficient increasing with downstream distance and confirms the positive pressure gradient. The wake decay and growth are generally characterized by the maximum velocity defect $\bar{U}_{1m}$ and the width b that vary only in longitudinal direction (ξ_1/d). Their product, $\bar{U}_{1m}b$, exhibits a major parameter in describing the free turbulent flow and in modeling the free turbulent Reynolds stresses. For straight wakes at zero pressure gradient, this product is a constant for all longitudinal locations as shown by Eifler (1975) and Reichardt (1950). Recent investigations by Schobeiri et al. (1994) show that the product $\bar{U}_{1m}b$ has a nearly constant value for zero streamwise pressure gradient curved wakes. Figure 5 shows the product $\bar{U}_{1m}b$ at various longitudinal locations for the positive streamwise pressure gradient case presented in this paper. As seen, the product $\bar{U}_{1m}b$ increases with the downstream location. The values of the maximum velocity defect, wake width, potential velocity at the wake center and the average velocity upstream of the cylinder at various downstream locations are given in Table 1.

Mean Velocity Distribution. Figure 6 shows typical plots of the streamwise velocity component as a function of the lateral distance for six longitudinal locations. The velocity distributions
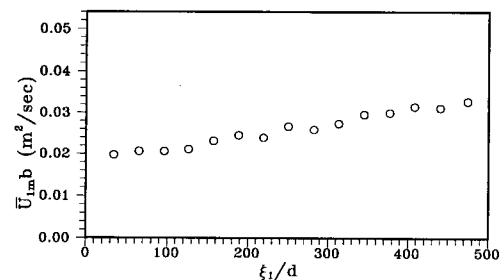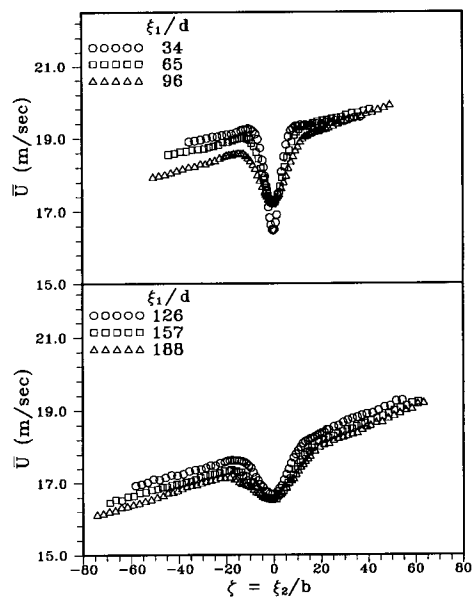

Fig. 5 Integral parameter $U_{1m}b$ as a function of longitudinal position. The uncertainty of the longitudinal velocity measurement essential for calculating the velocity defect is 1.2 percent.

Table 1   Values of selected quantities of the wake at positive longitudinal pressure gradient
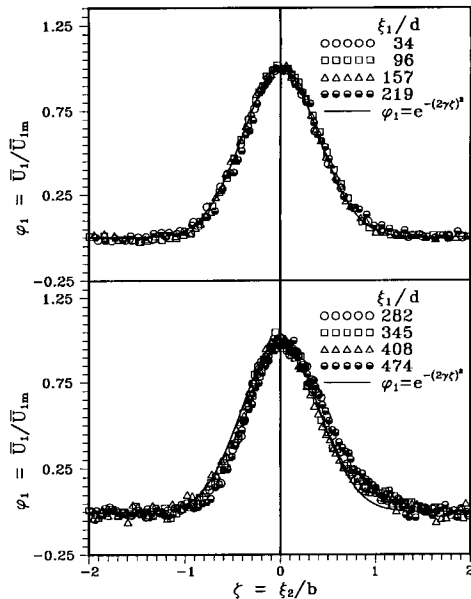
θ (o)	ξ_1/d	$\bar{U}_{1m}$ (m/s)	b (mm)	$\bar{U}_{po}$ (m/s)	$\overline{u_o^2}$ (m²/s²)	$\overline{v_o^2}$ (m²/s²)	$\bar{V}_{in}$ (m/s)
0	34	2.793	7.06	19.27	1.833	1.965	19.10
5	65	1.952	10.56	19.17	0.876	0.704	19.10
10	96	1.550	13.30	18.85	0.631	0.444	19.09
15	126	1.311	16.13	18.00	0.510	0.333	19.20
20	157	1.216	18.97	17.76	0.470	0.294	19.07
25	188	1.075	22.77	17.68	0.446	0.279	19.06
30	219	0.954	25.00	17.37	0.419	0.262	19.08
35	250	0.898	29.76	16.94	0.380	0.258	18.94
40	282	0.780	33.17	17.02	0.374	0.267	18.92
45	313	0.778	35.28	16.63	0.361	0.273	19.07
50	345	0.716	41.37	16.33	0.346	0.285	18.99
55	377	0.698	43.03	16.34	0.334	0.297	18.99
60	408	0.649	48.58	15.61	0.303	0.288	19.08
65	440	0.609	51.27	15.66	0.297	0.301	19.08
70	474	0.578	56.68	15.64	0.279	0.303	19.09

Fig. 7   Lateral distribution of velocity defect at different longitudinal positions. The uncertainty of the longitudinal velocity measurement essential for calculating the velocity defect is 1.2 percent.

for other longitudinal locations are similar to those plotted in Fig. 6. The velocity distribution in Fig. 6 is asymmetric with respect to the wake center with a higher value on the positive side of ξ_2. This asymmetric behavior is a result of the existing lateral pressure gradient, which the curvature generates. Note that, because of the lack of the lateral pressure gradient, the velocity distributions within straight channels at zero or positive streamwise pressure gradient are fully symmetric (see Eifler, 1975 and Gartshore, 1967). The wake velocity defect decreases and the wake width increases with downstream location. A close examination of the velocity data points outside the wake for the initial three longitudinal locations reveals a nonuniform decrease in potential velocity across the channel. This nonuniform decrease in potential velocity across the channel, which is due to the turning of flow from a straight section to the curved channel, occurs up to the longitudinal location $\xi_1/d = 96$.

Figure 7 shows the lateral distribution of the nondimensional mean velocity defect for different longitudinal locations. The mean velocity defect is normalized by its maximum value and the lateral distance by the wake width b. The purpose for normalizing the lateral distance with length scale b and the velocity defect with velocity scale $\bar{U}_{1m}$ is to check the existence of simi-

larity for mean velocity defect profiles. Figure 7 confirms the existence of similarity for mean velocity defect profiles. The solid line represents the results for the curved channel wake at zero streamwise pressure gradient by Schobeiri et al. (1994) and straight channel wake by Eifler (1975) given by the function φ_1. The mean velocity defect profiles are symmetric and almost identical to the straight wake except that they are slightly wider on the inner side of the wake (concave side of the trajectory of wake centerline, i.e., $\xi_2 > 0$) at higher longitudinal locations. Overall, it may be considered that the effect of curvature on mean velocity defect distribution is small.

Figure 8 shows the lateral distribution of the nondimensionalized lateral velocity component $\bar{V}/\bar{U}_{1m}$ for various longitudinal locations. The lateral distribution at the first measurement location shown in Figure 8 is similar to the straight wake results, where the distribution is slightly asymmetric with a minimum at $\zeta > 0$, a maximum at $\zeta < 0$ and zero lateral velocity at the center. The $\bar{V}/\bar{U}_{1m}$ distribution for straight wake approaches zero at the edges. The lateral velocity distribution shown for other locations can be considered as a superposition of the distribution at zero streamwise pressure gradient straight wake on a normalized hypothetical potential distribution of lateral component of velocity. The profile of the hypothetical potential distribution of $\bar{V}$ is dictated by the longitudinal pressure gradient and streamline curvature. The hypothetical potential velocity distribution of $\bar{V}$ in the wake region is almost linear with a positive slope up to a longitudinal location $\xi_1/d = 400$. The hypothetical potential velocity distribution at the last two measurement locations in Fig. 8 deviate from other locations. This deviation is attributed to the effect of boundary layer growth on the concave, convex and the side walls. For the longitudinal locations $\xi_1/d > 400$, this boundary layer growth influences the hypothetical potential velocity distribution and affects the two-dimensionality of the wake flow as previously indicated.

Reynolds Stresses.   Figures 9–11 show the lateral distributions of the nondimensionalized Reynolds stresses. The Reynolds normal stresses are normalized with respect to their values at the wake center. These values are given in Table 1. The normalized Reynolds stress component in the longitudinal direction is shown in Fig. 9. Similar to the straight and curved wakes with zero streamwise pressure gradient (Eifler, 1975; Schobeiri
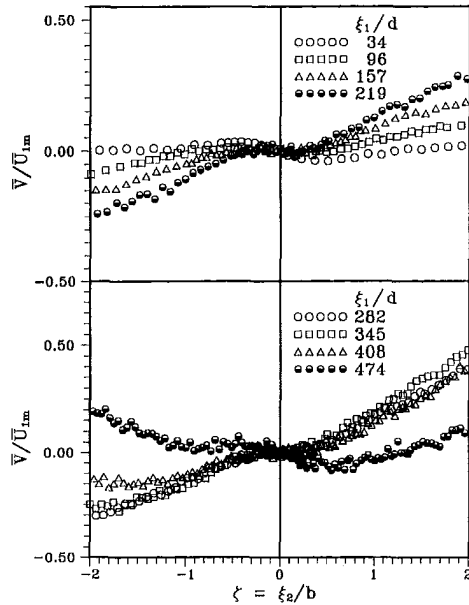

Fig. 6   Lateral distribution of longitudinal component of velocity with an uncertainty of 1.2 percent at different longitudinal positions

Fig. 8 Lateral distribution of lateral velocity component with an uncertainty of 3.0 percent at different longitudinal positions

Fig. 10 Lateral distribution of lateral component of Reynolds normal stress at different longitudinal positions. The measurement uncertainty of the lateral velocity component essential for calculating the lateral component of Reynolds normal stress is 3.0 percent.

et al., 1994), the experimental results for different ξ_1/d shown in Fig. 9 collapse together. This confirms the hypothesis of Prandtl (1942) concerning the local dependency and longitudinal similarity of the turbulence quantities. For the above mentioned zero streamwise pressure gradient cases, it was shown (Schobeiri et al., 1994; Eifler, 1975) that the nondimensionalized Reynolds normal stress components are functions of ζ and R only resulting in functional relationships that describe $\overline{u^2}/y_0^2 = f_1(R, \zeta)\varphi_1$ and $\overline{v^2}/v_0^2 = f_2(R, \zeta)\varphi_1$. In comparison with the straight wake data, the present results exhibit an asymmetric feature due to the curvature of the wake path previously discussed. For straight wakes with zero or positive streamwise pressure gradient (Eifler, 1975; Gartshore, 1967), the longitudinal component of Reynolds stress is symmetric with respect to

the wake center with a maximum on each side of the wake center and with a minimum at the wake center. The asymmetry of the Reynolds stresses in the present data are due to the asymmetric velocity distribution of $\overline{U}$ as a result of the existing lateral pressure gradient that is generated by the curvature. The turbulence in a curved shear flow is suppressed if there is a positive velocity gradient in the positive radial direction. On the other hand, a negative velocity gradient in the radial direction promotes the turbulence. For the measurements at all longitudinal locations, the gradient of longitudinal velocity in the positive radial direction is negative on the inner half of the wake. As opposed to this, the gradient of longitudinal velocity in the
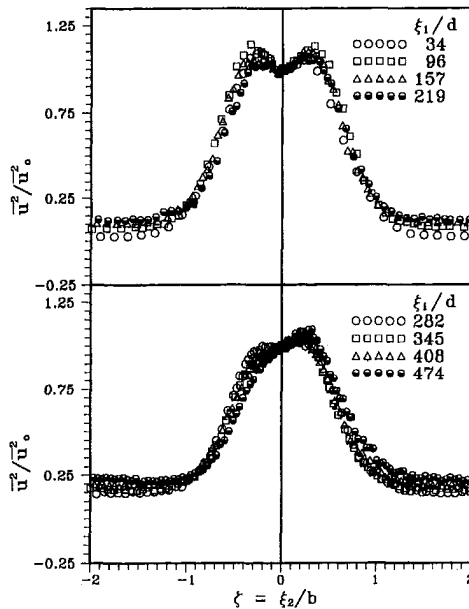

Fig. 9 Lateral distribution of longitudinal component of Reynolds normal stress at different longitudinal positions. The uncertainty of the longitudinal velocity measurement essential for calculating the longitudinal component of Reynolds normal stress is 1.2 percent.

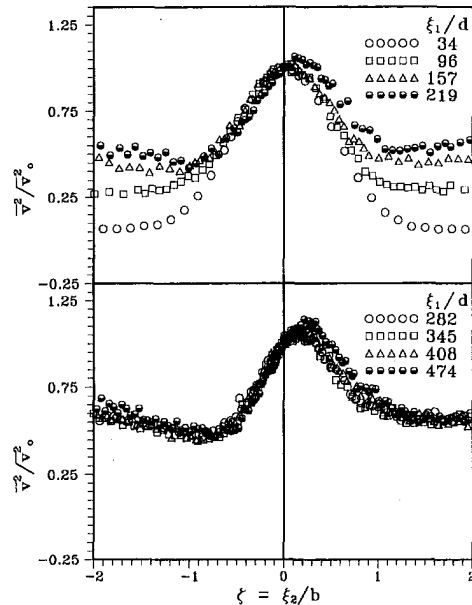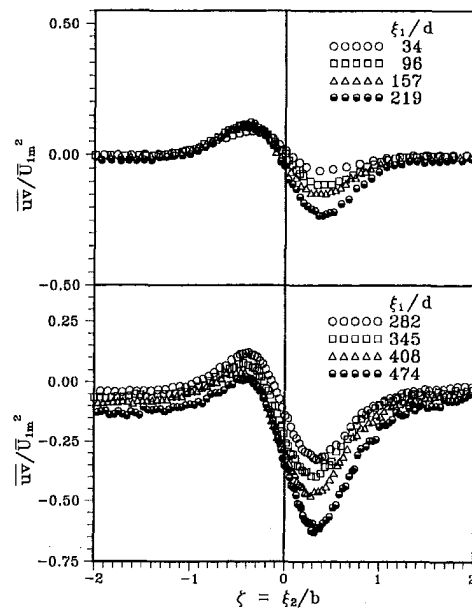**Fig. 11 Lateral distribution of Reynolds shear stress at different longitudinal positions. The uncertainties of the longitudinal and lateral velocity component measurements essential for calculating the Reynolds shear stress component are 1.2 and 3.0 percent.**

positive radial direction is positive in the outer half (convex side of the trajectory of the wake centerline, i.e., $\xi_2 < 0$) of the wake. Therefore, the turbulent stresses should be higher on the inner half of the wake than the outer half of the wake. This is the case for all measurement locations except for the first two measurement locations. The asymmetric nature of the longitudinal component of Reynolds stress is qualitatively similar to the results obtained by Koyama (1983) and Nakayama (1987). Note that the asymmetry of the longitudinal component of Reynolds stress increases with the downstream location. The deviationary behavior in the asymmetric nature of the turbulent stresses at the first two measurement locations may be due to the existence of varying longitudinal pressure gradients across the channel as the flow enters the curved channel from the straight section.

The lateral distribution of the lateral component of Reynolds stress is plotted in Fig. 10. Similar to the longitudinal component, the maximum value of lateral component of Reynolds stress occurs at the inner half of the wake. The asymmetry of the lateral component of Reynolds stress is more than the longitudinal component. In other words, the lateral component of Reynolds normal stress exhibits more distortion from the symmetrical straight wake results.

The lateral distribution of Reynolds shear stress at various longitudinal locations is plotted in Fig. 11. The Reynolds shear stress is nondimensionalized by the square of the maximum velocity defect. The Reynolds shear stress distribution shows the strong asymmetry due to the curvature. The nature of curvature of the wake centerline and the gradient of longitudinal velocity suggest a higher value of Reynolds shear stress on the inner half of the wake. This is observed at every longitudinal location except for the very first two measurement locations, where, as explained before, the pressure gradient dominates over the curvature effect. It appears that the Reynolds shear stress distribution in the outer half of the wake is closer to a self preservation state than the inner half of the wake. The Reynolds shear stress at the center of the wake is not zero, although the lateral gradient of longitudinal velocity is zero at the wake center. Raj and Lakshminarayana (1973) also observed nonzero value of Reynolds shear stress at the wake center. Recent theoretical and experimental investigations by Schobeiri et al. (1994) revealed similar behavior for the Reynolds shear stress at the center of a curved wake at a zero streamwise pressure gradient. Their theoretical results based on the transformed conservation equations of continuity and motion show that for a wake flow with a given curvature, the shear stress values at the wake center as well as at the edges are always different from zero. The shear stress may assume zero values at these lateral locations only if the radius of curvature approaches infinity, which results in straight wake flow.

An overall comparison of the Reynolds shear stress for the wake development in the curved channel at zero and positive longitudinal pressure gradients can be made by plotting the maximum and minimum values of Reynolds shear stress as function of downstream distance as shown in Fig. 12. The symbol $\overline{uv}_m$ stands for a maximum value of Reynolds shear stress at the outer half of the wake and minimum value of Reynolds shear stress at the inner half of the wake. The maximum and minimum values of Reynolds shear stress nondimensionalized with the square of the average velocity upstream of the wake generating cylinder is shown in Fig. 12(a). Figure 12(b) shows the maximum and minimum values of Reynolds shear stress normalized with the square of the maximum velocity defect. The filled symbols represent the maximum value of Reynolds shear stress that occurs at the outer half of the wake and the open symbols represent the minimum value of Reynolds shear that occurs at the inner half of the wake. For a straight wake, the absolute value of maximum and minimum Reynolds shear stress should be the same. Figure 12 shows that the absolute
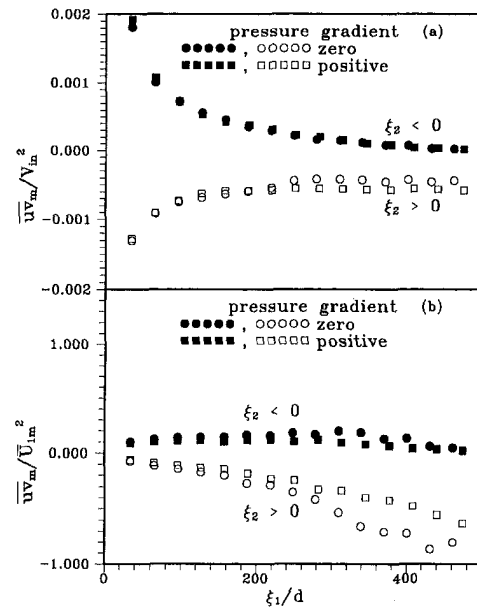
Fig. 12 Longitudinal variation of the maximum value of Reynolds shear stress at zero and positive pressure longitudinal pressure gradients. The uncertainties of the longitudinal and lateral velocity component measurements essential for calculating the Reynolds shear stress component are 1.2 and 3.0 percent.

value of the minimum Reynolds shear stress occurring at the inner half of the wake is higher than the maximum value of Reynolds shear stress occurring at the outer half of the wake, except for the initial two measurement locations. In the outer wake, as shown in Fig. 12(a), the maximum value of the Reynolds shear stress nondimensionalized with the averaged inlet velocity has almost the same value for the longitudinal locations plotted in Fig. 12(a) for both pressure gradients. In the inner half of the wake, the absolute value of minimum Reynolds shear stress nondimensionalized with the square of average velocity decreases with downstream location at a higher rate for zero streamwise pressure gradient than for positive pressure gradient. Figure 12(b) shows that the absolute value of Reynolds shear stress normalized with the square of maximum velocity defect increases with downstream location. This is the case for both the inner and outer halves of the wake except for the outer half of the wake at the last five downstream locations where the normalized Reynolds shear stress decreases slightly. At a particular longitudinal location, the absolute value of normalized shear stress has a higher value for zero streamwise pressure gradient than for positive pressure gradient. This is similar to the results obtained by Gartshore (1967) for a straight wake subjected to adverse pressure gradient where he observed a lower value of normalized Reynolds shear stress compared to the value of normalized Reynolds shear stress for a zero streamwise pressure gradient straight wake.

5 Conclusions

The wake development behind a stationary cylinder in a curved channel at positive longitudinal pressure gradients is experimentally investigated. The results of the investigation revealed the following aspects of the influence of streamline curvature and longitudinal pressure gradient on the development of wakes. 1.) Comparison of the wake development in the curved channel between zero and positive longitudinal pressure gradients shows that the decay of the non-dimensionalized velocity defect is faster at zero streamwise pressure gradient than at a positive pressure gradient. Conversely, the growth of the wake width is slightly faster at positive pressure gradient than at a

zero streamwise pressure gradient. 2.) The product $\bar{U}_{1m}b$ as a function of longitudinal location, while being approximately constant at zero streamwise pressure gradient, increases at positive pressure gradient. 3.) Even though the longitudinal component of mean velocity is asymmetric with respect to the wake center, the mean velocity defect profiles in similarity coordinates are almost symmetric and follow the Gaussian function for straight wake data. However, small deviations are observed particularly at far downstream locations and wake edges, where the wake is slightly wider on the inner half. In general, it may be considered that for mild curvature wake with small d/R range of 0.002 to 0.003 as presented in this investigation, the effect of curvature on mean velocity defect distribution is small. 4.) The Reynolds stress distributions in similarity coordinates are strongly influenced by the curvature. Pronounced asymmetric features are observed for all three components of Reynolds stresses measured. The value of longitudinal component of Reynolds stress at the inner half of the wake is higher than the outer half. The asymmetry in lateral component of Reynolds normal stress is higher than the asymmetry in the longitudinal component of Reynolds normal stress. The Reynolds shear stress distribution has higher values at the inner half than outer half. The asymmetry of Reynolds stress distribution increases with downstream location. At a particular longitudinal location, the absolute value of Reynolds shear stress normalized with the square of the maximum velocity defect has a higher value for zero streamwise pressure gradient than for positive pressure gradient.

Acknowledgment

References

Eifler, J., 1975, "Zur Frage der freien turbulenten Strömungen, insbesondere hinter ruheneden und bewegten Zylindern," Diss. D-17, Techische Hochschule Darmstadt, Germany.

Gartshore, Ian S., 1967, "Two-Dimensional Turbulent Wakes," *Journal of Fluid Mechanics*, Vol. 30, part 3, pp. 547–560.

Hill, P. G., Schaub, U. W., Senoo, Y., 1963, "Turbulent Wakes in Pressure Gradients," ASME *Journal of Applied Mechanics*, pp. 518–524.

John, J., and Schobeiri, T., 1993, "A Simple and Accurate Method of Calibrating X-Probes," ASME JOURNAL OF FLUIDS ENGINEERING, Vol. 115, pp. 148–152.

John, J., 1993, "A Study of the Development of Steady and Periodic Unsteady Turbulent Wakes through Curved Channels at Positive, Zero, and Negative Streamwise Pressure Gradients," Dissertation, Texas A&M, Dec.

Koyama, H., 1983, "Effect of Streamline Curvature on Laminar and Turbulent Wakes," *Proc. of Fourth Symp. on Turbulent Shear Flows*, University of Karlsruhe, Karlsruhe, Germany, pp. 141–155.

Margolis, D. P., Lumley, J. L., 1965, "Curved Turbulent Mixing Layer," *The Physics of Fluids*, Vol. 8, No. 10, pp. 1775–1784.

Nakayama, A., 1987, "Curvature and Pressure-Gradient Effects on a Small-Defect Wake," *Journal of Fluid Mechanics*, Vol. 175, pp. 215–246.

Pfeil, H., and Eifler, J., 1975a, "Zur Frage der Schubspannungsverteilung für die ebenen freien turbulenten Strömungen," *Forschung im Ingenieurwesen*, Vol. 41, Nr. 4, pp. 105–112.

Pfeil, H., and Eifler, J., 1975b, "Messungen im turbulenten Nachlauf des Einzelzylinders," *Forschung im Ingenieurwesen*, Vol. 41, Nr. 5, pp. 137–145.

Prandtl, L., 1942, "Bemerkungen zur Theorie der freien Turbulenz," *Zeitschrift für angewandte Mathematik und Mechanik (ZAMM)*, Vol. 22, Nr. 5, pp. 241–254.

Raj, R., and Lakshminarayana, B., 1973, "Characteristics of the Wake behind a Cascade of Airfoils," *Journal of Fluid Mechanics*, Vol. 81, part 4, pp. 707–730.

Reichardt, H., 1950, "Gesetzmäßigkeiten der freien Turbulenz," *VDI-Forschungsheft*, 414.

Savill, A. M., 1983, "The Turbulent Structure of a Highly Curved Two-Dimensional Wake," *Structure of Complex Turbulent Shear Flow, IUTAM Symposium 1982*, R. Dumas and L. Fulachier, eds., Springer, New York, pp. 185–197.

Schlichting, H., 1930, "Über das ebene Windschattenproblem," Dissertation Göttingen, *Ingeniuer-Archiv 1*, pp. 537–571.

Schobeiri, T., Pardivala, D., 1992, "Establishment of a Research Facility for Investigating the Effects of Periodic Unsteady Inlet Flow, Pressure Gradient and Curvature on Boundary Layer Transition, Wake Development And Heat Transfer," *Rotating Machinery Transport Phenomenon*, Hemisphere Publishing, Washington D.C.

Schobeiri, M. T., John, J., K., Pappu, 1994, "Theoretical and Experimental Investigations of Two-Dimensional Wakes within a Curved Channel," ASME Paper No. 94-GT-367 and to appear in the ASME *Journal of Turbomachinery*.

Townsend, A. A., 1947, "Measurements in the Turbulent Wake of a Cylinder," *Proc. Roy. Soc. Lond.*, Series A190, pp. 551–561.

Townsend, A. A., 1949a, "Momentum and Energy Diffusion in the Turbulent Wake of a Cylinder," *Proc. Roy. Soc. Lond.*, A197, pp. 124–140.

Townsend, A. A., 1949b, "The Fully Developed Turbulent Wake of a Circular Cylinder," *Aust. J. Sci. Res.*, Vol. 2, pp. 451–468.

Wattendorf, F. L., 1935, "A Study of the Effect of Curvature on Fully Developed Turbulent Flow," *Proc. Roy. Soc. Lond.*, Vol. 148, pp. 565–598.

The Turbulent Incompressible Jet in a Curved Coflow

M. V. Ötügen
Associate Professor.

F. Girlea
Graduate Assistant.

P. M. Sforza
Professor.

Polytechnic University,
Mechanical, Aerospace and Manufacturing
Engineering,
Six Metrotech Center,
Brooklyn, NY 11201

The effects of small streamline curvature on the growth and axial flow development of a turbulent incompressible jet in a curved coflow was investigated experimentally. The jet streamline curvature was achieved by introducing the initially round jet tangentially into a stream flowing through a curved channel of square cross-section. The jet issued from a straight pipe and had a fully developed velocity profile at the exit plane. The jet Reynolds number and the coflow-to-jet-velocity ratio were 4300 and 0.11, respectively. A single component laser Doppler anemometer was used to measure the streamwise velocity. Axial mean velocity and turbulence intensity profiles were measured at various streamwise locations in both the plane of curvature and the surface perpendicular to the plane of curvature. The results indicate that the jet growth and turbulence intensity are influenced by the small streamline curvature. The growth rate of the curved jet in the plane of curvature is slightly increased compared to that of a straight jet. However, the growth of the same curved jet is suppressed in the plane perpendicular to the plane of curvature. In the plane of curvature, the inner jet half-width is larger than the outer jet half-width. The mean velocity profiles in this plane are nearly Gaussian when the lateral distance is normalized by the respective inner and outer side jet half-widths. The axial turbulence intensity profiles show asymmetry in the plane of curvature with a pronounced peak on the outer side of the jet.

Introduction

Although turbulent flows have been studied for a long time, little attention has been paid to turbulent curved flows with three-dimensional influences compared to that directed toward shear flows with negligible or no streamline curvature. It is known that an inviscid instability arises in a turbulent flow where the angular momentum decreases away from the center of curvature. This instability, which is brought on by the centrifugal force gradient in the primary strain rate direction, is expected to increase turbulent stress levels and three-dimensional effects (So, 1975). On the other hand, when the angular momentum increases away from the center of curvature, the flow experiences a stabilizing effect and turbulent stress levels and three-dimensional effects are expected to be suppressed. Indeed, earlier studies of curved boundary layers showed that turbulence is suppressed in a boundary layer over a convex curvature (So and Mellor, 1973) and enhanced when the boundary layer is subjected to a concave curvature (So and Mellor, 1975). A review of streamline curvature effects on turbulent flow structure is provided by Bradshaw (1973).

In the case of free shear flows with streamline curvature, mixing layers have received the bulk of the attention (Rapp and Margolis, 1967; Wyngaard et al., 1967; Castro and Bradshaw, 1976). These studies showed that the mixing layer is stable when the velocity gradient is positive in the radial outward direction, and conversely, it is unstable when this gradient is negative. Through these studies it was also observed that the initially two-dimensional shear layer becomes three-dimensional when subjected to destabilizing streamline curvature. This behavior is attributed to the development of an instability-driven secondary flow structure.

The structure of turbulent jets with streamline curvature is intrinsically more complex. While mixing layers have their turbulence either augmented or suppressed, depending on the sign of the velocity gradient in the primary strain rate direction, turbulent jets possess both turbulence-augmented and turbulence-suppressed regions simultaneously. The outer side of the jet is subjected to unstable angular momentum stratification, while the inner side of the jet experiences a stable angular momentum stratification. Most previous investigations of curvature effects in jets were performed either by placing a jet in a cross-flow (Hanui and Ramaprian, 1989) or by injecting it into a large cavity in order to obtain streamline curvature (Masuda and Maeda, 1986, Masuda and Andoh, 1989). These studies indicate that in the initial jet region, while the mean axial velocity profiles remain symmetric, the fluctuating velocity and Reynolds shear stress show strong asymmetry, pointing to an altered turbulent transport process. In the initially developing region of a plane jet, the ratio of unstable-side maximum Reynolds stress to stable-side maximum Reynolds stress grows rapidly with increasing axial distance and reaches the value of 2 by ten nozzle widths from the exit plane.

In the curved wake, the stable and the unstable sides of the shear layer are interchanged; the inner side of the wake is unstable and the outer side is stable. A study of the effects of streamline curvature on the three-dimensional structure of a plane wake has been conducted by Weygandt and Mehta (1993). The effects of curvature were most apparent in the Reynolds stress results, especially those for the primary shear stress. The distributions of both the turbulent kinetic energy and shear stress are affected by curvature. The peak levels of the turbulent shear stress were increased on the unstable side and decreased on the stable side, compared to those in a straight wake. Streamline curvature also produced a larger wake growth rate. Ramjee and Neelakandan (1989) investigated the two-dimensional wake of a rectangular cylinder in a curved stream. Their results indicate that the streamline curvature affects the turbulence field of the wake quite significantly, with the strongest effects on the far field Reynolds shear stress distribution.

The present investigation aims to study the structure of a turbulent jet subjected to a small streamline curvature. The geometry of the flow is different than those of the previous curved jet investigations discussed above. In this study an initially round turbulent jet with a fully developed turbulent pipe flow
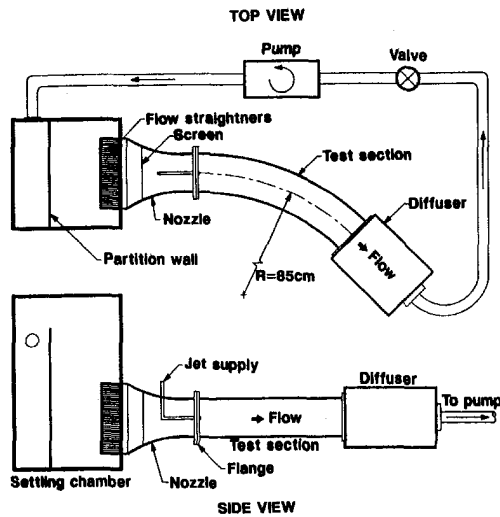
TOP VIEW

SIDE VIEW

Fig. 1 Schematic diagram of the water tunnel facility

velocity profile is injected tangentially into a co-flowing stream in a curved rectangular duct. With co-flow-to-jet velocity ratio of 0.11, the jet trajectory does not exactly follow the test channel curvature, but undergoes an even milder streamline curvature. By its nature, the jet contains both the stable inner side and the unstable outer side. In selecting this three-dimensional geometry, emphasis is placed on elimination of wall effects, and of the pressure gradients of a jet in a crossflow, so that the jet is influenced by the streamline curvature alone.

Experimental Facility and Procedure

The facility consisted of a closed-return low speed water tunnel, a jet injection system, a laser Doppler velocimeter (LDV) system with a seed generator, and a traversing mechanism for the optical system. A schematic diagram of the water tunnel and the jet assembly are shown in Fig. 1. The pump was placed as far as possible from the diffuser (3 m) to minimize the propagation of possible pressure fluctuations into the test section. The settling chamber, with dimensions of 0.61 × 0.61 × 1.13 m, was divided into two regions by a vertical partition wall whose purpose was to prevent large scale turbulent motion from propagating into the test section. The flow returning from the pump outlet was introduced in the small region of the settling tank just below the water level. Water was allowed to gently spill from this region over the partition wall into the large section of the settling tank. The converging nozzle before

the test section was 0.48 m long with a contraction ratio of 4.5. The flow straighteners at the inlet of the nozzle were sandwiched between two fine wire square mesh screens. Another fine wire screen was placed 0.10 m downstream of the nozzle inlet. The turbulence intensity in the test section was measured to be 2 percent at a Reynolds number of 23,000 based on the hydraulic diameter of the test section.

The curved test section had a square cross-section of 0.16 × 0.16 m. The test channel center line had a radius of curvature of 0.85 m and an arc length of 57 degrees. Mean velocity at the test section inlet was 0.15 m/s. The Reynolds and Dean numbers characterizing the free stream in this investigation were Re_o = 23,000 and De = 1,000, respectively. The jet was injected into the test section through a 3.175 mm diameter stainless steel tube, which was introduced from the top wall of the nozzle approximately 15 cm upstream of the test section inlet. The tube was bent 90 degrees at the test section centerline, thus bringing it parallel to the direction of the mean flow. From the point of the bend the tube extended 16 cm, thus positioning the exit plane of the jet approximately 1 cm downstream of the test section inlet. This arrangement made the initial trajectory of the jet tangent to the test section centerline. An air-pressurized cylinder was used to control the jet so that precise adjustments of the jet flow rate could be made. The loss of water volume in the cylinder, and thus the hydrostatic head, was compensated for by continuously adding water into this cylinder via a variable mass flow valve. The additional mass introduced into the closed-loop water tunnel by the jet was removed through a tube exiting from one side of the settling chamber and a mass flow meter. Throughout the study, the variation of the jet and coflow mean and turbulent velocity measured by the LDV system was within ±0.3 percent.

The single-component LDV system was configured to operate in the backscatter mode and was powered by a 15 mW Helium-Neon laser at the 632.8 nm line. The measuring volume formed by the crossing of the two beams was aligned with the local streamline direction to measure the streamwise component of velocity. The ellipsoid LDV probe volume had a diameter of 0.13 mm and an effective length of 0.6 mm. Silicon carbide particles with a nominal diameter of 14 μm were used to seed the jet and the co-flow fluids. A 5 μm filter was used to remove contaminant particles in the water supply for both the jet and the co-flow before introducing the seed material. A TSI model 1980 B counter was used to process the signal output from the photo-multiplier tube. Before being timed by the counter, the Doppler bursts were conditioned by high-pass and low-pass filtering at corner frequencies of 600 kHz and 30 kHz, respectively. Eight cycles of the Doppler burst were used to determine its frequency and only those bursts which passed the 1 percent

---

Nomenclature

b_y = jet half-width in the plane of curvature

b_z = jet half-width in the normal plane

d = jet diameter at exit

D = hydraulic diameter of test channel

D_e = Dean number ($= (U_0 h/v)(h/R_i)^{1/2}$)

h = test channel width

r = jet radius at exit

R_{av} = jet average radius of curvature

R_c = test channel center line radius of curvature

R_i = test channel inner wall radius of curvature

Re_j = jet Reynolds number ($= U_{av}d/v$) .

Re_o = coflow Reynolds number ($= U_0 D/v$)

U = mean velocity component in the x (streamwise) direction

U_m = maximum mean velocity in x direction

U_j = maximum jet velocity at exit

U_{av} = average jet velocity at exit

U_o = coflow mean velocity at test section entrance

U^* = nondimensional velocity ($= (U - U_o)/(U_m - U_o)$)

u' = fluctuating velocity component in the streamwise direction

u'_m = maximum fluctuating velocity component

u'_o = coflow fluctuating velocity at test section entrance

δ = radial location of maximum velocity measured from test channel centerline

v = dynamic viscosity

x = local streamwise coordinate for jet ($= (R_c + \delta)\phi$)

y = local radial coordinate for jet

z = local coordinate for jet normal to x and y

X, Y = rectangular coordinates measured from the center of curvature of test channel

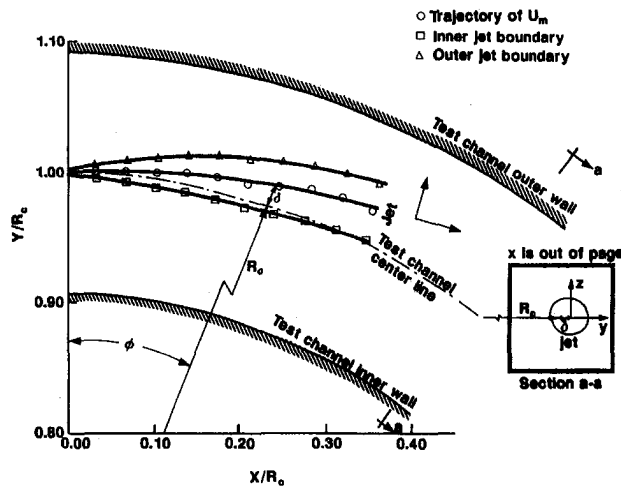ϕ = polar coordinate measured from jet exit

---

Fig. 2 Jet trajectory and coordinate system

comparison test (8 cycle-to-4 cycle frequency comparison) were validated. To prevent velocity biasing, the analog output of the counter was used for data acquisition. The analog output of the counter was digitized by a 12-bit 8-channel analog-to-digital converter. In the experiments, the validated burst rates were over an order of magnitude higher than the data acquisition rate. An IBM AT-type (Intel 80286-based microprocessor) personal computer controlled the data acquisition. Data was acquired at a rate of 65 samples per second. The sample record length was determined by an analysis of its effect on the mean and rms velocity values. Based on this analysis, 11,700 samples were obtained per point which translates into approximately 180 seconds of sampling time. The LDV system was placed on an aluminum traverse table in an arrangement which allowed the probe to be positioned in three-dimensional space at any point inside the test section. The positioning accuracy of the traverse system is ±0.5 mm in the x direction and ±0.05 mm in y and z directions.

The uncertainty in the measurement of U and u' were estimated to be within 3 and 4 percent, respectively. The corresponding uncertainty in the determination of the jet half-width, b, was less than 8 percent. The uncertainty in the measurements was obtained taking into account the various potential sources of error including the positioning accuracy of the optical traverse system and the inherent precision limit of the LDV system. In the uncertainty estimate of u', additional potential errors due to the finite probe length, electronic noise and the bit resolution of the analog-to-digital converter were also taken into account.

Results and Discussion

The average jet exit and the uniform co-flow velocities were 1.35 m/s and 0.15 m/s, respectively. The velocity profile at the exit plane is that of a fully developed pipe flow. The streamwise distance, x/d, in terms of the angle, ϕ, was chosen as (see Fig. 2)

$$\frac{x}{d} = \frac{(R_c + \delta)\phi}{d} \tag{1}$$

This definition was used to better account for the actual trajectory of the jet with respect to the channel centerline. The local coordinates in the x, z surface were determined by the values of $R_c + \delta$ corresponding to a particular streamwise position. Therefore, the x, z surface was located at a radial distance where the velocity in the x, y plane attained a maximum value (Fig. 2). Both y and z locations were referenced from the point of maximum mean velocity in the x direction. Negative y and z

correspond to locations in the inner curvature and lower regions of the jet, respectively.

The jet exit mean and rms velocity profiles in both the x, y and x, z planes and passing through the duct centerline are shown in Fig. 3. At $x/d = 1$, it is observed that the mean velocity profiles in the two planes are essentially coincident indicating that the jet in the initial stage is axisymmetric. Close to the edge of the jet the nondimensional mean velocity assumes a small negative value indicating a drop in the local velocity to a level below that of the coflow. This is due to the wake developing downstream of the wall of the tube from which the jet emerges. The maximum mean velocity at the exit was $U_j = 1.7$ m/s. From the profiles, the average (bulk) velocity at jet exit is calculated to be 1.35 m/s. The turbulence intensities reach their maximum value (approximately 14 percent) away from the jet axis. These maxima occur roughly around the location of maximum mean shear.

Jet Trajectory. Figure 2 shows the jet trajectory in the plane of curvature (x, y plane) up to $x/d = 97.5$. This schematic represents the physical location of the time averaged jet in the test section and is obtained by superimposing the jet on the geometry of the test channel. Here, the jet boundary is represented by the symbols and is defined as the location where the local excess velocity becomes 10% of the maximum value for a given profile. The solid lines are drawn through the data as a visual aid. Throughout the study, the trajectory of the maximum mean velocity, U_m, is taken to be the centerline of the jet. The global coordinate system X, Y was non-dimensionalized with respect to the test channel center line radius of curvature, R_c. The jet centerline does not follow the exact curvature of the test channel, but exhibits a milder curvature. This was expected based on initial flow visualizations using a dye tracer. The visualizations showed that it was not possible to achieve a jet trajectory which completely follows the test channel curvature and at the same time maintain an initial jet Reynolds number high enough to ensure a near equilibrium free turbulent jet flow. The mean radius of curvature of the jet, R_{av}, was determined by fitting a circle to the data points in Fig. 2 which results in the following expression:

$$\frac{R_{av}}{R_c} = \frac{1 - Y_j/R_c}{2 \sin^2 \alpha_j} = \frac{(X_j/R_c)^2}{2(1 - Y/R_c) \cos^2 \alpha_j} \tag{2}$$

Here, X_j and Y_j denote the location of the jet axis in the coordinate system shown while α_j is defined by the following equation:
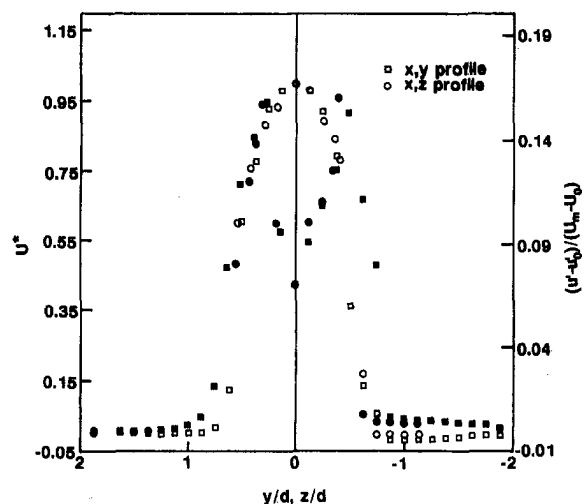

Fig. 3 Mean velocity and turbulence intensity profiles at $x/d = 1$ (solid symbols represent turbulence intensity)
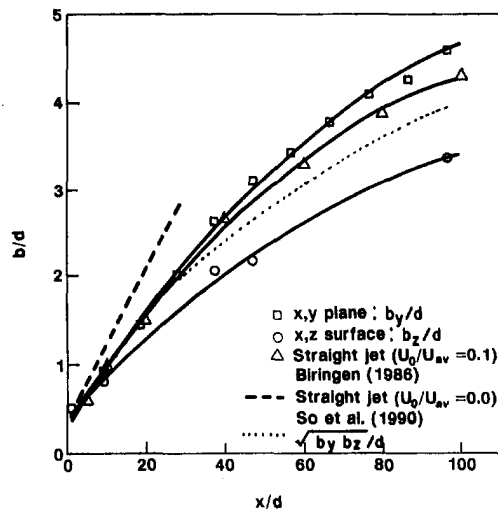
Fig. 4   Jet half-widths

$$\alpha_j = \tan^{-1}\left(\frac{1 - Y_j/R_c}{X_j/R_c}\right) \tag{3}$$

Using the first and the last points along the jet axis yields $R_{av}/R_c = 2$ which again illustrates the inability of the jet to completely follow the outer stream direction. Since the test section centerline curvature is $R_c = 0.85$ m and the jet diameter $d = 3.175$ mm, the ratio $d/R_{av} = 1.87 \times 10^{-3}$, indicating a modest curvature for the turbulent jet.

Jet Growth Rate. The growth of the jet with downstream distance in both the x, y, and the x, z planes is presented in Fig. 4. Here, b_y is the average value (inner and outer side) of the jet half-width in the plane of curvature and b_z is that in the surface normal to the plane of curvature. The jet half-width is defined as the distance from jet centerline to the point where the mean excess velocity is equal to 0.5 $(U_m - U_o)$. The solid lines in Fig 4 are drawn through the data points as a visual aid. The growth of the present jet half-width in both planes is compared to the growth of two circular straight jets; one with no co-flow (So et al., 1990) and the other in a coflowing stream (Biringen, 1986). Biringen reports a coflow-to-jet exit velocity ratio of $U_o/U_{av} = 0.1$ for his study, which closely matches the present value of $U_o/U_{av} = 0.11$. This close correspondence allows the comparison of the structure of the two jets without significant concern of velocity ratio effects. So and Huang (1989) show that the effect of coflow-to jet velocity ratio on jet growth is substantial only when that ratio is small. Their results indicate that traversing from a ratio of 10 to 11 percent incurs only a small (less than 3 percent) reduction in jet spreading rate. Therefore, using Biringen's (1986) straight jet results in Fig 5 as a comparison case by which to assess curvature effects seems reasonable. Note that the average growth of the curved jet as given by $\sqrt{b_y b_z}/d$, is slightly smaller compared to the growth, b/d, of the straight jet which could be attributed to the difference in the coflow-to-jet velocity ratio.

The nonlinear growth rate is characteristic of all coflowing jets. Furthermore, it has also been observed that, with a fixed set of initial conditions, the growth rate of the co-flowing straight jet decreases with increasing U_o/U_{av} (Maczynski, 1961; Antonia and Bilger, 1973; Biringen, 1986). This change in the growth rate is generally attributed to the annular shear layer instability modes in the initial jet region. These modes are sensitive to the velocity ratio and in turn can have a significant impact on the far field jet growth and mixing. The experimental data points for the co-flowing jets were fit with a second order polynomial as shown by the solid lines in Fig. 4. The curved

jet grows faster in the x, y plane (i.e., the plane of curvature) than it does in the x, z surface. While the average width, b_y, in the plane of curvature (i.e., the x, y plane) is slightly larger than that of the straight jet of Biringen, the corresponding jet half-width b_z, in the x, z plane, which is normal to the plane of curvature, is significantly suppressed. At $x/d = 97.5$, b_y is approximately 35 percent larger than b_z. This is evidence that at large streamwise distances the time-mean cross-section of the jet is no longer circular. This structural feature of the curved jet was confirmed through laser sheet flow visualizations.

Careful examination of the velocity profiles in the plane of curvature reveals that in addition to the average half-width b_y being larger than its counterpart b_z, it also displays a clear asymmetry between the inner and outer sides for $x/d \ge 50$. The growth of the outer and inner side jet half-widths, $b_{y,o}$ and $b_{y,i}$, respectively, is shown in Fig. 5. Up to $x/d = 50$, the half-widths on either side of the jet in the plane of curvature are nearly equivalent, but beyond that there is a definite difference in their size, with the most substantial difference showing up around $x/d = 70$. This asymmetry strongly suggests that the effects of curvature, which are different on each side of the jet, are responsible for this behavior. In the present case, there is competition between two distinct effects of streamline curvature. First, the enhanced instability (hence increased turbulent momentum transport) on the outer side would tend to cause that side of the jet to grow more rapidly than the corresponding straight jet. Second, the mismatch between the jet curvature and the co-flow curvature results in the development of a secondary flow which tends to retard the growth on the outer side. The converse is true for the inner side of the jet. In this respect, the jet in a curved co-flow acts like a jet inclined at a slight angle to a small crossflow because its momentum permits it to defeat, in part, the guiding effect of the weak coflow. A wake in a curved coflow is swept along, passively by the guiding outer flow. In general then, jets in a curved coflow will be subjected to these competing effects outlined above until the initial jet-to-co-flow velocity ratio falls below unity and a wake-like flow is established. In this respect, the behavior of a round turbulent jet injected into a curved coflow is substantially different than that of a boundary layer with a streamline curvature. The two-dimensional boundary layer is partially guided by the convex
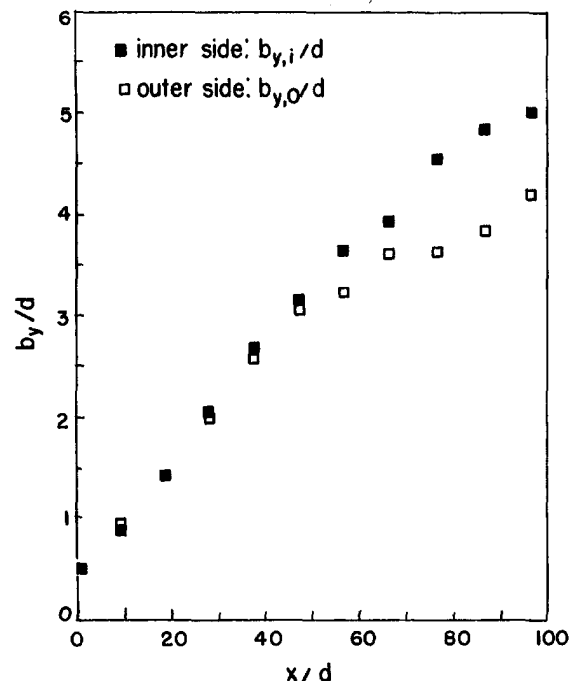

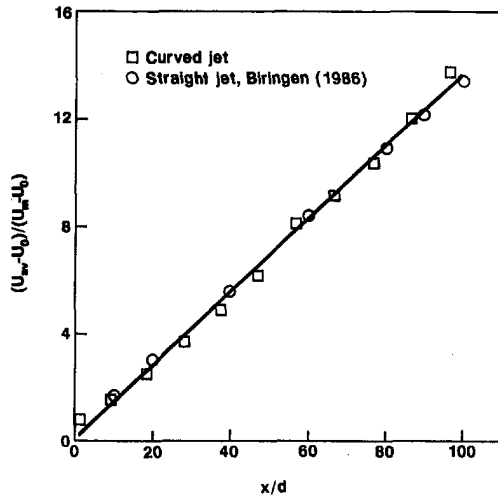**Fig. 5   Inner and outer jet half-widths in the x, y plane**

Fig. 6 Mean centerline excess velocity decay

Fig. 7(a) $x/d < 50$

Fig. 7(b) $x/d > 60$

Fig. 7 Mean velocity profiles in the x, y plane; the solid line is given by Eq. (5)

or concave wall and the exchange of momentum takes place only at its interface with the freestream; thus, the growth of the layer is controlled essentially by turbulent transport. In contrast, the three-dimensional jet in a curved coflow is free to exchange momentum all around its periphery and turbulent transport is not necessarily the dominant mechanism for growth. This partially explains the seemingly contradicting trend of reduced growth rate of the unstable side of the jet when compared to the enhanced pattern of growth observed in a turbulent boundary layer over a concave surface.

Centerline Velocity Decay. The streamwise distribution of the maximum mean (or centerline) velocity, U_m, of the curved jet is shown in Fig. 6 along with the results of the straight jet of Biringen (1986) in a coflow. When normalized using the initial jet excess velocity, the agreement between the decay patterns of ($U_m - U_o$) for the two jets is remarkably good. The solid line is the expression

$$(U_{av} - U_o)/(U_m - U_o) = k(x/d) + k_o \qquad (4)$$

with $k = 0.136$ and $k_o = 0$. For a free jet in a nonmoving environment, the value of k is typically between 0.23 (So et al., 1990) and 0.2 (Wygnanski and Fiedler, 1969). Therefore, the maximum velocity decays at a lower rate in a jet with a coflow as compared to the free jet. On the other hand, the addition of the mild streamline curvature to the co-flowing jet apparently does not otherwise change the center-line velocity decay pattern.

Mean Velocity Profiles. Figure 7 shows the jet mean velocity profiles in the plane of curvature. Here, the mean excess velocity is nondimensionalized with the local maximum velocity excess and the lateral coordinate is normalized with the appropriate jet half-width, $b_{y,i}$ or $b_{y,o}$. This non-dimensionalization is applied because it is considered appropriate to scale each side of the jet by the different growths observed. It is clear that this approach provides a good collapse of the data into a nearly self-preserving form for $U^* > 0.2$. The behavior below that value is neither self-preserving in appearance nor symmetrical. Furthermore, at $x/d \geq 40$, in Fig 7a, there is a clear departure of the data from the Gaussian on the outer side of the jet and this is maintained at larger x/d as seen in Fig. 7(b). As a guide for comparison purposes, the Gaussian profile given by

$$\frac{U - U_o}{U_m - U_o} = \exp[-\ln 2(y/b)^2], \qquad (5)$$

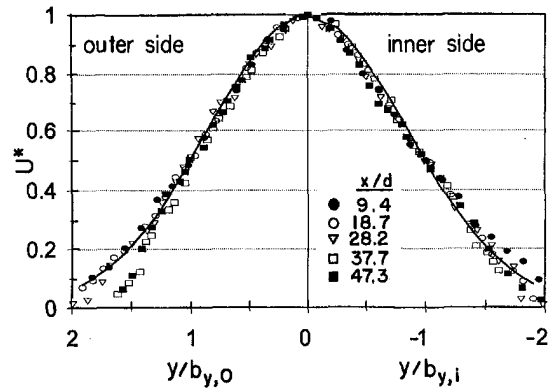where b is $b_{y,o}$ for $y > 0$ and $b_{y,i}$ for $y < 0$, is also shown in Fig. 7.
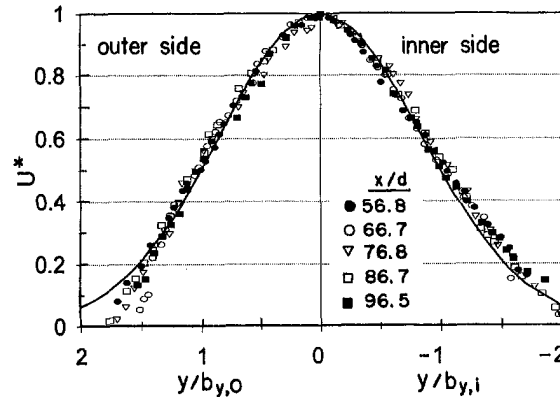
Figure 8 shows the normalized mean excess velocity profiles in the x, z plane. Unlike their x, y plane counterparts, these profiles show a good degree of symmetry about the jet centerline throughout the measurement domain. Also, they collapse well onto one curve indicating that the mean velocity profiles attain a "self-preserving" shape at least in the x, z plane. The same Gaussian curve given by Eq. 5 is repeated here for comparison.

Turbulence Intensity. Turbulence intensity profiles were obtained at several streamwise locations both in the plane of curvature and in the surface normal to it. The profiles in the
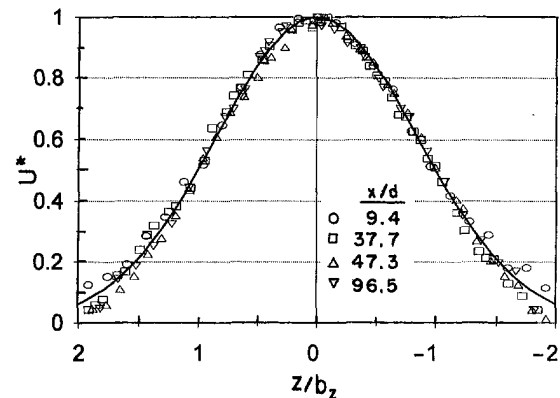

Fig. 8 Mean velocity profiles in the x, z plane; the solid line is given by Eq. (5)

plane of curvature are presented in Fig. 9. An asymmetry is observed in these profiles with significantly higher levels of turbulence on the outer side of the jet. The asymmetry starts to manifest itself at $x/d = 50$, the same location where the velocity profiles in the plane of curvature on the outer side show a marked departure from their previous behavior. This is also the location where the growth in b_y on either side of the jet begins to show asymmetry. By a streamwise location of $x/d \approx 80$ (Fig. 9(b)) the peak intensity has increased more than 30 percent over its maximum at distances $x/d \leq 50$ (Fig. 9(a)). When $x/d = 100$ is reached the turbulence intensity distribution has declined back almost to the original levels. Obviously, there is some enhanced production of turbulence starting around $x/d = 50$ and peaking at about $x/d = 80$, with an apparent relaxation occurring by $x/d = 100$.

As discussed earlier, this behavior is due to the existence of a pair of stability-mismatched sides. For $y > 0$ the gradient of the centrifugal force is negative. This source of instability leads to augmented turbulence. On the other hand, for $y < 0$, the centrifugal force is stably stratified which discourages the exchange of momentum between adjacent layers of fluid. Therefore, on this side of the jet, the turbulence intensities are smaller. The higher turbulence levels in the outer side of the jet can also be attributed to the increasing mean strain rate with streamwise distance. It provides the additional source of turbulence production, and thus higher turbulence intensities. Again, however, the root cause is the inviscid instability in the outer jet. It is this instability which causes the larger velocity gradients occurring on this side of the jet. As to the occurrence of a maximum of outer side turbulence around $x/d = 80$, this could be the due to the continuously changing jet streamline curvature with streamwise distance which most likely becomes too weak to
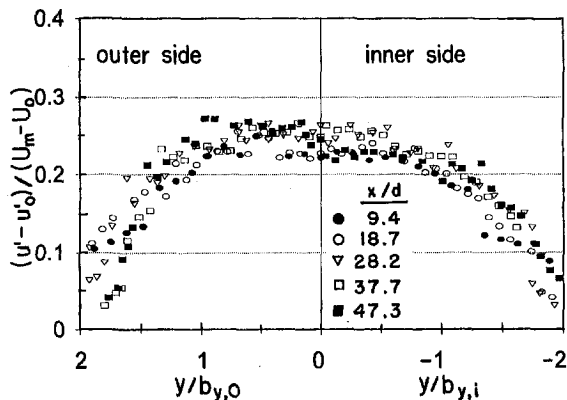

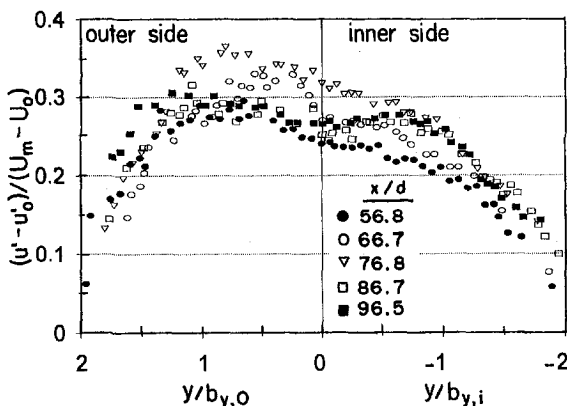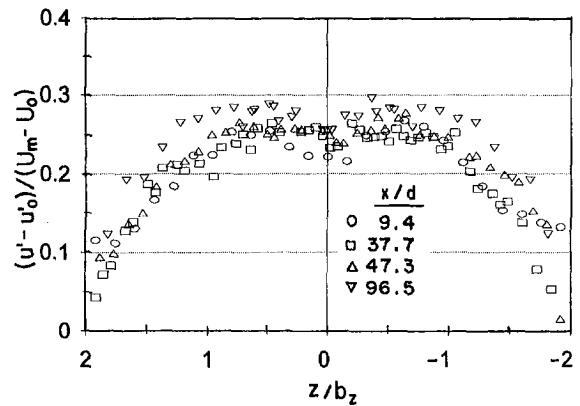Fig. 10 Turbulence intensity profiles in the x, z plane

produce extra strain rate beyond $x/d = 80$, and the turbulence field starts relaxing back to equilibrium levels. In contrast, the turbulence intensity profiles in the x, z surface are nearly symmetric (Fig. 10) and essentially similar in nature to those for straight jets. The turbulence levels remain relatively uniform with streamwise distance and for $x/d > 50$ turbulence in the x, z plane is significantly smaller than that on the plane of curvature.

Conclusions

The structure of an incompressible, curved turbulent jet was experimentally investigated. In order to study the effects of a mild streamline curvature on the flow structure, the jet was introduced parallel into a stream flowing through a curved channel. The jet issued from a straight pipe and had a fully developed velocity profile at the exit. The jet's streamline curvature was milder than that of the coflow. Streamwise velocity measurements were performed using an LDV system. The results indicate that even a mild streamline curvature can alter the global structure of the jet with the strongest effects on the jet growth pattern. The major conclusions can be listed as follows:

(1) The jet grows faster in the plane of curvature than it does along the surface normal to the plane of curvature. At approximately 100 jet diameters downstream from the exit, the jet half-width in the plane of curvature is 35 percent larger than its counterpart in the surface perpendicular to the plane of curvature.

(2) The mean velocity profiles in the plane of curvature are asymmetric when $x/d \geq 50$ with the outer jet half-width always smaller than the inner jet half-width. On the other hand, the streamline curvature does not seem to have any effect on the decay rate of the maximum mean excess velocity. The curved jet essentially has the same center-line velocity decay rate as the straight jet with the same jet-to-co-flow ratio.

(3) The jet turbulence structure is significantly altered by the streamline curvature. Turbulence intensity profiles show a strong asymmetry in the plane of curvature. Turbulence levels are higher on the outer side where the mean angular momentum is unstably stratified as compared to those levels in the inner side where the angular momentum gradient imposes stability. The outer side turbulence intensity reaches a maximum around $x/d = 80$. Beyond this point, it relaxes back to the levels for $x/d < 60$.

Fig. 9(a) $x/d < 50$

Fig. 9(b) $x/d > 60$

Fig. 9   Turbulence intensity profiles in the x, y plane

Acknowledgments

References

Antonia, R. A., and Bilger, R. W., 1973, "An Experimental Investigation of an Axisymmetric Jet in a Co-Flowing Air Stream," *Journal of Fluid Mechanics*, Vol. 61, pp. 805–822.

Biringen, S., 1986, "An Experimental Investigation of a Turbulent Round Jet in a Coflowing Airstream," Presented at the Winter Annual Meeting of ASME, Anaheim, CA, December 7–12.

Bradshaw, P., 1973, "Effects of Streamline Curvature on Turbulent Flow," *AGARDograph* No. 169.

Castro, I. P., and Bradshaw, P., 1976, "The Turbulence Structure of a Highly Curved Mixing Layer," *Journal of Fluid Mechanics*, Vol. 73, pp. 265–304.

Hanui, H., and Ramaprian, B. R., 1989, "Studies on Two-Dimensional Curved Non-Buoyant Jets in Cross Flows," ASME JOURNAL OF FLUIDS ENGINEERING, Vol. 111, pp. 78–86.

Maczynski, J. F. J., 1961, "A Round Jet in an Ambient Co-Axial Stream," *Journal of Fluid Mechanics*, Vol. 13, pp. 597–608.

Masuda, W., and Maeda, Y., 1986, "Measurement in a Two-Dimensional Curved Jet Along a Circular Arc," *Transactions of the Japanese Society for Aeronautical and Space Sciences*, Vol. 29, pp. 67–76.

Masuda, W., and Andoh, S., 1989, "Effects of Curvature on the Initial Mixing Region of a Two-Dimensional Jet," *AIAA Journal*, Vol. 27, pp. 52–56.

Masuda, W., and Andoh, S., 1989, "Turbulence Structure in an Initial Mixing Region of a Two-Dimensional Curved Jet," *AIAA Journal*, Vol. 27, pp. 1038–1043.

Namer, I., and Ötügen, V., 1988, "Velocity Measurements in a Plane Turbulent Air Jet at Moderate Reynolds Numbers," *Experiments in Fluids*, Vol. 6, pp. 387–399.

Ramjee, V., and Neelakandan, D., 1989, "Development of Wake of a Rectangular Cylinder in a Curved Stream," *Experiments in Fluids*, Vol. 7, pp. 395–349.

Rapp, A. F., and Margolis, D. P., 1968, "Turbulence and Pressure Transport in a Curved Mixing Layer," *Physics of Fluids*, Vol. 11, pp. 1347–1348.

So, R. M. C., and G. L. Mellor, 1973, "Experiment on Convex Curvature Effects in Boundary Layers," *Journal of Fluid Mechanics*, Vol. 60, pp. 43–62.

So, R. M. C., 1975, "A Turbulent Velocity Scale for Curved Shear Flows," *Journal of Fluid Mechanics*, Vol. 70, pp. 37–57.

So, R. M. C., and Mellor, G. L., "Experiment on Turbulent Boundary Layers on a Concave Wall," *Aeronautical Quarterly*, Vol. 26, pp. 26–40.

So, R. M. C., and Huang, B. C., 1989, "On Incompressible, Turbulent, Heated Round Jets in a Co-Flowing Stream," *The Aeronautical Journal of the R.A.S.*, Mar., pp. 100–110.

So, R. M. C., Zhu, J. Y., Otugen, M. V., and Hwang, B. C., 1990, "Some Measurements in a Binary Gas Jet," *Experiments in Fluids*, Vol. 9, pp. 273–284.

Weygandt, J. H., and Mehta, R. D., 1993, "The Three-Dimensional Character of a Curved Wake," Presented at the 30th AIAA Aerospace Sciences Meeting, January 6–9, Reno, NV.

Wygnanski, I., and Fiedler, H., 1969, "Some Measurements in the Self-Preserving Jet," *Journal of Fluid Mechanics*, Vol. 38, pp. 577–612.

Wyngaard, J. C., Tennekes, H., Lumley, J. L., and Margolis, D. P., 1968, "Structure of Turbulence in a Curved Mixing Layer," *Physics of Fluids*, Vol. 11, pp. 1251–1253.

Effect of Dispersed Phase on Modification of Turbulent Flow in a Wall Jet

Yohei Sato
Ph.D. Candidate.

Koichi Hishida
Associate Professor.

Masanobu Maeda
Professor.

Department of Mechanical Engineering,
Faculty of Science and Technology,
Keio University,
3-14-1 Hiyoshi, Kohoku-ku, Yokohama,
223 Japan

The interaction between dispersed particles and fluid turbulence for a vertical downflow turbulent wall jet embedded in a uniform stream was investigated experimentally and numerically. Three kinds of size classified spherical particles, which were smaller than the Kolmogorov lengthscale of the flow, were dispersed in the jet upstream of the test section. The particle mass loading ratios were set at up to 0.3. Particle and gas-phase velocities were measured by laser Doppler velocimetry with particle size discrimination, and numerical simulations were carried out considering momentum exchange between both phases. Motion of small particles with Stokes number of around unity was influenced by strong shear in the developing region. Streamwise turbulence intensity was strongly attenuated by the addition of particles in the free shear layer region, while transverse turbulence intensity was suppressed in the fully-developed region of both the free and wall shear regions. Modifications of the mean fluid velocity by the particles induced reduction in the Reynolds stress, which alters the turbulence production. Turbulence modification by particles, with Stokes number of order of unity, is due primarily to the extra dissipation which is a function of particle mean concentration and fluid turbulence in the fully-developed region.

1 Introduction

Particle-laden flows occur in essentially all areas of engineering and understanding the particle-turbulence interaction problem is of great importance. Experimental and numerical efforts in turbulence modification by addition of solid particles in air flow have revealed that reduction of gas-phase turbulence intensity is strongly correlated with particle Stokes number and particle mass loading. Eaton (1994) recently reviewed the experiments and simulations in turbulence modification of simple flows and showed significant turbulence attenuation for mass loading ratios greater than 0.1. Gore and Crowe (1989) compiled data in recent reviews concluding that small particles attenuate turbulence and large particles augment it. They used the particle diameter normalized by a turbulence length scale. Adding particles to a single-phase flow dramatically increases the number of dimensionless parameters needed to characterize the flow and particle behavior. At present, it is difficult to resolve all the parameters involved in the development of models for turbulence modification by particles.

Turbulence modification has been extensively studied in fully-developed pipe flows (e.g., Maeda et al., 1980; Tsuji et al., 1984), axisymmetric jet flows (e.g., Modarress et al., 1984; Shuen et al., 1985; Fleckhaus et al., 1987; Hardalupas et al., 1989), turbulent boundary layer flow (Rogers and Eaton, 1991), fully-developed channel flow (Kulick et al., 1994) and homogeneous isotropic turbulence (Squires and Eaton, 1990; Elghobashi and Truesdell, 1993). Development of turbulence models for particle-laden flows has created a demand for accurate experimental data in inhomogeneous flows to extend the understanding of the effect of particles on turbulence in complex flows.

The most commonly used turbulence models in dilute two-phase flow are based on the k-ϵ two-equation model. These models are represented by the approach of Elghobashi and Abou-Arab (1983) and Rizk and Elghobashi (1989). Transport

equations of turbulence kinetic energy and its dissipation rate are retained with the addition of extra terms by particles. The constants in the original single-phase model are left unchanged, however these constants were found to change rapidly with increasing mass loading of light particles from the direct numerical simulation database of particle-laden isotropic turbulence (Squires and Eaton, 1994). The most prominent problem in numerical modeling is to model the destruction of extra dissipation by the presence of particles in ϵ-equation. Values of a new constant for the destruction of extra dissipation by particles have been used indicating that the model is poorly established at this time (Eaton, 1994). If turbulent velocity fluctuations along particle path are known, the destruction of dissipation by particles can be calculated (Elghobashi and Abou-Arab, 1983). Berlemont et al. (1990) have made considerable effort and progress in this area.

The objective of this study is to extend the understanding of turbulence modification by particles in complex flows and turbulent wall jet embedded in a uniform stream is considered to investigate how particles respond to turbulence in a wall jet with freestream and how turbulence is modified by the presence of particles. The wall jet is thought of as a two-layer shear flow comprising an inner region in which the flow is similar to a turbulent boundary layer, and an outer layer where the shear-layer character is more like that of a free shear flow (Launder and Rodi, 1983). The turbulent wall jet was selected in order to examine that the particle motion and the turbulence modification are influenced by the strong shear in both the free and wall shear regions, which cannot be observed in boundary layer and channel flows in which the velocity gradient is steep only near the wall. The present study considered the effects of variations in particle Stokes number (ratio of particle relaxation time to fluid turbulence) and particle mass loading, on the development of the boundary layer and the free shear layer in the self-similar region of the wall jet starting from 20 slot widths downstream of the nozzle, which was confirmed by the experiments of Zhou and Wygnanski (1993). In this work, both fluid and particle velocities were measured by laser Doppler velocimetry with particle size discrimination, and numerical simulations were performed by a low-Reynolds-number k-ϵ model considering

Copyright © 1996 by ASME

Table 1 Fluid flow parameters

Parameters	
width of jet b	5 mm
jet velocity at nozzle exit $\bar{U}_{\text{jet}}$	10 m/s
freestream velocity $\bar{U}_\infty$	2 m/s
Reynolds number Re_{jet}	3300
$\bar{U}_\infty/\bar{U}_{\text{jet}}$	0.2
momentum thickness θ_o	11 mm
friction velocity u_τ^*	0.15–0.19 m/s
Kolmogorov microscale at Y_{max} η^*	860–1100 μm

* Values in the fully-developed region ($x/b = 30$–50).

The test section was a rectangular channel, 150×100 mm^2, and 800 mm long. The side walls of the test section were optical glass for LDV. The particles were then recovered after the test section using a cyclone separator.

Pressure taps were located along the centerline of the jet-side wall, for measuring the streamwise pressure gradient. Jet efflux velocity was 10 m/s yielding jet Reynolds number of 3300. Some of the properties of the flow are presented in Table 1. The momentum thickness of the upstream boundary layer was calculated from velocity measurements made near the jet exit ($x/b = 0.2$) by

$$\theta_o = \int_0^\infty (\bar{U}_f/\bar{U}_\infty - 1)(\bar{U}_f/\bar{U}_\infty)dy\big|_{x/b=0.2}. \qquad (1)$$

Friction velocities were estimated by using the relation between wall shear stresses, τ_w, and coefficients of skin friction, C_f, (Bradshaw and Gee, 1962), which was confirmed by the experiments of a self-preserving plane wall jet by Irwin (1973):

$$C_f = 0.026 \left(\frac{\bar{U}_{\text{max}}Y_{\text{max}}}{\nu}\right)^{-0.18}, \qquad (2)$$

$$u_\tau = \sqrt{\frac{\tau_w}{\rho_f}} = \left(\frac{1}{2} \bar{U}_{\text{max}}^2 C_f\right)^{1/2}. \qquad (3)$$

The Kolmogorov micro lengthscales at Y_{max} were estimated in this study (Tennekes and Lumley, 1972)

$$\eta = \kappa^{1/4}Y_{\text{max}}\left(\frac{Y_{\text{max}}u_\tau}{\nu}\right)^{-3/4} (\kappa = 0.41). \qquad (4)$$

Three classes of particles were used in the present set of experiments and their characteristics are compiled in Table 2.

Fig. 1 Schematic of air and particle feed system

1 Tracer feeder
2 Settling chamber
3 Valve
4 Particle feeder
5 Orifice
6 Manometer
7 Straightener
8 Screen
9 Splitter plate
10 Settling duct
11 Contraction nozzle
12 Test Section
13 Orifice
14 Manometer
15 Valve
16 Blower
17 Cyclone separator
18 Valve
19 Particle collector

momentum exchange between both phases and particle Lagrangian simulation techniques (Berlemont et al., 1990). Validation of the present numerical technique is discussed by comparing with experiments.

2 Experimental Facility and Techniques

The present experiments were performed in a blower-driven, two-dimensional, vertical turbulent wall jet wind-tunnel. The air flow was directed vertically downwards and the jet, but not the freestream, was uniformly loaded with particles, which was checked by laser Doppler velocimetry (LDV) at the nozzle exit. Figure 1 depicts the basic air flow and particle supply system. The air passed through a mixing chamber where aluminum powder of approximately 1 μm was added as a tracer of the air. The flow was then divided into two streams and passed through a set of grids. After the grids, the flow passed though a 7:1 contraction to the test section. The uniformity of the freestream was measured with LDV at three spanwise stations.

--- Nomenclature ---

c = fluctuating particle concentration
$\bar{C}$ = mean particle concentration
f_{D_i} = ith component of fluctuating particle drag force
$\tilde{f}_{D_i}$ = ith component of instantaneous particle drag force ($\bar{F}_{D_i} + f_{D_i}$)
$\bar{F}_{D_i}$ = ith component of mean particle drag force
m_p = particle mass
u = streamwise velocity fluctuation
$\tilde{u}_{f_i}$ = ith component of fluid instantaneous velocity
$\tilde{u}_{p_i}$ = ith component of particle instantaneous velocity
$\bar{U}$ = streamwise mean velocity

$\mathbf{U}_f$ = instantaneous fluid velocity vector
$\bar{U}_{\text{max}}$ = local maximum velocity in the jet
v = transverse velocity fluctuation
$\bar{V}$ = transverse mean velocity
$\mathbf{V}_p$ = instantaneous particle velocity vector
x = streamwise direction
y = transverse direction
Y_{max} = distance from the surface where the local velocity is maximum
$Y_{\text{max}/2}$ = distance from the surface where the local velocity is reduced to one-half of its maximum value ($Y_{\text{max}/2} > Y_{\text{max}}$)

κ = von Kármán constant ($\kappa = 0.41$)
μ = viscosity of air
ν = kinematic viscosity of air
ν_T = eddy viscosity ($c_\mu f_\mu(k^2/\epsilon)$)
ρ = density
τ_p = particle time constant ($\rho_p d_p^2/18\rho_f\nu$)
$\bar{\tau}_p^c$ = corrected particle time constant

Subscripts

f = fluid property
p = particle property

Superscripts

$-$ = mean value

Table 2   Particle properties

Properties	Glass	Glass	Nickel
number mean diameter d_p	49.3 μm	140 μm	50.3 μm
stan. dev. of diameter σ_p	4.85 μm	8.9 μm	6.68 μm
density ρ_p	2590 kg/m^3	2590 kg/m^3	8404 kg/m^3
particle time constant τ_p	19.1 ms	154 ms	64.6 ms
corrected time constant $\overline{\tau_p^c}$*	13.6–15.6 ms	70.5–124 ms	45.2–64.6 ms
terminal velocity V_t ($=\tau_p \cdot g$)	0.18 m/s	1.51 m/s	0.63 m/s
particle Stokes number St*	0.56–2.2	2.7–17	1.2–9.7
particle mass loading ratio ϕ	0.1	0.3	0.3
particle volumetric fraction	4.6 $\times$ 10^{-5}	1.3 $\times$ 10^{-4}	4.3 $\times$ 10^{-5}
particle Reynolds number range Re$_p$*	2.0–5.4	2.0–20	0.27–6.5

* Values in the fully-developed region ($x/b = 30$–50).

The corrected particle time constant, for a non-Stokesian particle, which can be written as

$$\overline{\tau_p^c} = \frac{4 d_p \rho_p}{3 \rho_f C_D \sqrt{(\bar{U}_p - \bar{U}_f)^2 + (\bar{V}_p - \bar{V}_f)^2}}, \qquad (5)$$

is the time required for a particle in free-fall to accelerate from rest to 63 percent of its terminal velocity, which time was computed using the drag law given by Morsi and Alexander (1972). The coefficient of drag, C_D, is a function of the particle Reynolds number which is defined by

$$Re_p = \frac{d_p |V_p - U_f|}{\nu}. \qquad (6)$$

The particle size distributions were determined by using successively smaller sieves and the particle sphericity was checked using a microscope. The Stokes number is based on the corrected particle time constant and the characteristic timescale of energy-containing eddy based on the turbulence kinetic energy, k, and its dissipation rate, ϵ, from the computational results.

Velocity statistics of both gas and particle phases were obtained using a He-Ne three-beam LDV (Fleckhaus et al., 1987) for simultaneous two-component velocity measurements by employing the polarization of the laser beam. Discrimination between gas-phase tracers and the particles was done by comparing peak value of amplitude of the pedestal signals and Doppler frequency was detected by using FFT-type signal processor with Digital Signal Processor for a poor signal to noise ratio (Kobashi et al., 1991).

Pressure was measured through taps located on the wall of the jet side along the centerline. The static pressures were measured by a digital manometer with resolution of 9.8 $\times$ 10^{-2} Pa. The streamwise gradient of wall-pressure was 47.8 Pa/m in the test section.

3   Overview of the Simulation

3.1   Particle Lagrangian Simulation. The particle Lagrangian simulation (Berlemont et al., 1990), which was performed in the present study, relies on calculating the particle trajectory. The influence of the turbulence field on particles is represented by tracking a discrete particle and a fluid particle simultaneously. The difference between the two trajectories is represented through Eulerian correlations which transfer information from the fluid to particle. The instantaneous field velocity, $\tilde{u}_{f_i}$, was calculated assuming that the pdf of the fluctuating velocity field is Gaussian and the statistical properties of the field are determined by Lagrangian correlations. For dense particles in air flow, the equation of particle motion reduces to

$$m_p \frac{d V_p}{dt}$$

$$= -\frac{3}{4} \frac{m_p}{d_p} \frac{\rho_f}{\rho_p} C_D (V_p - U_f) |V_p - U_f| + m_p g + F_L, \qquad (7)$$

and the coefficient of drag, C_D, is given by Morsi and Alexander (1972). The Saffman lift force (1965)

$$F_{L_j} = 1.615 \, \mu d_p^2 \left(\frac{1}{\nu} \left| \frac{\partial \tilde{u}_{f_i}}{\partial x_j} \right| \right)^{1/2} (\tilde{u}_{f_i} - \tilde{u}_{p_i}), \qquad (8)$$

may influence particle motion in regions of strong shear. In the present investigation, however, it is impossible to estimate the instantaneous gradient of fluid velocity at each particle point. Therefore the lift force term is estimated by

$$F_{L_j} \approx 1.615 \, \mu d_p^2 \left(\frac{1}{\nu} \left| \frac{\tilde{u}_{f_i} - \bar{U}_{f_i}}{\Delta x_j} \right| \right)^{1/2} (\tilde{u}_{f_i} - \tilde{u}_{p_i}), \qquad (9)$$

where $\bar{U}_{f_i}$ is fluid mean velocity at a grid near a particle point and Δx_j is distance between a grid and the particle point.

Estimation of turbulence scales which affect particle dispersion is of importance in the Lagrangian approach (Berlemont et al., 1993). The Lagrangian integral time scales are defined as follows:

$$\tau_{L_{11}} = 0.2 \frac{\overline{u^2}}{\epsilon} \quad \text{(Berlemont et al., 1990)}, \qquad (10)$$

$$\tau_{L_{22}} = \frac{1}{3} \frac{\overline{v^2}}{\epsilon} \quad \text{(Tennekes and Lumley, 1972)}. \qquad (11)$$

The Eulerian spatial correlation scales which are used in the computation of the correlations between fluid and particle are given by (Tennekes and Lumley, 1972)

$$L_{E_{11}} = \frac{3}{2} \tau_{L_{22}} \overline{v^2}, \qquad (12)$$

$$L_{E_{22}} = \frac{1}{2} L_{E_{11}}. \qquad (13)$$

3.2   Eulerian Field Simulation. The turbulence quantities are obtained by solving the continuity equation, the Reynolds-averaged Navier-Stokes equation and the following transport equations of turbulence kinetic energy and its dissipation rate:

$$\frac{Dk}{Dt} = P_k + T_k + \Pi_k + D_k - \epsilon - \epsilon_p, \qquad (14)$$

$$\frac{D\epsilon}{Dt} = P_\epsilon^1 + P_\epsilon^2 + P_\epsilon^3 + P_\epsilon^4 + T_\epsilon + \Pi_\epsilon + D_\epsilon - D - D_p. \qquad (15)$$

Each modeled term appeared in the low-Re k-ϵ model proposed by Nagano and Shimada (1993) is compiled in Table 3. Squires

Table 3(a)   Modeled terms in k-equation

T_k (normal component)	Π_k (normal component)
$\dfrac{\partial}{\partial y}\left(f_T \dfrac{\nu_T}{\sigma_k} \dfrac{\partial k}{\partial y} \right)$	$-0.5\nu \dfrac{\partial}{\partial y}\left(\dfrac{k}{\epsilon} \dfrac{\partial \epsilon}{\partial y} f_{w1} \right)$

$\sigma_k = 1.2$
$f_T = 1 + 3.5 \exp\{-(R_T/100)^{3/4}\}$, $\quad f_{w1} = \exp\{-(y^+/9)^2\}$, $\quad R_T = k^2/(\nu\epsilon)$

Table 3(b)   Modeled terms in ϵ-equation

$P_\epsilon^1 + P_\epsilon^2 + P_\epsilon^4 - D$	P_ϵ^3	T_ϵ (normal component)	Π_ϵ (normal component)
$c_{\epsilon 1} \dfrac{\epsilon}{k} P_k - c_{\epsilon 2} f_2 \dfrac{\epsilon^2}{k}$	$f_{w2} \nu \nu_T \left(\dfrac{\partial^2 \bar{U}_f}{\partial y^2} \right)^2 + c_{\epsilon 3} \nu \dfrac{k}{\epsilon} \dfrac{\partial k}{\partial y} \dfrac{\partial \bar{U}_f}{\partial y} \dfrac{\partial^2 \bar{U}_f}{\partial y^2}$	$\dfrac{\partial}{\partial y} \left(f_T \dfrac{\nu_T}{\sigma_\epsilon} \dfrac{\partial \epsilon}{\partial y} \right)$	$-c_{\epsilon 4} \nu \dfrac{\partial}{\partial y} \left[(1 - f_{w1}) \dfrac{\epsilon}{k} \dfrac{\partial k}{\partial y} f_{w1} \right]$

$\sigma_\epsilon = 1.3$, $\quad c_{\epsilon 1} = 1.45$, $\quad c_{\epsilon 2} = 1.9$, $\quad c_{\epsilon 3} = 0.005$, $\quad c_{\epsilon 4} = 0.5$

$f_2 = [1 + \exp\{-2 \times 10^{-4} R_S^{13}\} \{1 - \exp(-2.2 R_S^{1/2})\}] \times (1 - f_{w1})$, $\quad R_S = \dfrac{k}{\epsilon} \dfrac{u_\tau^2}{\nu + \nu_T} \dfrac{1}{R_T^{1/2}} f_{w1}$, $\quad f_{w2} = \exp\{-(y^+/44)^2\}$

and Eaton (1994) showed that there is a change in $c_{\epsilon 2}$ of the destruction of dissipation term, D, with increased mass loading of particles from direct numerical simulation data of particle-laden isotropic turbulence. To avoid changing in the single-phase model constants, all the terms are included in the k- and ϵ-equations which were neglected in the standard model (Launder and Spalding, 1974). Figure 2 compares the calculated mean fluid velocity profiles with the experimental results, showing good agreement in the fully-developed region ($x/b = 30$–50).

In the two-way-coupling simulation momentum exchange between dispersed phase and turbulence must be considered (Shuen et al., 1985; Berlemont et al., 1990). The mean drag force on particles, $\overline{F_{D_i}}$, is added to the momentum equation. The source or sink of k due to momentum exchange with the particles, ϵ_p, is given by

$$\epsilon_p = \overline{u_{f_i} f_{D_i}} = \overline{\tilde{u}_{f_i} \tilde{f}_{D_i}} - \bar{U}_{f_i} \cdot \overline{F_{D_i}}. \tag{16}$$

The destruction of extra dissipation by the presence of particles, D_p, is expressed as the destruction of dissipation term, D:

$$D_p = c_{\epsilon p} \frac{\epsilon}{k} \epsilon_p. \tag{17}$$

The model constant $c_{\epsilon p}$ is usually calibrated to yield good agreement with a particular laboratory experiment. We calculated particle-laden turbulent channel flow of Kulick et al. (1994) and the present experiments with several values ranging from 1.0 to 2.0. Then the value of 1.6 was optimized.

3.3   Boundary Conditions.   The initial condition of particle injection has influenced the Lagrangian statistics. We calculated the initial quantities of dispersed phase by a two-way-coupling simulation in a fully-developed channel flow with periodic boundary condition. Range of particle diameter distribution was not considered at the inlet.

The boundary conditions of flow field are: $\bar{U}_f = \bar{V}_f = k = 0$, $\epsilon_w = 2\nu(\partial \sqrt{k}/\partial y)_w^2$ at the wall; and $\partial \bar{U}_f/\partial x = \partial \bar{V}_f/\partial x = \partial k/\partial x = \partial \epsilon/\partial x = 0$ at the outlet. The inlet quantities of the wall jet were calculated by a fully-developed channel flow simulation with periodic boundary condition. The inlet conditions of the free stream were specified from the experimental data: $k = (3/4)(u_f^2 + v_f^2)$, and the dissipation rate of turbulence kinetic

energy was set equal to the centerline value of the wall jet. At the wall boundaries it was assumed that particles collided in a perfectly elastic and frictionless manner. This assumption worked well for particles of a size significantly larger than the scale of wall roughness. Particle volumetric fractions in this experiments were less than 5.0×10^{-4}, so that particle-particle collisions could be neglected and the continuity equation for carrier fluid remained unchanged by the addition of the particles (Rizk and Elghobashi, 1989).

## 4   Uncertainties in Experiment and Simulation

LDV velocity measurements used 2000 samples. The measurement uncertainties in the present experiments, for a 95 percent confidence level, are compiled in Table 4. The two-dimensional nature of the flow in the test section was assured by making spanwise measurements across the flow. The mean streamwise velocity was found to vary within 3 percent across the span of wall jet.

Two types of grid systems (283×188 and 143×165) were used to evaluate the grid dependence of the computational results. The comparisons of Fig. 2 suggest grid-independent solutions in the calculations. Comparison between the simulation results from 16384 and 32768 ($=32^3$) particles indicated negligible differences.

5   Results and Discussion

A Cartesian coordinate system (x, y) with the origin on the jet side wall at the centerline (Fig. 1) is used for all data presentation. Results are presented in the fully-developed region ($x/b = 40$ and 50). All of the numerical results in this section were obtained by ensemble averaging over the trajectories of 32768 particles in the 143×165 grid. The term 'unladen flow' refers to the gas flow without particles and 'laden flow' to the gas flow in the presence of particles.

5.1   Particle Response to Turbulence.   Particles used in the present experiments can be classified according to the ability of the particles to respond to shear flows. 'Responsive' particles are those for which the particle Stokes number, St, is around unity, which refer to 50 μm glass particles in this study. 140 μm glass and 50 μm nickel particles are 'partly responsive' particles (Hardalupas et al., 1989) which have St of the order of unity in the fully-developed region. The mean St, which is based on the characteristic mean timescale of the flow defined as $b/(\bar{U}_{jet} - \bar{U}_\infty)$, shows larger values, for example, St = 21–24 for 50 μm glass particles. In the present study, however, discussion with the mean St is quite controversial, so that the
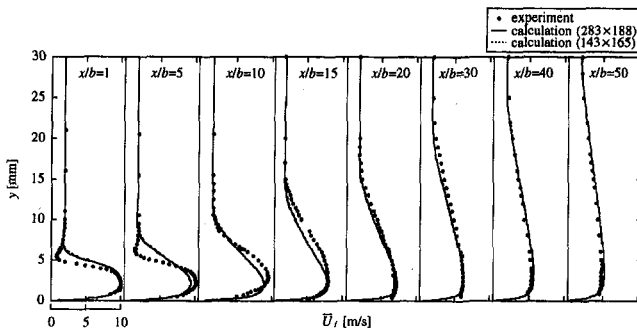
Fig. 2   Mean streamwise velocity profiles of unladen air flow

Table 4   Measurement uncertainties

	Mean velocity	Fluctuating velocity
gas phase in the presence of particles	3%	5%
particles	0.3%	3%
particle number density	4%	
static pressure	9.8×10^{-2} Pa	

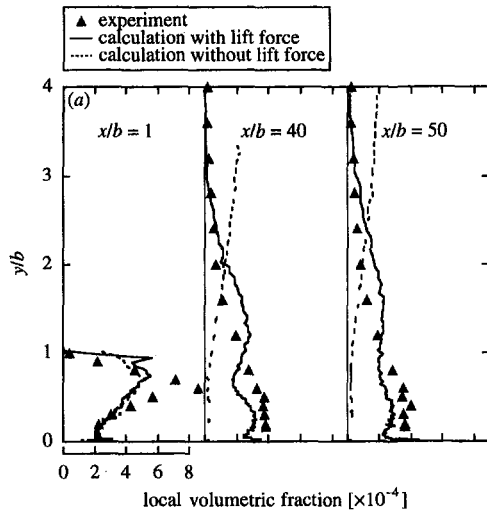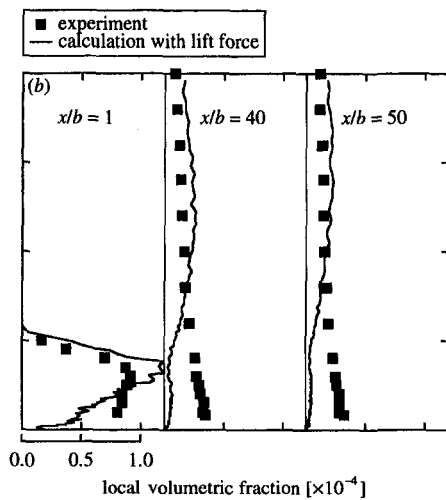**Fig. 3(a)** 50 μm glass particle local volumetric fraction profiles

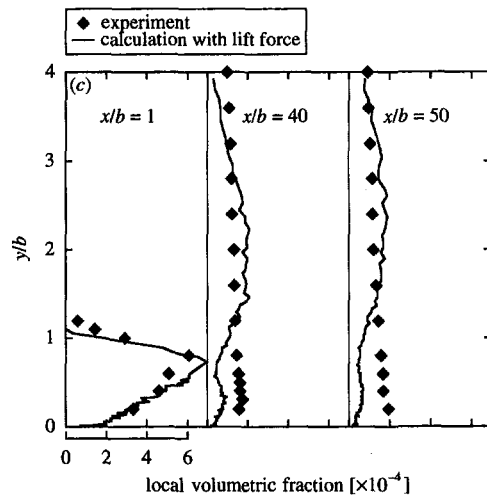**Fig. 3(b)** 140 μm glass particle local volumetric fraction profiles

Fig. 3(c) 50 μm nickel particle local volumetric fraction profiles

experimental results suggest that responsive particles accumulated the wall and partly responsive particles dispersed uniformly in the fully-developed region. The computational results for responsive particles considering the lift force show the same trend, in contrast to the results without the lift force. The evaluation of the lift force indicated that if the particle relative velocities and the instantaneous velocity gradients have same values for all the particles, the lift force acting on 50 μm glass particles is approximately three times that on partly responsive particles. It is observed that effect of the lift force for responsive particles on particle motion is significant compared to partly responsive particles. The lift force used in this study was 'modeled' and the experiments of Segré and Silverberg (1962) demonstrated that, with minor corrections, Saffman's derivation applies to particles with $Re_p < 10$ (for 140 μm glass particles, $2 < Re_p < 20$). Thus discussion may not be beyond controversy, but the experimental and computational evidence supports the importance of the lift force on smaller particles.

In the wall jet the shear stress near the nozzle exit is stronger than that in the fully-developed region, so that it can be seen that the lift force is significant in the developing region. Figure 4 shows profiles of probability density of transverse location for responsive particles at $x/b = 1-10$ from the computational results. It must be noted that responsive particles have tendency to accumulate near the wall ($y/b < 1$) due to the lift force. Without the lift force responsive particles dispersed faster, and the influence in the developing region remained in the fully-developed region, which means particles dispersed uniformly in the free shear region shown in Fig. 3(a). The computational results for partly responsive particles show negligible differences between with and without the lift force, however, show higher dispersion compared to the experimental results.

Figures 5(a)–(c) show the variation of particle mean streamwise velocity with distance from the nozzle exit, distance from the wall, and particle Stokes number, which are compared with the same quantities for the unladen and laden air flow. 50 μm and 140 μm glass particles exceed the air flow, which was predicted by the numerical simulation, due primarily to particle inertia. Behavior of 50 μm nickel particles, however, shows different trend. The computational results suggest that particles exceed the air flow, but it is observed that the streamwise particle relative velocities are small in the experiments. The terminal
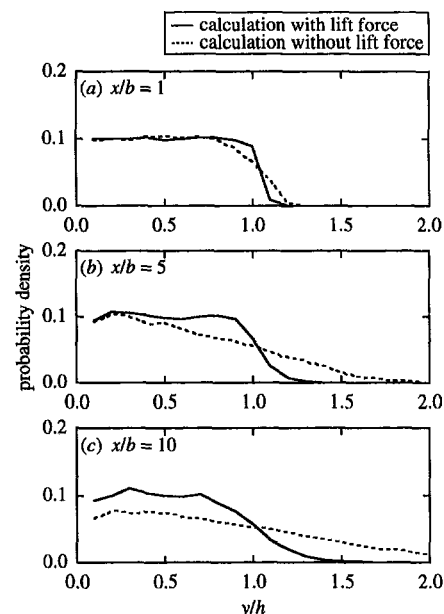

Fig. 4 Probability density of transverse location of 50 μm glass particle at (a) $x/b = 1$; (b) $x/b = 5$; (c) $x/b = 10$

turbulent St based on the characteristic timescale of energy-containing eddy with the aid of the computational results was used.

Figures 3(a)-(c) show profiles of particle local volumetric fraction which was evaluated by particle number density. The
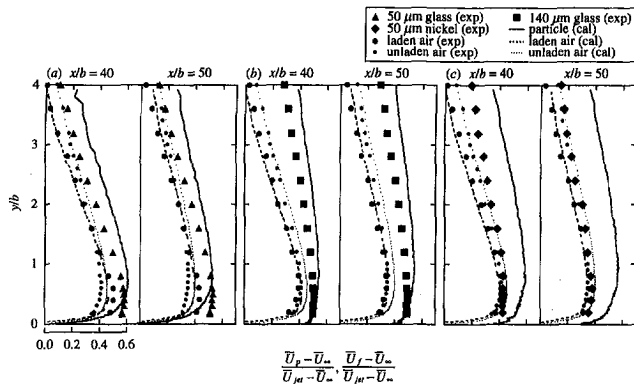
Journal of Fluids Engineering

Fig. 5 Mean streamwise velocity profiles of particles and air in the presence of (a) 50 μm glass particles; (b) 140 μm glass particles; (c) 50 μm nickel particles

Fig. 7 Transverse velocity fluctuations profiles of particles and air in the presence of (a) 50 μm glass particles; (b) 140 μm glass particles; (c) 50 μm nickel particles

velocity of a single 50 μm nickel particle is 0.63 m/s; in comparison, at a mass loading of 0.3 the mean slip velocity is approximately 2 m/s. It is difficult to explain the relationship between the nickel-particle mean slip velocity and loading. Simple analyses rule out a significant effect of particle-particle collisions. A possibility is that a large charge could have built up on the walls, possibly causing the observed difference in the particle mean velocity profiles. The amount of charge accumulated on the walls would probably affect motion of nickel particles.

Streamwise particle velocity fluctuations are displayed in Figs. 6(a)–(c). Responsive particles had nearly the same fluctuation intensity as the turbulence intensity in both the free and wall shear regions. 140 μm glass and 50 μm nickel particles 'partly' responded to fluid turbulence. The computational results for 140 μm glass predicted well, and for 50 μm glass particles differences was observed. It is found that the equation of particle motion used in the present study has ability to express motion of a particle with a large particle time constant. It is widely known that the k-ε model hardly predicts developing region of fluid turbulence, for example, in this study computed turbulence intensities show twice as those of experiments at x/b = 1 and 5, and half those at x/b = 10–20. Thus behavior of lighter particle, which is expressed by Eq. (7), is mostly influenced by predicted fluid turbulence in the developing region in a turbulent wall jet.

Profiles of transverse particle velocity fluctuations are presented in Figs. 7(a)–(c). Particle velocity fluctuations were smaller than flow turbulence intensities in the transverse direction, because fluid transverse velocity fluctuations occur at higher frequencies than do streamwise fluctuations, to which frequencies particles were less able to respond.
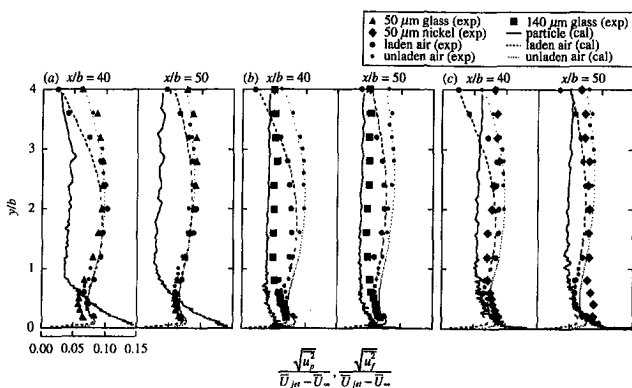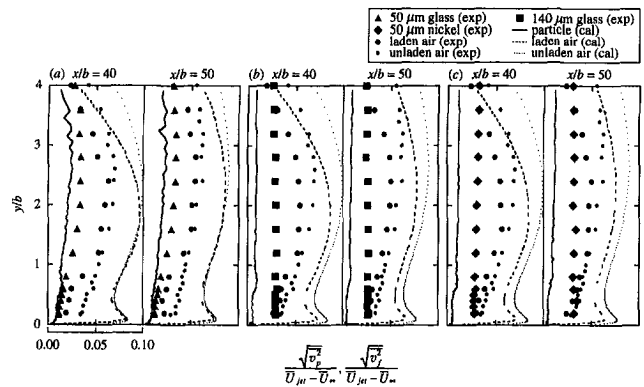

Fig. 6 Streamwise velocity fluctuations profiles of particles and air in the presence of (a) 50 μm glass particles; (b) 140 μm glass particles; (c) 50 μm nickel particles

5.2 Turbulence Modification by Particles. Profiles of mean streamwise velocity of the gas phase in the presence of particles are shown in Figs. 5(a)–(c). Partly responsive particles have a mean slip velocity between both phases that cause momentum transfer from the particles to the gas phase. In the fully-developed region the laden fluid mean velocities were decelerated due to partly responsive particles. The numerical simulation used in this study has an ability to predict the same behavior, therefore the momentum exchange between particles and fluid turbulence is mainly due to the particle drag. The laden air velocities in the presence of responsive particles exceed the unladen air near the wall ($y/b < 1$), which was not observed in the computational results. Simple analysis shows that the effect of mean particle drag on the mean momentum equation may be positive, which is impossible in the present simulations.

Profiles of streamwise turbulence intensity are illustrated in Figs. 6(a)–(c). Streamwise turbulence intensities were attenuated more strongly in the free shear layer region than near the wall in the fully-developed region. Attenuation of streamwise turbulence intensity by partly responsive particles is increased with distance from the wall. The present numerical simulations agree well with the experimental results in the streamwise direction. The model constant $c_{\epsilon p}$ has a wide range of values in the k-ε model. Rizk and Elghobashi (1989) used $c_{\epsilon p} = 2$, Berlemont et al. (1990) used $c_{\epsilon p} = 1.9$, and Rizk et al. (1993) used $c_{\epsilon p} = 1.7$. The value of 1.6 was determined to use in order to obtain the same degree of attenuation of turbulence kinetic energy; in the experiments the turbulence kinetic energy was estimated from the streamwise and transverse turbulence intensities, $k = (3/4)(u_f^2 + v_f^2)$.

It was observed from Fig. 6(a) that streamwise turbulence intensities in the presence of responsive particles were augmented for $y/b < 2.5$ in the experiments. While the computational results show no change compared with the unladen flow. Several reasons may be considered. The first is that change in mean streamwise velocity gradients modifies the streamwise turbulence intensities and particles augment streamwise turbulence. The second is that particle-turbulence interactions cause the streamwise turbulence augmentation. The present numerical simulations suggest that momentum exchange between responsive particles and fluid turbulence cannot represent augmentation of streamwise turbulence intensity, which means that change in velocity gradients do not contribute the augmentation.

Profiles of transverse turbulence intensity are displayed in Figs. 7(a)–(c). The variation of transverse turbulence intensity with Stokes number and distance from the wall differs in several respects from that in the streamwise direction. The degree of turbulence attenuation in the transverse direction was larger than that in the streamwise direction. Especially in the presence of responsive particles, the transverse turbulence intensities
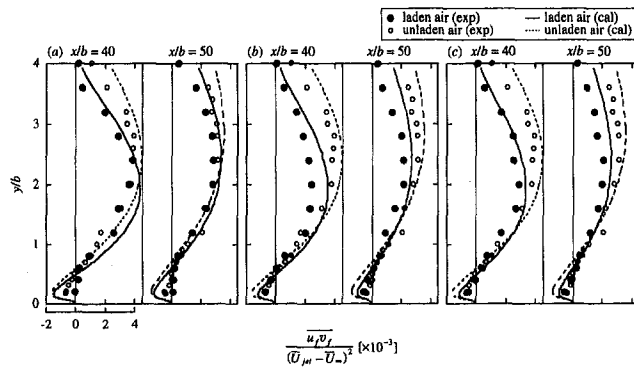
Fig. 8 Profiles of Reynolds stress of the gas phase in the presence of (a) 50 μm glass particles; (b) 140 μm glass particles; (c) 50 μm nickel particles

were suppressed both the free and wall regions, which shows the opposite trends compared to the streamwise turbulence intensities. The computational results show reduction of transverse turbulence intensity by partly responsive particles, in spite of overpredicted values. However, the present numerical simulations cannot predict strong reduction of transverse turbulence intensity near the wall by responsive particles.

Figures 8(a)–(c) show profiles of Reynolds stress of the gas phase in the presence of particles. Reynolds stresses in the free shear layer region were strongly modified by all the particles. The computational results show good agreement in the presence of partly responsive particles. Apparent changes in Reynolds stress by particles in the free shear region were primarily attributed to modifications of the mean velocity gradient.

It can be concluded that turbulence attenuation by partly responsive particles is mainly due to momentum exchange between the two phases, which is ensured by the present numerical simulation techniques.

5.3 Analytical Examination of Effect of Small Particles on Turbulence Modification.

Modifications of the gas-phase mean velocity profiles (Fig. 5) and changes in the Reynolds stress (Fig. 8) alter the rates of production of turbulence kinetic energy, as displayed by the profiles at $x/b = 50$ in Figs. 9(a)–(c). Each term is normalized by velocity difference and kinematic viscosity of air. Production term for the experimental case is calculated by

$$P_k = -\overline{u_f v_f}\frac{\partial \bar{U}_f}{\partial y}. \tag{18}$$

The extra dissipation due to particles, ϵ_p, (Eq. (17)) reduces to

$$\epsilon_p \approx \frac{\bar{C}}{\rho_f \overline{\tau}_p^c}(\overline{u_{f_i}u_{f_i}} - \overline{u_{f_i}u_{p_i}}) + \frac{1}{\rho_f \overline{\tau}_p^c}(\bar{U}_{f_i} - \bar{U}_{p_i})\overline{cu_{f_i}}$$

$$+ \frac{1}{\rho_f \overline{\tau}_p^c}(\overline{cu_{f_i}u_{f_i}} - \overline{cu_{f_i}u_{p_i}}), \tag{19}$$

where $\overline{\tau}_p^c$ is mean corrected particle time constant. The values of $\overline{\tau}_p^c$ were calculated by the experimental value of particle mean slip velocity for each component, while $\overline{\tau}_p^c$ was obtained to ensemble in each control volume in the simulations. Squires and Eaton (1990) showed that if the particle concentration distribution is random the correlation term $\overline{cu_{f_i}}$ and the triple correlations terms $\overline{cu_{f_i}u_{f_i}}$ and $\overline{cu_{f_i}u_{p_i}}$ are negligible compared to the other terms with direct numerical simulation data of particle-laden isotropic turbulence. Correlation between fluid and particle velocity fluctuations is unknown in the experiments, so that Eq. (19) simplifies to

$$\epsilon_p \approx \frac{\bar{C}}{\rho_f \overline{\tau}_p^c}2k, \tag{20}$$

where $\bar{C}$ is mean particle concentration which was calculated by the experimental values of particle local volumetric fraction multiplied by particle density. In Fig. 9, the extra dissipation term for the experimental case was evaluated by Eq. (20) and for the numerical case was calculated by Eq. (16).

Figures 9(b) and 9(c) show that turbulence production was strongly affected by partly responsive particles in the free shear layer region, due primarily to modifications in gas-phase mean velocity. It is observed that the dissipation rate of turbulence kinetic energy in the simulations decreased and the simplified extra dissipation by particles was a significant factor in turbulence attenuation by 'partly responsive' particles. In the presence of 'responsive' particles the simplified extra dissipation term had large values compared to the computed extra dissipation term. The present numerical simulation techniques have no ability to predict the streamwise turbulence augmentation (Fig. 6(a)), strong attenuation of transverse turbulence intensity near the wall (Fig. 7(a)) and different values of Reynolds stress near the wall (Fig. 8(a)) in the presence of 50 μm glass particles.

Correlation between fluid and particle velocity fluctuations, $\overline{u_{f_i}u_{p_i}}$, which was neglected in equation (20) is a possibility to analyze turbulence modification by 50 μm glass particles. The fluid/particle correlation $\overline{u_{f_i}u_{p_i}}$ is estimated by numerical results:

$$\overline{u_{f_i}u_{p_i}} = \overline{\tilde{u}_{f_i}\tilde{u}_{p_i}} - \bar{U}_{f_i}\cdot\bar{U}_{p_i}. \tag{21}$$

Figures 10(a)-(c) depict profiles of correlation between fluid and particle velocity fluctuations in the presence of particles at $x/b = 50$ from the computational results. Fluid/particle correlation was smaller than the turbulence intensity, which means the term $\overline{u_{f_i}u_{f_i}} - \overline{u_{f_i}u_{p_i}}$ is always positive. As particle velocities exceeded the gas-phase velocities, the spectrum of turbulencefluctuations seen by a particles may shift to a high frequency. This decreases the fluid/particle correlation and increases turbulence attenuation. Although the influence of fluid/particle correlation on turbulence attenuation must be small when particle Stokes
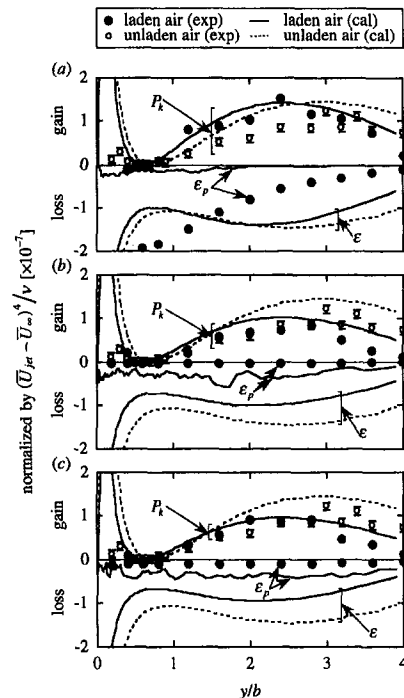

Fig. 9 Profiles of turbulence kinetic energy budget of the gas phase in the presence of (a) 50 μm glass particles; (b) 140 μm glass particles; (c) 50 μm nickel particles at $x/b = 50$
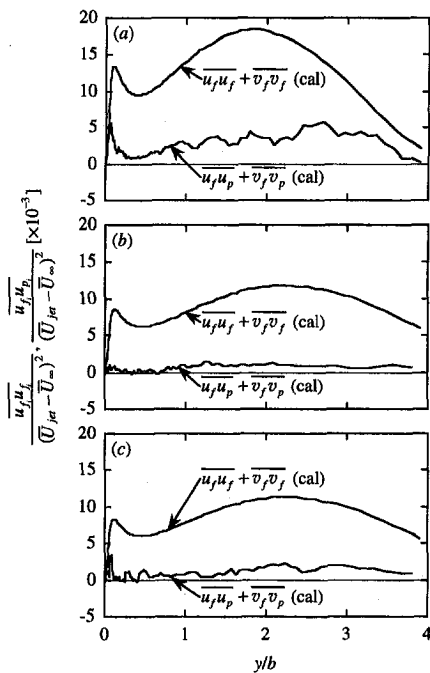
Journal of Fluids Engineering

Fig. 10 Profiles of correlation between fluid and particles velocity fluctuations in the presence of (a) 50 μm glass particles; (b) 140 μm glass particles; (c) 50 μm nickel particles at $x/b = 50$

number is of order of unity, measurements of this quantity are required. Knowledge of the spectrum of the fluid velocity fluctuations along the path of a moving particle is needed to estimate the fluid/particle correlation and the dissipation of turbulence kinetic energy by particles (Elghobashi and Abou-Arab, 1983; Eaton, 1994).

Based on the Gore and Crowe (1989) correlation the ratio of diameter of 50 μm glass particles, d_p, to characteristic length scale, l_e, by turbulence kinetic energy k and its dissipation rate ϵ from the computational results shows 0.005. This means that 50 μm glass particles always attenuate turbulence intensity because of $d_p/l_e < 0.1$. However, the Gore and Crowe correlation cannot be used to represent the responsive difference between 50 μm glass and nickel particles and to show the turbulence modification by 50 μm glass particles in the present wall jet.

It can be concluded from Figs. 9 and 10 that the extra dissipation which is a function of particle mean concentration and fluid turbulence makes a contribution to turbulence attenuation by partly responsive particles in the fully-developed region. Figures 9(a) and 10(a) suggest that turbulence model based on single time scale considering momentum exchange between both phases cannot represent turbulence modification by 50 μm glass particles at a low mass loading.

6 Conclusions

Particle response and turbulence modification by particles in a turbulent wall jet with free stream were examined. Motion of responsive particles, which have the particle Stokes number of around unity was influenced by the strong shear in the developing region, and accumulated near the wall and responded to the streamwise turbulence intensity in the fully-developed region. Partly responsive particles, which have the particle Stokes number of order of unity, were dispersed uniformly in the fully-developed region, which was affected by the shear region in the developing region. All the particles less responded to transverse flow turbulence, because the transverse velocity fluctuations occur at higher frequencies to which particles were less able to respond. The particle Lagrangian and Eulerian field

simulations predicted well behavior of particles, which was influenced by the lift force.

Fluid mean streamwise velocities were modified by the addition of particles in the free shear layer region, which induced the modifications of the Reynolds stress profiles. In the fully-developed region particles reduced strongly the streamwise turbulence in the free shear layer region, while the transverse turbulence intensity was attenuated both near the wall and in the free shear layer region. It was revealed from turbulence kinetic energy budget profiles and small value of the correlation between fluid and particle velocity fluctuations that the extra dissipation, which is a function of particle mean concentration and fluid turbulence, contributed to turbulence attenuation by "partly responsive" particles in the fully-developed region.

References

Berlemont, A., Desjonquères, P., and Gouesbet, G., 1990, "Particle Lagrangian simulation in turbulent flows," *International Journal of Multiphase Flow*, Vol. 16, No. 1, pp. 19–34.

Berlemont, A., Desjonquères, P., and Gouesbet, G., 1993, "Particle Tracking in Turbulent Flows," *Gas-Solid Flows*, ASME FED-Vol. 166, pp. 121–129.

Bradshaw, P., and Gee, M. T., 1962, "Turbulent Wall Jets with and Without an External Stream," *Aero. Res. Counc. R. & M.*, p. 3252.

Eaton, J. K., 1994, "Experiments and Simulations on Turbulence Modification by Dispersed Particles," *Applied Mechanics Reviews*, Vol. 47, No. 6, Part 2, part of "Mechanics USA 1994" Kobayashi, A. S., ed., pp. S44–S48.

Elghobashi, S. E., and Abou-Arab, T. W., 1983, "A Two-Equation Turbulence Model for Two-Phase Flows," *Physics of Fluids*, Vol. 26, No. 4, pp. 928–937.

Elghobashi, S. E., and Truesdell, G. C., 1993, "On the Two-Way Interaction Between Homogeneous Turbulence and Dispersed Solid Particles. I: Turbulence Modification," *Physics of Fluids*, Vol. 5, No. 7, pp. 1790–1801.

Fleckhaus, D., Hishida, K., and Maeda, M., 1987, "Effect of Laden Solid Particles on the Turbulent Flow Structure of a Round Free Jet," *Experiments in Fluids*, Vol. 5, No. 5, pp. 323–333.

Gore, R. A., and Crowe, C. T., 1989, "Effect of Particle Size on Modulating Turbulent Intensity," *International Journal of Multiphase Flow*, Vol. 15, No. 2, pp. 279–285.

Hardalupas, Y., Taylor, A. M. K. P., and Whitelaw, J. H., 1989, "Velocity and Particle-Flux Characteristics of Turbulent Particle-Laden Jets," *Proceedings of the Royal Society of London Series A*, Vol. 426, No. 1870, pp. 31–78.

Irwin, H. P. A., 1973, "Measurements in a Self-Preserving Plane Wall Jet in a Positive Pressure Gradient," *Journal of Fluid Mechanics*, Vol. 61, pp. 33–63.

Kobashi, K., Hishida, K., and Maeda, M., 1991, "Measurement of Fuel Injector Spray Flow of I.C. Engine by FFT Based Phase Doppler Anemometer—An Approach to the Time Series Measurement of Size and Velocity," *Applications of Laser Techniques to Fluid Mechanics* Adrian, R. J. et al., eds., Springer-Verlag, pp. 268–287.

Kulick, J. D., Fessler, J. R., and Eaton, J. K., 1994, "Particle Response and Turbulence Modification in Fully Developed Channel Flow," *Journal of Fluid Mechanics*, Vol. 277, pp. 109–134.

Launder, B. E., and Rodi, W., 1983, "The Turbulent Wall Jet—Measurements and Modeling," *Annual Review of Fluid Mechanics*, Vol. 15, pp. 429–459.

Launder, B. E., and Spalding, D. B., 1974, "The Numerical Computation of Turbulent Flows," *Computer Methods in Applied Mechanics and Engineering*, Vol. 3, pp. 269–289.

Maeda, M., Hishida, K., and Furutani, T., 1980, "Optical Measurements of Local Gas and Particle Velocity in an Upward Flowing Dilute Gas-Solids Suspension," *Proceedings of Polyphase Flow and Transport Technology*, Century 2-ETC, San Francisco, pp. 211–216.

Modarress, D., Tan, H., and Elghobashi, S. E., 1984, "Two Component LDA Measurement in a Two-Phase Turbulent Jet," *AIAA Journal*, Vol. 22, No. 5, pp. 624–634.

Morsi, S. A., and Alexander, A. J., 1972, "An Investigation of Particle Trajectories in Two-Phase Flow Systems," *Journal of Fluid Mechanics*, Vol. 55, pp. 193–208.

Nagano, Y., and Shimada, M., 1993, "Modeling the Dissipation-Rate Equation for Wall Shear Flows (Comparison With Direct Simulation Data)," *Transaction of JSME Series B*, Vol. 59–559, pp. 78–83.

Rizk, M. A., and Elghobashi, S. E., 1989, "A Two-Equation Turbulence Model for Dispersed Dilute Confined Two-Phase Flows," *International Journal of Multiphase Flow*, Vol. 15, No. 1, pp. 119–133.

Rizk, M. A., Mostafa, A. A., and Abolfadi, M. A., 1993, "Calculation of a Particle-Laden Flat Plate Turbulent Boundary Layer," *Gas-Solid Flows,* ASME FED-Vol. 166, pp. 169–175.

Rogers, C. B., and Eaton, J. K., 1991, "The Effect of Small Particles on Fluid Turbulence in a Flat-Plate, Turbulent Boundary Layer in Air," *Physics of Fluids A,* Vol. 3, No. 7, pp. 928–937.

Saffman, P. G., 1965, "The Lift on a Small Sphere in a Slow Shear Flow," *Journal of Fluid Mechanics,* Vol. 22, pp. 385–400 and *corrigendum, ibid.* (1968), Vol. 31, p. 624.

Segré, G., and Silverberg, A., 1962, "Behaviour of Macroscopic Rigid Spheres in Poiseuille Flow. Part 1," *Journal of Fluid Mechanics,* Vol. 14, pp. 115–135.

Shuen, J-S., Solomon, A. S. P., Zhang, Q-F., and Faeth, G. M., 1985, "Structure of Particle-Laden Jets: Measurements and Predictions," *AIAA Journal,* Vol. 23, No. 3, pp. 396–404.

Squires, K. D., and Eaton, J. K., 1990, "Particle Response and Turbulence Modification in Isotropic Turbulence," *Physics of Fluids A,* Vol. 2, pp. 1191–1203.

Squires, K. D., and Eaton, J. K., 1994, "Effect of Selective Modification to Turbulence in Two-Equation Models for Particle-Laden Turbulent Flows," ASME JOURNAL OF FLUIDS ENGINEERING, Vol. 116, pp. 778–784.

Tennekes, J., and Lumley, J. L., 1972, *A First Course in Turbulence,* The MIT Press, Cambridge.

Tsuji, Y., Morikawa, Y., and Shiomi, H., 1984, "LDV Measurements of an Air-Solid Two-Phase Flow in a Vertical Pipe," *Journal of Fluid Mechanics,* Vol. 139, pp. 417–434.

Zhou, M. D., and Wygnanski, I., 1993, "Parameters Governing the Turbulent Wall Jet in An External Stream," *AIAA Journal,* Vol. 31, No. 5, pp. 848–853.

Effect of Nonaxisymmetric Forcing on a Swirling Jet With Vortex Breakdown

Ismet Gursul

Assistant Professor,
Department of Mechanical, Industrial
and Nuclear Engineering,
University of Cincinnati,
Cincinnati, OH 45221-0072

Nonaxisymmetric forcing was applied to the vortex breakdown flowfield of a strongly swirling jet and its effects were investigated experimentally. It is shown that the spreading rate of the jet can be increased due to the excitation of the helical mode instability of the breakdown flowfield. This can be achieved for extremely low amplitudes of excitation.

1 Introduction

Early experiments on strongly swirling jets showed that a large recirculation region exists around the jet exit (Syred and Beer, 1974). It is now well known that this recirculation region is a result of the vortex breakdown phenomenon. Vortex breakdown, which is a rapid axial deceleration of the core of a swirling flow, has been observed in many technological and natural flow fields: swirl combustors (Syred and Beer, 1974), suction tubes of pumps and draft tubes of turbines (Escudier, 1987; Falvey, 1971), leading-edge vortices over delta wings (Peckham and Atkinson, 1957), tornadoes and dust devils (Burggraf and Foster, 1977; Lugt, 1983). While it is undesirable in many cases, it has favorable effects in swirl combustors. The breakdown produces a reversed flow region and enhances the mixing between fuel and air (Syred and Beer, 1974). The present experiments were performed to investigate the feasibility of flow control in vortex breakdown flowfields with an application to improve mixing.

Several experimental studies have been conducted in order to understand the nature of vortex breakdown. These observations and different explanations of the phenomena based on instability, wave propagation and flow stagnation are summarized in several review articles (Hall, 1972; Leibovich, 1984; Escudier, 1988). Although the fundamental cause of breakdown is not well understood, the nature of the wake region was subject to several investigations. Periodic oscillations were observed in a variety of swirling flows after breakdown occurred. Among them are a confined vortex in a tube (Garg and Leibovich, 1979), swirling jets (Chanaud, 1965; Cassidy and Falvey, 1970), wing tip vortex (Singh and Uberoi, 1976) and leading-edge vortices over delta wings (Roos and Kegelman, 1990; Gursul, 1994). Garg and Leibovich (1979) carried out single point LDV measurements in the wakes of breakdown in a tube and observed coherent oscillations. They suggested that the measured frequencies correspond to the theoretical predictions by Lessen et al. (1974) for the first helical mode of the time-averaged mean flow profiles, assuming that the oscillations are the disturbances with the maximum growth rate. The disturbances are represented as $\exp\{i(\alpha x + n\phi - \omega t)\}$, where ω is the frequency, α the wavenumber in the axial direction and n the wavenumber (an integer) in the angular direction. The experiments in a tip vortex (Singh and Uberoi, 1976) also showed coherent velocity fluctuations, which were shown to be a helical mode with the help of simultaneous two-point hot-wire measurements at $\phi = 0$ deg and $\phi = 180$ deg. However, all these previous experiments could not distinguish between n

$= +1$ and $n = -1$. Experiments on leading-edge vortices over delta wings (Gursul, 1994) with the help of two-point pressure and velocity measurements by varying the azimuthal angle showed that $n = +1$. In all these swirling flows, vortex breakdown was the common feature. Thus, the evidence indicates that the flow in the breakdown region is unstable to helical disturbances. It should be noted that the helical mode instability is an indication of a centrifugal instability (Leibovich, 1984).

Several theoretical studies of helical mode instabilities in swirling flows are available (Lessen et al., 1974; Duck and Foster, 1980; Khorrami, 1991; Mayer and Powell, 1992). These researchers studied the stability of the Q-vortex, where the axial velocity profiles is represented as $W = \exp(-r^2)$. However, as discussed earlier by Panda and McLaughlin (1994), axial velocity profiles of the strongly swirling jets (with vortex breakdown), as in this experimental work, are different than the one given for the Q-vortex. The experimental velocity profiles are wake-like near the jet axis, but have a local maximum at a certain radius and vanish at large distances away from the axis. The shear layer around the wake profile can support the Kelvin-Helmholtz waves. It is also certain from the experimental investigations (Syred and Beer, 1974) that the helical mode instability exists in the vortex breakdown flow field of jets. Moreover, the growth of the Kelvin-Helmholtz instability waves around a strongly swirling jet (with vortex breakdown) is relatively small and vortex pairing is suppressed (Panda and McLaughlin, 1994). Therefore, the increased entrainment and spreading rates of strongly swirling jets cannot be related to the Kelvin-Helmholtz instability. It has been suggested by Panda and McLaughlin (1994) that the centrifugal instabilities may be responsible for larger entrainment in the shear layer. Although the exact mechanism for larger entrainment and spreading rates is not known, it can be argued that vortex breakdown plays an important role.

The helical mode instability (which is related to the centrifugal instability) may be a key aspect of the enhanced mixing and entrainment mechanism in strongly swirling jets. The purpose of the present investigation is to excite the helical mode instability of the vortex breakdown flow field. It is expected that this excitation may affect the development of the flow field and enhance the mixing and entrainment. Nonaxisymmetric forcing was applied to the breakdown flow field of a strongly swirling jet. This led to excitation of the helical mode at any desired frequency. Effects of forcing on the flow field were investigated.

2 Experimental Facility

Experiments were conducted in air using the setup shown in Fig. 1, which consisted of a stagnation chamber and a nozzle. The chamber has a circular cross-section of 38 cm in diameter and the nozzle diameter is 5 cm. The air, which is supplied by a blower, passes through a baffle, honeycomb and screens before
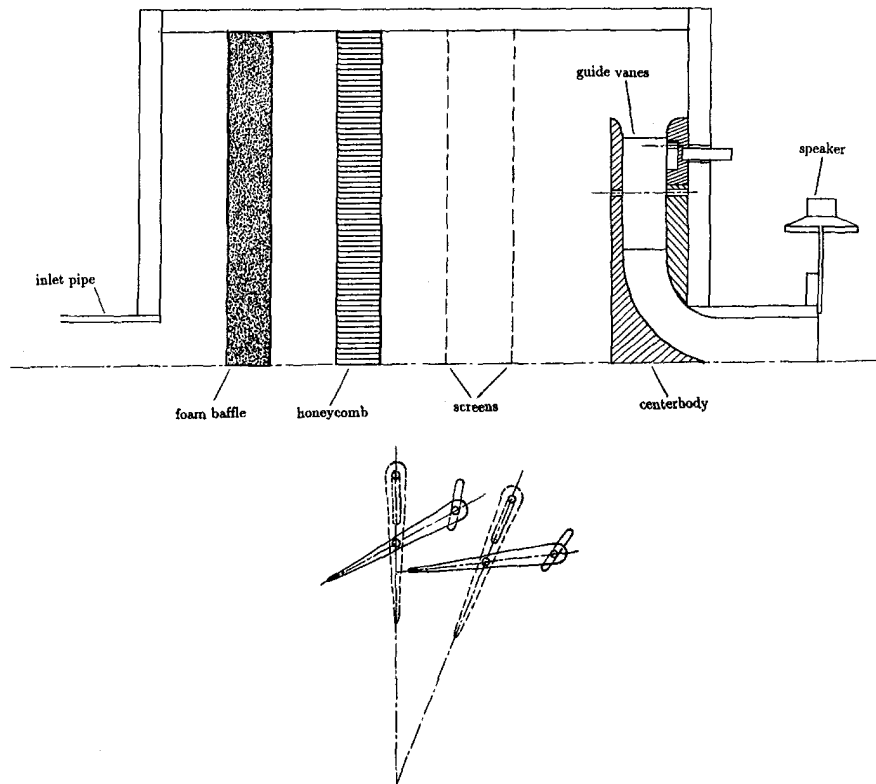
Fig. 1 Experimental setup (top); vane geometry and mechanism for swirl adjustment (bottom)

entering the swirl section. A set of guide vanes consisting of 16 streamlined foils, placed symmetrically in the azimuthal direction is used to generate swirl. The amount of swirl is controlled by adjusting the angle of the guide vanes. The turbulence level at the nozzle exit for the nonswirling jet was 0.5 percent.

The purpose of this experiment was to introduce perturbations to the core of the vortex whose vorticity originates from the boundary layer shed from the centerbody (see Figure 1). The nonaxisymmetric forcing was generated by a 25.4 cm diameter woofer connected to the jet exit by a tube of 3 mm diameter as shown in Fig. 2. The woofer was driven by a power amplifier and function generator. This type of forcing was shown to be effective because of pumping the fluid rather than emitting acoustic waves (Williams et al., 1991). Since the fluid is pumped periodically in the radial direction, the forcing induces radial velocity fluctuations on the axis and excites the first helical mode $|n| = 1$, which is the *only* mode that has nonzero
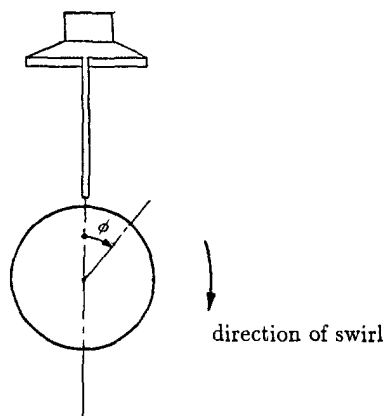

Fig. 2 Schematic of nonaxisymmetric forcing by woofer

radial velocity on the axis (Leibovich, 1984). For all other modes, the radial velocity must be zero on the centerline. (This comes from the requirement of bounded velocity on the axis of rotation and can be proved with the continuity equation (Lessen et al., 1974)). The rms velocity fluctuation level at the exit of the 3 mm diameter tube (with no jet flow) was measured with a hot-wire anemometer and was used as a reference for the forcing level. Since the forcing system is completely closed, there is no net mass addition. However, there is a net momentum addition (Williams et al., 1991). The dimensionless momentum coefficient is defined as the ratio of the momentum flux from the forcing tube to the momentum flux of the jet, $C = (v'/ \bar{U})^2 (d/D)^2$, in which v' is the rms velocity fluctuation level at the exit of the 3 mm diameter tube, $\bar{U}$ is the average axial velocity at the nozzle exit, d and D are the diameters of the forcing tube and nozzle respectively. Throughout the experiments, the momentum coefficient was kept constant at a very small value ($C = 0.0001$).

Near-field pressure measurements were made outside the jet with a piezoelectric transducer (PCB, model 103A). The pressure transducer is 5.6 mm high, 9.4 mm in diameter and has a pressure orifice measuring 2.54 mm in diameter. A single hot-wire probe was also used to monitor the spectral features of the unsteady flow. Pressure and velocity signals were processed by a two channel signal analyzer (HP 35660A). The time-averaged velocity measurements were made with a five-hole probe (United Sensor, 3.1 mm in diameter) connected to a differential pressure transducer (Setra, model 239). Although the probe interference resulting in premature breakdown is a concern in this type of flows, the velocity measurements are found much less sensitive to a probe placed sufficiently downstream of the breakdown point (where the axial velocity becomes zero) (Payne et al., 1989). In this study, the measurements were taken well downstream of the breakdown location and the near-field pressure fluctuations were monitored. There was no noticeable difference in pressure fluctuations with and without the velocity
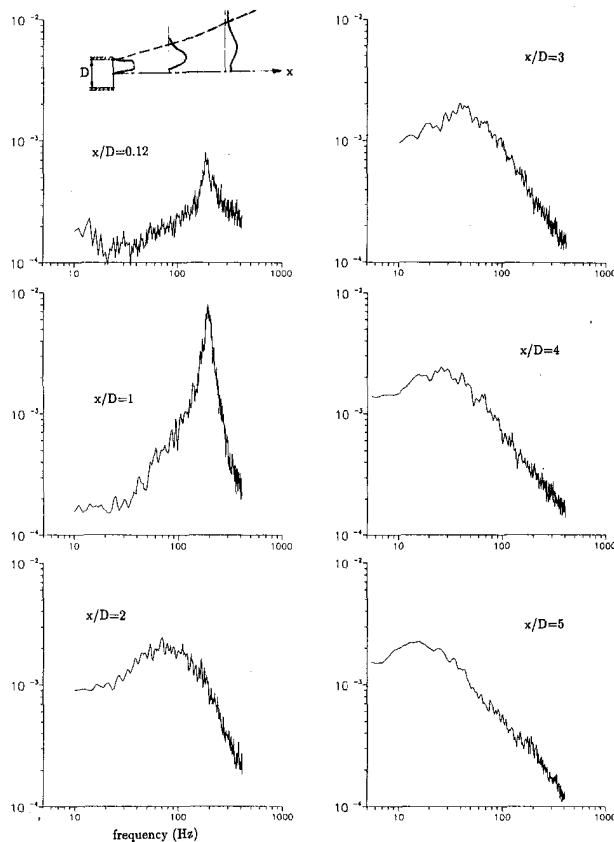
Fig. 3 Near field pressure spectra along the jet boundary for the unforced jet. Vertical scale is logarithmic in arbitrary units.

probe in the flowfield. Experimental uncertainty for mean velocity measured by the five-hole probe was estimated as 1 percent, based on the uncertainty in pressure measurements and the uncertainty in measuring the flow angles during the calibration process, using the standard procedures (Kline, 1985). The uncertainty for velocity fluctuations measured by the hot-wire probe was estimated as 3 percent, using the results given by Perry (1982). For pressure fluctuations, the uncertainty was estimated from the calibration of the pressure transducer as 5 percent. The location of the breakdown was observed by releasing smoke on the axis of the centerbody of the apparatus.

3 Results

For small amounts of swirl, the breakdown location is far downstream, and moves upstream with increasing swirl level. It enters the nozzle and reaches the centerbody for $\Gamma/\bar{U}D \geq 0.6$, where Γ is the circulation. The circulation at the trailing-edge of the swirl vanes was used in the swirl parameter $\Gamma/\bar{U}D$ and it was calculated from the geometry of the guide vanes (Sarpkaya, 1971). The experiments were carried out for $\Gamma/\bar{U}D = 0.82$, therefore the vortex breakdown is located near the centerbody. Detailed measurements of the azimuthal component of velocity with the five-hole probe provided a value of circulation that is 4 percent larger than the above estimate. The Reynolds number based on jet exit diameter was 50,000.

For the unforced jet, pressure spectra along the jet boundary are shown in Fig. 3. The jet boundary was defined as the location where the local mean velocity was 5 percent of the maximum jet velocity at the jet exit. The jet boundary is shown with the dashed lines (see inset in Figure 3) along with a sketch of the axial velocity profiles. The sharp peak near the jet exit is due to the fluctuations induced by the natural helical mode instability. This was verified by using two transducers and measuring

the phase angle between the two pressure signals at $x/D = 0.12$. The first transducer was located at $\phi = 0$ deg while the second one was located at different azimuthal angles (45, 90 and 180 deg). Cross-spectral analysis provided the phase angle between the pressure fluctuations measured with the two transducers. If the pressure fluctuations at $\phi = 0°$ and $\phi = \phi$ are represented as $\cos(\omega t)$ and $\cos(\omega t - \theta)$ respectively, variation of the phase angle θ is shown as a function of the azimuthal angle ϕ in Fig. 4. The slope of the straight line is 45° which means that the azimuthal wavenumber is unity ($n = 1$). Note that the positive azimuthal direction is the swirl direction (Fig. 2). It is also clear that the disturbance rotates in the same direction as the vortex. It is well known from linear stability theory (Lessen et al., 1974) that, for a jet-like axial velocity profile, the flow is most sensitive to the helical mode disturbances rotating in opposite direction to the mean swirl. These are the inviscid modes with the maximum growth rates two orders of magnitude larger than the viscous modes. However, as Khorrami (1991, p. 200) points out: ". . . the translation or inversion of the axial velocity affects the frequency only while the growth rate remains unchanged. This is correct but it should also be noted that inversion of the axial velocity profile causes the sign of the unstable azimuthal wavenumber, n, to change." For a wake-like velocity profile, the flow is most sensitive to the helical mode disturbances rotating in the same direction as the mean swirl. Since the breakdown flow fields always have wake-like axial velocity profile, they support instabilities rotating in the same direction as the main vortex. Although the theory cannot predict which azimuthal wavenumber will be amplified, the experiments in a tube (Garg and Leibovich, 1979), tip vortex (Singh and Uberoi, 1976) and leading-edge vortices over delta wings (Gursul, 1994) suggest that $n = 1$, whenever vortex breakdown occurs.

An attempt was made to compare the measured frequency of the helical mode instability with the results of the stability theory. The measured velocity profiles differ from that of the Q-vortex, except very near the nozzle exit, as will be shown later. The axial and swirl velocity profiles for the Q-vortex are given, respectively, in the following form:

$$W = \exp(-r^2)$$

$$V = q[1 - \exp(-r^2)]/r$$

Using the velocity profile at $x/D = 0.12$ and curve-fitting, the parameter q was found to be 1.04. Lessen et al. (1974) provided the axial wavenumber and phase speed of the most amplified disturbances for the first helical mode. By using this informa-
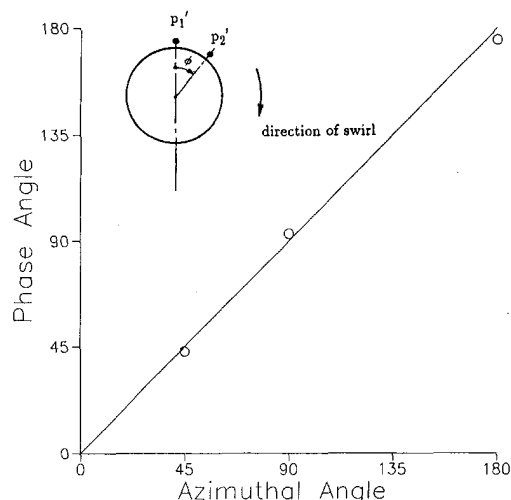

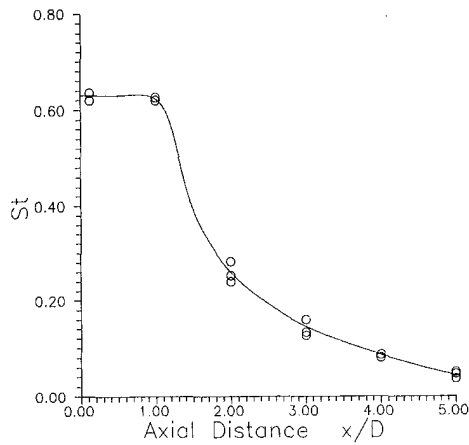**Fig. 4 Variation of phase angle as a function of azimuthal angle**

Fig. 5 Variation of Strouhal number as a function of streamwise distance

tion, the frequency was estimated as $f_{th} = 160$ Hz, while the dominant frequency of the spectrum in Figure 3 was $f_{exp} = 190$ Hz. The agreement is reasonable, considering the very rapid variations in the velocity profiles near the jet nozzle.

Returning to Fig. 3, the spectra near the jet exit, $x/D = 0.12$, and at $x/D = 1$ show approximately the same peak frequency. However, for $x/D \geq 1$, the peak of the spectra shifts to smaller frequencies with increasing streamwise distance, while the energy around the peak frequency becomes more distributed. Variation of the Strouhal number based on the peak frequency, St $= fD/\bar{U}$, as a function of streamwise distance is shown in Fig. 5. The rapid decrease of the peak frequency is believed to be due to the rapid spreading of the jet. The mean axial velocity profiles for swirling and nonswirling jets are shown at three different streamwise location in Fig. 6(a). The mean velocity distributions show that the jet diverges quickly for $x/D \geq 1$. For the swirling jet, the swirl velocity profiles (not shown here) are similar to a solid body rotation near the centerline and to a potential vortex at large distances from the centerline. The maximum axial and swirl velocity (normalized by the maximum axial velocity at the jet exit) are shown in Fig. 6(b) as a function of streamwise distance. The mean axial and swirl velocities decay very quickly with the streamwise distance. Since the first helical mode instability ($n = 1$) appears to be rotating at the solid body rotational speed (Roos and Kegelman, 1990; Syred and Beer, 1974), the rapid decrease of the swirl velocity is the reason for large changes in the Strouhal number.

In order to study the jet response to forcing, a single hot-wire probe was located at $r = D/2$ at different streamwise positions (for $\phi = 90$ deg). The excitation frequency was varied while keeping the momentum coefficient constant ($C = 0.0001$). This required adjustment of the input voltage to the acoustic driver. Since the acoustic pressure intensity strongly depends on forcing frequency, velocity fluctuations are a better measure of forcing. It should be kept in mind that the results are only qualitative, because the single hot-wire probe is sensitive to the magnitude of the velocity vector in the three-dimensional flow field. Figure 7 shows the amplitude of velocity fluctuations as a function of the forcing frequency. The frequency at which the amplitude of velocity fluctuations is maximum varies with streamwise distance. This most amplified frequency at a particular streamwise location is the same as the dominant frequency for the unforced jet (see Fig. 3) at the same location. This confirms that the helical mode instability is indeed excited with this forcing. The most amplified frequency varies accordingly as the local velocity profiles develop in the streamwise direction.

This result suggests that forcing at high frequencies (corresponding to $x/D < 1$) may not be effective. Therefore, it was decided to study the effect of forcing at lower frequencies. Forcing was applied at St $= fD/\bar{U} = 0.08$, which corresponds
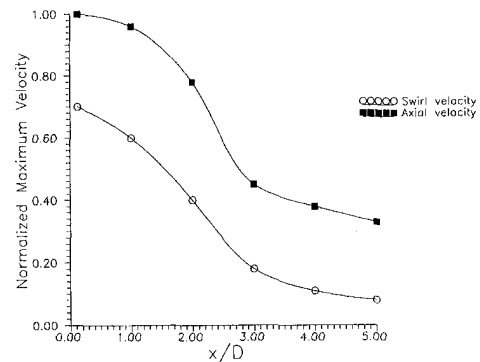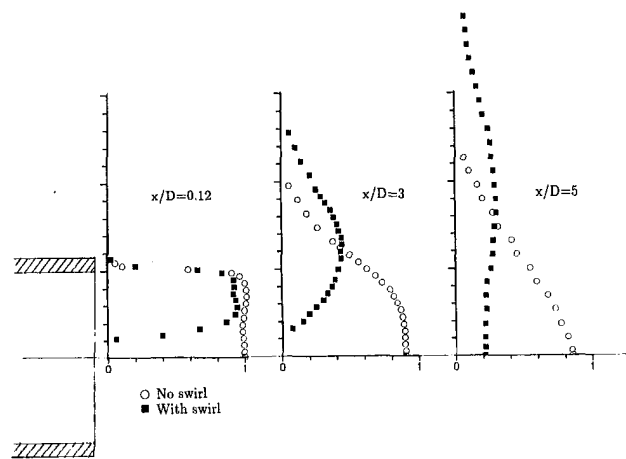

Fig. 6 (a) Axial velocity profiles for swirling and nonswirling jets (top); (b) normalized maximum axial and swirl velocities as a function of streamwise distance (bottom)

to the most amplified frequency for $x/D \approx 4$. The mean axial velocity distributions, with and without forcing, are compared in Fig. 8. The mean velocity measurements were carried out along the radius at azimuthal angle $\phi = 90$ deg. (Recall that forcing is applied at $\phi = 0°$). The symmetry checks showed that the mean flow is symmetrical within the measurement domain ($x/D \leq 5$). Due to the inability of the five-hole probe to detect reversed flow, no measurement is available near the axis around the jet exit. Figure 8 shows that, while there is not much difference near the jet exit, forcing increases the spreading of the swirling jet for $x/D \geq 2$. It should also be noted that the axial
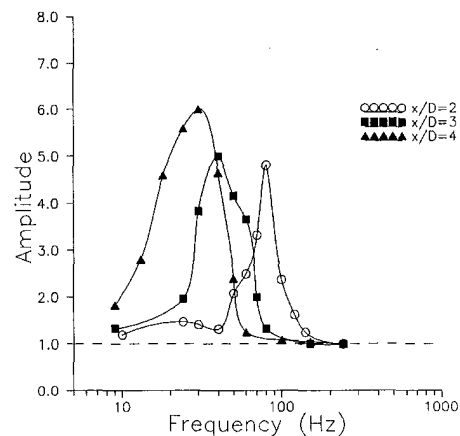

Fig. 7 Amplitude of the velocity fluctuations at $r = D/2$ normalized by the value for unforced case as a function of the forcing frequency
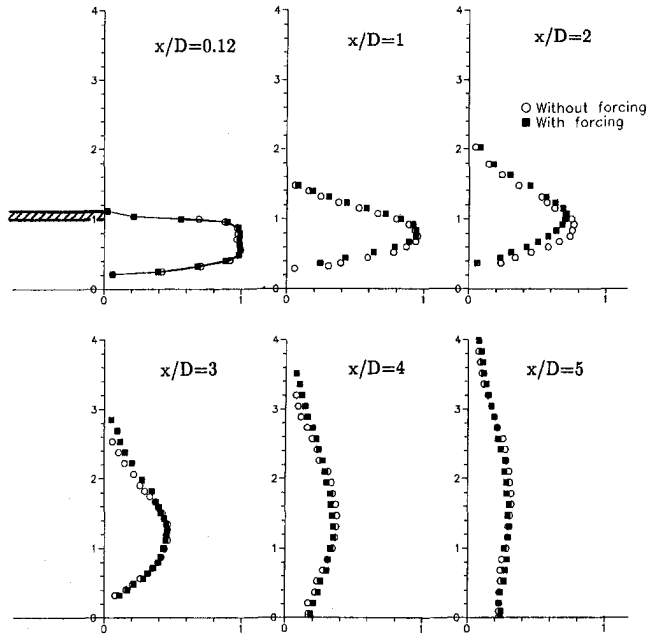
Fig. 8 Mean axial velocity profiles for unforced and forced (St = 0.08) jets

Fig. 10 Near field pressure spectra along the jet boundary for unforced (dashed lines) and forced (solid line) jets. Vertical scale is linear in arbitrary units, St = 0.08. Forcing frequency is indicated with an arrow.

velocity profiles near the nozzle exit and farther downstream are very different. Initially, the velocity profile is wake-like with reversed flow around the axis. Except for the thin region of boundary layer near the wall, the axial velocity is fairly uniform in the rest of the profile. This profile is similar to the Q-vortex (which was studied extensively by Lessen et al., 1974), if the boundary layer near the wall is neglected. On the other hand, farther downstream, the velocity profiles show a minimum on the axis and have a local maximum at a certain radius and vanish at large distances away from the axis.

The variation of momentum thickness for two different forcing frequencies is shown together with that of the unforced jet in Fig. 9. The forced jets become thicker than the unforced jet. At the higher forcing frequency, the enhanced spreading of the jet starts earlier. However, at large distances, the two cases reach approximately the same momentum thickness. Comparison of near-field pressure spectra along the jet boundary for the unforced and forced jet is shown in Fig. 10 for St = 0.08. It is evident that the dominant frequencies of the spectra of the unforced jet are still observed for the forced jet. The amplitude at the forcing frequency is very small near the jet exit. The spectra show the growth of the amplitude at the forcing frequency up
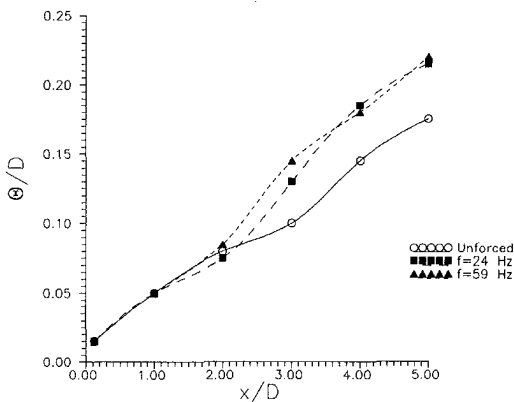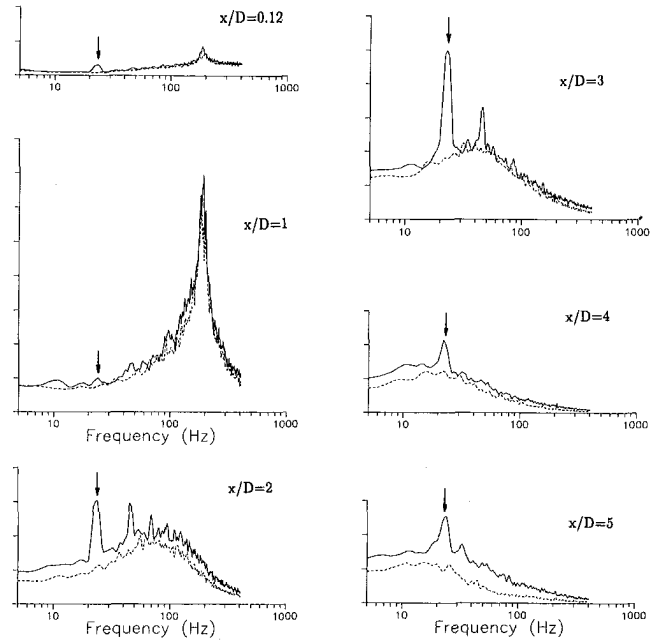
to x/D = 3, thereafter a gradual decay. Higher harmonics of the forcing frequency are also observed in the spectra for x/D = 2 and 3. The energy of the fluctuations appears to increase with forcing. The variation of rms pressure fluctuations along the jet boundary for unforced and forced jets is compared in Fig. 11. All the evidence presented here indicates that the helical mode becomes more energetic as a result of forcing. This, in turn, increases the spreading of the jet. Although the exact mechanism of how the forcing produces increases in jet spreading is not clear, its relation to the helical mode instability of vortex breakdown flowfield has been demonstrated.

4 Conclusions

Nonaxisymmetric forcing was applied to the vortex breakdown flowfield of a strongly swirling jet and its effects were investigated. Due to the large swirl parameter, vortex breakdown was already located inside the jet nozzle for the unforced jet. It was shown that, for the unforced jet, periodic oscillations are due to the helical mode instability of the vortex breakdown
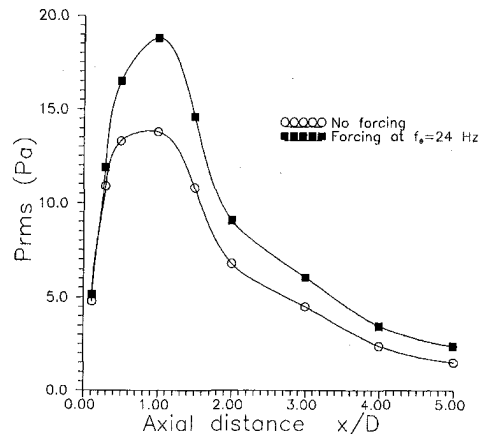

Fig. 9 Variation of momentum thickness for unforced and forced (St = 0.08 and 0.20) jets

Fig. 11 Variation of rms pressure fluctuations along the jet boundary for unforced and forced jets, St = 0.08

flowfield. The dominant frequency detected in the spectrum decreases quickly in the streamwise direction due to the rapid spreading of the jet. Radial velocity perturbations generated by a woofer were introduced into the flow near the jet exit. The radial velocity fluctuations induced on the axis excite the first helical mode, which is the only mode that has nonzero radial velocity on the axis. With this closed forcing system, zero net mass is added, however, there is nonzero momentum addition. The mean velocity profiles show that forcing increases the spreading of the swirling jet. The initial variation of momentum thickness depends on the forcing frequency, whereas the asymptotic behavior is the same. It is concluded that the helical mode becomes more energetic as a result of the forcing and increases the spreading of the jet. It should be noted that this has been achieved for an extremely low level of excitation (momentum coefficient $C = 0.0001$).

Acknowledgment

References

Burggraf, O., and Foster, M. R., 1977, "Continuation or Breakdown in Tornado-Like Vortices," *Journal of Fluid Mechanics*, Vol. 80, Part 4, pp. 685–703.

Cassidy, J., and Falvey, H. T., 1970, "Observations of Unsteady Flow Arising After Vortex Breakdown," *Journal of Fluid Mechanics*, Vol. 41, pp. 727–736.

Chanaud, R. C., 1965, "Observations of Oscillatory Motion in Certain Swirling Flows," *Journal of Fluid Mechanics*, Vol. 21, pp. 111–127.

Duck, P. W., and Foster, M. R., 1980, "The Inviscid Stability of a Trailing Line Vortex," *Journal of Applied Mathematics and Physics (ZAMP)*, Vol. 31, pp. 524–532.

Escudier, M., 1987, "Confined Vortices in Low Machinery," *Annual Review of Fluid Mechanics*, Vol. 9, pp. 27–52.

Escudier, M., 1988, "Vortex Breakdown: Observations and Explanations," *Progress in Aerospace Sciences*, Vol. 25, pp. 189–229.

Falvey, H. T., 1971, "Draft Tube Surges. A Review of Present Knowledge and an Annotated Bibliography," US Bureau of Reclamation, Rep. REC-ERC-71-42.

Garg, A. K., and Leibovich, S., 1979, "Spectral Characteristics of Vortex Breakdown Flowfields," *The Physics of Fluids*, Vol. 22, pp. 2053–2064.

Gursul, I., 1994, "Unsteady Flow Phenomena over Delta Wings at High Angle of Attack," *AIAA Journal*, Vol. 32, No. 2, pp. 225–231.

Hall, M. G., 1972, "Vortex Breakdown," *Annual Review of Fluid Mechanics*, Vol. 4, pp. 195–217.

Khorrami, M., 1991, "On the Viscous Modes of Instability of a Trailing Line Vortex," *Journal of Fluid Mechanics*, Vol. 225, pp. 197–212.

Kline, S. J., 1985, "The Purpose of Uncertainty Analysis," ASME JOURNAL OF FLUIDS ENGINEERING, Vol. 107, June, pp. 153–160.

Leibovich, S., 1984, "Vortex Stability and Breakdown: Survey and Extension," *AIAA Journal*, Vol. 22, pp. 1192–1206.

Lessen, M., Singh, P. J., and Paillet, F., 1974, "The Stability of a Trailing Line Vortex. Part 1. Inviscid Theory," *Journal of Fluid Mechanics*, Vol. 63, pp. 753–763.

Lugt, H. J., 1983, *Vortex Flow in Nature and Technology*, John Wiley, New York, pp. 191–194.

Mayer, E. W., and Powell, K. G., 1992, "Viscous and Inviscid Instabilities of a Trailing Vortex," *Journal of Fluid Mechanics*, Vol. 245, pp. 91–114.

Panda, J., and McLaughlin, D. K., 1994, "Experiments on the Instabilities of a Swirling Jet," *Physics of Fluids*, Vol. 6, pp. 263–276.

Payne, F. M., Ng, T. T., and Nelson, R. C., 1989, "Seven Hole Probe Measurement of Leading-Edge Vortex Flows," *Experiments in Fluids*, Vol. 7, pp. 1–8.

Peckham, D. H., and Atkinson, S. A., 1957, "Preliminary Results pf Low Speed Wind Tunnel Tests on a Gothic Wing of Aspect Ratio 1.0," Aero. Res. Council., CP 508, pp. 16–17.

Perry, A. E., 1982, *Hot-Wire Anemometry*, Oxford University Press, New York.

Roos, F. W., and Kegelman, J. T., 1990, "Recent Explorations of Leading-Edge Vortex Flowfields," NASA High Angle-of-attack Technology Conference, NASA Langley Research Center, VA, Oct. 30–Nov. 1.

Sarpkaya, T., 1971, "On Stationary and Traveling Vortex Breakdowns," *Journal of Fluid Mechanics*, Vol. 45, pp. 545–559.

Singh, P. I., and Uberoi, M. S., 1976, "Experiments on Vortex Stability," *The Physics of Fluids*, Vol. 19, No. 12, pp. 1858–1863.

Syred, N., and Beer, J. M., 1974, "Combustion in Swirling Flows: A Review," *Combustion and Flame*, Vol. 23, pp. 143–201.

Williams, D., Acharya, M., Bernhardt, J., and Yang, P., 1991, "The Mechanism of Flow Control on a Cylinder with the Unsteady Bleed Technique," AIAA 91-0039, 29th Aerospace Sciences Meeting, January 7–10, 1991, Reno, NV.

K. R. Mutama
Ventilation & Air Conditioning Engineer,
BHP Copper Inc.,
Box M,
San Manuel, AZ 85631
Assoc. Mem. ASME

A. E. Hall
Associate Professor.
Ventilation Laboratory
University of British Columbia,
Department of Mining & Mineral
Process Engineering,
6350 Stores Rd.,
Vancouver, B.C. Canada V6T 1Z4

The Experimental Investigation of Jet Fan Aerodynamics Using Wind Tunnel Modeling

Jet fan aerodynamic behavior was investigated using wind tunnel modeling. Conditions were created to simulate mine and vehicular tunnel ventilation where these fans are finding increased application. Results showed that the ability of a jet fan to entrain air depends on its proximity to the tunnel wall. Moving the jet fan toward the wall increased the initial pressure drop below ambient in a significant length of the tunnel. This increased the volume of air entrained despite the existence of a large recirculation eddy or back flow whose size diminished as the jet fan was traversed toward the tunnel axis. When the jet fan was located at the tunnel axis the flow was very unstable close to the walls of the tunnel and it had a tendency to reverse itself with periods coinciding with the jet oscillation behavior. The complete set of measurements obtained are suitable for CFD code validation and modeling.

Introduction

Jet fans are free-standing, unducted axial flow fans used in mine and vehicular tunnel longitudinal ventilation. Their application in mining operations includes pressure boosters and ventilation of development ends, underground workshops, battery charging bays, pump and machine chambers. In industrial applications, they are used for road tunnel ventilation, cooling of furnaces and kilns, degassing of tanks and ship hulls; and ventilation of service tunnels during repairs. They operate by discharging an air jet in the area to be ventilated.

The jet fan exchanges its momentum with the surrounding secondary air in exactly the same manner as jet pumps, hence the fan delivers a volume much greater than its own inlet volume. Abramovich (1963) describes the air distribution in a dead end channel supplied by a jet. In underground mine auxiliary ventilation, jet fans are used to boost air pressure and to direct airflow where mining operations are in progress. The usual mining practice is to use a ducted system in which a long tube conveys the air from the fan. The disadvantage of a ducted system is that it results in very high velocities at discharge but relatively low velocities throughout the body of the opening. It restricts the cross section of the opening available for the passage of machinery. High velocities in long ducts of small area result in large energy costs. Ducts have to be replaced frequently because of damage which causes excessive leakage. Jet fan ventilation is very effective because it uses the opening itself as a duct and can be operated remotely with the aid of computer control.

Jet fan mine ventilation research has been very limited. Matta et al. (1978) used sulfur hexafluoride (SF6) tracer gas to determine the effectiveness of a jet fan in distributing fresh air in large mine openings and purging gaseous pollutants. Thimons et al. (1986) showed that jet fans were effective in clearing diesel exhaust and methane gases whereas a ducted fan system was more effective in clearing out mine blast gases and methane layering. Mizuno and Araie (1990) observed that as much as 15 percent of the momentum is lost due to friction when the jet fan is in contact with the wall in their model tunnel experiment.

Ventilation is necessary in vehicular tunnels in order to avoid build up of toxic exhaust emissions from automobiles. In the event of a fire, fumes are cleared. The present work is aimed at improving jet fan ventilation design by providing some fundamental data on the subject. The main objectives of this study were to study the pressure and flow field of a jet fan traversed from one wall to the axis of a tunnel. The optimum positioning of the jet fan can be obtained by understanding its aerodynamic characteristics. This is of paramount importance in mine and automobile tunnel ventilation design. There is a lack of comprehensive data on jet fans, and more studies are required to address the subject fully.

Experimental Apparatus and Methodology

Figures 1 and 2 describe the apparatus used in this investigation which comprises (i) a wind tunnel and (ii) a jet fan simulation mechanism. The wind tunnel was specifically designed for airflow studies in mines and tunnels. The wind tunnel design, construction, and testing is described by Mutama and Hall (1993) and is of 900 by 900 mm square cross section, suction type. The wind tunnel working section is over 8 metres long and its sides are made of plexiglass. Thirty-six static pressure holes are drilled on the north wall side of the tunnel as shown in Fig. 1(a). The south wall side of the tunnel has six sets of 5 holes positioned as shown in Fig. 1(b). Each set of 5 holes from the tunnel roof to the floor comprises one measurement station and the holes are 150 mm apart vertically. Complete velocity and pressure traverses can be made on the entire cross section and length of the tunnel. The jet fan was simulated by an aluminum pipe 100 mm in diameter connected to a centrifugal blower which supplied the airflow. An air jet of velocity range 20–40 m/s which represents the typical jet fan outlet velocities was the important aspect of this simulation. The pipe was inserted 12 jet nozzle diameters inside the tunnel. The jet fan to wind tunnel diameter ratio D_R was 0.11. Figure 2 shows a cross section of the jet fan—tunnel system. The jet fan simulation mechanism is mounted on traversing rails and can be made to slide from the north wall to the axis of the wind tunnel, at half its height of 450 mm from the roof as shown in Fig. 2.

Figure 3 shows a diagrammatic layout of the instrumentation used. Velocity measurements were performed using a hot wire anemometer probe and also a multi function digital micromanometer in conjunction with a pitot static tube. The velocity readings were recorded on a data logger or an IBM PC. An electronic vane anemometer of 25 mm diameter specially adapted for this study was used to determine the magnitude and direction of the flow and could be traversed across the wind

Pressure hole positions (mm) from jet nozzle							
No.	mm	No.	mm	No.	X mm	No.	X mm
1	150	10	1870	19	3760	28	5550
2	330	11	2050	20	3940	29	5730
3	510	12	2230	21	4120	30	5910
4	690	13	2580	22	4300	31	6190
5	870	14	2760	23	4480	32	6370
6	1050	15	2940	24	4660	33	6550
7	1330	16	3120	25	5010	34	6730
8	1510	17	3300	26	5190	35	6910
9	1690	18	3480	27	5370	36	7090

(a) Tunnel North Wall showing static pressure holes

(b) South wall showing hot wire probe access holes
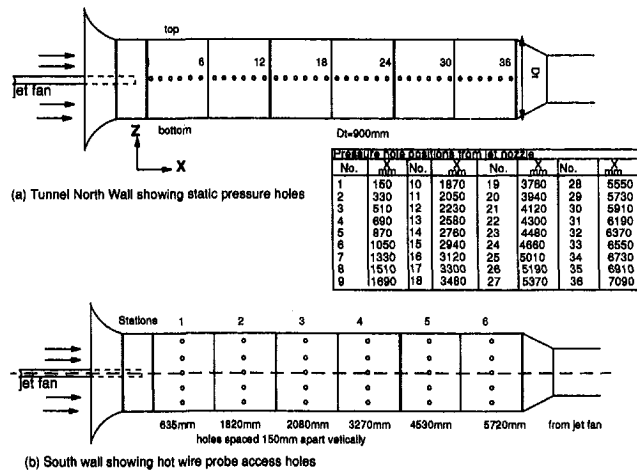
Fig. 1 Details of wind tunnel sides (not to scale)

Legend

Tunnel diameter Dt=900mm

Fp is normalized jet fan position from wall (Y/Dt)

Fp values 0.06, 0.11, 0.17, 0.22, 0.28, 0.33, 0.39, 0.44, 0.5

Fig. 2 Cross-sectional view of jet fan traverse across tunnel

tunnel. All the velocity and pressure traversing probes were coupled to an electronic traversing ruler. Pressure measurements were carried out using an array of transducers connected to an analog-digital data acquisition board.

The fan was set to deliver jets with outlet velocities of 20.8 and 40 m/s, corresponding to Reynolds numbers of 13714 and 26374, respectively. The jet fan position was varied from the wall contact to the tunnel axis position. The first task was to record axial static pressure distributions on both sides of the wind tunnel. A large number of readings were recorded for each static pressure position so that a representative average could be determined.

Complete tunnel cross-sectional velocities were determined at first and were sufficient to define the flow in two dimensions at the height of 450 mm from the tunnel floor for all the six stations and at each fan position. A complete velocity grid was obtained at downstream positions of $X/D_j = 45.3$ and 57.2 in order to obtain the total tunnel flow rate.

Results and Discussion

The complete set of measurements obtained characterizes the aerodynamics of a jet fan traversed at different positions in relation to the tunnel walls. The results give a clear picture of the pressure and flow fields established in the tunnel. Figure 4 typifies the axial development of pressure and velocity measurements for a jet fan positioned at $F_p = 0.17$. F_p is the fractional distance (Y/D_t) from the north wall to the axis of the tunnel (see Fig. 2). Flow field measurements were used to determine the total volume flow out of the tunnel and the air entrainment rate of the jet fan at various positions. Uncertainties in measured and derived quantities are quoted below each figure.

Pressure Measurements

Pressure results are necessary in the understanding of entrainment and the pressure rise characteristic is important in the calculation of power performance curves. A detailed analysis of the pressure variation is described and the pressure field was found to be affected significantly by the positioning of the jet

————— Nomenclature —————

A_j = area of jet fan nozzle (m^2)
$A_e = (A_t - A_j)$ inlet area for the entrained flow (m^2)
A_t = cross-sectional area of tunnel (m^2)
D_R = diameter ratio (D_j/D_t)
D_j = diameter of jet fan nozzle (meters)
D_t = diameter of tunnel (meters)
E_{in} = energy in jet fan flow (J/s)
E_{out} = energy in the tunnel discharge flow (J/s)
E_{fl} = frictional energy loss (J/s)
E_r = recirculation energy loss (J/s)
E_{ml} = mixing energy loss (J/s)
E_{fl} = jet energy loss (J/s)
F_p = fractional diameter of tunnel (Y/D_t) used to define jet fan traverse from one tunnel wall
Y = distance of jet fan traverse from one tunnel wall
P = pressure (N/m^2)
P_e = pressure of the entrained flow
P_j = total pressure of the jet at the nozzle
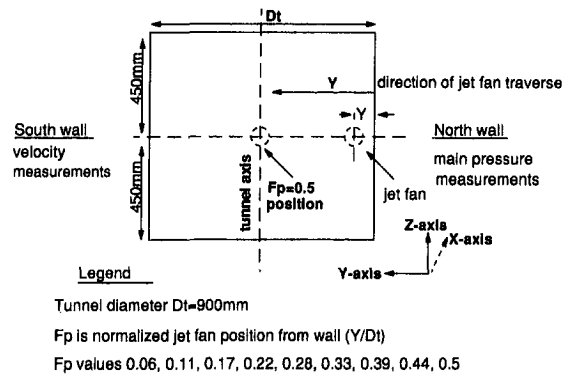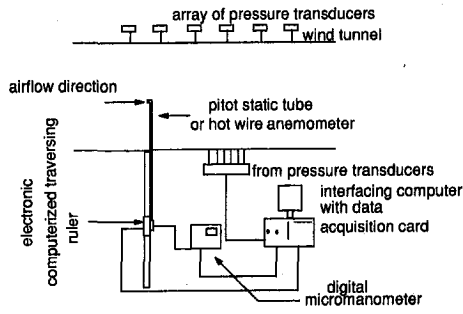P_{tn} = static pressure of the tunnel flow

$(P_{tn} - P_e)_{exp}$ = measured pressure difference between entrained flow and tunnel end
$(P_{tn} - P_e)_{th}$ = theoretical pressure difference between entrained flow and tunnel end for zero friction loss
Q_j = jet discharge flow (m^3/s)
Q_e, Q_s = entrained or secondary flow (m^3/s)
$Q_T = (Q_e + Q_i)$ total tunnel flow (m^3/s)
Q_R = recirculated volume flow (m^3/s)
n = m$_e$/m$_j$ = Q_e/Q_j flow ratio of secondary stream to jet discharge quantity
m_e = entrained mass flow
m_j = jet discharge mass flow
U = velocity (m/s)
E_u = velocity of entrained flow
U_j = jet fan discharge velocity (m/s)
U_t = average tunnel velocity (m/s)

U_c = tunnel centreline or axis velocity (m/s)
u' = turbulence fluctuation
$\sqrt{u'^2}/U_c$ = rms or turbulence level of the fluctuating velocity at the tunnel axis
W_R = width of back flow at any axial distance (meters)
W_R/D_t = dimensionless backflow width
X = axial distance from jet fan nozzle (meters)
X/D_j = dimensionless distance from jet fan nozzle
η_i = induction efficiency defined by Eq. 3
Φ = tunnel to jet velocity ratio U_t/U_j ratio
$\theta = (Q_j + Q_s)(D_j/2)/(Q_jD_t)$ Thring and Newby similarity parameter
$C_t = \theta$ Craya-Curtet parameter for ducted confined jets
$\alpha = A_j/A_e$ area ratio of jet fan to secondary stream inlet area
$\Omega = A_j/A_t$ area ratio of jet fan to tunnel ρ air density (kg/m^3)

Fig. 3 Arrangement of instrumentation

fan. Figures 5(a), 5(b), 5(c), and 5(d) show the axial static pressure variation at the jet fan positions F_p of 0.06, 0.11, 0.17, 0.22, 0.28, 0.33, 0.39, 0.44, and 0.5. The wall static pressures are normalized by the jet dynamic pressure $(1/2 \ \rho u_j^2)$. The symbol P_e denotes the suction or entry pressure of the entrained or secondary stream measured at about $X/D_j = -10$ and is almost close to ambient in this experiment. In Fig. 5(a) at the position $F_p = 0.06$, the axial static pressure starts by rising from slightly above ambient i.e., above the zero pressure line to a peak of 0.9 percent of jet exit dynamic pressure at 4 nozzle diameters after which it drops significantly below ambient. At 18 nozzle diameters the pressure rises slightly and then drops to a minimum of -0.009 jet discharge dynamic pressure at 27 nozzle diameters. It rises monotonically to its maximum of just 1.5 percent jet discharge dynamic pressure and remains invariant with axial distance after 50 nozzle diameters over the tunnel test section. The same pattern of variation is observed for the jet fan positions F_p of 0.11 and 0.17 except that the initial peaks occur at 9 and 15 nozzles diameters respectively and minimum pressure is attained at around $X/D_j = 25$. The fan position $F_P = 0.06$ experiences the largest pressure drop for $X/D_j \leq 30$. In all cases the rate of pressure rise is similar and the maximum pressure values achieved are close.

The variation of static pressure for F_p values of 0.22, 0.28, 0.33, 0.39, 0.44 and 0.5 (Fig. 5(b)) show remarkable similarity. The pressure drops to a minimum at about 19 nozzle diameters after which it rises to a maximum of about 1.7 percent of jet discharge dynamic pressure and remains unchanged over the tunnel test section. The initial static pressure variation described for $F_p < 0.22$ differs somewhat from that of $F_p > 0.17$, because at $F_p \geq 0.22 < 0.5$ maximum pressures are attained at about $X/D_j = 40$ and at around $X/D_j = 50$ for $F_p \leq 0.17$. On the south tunnel side ($F_p = 0.83$, Figure 5(c)) pressure development is much more rapid.

In Figs. 5(c) and 5(d) wall static pressures are presented for two jet outlet velocities of 20.8 and 40 m/s and at $F_p = 0.17$, 0.33 and 0.83. The normalized pressure magnitudes are similar up to $X/D_j = 30$ for $F_p = 0.17$ and $X/D_j = 15$ for $F_p = 0.33$. The normalized peak pressures are lower for the lower discharge velocity. The actual measured peak pressures (in pascals) differ by a factor of 5 to 6 for the two jet fan discharge velocities. Figure 5(c) and 5(d) show that for similar F_p settings confining walls rather than the jet Reynolds number play a major role in the pattern or qualitative manner in which the pressure varies.

For $F_p \leq 0.17$ the pressure variation can be explained partly due to the jet being unable to expand freely on the side close to the wall. On reaching the wall it experiences wall friction and is deflected inwards after which the pressure falls again to reach a negative minimum. From there it rises until it attains a maximum. Therefore the proximity to the confining walls affects the sign and steepness of the pressure gradient and consequently the mixing process of the primary and secondary streams. The momentum distribution and boundary layer growth are also affected. The situation is simpler at $F_p \geq 0.22$ where the pressure falls and rises monotonically to reach a peak which is maintained over the tunnel test section. The jet development in all cases can be summarized as in Fig. 4 but for jet fan position $F_p \geq 0.22$ the pressure development within $X/D_j \leq 20$ is less complex. It is worth pointing out that there is no noticeable variation in wall static pressure for each side of the tunnel, in the vertical distance Z (normal to the X-axis). The wall static pressure measured on the south side of the tunnel develops more rapidly than that on the opposite (north) side where the jet fan is traversed from. The pressure rise is also much steeper on the south side where jet fan position $F_p \geq 0.5$ (see Fig. 5(c) for $F_p = 0.83$). Thus the axial static pressure variation is not symmetrical even though the same pattern is followed.

In Fig. 6 the measured to theoretical tunnel end pressure rise $(P_{tn} - P_e)_{\text{exp}}/(P_{tn} - P_e)_{th}$ at $X/D_j > 50$ is plotted as a function of jet fan position F_p. The pressure $(P_{tn} - P_e)_{th}$ is calculated from the momentum balance equation of the jet, entrained air and total tunnel flow for zero friction loss:

$$(P_{tn} - P_e)A_t = m_j U_j + m_e U_e - m_t U_t \qquad (1)$$

The symbols m, U and A represent mass flow, velocity and area. The subscripts j, e, and t denotes conditions for the jet fan, secondary stream and tunnel respectively. Equation (1) can be expressed in terms of the jet outlet velocity by using continuity relations to become:

$$P_{tn} - P_e = \alpha \rho U_j^2 (1 - \alpha n)^2 \qquad (2)$$
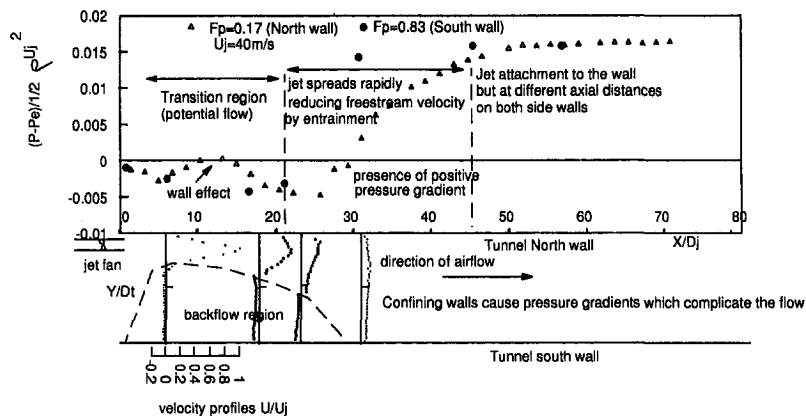

Fig. 4 Axial static pressure plotted together with velocity U/Uj (position of jet fan is $F_p = 0.17$ backflow region is clearly shown) (uncertainty in U/Uj is 2.75 percent and in normalised pressure is 2.67 percent)
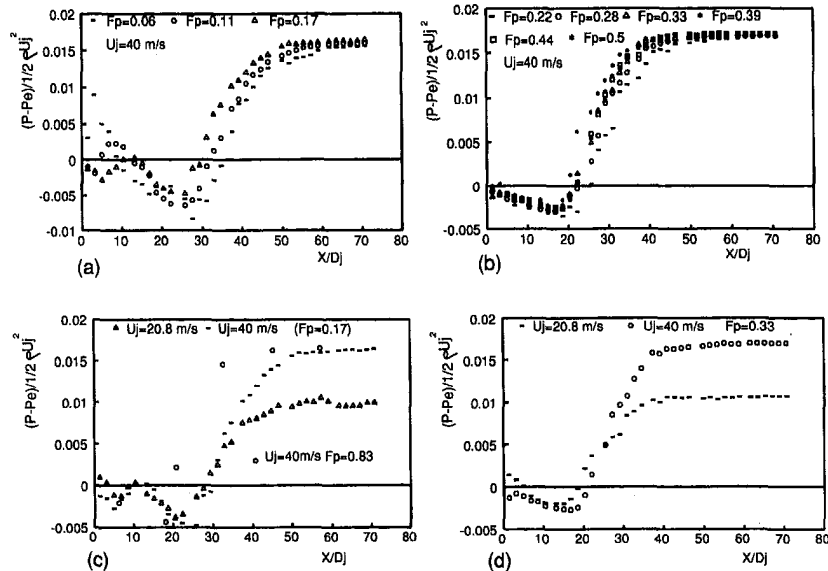
Fig. 5 Axial wall static pressure variation at various positions (uncertainty in normalized pressure is 2.67 percent)

where α, n and ρ are the jet fan outlet to secondary flow entry area ratio (A_j/A_e, $A_e = A_t - A_j$), flow ratio (m_e/m_j or Q_e/Q_j) and air density respectively. The symbol P_e denotes the secondary stream entry pressure (at about $X/D_j = -10$) and P_{tn} is the maximum pressure achieved by the mixed flow in the tunnel, downstream of the jet discharge ($X/D_j \gg 0$). The tunnel end pressure rise is higher when the jet fan is moved away from the wall. When the jet fan is close to the wall ($F_p = 0.06$) the measured pressure rise is 15% less than the theoretical one. Mizuno and Araie's (1990) also observed that measured pressure was less than the theoretical pressure when the jet was close to the wall. The difference between theoretical and measured tunnel end pressure rise is about nine percent when the jet fan is at the axis of the tunnel. In Fig. 6 another pressure ratio ($P_{tn} - P_e$)/($P_j - P_{tn}$) is plotted against fan position. The total pressure P_j is measured at the jet nozzle discharge. This ratio in essence is the excess pressure rise of the mixed flow to the pressure drop of the jet flow. It is also observed that this pressure ratio is higher for $F_p \geq 0.33$ than $F_p < 0.33$. Therefore the pressure or momentum of the jet is affected quite significantly by the closeness of the jet fan to the wall.

Velocity Measurements

The velocity profile results describe the axial jet development as shown in Fig. 7. The profiles show a back flow on one tunnel side for jet fan positions closer to the wall. The back flow diminishes when the jet fan is moved toward the tunnel axis. In Fig. 7(a) at jet fan position $F_p = 0.06$ the back flow covers $\frac{2}{3}$ of the tunnel diameter at $X/D_j = 6.35$. Jet fan positions $F_P > 0.33$ up to the tunnel axis position ($F_P = 0.5$) have no active reverse current. However, at the tunnel axis position ($F_P = 0.5$) within $\frac{1}{6}$ of D_t from the side walls the flow is very unstable because it produces both positive and negative velocities in periods of 2 to 4 seconds. In Fig. 7(d) only the negative velocities are shown in the regions where this flow instability occurs. Thus the nature of the backflow observed for jet fan positions $F_P \leq 0.33$ (Figs. 7(a) to 7(c)) is different from the tunnel wall flow instability observed for the tunnel axis position. At all the positions the jet was observed to oscillate when thin cotton wool "whiskers" were attached on either side of the discharge nozzle. The back flow was visualized using strips of ribbons of half the tunnel height in length fastened to a common string and attached across the wind tunnel. The flow visualiza-

tion revealed the presence of a back flow clearly and also confirmed the strong shear between the mainstream and the backflow. Figures 7 and 8 show that backflow diminishes as F_p is increased.

Figures 7(b) and 7(c) show the velocity profiles for jet fan positions F_p of 0.17 and 0.33 at 6.35, 18.2, 20.8 and 32.7 nozzle diameters. The magnitudes of the negative velocities were quite significant and in some cases up to $-0.075U_j$. At the jet fan position $F_p = 0.5$ the flow profiles are symmetrical.

An approximate theory on confined jets and recirculation was developed by Curtet (1958) in an attempt to give a full account of the effects of furnace walls and the surrounding environment on turbulent diffusion flames for a jet located on the duct axis ($F_p = 0.5$). Higher velocities were used and the amount of secondary fluid entrained by the jet was controlled and backflow was obtained under these conditions on both walls of the confining duct. The resulting profiles resemble those from the present study for ($F_p = 0.5$) as in Fig. 7(d). The Craya-Curtet parameter C_t which is similar to Thring and Newby (1953) similitude parameter $\theta = (Q_j + Q_s)(D_j/2)/Q_jD_t$ defines a possibility of recirculation. The terms Q_j, Q_s, D_j and D_t are the jet discharge, secondary stream flow, jet diameter, and tunnel diameter respectively. For values of C_t of around 0.075 the extent of the back flow is quite significant decreasing with increase of C_t. According to Barchilon and Curtet (1964) at C_t above 0.9 the back flow is absent. In this study the values of C_t are less than 0.25 and recirculation is observed at all jet fan
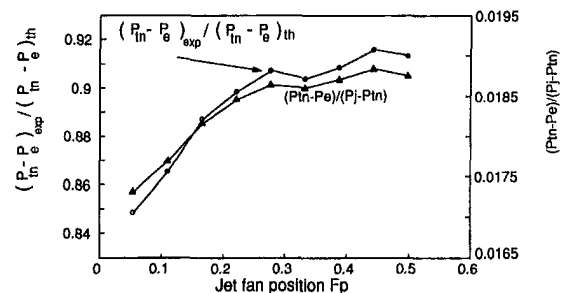

Fig. 6 Pressure ratio versus jet fan position (uncertainty in $(P_{tn} - P_e)_{exp}/(P_{tn} - P_e)_{th}$ is 1.44 percent); (uncertainty in $(P_{tn} - P_e)_{exp}/(P_j - P_{tn})$ is 2.77 percent)
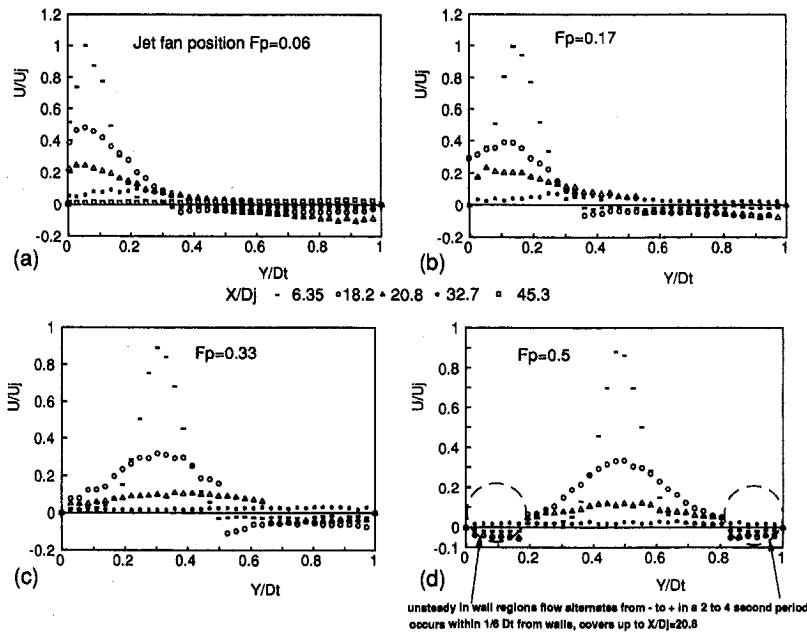
Fig. 7 Velocity profiles of tunnel at various jet fan positions, U_j = 40 m/s (uncertainty in U/U_j is 2.75 percent)

positions $F_p < 0.44$. Recirculation in most cases occurs when the jet has entrained all the surrounding secondary fluid and then entrains its own fluid upon reaching the confining walls. The controlling factors for the onset of backflow are the jet fan and tunnel diameter ratios (D_j/D_t), fan position F_p, velocity ratio U_t/U_j and the presence of a severe pressure gradient. Figure 9 shows the backflow as a fraction of both the jet discharge (Q_R/Q_j), and total tunnel flow (Q_R/Q_T). The backflow fraction Q_R/Q_j falls with jet fan position from 1.4 to about 1.15. The backflow fraction Q_R/Q_T changes relatively little with position ($F_p \leq 0.33$) and is around 0.72. Backflow must be understood because it wastes energy and in certain mine ventilation situations, unwanted pollutants are recirculated.

Longitudinal Turbulence Levels

The importance of longitudinal turbulence levels was to establish whether they enhanced entrainment rates and to help understand the structure of the flow field at the tunnel axis. Longitudinal turbulence levels are plotted in Fig. 10 for three jet fan positions F_p of 0.06, 0.33 and 0.5. They were measured from 6.35 nozzle diameters and onwards at the tunnel axis. At positions $F_p = 0.06$ and 0.33 the tunnel axis does not correspond to the jet axis and this partly explains the initial high turbulence levels of above 50%. There is a minimum level at $X/D_j = 20.8$ for the jet fan position $F_p = 0.06$ and 0.33. This is followed by

a continuous rise which assumes a value of nearly 65 percent at $X/D_j = 57.2$ in the former case. Turbulence levels reach a peak and decrease downstream at the other jet fan positions. The situation is somewhat different when the jet is located at the tunnel axis ($F_p = 0.5$) because the turbulence levels are lower at $X/Dj = 6.35$ (about 10 percent), with a marked rise after 18.2 nozzle diameters. A peak of 75 percent is reached at 45.3 nozzle diameters followed by a sharp decrease to a value of about 35 percent at $X/D_j = 57.2$. The turbulence levels are comparable in magnitude with those of Curtet (1958) but are much higher than those of a free jet after 18 nozzle diameters. Qualitatively the longitudinal turbulence variation mimics that of the axial wall static pressure. There is a high level of turbulent mixing in the tunnel between the two fluid streams and recirculating currents probably contribute to the high level of velocity fluctuations observed.

Entrainment Rates

The pressure and flow results including the turbulence levels are important in understanding the entrainment data. The entrainment results are a direct measure of jet fan performance in the tunnel. Figure 11 shows the quantity of air entrained with respect to jet fan position. When the jet is closer to the wall the quantity of air entrained is greater than when it is moved
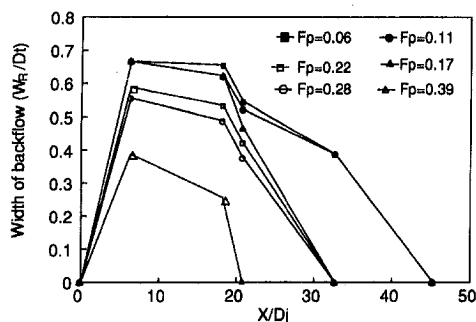

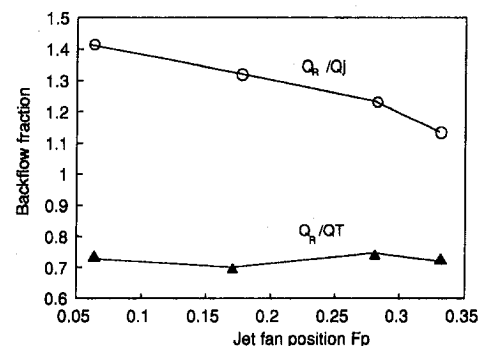**Fig. 8** Width of backflow vs axial distance (uncertainty in (W_R/D_t) is 8.6 percent)

Fig. 9 Backflow fraction vs jet fan position (uncertainty in Q_R/Q_j and Q_R/Q_T are 8.74 percent and 10.67 percent, respectively)
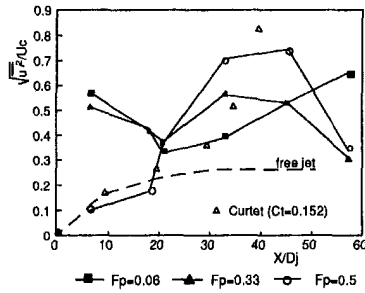
Fig. 10 Tunnel centerline longitudinal turbulence levels (uncertainty is 6.05 percent)

Fig. 12 Efficiency versus jet fan position (uncertainty in both pressure related quantities is 7.08 percent)

toward the tunnel axis. The lowest amount of air entrained is obtained when the jet fan is positioned at $F_p = 0.39$. After this position the entrainment rate increases but it does not reach the same levels as when the jet is close to the wall. This observed decrease in flow ratio as F_P increases is different from the pressure characteristic $(P_{tn} - P_e)/(P_j - P_{tn})$ plotted in Fig. 6, which increases as F_P is increased. An explanation for this observation can be obtained with the aid of Fig. 5. When the jet fan is located at positions $F_p < 0.22$ the extent to which the pressure drops below ambient and therefore attaining negative values, is greater for decreasing F_P. This tends to improve the suction effect as in a jet pump because of the negative pressure difference created. For the jet fan position $F_P = 0.06$ the pressure is negative up to almost 40 nozzle diameters. A combination of these large pressure drops and wall friction could partly explain the lower pressure characteristics for near wall jet fan positions in Fig. 6. The fact that where the entrainment processes are high, the extent of the back flow is quite significant on one side of the tunnel is difficult to explain. The amount of total flow Q_T discharged from the tunnel varies from just over 1.6 times to about twice the initial jet volume flow Q_j. The entrainment volume flows Q_e are also plotted in Fig. 11 as a function of F_p.

The ratio of the energy in the discharge flow to the energy input from the jet fan nozzle $Q_e(P_{tn} - P_e)/(Q_j(P_j - P_{tn}))$ or $n(P_{tn} - P_e)/(P_j - P_{tn})$ is expressed as percent efficiency in Fig. 12. The symbols Q_e, Q_j, and n are the entrained, jet discharge and flow ratio Q_e/Q_j respectively. High tunnel end pressure P_{tn}, low jet discharge total pressure P_j and high flow ratio n increase the performance of the jet fan. This definition of efficiency is widely accepted in jet pump or ejector theory. The variation in efficiency of the system follows that of flow ratio Q_T/Q_j with varying position F_p.

An induction efficiency is described by Reale (1973) as the ratio of the ventilation power output to the power transmitted to the fluid by the fan:

$$\eta_i = 2\Phi(1 - \Phi)/((1 + \Phi)(1 - \Omega)) \qquad (3)$$

where Φ is the velocity ratio U_t/U_j and Ω is the area ratio A_j/A_t. This efficiency is similar to the parameter $Q_T(P_{tn} - P_e)/$
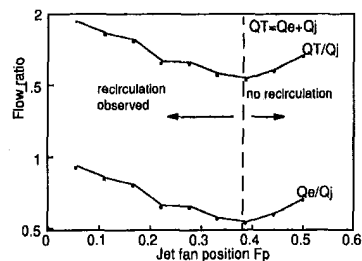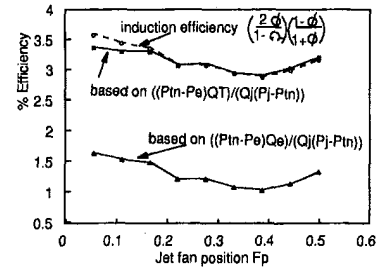
$(Q_j(P_j - P_{tn}))$ where Q_T is now used instead of Q_e unlike before and is a form of measured induction performance (Fig. 12). Although the values appear low, this type of ventilation is still effective, and in order to evaluate it fully one has to consider the factors involved. An overall energy balance of the system can be formulated as follows:

$$E_{in} = E_{out} + E_{fl} + E_r + E_{ml} + E_{jl} \qquad (4)$$

where E_{out} is work output of the secondary flow, E_{fl}, E_r, E_{ml}, and E_{jl} are the energy losses due to friction, back flow, mixing and jet loss respectively. The backflow, mixing and friction losses account for a significant amount of the losses incurred on the system.

Conclusions

The present experimental studies have examined the overall flow produced by a jet fan located at various positions in a wind tunnel. Pressure and velocity field results have revealed that the jet fan performance is enhanced when it is closer to one tunnel wall despite apparent frictional pressure losses. The axial static pressure results support this conclusion and because of the high pressure drops created initially (up to $X/D_j = 30$) when the jet fan is close to the wall more secondary air is induced to flow in the tunnel. One important observation made in this study is the existence of backflow when the jet fan is located close to the wall for positions $F_p < 0.44$. The existence of backflow has never been addressed fully before. The present wind tunnel studies provide a significant contribution to the formulation of realistic guidelines in mine and tunnel ventilation. Backflow fraction Q_R/Q_T is found to be about 0.72 for $F_p < 0.44$ in this study and is important data in jet fan ventilation design. If the causes of backflow are known it can be avoided by careful design. When the jet fan is located at the tunnel axis there is no backflow but unstable flow occurs in the wall region approximately within 0.17 tunnel diameters from the walls. The flow is subject to directional changes every few moments suggesting oscillation of the flow field. The period of this oscillation is of the order of 2 to 4 seconds.

Turbulent quantities are observed to be quite high suggesting a high degree of mixing of the two streams.

Acknowledgments

Fig. 11 Flow ratio vs jet fan position (uncertainty in Q_e/Q_j and Q_T/Q_j is 6.52 percent)

References

Abramovich, G. N., 1963, *The Theory of Turbulent Jets*, MIT Press, Cambridge, MA, pp. 444–475, pp. 633–654.

Barchilon, M., and Curtet, R., 1964, "Some Details of the Structure of an Axisymmetric Confined Jet with Back Flow," ASME *Journal of Basic Engineering*, pp. 777–787.

Curtet, R., 1958, "Confined Jets and Recirculation Phenomena with Cold Air," *Combustion and Flame*, Vol. 2, pp. 383–411.

Matta, J. E., Thimmons, E. D., Kissell, F. N., 1978, "Jet Fan Effectiveness as Measured with SF6 Tracer Gas," *Report of Investigations 8310*, U.S.B.M., 14p.

Mizuno, A., and Araie, K., 1989, "Measurement of Pressure Rise Performance of a Jet Fan in a Tunnel by Model Experiment," *Nippon Kikai Gakkai Ronbunshu, B. Hen/Trans. of the Japan Society of Mechanical Engineers*, Part B, No. 514, pp. 1613–1617.

Mutama, K. R., and Hall, A. E., 1993, "Development of a Wind Tunnel for Mine Ventilation Aerodynamic Measurements," *Proceedings of the 6th US Mine Ventilation Symposium*, Chapter 61, R. Bhaskar, ed., pp. 407–412.

Reale, F., 1973, "Fundamentals and Applications of Induction Ventilation Systems of Vehicle Tunnels," *Int. Symposium on the Aerodynamics and Ventilation of Tunnels*, BHRA Fluid Engineering, England.

Thimons, E. D., Brechtel, C. E., Adam, M. E., and Agapito, J. F. T., "Face Ventilation for Oil Shale Mining," *Infor. Circular 9118*, U.S. Bureau of Mines, 15p.

Thring, M. W., and Newby, M. P., 1953, *Fourth Symposium (International) on Combustion*, Williams and Wilkins, Baltimore, p. 789.

D. Sivakumar
Research Student.

B. N. Raghunandan
Professor.

Department of Aerospace Engineering,
Indian Institute of Science,
Bangalore, 560012 India

Jet Interaction in Liquid-Liquid Coaxial Injectors

Interaction between two conical sheets of liquid formed by a coaxial swirl injector has been studied using water in the annular orifice and potassium permanganate solution in the inner orifice. Experiments using photographic techniques have been conducted to study the influence of the inner jet on outer conical sheet spray characteristics such as spray cone angle and break-up length. The core spray has a strong influence on the outer sheet when the pressure drop in the latter is low. This is attributed to the pressure variations caused by ejector effects. This paper also discusses the merging and separation behavior of the liquid sheets which exhibits hysteresis effect while injector pressure drop is varied.

Introduction

In rocket engine combustion chambers, the evaporation rate of fuel and oxidizer droplets is one of the principal factors determining the combustion efficiency. This is governed by the injector design and the mixing of fuel and oxidiser jets in the combustion chamber. Distribution of propellants in the combustion chamber is itself accomplished by suitable combination of injector elements. Coaxial jet mixing is known to be one of the efficient ways to achieve good mixing in the combustion chamber. There are number of rocket motors both of storable and cryogenic propellants functioning with such injectors.

Atomization characteristics of coaxial injectors have been studied by many authors. In a study to simulate FLOX/methane injector element, Burick (1972) has discussed the effect of geometrical configuration of coaxial injector on drop size distribution and mixing efficiency. By increasing the oxidizer post-recess length in the injector configuration, which is the projection of oxidizer orifice beyond the fuel orifice, SMD increases and mixing efficiency reaches a maximum and then reduces. York et al. (1953) have studied the disintegration of plane liquid sheets theoretically through a mathematical analysis and qualitative comparisons have been made with experimental results. They concluded that instability and wave formation at the interface are the major factors in the break-up of the sheet of liquid into drops. Dombrowski and Tahir (1977) have made a systematic study on atomization characteristics of swirl pressure nozzles using oils covering wide viscosity range. Correlations were obtained for mean drop size, size distribution and break-up length in terms of the operating variables. Wang et al. (1986) conducted experiments on air-assist nonswirl atomizers and concluded that the ratio of water to air flow rates governed the uniformity of drop size distribution across the spray. A similar conclusion was arrived at for air-assist swirl atomizer by Mao et al. (1986, 1987) who studied the drop size distribution at several axial and radial locations using Fraunhofer diffraction particle sizing instrument and Phase/Doppler spray analyser. It has also been shown that SMD increased with distance downstream along the center line and also with the radial distance from the axis. The study of Eroglu and Chigier (1991) is focussed on the SMD variation and velocity distribution of coaxial liquid/air jets. It was found that SMD distribution is strongly affected by the structure and behavior of the preceding liquid intact jet. It has been shown that increase in liquid supply pressure increases the momentum of the water jet making it more

stable and the increase in air supply pressure increases the relative velocity at the liquid/air interface which reduces the SMD. In their detailed studies with coaxial rocket injectors, Sankar et al. (1991, 1992) have examined the effects of geometric variable and the ambient environment. It was observed in their experiment with water–air, $LN_2 - GN_2$ systems that recess length of the coaxial injector seems to have a greater effect on the atomization of water than on liquid nitrogen. With this work, it was concluded that the presence of larger particles at high chamber pressures is attributed to the diminished effect of secondary atomization resulting from a decrease in the relative shear velocity between the droplets and the gas flow. Hardalupas and Whitelaw (1994) have studied the spray characteristics of coaxial airblast atomizers by simulating the space shuttle main engine preburner spray condition. The effect of converging exit path for the gas and liquid tube recess have been examined by the author. It was found that the presence of a converging nozzle at the exit of the gaseous jet improved the atomization. Recess of the liquid tube by two or three liquid tube diameters increased the rate of spread of the sprays and reduced the extent of atomization for the straight and converging gaseous jet exit nozzles. Care and Ledoux (1991) have studied the coaxial airblast atomizer both experimentally and theoretically. Spray structure, SMD, air-liquid velocities, and spray angles have been reported by the author.

The most notable feature of the studies reported above is that the initial interaction of the outer and central jets governs the eventual dropsize and mixing characteristics. All of the above studies with coaxial injectors are made with gaseous outer jet and the literature on liquid–liquid coaxial jets is rather scanty. The present work motivated by coaxial elements of storable propellant systems deals with liquid–liquid type of injection with emphasis on the initial interaction between the liquid sheets.

In a spray from coaxial swirl injector, the liquid oxidizer conical sheet is in the aircore of the liquid fuel cone. At very low injection pressure drop, the liquid sheets are separated from each other. With an increase in the injection pressure drop, (Δp) across the fuel and oxidizer orifices, the liquid sheets move closer and merge at certain condition. Merging of the liquid sheets and the consequent mixing of fuel and oxidizer components are essential in the rocket thrust chamber. This requirement is especially important for hypergolic combinations. The process of merging of the concentric liquid sheets as injector pressure drops across the orifices are gradually increased involve some interesting physical phenomena. The presence of a central sheet in the core of the outer conical liquid sheet affects the spray characteristics of the outer conical sheet and vice versa. Understanding of this merging behavior of liquid sheets is important, especially when one is interested in the
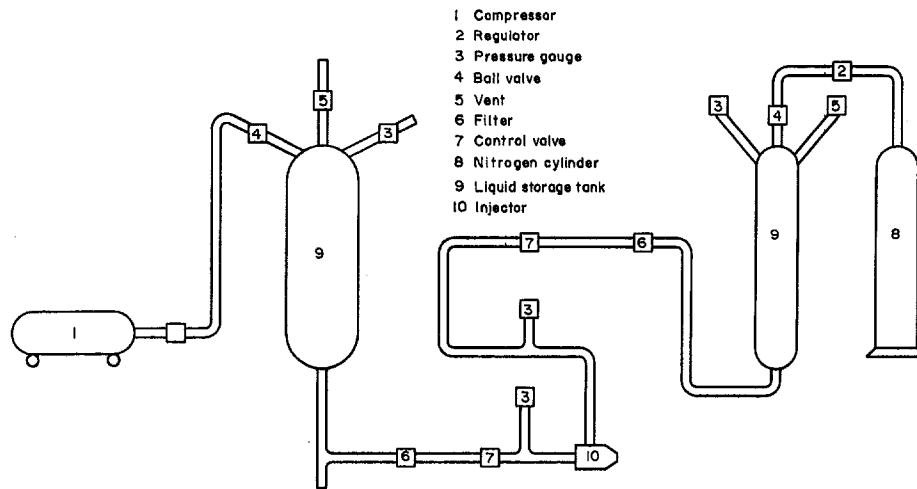
Fig. 1 Schematic diagram of experimental setup

throttling of the rockets. Hence the present experimental study is mainly aimed to throw light on some basic features of this phenomenon in the coaxial swirl injectors.

The range of Reynolds number for the test condition is 15,000–40,000 and that of Weber number, based on hydraulic diameter (We $= \rho_a u_r^2 d_h / \sigma$), 3–20 which are close to the actual injector conditions in a typical rocket engines. The experimental conditions of relatively large sized injector, low pressure drop across the orifice and the ambient pressure are chosen such that the study of liquid sheet interaction is feasible. The description of the phenomenon and the main observations are nevertheless applicable to rocket combustion chamber where the liquid sheets meet at distances much closer to the injector face.

Experimental Details

The schematic representation of the experimental setup is given in Fig. 1. Two separate tanks are used for storing the experimental liquids—here water and potassium permanganate solution. The tanks are pressurized either by nitrogen cylinder or by an air compressor capable of maintaining a steady pressure of 8–10 atm in the tanks during discharge. Pressure regulators and pressure gauges are employed to control and monitor the pressure drops across the orifices. All pressure gauges are calibrated with respect to a standard HEISE pressure gauge. The error in (Δp) is a combination of errors due to instrument resolution and shift in calibration as found out from repeated calibration. Thus the highest uncertainty error in (Δp) is estimated to be 4.4 percent. In the discharge line from the tank to the injectors, filters are used to trap fine particles which may clog the injector. Metal wire square mesh of size about 45–50 μm is employed in this filter. Control valves and additional pressure gauges just ahead of the injectors to measure the injection pressure drop are also present in the lines.

Considerable amount of published information is available on the design of swirl injectors to meet mass flow and cone angle criteria. These have been extended to the coaxial injector in the present work. A coaxial injector is fabricated here primarily to study the behavior of two coaxial liquid conical sheets. The schematic view of the injector is given in Fig. 2, which also describes all the geometric parameters. These values are arrived at from the mixture ratio of a typical propellant combination. A practical difficulty in designing this injector was in making the orifice accurately coaxial and coplanar. With con-
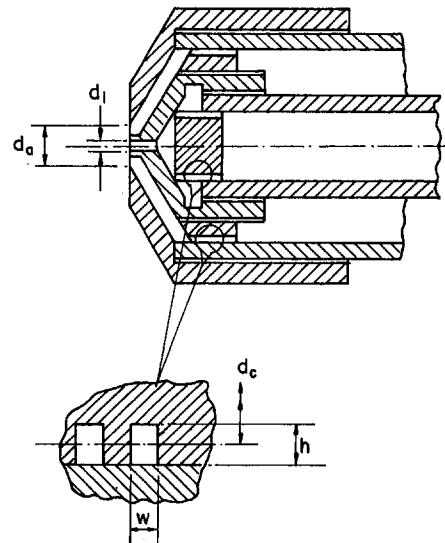

Fig. 2 Schematic diagram of the coaxial injector

——— Nomenclature ———

d_a = annular orifice diameter
d_c = mean diameter of the swirler
d_h = equivalent hydraulic diameter of the orifice
d_i = inner orifice diameter
d_o = orifice diameter
h = depth of the rectangular helical passage
K = swirl number given by Lefebvre

(Δp) = injection pressure drop
(Δp)$_i$ = inner orifice injection pressure drop
(Δp)$_a$ = annular orifice injection pressure drop
(Δp)$_{i,m}$ = merging pressure
(Δp)$_{i,s}$ = separation pressure
S_i = inner orifice swirl number
S_a = annular orifice swirl number

u_r = relative velocity between liquid and air
w = width of the rectangular helical passage
We = Weber number
α = spray cone angle
δ = annular gap in the outer orifice
σ = liquid surface tension
ρ_a = air density

Table 1 Swirl numbers used in the present study

Inner swirler S_i	Annular swirler	
	S_{a1}	S_{a2}
13.9 (d_i = 1 mm)	54.6 (d_a = 2.8 mm, δ = 0.4 mm)	110.6 (d_a = 2.8 mm, δ = 0.4 mm)
	75.2 (d_a = 3.1 mm, δ = 0.55 mm)	152.1 (d_a = 3.1 mm, δ = 0.55 mm)

ventional lathe machines, it is very difficult to achieve both the requirements. To get a coaxial configuration of both the orifices with good accuracy, a little movement is provided for the inner orifice. Required coaxial conical liquid sheets necessary for the study can be obtained by moving the inner orifice over a small distance (<1 mm) at which condition the exit orifices of inner and outer sprays are coaxial but not necessarily coplanar. The swirling motion is generated by passing the liquids through single start rectangular helical passages as shown in Fig. 2. The swirl intensity is given by swirl number, S by Beer and Chigier (1983) as

$$S = \frac{G_\phi}{G_x R}$$

where G_ϕ is the axial flux of the angular momentum, G_x is the axial thrust, and R is the exit radius of the nozzle. When there is an orifice downstream of the swirler which enhances axial velocity while conserving angular momentum, the swirl number takes the form

$$S_i = \frac{\pi d_o d_c}{4wh}$$

for inner swirler and

$$S_a = \frac{\pi \delta d_c}{wh}$$

for annular swirler. The terms in this expression are clearly shown in Fig. 2. Values of S used in the present study are given in Table 1. It may be noted that K value defined for swirl intensity by Lefebvre (1989) works out to be $1/4S$. Liquid flow rate through the injector is measured by collection method. The error in liquid flow rate arises from pressure measurement and the collection technique. This uncertainty is estimated to be about 1.5 to 2 percent. The liquid flow rate is plotted with (Δp) in Fig. 3 for both inner spray and annular spray.

Photographic technique has been used to visualize the spray pattern. A 35mm still camera is used to take color and black and white photographs at shutter speeds less than 1/15 s. Wherever required high speed films (400 ASA) have been used. Spray is illuminated by a strobe light at right angles to the line of sight of the camera. The measurements on film negatives are made using a microfilm reader of 17.5X.

Results and Discussion

Mutual Influence of Sheets on Spray Cone Angle. An interesting observation is that each sheet experiences the influence of the other even when the jets do not merge. Figure 4 shows some typical photographs to illustrate this point. These photographs have been taken at a constant annular orifice injection pressure drop, (Δp)$_a$ with different values of the inner orifice injection pressure drop, (Δp)$_i$. Figure 4(a) corresponds to the outer spray in the absence of any flow in the core. A large spread of the liquid sheet and the droplets is clearly seen. In Fig. 4(b), the influence of inner jet at a (Δp)$_i$ = 0.169 MPa may be observed. At this condition the inner spray is still in its tulip stage and yet the spray cone angle is lower and the liquid jet as well as the disintegrated spray seem to bend inwards. The effect is further enhanced at a higher (Δp)$_i$ of 0.19 MPa as seen in Fig. 4(c). The inner jet is now a conical spray and the expansion of the outer spray is curtailed.

A number of experiments are carried out to get the quantitative variation of spray cone angle of outer spray. Water and potassium permanganate solution are used as the experimental liquids for annular orifice and inner orifice respectively, to distinguish the two liquid sheets. Color photographs are made use of to get the spray cone angle variation of both the liquid sheets at a particular (Δp)$_a$. The error in spray cone angle, α arise due to (i) uncertainty in the identification of the spray cone surface from the photograph and the consequent length measurement which is used to compute α and is estimated to be 2.14 percent and (ii) repeatability of data in view of the very weak unsteadiness present in the system which has a maximum uncertainty of 3 percent. Thus the upper bound of uncertainty in cone angle is expected to be 3.68 percent. The typical variations of spray cone angles of both the liquid jets are plotted in Fig. 5 at a particular (Δp)$_a$. Clearly the cone angle of the outer spray significantly drops as the (Δp)$_i$ is increased. The gradual increase in the inner spray cone angle is not as much as it would be in the absence of the outer spray. These mutual interference effects are more clearly seen in Figs. 6 and 7 where the effect of one on the other is depicted. Any prediction of the distance of the merging point from the injector face must take this effect into consideration.

The explanation for the behavior lies in the fact that the sheet in the core induces some velocity in the air core, much like an ejector effect, resulting in a drop in static pressure. This tends to bend the outer conical sheet of liquid inwards. This is verified by conducting experiments with air flow at different velocity through the inner orifice. The outer spray exhibits the same bending effect confirming the above observation.

Merging and Separation of Liquid Sheets. The liquid jets coming out of the two orifices are in the form of conical sheets for a short distance. As mentioned earlier, due to mutual interaction they bend inwards further downstream before breaking up into droplets. At a given (Δp)$_a$, if (Δp)$_i$ is gradually increased, at some value of (Δp)$_i$ the two sheets merge with each other
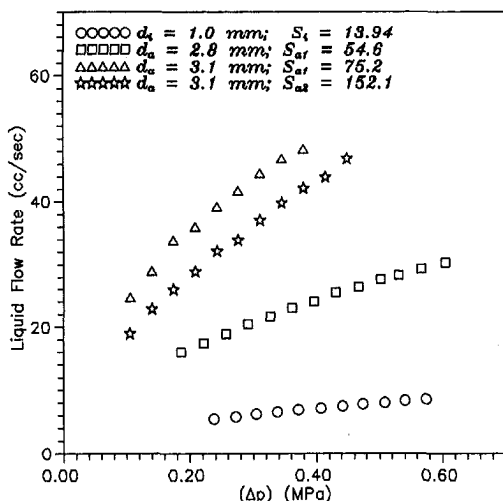
Fig. 3 Liquid flow rate variation with injection pressure drop

$(\Delta p)_a = 0.19$ MPa
$(\Delta p)_i = 0$

$(\Delta p)_a = 0.19$ MPa
$(\Delta p)_i = 0.169$ MPa

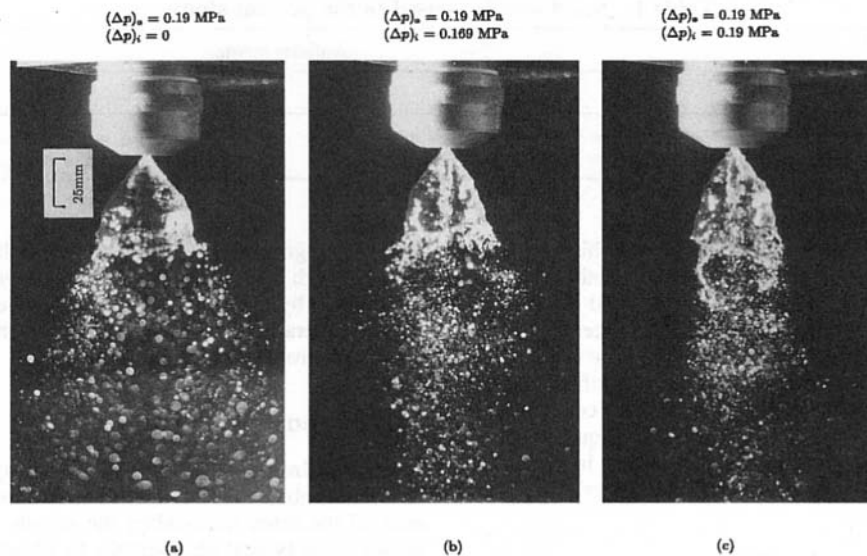$(\Delta p)_a = 0.19$ MPa
$(\Delta p)_i = 0.19$ MPa

(a) (b) (c)

Fig. 4 Influence of inner conical sheet on outer conical sheet

and the merging point immediately moves upstream very close to the injector orifice. This is henceforth referred as the 'merging pressure', $(\Delta p)_{i,m}$. Beyond this value of $(\Delta p)_{i,m}$ the two jets remain merged and the break up of the combined jet follows at a short distance from the injector orifice exit. If the approach is reversed, namely from the merged condition if $(\Delta p)_i$ is decreased keeping $(\Delta p)_a$ constant, there is a condition of $(\Delta p)_{i,s}$ at which the two jets separate from each other. This separation pressure is however lower than the merging pressure at all $(\Delta p)_a$.

The process of merging is primarily dictated by the cone angles of liquid sheets at corresponding pressure drops, but modified by the interactions described earlier. However, after merging, the two conical liquid sheets are pulled closer to each other and the point of merging moves upstream. A new state of equilibrium is achieved where the surface tension balances the components of inertial forces trying to pull the sheets apart. Therefore the process of separation will require lower pressure levels at which cone angles tend to be lower, to overcome the surface tension forces. This results in the hysteresis seen in Fig. 8.
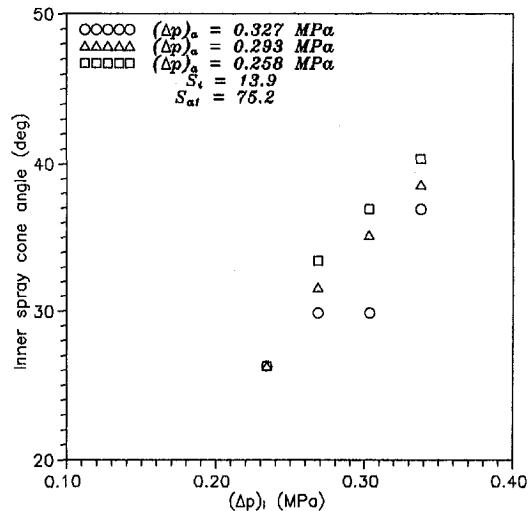

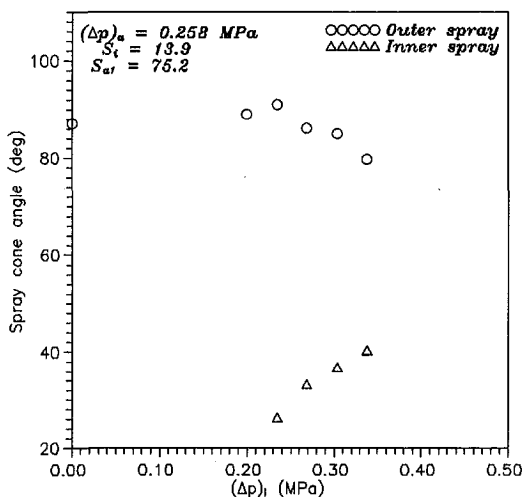Fig. 6 Effect of $(\Delta p)_a$ on inner spray cone angle

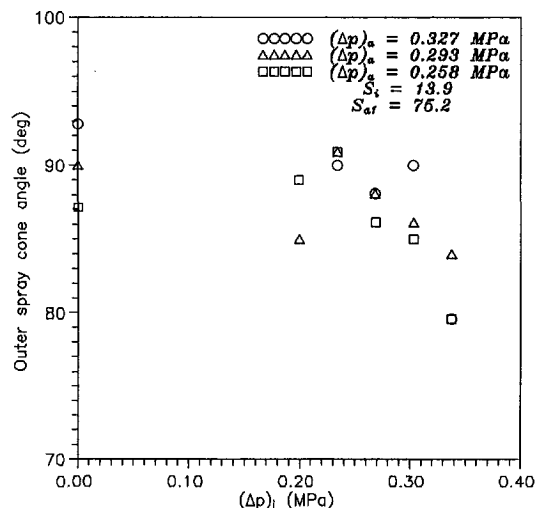Fig. 5 Effect of $(\Delta p)_i$ on outer and inner spray cone angles

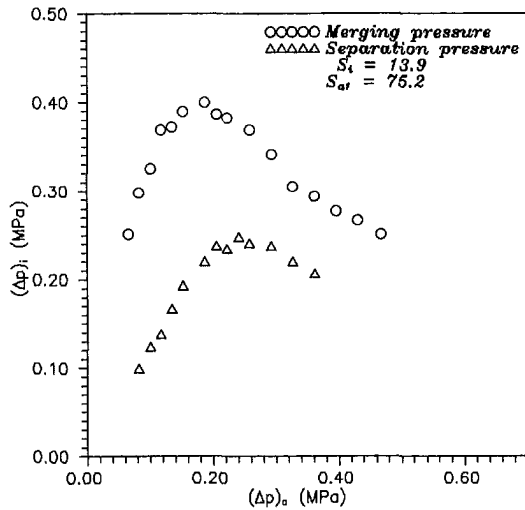Fig. 7 Effect of $(\Delta p)_i$ on outer spray cone angle

Fig. 8 Merging and separation behavior of conical sheets

Fig. 10 Effect of $(\Delta p)_i$ on outer conical sheet break-up length (before merging)

The trends of variation $(\Delta p)_{i,m}$, as well as $(\Delta p)_{i,s}$, show a maxima as can be seen in Fig. 8. It is important to note that merging itself is a consequence of inward bending of the outer conical sheet. In the lower range of $(\Delta p)_a$, there is a substantial increase in the cone angle of the outer spray as $(\Delta p)_a$ increases. So the extent of bending required for merging to take place will also become higher which can be met only by increasing the core pressure drop $(\Delta p)_i$. This explains the rising part of the curve in Fig. 8. However, in the higher range of $(\Delta p)_a$ beyond the maximum, the phenomenon is different. Here the outer liquid sheet breaks up into a spray at a very short distance. The consequent dense spray induces a quicker interaction with the inner jet. As the break-up length decreases as a result of gradual rise in $(\Delta p)_a$, lower $(\Delta p)_i$ suffices for the merging process. It is extremely difficult to measure the distance from the injector face to the location where the merging process gets initiated. The reasons are that the transition occurs at a very small change in $(\Delta p)_i$ and the point of merging quickly moves upstream. Efforts are on to delineate this phenomenon in detail.

Influence of Sheet Interaction on Break-Up Length. Break-up length of a jet is one of the major parameters which affect the spray penetration and distribution in the combustion chamber. The error in breakup length as measured from photographs arises due to (i) circumferential variation as viewed
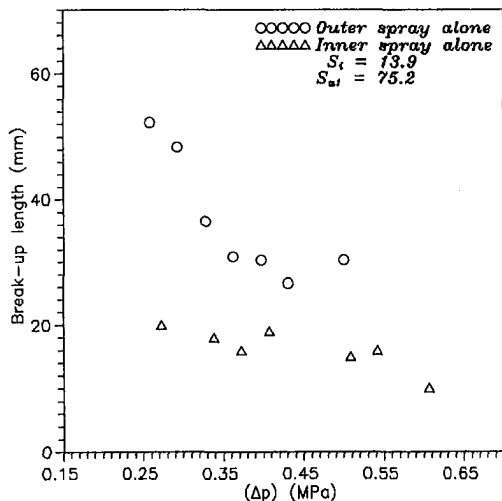
from different angles which has been estimated to be 5 percent and (ii) error in the measurement of length from magnified photographs which is estimated to be 2.5 percent. Thus the uncertainty in the breakup length is 5.59 percent. The variation of break-up length of individual conical sheets with (Δp) is plotted in Fig. 9 in the absence of the other spray. As observed in the spray cone angle variation, the break-up length of outer conical sheet at particular condition is also affected by the presence of inner sheet. The presence of inner sheet in the air core of the outer spray introduces perforations and oscillations in the outer conical sheet as it bends towards the inner jet. This perturbation increases at higher $(\Delta p)_i$ and makes the outer conical sheet disintegrate at a shorter distance. Experiments are conducted by varying $(\Delta p)_i$ at constant $(\Delta p)_a$. It is difficult to discern this phenomenon at higher $(\Delta p)_a$ in the presence of inner spray because the break-up length of outer conical sheet even in the absence of inner spray is lower. Hence most of the experiments were conducted at lower range of $(\Delta p)_a$.

Figure 10 represents the variation of break-up length of outer conical sheet with the variation in $(\Delta p)_i$ at a particular $(\Delta p)_a$. It is observed that there is a considerable reduction in break-up length in lower range of $(\Delta p)_i$ and also at higher $(\Delta p)_i$ (near

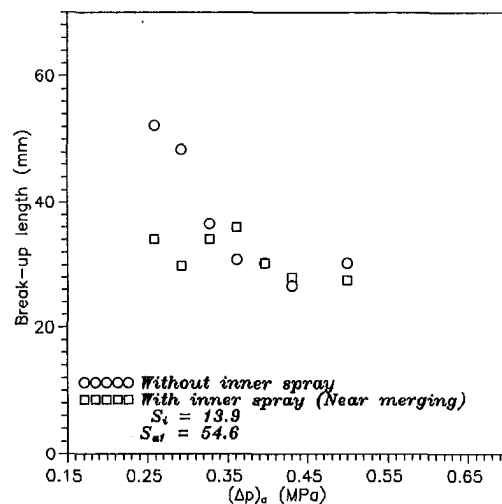**Fig. 9 Break-up length variation with (Δp) of individual conical sheets**

Fig. 11 Break-up length variation of outer conical sheet in the absence and presence of inner spray (near merging refers to the state $((\Delta p)_{i,m} - (\Delta p)_i) < 10.3$ KPa)

Journal of Fluids Engineering

merging stage). In an intermediate range of $(\Delta p)_i$, the oscillation of the sheet is rather intense and therefore there is a spread of data as obtained from still photographs. As the outer conical sheet bends toward the inner sheet, the drops formed from the inner spray collide with the outer conical liquid sheet reducing its break-up length. As $(\Delta p)_i$ increases the bending effect of outer liquid sheet, as well as the spread of inner liquid sheet, increases and makes the outer liquid sheet break at a shorter distance.

Figure 11 represents the same influence as described above for different states of the outer conical sheet at conditions of the inner sheet just prior to merging. In effect, the break-up length of the outer conical sheet is very much affected near the merging point at lower injection pressure drop. At higher injection pressure drop of outer jet, the influence of inner sheet is not as high.

Concluding Remarks

Significant interaction between the conical liquid sheets from coaxial swirl injectors occurs before final break-up. Pressure variation caused by ejector effects of one affects the other. The coaxial liquid sheets exhibit hysteresis effects in terms of merging and separation while throttling is effected. This is attributable to surface tension effects, which however calls for further examination. Similarly jet break-up lengths also exhibit mutual influence. In the light of this study, data generated by separately testing core and annular jets differ considerably from actual combined operation especially at lower pressure drops.

Acknowledgment

References

Beer, J. M., and Chigier, N., 1983, *Combustion Aerodynamics,* Robert E. Krieger Publishing Company.

Burick, R. J., 1972, "Atomization and Mixing Characteristics of Gas/Liquid Coaxial Injector Elements," *Journal of Spacecraft and Rockets,* Vol. 9, No. 5, May, pp. 326–331.

Care, I., and Ledoux, M., 1991, "Study of an Air Blast Coaxial Atomiser: Experiments and Modelisation," *Proceedings of the 5th International Conference on Liquid Atomisation and Spray Systems (ICLASS)* (Gaithersburg, MD), pp. 763–770 (Paper 85).

Dombrowski, N., and Tahir, M. A., 1977, "Atomization of Oils by Swirl Spray Pressure Nozzles," *Journal of the Institute of Fuel,* June, pp. 59–67.

Eroglu, H., and Chigier, N., 1991, "Initial Drop Size and Velocity Distributions for Airblast Coaxial Atomizers," ASME JOURNAL OF FLUIDS ENGINEERING, Vol. 113, Sept., pp. 453–459.

Hardalupas, Y., and Whitelaw, J. H., 1994, "Characteristics of Sprays Produced by Coaxial Airblast Atomisers," *Journal of Propulsion and Power,* Vol. 10, No. 4, July-Aug, pp. 453–460.

Lefebvre, A. H., 1989, *Atomisation and Sprays,* Hemisphere, New York.

Mao, C. P., Wang, G., and Chigier, N., 1986, "The Structure and Characterization of Air-assisted Swirl Atomiser Sprays," *Atomisation and Spray Technology,* Vol. 2(2), pp. 151–169.

Mao, C. P., Oechsle, V., and Chigier, N., 1987, "Drop Size Distribution and Air Velocity Measurements in Air Assist Swirl Atomizer Sprays," ASME JOURNAL OF FLUIDS ENGINEERING, Vol. 109, Mar. pp. 64–69.

Sankar, S. V., Brena de la Rosa, A., Isakovic, A., and Bachalo, W. D., 1991, "Liquid Atomisation by Coaxial Rocket Injectors," *AIAA Paper* 91-0691, Jan.

Sankar, S. V., Wang, G., Brena de la Rosa, A., Isakovic, A., and Bachalo, W. D., 1992, "Characterisation of Coaxial Rocket Injectors Under High Pressure Environments," *AIAA Paper* 92-0228, Jan.

York, J. L., Stubbs, H. F., and Tek, M. R., 1953, "The Mechanism of Disintegration of Liquid Sheets," *Trans. ASME,* Vol. 75, pp. 1279–1286.

Numerical Study of Viscous Flows Inside Partially Filled Spinning and Coning Cylinders

Mohamed Selmi
Assistant Professor,
Department of Mechanical Engineering,
Qatar University, P.O. Box 2713, Doha,
Qatar. Mem. ASME

This paper is concerned with the solution of the 3-D-Navier-Stokes equations describing the steady motion of a viscous fluid inside a partially filled spinning and coning cylinder. The cylinder contains either a single fluid of volume less than that of the cylinder or a central rod and a single fluid of combined volume (volume of the rod plus volume of the fluid) equal to that of the cylinder. The cylinder rotates about its axis at the spin rate ω and rotates about an axis that passes through its center of mass at the coning rate Ω. In practical applications, as in the analysis and design of liquid-filled projectiles, the parameter $\epsilon = \tau \sin \theta$, where $\tau = \Omega/\omega$ and θ is the angle between spin axis and coning axis, is small. As a result, linearization of the Navier-Stokes equations with this parameter is possible. Here, the full and linearized Navier-Stokes equations are solved by a spectral collocation method to investigate the nonlinear effects on the moments caused by the motion of the fluid inside the cylinder. In this regard, it has been found that nonlinear effects are negligible for $\tau \approx 0.1$, which is of practical interest to the design of liquid-filled projectiles, and the solution of the linearized Navier-Stokes equations is adequate for such a case. However, as τ increases, nonlinear effects increase, and become significant as ϵ surpasses about 0.1. In such a case, the nonlinear problem must be solved. Complete details on how to solve such a problem is presented.

1 Introduction

Spin-stabilized liquid-filled projectiles are known to experience severe dynamical instabilities owing to the motion of their liquid payload. For cylinders completely filled with a single fluid we know two types of instabilities. One of the instabilities is caused by resonance with inertial waves at critical coning frequencies (ratio of the coning rate Ω to the spin rate ω) and is most pronounced for fluids of low viscosity, i.e., high Reynolds numbers. We define the Reynolds number as Re $= \omega a^2/\nu$, where a is the radius of the cylinder and ν is the kinematic viscosity of the fluid. This instability is known to depend strongly on the cylinder aspect ratio (ratio of the length $2c$ of the cylinder to its diameter $2a$). For stable designs, the aspect ratio is properly chosen to avoid resonance for a given coning frequency. The other kind of instability is due to viscous stresses applied on the walls of the payload container and is most pronounced for fluids of high viscosity, i.e., low to medium Reynolds numbers, for a wide range of aspect ratios and coning frequencies.

A number of approximations to solve for the fluid motion inside a completely filled cylinder have been devised for the purpose of understanding the causes of flight instabilities of liquid-filled projectiles. The boundary-layer approximation is the basis of the Stewartson-Wedemeyer theory (Stewartson, 1959; Wedemeyer, 1966). Since this approximation is only valid for flows at sufficiently large Reynolds numbers, say Re $= 1000$, the theory is primarily suited to predict instability caused by inertial waves. Analysis based on the Navier-Stokes equations (Herbert and Li, 1990) shows, however, that resonance with inertial waves may severely influence the liquid moments at Reynolds numbers as low as Re $= 100$. An improvement to the Stewartson-Wedemeyer theory has been proposed by Kitchens, Gerber, and Sedney (KGS) (see for example Mur-

phy et al., 1989). While the Stewartson-Wedemeyer theory uses the boundary layer approximation in both the radial and axial directions, the KGS method employs the boundary layer approximation in the axial direction and solves the linearized Navier-Stokes equations in the radial direction.

The linearized Navier-Stokes equations when the coning angle is sufficiently small is the basis of the approach suggested by Hall, Sedney, and Gerber (HSG) (Hall et al., 1990). This approach expands velocity components and pressure in a series of products of complex trigonometric functions in axial direction and radial "eigenfunctions" that satisfy homogeneous boundary conditions at the side wall. The expansion coefficients of the series can be found from the boundary conditions at the end walls by collocation or least squares.

Selmi, Li, and Herbert (SLH) (Selmi et al., 1992) have developed an alternative method to calculate the moments exerted by the liquid inside the cylinder from the linearized Navier-Stokes equations. The SLH approach is based on the observation that when using a control volume analysis to calculate the moments, these moments depend essentially on the axial velocity. They have derived a single sixth-order partial differential equation for the axial velocity component and solved it by eigenfunction expansion. An extension of this approach to solve for the moments inside partially filled cylinders and cylinders containing a central rod is given by Selmi and Herbert (1995).

Although solving the linearized Navier-Stokes equations as done by Selmi and Herbert (1995) yielded fast numerical codes for the evaluation of the moments, these codes can handle only linear problems. Full Navier-Stokes equations, however, must be solved to know the effect of nonlinearities on these moments. In this paper, we solve the nonlinear problem by solving the full Navier-Stokes equations by a spectral collocation method to determine whether nonlinear effects are significant for flows in spinning and coning cylinders containing a partial fill or a central rod. Our main goal in studying the above flow configurations is to gain insight and analytical capabilities for the design of stable configurations. While a central rod or partial fill may serve to intentionally change liquid moments and resonant frequencies, partial fills are also frequent off-design products.

2 Governing Equations

We consider the flow of an incompressible fluid of density ρ and viscosity μ inside a cylinder of radius a and length $2c$. The cylinder is rotating about its axis at the spin rate ω and rotating about an axis that passes through its center of mass at the coning rate Ω. We will consider two internal configurations that can be treated in a similar manner. In one configuration, the cylinder contains a central rod of radius $a_0 < a$ and the fluid completely fills the annulus bounded by the surface of the rod and the end and side walls of the cylinder. Thus the volume of the fluid and the volume of the rod equals the volume of the cylinder. In the second configuration the cylinder is partially filled with a fluid of fill radius $a_0 < a$. We define the fill radius as the radial distance from the center of the cylinder to the location of the free surface of the fluid that results under the influence of centrifugal forces when the cylinder is spinning about its axis and there is no coning motion.

Another measure of the fluid quantity inside the cylinder is the fill ratio f defined as the ratio of the volume of the liquid V_1 to the volume of the cylinder V. When the cylinder is spinning and coning simultaneously, the fill radius, that we denote by a_f, is no longer constant, but varies with the axial and azimuthal directions. When the spinning rate is much larger than the coning rate, as in practical applications, the deviation of a_f from a_0 is small. In this study it is assumed that this is the case.

We use Cartesian coordinates (x, y, z), where z is the spin axis and x is normal to z and coplanar with both the spin axis and the coning axis Z. The angle between spin axis and coning axis is denoted by θ, as shown in Fig. 1. We also use cylindrical coordinates (r, ϕ, z) where r is along the radial direction and ϕ is along the azimuthal direction. The coning system (x, y, z) or (r, ϕ, z) rotates about the Z-axis of the inertial system (X, Y, Z) at the coning rate Ω. The flow quantities are made dimensionless by using ρ to scale mass, a to scale length, and ω to scale time. The problem then depends on the aspect ratio $\eta = a/c$, the coning frequency $\tau = \Omega/\omega$, the coning angle θ, the fill radius $r_0 = a_0/a$ (or the fill ratio $f = V_1/V$), and the Reynolds number $\text{Re} = \omega a^2/\nu$, where ν is the kinematic viscosity. For a cylinder containing a partial fill, the dimensionless radial distance locating the free surface is $r_f = a_f/a$ and is an unknown function of ϕ and z that needs to be determined. For convenience, we write $r_f = r_0 + \zeta(z, \phi)$, where $\zeta(z, \phi)$ is the radial deviation of the interface from the axisymmetric surface of radius r_0. Moreover, we split the velocity field into a component due to rigid-body rotation ($r e_\phi$, e_ϕ being a unit vector in
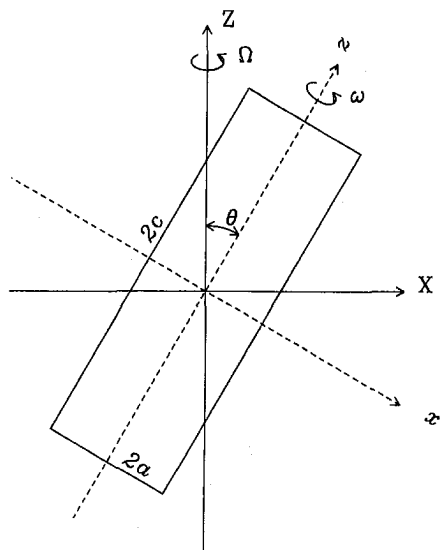
the azimuthal direction) and a deviation from rigid-body motion ($\mathbf{v}$). While we split the pressure according to

$$P = \tfrac{1}{2}[(1 + \tau_z)^2(r^2 - r_0^2) + r^2\tau_\phi^2$$

$$+ z^2\epsilon^2 - 2rz\tau_z'\tau_r] + p^d, \quad (1)$$

where $\tau_r = -\epsilon \cos\phi$, $\tau_\phi = \epsilon \sin\phi$, $\tau_z = \tau \cos\theta$, and $\epsilon = \tau \sin\theta$. The equations governing the velocity components $\mathbf{v} = (v_r, v_\phi, v_z)$ and pressure p^d have been derived by Herbert (1985). They take the form

$$\frac{1}{r}\frac{\partial}{\partial r}(rv_r) + \frac{1}{r}\frac{\partial v_\phi}{\partial \phi} + \frac{\partial v_z}{\partial z} = 0, \quad (2a)$$

$$D'v_r - \frac{v_\phi^2}{r} - 2(1 + \tau_z)v_\phi + 2\tau_\phi v_z$$

$$= -\frac{\partial p^d}{\partial r} + \frac{1}{\text{Re}}\left[D''v_r - \frac{v_r}{r^2} - \frac{2}{r^2}\frac{\partial v_\phi}{\partial \phi}\right], \quad (2b)$$

$$D'v_\phi + \frac{v_r v_\phi}{r} + 2(1 + \tau_z)v_r - 2\tau_r v_z$$

$$= -\frac{1}{r}\frac{\partial p^d}{\partial \phi} + \frac{1}{\text{Re}}\left[D''v_\phi - \frac{v_\phi}{r^2} + \frac{2}{r^2}\frac{\partial v_r}{\partial \phi}\right], \quad (2c)$$

$$D'v_z + 2\tau_r v_\phi - 2\tau_\phi v_r = -\frac{\partial p^d}{\partial z} - 2r\tau_r + \frac{1}{\text{Re}}[D''v_z], \quad (2d)$$

where

$$D' = \frac{\partial}{\partial t} + \frac{\partial}{\partial \phi} + v_r\frac{\partial}{\partial r} + \frac{v_\phi}{r}\frac{\partial}{\partial \phi} + v_z\frac{\partial}{\partial z},$$

and

$$D'' = \frac{\partial^2}{\partial r^2} + \frac{1}{r}\frac{\partial}{\partial r} + \frac{1}{r^2}\frac{\partial^2}{\partial \phi^2} + \frac{\partial^2}{\partial z^2}.$$

For a cylinder containing a central rod, Eqs. ($2a$) through ($2d$) are supplemented with the no-slip conditions at the end walls ($z = \pm\eta$), side wall ($r = 1$), and at the surface of the central rod ($r = r_0$), namely,

$$v_r = v_\phi = v_z = 0. \quad (3)$$

While for a cylinder containing a partial fill, in addition to the no-slip conditions (3) applied at the side wall ($r = 1$) and at the end walls ($z = \pm\eta$), Eqs. ($2a$) through ($2d$) are supplemented with the conditions of vanishing stresses at the free surface interface. When the cylinder is only rotating about its axis ($\epsilon = 0$), the radial interface deviation ζ vanishes. Moreover, when $\epsilon = 0$, the governing equations admit the trivial solution $\mathbf{v} \equiv \mathbf{0}$ and $p \equiv 0$, and since the forcing of the flow quantities are $\mathcal{O}(\epsilon)$, then the velocity deviation from solid body rotation $\mathbf{v}$ and ζ are $\mathcal{O}(\epsilon)$. Hence it is well justified for small ϵ (and consequently small ζ) to linearize the free stress conditions at the interface with ϵ. When this is done these conditions take the form

$$\frac{\partial v_z}{\partial r} + \frac{\partial v_r}{\partial z} = 0, \quad (4a)$$

$$r\frac{\partial}{\partial r}\left(\frac{v_\phi}{r}\right) + \frac{1}{r}\frac{\partial v_r}{\partial \phi} = 0, \quad (4b)$$

$$-p^d + \frac{2}{\text{Re}}\frac{\partial v_r}{\partial r} = \frac{1}{2}[2r_0\zeta(1 + \tau_z)^2 + 2r_0 z\tau_z\epsilon \cos\phi]. \quad (4c)$$

Fig. 1 Description of geometry

Table 1 Convergence of the moments for a cylinder containing a coaxial rod at $\eta = 4.368$, $\tau = 0.16667$, $\theta = 20°$, $r_0 = 0.2$, and Re $= 20$

K	$2L + 1$	M	M_x	M_y	M_z
5	3	5	7.797500E-02	6.507513E-02	2.838058E-02
7	3	7	7.816556E-02	6.526656E-02	2.844994E-02
9	3	9	7.818229E-02	6.528047E-02	2.845603E-02
11	3	11	7.818312E-02	6.527786E-02	2.845633E-02
5	5	5	7.813800E-02	6.517547E-02	2.843991E-02
7	5	7	7.833498E-02	6.534655E-02	2.851160E-02
9	5	9	7.835370E-02	6.535958E-02	2.851841E-02
11	5	11	7.835426E-02	6.535732E-02	2.851862E-02

Table 2 Convergence of the moments for a cylinder containing a partial fill at $\eta = 4.368$, $\tau = 0.16667$, $\theta = 20°$, $r_0 = 0.2$, and Re $= 20$

K	$2L + 1$	M	M_x	M_y	M_z
5	3	5	8.159883E-02	7.683548E-02	2.969954E-02
7	3	7	8.169305E-02	7.720829E-02	2.973384E-02
9	3	9	8.162443E-02	7.721073E-02	2.970886E-02
11	3	11	8.161829E-02	7.719745E-02	2.970663E-02
5	5	5	8.188372E-02	7.691139E-02	2.980324E-02
7	5	7	8.196267E-02	7.728367E-02	2.983197E-02
9	5	9	8.188500E-02	7.729080E-02	2.980370E-02
11	5	11	8.187803E-02	7.727703E-02	2.980117E-02

From kinematics and for small ζ, ζ is related to the radial velocity by $v_r(r_0, \phi, z) = \partial\zeta/\partial\phi$, and this relation is used to eliminate ζ from the interface condition $(4c)$,

$$-\frac{\partial p^d}{\partial\phi} + \frac{2}{\text{Re}}\frac{\partial^2 v_r}{\partial r\partial\phi} - r_0 v_r(1 + \tau_z)^2 = -r_0 z\tau_z\epsilon \sin\phi. \quad (5)$$

Equations $(2a)$ through $(2d)$ support the following symmetries: if $(v_r, v_\phi, v_z, p^d, \zeta)$ is the solution at (r, ϕ, z), the solution at $(r, \phi + \pi, -z)$ is $(v_r, v_\phi, -v_z, p^d, \zeta)$. These symmetries are exploited to save computational power. If we further linearize the governing equations with ϵ, the continuity equation remains unchanged, while the steady-state momentum equations could be written in vector form as,

$$\frac{\partial}{\partial\phi}\mathbf{v} + 2r\tau_z\mathbf{e}_z + 2\boldsymbol{\tau} \times \mathbf{v} + \nabla p^d - \frac{1}{\text{Re}}\nabla^2\mathbf{v} = 0 \quad (6)$$

where $\mathbf{e}_z$ is a unit vector in the z direction, ∇ is the gradient operator, $\nabla^2 = D''$ is the Laplacian, and $\boldsymbol{\tau} = (0, 0, 1 + \tau_z)$. These equations support the additional symmetries: $\mathbf{v}(r, \phi + \pi, z) = -\mathbf{v}(r, \phi, z)$, $p^d(r, \phi + \pi, z) = -p^d(r, \phi, z)$, and $\zeta(\phi + \pi, z) = -\zeta(\phi, z)$. Our ultimate objective is to compare the solution of the linear problem to that of the nonlinear problem for practical geometrical and flow parameters.

3 Evaluation of Moments

Our main objective is to calculate the moment induced by the liquid inside the cylinder. For convenience, we use the aeroballistic reference frame (x, y, z) to express the moment in terms of Cartesian components (M_x, M_y, M_z). For small ζ, it can then be shown (Murphy, 1985; Murphy et al., 1989; Herbert and Li, 1990) that these components are related to the flow velocities by

$$M_x = 2\frac{\Omega}{\omega}(\rho\omega^2 a^5)\cos\theta \int_{-\eta}^{\eta}\int_0^{2\pi}\int_{r_0}^1 v_z r^2 \cos\phi \, dr d\phi dz, \quad (7a)$$

$$M_z = M_x \tan\theta, \quad (7b)$$

$$M_y = 2\frac{\Omega}{\omega}(\rho\omega^2 a^5)\cos\theta \int_{-\eta}^{\eta}\int_0^{2\pi}\int_{r_0}^1 v_z r^2 \sin\phi \, dr d\phi dz$$
$$+ \frac{\Omega}{\omega}(\rho\omega^2 a^5)\sin\theta \int_{-\eta}^{\eta}\int_0^{2\pi}\int_{r_0}^1 v_\phi r^2 dr d\phi dz. \quad (7c)$$

The above formulas are only valid for steady-state conditions as it is the case here. For unsteady flows, the reader is referred to the study by Li and Herbert (1991) for appropriate evaluation of the moments.

If we represent the velocity field by the Fourier series

$$\mathbf{v}(r, \phi, z) = \sum_{n=-\infty}^{\infty} \mathbf{v}_n(r, z)e^{in\phi},$$

$$\mathbf{v}_n = (u_n, v_n, w_n), \quad i^2 = -1, \quad (8)$$

then it is evident from the expressions of the moments, upon performing the integrations over ϕ, that we need only to consider the Fourier components w_1 and v_0. If the flow quantities are expanded in powers of ϵ, it becomes obvious that w_1 is $\mathcal{O}(\epsilon)$ (since the forcing term in the equations of $\mathcal{O}(\epsilon)$ is simply periodic) and v_0 is $\mathcal{O}(\epsilon^2)$. Sine v_0 is $\mathcal{O}(\epsilon^2)$ it cannot be determined by simply solving the linear Navier-Stokes equations of $\mathcal{O}(\epsilon)$.

4 Discussion

Details of how to discretize the governing equations along with the boundary conditions using the spectral collocation method for both configurations are given in the Appendix. The nonlinear system resulting from the discretization is solved iteratively, and requires a guessed solution to start the iteration. In the first step, the linear algebraic system resulting from linearization of the governing equations in ϵ (Eqs. (6)) is solved by Gauss elimination. Subsequently, the nonlinear problem is solved iteratively by the modified Newton's method. For each iteration step, the nonlinear terms are evaluated using the solution at the previous step. This modifies only the right-hand side of the linear system solved in the first step and, consequently, the whole iteration process is equivalent to solving a linear system with different right-hand sides. This approach is computationally less expensive than that of Newton-Raphson iteration where each step requires solving a new algebraic system of relatively large size to obtain the corrections to the previous approximations. However, the modified Newton's method sometimes does not lead to a converging solution especially when nonlinear effects are strong. When this happens, the Newton-Raphson method is utilized instead. Therefore three codes based on the spectral collocation techniques discussed in the Appendix have been written; one solves only the linear system, the second reads a guessed solution and solves for the nonlinear solution using the modified Newton's method, and the third reads a guessed solution and solves for the nonlinear solution using the Newton-Raphson method.
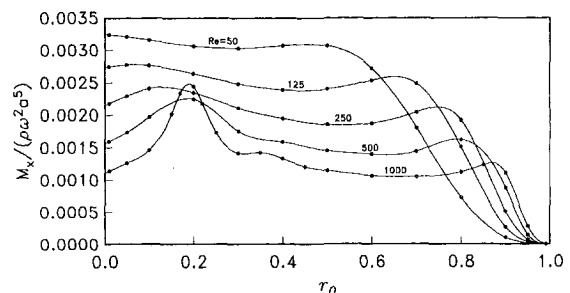
Fig. 2 Dimensionless yaw moment versus dimensionless fill radius for a cylinder containing a central rod at $\tau = 0.1$, $\eta = 4.5$ and $\theta = 2$ deg. Comparison of the linear results (solid lines) and nonlinear results (circles).
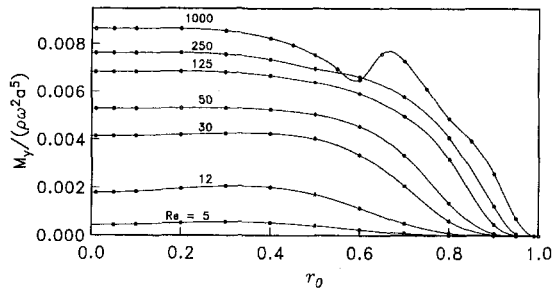
Fig. 3 Dimensionless pitch moment versus dimensionless fill radius for a partially filled cylinder at $\tau = 0.1$, $\eta = 4.5$ and $\theta = 2$ deg. Comparison of the linear results (solid lines) and nonlinear results (circles).

Fig. 5 Dimensionless yaw moment versus dimensionless fill radius for a cylinder containing a central rod at Re $= 450$, $\tau = 0.1111$, $\eta = 3$ and $\theta = 2$ deg. Comparison of the results with those of Murphy et al. obtained by the KGS method and those of Selmi obtained by the SLH method.

The spectral collocation codes that we have written are operational for Reynolds numbers up to Re $= 1000$. The code based on the modified Newton's method requires about 87 seconds CPU time on a Cray YM-P/864 for resolutions of $11 \times 11 \times 5$ polynomials in the r, z, and ϕ directions, respectively. Beyond this resolution, which is needed for flows at Reynolds number above 1000 and especially at parameters leading to resonance, the code becomes relatively expensive not in terms of CPU time but in terms of memory requirement. Tables 1 and 2 show the convergence of the moments as calculated by Eqs. (7) for different resolutions. We can see from these tables that we achieve at least 5 digits of accuracy with resolutions of $11 \times 11 \times 5$ polynomials in the r, z, and ϕ directions, respectively.

5 Results

We have used the control volume expressions presented in Section 3 to calculate the moments exerted by the liquid payload on the walls of the cylinder. Figures 2 and 3 present the variation of the dimensionless yaw moment $(M_x/(\rho\omega^2 a^5))$ and dimensionless pitch moment $(M_y/(\rho\omega^2 a^5))$ with the dimensionless fill radius r_0 for different Reynolds numbers and for an aspect ratio of $\eta = 4.5$, a coning frequency of $\tau = 0.1$, and coning angle of $\theta = 2$ deg. The aspect ratio and coning frequency chosen are typical of what is recorded in flight for liquid-filled projectiles (Miller, 1991). The coning angle, however, was chosen so small for the sake of determining if there are any nonlinear effects on the moments at small coning angles. The figures compare the nonlinear results (shown as circles) with the linear ones (shown as solid lines). As can be seen, these figures indicate no difference in both results even for the pitch moment which requires the mean of the azimuthal velocity v_0 (which cannot be determined from linear analysis) and the fundamental of the axial velocity w_1 (which can be determined from linear analysis).

We have also computed the moments at the same coning frequency and aspect ratio as the above results, but at high
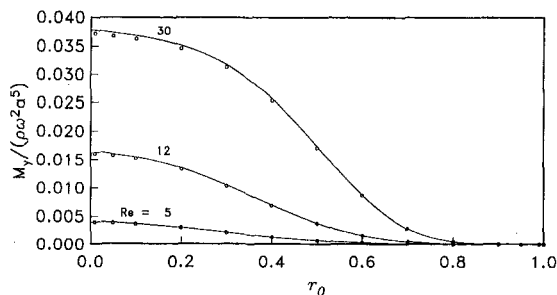
coning angle, $\theta = 20$ deg. The results show no nonlinear effects on the yaw moment (M_x) and roll moment (M_z) for fill radii not too close to that causing resonance with inertial waves and a negligible effect for fill radii close to that causing resonance with inertial waves. A detailed discussion of resonance is given by Selmi and Herbert (1995). There is, however, a slight nonlinear effect on the pitch moment M_y as can be seen from Fig. 4. This effect is seen for any fill radius and it is due to the contribution of the mean component of the azimuthal velocity. Nevertheless, this effect is insignificant for all engineering practices. The difference between linear and nonlinear results does not surpass 2 percent.

Figure 5 compares our results with those obtained by Selmi (1991) using the SLH method of Selmi et al. (1992) and those obtained by Murphy et al. (1989) using the KGS method. The slight discrepancy between our linear results and the linear results of Selmi (1991) is due to difference in resolution with the eigenfunction approach being the most accurate since a large number of eigenfunctions are used in the SLH expansion as compared to the number of Chebyshev polynomials used here. In this study, we have used 11×11 Chebyshev polynomials in r and z and 5 Fourier functions in ϕ. In the eigenfunction approach as many as 120 eigenfunctions in z are used as it does not require intensive CPU time since it converts the three-dimensional problem into a one-dimensional one. The slight discrepancy between our results and the linear results of Murphy et al. is probably due to the boundary layer approximation used in the KGS method.

All of the above moments have been computed for relatively small coning frequencies ($\tau \approx 0.1$) which are of practical interest in the case of flights of liquid-filled projectiles. However, our method can handle the computation of moments at higher values of the coning frequency. Figures 6 and 7 show the yaw

Fig. 4 Dimensionless pitch moment versus dimensionless fill radius for a cylinder containing a central rod at $\tau = 0.1$, $\eta = 4.5$ and $\theta = 20$ deg. Comparison of the linear results (solid lines) and nonlinear results (circles).
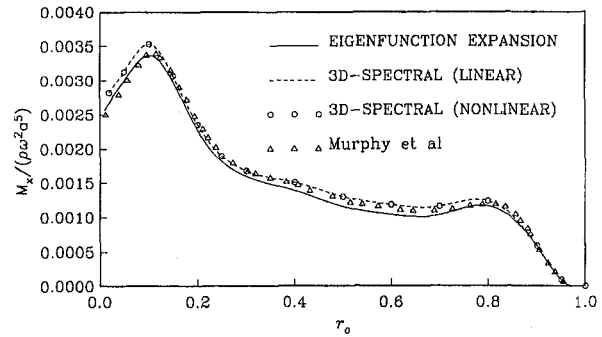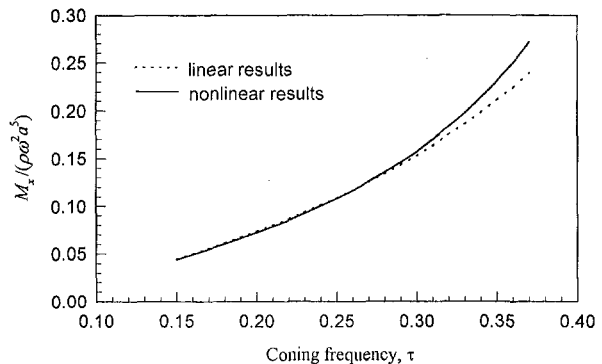

Fig. 6 Dimensionless yaw moment versus coning frequency for a cylinder containing a central rod at Re $= 500$, $\eta = 4.368$, $\theta = 20$ deg, and $r_0 = 0.2$. Comparison of the linear results (- - -) and nonlinear results (—).
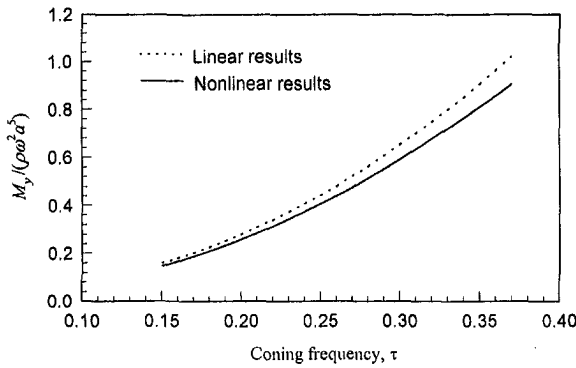
Fig. 7 Dimensionless pitch moment versus coning frequency for a cylinder containing a central rod at Re = 500, η = 4.368, θ = 20 deg, and r_0 = 0.2. Comparison of the linear results (---) and nonlinear results (—).

and pitch moments versus the coning frequency respectively for a cylinder containing a coaxial rod. As can be seen from the figures and as it is expected nonlinear effects increase as the coning frequency increases. For the case depicted in both figures, we see that the moments computed using nonlinear analysis start to deviate significantly from those computed using linear analysis as the coning frequency surpasses about 0.3.

6 Conclusions

We have described in details how to solve the steady three-dimensional Navier-Stokes equations describing the motion of a liquid inside a spinning and coning cylinder containing a partial fill or a central rod at arbitrary Reynolds number, coning frequency, coning angle, and fill ratio by the spectral collocation technique. We have also presented how to calculate the moments caused by the liquid inside the cylinder.

The spectral collocation codes which solve the three-dimensional Navier-Stokes equations have shed some lights into how significant nonlinear effects are on the moments for Reynolds numbers up to 1000 and for flight parameters of practical interest ($\tau \approx 0.1$). In this regard, it was found that for small coning angles, there is no effect at all. However, as the coning angle increases there is a small effect on the Roll and Yaw moments near resonance and there is a small effect on the pitch moment which is due to the contribution of the mean of the azimuthal velocity. Nevertheless, this effect is negligible from the viewpoint of engineering design and analysis. It has also been found that as τ increases, nonlinear effects increase, and they become significant as ϵ surpasses 0.1.

Acknowledgments

References

Hall, P., R. Sedney, and N. Gerber, 1990, "Dynamics of the Fluid in a Spinning Coning Cylinder," *AIAA Journal*, Vol. 28, No. 5, pp. 828–835.

Herbert, T., 1985, "Viscous Fluid Motion in a Spinning and Nutating Cylinder," *Journal of Fluid Mechanics*, Vol. 167, pp. 181–198.

Herbert, T., and R. Li, 1990, "Computational Study of the Flow in a Spinning and Nutating Cylinder," *AIAA Journal*, Vol. 28, No. 9, pp. 1596–1604.

Li, R., and T. Herbert, 1991, "Numerical Study of Unsteady 3D Flows in a Spinning and Nutating Cylinder," *Proceedings of the 1991 AHPCRC Workshop on Problems of Rotating Liquids*, Report CRDEC-SP-038, edited by D. D. Joseph and M. C. Miller, pp. 159–174.

Murphy, C. M., 1985, "A Relation Between Liquid Roll Moment and Liquid Side Moment," *Journal of Guidance, Control, and Dynamics*, Vol. 8, pp. 287–288.

Murphy, C. H., J. W. Bradley, and W. H. Mermagen, 1989, "Side Moment Exerted by a Spinning, Coning, Highly Viscous Liquid Payload," Ballistic Research Laboratory, Technical Report BRL-TR-3074.

Selmi, M., 1991, "Resonance Phenomena in Viscous Fluid Configurations Inside a Spinning and Coning Cylinder," Ph.D. dissertation, The Ohio State University, Columbus, Ohio.

Selmi, M., R. Li, and T. Herbert, 1992, "Eigenfunction Expansion of the Flow in a Spinning and Nutating Cylinder," *Physics of Fluids A*, Vol. 4, No. 9, pp. 1998–2007.

Selmi, M., and T. Herbert, 1995, "Resonance Phenomena in Viscous Fluids Inside Partially Filled Spinning and Nutating Cylinders," *Physics of Fluids*, Vol. 7, No. 1, pp. 108–120.

Stewartson, K., 1959, "On the Stability of a Spinning Top Containing Liquid," *Journal of Fluid Mechanics*, Vol. 5, No. 4, pp. 577–592.

Wedemeyer, E. H., 1966, "Viscous Corrections to Stewartson's Stability Criterion," Ballistic Research Laboratory, Report 1325.

A Solution Procedure

For convenience, we treat both configurations simultaneously by introducing the parameter α, where $\alpha = 0$ is used in case of a cylinder with a central rod and $\alpha = 1$ is used in case of a partially filled cylinder. We approximate the flow quantities by

$$v_r = \sum_{k=0}^{K+\alpha-1} \sum_{l=0}^{L} \sum_{m=0}^{M-1} u_{klm} R_k^u(\tilde{r}) \cos(l\phi) Z_m^u(z/\eta)$$
$$+ \sum_{k=0}^{K+\alpha-1} \sum_{l=1}^{L} \sum_{m=0}^{M-1} \tilde{u}_{klm} R_k^u(\tilde{r}) \sin(l\phi) Z_m^u(z/\eta) \quad (9)$$

and similar expressions for v_ϕ, v_z, and p^d, where $\tilde{r} = (2r - 1 - r_0)/(1 - r_0)$ is an algebraic mapping that maps the radial domain $[r_0, 1]$ into the interval $[-1, 1]$, $R_k^\beta(\tilde{r})$ and $Z_m^\beta(z/\eta)$, with $\beta = u$, v, w, or p, are linear combinations of Chebyshev polynomials suitably chosen for each flow configuration to satisfy both symmetry and boundary conditions. If T_m denotes a Chebyshev polynomial of order m, these functions are

$$Z_m^u\left(\frac{z}{\eta}\right) = Z_m^v\left(\frac{z}{\eta}\right)$$

$$= \begin{cases} T_{2m+2}\left(\dfrac{z}{\eta}\right) - T_{2m}\left(\dfrac{z}{\eta}\right), & \text{if } l \text{ is even,} \\[2ex] T_{2m+3}\left(\dfrac{z}{\eta}\right) - T_{2m+1}\left(\dfrac{z}{\eta}\right), & \text{if } l \text{ is odd,} \end{cases} \quad (10)$$

$$Z_m^w\left(\frac{z}{\eta}\right) = \begin{cases} T_{2m+2}\left(\dfrac{z}{\eta}\right) - T_{2m}\left(\dfrac{z}{\eta}\right), & \text{if } l \text{ is odd,} \\[2ex] T_{2m+3}\left(\dfrac{z}{\eta}\right) - T_{2m+1}\left(\dfrac{z}{\eta}\right), & \text{if } l \text{ is even,} \end{cases} \quad (11)$$

$$R_k^u(\tilde{r}) = R_k^v(\tilde{r}) = R_k^w(\tilde{r})$$

$$= \begin{cases} T_{k+2}(\tilde{r}) - T_k(\tilde{r}), & \text{for the rod case,} \\ T_{k+1}(\tilde{r}) - T_k(\tilde{r}), & \text{for partial fill case,} \end{cases} \quad (12)$$

$$Z_m^p\left(\frac{z}{\eta}\right) = \begin{cases} T_{2m}\left(\dfrac{z}{\eta}\right), & \text{if } l \text{ is even,} \\[2ex] T_{2m+1}\left(\dfrac{z}{\eta}\right), & \text{if } l \text{ is odd,} \end{cases} \quad (13)$$

$$R_k^p(\tilde{r}) = T_k(\tilde{r}). \quad (14)$$

All these expansion functions satisfy all boundary conditions implicitly except for the case of partial fill. For this case, expansion (12) does not allow satisfying the interface conditions implicitly. They are satisfied explicitly and that's why in series (9) one extra expansion function in the radial direction is assumed for the partial fill case. When series (9) are substituted into the governing Eqs. (2) and the resulting equations are satisfied at the collocation points,

$$\left(\tilde{r}_k, \phi_l, \frac{Z_m}{\eta} \right)$$

$$= \left(\cos \frac{2k+1}{2K} \pi, 2\pi \frac{l-1}{2L+1}, \cos \frac{2m+1}{4M} \pi \right), \quad (15)$$

where $k = 0, 1, 2, \ldots, K - 1$, $l = 1, 2, \ldots, 2L + 1$, and $m = 0, 1, 2, \ldots, M - 1$, a system of nonlinear algebraic equations for the $4 \cdot (K + \alpha) \cdot (2L + 1) \cdot M$ unknown expansion coefficients results. This system of equations can be written as

$$\mathbf{f}(\mathbf{C}) = 0, \quad (16)$$

where $\mathbf{f}$ is a vector function representing the governing equations at the collocation points and $\mathbf{C}$ is a vector whose entries are the expansion coefficients. Since this system is nonlinear, it must be solved iteratively. If $\mathbf{C}^{old}$ denotes a known approximate solution, then a closer solution to the right one, $\mathbf{C}^{new}$, could be obtained by Newton-Raphson iteration,

$$\mathbf{C}^{new} = \mathbf{C}^{old} - J^{-1} \mathbf{f}(\mathbf{C}^{old}), \quad (17)$$

where J is the Jacobian of the system. Of course it is not needed that J be inverted, but a correction, $\delta\mathbf{C}$, to the old solution is found first by solving the linear system,

$$J\delta\mathbf{C} = -\mathbf{f}(\mathbf{C}^{old}), \quad (18)$$

then, the new solution is formed as follows: $\mathbf{C}^{new} = \mathbf{C}^{old} + \delta\mathbf{C}$. The iteration is repeated till the new solution becomes the same as the old one within a small prescribed error. This method requires solving a new system in each iteration and could be quite expensive. A less expensive method is the modified Newton's method. If we let

$$\mathbf{C} = \bar{\mathbf{C}} + \delta\mathbf{C}, \quad (19)$$

where $\bar{\mathbf{C}}$ is a known solution, and substitute it into Eq. (16), the following system results

$$J\delta\mathbf{C} = -\mathbf{f}(\bar{\mathbf{C}}) + \mathbf{g}(\delta\mathbf{C}) \quad (20)$$

where $\mathbf{g}$ is a nonlinear vector function of $(\delta\mathbf{C})$. The above system is also solved iteratively. In the first step, the nonlinear terms are neglected, that is we solve

$$J\delta\mathbf{C}^0 = -\mathbf{f}(\bar{\mathbf{C}}) \quad (21)$$

for $\delta\mathbf{C}^0$ which is a first guess for $\delta\mathbf{C}$. In the subsequent steps, if the superscript i denotes the ith iteration, we solve

$$J\delta\mathbf{C}^i = -\mathbf{f}(\bar{\mathbf{C}}) + g(\delta\mathbf{C}^{i-1}). \quad (22)$$

The iteration is stopped when $\delta\mathbf{C}^i$ becomes within a small error of $\delta\mathbf{C}^{i-1}$.

The above analysis could be quite confusing as far as how to generate the discrete system and how to solve it. A simpler way to understand this is as follows. We split the flow variables as

$$v_r = \bar{U} + U, \quad v_\phi = \bar{V} + V,$$
$$v_z = \bar{W} + W, \quad p^d = \bar{P} + P, \quad (23)$$

where $\bar{U}$, $\bar{V}$, $\bar{W}$, and $\bar{P}$ represent a known approximate solution. This could be an exact solution at a different Reynolds number than the desired one. The purpose now is to solve for the correction variables U, V, W, and P. We substitute Eqs. (23) into the governing Eqs. (2) and expand U, V, W, and P in series as in expansion (9). If the resulting equations are satisfied at the collocation points (15) and the expansion coefficients are stored in the vector $\delta\mathbf{C}$, we obtain the system of Eqs. (20). Now if the nonlinear terms are neglected and the approximate solution (represented by $\bar{U}$, $\bar{V}$, $\bar{W}$, and $\bar{P}$ or $\bar{\mathbf{C}}$) is updated during each iteration, the Jacobian changes and a linear system is solved for the corrections U, V, W, and P or $\delta\mathbf{C}$ during each iteration. This method is known as the Newton-Raphson's method. If, however, the nonlinear terms are kept and the original approximate solution is kept unchanged during each iteration, the Jacobian does not change and a linear system is solved once and only the right hand side of the system changes during each iteration. This method is known as the modified Newton's method.

Friction Factor In Sine-Pipe Flow

C. O. Popiel

Professor,
Heat and Fluid Flow Group,
Poznan University of Technology,
60-965 Poznan, Poland

D. F. van der Merwe

Professor,
Energy Laboratory,
Rand Afrikaans University,
Johannesburg, South Africa

Measurements of pressure losses in a sine-waved hydraulically smooth pipe, having a centerline described by the formula $y = h \sin (2\pi x/\lambda)$, are presented. The effect of the dimensionless wave-length (λ/d) and amplitude (h/d) on the Darcy friction factor was investigated in the range of the Reynolds number from about 100 to 10 000, and in the ranges of wavelength from $\lambda/d = 17.7$ to 150 and amplitude from $h/d = 1.5$ to 32. The Dean number, based on the minimum radius of the sine-waved centerline curvature, below which the influence of the sine-pipe shape in comparison to the straight tube was not seen is $De \leq \sim 20$. A smooth transition from laminar to turbulent region in the friction factor versus Reynolds number plot was observed. In turbulent region the effect of the sine-pipe shape can be neglected for $\lambda/d \geq 1.36*h/d + 36.2$.

Introduction

The sine-waved pipe can be one of the most efficient tube shapes used in many heat transfer equipment because of the more vigorous mixing of fluid provided by the alternating bends than, for example, in coiled pipes (Shimizu et al., 1982) and a good relaxation of possible thermal stresses. This tube configuration should find wider application when the fluid and heat flow characteristics are known and the optimization of the tube geometry is possible. At present, the sine-waved tubes are used, for example, in shell-and-tube heat exchangers for domestic and industrial water heating systems, in floor heating systems and in plate solar collectors.

Flows in helical coils and in single bends of the pipe of circular cross-section are well recognized (for example: Ward-Smith, 1980; Berger and Talbot, 1983; Ito, 1987). Fluid in the central part of the pipe having higher velocity is subjected to a larger centrifugal force than the slower fluid at the pipe walls. This causes the fluid to move outward from a central region of the pipe towards the side walls producing a secondary flow imposed on the main axial flow which is seen as a counter-rotating helical vortex pair (originally described by Dean, 1927). For flow in a single bend, for example in a 90 deg bend having a curvature ratio (ratio of centerline curvature radius to the tube radius) lower than $2R_c/d = 3$, a separation and reversed flow can occur. Strong influence of the single bend curvature on the pressure difference between outer and inner walls appears about two diameters upstream and exists about three diameters downstream from the bend (Ito, 1960). One can expect that the velocity profile distorted by the bend will be observed for much longer downstream distance. Flow in a wavy pipe approaching a consecutive bend (sine crest) will be much more complex. Pressure losses of the flow in a sine-wavy pipe will be a result of the very complex velocity gradient distribution and friction at the pipe wall and of the dissipation of energy of the vortex pair produced by each consecutive bend. The only data concerning pressure drop in a sine pipe flow (only at $h/d = 10$) were reported by Abou-Arab et al. (1991).

In our paper, the results of measurements of pressure losses in a sine-wavy pipe flow are presented for a wide range of the two nondimensional geometrical parameters (i.e., h/d-sine-wave amplitude and λ/d-sine-wavelength) and of the Reynolds number.

Experimental Setup

Pressure losses in a sine-wavy pipe flow were measured using the set up shown schematically in Fig. 1. Constant pressure

before the test section assured a constant flow rate during each run when a flow rate, pressure loss, and temperature were recorded. A fully developed pipe velocity profile at the entrance to the test section was obtained with the developing section of the 100d long straight pipe. For the developing and test sections a high quality thick-walled plastic pipe of 5.66 mm in diameter was used. A precise determination of the internal diameter of the test section plastic pipe was achieved by weighing the mass of water filling the pipe of known length. The length of the pipe of the test section was 5 m. The centerline of the sine-waved pipe was determined by the formula $y = h* \sin (2\pi x/\lambda)$. The sine-waved pipe projected contour was traced on the soft flat plywood plate with the two rows of a number of guiding pins and then the plastic pipe was inserted in between. At small curvature radius (close to $2R_c/d = 3$) some deformation of the circular cross-section of the pipe was compensated by pressing the pipe bends to the plate with semicircular clamps.

Water mass flow rate was measured with a weight technique using two electronic precise scales of 3.5 and 20 kg in range. Pressure losses were measured with 1 m long mercury and 2.5 m long water U-tube manometers, and for very low pressure losses a U-tube water manometer was inclined at a ratio 1:10. It was important to keep the temperature of water in U-tube manometer, in both pressure impulse plastic pipes and in the test section, on the same level. To reduce the entry and exit effects the pressure taps were located in the side plane wall of the sine-waved pipe. The upstream pressure tap was located at the distance 3d before the first bend. Flow rate of water was controlled with the upstream and downstream valves to obtain a stable flow.

Before the main measurements were started a calibration test was executed with the 5 m long straight test section pipe. A very good agreement of the measured pressure losses with the theoretical solution based on the Hagen-Poiseuille law ($f_s = 64/Re$) in a laminar region and with the formula of Blassius ($f_s = 0.3164/Re^{0.25}$) in turbulent region valid for a hydraulically smooth pipe has been observed (Fig. 2). A laminar-turbulent transition was located at the Reynolds number Re = 4000 suggesting relatively calm flow conditions at the inlet to the test section despite the upstream control valve disturbances. Density and viscosity of water were determined with the formulas provided by Gluck (1986). Due to a precise instrumentation and techniques employed a high accuracy of each experimental point was achieved (except some measurements at very low flow rates). The maximum overall uncertainties based on the single sample analysis (e.g., Moffat, 1988) in measurements of the friction factor f were ±4.5 percent at the Re = 100, ±2.5 percent at the Re = 300 and below ±1.5 percent at the Re ≥ 1000 with 95 percent certainty. These values were dominated by the errors associated with the pressure measurements. The
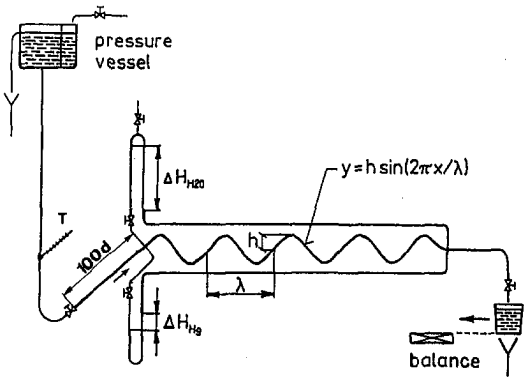
Fig. 1 Line diagram of experimental rig for pressure-loss measurements

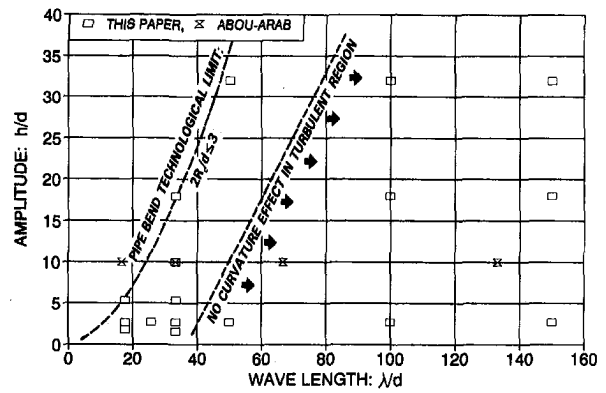$y = h \sin(2\pi x / \lambda)$

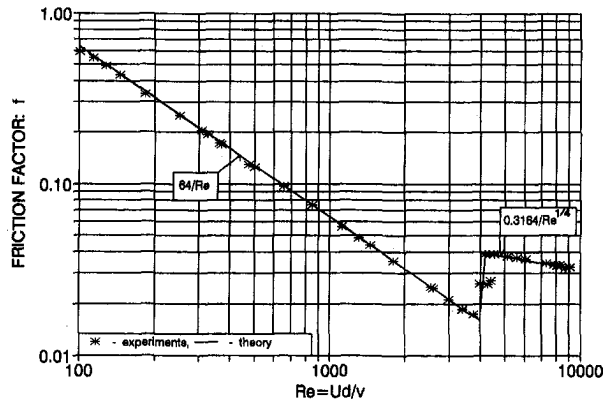Fig. 3 Map of investigated geometrical configurations of a sine-wavy pipe

Fig. 2 Friction factor for a straight pipe flow
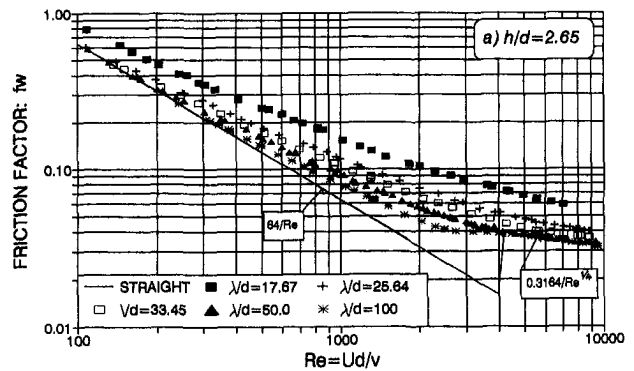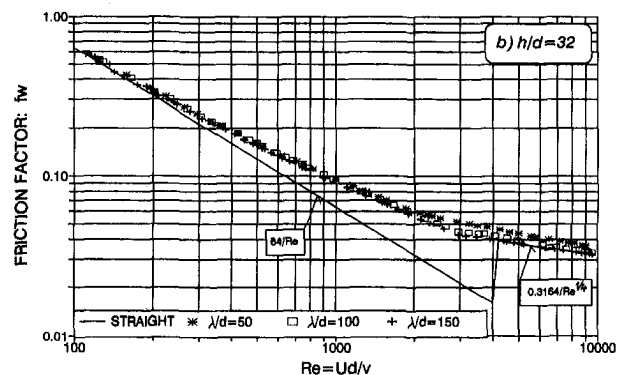

Fig. 4(a)

Fig. 4(b)

Fig. 4 Friction factor as a function of Reynolds number at h/d = const. (effect of λ/d)

uncertainty in determination of the Re number was ± 0.6 percent with 95 percent certainty.

The lowest number of bends of the sine-waved pipe test section in some cases was about 10 (see Table 1). In these cases the distances between the points of the minimum curvature radius were relatively long (about 90d) and the pressure drops on the first, second and subsequent bends were very close. In the remaining cases due to the larger number of bends these differences did not introduce significant errors. Therefore we may say that the obtained results represent the data valid for the periodically developed flow in the sine-waved pipe.

Results and Discussion

A map of 17 geometrical configurations for which a series of measurements of pressure losses versus flow rate were performed, is shown in Fig. 3. A general strategy of the distribution of the geometrical parameters of the sine-wave pipe was to cover the practical area of application as well to find the limits of the effect of the sine-wave curvature. There are no experimental points at high amplitude and low wavelength because it was rather difficult to produce pipe bends having a curvature ratio below $2R_c/d = \sim 3$.

Total pressure losses for a sine-wavy pipe flow are presented in a form of the Darcy friction factor versus Reynolds number $f_w = f(\text{Re})$ in Figs. 4 and 5 where the effects of the wave

Nomenclature

d = diameter of tube

De $= \text{Re}(d/2R_c)^{1/2}$ = Dean number

$f = \Delta P/(0.5*U^2\rho L/d)$ = Darcy friction factor

h = sine-wave amplitude

L = length of tube

ΔP = pressure losses

$R_c = (\lambda/2\pi)^2/h$ = minimum radius of the sine-wave curvature

Re $= U*d/\nu$ = Reynolds number

U = mean velocity

λ = sine-wave length

ρ = density of water
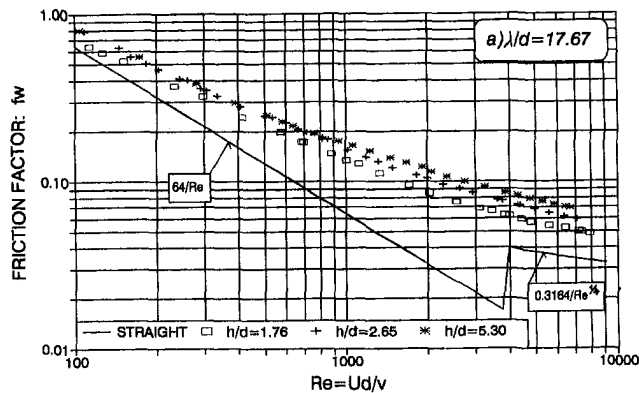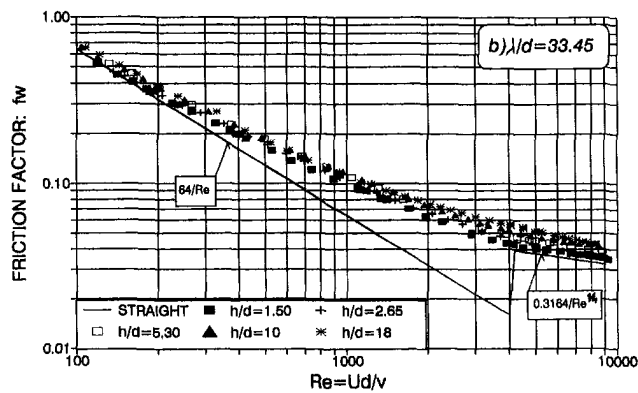
ν = kinematic viscosity of water

Fig. 5(a)

Fig. 5(b)
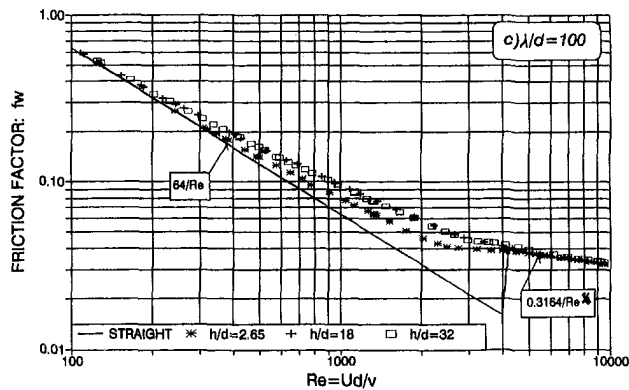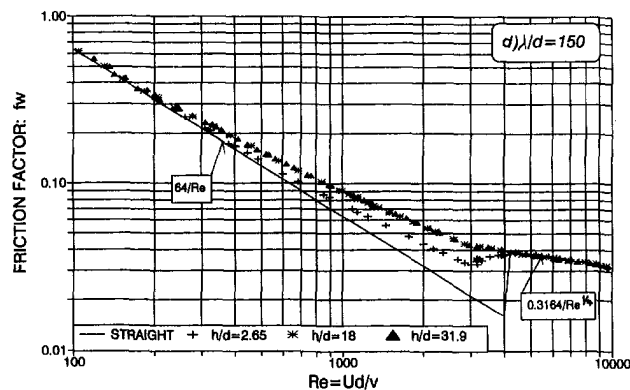

Fig. 5(c)

Fig. 5(d)

Fig. 5   Friction factor as a function of Reynolds number at λ/d = const (effect of h/d)

amplitude h/d and wavelength (λ/d) as parameters are shown, respectively. All these data do not show an abrupt laminar to turbulent transition. A similar behavior of the friction factor against Reynolds number was found in the helical pipe flow (Wojtkowiak and Popiel, 1995). It is known that curvature of the helical pipe increases the critical Reynolds number. In our case one can expect more complex mixing and rather early laminar to turbulent transition. But it is not precisely clear when and how a laminar counter-rotating vortex flow in a helical or sine-waved pipe changes into another flow pattern as the Reynolds number increases to the turbulent flow regime.

Similar lack of clarity was mentioned by Cheng and Yuen (1987) in their experimental study of the flow in a 180 deg pipe bend. From the smooth laminar-turbulent flow transition displayed by the friction factor when plotted versus Reynolds (or Dean) number it was concluded that in the elongated transition region the laminar counter-rotating vortex pair is gradually replaced by a well-mixed turbulent flow. Closer comparison of all data at constant h/d or λ/d (Figs. 4 and 5) shows that the friction factor depends on two parameters describing a sine-centerline and none of them can be overlooked as was done by Abou-Arb et al. (1991) who performed measurements at h/d = 10 only. The best agreement of our data with the results of Abou-Arab et al. was obtained using results taken from their Figs. 7 and 8 and what is shown in our Fig. 6 for λ/d = 33.45 and h/d = 10. In laminar region, an inclination line of their results slightly differs from the trend of our results, in turbulent region their results are lower by about 15 percent. It seems that there are some discrepancies between the data of Abou-Arab et al. shown in their Fig. 5 and in the formula for laminar case, and the rest of their results.

In the straight tube turbulent flow region the effect of the sine-waved pipe curvature on the friction factor can be neglected for some geometrical configurations (Fig. 3), for instance, at h/d = 2.65 for $\lambda/d \geq$ ~40, at h/d = 18 for $\lambda/d \geq$ ~60, and at h/d = 32 for $\lambda/d \geq$ ~80, i.e., at

$$\lambda/d \geq 36.2 + 1.36 * h/d$$

In the laminar region this effect vanishes below the Dean number De = ~20 for all tested geometrical parameters, as shown clearly in Fig. 7.

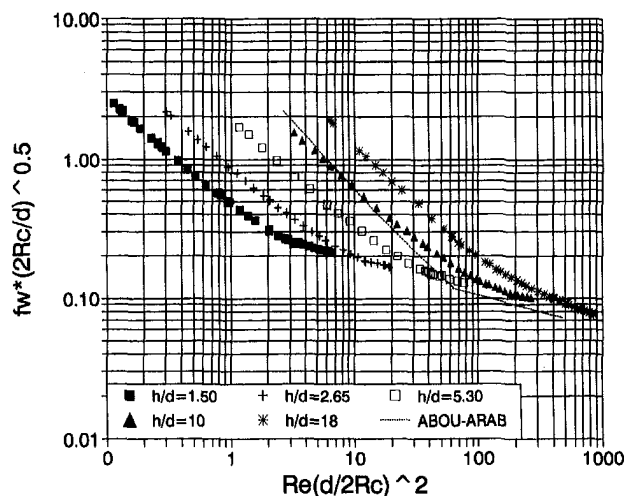Fig. 6   Modified friction factor as a function of the modified Dean number at λ/d = 33.45
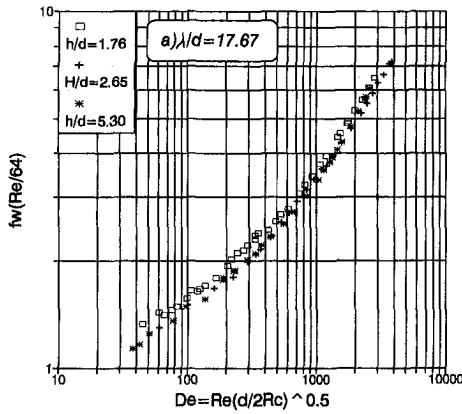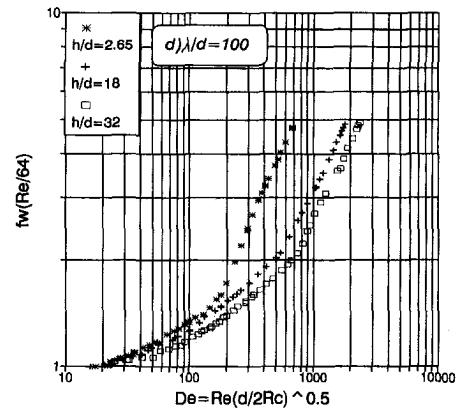
Fig. 7(a)

Fig. 7(b)

Fig. 7(c)

Fig. 7(d)
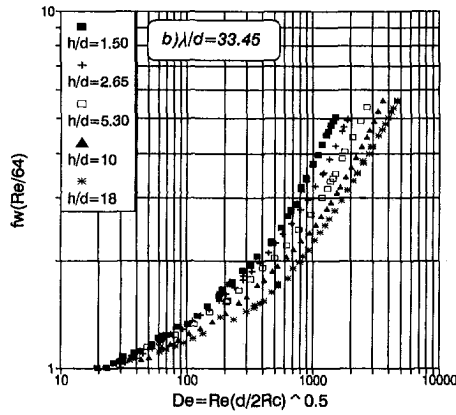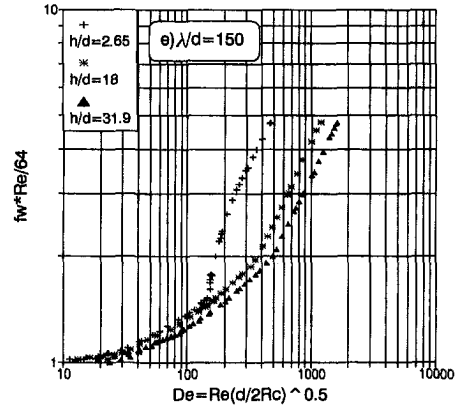
Fig. 7(e)
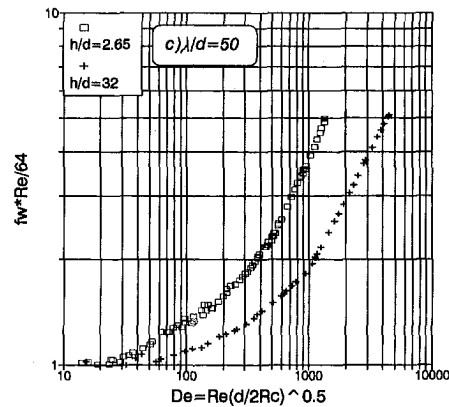
Fig. 7 Normalized friction factor versus modified Dean number at λ/d = const.

pair on the pressure losses is gradually replaced by the growing turbulent mixing as the Reynolds number is increased.

The effect of the sine-wavy pipe curvature vanishes below the Dean number De = ~20 for all tested geometrical configurations. In the turbulent region the effect of the sine-wavy shape can also be neglected for $\lambda/d > 1.36*h/d + 36.2$.

Acknowledgment

In Fig. 6, the experimental data for $\lambda/d = 33.45$ are presented in a form of the modified friction factor versus a modified Dean number (after Ito, 1987):

$$f_w^*(2R_c/d) = f[\text{Re}^*(d/2R_c)^2]$$

At higher values of $\text{Re}^*(d/2R_c)^2$ data have a tendency to follow one line. However, it is not easy to correlate all the data with a single formula for all values of λ/d.

Concluding Remarks

The Darcy friction factor versus Reynolds number plot for a sine-waved pipe flow shows a smooth transition from the laminar to the turbulent regime. In this elongated transition region presumable the effect of the counter-rotating laminar vortex

Table 1 Geometrical parameters of the investigated sine-waved pipe (L = 5 m, d = 5.66 mm)

h/d	λ/d	$2R_c/d$	No. of bends
1.5	33.45	37.8	51
1.76	17.67	9.00	92.4
2.65	17.67	5.97	84
2.65	25.6	12.57	63.7
2.65	33.45	21.4	50
2.65	50	47.9	34.7
2.65	100	191	17.5
2.65	150	430	11.6
5.3	17.67	2.93	62
5.3	33.45	10.7	44
10	33.45	5.67	32.5
18	33.45	3.15	21.9
18	100	28.1	14
18	150	63.3	10.43

References

1 Abou-Arab, T. W., Aldoss, T. K., and Mansour, A., 1991, "A Pressure Drop in Alternating Curved Tubes," *Applied Scientific Research*, Vol. 48, pp. 1–9.

2 Burger, S. A., Talbot, L., and Yao, L. S., 1983, "Flow in Curved Pipes," *Annual Review of Fluid Mechanics*, Vol. 15, pp. 461–512.

3 Cheng, K. C., and Yuen, F. P., 1987, "Flow Visualization Studies on Secondary Flow Patterns in Straight Tubes Downstream of a 180 deg Bend and in Isothermally Heated Horizontal Tubes," ASME *Journal of Heat Transfer*, Vol. 109, pp. 49–54.

4 Dean, W. R., 1927, "Note on the Motion on Fluid in a Curved Pipe," *Philos. Mag.*, Vol. 4, pp. 208–223.

5 Gluck, B., 1986, *Zustands-und Stoffwerte, Wasser, Dampf, Luft*. VEB-Verlag, Berlin.

6 Ito, H., 1960, "Pressure Losses in Smooth Pipe Bends, ASME *Journal of Basic Engineering*, Vol. 82, pp. 131–143.

7 Ito, H., 1987, "Flow in Curved Pipes," *Int. Journal J.S.M.E.*, Vol. 30, pp. 543–552.

8 Moffat, R. J., 1988, "Describing the Uncertainties in Experimental Results," *Experimental Thermal and Fluid Science*, Vol. 1, pp. 3–17.

9 Shimizu, Y., Sugino, K., Kuzuhara, S., and Murakami, M., 1982, "Hydraulic Losses and Flow Patterns in Bent Pipes (Comparison of the Results in Wavy Pipes and Quasi-Coiled Ones)," *Bulletin J.S.M.E.*, Vol. 25, pp. 24–31.

10 Ward-Smith, A. J., 1980, *Internal Fluid Flow. The Fluid Dynamics of Flow in Pipes and Ducts. Chapter B: Bends*, Clarendon Press, Oxford, pp. 248–306.

11 Wojtkowiak, J., and Popiel, C. O., 1995, "Flow Resistance Coefficient for a Helical Pipe," *Inzynieria Chemiczna i Procesowa*-PAN, No. 2, pp. 273–281 (in Polish, extended English abstract).

N. J. Locke
Research Engineer.

P. S. Jackson
Professor.

R. G. J. Flay
Senior Lecturer.

Department of Mechanical Engineering,
University of Auckland,
Private Bag 92019,
Auckland 1, New Zealand

Lift and Drag Distributions of Yacht Sails Using Wake Surveys

The theory and numerical methods used to determine the lift and drag of a yacht model from wind-tunnel wake measurements are discussed. The results from wake surveys taken downstream of a 1/40th scale IACC model yacht are presented. The lift and drag distributions are given as well as plots of the total pressure loss, vorticity, and stream-function, which are helpful in understanding the flow structure.

Introduction

Computer models which predict the performance of yachts at the design stage are widely used by modern yacht designers. Given the heading of the yacht relative to the wind and the wind speed, these models balance the hydrodynamic and aerodynamic forces and moments acting on the hull and sails in order to predict the hull speed (a good survey of this field is given by Larsson, 1990). An essential prerequisite for this process is a reliable model for the sail aerodynamics, which is capable of predicting the lift, drag, and moment of multiple interacting sails of any planform at any heel angle and over a range of angles of attack from 0 to 180 degrees. In addition, any sail while in use may have its camber altered from 5 to 20 percent, and its geometric twist over the span varied from 15 to 30 degrees. This is obviously a very demanding task, and the key to the development of suitable models is an understanding both of the nature of the flow over yacht sails and of the way in which this is affected by changes in sail shape. While it is possible to measure the total forces and moments on a set of sails it is far more difficult to make direct measurements of the distribution of the lift and drag over the span, and this is also a serious obstacle to the calibration of the numerical methods needed to provide a better understanding of the effect of sail shape on performance. The difficulty arises because pressure measurements must be made without interfering either with the flow or the flexibility of the sails, and this is very difficult to achieve on a model.

One way to determine the distribution of lift and drag along the span, and to break down the components of drag into induced drag and profile drag, is to infer them from measurements made in the wake of the sails. This technique is well established in the testing of lifting surfaces (Brune, 1994) and has been widely used in developing an understanding of the drag of bluff bodies such as vehicles (Ahmed et al., 1984). This paper investigates the use of this technique for yacht sails, and presents some typical results.

Wake surveys were carried out downstream of a model yacht that was mounted in an open-jet, slotted-wall, wind-tunnel. The velocity components and total pressure loss in the wake were measured using a 5-hole pressure probe that was moved over the wake plane using a 2-D traversing rig. The theory used to determine the lift and drag distributions from the experimental wake measurements is discussed, and sail test results from a 1/40th scale I.A.C.C. (International Americas Cup Class) model yacht are presented. The structure of the flow in the wake is of

particular interest, and shows quite clearly the sources of the various kinds of drag.

The yacht sail problem is further complicated by the increase in true wind speed with height over the water, which causes the apparent wind speed and direction for the sails to vary along the span of the mast. This causes difficulties in applying the ideas of classical aerodynamics, including the wake theory outlined below. It also means that wind-tunnel testing cannot simulate the true flow conditions unless the same incident twist and shear are modeled, but while the simulation of incident shear is well established the modeling of incident twist is far more difficult in a wind-tunnel. For these reasons, the tests reported here were done in a uniform flow.

Drag From Wake Measurements

Wake integration procedures are now used routinely for the determination of lift and drag forces acting on a body in a wind-tunnel. The necessary relationships are derived by applying the momentum equation to a control volume made up, as shown in Fig. 1, of transverse planes of area A upstream and downstream of the body and an intervening tube that is taken to lie just inside the wind-tunnel walls (the effect of the slotted walls used here is considered later). In the streamwise direction this equation gives the body drag in incompressible flow as

$$D = \int_A (p_o - p + \rho U_o^2 - \rho u^2)dA \qquad (1)$$

where the integration is taken over the downstream plane, and the upstream plane is sufficiently removed that free-stream conditions apply (as indicated by the zero subscript). Introducing the total pressure, $P = p + (\rho/2)(u^2 + v^2 + w^2)$, this becomes

$$D = \int_A (P_o - P)dA + \frac{\rho}{2}\int_A (U_o^2 - u^2)dA$$

$$+ \frac{\rho}{2}\int_A (v^2 + w^2)dA \qquad (2)$$

Betz (1925) and Maskell (1972) made significant contributions towards the evaluation and understanding of the second term, using an idea best expressed by splitting the downstream axial velocity into three components as shown in Fig. 2;

$$u = U_o + u_p - u_v, \qquad (3)$$

where U_o is the undisturbed flow, u_p is the flow disturbance in the inviscid region outside the wake (regarded as extending through the wake), and u_v is the reduction in velocity in the wake due to viscous effects. The sum $U^* = U_o + u_p$ may also be regarded as the fictitious axial velocity needed in the wake
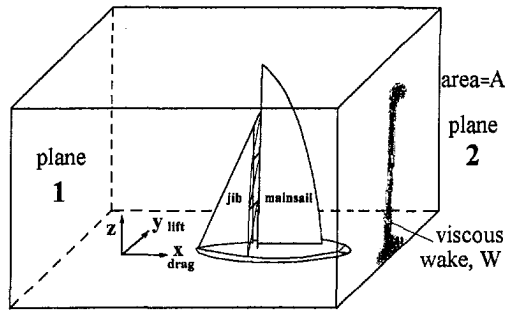
Fig. 1 Control volume, with yacht model and wake

to restore the total pressure there to its upstream value (the concept due to Betz). If there is no flux through the side surfaces S of the control volume, conservation of mass requires the downstream flux of u through the area A to equal the upstream flux of U_o through the same area, and this in turn implies that the fluxes of u_p and u_v must be equal. It is then not difficult to show that the drag may be written as the sum

$$D = D_1 + D_2 + D_3 + D_4,$$

where

$$D_1 = \int_W (P_o - P)dA, \quad D_2 = -\frac{\rho}{2}\int_A u_p^2 dA,$$

$$D_3 = \frac{\rho}{2}\int_W u_v(2u_p - u_v)dA \quad D_4 = \frac{\rho}{2}\int_A (v^2 + w^2)dA. \quad (4)$$

Here the area W is that part of the downstream plane which is intercepted by the viscous wake, as shown in Fig. 1, as by definition it is only here that u_v and $P_o - P$ are nonzero.

This gives a complete set of equations which enables the drag to be calculated from measurements across a wake plane of the total and static pressures and the three components of velocity. It is clear that D_1 and D_3 are due to viscous effects and must be related to profile drag, while D_4 is due to crossflow in the wake and must be related to vortex drag. The significance of D_2 was demonstrated by Wu et al. (1979), who first wrote the crossflow integral D_4 in terms of the stream function ψ and potential ϕ for the two-dimensional flow in the transverse downstream plane associated with the axial vorticity ξ and dilatation f. The governing equations for ψ and ϕ are

$$\frac{\partial^2 \psi}{\partial y^2} + \frac{\partial^2 \psi}{\partial z^2} = -\xi = \frac{\partial v}{\partial z} - \frac{\partial w}{\partial y},$$

$$\frac{\partial \phi^2}{\partial y^2} + \frac{\partial \phi^2}{\partial z^2} = f = \frac{\partial v}{\partial y} + \frac{\partial w}{\partial z} \quad (5)$$

It follows that

$$v = \frac{\partial \psi}{\partial z} + \frac{\partial \phi}{\partial y}, \quad w = -\frac{\partial \psi}{\partial y} + \frac{\partial \phi}{\partial z} \quad (6)$$

which may be used with the divergence theorem to rewrite D_4 as

$$D_4 = D_5 + D_6$$

where

$$D_5 = \frac{\rho}{2}\int_W \psi\xi dA - \frac{\rho}{2}\int_C \psi v_T dA,$$

$$D_6 = -\frac{\rho}{2}\int_A \phi f dA + \frac{\rho}{2}\int_C \phi v_N dA \quad (7)$$

and v_T, v_N are the tangential and normal velocities around the boundary of the downstream plane. If C corresponds to the solid wall of a wind tunnel then the contour integrals vanish, but as here the tunnel has a slotted wall they are retained and calculated as described below. Equations (4) and (7) together form the Hackett and Sugavanam (1984) "gross" form for the drag, which is valid in near wakes as no approximations have been made.

In the case of a potential flow with no trailing vorticity the total drag must vanish. In these circumstances it is also clear that all terms except D_2 and D_6 must be zero, so that these terms must then be complementary. D_2 is therefore the drag due to the axial flow associated with source-like disturbances while D_6 is the drag due to the corresponding crossflow, and these must be equal and opposite. In a real flow therefore, $D_1 + D_3$ are directly associated with viscosity and may be combined to form the profile drag, while D_5 arises from trailing vorticity and is therefore the vortex drag. The evaluation of all three of these terms requires measurements over the wake only. The remaining $D_2 + D_6$ is the drag associated with apparent sources in the flow, and requires measurements over the whole downstream plane.

As noted at the start of this section, this analysis applies to a control volume in which there is no flux across the sidewalls. However, the measurements described below were made in a slotted-wall tunnel in which this condition cannot be guaranteed, and so further contributions to the conservation equations for mass and momentum have to be admitted. It is quite straightforward to show that these two equations lead to an additional component in the drag

$$D_7 = -\rho \int_S u_p v_N dA$$

where S is the side surface of the control volume (the tunnel walls) and v_N as before is the velocity normal to this surface. Since the function of slotted walls is to minimize the effect of tunnel walls on the flow, a properly designed tunnel should result in a negligible value for D_7 and indeed this tunnel has been optimised to give low blockage effects on the drag of bluff bodies (a recent summary of slotted-wall testing for bluff bodies is given by Mokry, 1995).

Although D_7 has not been measured here several remarks may be made regarding its likely magnitude. First, for a source-

---

Nomenclature

p, P = local static and total pressures

u, v, w = local components of velocity

ρ = air density

b = reference length, mast height = 0.83 m

U_o, q_o, P_o = incident mean speed, dynamic, and total pressures

L, D = lift (parallel to the wind tunnel floor) and drag

C_L, C_D = overall force coefficients, using sailplan area as reference

C_l, C_d = sectional force coefficients, using local total sail chord as reference

Wake Section Properties;

ξ, f = axial vorticity and apparent source density of the crossflow

ψ, ϕ = streamfunction and potential of the crossflow

u_p = increase in axial speed due to potential flow effects of body and wake

u_v = decrease in axial speed due to viscous effects

like disturbance u_p will be antisymmetric upstream and down-stream of the source while v_N will be symmetric, so that an integral for D_7 extending both upstream and downstream of the body should be small. Similarly, a transverse vortex (a lifting-line) will also produce symmetric and antisymmetric velocity components, while a trailing vortex will produce no u_p components at all. Second, Hackett and Sugavanam (1985) point out that the $D_2 + D_6$ contribution from apparent sources is usually found to be a small fraction of the drag, even for bluff bodies, and is also difficult to determine accurately because the perturbations outside the wake are so small. Since here the thin sails can only have small displacement effects even close to the sails, source-like contributions to u_p and v_N on the boundary S must be very small indeed. Our approach is therefore to ignore D_7 entirely and to define the vortex drag as simply being the total $D_5 + D_2 + D_6$ and the profile drag as $D_1 + D_3$.

A further contribution to the drag may arise from fluctuating components of velocity—this is readily seen in Eq. (2), where a time-average of fluctuating velocities will leave residual Reynolds stresses in the integrals (with the axial component being of opposite sign to the others). However, unless the position of the wake itself is highly unsteady, as in the case of vortex-shedding from a bluff body, these components will vanish outside the wake where there is no turbulence. Within the wake the turbulent kinetic energies may be expected to be small compared with that of the mean velocity defect, but they were not measured separately here.

Evaluation of the Crossflow

The evaluation of the drag terms D_5 and D_6 first requires the source density f and axial vorticity ξ to be found for the measured crossflow, and then the solutions for the streamfunction ψ and potential ϕ from Eqs. (5). Here f and ξ were evaluated using a finite difference representation of the equations using measurements of v and w made on a regular grid across the downstream plane. Derivatives were calculated at the cell centres by averaging the two first order derivatives found on the edges of the cell. Then f and ξ were evaluated at each mesh node by averaging the 4 adjacent values at the cell centres, except at the boundaries where a first-order approximation was applied directly to the mesh node. The calculation of ξ is the most critical in terms of accuracy; since it has the primary influence on the vortex drag integral, it effectively determines the boundary conditions used to solve for ψ (as discussed below), and it also directly determines the value calculated for the lift.

The stream function ψ was found by solving Eq. (5a) using the method of the false transient (Mallinson and de Vahl Davis, 1973), with a semi-implicit, finite-difference method (the Samarskii Andreyev alternating-direction method) being used to solve the set of equations formed when the finite difference form is applied at each grid node. The second derivatives were represented using central differences.

Most of the work done previously with this wake theory has been carried out in wind tunnels with solid walled test sections. Under such conditions, the boundary conditions needed to solve (5) are found easily and accurately at the wind tunnel walls where $\psi = 0$. However, the flow through the slotted wall wind tunnel used in this study meant that this simple boundary condition could not be applied (except at the floor where $\psi = 0$). To find the ψ boundary values it was instead assumed that the slotted wall wind tunnel performed ideally—that is, it simulated an infinite flow with no subsequent blockage effect. The flow outside the viscous wake can, therefore, be constructed from three potential flows: a vorticity driven flow, a source induced flow and a uniform onset flow. In the wake survey plane, the vorticity calculated at each mesh node was thought of as representing a line vortex, with the combined influence from each line being responsible for the vortex component of the flow.
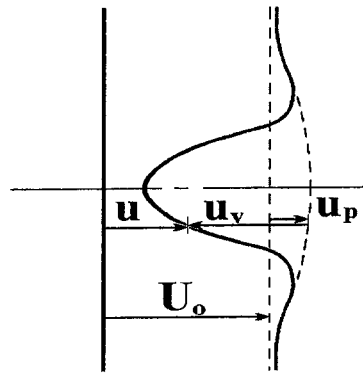

Fig. 2 Sketch defining the components of axial velocity in the wake

Since the stream function should only reflect the flow due to vorticity, the ψ boundary values can be calculated using the potential flow expression for the streamfunction due to a point vortex;

$$\psi_S = \frac{1}{2\pi} \int_W \ln{(r)}dA$$

where r is the distance from a vortex in the wake to the field point on the flow boundary S. At each boundary point the contribution to ψ of each point vortex and its image vortex (using the wind-tunnel floor as a reflection plane) were summed to give the ψ boundary values. The source density ϕ was found using the same procedure as for ψ.

Lift

A similar analysis for the lift L (in the y direction for a yacht) gives

$$L + L_1 = L_2 + L_3$$

where L_1 is the net pressure force acting in the sidewalls of the tunnel for all the flow upstream of the downstream wake plane being considered, and

$$L_2 = \rho U_o \int_A v\,dA = \rho U_o \int_W z\xi\,dA,$$

$$L_3 = \rho \int_A v(u_p - u_v)\,dA. \qquad (8)$$

The term L_2 is the usual term relating lift to the circulation of the lifting body, while Wu and Wu (1989) interpret the last integral as lift penalties due to crossflow in the wake and viscous effects. It is assumed now that the velocity perturbations in the wake and on the sidewalls are small in comparison with U_o, so that only L_2 need be retained.

Instrumentation and Errors

Wake surveys were taken for a 1/40th scale International Americas Cup Class model yacht in a slotted-wall wind-tunnel of cross-section 1.5 m $\times$ 1.5 m and 3.0 m working length, as shown in Fig. 3, the slots extending 1.0 m and 1.4 m upstream and downstream of the model. The wind speed of 11.4 m/s gave a Reynolds number of 3.4×10^5 based on the maximum combined chord of the jib and mainsail (0.45 m). To reduce the effect of the incident floor boundary layer a ground board 1.2 m wide and 2 m long was placed 105 mm above the floor with its leading edge 0.4 m upstream of the model bow. The wake survey data were collected 0.375 m downstream of the mast base, or 0.075 m downstream of the stern of the hull. A non-nulling five-hole probe of 2.5 mm radius was used to measure the pressures and velocities over a sampling grid spaced
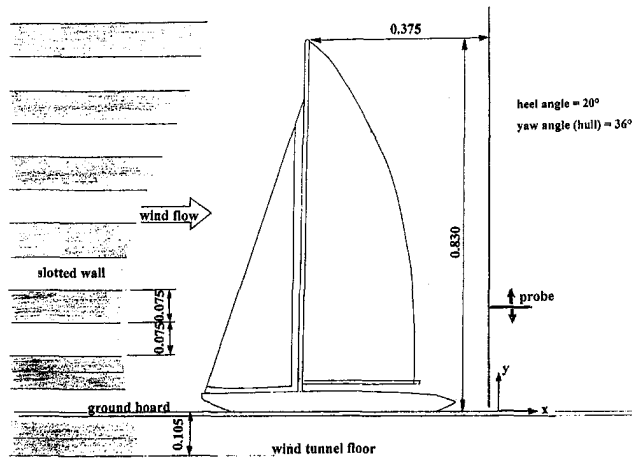
Fig. 3 Sail plan for the model

15 mm in both the horizontal and vertical directions, with the traversing rig having positional accuracy in the vertical and horizontal directions of 0.01 and 0.29 mm, respectively. The density of the data was then numerically increased to a 5 mm × 5 mm grid by fitting cubic splines to the raw data. The net forces calculated from the wake data were non-dimensionalised using the planform area of the sails, and for the moments the mast height was used as the reference length. The sectional forces along the span were evaluated on a horizontal strip 5 mm wide, and the corresponding sectional coefficients were found using the total chord defined as the sum of main and jib chords at each section.

The probe calibration showed a standard deviation for total and dynamic pressures of 0.55 and 0.67 Pa and for flow direction 0.24 deg, and its associated pressure transducer was also accurate to 0.5 Pa. The resulting uncertainty (95 percent confidence) for the pressure loss in the wake and the crossflow speeds, vorticity and streamfunction are shown in the figure captions which follow. This error does not include the averaging effect caused by a probe of nonzero dimensions, which may be significant in the regions of steep gradients (the vortex cores).

Distribution of Lift and Drag for a IACC Yacht Sailplan

The results presented here are for a case with the yacht hull set at 36 deg incidence and heel angle of 20 deg, and the

Table 1 Parameters for the sail shapes

Height z (mm)	Chord (mm)	Twist to tunnel axis	Position of max camber (% of chord)	Value of max camber (% of chord)
		Mainsail		
774	48	−4	48	14
689	103	−4	46	12
603	151	1	43	11.5
514	191	3	46	14
411	223	5	45	13
310	239	7	43	14
203	249	11	44	12.5
92	252	16	47	9.5
		jib		
514	50	−8	31	12
411	90	−2	29	13
310	129	5	27	15.5
203	170	9	34	12
92	213	10	46	9
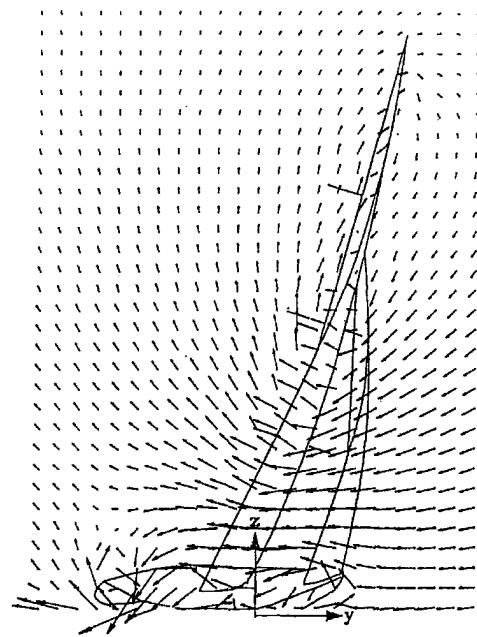
Fig. 4 Velocity vectors, showing direction and relative speeds of the wake crossflow (uncertainty 4.7 percent)

sails adjusted to give smoothly attached flow (as determined by tufts). Data for the resulting sail shapes (as measured from photographs) are given in Table 1. The measured crossflow velocities and total pressure loss are shown in Figs. 4 and 5, and the calculated vorticity and stream-function fields in Figs. 6 and 7. The separate wakes of the main- and head-sails are easily distinguished. A strong vortex core is present at the foot of the sails (in the wake centre and near the floor in Fig. 5), which is due to the significant gap beneath the foot of the mainsail—the rapid unloading of this sail toward the foot results in the usual concentrated trailing vortex. However, there is no corresponding vortex core at the head of the sails, which
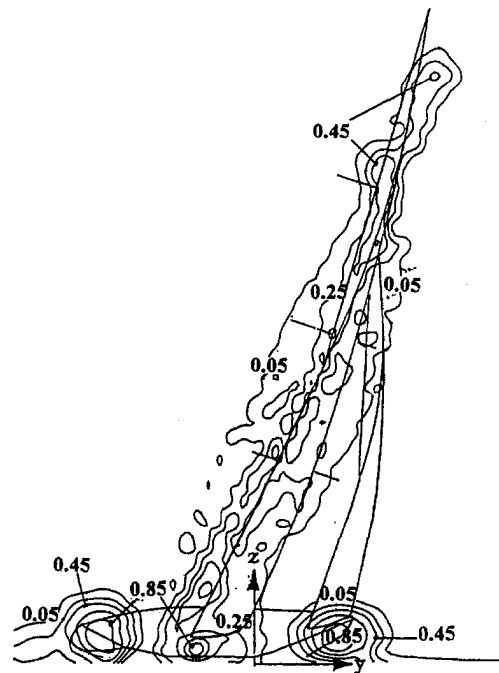
Fig. 5 Total pressure loss contours in the sail wake, $(P_o - P)/q_0$ (4 levels in the range 0.05 to 0.85, uncertainty 3.2 percent)

Fig. 8 Distribution of the lift force and drag coefficients across the span

Fig. 6 Contours of crossflow vorticity in the wake, $\xi b/U_o$ (10 levels in the range −31 to +39, 10.3 percent uncertainty)

is due to the continuous decrease in sail chord and increase in twist along the span. As seen below, the sail unloads more or less uniformly along its span and so sheds vorticity continuously instead of as a concentrated tip vortex. Not unexpectedly, there is a large head loss at the top of the headsail where the two sails join, and again in the vortex core from the foot of the main.
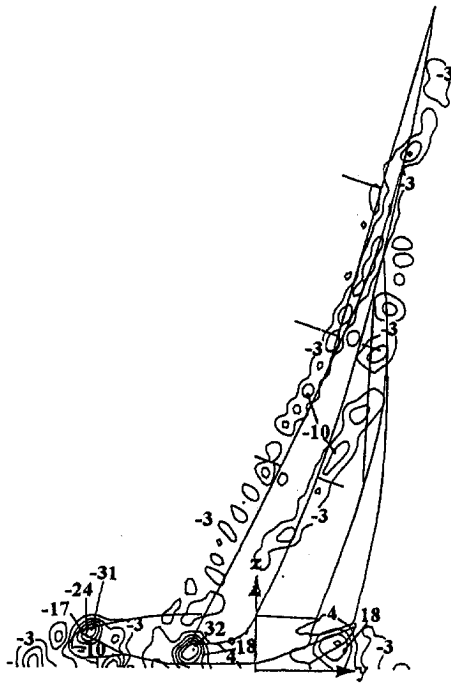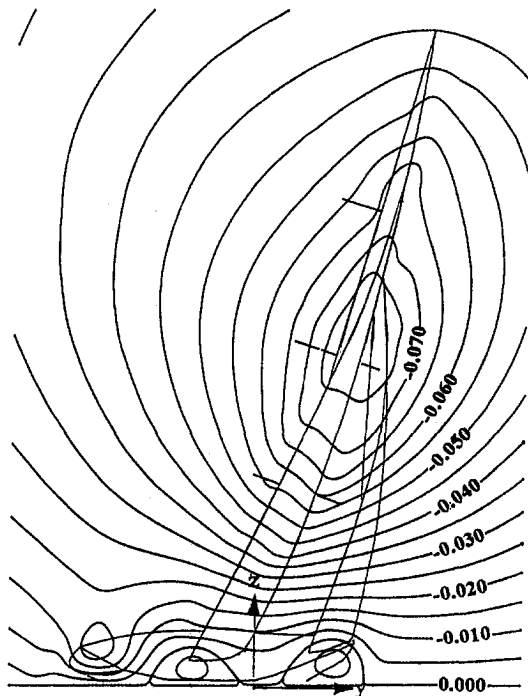

Fig. 7 Streamfunction contours in the wake, ψ/bU_o, superimposed on the projection of the model (16 levels in the range −0.075 to +0.005, 1.5 percent uncertainty)
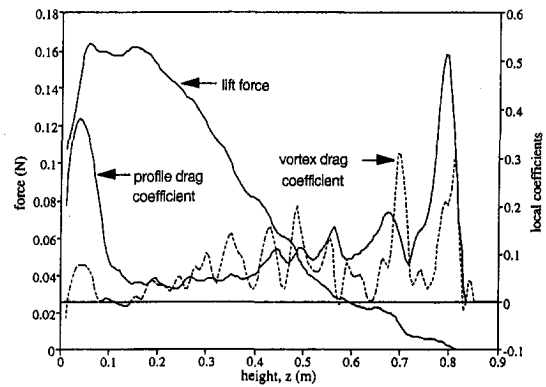
However, there are two further vortex cores (the outer two of Fig. 5) whose presence has hitherto not been suspected, but which is easily explained with hindsight; the hull is a bluff body on the tunnel floor, and therefore the incident floor boundary layer forms a horseshoe vortex around the hull whose trailing legs form the cores. Since they contain fluid from the floor boundary layer upstream of the model, a high loss in total pressure is observed within these cores. This horseshoe vortex is only partly an artefact of testing in a wind-tunnel as a real yacht also moves into a flow containing incident shear—since the yacht itself is moving the apparent wind does not fall to zero speed at sea level, but the presence of significant incident shear there is likely to lead to the same horseshoe vortex wake and an aerodynamic drag for the hull that is larger than expected.

Figure 8 shows the distributions of the sectional lift force and the sectional coefficients of vortex drag ($D_2 + D_5 + D_6$) and profile drag ($D_1 + D_3$). The lift distribution is clearly far from the aerodynamic ideal of elliptic loading, but will be closer to the optimum loading shape when rolling moment limitations are imposed (as detailed by Jones, 1950). The sharp decrease in lift below $z = 0.1$ m corresponds to the unloading around the foot of the sails. The vortex drag coefficient is quite irregular along the span, and inspection of the vorticity plot in Fig. 6 shows a "lumpy" distribution along the span with a number of small vortex cores being evident. Since the location and number of these lumps do not correlate with the measurement grid (which used about 50 points along the sail span), and the lumpiness was not observed on a solid wing which was used as a test case, this lumpiness is thought to be due to the numerous irregularities in the construction and support of the sail. The sail had four seams and eight battens (stiffening strips) in the streamwise direction and the mast had three spreaders (transverse struts), all of which would disturb the flow directly or cause small local variations in sail shape. The same elements would be present on a full-size sail.

The profile drag is large for the hull, and for the sail is largest close to $z = 0.5$ m where the mainsail planform has begun to taper and the main and headsails attach. However, the profile drag coefficient is higher at the head, because as the mast diameter becomes progressively larger relative to the chord so its separation drag becomes progressively more significant. The "source" drag D_6 was found to be negligible along the whole of the span, while the "Betz" term D_3 was significant only in the hull wake and near the masthead.

Finally, Fig. 9 shows the distribution of the force components in the directions of the hull axis and its normal (thrust and sideforce). The thrust is being generated primarily by the lower half of the sails, with the top of the mainsail producing a slightly negative thrust but significant sideforce which is obviously undesirable. The heeling moment (first moment of the sideforce distribution) from the top of the sail would also be high, and this is also undesirable in practice. A significant improvement
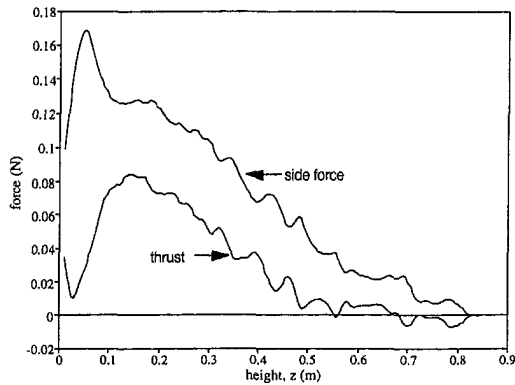
Fig. 9 Distribution of sideforce and thrust across the span

information for the design and analysis of sails than balance measurements, and is the only practical way of determining the distribution of forces along the span which is essential for the understanding of complex phenomena like sail interaction and for the calibration of numerical methods.

The single set of results presented here contains a wealth of information about sail aerodynamics which has not been shown before, and further tests can only add to this. Although they apply to only one of the infinite number of sail shapes achievable with this same sail plan, they illustrate the level of detail that may be obtained and show many features common to results for other sail shapes. A very strong vortex is observed at the foot of the sails, as expected, but no corresponding trailing vortices are observed at the head. An additional vortex pair has been discovered, and is due to the influence of the hull on the vorticity in the floor boundary layer of the incident flow.

Acknowledgments

References

Ahmed, S. R., Ramm, G., and Faltin, G., 1984, "Some Salient Features of the Time-Averaged Ground Vehicle Wake," SAE Int Congr Michigan, SAE Paper 840300.

Betz, A., 1925, "A method for direct determination of profile drag," (German) *Z. Flugtechnik Motorluftschiffahrt*, Vol. 16, pp. 42–44.

Brune, G. W., 1994, "Quantitative low-speed wake surveys," *J Aircraft*, Vol. 31, No. 2, pp. 249–255.

Hackett, J. E., and Sugavanam, A., 1984, "Evaluation of a Complete Wake Integral for the Drag of a Car-Like Shape," SAE paper 840577, Ann. SAE Congress, Detroit.

Jones, R. T., 1950, "The Spanwise Distribution of Lift for Minimum Induced Drag of Wings Having a Given Lift and a Given Bending Moment," NACA TN 2249, 1950.

Larsson, L., 1990, "Scientific Methods in Yacht Design," *Ann Rev Fluid Mech*, Vol. 22, pp. 349–85.

Mallinson, G. D., and Vahl Davis, G. de, 1973, "The Method of the False Transient for the Solution of Coupled Elliptic Equations," *J Computational Physics*, Vol. 12, pp. 435–461.

Maskell, E. C., 1972, "Progress Towards a Method for the Measurement of the Components of the Drag of a Wing of Finite Span," RAE Tech Rept 72232, U.K.

Mokry, M., 1995, "Wall Interference Correction to Drag Measurements in Automotive Wind Tunnels," *J Wind Eng. Ind. Aerodyn.*, Vol. 56, pp. 107–122.

Wu, J. C., Hackett, J. E., and Lilley, D. E., 1979, "A Generalized Wake-Integral Approach for Drag Determination in Three-Dimensional Flows," AIAA Paper No 79-0279.

Wu, J. C., and Wu, J. M., 1989, "Vortical Sources of Aerodynamic Force and Moment," SAE Paper 892346, SAE Annual Congress, Detroit.

in sail trim would therefore result if the lift of the top of the mainsail could be increased relative to its drag; as the lift coefficient of the head of the sails is well below that of the lower half, this suggests that a sail setting with less twist along the span would show a better performance.

Changing the incidence of the hull and sails was found to alter the results quantitatively, but not qualitatively. For example with the hull and sails set for "close-hauled" (sailing as close to the wind direction as possible), the flow patterns showed that the two vortex cores near the floor and having the same sign had almost merged and the wakes of the two sails were less distinguishable (on this heading there is much less gap between them), but otherwise the general features were the same. The components of both the lift and drag were reduced substantially, as would be expected for sails with less incidence to the wind, but their distribution along the span was similar.

Conclusions

Wake surveys have been shown to be a very useful way of measuring the lift and drag of sails, and of providing a breakdown for the various sources of drag. The greatest drawback of the method is the time needed to make the measurements, and given that each sail plan has to be tested with the sails in numerous different trim settings for incidence and twist, it would not be a feasible to carry out an exhaustive set of tests. Rather the advantage of the method lies in the information it provides about the structure of the flow, especially when combined with computer graphics. The technique provides far better

Three-Dimensional Particle Tracking Velocimetry With Laser-Light Sheet Scannings

Satoru Ushijima

Nobukazu Tanaka

Central Research Institute of
Electric Power Industry (CRIEPI)
1646 Abiko, Abiko-shi, Chiba-ken,
270-11, Japan

This paper describes three-dimensional particle tracking velocimetry (3D PTV), which enables us to obtain remarkably larger number of velocity vectors than previous techniques. Instead of the usual stereoscopic image recordings, the present 3D PTV visualizes an entire three-dimensional flow with the scanning laser-light sheets generated from a pair of optical scanners and the images are taken by a high-speed video system synchronized with the scannings. The digital image analyses to derive velocity components are based on the numerical procedure (Ushijima and Tanaka, 1994), in which several improvements have been made on the extraction of particle images, the determination of their positions, the derivation of velocity components and others. The present 3D PTV was applied to the rotating fluids, accompanied by Ekman boundary layers, and their complicated secondary flow patterns, as well as the primary circulations, are quantitatively captured.

1 Introduction

Recently, digital image processing has been extensively utilized to analyze flow-visualization images in an attempt to understand large-scale structures and other spatial characteristics in flows. Among various image processing techniques (see e.g., Hesselink, 1988), particle tracking velocimetry (PTV) is one of the most effective techniques which enable us to make accurate and high-quality velocity measurements in a variety of laboratory-scale flows of gases and liquids over a wide range of velocity (Adrian, 1991).

The early attempt to apply PTV to three-dimensional flows was made by Chang and Tatterson (1983). The principle of their 3D PTV was based on the stereoscopic photogrammetry with the aid of a Bolex stereoscopic lens and a high-speed 16-mm camera. The similar techniques were employed by Racca and Dewey (1988) and Economikos et al. (1990). On the other hand, multiple cameras were utilized to improve the viewing angles in the stereoscopic recording (Adamczyk and Rimai, 1988). In addition, to make more accurate measurements, three-camera systems were used by Nishino et al. (1989), Sata and Kasagi (1992), and Maas et al. (1993).

While the minor differences are found in the recording techniques adopted by the 3D PTV proposed in the past, as described above, it can be seen that they are essentially identical in terms of the stereoscopic recording of image sequences. However, the stereoscopic recording has fundamental drawbacks since this method projects all of the tracer-particle images included in a measuring volume onto only a few two-dimensional frames. As a result, when the number of tracer particles largely increases, the procedures inherent in the previous 3D PTV, for example the identification of a particle image recorded by multiple cameras and the reconstruction of the three-dimensional particle positions, become almost impossible. This evidence is given by the fact that the numbers of the derived velocity vectors range from only around ten to several hundred at most in the previous measurements (Kasagi and Nishino, 1991).

This study describes 3D PTV which makes use of a pair of optical scanners generating horizontally and vertically scanning laser-light sheets. The images of the tracer particles on the

visualized sections are recorded by a high-speed video system capable of 500 frames per second, whose recording is synchronized with the scannings. Since the stereoscopic recording is dismissed in the present 3D PTV, it is possible to obtain quite lager number of velocity vectors than usual and the complicated calibration of multiple cameras is not necessary.

The digital image analyses are based on the numerical procedure proposed by Ushijima and Tanaka (1994). In this method, several improvements have been made on the extraction of particle images, positioning of them with sub-pixel accuracy, determination of velocity vectors, variable tracking frame numbers, and others. Consequently, the accuracy is made higher than the image analyses performed by the usual PTV. The derived velocity components are spatially interpolated with cubic spline functions at regular grid points in three-dimensional space and the theoretical model based on variational analysis is applied to the results so that the nondivergent conditions should be satisfied.

The developed 3D PTV is applied to the rotating fluids in a cubic cavity model equipped with a rotating disk. In experiments, various three-dimensional flow patterns are induced by locating the rotating shaft at the center and by shifting it to a corner of the cavity. The secondary flows occurring on vertical sections, as well as primary circulations caused by the rotating disk, are quantitatively measured with the present 3D PTV.

2 Procedure for Image Acquisition

Flow Visualization System. The PTV system using a scanning laser-light sheet was previously developed by Ushijima and Tanaka (1994), which allows us to obtain velocity vectors on multiple horizontal sections within sufficiently short sampling time. While two velocity components on multiple sections can be measured with this system, the velocity component normal to the scanning laser-light sheet was not directly obtained. In contrast, the present visualization system utilizes a pair of optical scanners which can generate horizontally and vertically scanning laser-light sheets in order to obtain all velocity components in a measuring volume.

Figure 1 illustrates the manner of the flow visualization and the video recordings. A couple of scanners in this visualization system have small mirrors whose rotating shafts are arranged in different directions each other. As shown in Fig. 1, the scanner-1 generates the vertical laser-light sheets which visualize multiple

Fig. 1 Flow visualization and image-recording system

Experimental case	Axis positions (x, y); unit: mm
Case 1	$(30, 30)$
Case 2	$(30 - 10\sqrt{2}, 30 - 10\sqrt{2})$
Case 3	$(30 - 20\sqrt{2}, 30 - 20\sqrt{2})$

quency ω of the rotating disk is set at $8\pi/15$ radian per second. As listed in Table 1, three cases of experiments were conducted, in which the axis position of the rotating disk is shift from the center (Case 1) to a corner of the cavity along a diagonal line (Cases 2 and 3).

The representative length scale L_0 is defined as the side length of the cavity ($L_0 = 60$ mm) and the Reynolds number based on L_0 and ω is estimated as about 6.0×10^3.

Tracer particles scattered in the fluid are made of high polymer (Eslen) with a specific gravity of 1.03. Their average diameter is around 400 μm. Since these tracer particles include fluorescent sodium, their clear images can be taken in the presence of laser-light sheets. In experiments, the saline water with suitably-adjusted density is used as a working fluid so that the tracer particles can have completely neutral buoyancy.

As illustrated in Fig. 2, the numbers of the visualized horizontal and vertical sections are 10, respectively, and total 20 sections are recorded with the high-speed VCR system. Since two frames are recorded per section, the time interval between two adjacent sections is 4 ms and the scanning time cycle (T_C) corresponds to 80 ms. In the present measurements, 10 frames are recorded for each section during 10 scanning cycles which is equivalent to the sampling time (T_S) of 0.796 seconds.

3 Digital Image Analyses

Determination of Particle Positions. The images on a frame recorded by high-speed VCR system are transformed to digital data consisting of 512×512 pixels with 256-gray-level resolution per a single pixel. After applying adequate filters (Rosenfeld and Kak, 1976), the particle images are separated from the background and their positions are determined with sub-pixel accuracy. This procedure is based on our previous numerical techniques (Ushijima and Tanaka, 1994).

The binarized images are first derived by means of the discriminant and least squares threshold selection (Otsu, 1978), which selects an optimum threshold level so that the summation of gray-level variances in two classes separated by the threshold should be minimum and that the variance between the two classes should be maximum on the basis of discriminant analysis. Instead of employing a single threshold level for a frame, the digital images on a frame are divided into 1024 subregions each consisting of 16×16 pixels and the optimum threshold is determined for each subregion. The binarized particle image is then replaced by 3×3 pixels area without changing its center point. Finally, the logical products are taken between the original images having grey levels and the binarized particle images. This procedure allows us to separate the tracer particle images preserving 256-gray-level resolution from the background.

It is effective for the accurate positioning of the tracer particles to make use of their gray-level distributions, rather than the binarized results, since the error resulting from the incorrect positioning is a dominant factor for the total uncertainties of the derived velocity components. Thus the second-order regression curvature is derived for the gray-level distribution of each particle on the basis of the method of the least squares. Then the tracer particle position is determined with second-order accuracy as the point where the regression curvature gives its peak value.

vertical sections. The visualized images are taken by a high-speed video cassette recorder (VCR) system through the front window of an experimental cavity model. On the other hand, the horizontal sections visualized by the scanner-2 are recorded with the same VCR system through a plane mirror placed below the transparent bottom window. Since the visualized horizontal and vertical sections are both included in the view of the high-speed video camera, only a single camera is needed in the present system.

The present VCR system (NAC HSV1000HS) is capable of taking 500 frames par second and its strobe (TTL) signals are utilized to synchronize the video recordings with the stepping movements of the scanners. Since two scanners are systematically operated by a control driver, which receives the TTL signals from the VCR system, the continuously visualized sections are suitably recorded on the appointed video frames. The exposure time per frame is set at 200 μs with the aid of an electrical shutter.

Cavity Model With a Rotating Disk. It has been known that complicated three-dimensional flows are generally observed in rotating fluids as well as their primary circulating motions (e.g., Greenspan, 1968). In a cavity model equipped with a rotating disk on its upper boundary, secondary flows, as well as horizontal main circulations, are expected to appear on the vertical sections owing to the Ekman boundary layer developed near the bottom surface.

Figure 2 shows a cubic cavity model with each side of 60 mm and a rotating disk 170 mm in diameter. The angular fre-
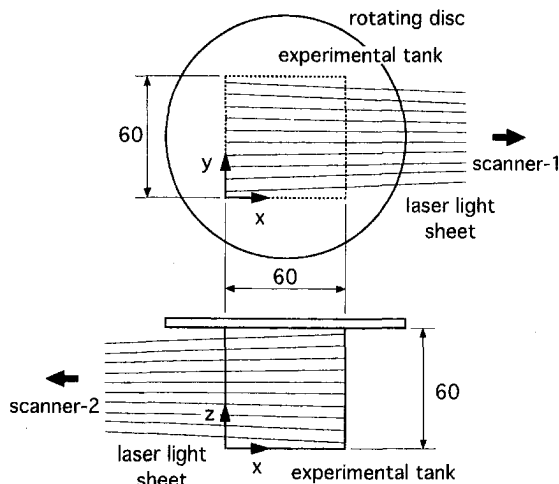

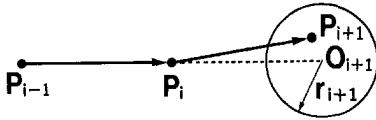Fig. 2 Cavity model with a rotating disk

Fig. 3 Search region on $i + 1$ frame

Particle Tracking. The particle tracking procedure as done by Ushijima and Tanaka (1994) is applied to specify an identical particle recorded on the multiple frames. Figure 3 shows the search region on the $i + 1$ frame, which is set up after the candidates of particle positions (P_1, P_2, ..., P_i) have been specified. The center of the circular search region is set at $2\mathbf{p}_i - \mathbf{p}_{i-1}$, where $\mathbf{p}_i$ is the position vector of P_i. The radius of the search region r_{i+1} on the $i + 1$ frame is set up as one-third of the average particle distance δ_{i+1} on the $i + 1$ frame, which is one of the criteria to determine the search region employed by Dracos and Malik (1992) and Malik et al. (1993). When a single center point is located within the search region, this becomes a new candidate on the $i + 1$ frame. In case that the multiple center points are included, the center point which gives the minimum variance of the local velocities calculated from P_{i-1}, P_i and P_{i+1} is selected. If there is no center point, all candidates (P_1, P_2, ..., P_i) are discarded. This tracking procedure is repeated over N_T frames ($N_T \geq 3$), where N_T is referred to as tracking frame number.

On the first frame of tracking, the circular search region is set up, having its center at P_1 and its radius r_1 equal to $(\frac{1}{2})\delta_1$. When multiple center points P_2 are included in the region, all of them are considered as valid and the tracking procedure described above continues to the following frames. While most of the misidentified center points are dropped in the process of the multiple trackings, a group of center points which gives the minimum variance of local velocities derived from all center points is selected if more than two groups are finally obtained. If there is no second point P_2 in the search region, the corresponding first center point P_1 is discarded.

Since the tracking procedure for N_T frames is carried out throughout all of the sampled frames, changing the first frame of tracking one by one, the number of total tracking procedures is given by $N_S - N_T + 1$, where N_S is the sampled frame number. In the present method, the lower and upper limitations (N_{T1} and N_{T2}, respectively) can be set for the tracking frame number in order to respond to high and low velocity regions coexisting in the visualized area (Ushijima and Tanaka, 1994). Thus the tracking procedure is conducted L_T times, which is given by

$$L_T = (N_S + 1)(N_{T2} - N_{T1} + 1) - \sum_{k=N_{T1}}^{N_{T2}} k \qquad (1)$$

Although the velocity components were usually derived only from the identified initial and terminal particle positions in previous works (e.g., Imaichi and Ohmi, 1982; Kobayashi et al., 1985), it is necessary for the accurate estimation of velocity vectors to take into consideration all intermediate particle positions as well as both ends. Thus, a quadratic function is approximated for a group of the identified positions with the method of least squares and the direction of velocity vector is defined as its tangential direction. In addition, the length of the velocity vector is calculated from the summation of all displacements (Ushijima and Tanaka, 1994).

When small number of error vectors are included in the results, bootstrap procedure (Efron, 1979; Diaconnis and Efron, 1983; Efron, 1983) is utilized to remove them. The bootstrap technique enables us to derive a frequency distribution for each of the obtained velocity components. After evaluating the average μ and the standard deviation σ from the frequency distribution, the velocity component located outside of the bandwidth $\mu \pm 3\sigma$ are judged as errors and replaced by the average.

Three-Dimensional Velocity Components. The velocity components obtained by the particle trackings are randomly distributed in accordance with the particle locations. Thus the results obtained by L_T times of tracking procedures are all superimposed and the average velocity vectors over the sampled frames are calculated at the appointed grid points. In terms of Nyquist sampling criterion, the resolution for the highest wavenumber is limited by $(\frac{1}{2})\delta_v$ (Agui and Jimenez, 1987), where δ_v is the average distance of the velocity vectors, which implies that meaningful grid intervals should be larger than $2\delta_v$. Since δ_v is estimated as 1.05 mm in the present study, the regular grid points of $13 \times 13 \times 13$ are set up in the cubic region in the cavity, which gives 5 mm interval between two adjacent grids.

Two velocity components are first interpolated at the grid positions on the visualized sections. The weighted averaging based on the Gaussian window is utilized in the interpolation, whose window width is set at $1.24\delta_v$ as proposed by Agui and Jimenez (1987). In this procedure, the error range for each interpolated result is also estimated with the bootstrap techniques as done by Ushijima and Tanaka (1994), which will be utilized in the spatial smoothing as described later.

As illustrated in Fig. 1, the visualized sections are not parallel and another spatial interpolation is operated in the direction normal to the sections. For the velocity components interpolated on the horizontal sections, one-dimensional cubic spline functions are derived to interpolate them in the vertical direction. The similar procedure is conducted for the velocity components on the vertical sections. As a result, the error ranges as well as the three velocity components are obtained at the regular grid points.

It is usual that the three-dimensional velocity components as obtained in laboratory measurements and in field observations do not completely satisfy the non-divergence condition even if they are carried out rigorously. The theoretical model based on variational analysis was proposed by Sasaki (1958, 1970a, b) and it was utilized by Sherman (1977) to adjust the observed wind fields over complex terrain. This model is also adopted in the present study in order that the fluid continuity should be satisfied in each control volume. The specific function in this model is given by

$$E(u_i) = \int_V \left[\alpha_i^2 (u_i - u_{i0})^2 + \lambda \frac{\partial u_i}{\partial x_i} \right] dx_1 dx_2 dx_3 \qquad (2)$$

where λ is the Lagrange multiplier. Here u_{i0} and u_i are measured velocity components and their adjusted values in x_i directions, respectively, where x_i with $i = 1$, 2 and 3 correspond to x, y and z coordinates. While the values of α_i are Gauss precision moduli related to the measurement errors in u_i, these values are almost same regardless of their directions in the present case. Thus we may put $\alpha_1^2 = \alpha_2^2 = \alpha_3^2 \equiv \alpha^2$. The Euler-Lagrange equations to minimize $E(u_i)$ are given by

$$u_i = u_{i0} + \frac{1}{2\alpha^2} \frac{\partial \lambda}{\partial x_i} \qquad (3)$$

$$\frac{\partial u_i}{\partial x_i} = 0 \qquad (4)$$

and the equation for λ is derived as

$$\frac{\partial^2 \lambda}{\partial x_i^2} = -2\alpha^2 \frac{\partial u_{i0}}{\partial x_i} \qquad (5)$$

Equation (5) is discretized in a finite difference scheme and solved by a successive overrelaxation method. The boundary conditions are $\lambda = 0$ on the bottom surface and $\partial \lambda / \partial n = 0$ on the other boundaries. The obtained λ is substituted into Eq. (3) and the adjusted velocity components are derived.

Finally, as conducted by Agui and Jimenez (1987), the velocity components are spatially smoothed by solving three-dimensional Laplace equations within the error ranges. As described above, the error ranges first obtained by the bootstrap method have already been interpolated at the grid points by means of cubic spline functions. The error ranges are now shifted so that the adjusted values for fluid continuity are taken into account:

$$err_{lmn}^i = \mu_{lmn}^i + \frac{1}{2\alpha^2}\frac{\partial \lambda}{\partial x_i} \pm \epsilon_{lmn}^i \qquad (6)$$

Here $\mu_{lmn}^i \pm \epsilon_{lmn}^i$ are the error ranges for u_i obtained at the grid points P_{lmn}. The solutions of Laplace equations at $n + 1$ step are compared with the shifted band widths calculated by Eq. (6) and when they are not included in these ranges, they are replaced with the upper or lower limit values. Since the difference of the average discrete dilation before and after the smoothing procedure is less than 0.1 percent with respect to the representative quantity calculated from L_0 and ω, the nondivergence condition is effectively satisfied.

4 Rotating Fluids Measured by 3D PTV

Measurement Conditions. As described above, three cases of experiments are carried out in this study. The conditions of sampling and tracking are listed in Table 2. In Table 2, the sampling frequency f_s is calculated from the scanning time cycle T_C. The total number of the obtained vectors (N_V) are listed in Table 3. From N_V, the number of the vectors per visualized section (n_{VS}) and the number per a tracking procedure (n_{VT}) are calculated as shown in Table 3. As listed in Table 3, the average number of the vectors obtained during 0.796 seconds amounts to more than 65,000, which enables us to derive nearly 3000 vectors per a single tracking procedure. Taking account that the maximum number of the vectors captured by usual 3D PTV remains several hundred at most, it is demonstrated that quite larger number of vectors can be acquired with the present 3D PTV.

**Table 2 Sampling and tracking conditions**

Case	f_s (1/s)	T_s (s)	N_T	L_T
Case 1	12.5	0.796	4~8	25
Case 2	12.5	0.796	3~5	21
Case 3	12.5	0.796	3~5	21

The average of the absolute velocity components (V_0) is about 2.9 mm/s, which may be one of the representative quantities in the cavity flows. The sampling time T_s corresponds to 3.8 percent with respect to the time scale based on V_0 and L_0. Thus, it can be concluded that the effectively instantaneous velocity components are measured by the present 3D PTV.

Experimental Results. Figure 4 shows the distributions of velocity vectors on horizontal (x-y) and vertical (x-z) planes measured in Case 1. The circulating flow patterns are observed in all horizontal sections and the intensity of velocity becomes weak near the bottom surface owing to the development of the Ekman boundary layer. While it can be seen that the circulating flows tend to diverge outside in the upper region in the cavity, the convergent circulations appear in the Ekman boundary layer

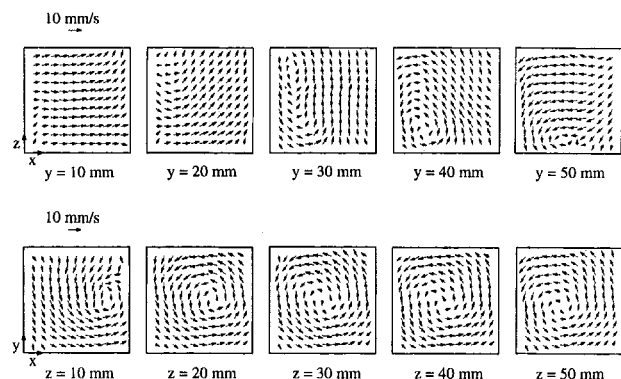**Table 3 Numbers of velocity vectors**

Numbers	Case 1	Case 2	Case 3	Average
N_V	82,189	58,659	55,395	65,414
n_{VS}	4,110	2,933	2,770	3,271
n_{VT}	3,288	2,793	2,638	2,906
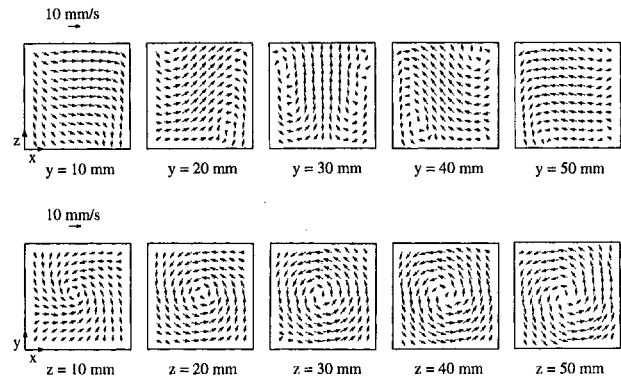
Fig. 4 Measured velocity vectors (Case 1)

in contrast. This typical flow pattern observed in a rotating fluid with Ekman boundary layers brings about the secondary flows observed on vertical sections; as shown in the x-z section at $y = 30$ mm, the ascending and descending flows arise in the center region and near the side boundaries, respectively. As shown on the vertical sections at $y = 20$ and 40 mm, the ascending flows are accompanied by circulation just outside of the center region. Figure 5 shows the results of Case 2. The rotating disk is shifted to a corner along a diagonal line by 20 mm in this case and the center positions of the circulations on x-y planes vary in accordance with the height; the center of the circulation, located slightly near the origin at $z = 50$ mm, once returns to the center of the cavity at $z = 40$ and 30 mm and then shifts to right side boundary on the lower horizontal sections. The similar tendency is also observed in Case 3 shown in Fig. 6, while at $z = 50$ mm the center of the circulation largely shifts to the origin. On the vertical sections at $y = 30$ mm in Case 2, the ascending flow is dominant on the right-hand side and, in contrast to a pair of eddies observed in Case 1, only a single eddy appears on the left side of the vertical flow. The small eddy observed near the bottom surface at $y = 50$ mm gradually develops at $y = 40$ and 30 mm with changing its center position. On the other hand, the flow patterns at $y = 10$ and 20 mm are largely different from them and it can be seen that the secondary flows also have asymmetric patterns. The similar secondary flow patterns are measured in Case 3, while the intensity of velocity vectors becomes slightly higher than that of Case 2.

The three-dimensional flow patterns in Case 1 are visualized with the aid of computer graphics as shown in Fig. 7. In this figure, the particles, initially located on a horizontal plane, are advected in the static velocity field which is assumed to be given by the measured results by the present 3D PTV. The time increment is 0.2 seconds and the particle positions are calculated

Fig. 5 Measured velocity vectors (Case 2)

10 mm/s

z ⊥ x
y = 10 mm   y = 20 mm   y = 30 mm   y = 40 mm   y = 50 mm

10 mm/s

y ⊥ x
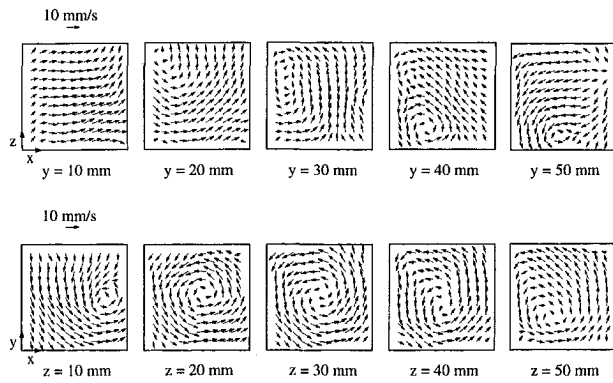z = 10 mm   z = 20 mm   z = 30 mm   z = 40 mm   z = 50 mm

Fig. 6 Measured velocity vectors (Case 3)

by a Runge-Kutta method. As observed in Fig. 4, the rotating ascending flow occurs in the center region of the cavity and the descending circulation appears near the side boundaries.

Estimation of Uncertainty. The uncertainties involved in PTV techniques have been widely investigated to specify the sources of errors and to evaluate their quantities (e.g., Imaichi and Ohmi, 1983; Kobayashi et al., 1985; Chang et al., 1985; Agui and Jimenez, 1987; Nishino et al., 1989). The results of the previous works allow us to evaluate the uncertainties in the present 3D PTV. According to Agui and Jimenez (1987), three different errors, visualization error ϵ_{vis}, sampling error ϵ_{sam}, and interpolation error ϵ_{int}, need to be taken into account.

The visualization error consists of the positioning error of the particles (ϵ_η) and the error associated with the traceability of particles to the fluid motion (ϵ_f). The positioning error may be evaluated by

$$\epsilon_\eta = \eta^* V_0 \qquad (7)$$

where η^* is the precision for a particle position normalized by the average length of the particle trajectories. Since the resolution of a pixel (Δ_p) corresponds to 120 μm and the average trajectory (Δ_t) is 0.93 mm, the present second-order positioning gives $\eta^* = (\Delta_p/\Delta_t)^2$ and the following result:

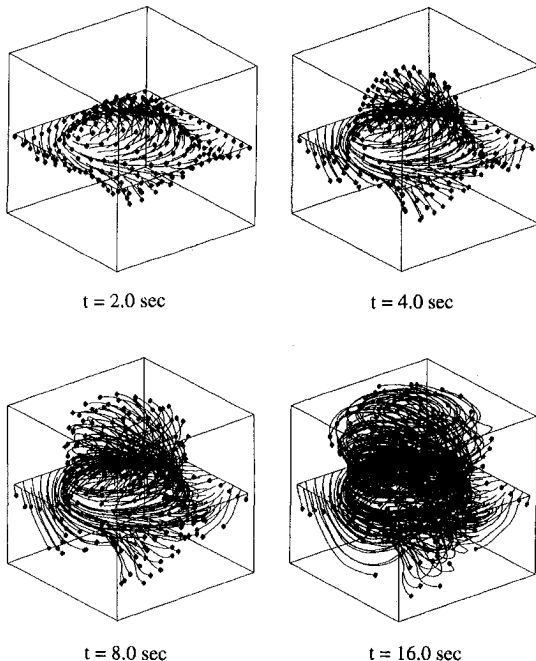t = 2.0 sec   t = 4.0 sec

t = 8.0 sec   t = 16.0 sec

Fig. 7 Flow patterns visualized with CG (Case 1)

$$\epsilon_\eta = 1.67 \times 10^{-2} V_0 \qquad (8)$$

On the other hand, the traceability error ϵ_f can be neglected in the present experiment, since the densities of the particles and the working fluid are almost same.

The sampling error ϵ_{sam} is evaluated by the following equation:

$$\epsilon_{sam} = u' \left(\frac{3\eta_L V_0}{Du'} \right)^{(m-1)/(m+1)} \qquad (9)$$

Here it is assumed that $m = \frac{5}{3}$ and $u'/V_0 = 0.1$ as done by Agui and Jimenez (1987). Then we obtain

$$\epsilon_{sam} = 2.5 \times 10^{-2} V_0 \qquad (10)$$

With reference to the results reported by Agui and Jimenez (1987), the present interpolation error ϵ_{int} can be estimated of the same order as their values, since our interpolation method is substantially based on their procedures: a convolution with an adaptive Gaussian window with the same window width (1.24δ), Class 3 bootstrap estimation and others.

Assuming that the interpolation error is 3 percent, the total error ϵ_T is calculated from the summation of the squares as

$$\epsilon_T = 4.2 \times 10^{-2} V_0 \qquad (11)$$

It is concluded that the present 3D PTV possibly involves about 4.2 percent uncertainty with respect to the representative velocity.

5   Concluding Remarks

A 3D PTV system, which enables us to obtain quite larger number of velocity vectors than usual, has been developed in order to measure effectively instantaneous all velocity components in the three-dimensional space. The developed system utilizes a pair of optical scanners which can generate horizontally and vertically scanning laser-light sheets. The images of the tracer particles on the visualized sections are recorded by a high-speed VCR system capable of 500 frames per second, whose recording is synchronized with the scannings. Since the usual stereoscopic recording by multiple cameras is dismissed, the present 3D PTV becomes free from the major drawbacks involved in previous 3D PTV: for example, identification of a particle image recorded by multiple cameras, camera calibrations and reconstruction of the three-dimensional particle positions. As a result, the number of the acquired velocity vectors becomes roughly ten times as many as that of the usual techniques (Kasagi and Nishino, 1991), which results in the higher spatial resolution in the present system.

The digital image analyses are based on the numerical procedure proposed by Ushijima and Tanaka (1994). In this method, several improvements have been made on the extraction of particle images having grey-level resolutions, positioning of them with sub-pixel accuracy, determination of velocity vectors, variable tracking frame numbers and others. Consequently, the accuracy is made higher than the image analyses done by the usual PTV. The derived velocity components are spatially interpolated with cubic spline functions at regular grid points in three-dimensional space and the theoretical model based on variational analysis is applied to the results so that the nondivergent conditions should be satisfied.

The developed 3D PTV was applied to the rotating fluids in a cubic cavity model equipped with a rotating disk. When the rotating shaft of the disk is set at the center of the cavity, the 3D PTV enables us to capture the primary circulating flows and vertical secondary flow patterns, which are typically observed in a rotating fluid with Ekman boundary layers. In case that the rotating shaft is shift to a corner of the cavity along a diagonal line, the varying center positions of the primary circulations and asymmetric secondary flow patterns are obtained. In these

measurements, more than 65,000 vectors are acquired within the sampling time of 0.796 seconds, which allows us to derive nearly 3000 vectors per a single tracking procedure. Taking account that the maximum number of the vectors captured by usual 3D PTV remains several hundred at most, it can be concluded that the present 3D PTV is quite advantageous in terms of spatial resolution.

Acknowledgments

The authors are grateful to Mr. H. Karube for his contribution to the experiments.

References

Adamczyk, A. A., and Rimai, L., 1988, "Reconstruction of a 3-Dimensional Flow Field from Orthogonal Views of Seed Track Video Images," *Experiments in Fluids,* Vol. 6, pp. 380–386.

Adrian, R. J., 1991, "Particle-Imaging Techniques for Experimental Fluid Mechanics," *Annual Review of Fluid Mechanics,* Vol. 23, pp. 261–304.

Agui, J., and Jimenez, J., 1987, "On the Performance of Particle Tracking," *Journal of Fluid Mechanics,* Vol. 185, pp. 447–468.

Chang, T. P., and Tatterson, G. B., 1983, "An Automated Analysis Method for Complex Three Dimensional Mean Flow Fields," *Proceedings 3rd International Symposium on Flow Visualization,* pp. 266–273.

Chang, T. P. K., Watson, A. T., and Tatterson, G. B., 1985, "Image Processing of Tracer Particle Motions as Applied to Mixing and Turbulent Flow—II. Results and Discussion," *Chemical Engineering Science,* Vol. 40, No. 2, pp. 277–285.

Diaconnis, P., and Efron, B., 1983, "Computer-Intensive Methods in Statistics," *Scientific American,* Vol. 248, No. 5, pp. 96–109.

Dracos, T., and Malik, N. A., 1992, "3D Particle Tracking Velocimetry—Its Possibilities and Limitations," *Proceedings 6th International Symposium on Flow Visualization,* Springer-Verlag, pp. 785–791.

Economikos, L., Shoemaker, C., Russ, K., Brodkey, R. S., and Jones, D., 1990, "Toward Full-Field Measurements of Instantaneous Visualization of Coherent Structures in Turbulent Shear Flows," *Experimental Thermal and Fluid Science,* Vol. 3(1), pp. 74–86.

Efron, B., 1979, "Computers and the Theory of Statistics: Thinking the Unthinkable," *SIAM Review,* Vol. 21, No. 4, pp. 460–480.

Efron, B., 1983, "Estimating the Error Rate of a Prediction Rule: Improvement of Cross-Validation," *Journal of American Statistical Association, Theory and Methods Section,* Vol. 78, No. 382, 316–331.

Greenspan, H. P., 1968, *The Theory of Rotating Fluids,* Cambridge Univ. Press.

Hesselink, L., 1988, "Digital Image Processing in Flow Visualization," *Annual Review of Fluid Mechanics,* Vol. 20, pp. 421–485.

Imaichi, K., and Ohmi, K., 1983, "Numerical Processing of Flow-Visualization Pictures—Measurement of Two-Dimensional Vortex Flow," *Journal of Fluid Mechanics,* Vol. 129, pp. 283–311.

Kasagi, N., and Nishino, K., 1991, "Probing Turbulence with Three-Dimensional Particle-Tracking Velocimetry," *Experimental Thermal and Fluid Science,* Vol. 4(5), pp. 601–612.

Kobayashi, T., Yoshitake, Y., Saga, T., and Segawa, S., 1985, "An Image Processing Technique for Determining Two-Dimensional Flow Fields with Reverse Flow," *Proceedings ASME Symposium on Physical and Numerical Flow Visualization,* pp. 39–46.

Maas, H. G., Gruen, A., and Papantoniou, D., 1993, "Particle Tracking Velocimetry in Three-Dimensional Flows," *Experiments in Fluids,* Vol. 15, pp. 133–146.

Malik, N. A., Dracos, Th and Papantoniou, D. A., 1993, "Particle Tracking Velocimetry in Three-Dimensional Flows Part II: Particle Tracking," *Experiments in Fluids,* Vol. 15, pp. 279–294.

Nishino, K., Kasagi, N., and Hirata, M., 1989, "Three-Dimensional Particle Tracking Velocimetry Based on Automated Digital Image Processing," ASME JOURNAL OF FLUIDS ENGINEERING, Vol. 111, pp. 384–391.

Otsu, N., 1978, "Discriminant and Least Squares Threshold Selection," *Proceedings 4th International Joint Conference on Pattern Recognition,* pp. 592–596.

Racca, R. G., and Dewey, J. M., 1988, "A Method for Automatic Particle Tracking in a Three-Dimensional Flow Field," *Experiments in Fluids,* Vol. 2, pp. 22.1.1–22.1.6.

Rosenfeld, A., and Kak, A. C., 1976, *Digital Picture Processing,* Academic Press, Inc.

Sasaki, Y., 1958, "An Objective Analysis Based on the Variational Method," *Journal of Meteorological Society of Japan,* Vol. 36(3), pp. 77–88.

Sasaki, Y., 1970a, "Some Basic Formalisms in Numerical Variational Analysis," *Monthly Weather Review,* Vol. 98, pp. 875–883.

Sasaki, Y., 1970b, "Numerical Variational Analysis Formulated under the Constraints Determined by Longwave Equations and Lowpass Filter," *Monthly Weather Review,* Vol. 98, pp. 884–898.

Sata, Y., and Kasagi, N., 1992, "Improvement toward High Measurement Resolution in Three-Dimensional Particle Tracking Velocimetry," *Proceedings 6th International Symposium on Flow Visualization,* Springer-Verlag.

Sherman, C. A., 1978, "A Mass-Consistent Model for Wind Fields over Complex Terrain," *Journal of Applied Meteorology,* Vol. 17, pp. 312–319.

Ushijima, S., and Tanaka, N., 1994, "Particle Tracking Velocimetry Using Laser-Beam Scanning and Its Application to Transient Flows Driven by a Rotating Disk," ASME JOURNAL OF FLUIDS ENGINEERING, Vol. 116, pp. 265–272.

B. Bouras
Research Engineer.

F. Karagiannis
Research Engineer.

G. Leoutsakos
Research Engineer.

K. C. Giannakoglou
Lecturer.

K. D. Papailiou
Professor.

Thermal Turbomachinery Laboratory,
National Technical University of Athens,
15710 Athens, Greece

Arbitrary Blade Section Design Based on Viscous Considerations. Background Information

Background information is presented on an arbitrary blade section design method which is outlined in a joint paper. This information concerns the assumptions, the development, and the predictive capabilities of the viscous flow calculation tool used in the design procedure. General properties of laminar and turbulent, unseparated or separated compressible shear layers, necessary for the blade optimization procedure, are discussed.

1 Introduction

The present paper and a joint paper (Bouras et al., 1991b) outline a method for the design of arbitrary peripheral cascades. The optimization of the blade design (Bonataki et al., 1993) is based to a large extent upon viscous considerations. Consequently, the accuracy of the prediction of viscous effects, especially when separation is present, becomes very important. Establishing basic information concerning the viscous flow calculation tool is the first aim of the present work. In this context, in Section 2 a brief description of the two-zone model is outlined, equations are developed in Section 3, and the semi-empirical background used for closure is discussed in Section 4. Section 5 provides some evidence of the predictive capabilities of the method. The development of such a theoretical tool, capable of predicting the design and off-design performance of arbitrary cascades and necessary for the design procedure presented in Bouras et al. (1991b) constitutes the second aim of this work.

The shear layer formulation mentioned above is used in this work in both direct (prediction) and inverse (design, optimization) modes. This, along with the establishment of the general properties of the laminar and turbulent shear layers, is outlined in Section 6. This last part forms the basis of the section design and optimization procedure from the viscous point of view and constitutes the third and last aim of this work.

Due to the limited space available, the background information is presented in brief and the reader should turn to the cited references for any additional information. The authors would like to underline the contribution of Jean Le Foll's (1965) ideas in the present development. His pioneering work for unseparated incompressible boundary layers forms the basis of this work.

2 The Two-Zone Model

The decomposition of a flow field into an inviscid and a viscous part is carried out through the second order flow model, Lock and Firmin, (1981), where the external inviscid flow properties may vary accross the shear layer. Matching the external

with the real flow velocity at the shear layer edge provide the necessary relations. The external flow is computed by applying a transpiration velocity $W_{n_{e_w}}$ along the solid boundaries and both sides of the dividing streamline in the wake, as

$$\rho_{e_w} W_{n_{e_w}} = \frac{d}{ds} (\rho_{e_w} W_{s_{e_w}} \delta_1) \tag{1}$$

A tangential velocity jump along the dividing streamline in the wake region results, in addition to the normal velocity jump, which the external inviscid flow calculation has to accommodate as well. The coupling of the inviscid and the viscous zones is carried out iteratively. A strong coupling is necessary, especially when separated flow regions exist.

3 The Development of the Canonical Equations

In this section a brief description of the development of the integral equations will be presented. Further details may be found in the first twelve cited references, while Papailiou, (1981) summarizes work performed until 1981.

The basic equations are considered in a rotating frame of reference, for turbulent flows. For laminar flows, similar expressions can be derived through the Stewartson's transformation, 1949. An orthogonal curvilinear coordinate system (s, n), where the s-lines coincide with the real flow streamlines, is used to express the continuity, the two momentum and the energy equations. For turbulent flows, the turbulent kinetic energy equation will be used, as well.

With some simplifications (Papailiou, 1990, Lock and Firmin, 1981), the equations for the external inviscid and the real flow are subtracted from each other, thus forming the corresponding deficit equations. These are integrated along the normal to the streamwise direction and after some rearrangements, they yield

(*a*) the streamwise momentum integral equation

$$\frac{1}{\rho_e R_w W_{s_{e_w}}^2} \frac{d}{ds} (\rho_{e_w} R_w W_{s_{e_w}}^2 \delta_2^*) + \frac{\delta_1}{W_{s_{e_w}}} \frac{dW_{s_{e_w}}}{ds}$$

$$= \frac{\delta_\rho}{W_{s_{e_w}}^2} \frac{d}{ds} \left(\frac{\omega^2 R_w^2}{2} \right) + \frac{C_f}{2} - \frac{1}{2\rho_{e_w} W_{s_{e_w}}^2} \frac{d}{ds}$$

$$\times [\rho_{e_w} W_{s_{e_w}}^2 K^*(\delta_1 + \delta_2)^2)] \tag{2}$$

Copyright © 1996 by ASME

(*b*) the energy integral equation

$$\frac{1}{\rho_{e_w}R_w W^3_{s_{e_w}}}\frac{d}{ds}(\rho_{e_w}R_w W^3_{s_{e_w}}\delta^*_3) + \frac{(\delta_1 - \delta_{1_k})}{W^2_{s_{e_w}}}\frac{dW^2_{s_{e_w}}}{ds}$$

$$= \frac{2(\delta_1 - \delta_{1_k})}{W^2_{s_{e_w}}}\frac{d}{ds}\left(\frac{\omega^2 R^2_w}{2}\right) + C_D \quad (3)$$

where the curvature $K^* = K_w + d^2\delta_1/ds^2$

The dissipation factor C_D and the skin friction coefficient C_f are given by

$$C_D = \frac{2}{\rho_{e_w}W^3_{s_{e_w}}}\int_0^\delta D\,dn, \quad C_f = \frac{2\tau_{sn_w}}{\rho_{e_w}W_{s_{e_w}}} \quad (4)$$

where $\int_0^\delta D\,dn$ is the dissipation integral.

The normal fluctuation terms are incorporated in the shear layer thicknesses, as

$$\delta^*_2 = \delta_2 - \int_0^\delta \frac{\rho\overline{W'^2_s} - \rho\overline{W'^2_n}}{\rho_{e_w}W^2_{s_{e_w}}}dn \quad (5)$$

$$\delta^*_3 = \delta_3 - \int_0^\delta \frac{\rho W_s(3\overline{W'^2_s} - \overline{W'^2_n} + \overline{W'^2_u})}{\rho_{e_w}W_{s_{e_w}}}dn \quad (6)$$

Equations (2) and (3) hold for compressible turbulent flows. It is a simple matter to obtain the corresponding equations for incompressible flows which read

$$\frac{1}{R_w W^2_{s_{e_w}}}\frac{d}{ds}(R_w W^2_{s_{e_w}}\delta^*_{2_k}) + \frac{\delta_{1_k}}{W_{s_{e_w}}}\frac{dW_{s_{e_w}}}{ds}$$

$$= \frac{C_f}{2} - \frac{1}{2W^2_{s_{e_w}}}\frac{d}{ds}[W^2_{s_{e_w}}K^*(\delta_{1_k} + \delta_{2_k})^2] \quad (7)$$

$$\frac{1}{R_w W^3_{s_{e_w}}}\frac{d}{ds}(R_w W^3_{s_e}\delta^*_{3_k}) = C_D \quad (8)$$

The corresponding equations for laminar flows are derived by dropping the normal fluctuation terms and considering that C_f corresponds to the laminar wall shear stress.

The Incompressible Shear Layer Equations. First, the last term in Eq. (7) is neglected. The kinetic energy dissipation is defined as

$$E = \rho\delta^*_{3_k}\frac{W^3_{s_{e_w}}}{2} = \rho\nu\,\mathrm{Re}_3\frac{W^2_{s_{e_w}}}{2} \quad (9)$$

where E, representing losses, increases with distance. From Eq. (8) it yields

$$\frac{dE}{E} = C_D\frac{ds}{\delta^*_{3_k}} \quad (10)$$

By taking $H^*_{32_k} = \delta^*_{3_k}/\delta^*_{2_k}$, and by introducing it into Eq. (9), differentiating and combining with Eq. (7), while using the definition $H^*_{12_k} = \delta^*_{1_k}/\delta^*_{2_k}$, one gets

$$\frac{1}{H^*_{12_k} - 1}\frac{dH^*_{32_k}}{H^*_{32_k}} = \frac{1}{H^*_{12_k} - 1}\left[1 - \frac{H^*_{32_k}C_f}{2C_D}\right]\frac{dE}{E} - \frac{dW_{s_{e_w}}}{W_{s_{e_w}}} \quad (11)$$

The proper way to handle the normal fluctuation terms will be considered later. For attached shear layers, however, a simple model can be used (Assassa and Papailiou, 1979), where the normal fluctuation terms effect on the energy equation is neglected ($H_{32k} = H^*_{32k}$) and the ratio $k = (H_{12k} - 1)/(H^*_{12k} - 1)$ is considered constant. For laminar flows, $k = 1$. Besides, H_{12k} can be considered as a unique function of H_{32k} (Papailiou, 1981), so that a new form factor L_k

$$dL_k = \frac{1}{H_{12_k} - 1}\frac{dH_{32_k}}{H_{32_k}} \quad (12)$$

is introduced, with the right-hand side being a total differential. A Reynolds number Re_4 and its neperian logarithm X are introduced

$$\mathrm{Re}_4 = \mathrm{Re}_3 e^{2L_k}, \quad X = \ln \mathrm{Re}_4 = \ln \mathrm{Re}_3 + 2L_k \quad (13)$$

The velocity logarithm q, instead of the velocity itself and the position Reynolds number Φ, instead of the arc length s, are also introduced

$$q = \ln\frac{W_{s_{e_w}}}{W_{ref}}, \quad \Phi = \int_0^s \frac{W_{s_{e_w}}ds}{\nu} \quad (14)$$

Then, if the grouping coefficient M is defined as

————— **Nomenclature** —————

$\mathbf{W}(W_s, W_n)$ = relative velocity vector
r = recovery factor
R = radius
δ = boundary layer thickness
δ_1 = displacement thickness

$$\rho_{e_w}W_{s_{e_w}}R_w\delta_1$$
$$= \int_0^\delta R(\rho_e W_{s_e} - \rho W_s)dn$$

δ_m = momentum ($m = 2$) and energy ($m = 3$) thickness

$$\rho_{e_w}W^m_{s_{e_w}}R_w\delta_m$$
$$= \int_0^\delta RW_s\rho(W^{m-1}_{s_e}$$
$$- W^{m-1}_s)dn$$

δ_{1k} = kinetic displacement thickness

$$\rho_{e_w}R_w W_{s_{e_w}}\delta_{1k}$$
$$= \int_0^\delta R\rho_e(W_{s_e} - W_s)dn$$

δ_ρ = density thickness

$$\rho_{e_w}R_w\delta_p = \int_0^\delta R(\rho_e - \rho)dn$$

K = curvature
ν = kinematic viscosity
Π = boundary layer equilibrium parameter
ω = rotation speed

Subscripts

e = external flow
k = kinematic
n = normal
s = streamwise
w = wall

$$M = \frac{1}{H_{12_k} - 1} \left[1 - \frac{H_{32_k} C_f}{2C_D} \right] \qquad (15)$$

Eqs. (11) and (10) yield

$$kdL_k = dq + kM \frac{dE}{E} \qquad (16)$$

$$\frac{dE}{E} = C_D \frac{d\Phi}{\text{Re}_3} \qquad (17)$$

Differentiating Eq. (9) and using Eqs. (16), (13), and (14), one additionally gets

$$(1 + 2kM) \frac{dE}{E} = dX \qquad (18)$$

It is important to note that in view of the number of equations available, only two independent variables can be chosen. These are the form factor L_k and the Reynolds number X and closure is effected via the semi-empirical frame. For laminar flows $M = M(L_k)$ and $C_D = C_D(L_k)$ while for turbulent ones $M = M(L_k, X)$ and $C_D = C_D(L_k, X)$. By eliminating dE/E between Eqs. (16) and (18) and between (17) and (18) the so-called canonical equations are obtained, namely,

$$dq = kdL_k + \beta dX \qquad (19)$$

$$d\Phi = \frac{1}{C} d \, \text{Re}_4 \qquad (20)$$

which relate the physical variables (q, Φ) to the shear layer intrinsic variables (L_k, X). The coefficients β and C are given by

$$\beta = - \frac{kM}{1 + 2kM}, \quad C = C_D(1 + 2M) \, \text{Re}_4 e^{2L_k} \qquad (21)$$

The Compressible Shear Layer Equations. The same analysis can be performed for compressible laminar and turbulent flows. The corresponding equations are derived following a development similar to the one presented in Papailiou and Bouras (1990) and Bouras (1992) and are

$$F_1 dL_k - F_{22} dq - \frac{C_D M}{\text{Re}_3} d\Phi$$
$$- \frac{F_{33}}{W_{s_{e_w}}^2} d\left(\frac{\omega^2 R_w^2}{2} \right) - A_m = 0 \qquad (22)$$

$$dX - 2dL_k + F_{44} dq - \frac{C_D d\Phi}{\text{Re}_3}$$
$$- \frac{F_{55}}{W_{s_{e_w}}^2} d\left(\frac{\omega^2 R_w^2}{2} \right) - A_e = 0 \qquad (23)$$

where the involved coefficients F_1, F_{22}, F_{33}, F_{44}, F_{55} and the normal fluctuation terms A_m and A_e are functions of the L_k, X and the external flow Mach number; they are all given in detail in Bouras et al. (1991a). In the case of a laminar shear layer, the corresponding equations are only slightly different from those used for the turbulent case, as discussed in the aforementioned reference.

4 The Semi-Empirical Frame

Closure of the system of integral equations is obtained by expressing the flow parameters, at any cross section, in terms of the two solution variables (Papailiou, 1981). A semi-empirical frame is required for laminar layers as well, in order to replace information lost during the integration. The shear layer proper-
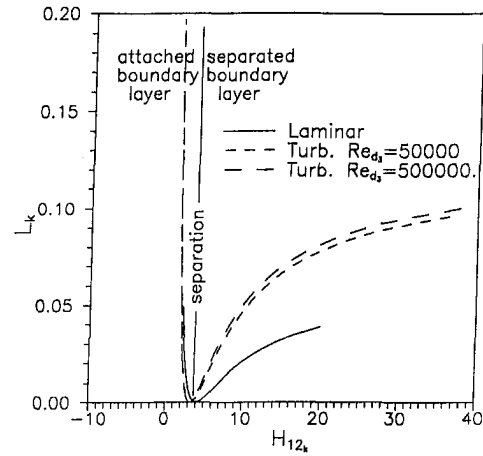

Fig. 1 The relation $L_k(H_{12k})$ for attached and separated incompressible shear layers, (a) laminar, (b) turbulent

ties at each station can be described by profiles corresponding to equilibrium, laminar or turbulent, shear layers. For laminar incompressible shear layers, similar solutions (Falkner and Skan, 1930) are used. For each equilibrium shear layers, the parameter

$$\Pi = \frac{\delta_1}{|\tau_{sn_w}|} \frac{dp_w}{ds} \qquad (24)$$

remains constant. In order to form the laminar shear layer semi-empirical frame, analytical expressions for both attached and separated velocity profiles are necessary. For laminar layers, the work reported by Cebeci and Keller (1971) was used, along with Stewartson's transformation. For turbulent incompressible shear layers, the Kuhn and Nielsen's (1973) work was used. For compressible flows, the generalized velocity of van Driest (1951) is used, through which the semi-empirical incompressible expressions are verified. This agrees with Morkovin's (1962) hypothesis which gives the possibility to use the incompressible flow turbulence properties for Mach numbers below 3. The turbomachinery range of application is thus largely covered.

While for laminar incompressible shear layers a unique relationship $H_{32k}(H_{12k})$ for attached and separated flows does exist, for turbulent ones, the experimentally established relation $H_{32k}(H_{12k})$ depends slightly upon the Reynolds number (Papailiou, 1981). On the other hand, for compressible laminar and turbulent shear layers, the curves $H_{32}(H_{12})$ depend strongly upon the Mach number. Considering, however, the curves $H_{32k}(H_{12k})$ based on the kinematic quantities, they come very close to those previously established for incompressible flows (Bouras, 1992; Papailiou and Bouras, 1990). These curves present a minimum very close to the location of zero wall shear stress, used here as the condition for flow separation. At this minimum, L_k is set to zero. The corresponding $L_k(H_{12k})$ curves are illustrated in Fig. 1. Although, the present theory relies upon a unique $H_{32k}(H_{12k})$ relationship, in practice the Reynolds number influence is taken into account, in the vicinity of separation. This improves considerably the accuracy of the calculation.

In deriving the basic equations, the normal fluctuation terms are retained and this is very important near separation and in the separated flow region. In Assassa and Papailiou (1979) these terms are modeled, based on limited experimental evidence. Other semi-empirical relations, established for the case of extended separated flow regions, Gerolymos et al. (1984) model the fluctuation terms, as they appear in Eqs. (2) and (3), including the case of the shock/turbulent shear layer interaction.

In view of what was presented above, β and C appearing in Eqs. (19) and (20) can be established. Figure 2 presents the curves $C(L_k)$ and $M(L_k)$, for laminar flows. Then $\beta(L_k)$ can
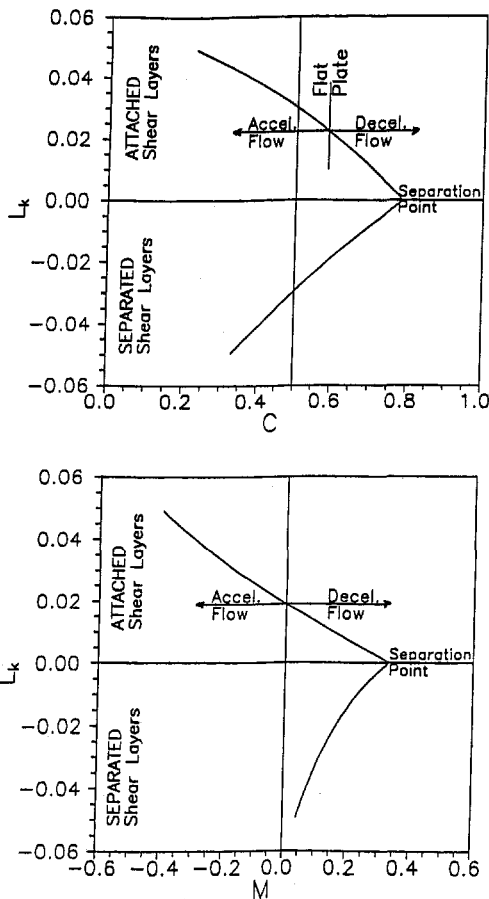
Fig. 2 The functions C and M for incompressible laminar, attached and separated shear layers

be computed according to (21). For turbulent flow, the values of $C_D(L_k, X)$ and $M(L_k, X)$ may be computed easily, $M(L_k, X)$ from Eq. (15) and $C_D(L_k, X)$ from (Papailiou, 1981)

$$\frac{C_D(1 + r(\gamma - 1)/2 \cdot M_{e_w}^2)}{H_{32}(\rho_{e_w}/\rho_w)C/2}$$

$$= \frac{\delta_1}{\delta_{1_k}} \frac{(H_{12} - 1) - r(\gamma - 1)M_{e_w}^2}{H_{12}} F_2\Pi + 1 \quad (25)$$

Corresponding curves for turbulent attached and separated incompressible shear layers are presented in Fig. 3.

5 The Direct Shear Layer Calculation and Its Prediction Capability

The calculation of the development of shear layers can be performed through the canonical equations and the semi-empirical frame, provided that the initial condition of the shear layer and the external flow data are known. The wall geometry and orientation must be also given, in order to evaluate the second order terms and the influence of Coriolis force and streamline curvature.

The canonical equations have been set up in a form convenient for the solution of the inverse problem. Papailiou (1981) has shown that using the present formulation in a direct mode, it is possible to pass through the separation point. However, since the inverse mode numerically behaves better than the direct one, it was decided to solve the equations in the inverse mode, even when dealing with a direct problem.

Ample evidence of the predictive capabilities of the method is given in the cited references, for decelerating transitional

flows (Leoutsakos, 1992), for shock/turbulent shear layer interactions with flow separation and reattachment (Kallas and Papailiou, 1987), and for flows with mild separation (Papailiou and Bouras, 1990, Bouras, 1992).

6 The Inverse Shear Layer Problem and the General Properties of the Image Plane

Le Foll's Idea. According to what has been said above, all quantities characterizing the state of a shear layer at a cross section can be specified, once two of them are known. Assuming that these are L_k and X, the canonical equations can be expressed in the form

$$F_i(W_{e_w}, s, L_k, X) = 0, \quad i = 1, 2 \quad (26)$$

The common way of utilizing these equations is to specify $W_{e_w}(s)$ and compute the properties of the shear layer in the form $L_k(s)$ and $X(s)$ (direct problem), or in the intrinsic form $L_k = L_k(X)$.

It is also possible, however, to start by specifying $L_k(X)$ and, through the same equations, compute the distribution $W_{e_w}(s)$. In other words, it is possible to select the desired shear layer properties and then calculate the velocity distribution which is necessary to produce it. Either the computed or the selected $L_k(X)$ curve can be traced on the (L_k, X)-plane. It is then evident that, if general shear layer properties are available on the same plane, one may select a curve $L_k(X)$ with the desired properties and produce, using Eqs. (26), the velocity distribution allowing such a shear layer to develop. Consequently, it is essential to identify as many general shear layer properties as possible on the (L_k, X)-plane, which will be referred to as the image plane.

The Laminar Image Plane. The laminar incompressible flow image plane is presented in Fig. 4 where the $M = $ const and the $C_D = $ const curves have been traced. The $M = $ const curves (as M depends only on L_k and $L_k = $ const defines a laminar equilibrium shear layer) are image curves of laminar
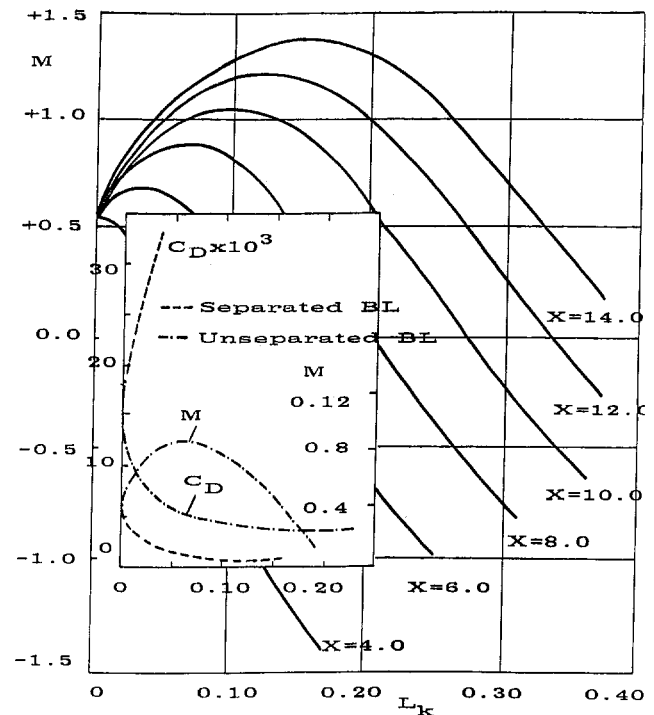

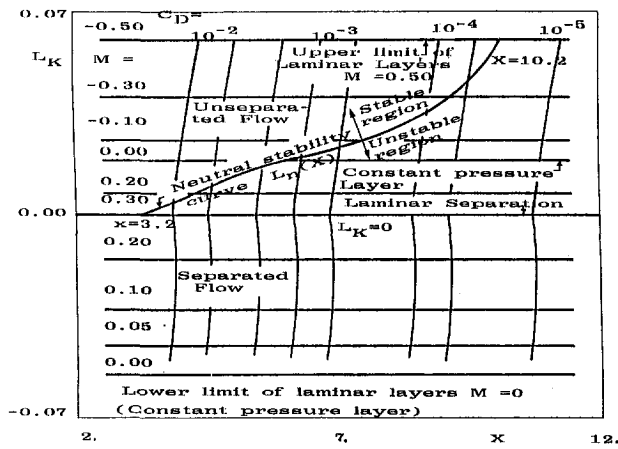Fig. 3 The functions M and C for turbulent attached and separated incompressible shear layers

Fig. 4 The Laminar Image Plane, for incompressible flows

Fig. 6 Turbulent equilibrium shear layers

equilibrium shear layers. The equilibrium shear layer $L_k = 0$ is, by definition, on the verge of separation and splits the image plane into an upper part ($L_k > 0$) containing all attached laminar shear layers and a lower part ($L_k < 0$) with the separated ones. For all equilibrium laminar shear layers, at successive stations, the velocity profiles are similar, the skin friction coefficient and form factors H_{12k}, H_{32k} and L_k are constant, while the Reynolds numbers $Re_1 = Re(\delta_1)$, $Re_2 = Re(\delta_2)$ and $Re_3 = Re(\delta_3)$ are increasing. Consequently, for all equilibrium shear layers, X is an increasing quantity with distance, justifying the choice of X as a solution variable. As dE/E, dX are both positive, Eq. (18) gives $M > -0.5$. The same reasoning can be applied for turbulent flows for which the quantity $(1 + 2kM)$ is also positive.
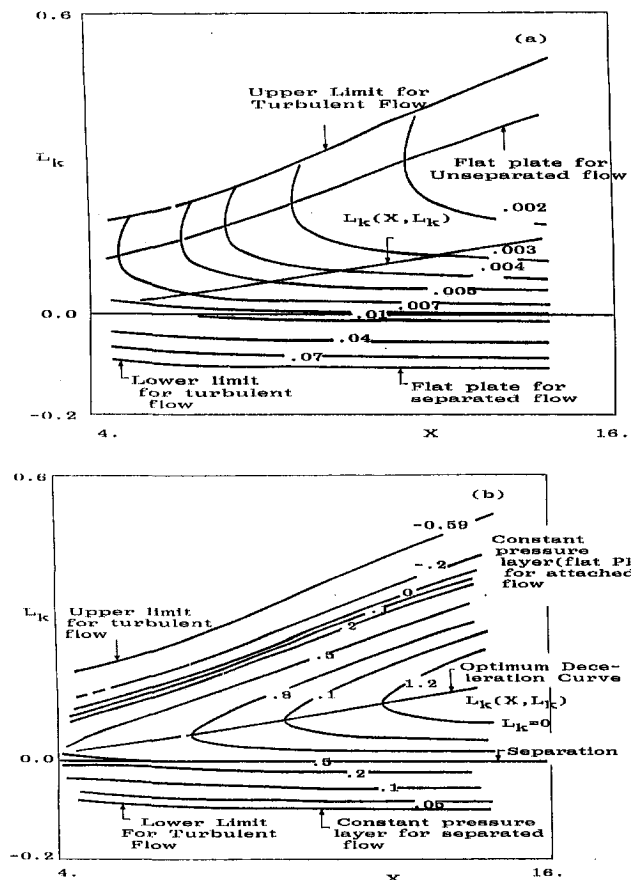

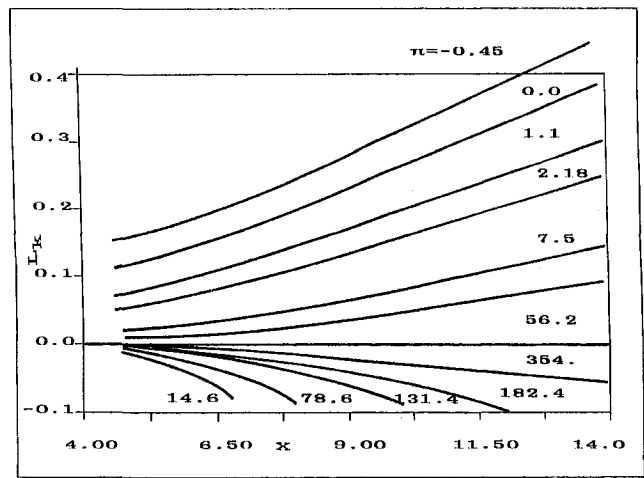Fig. 5 The Turbulent Image Plane (a) iso-C_D lines, (b) iso-M lines

The limit $M = -0.5$ where all shear layers cease to exist is shown in Fig. 4. For laminar separated shear layers, the limit is set by the equilibrium shear layer for which $dp/dx = 0$. This can be found in Schlichting (1962) who reports that two similar solutions exist for each value of Π in the interval between the flat plate laminar shear layer ($M = 0$) and the one corresponding to separation ($M = 0.329$); one for attached and the other for separated flow. Consequently, for $L_k < 0$, the lower limiting case is that of the flat plate equilibrium laminar shear layer.

It is also possible to trace Schlichting's neutral stability curve $L_n(X)$ on the image plane. It is known that two-dimensional disturbances of any frequency are damped for a Reynolds number smaller than the critical one. Below this curve the laminar shear layer is unstable in the Tollmien-Schlichting mode. Note that this curve cuts the limit $M = -0.5$ at $X = 10.2$. Consequently, for higher values of X, stable laminar layers do not exist. For low enough Reynolds numbers, the stability curve is compatible with the decelerating flow and cuts the laminar separation line at $X = 3.2$.

The Turbulent Image Plane. The turbulent image plane is presented in Fig. (5a) and (5b), where the $C_D = $ const and $M = $ const curves have been traced, respectively. Again, the locus $L_k = 0$ denotes separation. The upper limit for turbulent shear layers ($kM = -0.5$, or $M = -0.50$ for $k = 0.85$) appears on this plane. The turbulent equilibrium shear layers are presented separately in Fig. 6, for attached and detached flows.

Consider, now, Eq. (16) for an unseparated flow. According to this equation, the flow deceleration ($dq < 0$) can be obtained by either requiring dL_k to be negative or/and dE to be positive. The part of the deceleration which is done by increasing E is the one which is realized by consuming kinetic energy. The part which is done by decreasing L_k is the one which is realized without losses. During this decrease in L_k, the velocity profile is deformed and the outer layers transfer kinetic energy to the inner ones in order to overcome the imposed pressure gradient. The possibility of flow deceleration without consuming kinetic energy (that is, without losses) must be examined in connection to the negative limiting value of dL_k/dX. From Eq. (16) this part of deceleration may be computed through

$$k dL_k = dq \qquad (27)$$

We shall discuss now the maximum possible deceleration for attached turbulent shear layers, expressed by the maximum negative value that the slope dL_k/dX may assume. No theoretical answer can be given. However, it may be demonstrated (Le Foll, 1965), that an image curve $X = $ const which decelerates a shear layer without losses implies transfer of kinetic energy

from the shear layer to the external flow (negative entrainment). Even if this may be possible, although still debatable, one may consider as limiting case the following

$$\left(\frac{dL_k}{dX}\right) \geq -0.5 \qquad (28)$$

It can be shown, Papailiou (1981) that a very steep slope dL_k/dX, lower than -0.5 is experimentally possible. The practical consequences, however, of using lower dL_k/dX values being rather limited, we shall content ourselves with the limit of -0.5.

The range of L_k indicates that the part of the deceleration realized without losses (considering that separation is to be avoided) is rather small compared with the current applications demands. Eq. (16) shows that for a certain increase in losses, the maximum deceleration can be realized when the coefficient M is maximum, as k is constant. Consequently, the locus of maximum M is the locus of the optimum deceleration. For unseparated laminar shear layers, such a locus does not exist, because $M(L_k)$ (as can be seen in Fig. 2) is a monotonic function, increasing continuously up to separation. For turbulent unseparated shear layers, however, such a locus does exist, Fig. 3, in the attached region and far from separation. A minimum value of M exists in the separated flow region, which indicates that along the corresponding locus, a deceleration is carried out with the maximum of kinetic energy loss. The locus of optimum deceleration $L_k(X)$ is presented on the image plane, Fig. 5.

The Compressibility Effects. Results concerning compressible turbulent shear layers indicate that the equilibrium shear layers and the locus of maximum M maintain approximately their position on the image plane, provided that, instead of X, the quantity

$$X_k = \ln \mathrm{Re}_{3_k} + 2L_k \qquad (29)$$

is used as abscissa in the compressible image plane. Indicative results shown in Bouras (1991a) prove that the initial image plane remains practically unchanged for Mach numbers up to 2.5.

On the other hand, the equation corresponding to (16) for compressible rotating flow reads (Bouras et al., 1991a)

$$kF_1 dL_k = F_2 dq + kM\frac{dE}{E} + M_2 \frac{1}{W^2_{s_e}} d\left(\frac{\omega^2 R^2}{2}\right) \qquad (30)$$

We can see that the aforementioned reasoning concerning optimum deceleration, is still valid for Eq. (30), in spite of the presence of the functions F_1 and F_2, while the last term acts as moderator.

7 Conclusions

In this paper, theoretical work concerning the development of a direct and inverse viscous flow calculation method, capable to predict the behaviour of compressible shear layers (laminar and turbulent) developing along rotating or stationary blades

was presented. The method predicts both attached and separated flows. The general characteristics of laminar and turbulent shear layers are established and the background information for the development of a blade design and optimization method (which is outlined in a joint paper) is set up.

References

Assassa, G. M., and Papailiou, K. D., 1979, "An Integral Method for the Calculation of the Separated Turbulent Boundary Layer," ASME JOURNAL OF FLUIDS ENGINEERING, pp. 110–116.

Bonataki, E., Chaviaropoulos, P., and Papailiou, K. D., 1993, "An Inverse Inviscid Method for the Design of Quasi-Three Dimensional Turbomachinery Cascades," ASME JOURNAL OF FLUID ENGINEERING, Vol. 115, No. 121–127.

Bouras, B., Karagiannis, F., Leoutsakos, G., Giannakoglou, K., and Papailiou, K. D., 1991a, "Arbitrary Blade Section Design Based on Viscous Considerations: Background Information," International Symposium on Numerical Simulations in Turbomachinery, Joint ASME-JSME Fluids Engineering Meeting, Portland, Oregon, USA.

Bouras, B., Karagiannis, F., Chaviaropoulos, P., and Papailiou, K. D., 1991b, "Arbitrary Blade Section Design Based on Viscous Considerations. Blade Optimization," International Symposium on Numerical Simulations in Turbomachinery, Joint ASME-JSME Fluids Engineering Meeting, Portland, OR, also in this volume.

Bouras, V., 1992, "Integral Method for the Calculation and Optimization of Laminar and Turbulent Shear Layers in the Presence of Flow Separation," Ph.D. thesis, 1992, Dept. of Mech. Eng., NTUA, Greece.

Cebeci, T., and Keller, H. B., 1971, "Shooting Solutions of the Falkner-Skan Boundary Layer Equation," J. of Comp. Phys., Vol. 7, pp. 289–300.

Falkner, V. H., and Skan, S. W., 1930, "Some Approximate Solutions of the Boundary Layer Equations," Phil. Mag., Vol. 12, 865, 1931. ARC R and M 1314.

Gerolymos, G., Kallas, Y., and Papailiou, K. D., 1984, "The Behaviour of the Normal Fluctuation Terms in the Case of Attached or Detached Turbulent Boundary Layers," ASME Paper 84-GT-179.

Kallas, J., and Papailiou, K. D., 1987, "A Method for the Calculation of the Interaction of a Turbulent Boundary Layer with a Shock Wave," ISABE 87-7074. Proceedings of the 8th Intern. Society of Air Breathing Engines, Cincinnati, Ohio.

Kuhn, J. D., and Nielsen, J. N., 1973, "Prediction of Turbulent Separated Bounary Layers," AIAA Paper No. 73-663.

Le Foll, J., 1965, "A Theory of Representation of the Properties of Boundary Layers on a Plane," Proc. Seminar on Advanced Problems in Turbomachinery, VKI, Belgium.

Leoutsakos, G., 1992, "Transition Prediction in Attached and Separated Shear Layers Using an Integral Method," ASME Paper 92-GT-281.

Lock, R. C., and Firmin, M. C. P., 1981, "Survey of Techniques for Estimating Viscous Effects in External Aerodynamics," IMA Conference, London, UK.

Morkovin, M. V., 1962, "Effects of Compressibility on Turbulent Flows," Mecanique de la Turbulence, Colloques Internationaux du Centre National de la Recherche Scientifique, Marseille 1961, Editions du CNRS, France.

Papailiou, K. D., 1981, "Le Foll's Method and the Calculation of Attached and Separated Two-Dimensional Boundary Layers," Von Karman Institute, Lecture Series on "Separated Flows in Turbomachinery Components," VKI LS 1981-1.

Papailiou, K. D., and Bouras, B., 1990, "Arbitrary Blade Section Design Based on Viscous Considerations," AGARD VKI Special Course in Inverse Methods in Airfoil Design.

Schlichting, H., 1962, Boundary Layer Theory, 4th ed., McGraw-Hill.

Stewartson, K., 1949, "Correlated Incompressible and Compressible Boundary Layer," Proc. Roy. Soc. London, Series A 200, pp. 84–100.

van Driest, E. R., 1951, "Turbulent Boundary Layers in Compressible Fluids," Journal of Aero, Sciences, Vol. 18.

B. Bouras
Research Engineer.

F. Karagiannis
Research Engineer.

P. Chaviaropoulos
Research Engineer.

K. D. Papailiou
Professor.

Thermal Turbomachinery Laboratory,
National Technical University of Athens,
P.O. Box 64069, 15710 Athens, Greece

Arbitrary Blade Section Design Based on Viscous Considerations. Blade Optimization

A blade design and optimization procedure is presented in this work, which is based on viscous flow considerations. This procedure concerns the design of optimum rotating arbitrary compressible high subsonic compressor and turbine blade shapes. It takes into account the effects of wall curvature and Coriolis force on turbulence, while it allows the variation of stream surface radius, along which the blade shape is placed, as well as streamtube width, with meridional distance. In order to establish the inverse part of the viscous optimization procedure, aspects such as laminar stability, transition, optimum deceleration and, more generally, the behaviour of compressible attached and separated shear layers are discussed. A plane on which all the general properties of the compressible laminar and turbulent shear layers appear, is constructed and the generation of optimum shear layers for the critical side of the blade shape is established. The complete optimization (design) procedure is then described and discussed, while various designs realized by the present procedure are presented at the end of this paper.

1 Introduction

The material presented in this work can be used for different types of design. Furthermore, the design process is full of constraints and compromises, so that one cannot pretend that any one of the present day theories may give the optimum solution. What the designer desires to possess, however, is a reliable and flexible tool, which can help him evaluate the situation at hand. In addition, this tool must have a reasonably fast response, when an interactive computing procedure is used.

The main objective of the present work is to create a tool for optimizing the viscous behaviour of the flow, particularly in view of designing arbitrary compressor and turbine blade sections for Mach numbers, which may reach locally supersonic values.

Regardless of how the optimization problem is set and what constraints are imposed, two parameters are playing the most important role. The blade circulation (or the peripheral force) and the absolute total pressure losses. Then, constraints such as a desired low loss incidence interval (in order to ensure enough margin for stall) or an adequate blade thickness in the proper places and a convenient position of the center of gravity of the blade section (in order to ensure the desired mechanical properties) are considered separately, once the blade section shape is established. Consequently, two different computing tools are necessary; one, which deals with the viscous effects and a second one which deals with the inviscid external flow both in direct and inverse mode.

In Bouras et al. (1991), the background information was developed for both viscous calculation methods and the foundations for viscous optimization have been layed out. In Bonataki et al. (1993), the inverse inviscid calculation method is described. Centrifugal and Coriolis forces effects on turbulence as well as for the variation of the streamtube thickness along meridional distance are very important in turbomachinery appli-

cations. These effects are taken into account in the present work. If these effects were not taken into account, this may rule out application of this methodology to radial machines, while for axial machines there would be left too much room for interpretation. The direct inviscid calculation method is not presented here, as such methods constitute a standard calculation tool.

The inverse (design) procedure may be performed for one incidence only. Then, the direct inviscid calculation method, along with the direct counterpart of the viscous calculation method are used, in order to analyze the designed blading performance for a number of-off design incidences. For the complete calculation (direct and inverse), changes in the data used in the previous design used data are usually made and the procedure is repeated.

Since the first publication of the viscous flow calculation method by Le Foll (1965) concerning turbine cascade design and the subsequent publication of the work of Papailiou, 1981, on compressor cascade design, an important amount of work has been done relatively to the method, which, however, was published in a rather fragmentary way.

During this presentation, we did our best to describe the method in a brief but comprehensive way, putting emphasis on the parts that have not yet been published. In Section 2, it will be described how an optimum image curve is constructed. In Section 3 a very brief description of the wall curvature and Coriolis force effects on turbulence will be presented and in Section 4 various examples of blade section design will be presented and discussed.

2 Individual Shear Layers and the Optimum Image Curve

In Section 6, Bouras et al. (1991), Le Foll's idea, and the general properties of the image plane were analyzed. In this section it will be examined how we select an optimum image curve $L_k(X)$ for the most critical shear layer of the blading, that is the suction side for the axial flow machines and the pressure side for the radial flow ones. Axial machines will be considered first and only comments on radial machines will be given.
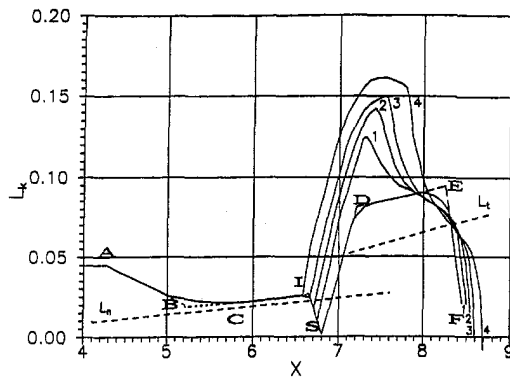
Fig. 1 Optimum image curve for the suction side of a blade section

The optimization is based on the following principle. The dissipation factor is one order of magnitude higher for turbulent than for laminar layers. In addition, the minimum value of the rate of dissipation which is represented by $1/M$ (see Eq. (23) in Bouras et al., 1991), is about three times smaller for turbulent layers. This minimum has been established for attached shear layers, far from separation. Therefore, the turbulent flow should be restricted to the decelerated flow region while deceleration must follow the optimum one, as close as possible.

The rest of the flow, starting from the leading edge, must be laminar. Near the leading edge, W_{sew} becomes proportional to the arc length, since this is the form of the potential flow close to a cylinder stagnation point. This is achieved with $L_k = .0436$ for $X \to -\infty$. For the laminar shear layer, Schlichting's curve (Schlichting H., 1962) presents an optimum image curve, since M takes its maximum possible value, as long as laminar instability has to be avoided (see Fig. 13(a) in Bouras et al., 1991).

The laminar part of the optimum image curve has been presented as OABCI in Fig. 1. The design is being done for the minimum Reynolds number of operation which is the most critical for turbulent shear layers. Following the initial stagnation point region, a part with $\beta_1 = 0$ (flat plate) is being used, if necessary, in order to avoid the deceleration part of Schlichting's (see Papailiou, 1981), and the corresponding velocity peak.

The segment (BC) that follows corresponds to a shifted Schlichting's neutral stability curve by a distance depending on the range of Reynolds number of operation. This is due to the fact that, as it has already been proved by Papailiou (1981) an increase in Reynolds number displaces the image curve to the right, while a decrease displaces the image curve to the left. This distance is selected, so that, when the overall Reynolds number is increased, the corresponding displacement of the image curve to the right never exceeds Schlichting's neutral stability curve.

"I" represents the point where instability (in the Tollmien-Schlichting 2-D mode) is first introduced for the lowest Reynolds number of operation. The distance between the point of instability and the region, where the actual transition takes place, depends, at least, on the turbulence level of the external flow and on the pressure gradient. A crude criterion is used here, which has been proposed by T. S. Wilkinson (see Papailiou, 1981, for details) and proved satisfactory for present purposes.

Assuming, that transition has taken place at S, the turbulent part of the image curve is examined. This part must realize an optimum deceleration and starts with a segment of a straight line and a slope which ensures the continuity of the derivative $dq/d\Phi$ at transition. Then, according to the principles established above for the optimum turbulent deceleration, the locus $L_t(X)$ is followed. In the last part of the image curve, the limit deceleration is employed until the locus $L_k = 0$ is reached, if we decide to avoid separation. Thus, one may profit, as much as possible from the part of the deceleration which can be realized without losses. Of course, this part can continue in the separated flow region, if incidence considerations permit it.

The first design image curve, shown by the dashed curve of Fig. 1, consists of segments of straight lines, which are selected as follows:

OA corresponds to the flow in the neighborhood of the leading edge, for which $W_{se} \sim s$. It is specified by $\beta_1 = 1$ and $L_k = .0436$.

AB a straight line joining OA to segment BC

BC a curve corresponding to $\beta_1 = 0$, in order to avoid the region of decelerated flow which is associated with Schlichting's curve ($X_B = 5.2$, $X_C = 5.8$).

CI the curve $L_k = L_n(X + 0.5)$

IS a line defined by the slope $dL_k/dX = -.2$, which is such that for levels of free stream turbulence greater than 1.5 percent, transition will occur between I and S.

SD a segment whose slope is defined by the condition that the derivative $dq/d\Phi$ of the velocity distribution should be continuous at the transition point.

DE the curve $L_k = L_t(X) + .03$, where .03 represents a safety margin ($X_E = 8.3$).

EF a final drop to close to separation with the maximum deceleration, i.e., $dL_k/dX = -.5$.

The velocity distribution corresponding to this initial image curve, can be obtained by integrating the established equations (Bouras et al., 1991), while a smoother velocity distribution can be obtained by rounding off the corners of the first image curve and this is the one plotted as a full curve on the Fig. 1.

Admitting that the external flow turbulence is such that transition takes place between points I and S, it is necessary to check that separation is avoided when transition point is any point of the segment (IS). To demonstrate this, calculations have been performed, using the external velocity distribution corresponding to the image curve ABCISDEF, assuming, in Fig. 1, that transition takes place at various points between I and S. They are presented in Fig. 1, where it can be seen that the image curve corresponding to point T_3 is just critical, bringing the final image point to incipient turbulent separation while the image curve corresponding to point T_4, presents a part of turbulent separated flow. From what has been said in Section 6, Bouras et al. (1991) it can be easily deduced that the same principles apply for the compressible case.

───────── **Nomenclature** ─────────

C_D = kinetic energy dissipation factor
C_f = skin friction coefficient
L_k = form factor
L_n = Schlichting's neutral stability curve
Re_s = Reynolds number based on arc length
Re_3 = Reynolds number based on energy thickness

s = arc length
$X = \ln (Re_3) + 2L_k$, abcissa of image plane
W = relative velocity
Φ = Reynolds number
ω = rotation speed

Subscripts

e = external flow

f, F = final
I = Instability
ref = reference values
s = tangent to the wall
T = transition
t = turbulent
w = value at wall
1 = inlet
2 = outlet

Looking at this optimum image curve we may see that, once the abscissas X_T and X_F have been defined (transition and final points), the whole optimum image curve has very closely been defined, as well. This last property may help us to solve the next problem, which is how to choose one particular image curve, once the general requirements of a particular design have been specified. These requirements are usually imposed in the physical plane, hence the necessity to relate the general properties of the two planes. This will be done in what follows.

The most interesting properties of a velocity distribution destinated for suction side are:

(a) The overall Reynolds number of operation, which is imposed.

(b) The maximum velocity appearing on the suction side. Mach number or noise considerations may demand it to be as low as possible.

(c) The mean velocity appearing on the suction side. Its value expresses the contribution of the suction side to the blade circulation.

(d) The losses or some other property of the shear layer.

Let us consider the absolute losses of the suction side. The pressure side losses have to be added to them and their sum has to be compared with the circulation per blade, before an estimate of the mass averaged loss can be made. Considering, now, the first three mentioned properties one may relate them to the two variables X_T and X_F, which define the optimum image curve.

Figure 2 presents curves relating the above mentioned velocity distribution properties with the shear layer intrinscid properties for all incompressible optimum image curves. Corresponding curves have been established for various exit Mach number levels as well, but are not presented here. Details concerning the construction of the graphs and the reasons for selecting the variables serving as abscissae, can be found in Papailiou (1973, 1981).

Closing this section, the importance of "centrifugal" forces has to be underlined. As centrifugal forces will be denoted nonconservative forces and more particularly their components normal to the mean flow direction. Their effects are particularly important for turbomachinery applications, Papailiou (1981) and expressions for dissipation factor C_D have already been developed following the work of Bradshaw (1967) and Johnston (1970). These expressions can be found in Papailiou (1981) for attached flow and in Bouras et al. (1991) for separated flow.

3 Results and Discussion

So far, various aspects of the design procedure for arbitrary blade sections in turbomachinery applications have been discussed. Before demonstrating how these tools may be used, it must be kept in mind that each application has its own peculiarities and constrains through a preliminary investigation. Consequently, it is important, that the designer is acquainted with the order of magnitude of the various design parameters and the shape and level of the various distributions of the input quantities. The inverse methodology offers considerable flexibility, giving no constrains at all to the geometric shape, but, on the other hand, it cannot take into account directly all the important constrains of the problem. In this respect, one has to keep in mind that the inverse tool alone doesn't provide the best results. A direct computational procedure must be used, for guidance.

An incompressible flow design case, Papailiou (1971) of a compressor blading will be considered, first, for which a 45 deg inlet air angle was specified with axial discharge. The blade chord Reynolds number was equal to 3×10^5. No additional constraints were imposed, other than that the blade ought to be manufacturable. For two-dimensional flow the velocity ratio $W_{se1}/W_{se2} = .707$ and, admitting that $W_{se,max}/W_{se1} = 1.3$, the ratio
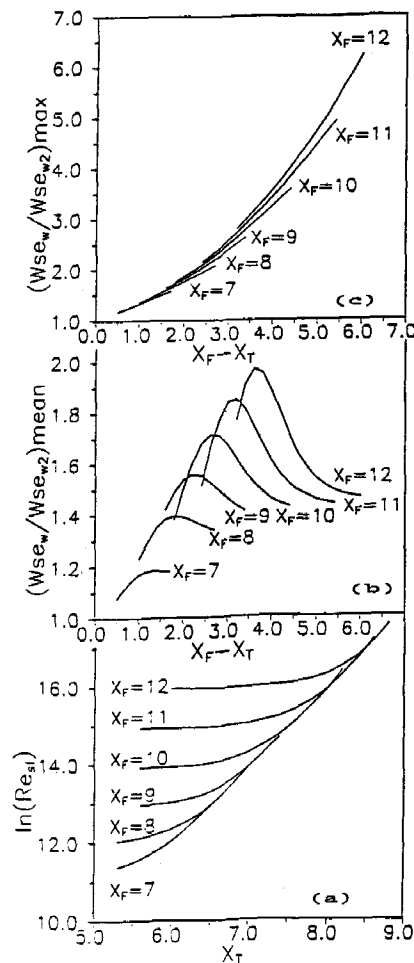

Fig. 2 Calculation results which connect the overall properties of the velocity distribution (mean velocity, maximum local velocity and Reynolds number based on total arc length) with the overall intrinscid properties (X_F and X_T) of an optimum image curve

$W_{se,max}/W_{se2}$ equals to 1.84. Considering Fig. 2, it is possible to see that combining the Reynolds number and the maximum velocity requirements, as well as the requirement to get a ratio $W_{Se,mean}/W_{se,2}$ as high as possible, a good first compromise may be achieved taking $X_F = 8.2$ and $X_F - X_T = 2.2$.

Once the overall intrinsic values of the image curve were specified, the optimum image curve for the blade suction side was constructed while the corresponding suction side velocity distribution was then calculated and is presented in Fig. 3. A pressure side velocity distribution was matched to it and, using a conformal mapping inverse method a blade shape was issued, Fig. 3.

One may find quite a few deficiencies in this first design, the most important being that the influence of curvature effects on turbulence were not taken into account. On the other hand, the corresponding blade shape was thin and the design was performed for incompressible flow. When the blade was tested in the VKI cascade wind tunnel, it was found that, due to the high loading, lateral flow convergence was important and, although it was assessed that transition was located were it was introduced theoretically, the velocity distribution was diverging from the theoretical one and so were the losses. This situation is described in Fig. 3. Subsequent tests conducted in Pratt & Whitney in 2-D conditions, however, demonstrated that the experimental velocity distribution was very close to the theoretical one and so were the losses. Experimental results obtained in Pratt & Whitney, demonstrate that the level of losses of the optimized
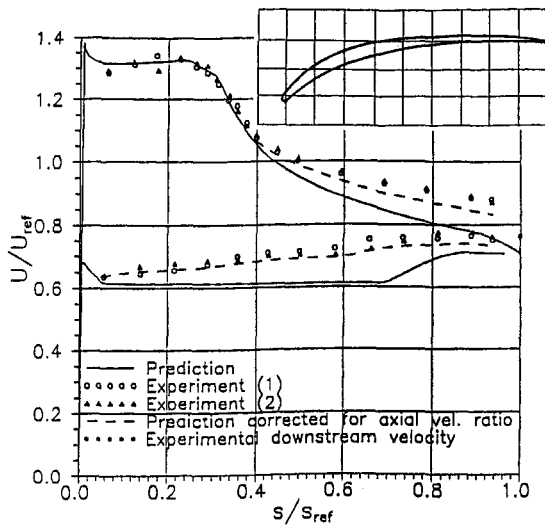
Fig. 3 Measured performance and blade shape of the optimized highly loaded compressor blading

Fig. 5(a) Velocity distribution and blade section shape

Fig. 5(b) Image curves for the suction side shear layers of the initial section and the optimized one

Fig. 5 Optimized hub blade section for an horizontal wind turbine

blade is quite below that of the NACA 65-series and that its off-designed behavior is quite remarkable.

A redesign of this case was undertaken, for an inlet Mach number of 0.7 and the same overall Reynolds number and inlet/outlet flow angles. In addition, it was aimed to obtain a thicker blade than the previous one. The same procedure with the one described for the previous case was employed for the redesign. Two more effects were taken into account during this proceduree. The first one concerned the influence of the exit Mach number on the curves presented in Fig. 2 and the second one the influence of the curvature on the locus of optimum deceleration. In fact, the optimum deceleration locus was displaced in agreement with the modified $M(L_k, X)$-curves, when curvature effects were introduced. Of course, these effects are not a priori known, depending on the curvature of the blade section. For this particular design the curvature effects of the first calculated blade section were taken into account.

Calculation results are presented in Fig. 4. It can be seen that the blade is thicker and the Mach number is locally almost sonic. In addition, the circulation is higher than that of the previous case, resulting to a higher pitch to chord ratio. Finally, the calculated level of mass averaged losses was found to be 0.028, a value which is low and quite comparable with the one reported for the previous case.

The case of a wind turbine will be examined, next. Analysing the hub blade section of an existing wind turbine, Bonataki et
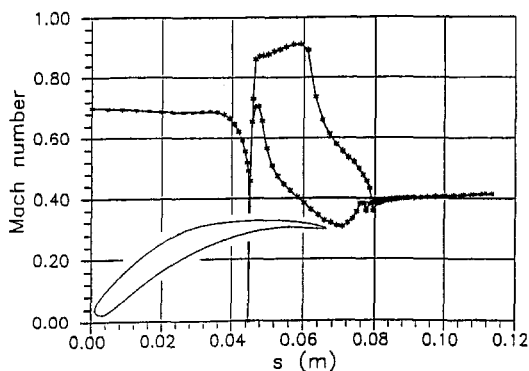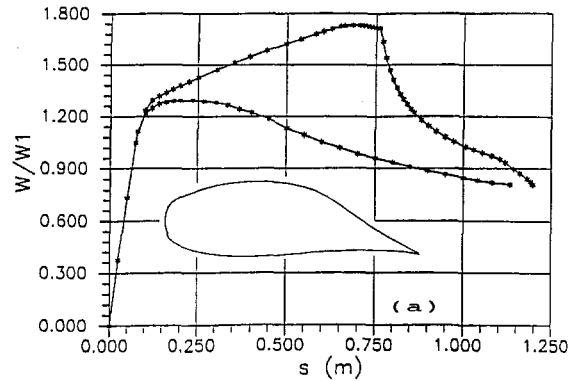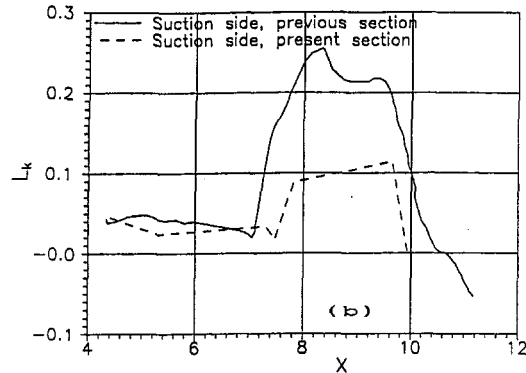

Fig. 4 Optimized high subsonic flow, high loaded compressor profile. Redesign of the profile presented in Fig. 3 with the same inlet and outlet flow angle.

al. (1991), it was found that considerable separation was present. The analysis was performed with the direct calculation tool presented in Section 5, Bouras et al. (1991). A redesign was decided, the target being to suppress separation for the incidence considered (design incidence of the machine) and optimize the losses. Besides, the same overall target was maintained (number of blades, circulation per blade and overall Reynolds number). Figure 5 presents the velocity distribution and resulting blade shape from the redesign. In the same figure, the suction side image curves are presented for the original and redesigned blade sections. In order to obtain this new design, a compromise was accepted on the basis of information supplied from Fig. 2. On the other hand, velocity distribution levels and details near the leading and trailing edges were chosen in order to conserve the original blade section maximum thicness. Of course, the design procedure was not straightforward and a small number of optimum suction side image curves were considered for the same overall Reynolds number, such that the corresponding $W_{se,mean}$ value was near maximum. As it can also be seen from the image curves presented in Fig. 5, no separation is present for the new design. On the other hand, from both inverse and direct calculations, It can be seen that the mass averaged losses for the redesigned blade section are four times less than those of the existing one.

The third case examined here will be an axial turbine one. The blade section, taken from the open literature and reported in Bonataki et al. (1993) was used as a basis for comparison. Its blade shape and the corresponding Mach number distribution are presented in Fig. 6. The blade was analyzed using the direct computational tool presented in Section 5, Bouras (1991) for design conditions. It can be seen Fig. 6 that the velocity peak near the inlet is important enough to induce transition at a distance from the leading edge equal to 12 percent of the chord. Very probably transition was intended to be located after the
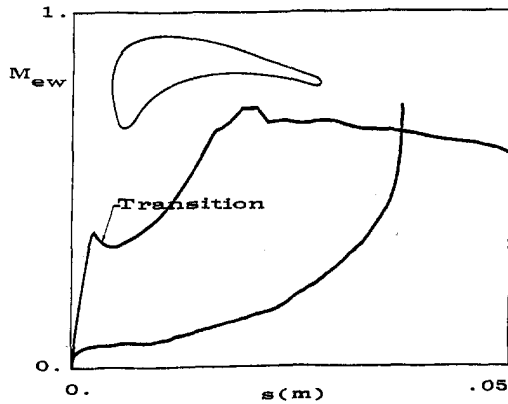
Fig. 6 A conventional turbine rotor blading and the corresponding Mach number distribution, taken from the open literature (see for details, Bonataki, 1991)

second velocity peak. As things stand, the calculated level of the losses is equal to 3.7 percent of the outlet dynamic head.

The present inverse calculation procedure was used, in order to obtain a new blading with the same circulation. The maximum suction side velocity level was kept about the same and so was the blade chord Reynolds number. Furthermore, the final value of X_F selected was lower than the corresponding value calculated for the original blading. The resulting blade shape is presented in Fig. 7 along with the external flow Mach number distribution. The losses for the new design were calculated equal to 2.8 percent of the outlet dynamic head. The difference in the level of losses between the original and the new blading is not surprising in view of the location of the transition point in the original design.

Finally, comparing the two designs, one may remark the larger leading edge radius of curvature of the new design and the somewhat unconventional shape resulting for a rotor, compared with the original design.

The inclusion of curvature and Coriolis force effects in the design procedure must be further discussed. Results of similar calculations performed for the suction side of the blade radial part of a centrifugal compressor demonstrate that, in the presence of strong Coriolis forces, the deceleration that this part of the blade can sustain is very limited. Consequently, the design of radial machines is influenced considerably by these effects. In fact, the design of a new version of a radial compressor, Cyffers et al. (1979) Bois et al. (1984) was realized taking them into account. The design aim was to reduce the axial length of the compressor for the obvious advantages of a multistage arrangement. The compressor pressure ratio was $\pi = 1.5$ and its mass flow rate $m_s = 8$ kg/s. Results of the calculations are
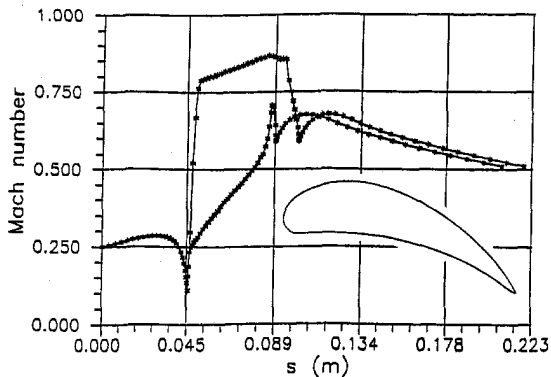

Fig. 7 The turbine blading and the corresponding Mach number distribution resulting from a redesign of the blading presented in Fig. 6
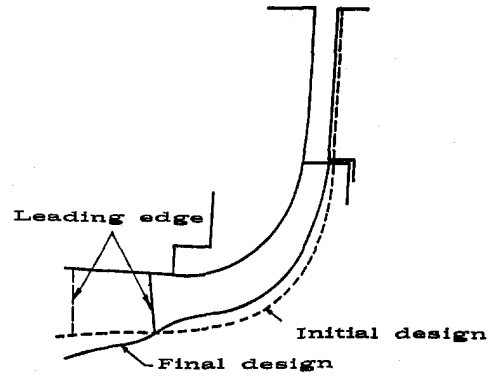

Fig. 8(a) Meridional compressor shapes (initial and final)
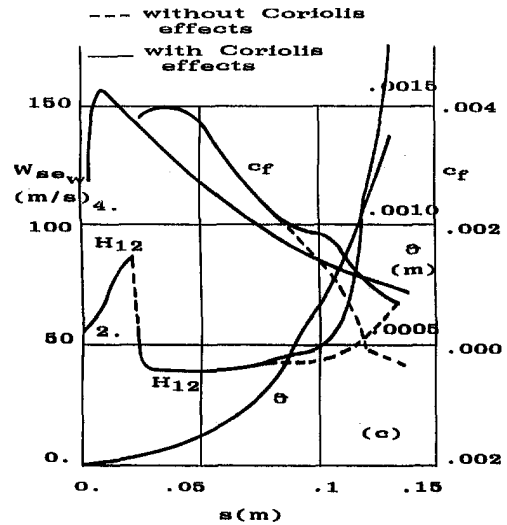
Fig. 8(b) Suction side case
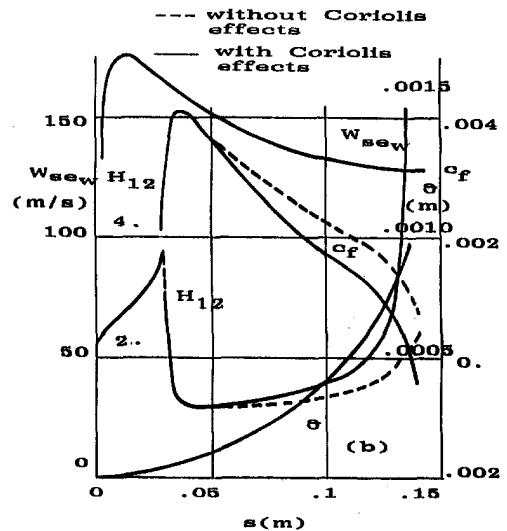
Fig. 8(c) Pressure side case

Fig. 8 Case of a radial compressor. Effect of Coriolis force on the suction and pressure side shear layers.

presented in Fig. 8. They concern the blade suction and pressure side velocity distributions along the mean stream surface. The variation of the streamtube width and radius was taken into account along with the effects of compressibility, wall curvature and Coriolis force. The shear layer calculation penetrated inside the reverse flow region.

It can be seen from Fig. 8 that the finally admitted velocity distributions are such that the deceleration is rather mild on the suction side and severe on the pressure side. The centrifugal force impact is such that finally separation is provoked near the suction side trailing edge, while it is suppressed all together on the pressure side.

Details on the radial compressor and the tests that were performed in the Ecole Centrale of Lyon, can be found in Bois et al. (1984). The overall isentropic efficiency of the compressor (including the scroll) at the design point was 0.84, a figure which can be considered rather satisfactory for this high hub to tip ratio design. The impeller efficiency at design point was found to be 0.90 and equal to the computed one. This figure, however, cannot alone explain the good overall efficiency. We believe that this was obtained due to the limited separation admitted for the impeller, which provided the diffuser with good inlet flow conditions. The unusual hub shape resulting from the redesign, was formed in this way in order to obtain the desired velocity distributions with easily manufacturable blades and the original casing.

5 Conclusions

In this work, a design procedure was presented, for the calculation of arbitrary blade sections for turbomachinery applications. This procedure which is fully inverse, takes into account the effects of viscosity. In addition, it establishes a number of elements, which can be used for optimization, putting the accent especially on viscous effects. Various examples were examined which are considered representative, but the whole domain of application is not covered yet. Although all aspects were not covered, it is evident that viscous effects cannot be neglected during the design process and that we possess the required information in order to take them into account.

References

Bois, G., and Papailiou, K. D., 1984, "A Contribution to the Study of the Design of an Industrial Centrifugal Compressor," ASME Paper 84-GT-60.

Bonataki, E., Chaviaropoulos, P., and Papailiou, K. D., 1993, "An Inverse Inviscid Method for the Design of Quasi-Three Dimensional Turbomachinery Cascades," ASME JOURNAL OF FLUIDS ENGINEERING, Vol. 115, No 121–127.

Bonataki, E., 1991, "Inviscid Subsonic Inverse Method for the Design of Blade Sections along Arbitrary Axisymmetric Stream Surfaces with Varying Stream Tube Width," Ph.D. thesis, NTUA, Greece.

Bouras, B., Karagiannis, F., Leoutsakos, G., Giannakoglou, K., and Papailiou, K. D., 1991, "Arbitrary Blade Section Design Based on Viscous Considerations. Background Information," International Symposium on Numerical Simulations in Turbomachinery, Joint ASME-JSME Fluids Engineering Meeting, Portland, Oregon, to appear in the ASME JOURNAL OF FLUIDS ENGINEERING.

Bradshaw, P., 1967, "The Analogy Between Streamline Curvature and Buoyancy in Turbulent Shear Flow," N. P. L. Aero Re. 1231, ARC 29048.

Cyffers, J., Crinquette, J. M., Papailiou, K. D., Bois, G., and Hong, A., 1979, "Etude d'un Etage Centrifuge a Grand Rapport de Moyeu, Destiné à la Realisation de Compresseurs Multietages en Ligne pour Gas Contenant Eventuellement des Particules en Suspension," Contrats DGRST, 75-7-1279, 75-7-1280, rapport final.

Johnston, J. P., 1970, "The Effects of Rotation on Boundary Layers in Turbomachine Rotors," Report MD 24, Thermoscience Div., Stanford Univ., USA.

Le Foll, J., 1965, "A Theory of Representation of the Properties of Boundary Layers on a Plane," Proc. Seminar on Advanced Problems in Turbomachinery, VKI March 29–30.

Lock, R. C., Firmin, M. C. P., 1981, "Survey of Techniques for Estimating Viscous Effects in External Aerodynamics," IMA Conference, London, UK.

Papailiou, K. D., 1971, "Boundary Layer Optimization for the Design of High Turbine Axial Flow Compressor Blades," ASME Journal of Engineering for Power, Vol. 93, pp. 147–155.

Papailiou, K. D., Satta, A., Nurzia, F., 1973, "On the Two-Dimensional Boundary Layers as they Appear on Turbomachine Blades," AGARD AG 164.

Papailiou, K. D., 1981, "Le Foll's Method and the Calculation of Attached and Seperated Two-Dimensional Boundary Layers," Von Karman Institute, Lecture Series on "Seperated Flows in Turbomachinery Components," VKI LS 1981-1.

Schlichting, H., 1962, Boundary Layer Theory, 4th ed., McGraw-Hill.

The Simulation of Mixing Layers Driven by Compound Buoyancy and Shear

D. M. Snider

Senior Engineer,
Science Applications
International Corporation,
2109 Air Park, SE,
Albuquerque, NM 87106

M. J. Andrews

Assistant Professor,
Department of Mechanical Engineering,
Texas A&M University,
College Station, TX 77843

Fully developed compound shear and buoyancy driven mixing layers are predicted using a k-ε turbulence model. Such mixing layers present an exchange of equilibrium in mixing flows. The k-ε buoyancy constant $C_{ε3} = 0.91$, defined in this study for buoyancy unstable mixing layers, is based on an approximate self-similar analysis and an accurate numerical solution. One-dimensional transient and two-dimensional steady calculations are presented for buoyancy driven mixing in a uniform flow field. Two-dimensional steady calculations are presented for compound shear and buoyancy driven mixing. The computed results for buoyancy alone and compound shear and buoyancy mixing compare well with measured data. Adding shear to an unstable buoyancy mixing layer does not increase the mixing growth rate compared with that from buoyancy alone. The nonmechanistic k-ε model which balances energy generation and dissipation using constants from canonical shear and buoyancy studies predicts the suppression of the compound mixing width. Experimental observations suggest that a reduction in growth rate results from unequal stream velocities that skew and stretch the normally vertical buoyancy plumes producing a reduced mixing envelope width.

Introduction

An unstable thermal stratification occurs when cold fluid overlays warm fluid under the influence of gravity. The buoyancy of the cool (heavy fluid) above the warmer (light fluid) makes the thermal interface unstable and causes the two fluids to mix. More generally, an acceleration directed from the heavy fluid to the light fluid imposes a pressure gradient at the density interface that drives the development of Rayleigh-Taylor instability (Taylor, 1950 and Chandrasekhar, 1961). The initial linear instability gives way to nonlinear mixing as heavy fluid falls through light fluid and light fluid rises through heavy fluid. In the nonlinear, three-dimensional process, vortices form between the moving fluid interfaces which leads to turbulent mixing. More typical of an application is that buoyancy often is accompanied by shear. Buoyancy produces a normal force at the interface, while parallel streams of unequal velocity produce a tangential shear force at the interface. Free shear perturbations arise as Kelvin-Helmholtz instabilities and are followed by growth and pairing of vortices that eventually form a turbulent mixing layer as observed by Brown and Roshko (1974).

Unstable thermal stratification occurs in both environmental and industrial processes (Sharp, 1984). Compound buoyancy and shear mixing occur in nature from effluent discharge into rivers and estuaries or from flow into ponds, lakes, or reservoirs (Imberger and Hamblin, 1982). Above the atmospheric boundary layer, buoyancy turbulence from phase change forms orderly plumes of cumulus clouds (Deardorff, 1970 and Vinnichenko et al., 1980). In heat exchangers, cold fluid enters the top of the exchanger, falls rapidly, and mixes with the warm fluid underneath. Swirl is used in pipes and internal combustion engines to generate an unstable thermal layer and promote heat transfer (Dhir and Chang, 1992). Furnaces and combustion chambers introduce cool fuel mixtures over hot gases, and chemical reactors mix chemicals of different densities. All these applications exhibit closely coupled compound buoyancy and shear flows. This close coupling between canonical shear and buoyancy results in compound interactions that are poorly understood and lead to a novel mixing process. Indeed, this compound buoyancy and shear presents an intriguing situation of two canonical equilibrium flows that exchange equilibria as the flow develops. Developed shear layers grow linearly with distance (Rajaratnam, 1976), while unstable buoyancy driven layers grow quadratically with streamwise distance (Youngs, 1984). The mixing process progresses through shear dominated flow with a linear growth rate to end with buoyancy mixing with a quadratic growth rate.

Calculations for developed shear layers have been made with turbulence models, such as that by Launder et al. (1973), and by direct numerical solution such as that by Comte et al. (1989) and Rogers and Moser (1994). Rayleigh-Taylor mixing from initially stagnant layers has been calculated using a transient, two-fluid model without a turbulence model by Youngs (1991), and a direct numerical solution by Li (1993). The prediction of compound buoyancy and shear mixing has been largely directed at the stable mixing layer (light fluid above heavy fluid). However, Andrews and Spalding (1990) reported "tilted" experiments where large scale overturning motion superimposed a shearing across a Rayleigh-Taylor mixing interface. Snider and Andrews (1994) presented detailed experiments of compound shear and unstable buoyancy mixing.

This study simulates fully developed compound shear and unstable buoyancy mixing in a plane layer using a two-equation turbulence model. Figure 1 illustrates a compound shear and buoyancy mixing layer. Turbulence transport is modeled by an eddy-diffusivity relation with closure completed using a two equation k-ε turbulence model. The k-ε turbulence closure model (Launder and Spalding, 1974) was chosen because of its popularity and its success in predicting a variety of turbulent flows. The model has recognized limitations (Bradshaw et al., 1991) with one major shortcoming being that its accuracy partly depends on empirical constants tailored for specific situations. This is especially true of the buoyancy dissipation constant $C_{ε3}$ (Eq. (7)). Reported values for $C_{ε3}$ range from 0.8 to 1.44 and are often defined together with a Richardson number (Rodi, 1991, 1993 and Yang and Aung, 1985). Launder (1988) used
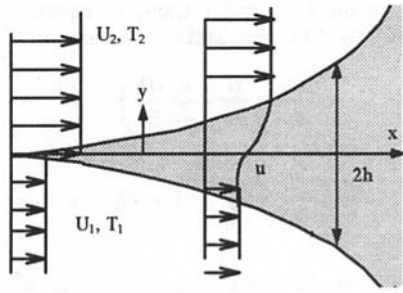
Fig. 1 Illustration of the buoyancy and shear mixing layer

$C_{c3} = C_{c1}$ in calculating flow near a heated vertical wall. Hanjalic and Vasic (1993) reported $C_{c3} = 0.8$ for an accurate prediction of pure buoyancy driven flows. In this study, the turbulence constant C_{c3} that appears in the buoyancy term of the dissipation is carefully evaluated from an analytical self-similar solution and an accurate numerical solution.

The turbulence model has been used successfully to simulate stable stratified flows where buoyancy suppresses the growth of the shear layer (Tennekes and Lumley, 1972). Calculations in this study are presented for unstable buoyancy and shear driven mixing. It might be expected that addition of the two unstable mixing mechanisms would increase the mixing layer growth rate beyond that of either of the two individual layers. This study shows that the k-ϵ model predicts a suppression of the buoyancy layer growth rate from addition of shear. The structure of experimentally measured data is examined to evaluate the validity of the calculated behavior. From a practical point this result indicates that shear can be used to mitigate the mixing growth due to unstable buoyancy, or conversely, unstable buoyancy can be used as a limited means to promote shear mixing.

Experimental Data. This numerical work makes use of experimental data from Snider and Andrews (1994) who developed a statistically steady experiment where buoyancy and shear were copresent and independently controlled. Details of the experiment can be found in Snider and Andrews (1994). Two parallel flowing water streams were separated by a thin splitter plate. At the end of the splitter plate, the flows met. A buoyancy unstable interface formed if the stream temperatures were different. An unstable shearing interface formed if the velocities were different, and a compound mixing layer formed if both temperatures and velocities were different. The mixing angle was chosen to be small to ensure parabolic flow.

Governing Equations and k-ϵ Model

The water mixing layer is a Newtonian incompressible fluid with constant kinematic viscosity. Temperature differences are small and density variations are limited to the buoyancy terms using the Boussinesq approximation. The ensemble averaged equations for conservation of mass, momentum, and energy equations are:

$$\frac{\partial u}{\partial x} + \frac{\partial v}{\partial y} = 0 \tag{1}$$

$$\frac{\partial u}{\partial t} + u \frac{\partial u}{\partial x} + v \frac{\partial u}{\partial y}$$
$$= -\frac{1}{\rho}\frac{\partial p}{\partial x} + \nu\left[\frac{\partial^2 u}{\partial x^2} + \frac{\partial^2 u}{\partial y^2}\right] - \left[\frac{\partial \overline{u'u'}}{\partial x} + \frac{\partial \overline{u'v'}}{\partial y}\right] \tag{2}$$

$$\frac{\partial v}{\partial t} + u \frac{\partial v}{\partial x} + v \frac{\partial v}{\partial y} = -\frac{1}{\rho}\frac{\partial p}{\partial y} + \nu\left[\frac{\partial^2 v}{\partial x^2} + \frac{\partial^2 v}{\partial y^2}\right]$$
$$- \left[\frac{\partial \overline{v'u'}}{\partial x} + \frac{\partial \overline{\partial v'v'}}{\partial y}\right] + \beta g(T - T_o) \tag{3}$$

$$\frac{\partial T}{\partial t} + u \frac{\partial T}{\partial x} + v \frac{\partial T}{\partial y}$$
$$= \frac{\kappa}{\rho C_p}\left[\frac{\partial^2 T}{\partial x^2} + \frac{\partial^2 T}{\partial y^2}\right] - \left[\frac{\partial \overline{T'u'}}{\partial x} + \frac{\partial \overline{T'v'}}{\partial y}\right] \tag{4}$$

where u and v are ensemble average velocities and p, ρ, and T are ensemble averaged pressure, density, and temperature, respectively. The expansion coefficient is $\beta = -(1/\rho_o)/(\partial \rho/\partial T)$, and T_o and ρ_o are the mean temperature and corresponding density. The u', v', ρ', and T' are fluctuating components. The $\overline{u'u'}$, $\overline{v'v'}$, and $\overline{u'v'}$ are the ensemble averaged Reynolds stresses, and $\overline{u'T'}$ and $\overline{v'T'}$ are the turbulent heat fluxes. Closure is completed using a Boussinesq approximation and a turbulent kinetic energy and kinetic energy dissipation model. The equations of closure are:

$$\overline{u'u'} = -\nu_t\left(2\frac{\partial u}{\partial x}\right) + \frac{2}{3}k \qquad \overline{v'v'} = -\nu_t\left(2\frac{\partial v}{\partial y}\right) + \frac{2}{3}k$$

$$\overline{u'v'} = -\nu_t\left(\frac{\partial u}{\partial y} + \frac{\partial v}{\partial x}\right) \tag{5a}$$

Nomenclature

A = Atwood number: $A = (\rho_1 - \rho_2)/(\rho_1 + \rho_2)$

C_μ, C_{c1},
C_{c2}, C_{c3} = constants in turbulence model

C_W, C_k,
C_ϵ, C_ρ = constants in assumed self-similar profiles

B = equation (20)
g = gravity acceleration
G_s = production of kinetic energy from shear
G_b = production of kinetic energy from buoyancy
h = half-width of the mixing layer (see Fig. 1 and Fig. 8)
k = ensemble averaged turbulent kinetic energy

l = turbulent length scale
p = ensemble averaged pressure
Ri = Richardson number
t = time
T = ensemble averaged temperature
T_0 = reference temperature
T_1, T_2 = freestream temperatures
u, v = ensemble averaged velocities
u', v' = fluctuating velocities
U_1, U_2 = freestream velocities
x, y = spatial coordinate in streamwise and vertical directions, respectively
α = buoyancy growth constant
β = coefficient of expansion
δ_ω = vorticity thickness
κ = thermal conductivity
ν = kinematic viscosity

ν_t = turbulent kinematic viscosity
T' = fluctuating temperature
$\overline{u_i' u_j'}$ = Reynolds stress
$\overline{T' u_j'}$ = fluctuating components of temperature
ϵ = ensemble averaged kinetic energy dissipation
ϵ_T = ensemble averaged turbulence heat flux dissipation
η = buoyancy similarity variable y/t^2
ρ = ensemble averaged density
ρ_1, ρ_2 = freestream densities
ρ_o = reference density at T_o
ρ' = fluctuating density
σ_T, σ_k, σ_ϵ, = Prandtl numbers

---

where the turbulent viscosity is $\nu_t = C_\mu(k^2/\epsilon)$. The closure for the turbulent heat flux is an eddy diffusivity model with the thermal time scale, $\overline{T'^2}/2\epsilon_T$, equal to the mechanical time scale, k/ϵ where ϵ_T is the molecular diffusion of turbulent temperature variance (Hanjalic, 1994):

$$\overline{T'u'} = -\frac{\nu_t}{\sigma_T}\left(\frac{\partial T}{\partial x}\right) \quad \overline{T'v'} = -\frac{\nu_t}{\sigma_T}\left(\frac{\partial T}{\partial y}\right) \quad (5b)$$

The simple gradient model neglects two important effects. First, the model does not predict an intensive turbulent heat flux where the mean temperature gradient is uniform or where the gradient may be in the same direction as the heat flux vector. Second, at a vertical heated wall where the major source of turbulence is induced by vertical heat flux, the temperature gradient in the vertical direction is small. This study of the unstable buoyancy layer does not suffer from the above two shortcomings. Buoyancy induced turbulence is in the direction of turbulent heat flux and opposite the temperature gradient.

The ensemble averaged turbulent kinetic energy and the dissipation equations are:

$$\frac{\partial k}{\partial t} + u\frac{\partial k}{\partial x} + v\frac{\partial k}{\partial y}$$

$$= \frac{\partial}{\partial x}\left(\frac{\nu_t}{\sigma_k}\frac{\partial k}{\partial x}\right) + \frac{\partial}{\partial y}\left(\frac{\nu_t}{\sigma_k}\frac{\partial k}{\partial y}\right) + G_s + G_b - \epsilon \quad (6)$$

$$\frac{\partial \epsilon}{\partial t} + u\frac{\partial \epsilon}{\partial x} + v\frac{\partial \epsilon}{\partial y} = \frac{\partial}{\partial x}\left(\frac{\nu_t}{\sigma_\epsilon}\frac{\partial \epsilon}{\partial x}\right) + \frac{\partial}{\partial y}\left(\frac{\nu_t}{\sigma_\epsilon}\frac{\partial \epsilon}{\partial y}\right)$$

$$+ C_{\epsilon 1}\frac{\epsilon}{k}G_s + C_{\epsilon 3}\frac{\epsilon}{k}G_b - C_{\epsilon 2}\frac{\epsilon^2}{k} \quad (7)$$

where k and ϵ are ensemble averaged kinetic energy and kinetic energy dissipation, respectively. The turbulent diffusivity is assumed much larger than the molecular diffusivity. The turbulent kinetic energy production from shear for two-dimensional incompressible flow is:

$$G_s = \nu_t\left[2\left(\frac{\partial u}{\partial x}\right)^2 + 2\left(\frac{\partial v}{\partial y}\right)^2 + \left(\frac{\partial u}{\partial y} + \frac{\partial v}{\partial x}\right)^2\right] \quad (8)$$

and the turbulent kinetic energy production from buoyancy is:

$$G_b = \frac{\nu_t g}{\sigma_T \rho_o}\frac{\partial \rho}{\partial y} = -\frac{\nu_t g}{\sigma_T}\beta\frac{\partial T}{\partial y} \quad (9)$$

where g is gravity, and σ_T is the Prandtl number.

The k-ϵ constants are $C_\mu = 0.09$, $C_{\epsilon 1} = 1.44$, $C_{\epsilon 2} = 1.92$, $\sigma_k = 1$, and $\sigma_\epsilon = 1.3$ (Launder and Spalding, 1974), and $\sigma_T = 0.6$ for the free mixing layer calculations (White, 1991). The constant $C_{\epsilon 3}$ is assigned the value 0.91 in this study.

Determination of $C_{\epsilon 3}$

The $C_{\epsilon 3}$ constant in Eq. (7) for Rayleigh-Taylor mixing in a plane layer is defined here. A value is determined from an approximate analytical self-similar solution and then with an accurate numerical solution.

Self-Similar Buoyancy Mixing. Here we describe a one-dimensional self-similar solution for the present problem similar to that of Andrews (1984) and a later analysis by Spitz and Haas (1991). In the experimental arrangement (Snider and Andrews, 1994) a buoyancy driven turbulent mixing layer grows when the upper and lower fluids have the same velocity, and the upper layer is colder than the lower layer as illustrated in Fig. 1. The mean vertical and horizontal velocities are zero in a Galilean frame moving with the mean velocity and, consequently, con-

vective terms in the k, ϵ, and T transport equations are zero. The governing Eqs. (4), (6), and (7) reduce to:

$$\frac{\partial T}{\partial t} = \frac{\partial}{\partial y}\left(\frac{\nu_t}{\sigma_T}\frac{\partial T}{\partial y}\right) \quad (10)$$

$$\frac{\partial k}{\partial t} = \frac{\partial}{\partial y}\left(\frac{\nu_t}{\sigma_k}\frac{\partial k}{\partial y}\right) + G_b - \epsilon \quad (11)$$

$$\frac{\partial \epsilon}{\partial t} = \frac{\partial}{\partial y}\left(\frac{\nu_t}{\sigma_\epsilon}\frac{\partial \epsilon}{\partial y}\right) + C_{\epsilon 3}\frac{\epsilon}{k}G_b - C_{\epsilon 2}\frac{\epsilon^2}{k} \quad (12)$$

The energy equation is recast in terms of density using a constant expansion coefficient, β.

$$\frac{\partial \rho}{\partial t} = \frac{\partial}{\partial y}\left(\frac{\nu_t}{\sigma_T}\frac{\partial \rho}{\partial y}\right) \quad (13)$$

Initial conditions are:

at $t = 0$ for $y \geq 0$: $\rho = \rho_2$, $k = 0$, $\epsilon = 0$

at $t = 0$ for $y < 0$: $\rho = \rho_1$, $k = 0$, $\epsilon = 0$

$$(14)$$

Exterior quiescent fluid boundary conditions are applied at the mixing layer boundary, $\pm h(t)$ shown in Fig. 1, as follows:

for $y > h$: $\rho = \rho_2$, $k = 0$, $\epsilon = 0$

for $y < -h$: $\rho = \rho_1$, $k = 0$, $\epsilon = 0$ $\quad (15)$

The above set of equations has a self similar solution using the similarity variables: $\eta = y/t^2$, $k(t, y) = t^2\tilde{k}(\eta)$, $\epsilon(t, y) = t\tilde{\epsilon}(\eta)$, $\rho(t, y) = \tilde{\rho}(\eta)$.

Introducing similarity variables into Eqs. (10) to (12) gives the following ordinary differential equations in $\tilde{k}$, $\tilde{\epsilon}$, and $\tilde{\rho}$:

$$-2\eta\frac{d\tilde{\rho}}{d\eta} = \frac{C_\mu}{\sigma_T}\frac{d}{d\eta}\left(\frac{\tilde{k}^2}{\tilde{\epsilon}}\frac{d\tilde{\rho}}{d\eta}\right) \quad (16)$$

$$2\tilde{k} - 2\eta\frac{d\tilde{k}}{d\eta} = \frac{C_\mu}{\sigma_k}\frac{d}{d\eta}\left(\frac{\tilde{k}^2}{\tilde{\epsilon}}\frac{d\tilde{k}}{d\eta}\right) + \frac{C_\mu}{\sigma_T}\frac{\tilde{k}^2}{\tilde{\epsilon}}\frac{g}{\rho_o}\frac{d\tilde{\rho}}{d\eta} - \tilde{\epsilon} \quad (17)$$

$$\tilde{\epsilon} - 2\eta\frac{d\tilde{\epsilon}}{d\eta} = \frac{C_\mu}{\sigma_\epsilon}\frac{d}{d\eta}\left(\frac{\tilde{k}^2}{\tilde{\epsilon}}\frac{d\tilde{\epsilon}}{d\eta}\right) + C_{\epsilon 3}\tilde{k}\frac{g}{\rho_o}\frac{d\tilde{\rho}}{d\eta} - C_{\epsilon 2}\frac{\tilde{\epsilon}^2}{\tilde{k}} \quad (18)$$

The constant $C_{\epsilon 3}$ is calculated from the integration of Eqs. (16) to (18) using approximate profiles for k, ϵ, and ρ. The turbulent kinetic energy and dissipation are approximated by parabolic profiles and the density within the mixing layer is approximated by a linear profile. It is shown later that these profiles are reasonable approximations to the true profiles. The approximate profiles are:

$$\tilde{k} = C_k(1 - \tilde{\eta}^2) \quad \tilde{\epsilon} = C_\epsilon(1 - \tilde{\eta}^2) \quad \tilde{\rho} = C_\rho\tilde{\eta} + \tilde{\rho}_1$$

where the self-similar length scale is normalized based on the mixing half width, $C_w = h/t^2$:

$$\tilde{\eta} = \frac{\eta}{C_w} = \frac{y}{h} \quad (19)$$

C_K and C_ϵ are constants, and for the linear density profile $C_\rho = (\rho_2 - \rho_1)/2$ and $\tilde{\rho}_1 = (\rho_1 + \rho_2)/2$. The equations are integrated across the mixing layer from $-1 < \tilde{\eta} < 1$, and the constants calculated:
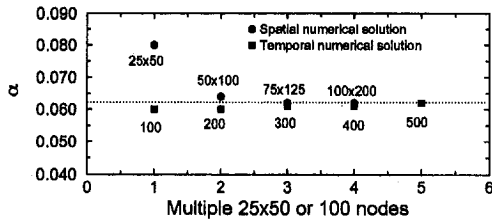
Fig. 2 Grid independence checks for spatial and temporal computed solutions

$$C_k = \frac{B^2 C_p^2 (C_{\epsilon2} - C_{\epsilon3})^3}{(4C_{\epsilon2} - 3)^2 (4C_{\epsilon3} - 3)} \frac{\sigma_T}{C_\mu} \quad C_\epsilon = \frac{(4C_{\epsilon3} - 3)}{(C_{\epsilon2} - C_{\epsilon3})} C_k$$

$$B = -\frac{C_\mu g}{\sigma_T \rho_o} \quad C_W = \frac{C_\mu (4C_{\epsilon2} - 3)}{BC_p \sigma_T (C_{\epsilon2} - C_{\epsilon3})} C_k \qquad (20)$$

$C_{\epsilon2}$, C_μ, and σ_T, in Eqs. (20), are the standard k-ϵ constants, C_p is given by the density differences between the layers, and the self-similar mixing width $C_W = h/t^2$ can be obtained from experimental data for the half-width of the mixing layer:

$$h = \alpha A g t^2 \qquad (21)$$

where A is the Atwood number and α is the growth rate constant of $\alpha = 0.07$ from Snider and Andrews (1994). Solving the C_W Eq. (30) for $C_{\epsilon3}$ gives a value of $C_{\epsilon3} = 0.88$.

Numerical One-Dimensional Transient Solution. The transient one-dimensional Eqs. (10) to (12) were solved numerically using a range of $C_{\epsilon3}$ values around the analytical self-similar value of 0.88. The numerical method used finite volumes, with staggered momentum nodes and a SIMPLE solution method (Patankar, 1980). Transient solutions were made using time steps from 0.05 s to 0.1 s and spatial grids ranging from 100 to 500 nodes uniformly spaced over a computational length of 0.5 m. The total volume error at each time step was less than 10^{-7} m^3. Solutions were found grid independent at nodalizations greater than 200 nodes as shown in Fig. 2.

Two methods can start the transient problem. In the first, the self-similar distribution of k, ϵ, and T are specified across the initial mixing width and the numerical solution quickly becomes self similar. In the second, which is used in this study, reasonable initial values for k, ϵ, and T are specified in an initial mixing width, and the numeric solution, like the experiment, progresses to a self-similar state. In the second approach, a virtual origin is defined which accounts for the development time to self-similar mixing. Both methods produced the same self-similar solution.

Figure 3 shows the growth rate constant, α, for the numerically calculated mixing layer plotted versus $C_{\epsilon3}$. The $C_{\epsilon3}$ from the self-similar solution is shown for comparison. The computed $C_{\epsilon3}$ ranges from 0.88 to 0.94 for the corresponding range of measured growth constants of $\alpha = 0.05$ to 0.077 reported in the literature by Read (1984), Youngs (1992), Linden et al. (1992), Andrews and Spalding (1990), and Snider and Andrews (1994). Figure 3 shows the value $C_{\epsilon3} = 0.8$ given by Hanjalic and Vasic (1993) gives a mixing layer growth rate $\alpha \sim 0.12$ which is larger than that measured. A value of $C_{\epsilon3} = 0.91$ gives an $\alpha = 0.07$ which compares well with measurements by Snider and Andrews (1994) and so is used in this study. The computed self-similar k, ϵ, and T compare reasonably with the approximate profiles used in the analytical self-similar solution, which explains the good agreement between analytical and computed $C_{\epsilon3}$.

Two-Dimensional Steady Boundary Conditions

A two-dimensional plane mixing layer generally forms as two parallel streams at different velocities and different temperatures

meet downstream from the splitter plate as illustrated in Fig. 1. The temperature of the bottom stream is higher than that of the top stream giving buoyancy unstable flow. With the same bottom and top velocities, the mixing is from buoyancy only, and with a uniform temperature field, the mixing is from shear only.

Constant freestream velocities U_1 and U_2 and temperatures T_1 and T_2 are applied at the inlet and in the far-field above and below the mixing region. The inlet k was set at 5 percent of the average free stream flow value based on measured data by Browand and Weidman (1976), which had experimental conditions close to those of this study. The inlet dissipation is based on a length scale associated with the 7 mesh/cm screen at the end of the splitter plate and is, $\epsilon_{\text{inlet}} = (k_{\text{inlet}}^{3/2}/l)$, where the length scale is taken as the mesh spacing $l = 0.12$ cm. The gradient of k and ϵ are zero in the far field above and below the mixing layer. The exit boundary condition is local one-way which gives an outflow with no exit streamwise diffusion. The outlet condition matches the parabolic design of the experiment (Snider and Andrews, 1994).

The calculation domain begins near the end of the splitter plate. Flow from the end of the splitter plate forms a wake that is complicated as boundary layers pass through a full screen. The k-ϵ model cannot be expected to work well in the near wake of the splitter plate because of the large change in anisotropy of the Reynolds stresses that occur as flow leaves the solid plate to a free density interface. This study focuses on calculating the developed turbulent mixing layer and requires only reasonable inlet values for the inlet mixing region. The experiment by Snider and Andrews (1994) used a full screen at the end of the splitter plate. Koop (1976) found that the full screen reduced boundary layer effects and gave nearly a step profile across the mixing layer. To model the experiment, the inlet velocity and temperature were specified as error functions across a narrow inlet mixing width. As detailed above the inlet value for k was taken from experimental data by Browand and Weidman (1976) and approximated by a bell shaped curve with a reasonable peak k value of 5 percent of the freestream flow. The initial mixing width was 2 to 3 computational nodes wide, which gave only a sparse representation of the curves. However, our interest was in the fully developed region downstream where profiles develop across many nodes.

Table 1 shows further details of the computations. The calculations are for buoyancy, shear, and compound shear and buoyancy mixing. Two-dimensional steady solutions are listed as "spatial" and the one-dimensional transient calculation is listed as "temporal."

The numerical method used two-dimensional, finite volumes with staggered momentum nodes. A hybrid numerical scheme (Spalding, 1972), and a SIMPLE solution scheme (Patankar, 1980) were employed. Steady calculations were made using node sizes ranging from 25×50 to 100×200 (axial-streamwise direction by vertical direction). The computation domain was 0.7 m in the streamwise direction and 1.2 m in the vertical
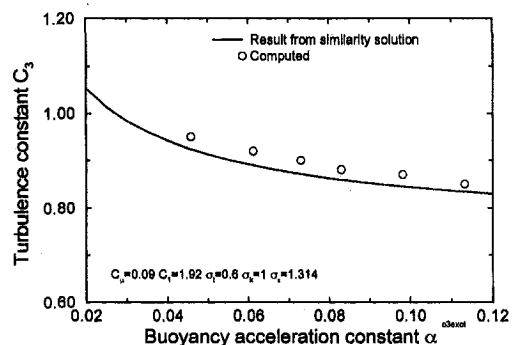

Fig. 3 Turbulence constant $C_{\epsilon3}$ compared to buoyancy growth constant α

Table 1 Boundary conditions and nodalization for numeric calculations. buoy: buoyancy calculation. shear: shear calculation. spatial: two-dimensional steady calculation. temporal 1-D: one-dimension transient solution.

Run	Exper[1].	Comment	U_1 (cm/s)	U_2 (cm/s)	T_1 (K)	T_2 (K)	Inlet h (cm)	Grid $X \times Y$
1		shear, spatial	3.4	5.4	300.0	300	0.90	50×100
2		shear, spatial	5.0	10.0	300.0	300	0.81	50×100
3		shear, spatial	4.1	4.7	300.0	300	0.72	50×100
4	2–68	buoy, temporal, 1-D	—	—	310.3	306.7	0.19	1×500
5	2–68	buoy, spatial	4.8	4.9	310.3	306.7	0.49	50×100
6	3–11	buoy and shear, spatial	4.1	4.7	311.2	306.8	0.67	50×100
7		buoy, spatial	4.4	4.4	311.2	306.8	0.54	50×100
8		buoy and shear, spatial	5.4	3.4	311.2	306.8	0.27	50×100

[1] Experiments listed are from Snider and Andrews (1994).

direction. Grid spacing was uniform in the streamwise direction and varied non-linearly in the vertical direction with the vertical grid size on the order of 0.24 cm at the slip line and 8 cm at the far field boundary. The total volume error for convergence was less than 10^{-7} m^3. Solutions were grid independent at node sizes greater than 50×100 as shown in Fig. 2. Applying variations in the specified inlet and initial mixing layer widths gave some change in distance (or time) to reach self-similar mixing but did not alter the developed mixing layer growth rate.

Buoyancy Mixing

Our work described above with a one-dimensional mixing model provided a value for $C_{\epsilon 3}$. This section gives results from two-dimensional steady calculations of the buoyancy mixing layer compared with measured data. The two-dimensional solution is motivated by a possible asymmetric behavior produced by shear. A transient analytical approximation of the free shear layer can be made for discontinuous flow (see Schlichting, 1958), but the common self-similar approach uses the two-dimensional boundary layer equations. The two-dimensional equations predict an asymmetric mixing layer that compares well with measured data with the asymmetry vanishing as the free stream velocity ratio exceeds 85 percent (Rajaratnam, 1976). Strong asymmetric mixing layers were not observed nor expected for the experiments predicted in this study, but to ensure that we fully capture the physical processes in both shear mixing, and compound shear and buoyancy mixing the full two-dimensional equations were solved.

Calculated and measured mixing half-widths, h, for a buoyancy layer are compared in Fig. 4. Snider and Andrews (1994) designed the experiment stream velocities to give a parabolic flow where the buoyancy mixing was carried in a moving frame of reference. The upper stream is cooler than the lower stream which gives a buoyancy unstable interface. Experimental results are formed from ensemble averaging a set of measurements. Further, Snider and Andrews (1994) showed that by nondimensioning experimental data, the data collapsed to a single curve in the developed mixing region. Calculated and measured results are presented for only two experiments in this study, but calculations for other tests compare equally well. Results from the spatial two-dimensional calculation (Run 5) and temporal calculation (Run 4) are compared with measured data from Test 2-68 in Fig. 4. There is a central region marked on the figure where the mixing is self-similar and the experimental and numerical results are comparable. Upstream the mixing is developing, and downstream of the marked self-similar region the channel ceiling and floor influence the mixing layer. The measured and calculated data are adjusted to a virtual origin to account for developing flow. Figure 4 shows growth rate differences between the spatial and temporal solutions at the start of the mixing layer. The difference arises from different temporal initial conditions and spatial inlet conditions. For established mixing ($x/W > 3$), the temporal and spatial calculations give

the same mixture growth rate independent of inlet or initial conditions, and both calculations compare well with measured data.

Shear Mixing Alone

A two-dimensional, steady calculation of the shear mixing layer with no temperature gradient was made. Table 1 gives the flow conditions for the three shear calculations, Run 1, Run 2, and Run 3. The width of the mixing layer is defined by the vorticity thickness $\delta_\omega = (U_1 - U_2)/(\partial u/\partial y)_{max}$. As expected for the shear layer, the calculated δ_ω grows linearly with streamwise distance except near the splitter plate. The slope of the calculated vorticity thickness is compared with measured data in Fig. 5. There is a significant spread in the measured data. However, it is evident that the calculated mixing layer thickness compares well and lies within the measured range.

Compound Buoyancy and Shear Mixing

In compound mixing both a temperature and velocity difference are applied between the upper and lower streams. The upper stream is cooler giving a buoyancy unstable interface. The governing equations are solved with turbulence constants defined from canonical shear and buoyancy mixing. Figure 6 compares measured data from Test 3-11 with the predicted mixing layer growth rate from compound shear and buoyancy calculation and from a buoyancy only calculation. Table 1 gives conditions for experimental Test 3-11. Again Test 3-11 is a typical compound mixing experiment where presented data are from ensemble averaging of measured data over the duration of the test. Both calculated and measured data are adjusted to a virtual origin. The steady compound mixing calculation and the pure buoyancy transient calculation agree well with measured data. Considering the good agreement with the pure buoyancy calculation, buoyancy appears as the dominate mixing process for the low shear values of Test 3-11 ($\Delta U = 0.6$ cm/
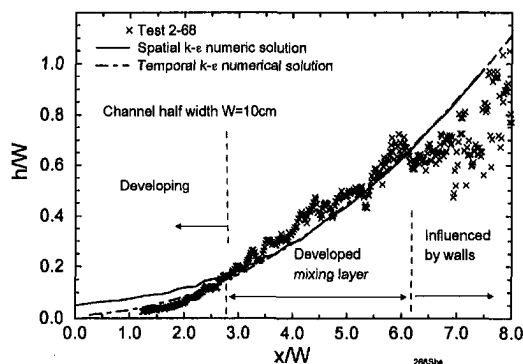
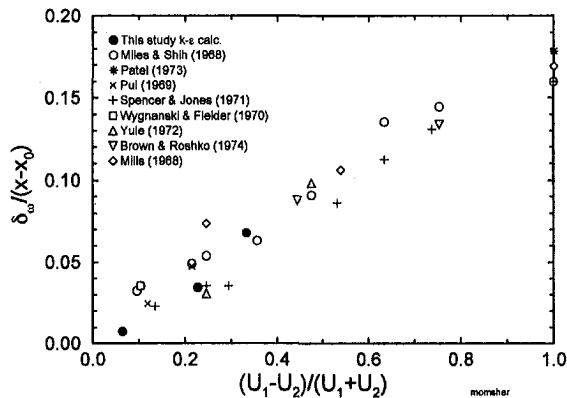Fig. 4 Calculated pure buoyancy mixing width compared with measured data

Fig. 5 Shear layer thickness

Fig. 7 (a) Compound mixing: Test 3-09, U_t = 5.2 cm/s, U_b = 4.3 cm/s Atwood No. = 0.00074, (b) Pure buoyancy mixing: Test 2-68, U_t = 4.9 cm/s, U_b = 4.8 cm/s, Atwood No. = 0.00064.

s), as might be expected from its quadratic growth. Figure 6 shows that buoyancy alone has a slightly greater mixing layer growth than for compound shear and buoyancy. We initially thought that the addition of shear to buoyancy mixing might increase the mixing width. However, the figure shows that addition of shear reduced the mixing width. Uncertainty in the experimental measured mixing width at low velocity differences was too large to verify the numerically observed effect of a reduced mixing layer from shear. However, it is important to note that the compound mixing in the experiment did not increase the mixing width, which is in agreement with the calculation.

The nonmechanistic k-ϵ model which balances energy generation and dissipation using constants from canonical shear and buoyancy studies predicts the suppression of the compound unstable shear and buoyancy mixing width. Indeed, numerical calculations beyond the limits of the experiments, with the same mean velocity but high shear rates, predict significant reduction in the mixing width from that of pure buoyancy. The k-ϵ terms represent a competition between the canonical shear and buoyancy mixing, and the ratio of buoyancy to shear turbulence production (Richardson number, $\mathrm{Ri} = -(g(\partial\rho/\partial y)/\rho(\partial u/\partial y)^2)$) near -1 suggests significant contribution by both mechanisms.

To understand better why compound shear and buoyancy do not produce a wider mixing region, we present two photographs in Figs. 7(a) and 7(b) for measured pure buoyancy mixing and compound mixing. Inspection of the photographs reveals that the cause of the reduced mixing width may be explained mechanistically as skewing and rounding of the normally vertical plumes by the velocity gradient. In a constant convective
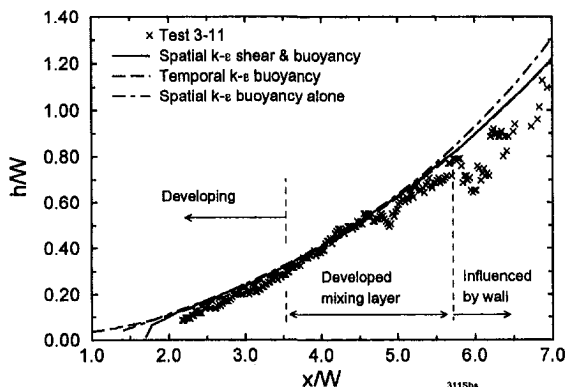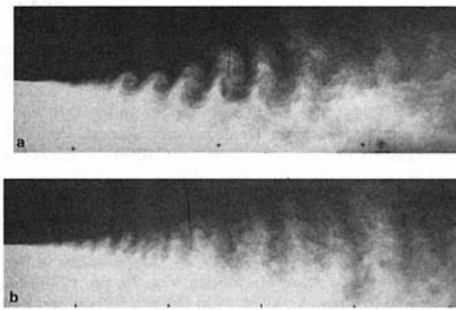
flow, buoyant plumes are fed from upper and lower streams at the same horizontal velocity and form vertical structures in a moving frame of reference as seen experimentally in Fig. 7(b) and illustrated on the left side of Fig. 8. Compound mixing of buoyancy with different stream velocities is seen experimentally in Fig. 7(a) and illustrated on the right side in Fig. 8. The buoyant heavy and light fluids interpenetrate each other at near the same rate as that in a constant moving frame of reference. However, the vertical velocity gradient stretches and thins the normally vertical plumes which in turn reduces the vertical height of the structures and the mixing width. Figure 8 illustrates the process where fast, heavy fluid (white) enters the mixing layer from the upper side, and slow, light fluid (gray) enters the mixing layer from the lower side. The high velocity stream entering the top of mixing layer pushes rising plumes of originally slow fluid, and the lower, slow stream drags descending plumes of originally fast fluid. This skews plumes and forms vortices that appear similar to shear layer mixing. The result of compound mixing is stretched, skewed plumes with rounded fronts and a reduced mixing growth rate.

Concluding Remarks

The k-ϵ model predicted well the pure buoyancy mixing layer and the compound shear and buoyancy mixing layer. A transient one-dimensional solution or a two-dimensional steady solution did equally well in predicting the pure buoyancy mixing layer. The turbulence constant $C_{\epsilon 3} = 0.91$ defined here for a buoyancy mixing layer provides good predictions for all cases.

Adding shear to an unstable buoyancy mixing layer does not increase the mixing growth rate beyond that from buoyancy alone. The measured flow structures suggest that shear skewing and stretching of vertical buoyant plumes reduces the growth of a unstable buoyancy mixing layer. The velocity difference in the available experimental data was too low to quantify differences in growth rate for buoyancy mixing width with and without shear. Further experiments with higher shear rates are required to resolve the differences.
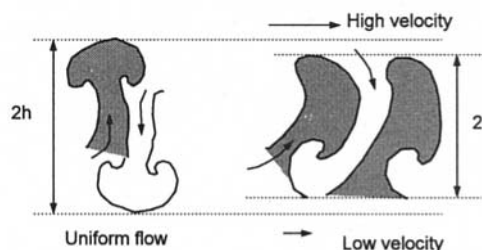

Fig. 6 Calculated combined shear and buoyancy mixing width compared with measured data

Fig. 8 Illustration of the buoyancy mixing and combined shear and buoyancy

References

Andrews, M. J., and Spalding, D. B., 1990, "A Simple Experiment to Investigate Two-Dimensional Mixing by Rayleigh-Taylor Instability," *Physics of Fluids*, Vol. 2, pp. 922–927.

Andrews, M. J., 1984, "The k-ϵ Model Applied to the Development of Rayleigh-Taylor Instability," Phoenix Demonstration Report, PDR/CFDU IC/13, Computational Fluid Mechanics Unit, Imperial College of Science and Technology, London, UK.

Bradshaw, P., Launder, B. E., and Lumley, J., 1991, "Collaborative Testing of Turbulence Models," ASME JOURNAL OF FLUIDS ENGINEERING, Vol. 113, pp. 3–4.

Browand, F. K., and Weidman, P. D., 1976, "Large Scales in the Developing Mixing Layer," *Journal of Fluid Mechanics*, Vol. 76, pp. 127–144.

Brown, G. L., and Roshko, A., 1974, "On Density Effects and Large Structure in Turbulent Mixing Layers," *Journal of Fluid Mechanics*, Vol. 64, pp. 775–816.

Chandrasekhar, S., 1961, *Hydrodynamic and Hydromagnetic Stability*, Oxford University Press.

Comte, P., Lesieur, M., Laroche, H., and Normand, X., 1989, "Numerical Simulation of Turbulent Plane Shear Layers," *Turbulent Shear Flow 6*, Springer-Verlag, Berlin, pp. 360–380.

Deardorff, J. W., 1970, "Convective Velocity and Temperature Scale for the Unstable Planetary Boundary Layer and for Rayleigh Convection," *Journal of Atmospheric Sciences*, Vol. 27, pp. 1211–1213.

Dhir, V. K., and Chang, F., 1992, "Heat Transfer Enhancement Using Tangential Injection," *ASHRAE Transactions*, BA-92-4-1.

Hanjalic, K., and Vasic, S., 1993, "Some Further Exploration of Turbulence Models for Buoyancy Driven Flows," *Turbulent Shear Flow 8*, Springer-Verlag, Berlin, pp. 319–341.

Hanjalic, K., 1994, "Achievements and Limitations in Modeling and Computation of Buoyant Turbulent Flows and Heat Transfer," *Proceedings Tenth International Heat Transfer Conference*, Brighton, UK, Vol. 1, Taylor Francis Publishing Co., pp. 1–18.

Imberger, J., and Hamblin, P. F., 1982, "Dynamics of Lakes and Cooling Ponds," *Annual Review of Fluid Mechanics*, pp. 153–187.

Koop, G. K., 1976, "Instability and Turbulence in a Stratified Shear Layer," Ph.D. thesis, University of Southern California.

Launder, B. E., Morse, A. P., Rodi, W., and Spalding, D. B., 1973, "The Prediction of Free-Stream Flows—A Comparison of the Performance of Six Turbulence Models," NASA SP 320.

Launder, B. E., 1988, "On the Computation of Convective Heat Transfer in Complex Turbulent Flows," ASME *Journal of Heat Transfer*, Vol. 110, pp. 1112–1128.

Launder, B. E., and Spalding, D. B., 1974, "The Numerical Computation of Turbulent Flows," *Computer Methods in Applied Mechanics and Engineering*, pp. 269–289.

Li, X. L., 1993, "Study of Three Dimensional Rayleigh Taylor Instabilities in Compressible Fluids Through Level Set Method and Parallel Computation," *Physics of Fluids A*, Vol. 5, pp. 1904–1913.

Linden, P. F., Redondo, J. M., and Caulfield, C. P., 1992, "Molecular Mixing in Rayleigh-Taylor Instability," *Advances in Compressible Turbulent Mixing*, W. P. Dannevik, A. C. Buckingham, and C. E. Leith, eds., pp. 95–104.

Miles, J. B., and Shih, J., 1968, "Similarity Parameter for Two-Stream Turbulent Jet-Mixing Region," *Journal AIAA*, Vol. 6, p. 1429.

Mills, R. D., 1968, "Numerical and Experimental Investigation of the Shear Layer Between Two Parallel Streams," *Journal of Fluid Mechanics*, Vol. 33, p. 591.

Patankar, S. V., 1980, *Numerical Heat Transfer and Fluid Flow*, Hemisphere Publishing Co.

Patel, R. P., 1973, "An Experimental Study of a Plane Mixing Layer," *Journal AIAA*, Vol. 11, p. 67.

Pui, N. K., 1969, "The Plane Mixing Layer Between Parallel Streams," M.A. Science thesis, University of British Columbia.

Rajaratnam, N., 1976, *Turbulent Jets*, Elsevier Science Publishing, Amsterdam, pp. 87–114.

Read, K. I., "Experimental Investigation of Turbulent Mixing by Rayleigh-Taylor Instability," *Physica 12D*, pp. 45–58, 1984.

Rodi, W., 1993, *Turbulence Models and Their Application in Hydraulics, A State of the Art Review*, Third edition, AA Balkema, Rotterdam, Brookfield.

Rodi, W., 1991, "Examples of Turbulence Model Applications," *Introduction to the Modeling of Turbulence*, vonKarmen Institute for Fluid Dynamics, Lecture Series 1991-02.

Rogers, M. M., and Moser, R. D., 1994, "Direct Simulation of a Self-Similar Turbulent Mixing Layer," *Physics of Fluids*, Vol. 6, pp. 903–923.

Sharp, D. H., 1984, "An Overview of Rayleigh-Taylor Instability," *Physica 12D*, p. 3.

Schlichting, H., 1958, *Boundary Layer Theory*, McGraw-Hill, NY, p. 489.

Spalding, D. B., 1972, "A Novel Finite-Difference Formulation for Differential Expressions Involving Both First and Second Derivatives," *International Journal for Numerical Methods Engineering*, Vol. 4, p. 551.

Spencer, B. W., and Jones, B. G., 1971, "Statistical Investigation of Pressure and Velocity Fields in the Turbulent Two-Stream Mixing Layer," *AIAA Paper* no. 71-613.

Spitz, P. B., and Haas, J., 1991, "Numerical Calibration of Rayleigh-Taylor Induced Turbulent Flows With k-ϵ Mix Model," *Proceedings of the 3rd International Workshop on the Physics of Compressible Turbulent Mixing*, Royaumont, pp. 511–521.

Snider, D. M., and Andrews, M. J., 1994a, "Rayleigh-Taylor and Shear Driven Mixing with an Unstable Thermal Stratification," *Boundary Layer and Free Shear Flows*, J. F. Donovan and J. C. Dutton, eds., ASME Fluids Summer Meeting 1994.

Taylor, G. I., 1950, "The Instability of Liquid Surfaces When Accelerated in a Direction Perpendicular to Their Planes I," *Proceedings of the Royal Society of London Series A*, Vol. CCI, pp. 192–196.

Tennekes, H., and Lumley, J. L., 1972, *A First Course in Turbulence*, MIT Press, pp. 97–102.

Vinnichenko, N. K., Pinus, N. Z., Shmeter, S. M., and Shur, G. N., 1980, *Turbulence in the Free Atmosphere*, Consultants Bureau, NY, pp. 145–164.

White, F. M., 1991, *Viscous Fluid Flow*, McGraw-Hill, Inc., pp. 482–483.

Wygnanski, I., and Fielder, H. E., 1970, "The Two-Dimensional Mixing Region," *Journal of Fluid Mechanics*, Vol. 41, p. 327.

Yang, R. J., and Aung, W., 1985, "Equations and Coefficients for Turbulence Modeling," *Natural Convection Fundamentals and Applications*, Hemisphere Publishing Co.

Yule, A. J., 1972, "Two-Dimensional Self-Preserving Turbulent Mixing Layers at Different Free Stream Velocity Ratios," *Aero. Res. Counc. R&M.*, no. 3683.

Youngs, D. L., 1991, "Three-Dimensional Numerical Simulation of Turbulent Mixing by Rayleigh-Taylor Instability," *Physics of Fluids A*, pp. 1312–1320.

Youngs, D. L., 1992, "Numerical Simulation of Turbulent Mixing by Experimental Investigation of Turbulent Mixing by Rayleigh-Taylor Instability," *Advances in Compressible Turbulent Mixing*, W. P. Dannevik, A. C. Buckingham, and C. E. Leith, eds., pp. 607–626.

Youngs, D. L., 1984, "Numerical Simulation of Turbulent Mixing by Rayleigh-Taylor Instability," *Physica 12D*, pp. 32–44.

V. E. Nakoryakov
Professor, Director.

O. N. Kashinsky
Professor, Head of Laboratory.

V. V. Randin
Senior Researcher.

L. S. Timkin
Research Scientist.

Russian Academy of Sciences,
Siberian Branch,
Institute of Thermophysics,
Lavrentyev Av., 1,
630090, Novosibirsk, Russia

Gas-Liquid Bubbly Flow in Vertical Pipes

(Data Bank Contribution)*

Gas-liquid bubbly flow was investigated in vertical pipes for different flow conditions: fully developed turbulent downward flow in a 42.3 mm diameter pipe and upward flow in a 14.8 mm diameter pipe with liquid of elevated viscosity. Wall shear stress, local void fraction, and liquid velocity profiles, shear stress, and velocity fluctuations were measured using an electrodiffusional method. Results obtained demonstrate the existence of "universal" near-wall velocity distribution in a downward bubbly flow. The reduction of turbulent fluctuations is observed in downward flow as compared to a single-phase turbulent flow. The development of bubble-induced liquid velocity fluctuations in a "laminar" bubbly flow was studied.

Introduction

Gas-liquid two-phase flow in a pipe has been the subject of a number of investigations in the last years. The structure of the flow was investigated mainly in vertical pipes due to the axial symmetry of the flow. Much attention has been paid to the study of upward gas-liquid flow. On the contrary, downward gas-liquid flow in vertical pipes has been explored less intensively. One of the first studies was made by Oshinovo and Charles (1974). It was demonstrated that in a bubbly flow regime gas bubbles were concentrated in the central part of the pipe. Detailed studies of void fraction and velocity profiles were performed by Ganchev and Peresadko (1985) and Wang et al. (1987). Gorelik et al. (1987) and Nakoryakov et al. (1986) have performed measurements of wall shear stress, void fraction, and liquid velocity in a 15 mm diameter pipe. They had observed the reduction of wall shear stress and velocity fluctuations at pipe Reynolds numbers corresponding to turbulent single-phase flow. No detailed measurements of the flow structure in the wall region have been performed for fully developed turbulent flow conditions.

Almost all the measurements in an upward gas-liquid flow were made for turbulent flow. This made it difficult to extract the effect of bubble-induced turbulence in the total two-phase turbulence. For this reason, experiments in gas-liquid flows for subcritical pipe Reynolds numbers are greatly desirable. A few attempts to study laminar bubbly flow were made theoretically by Achard and Cartellier (1985) and Antal et al. (1991) and experimentally by Valukina et al. (1979) and Kashinsky et al. (1993). Further investigations of these flow conditions are needed.

Measurements of fully developed turbulent downward bubbly flow and laminar upward bubbly flow in vertical pipes are presented in this paper. Experiments were performed using the same measuring techniques and present complete sets of data on the flow structure.

Experimental

Experimental Setup. Measurements of downward bubbly flow were performed on the experimental installation shown in

---

* Data have been deposited to the JFE Data Bank. To access the file for this paper, see instructions on p. 427 of this issue.

Contributed by the Fluids Engineering Division for publication in the JOURNAL OF FLUIDS ENGINEERING. Manuscript received by the Fluids Engineering Division August 26, 1994; revised manuscript received August 23, 1995. Associate Technical Editor: O. C. Jones.
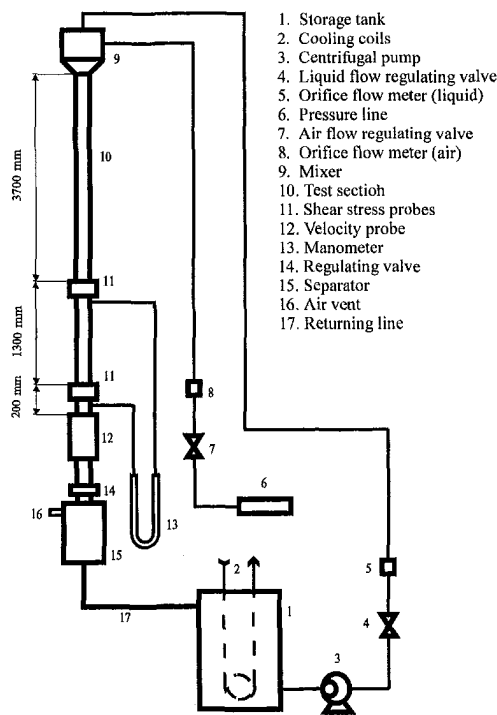
Fig. 1. It was a closed liquid flow loop. Liquid was pumped by a centrifugal pump through regulating valves and orifice meters to the top of the test section. The test section was a 42.3 mm i.d. pipe 5 m long. Air from a pressure line was supplied through regulating valves and orifice meter to the air injector in which gas-liquid flow was produced. Cocurrent gas-liquid bubbly flow moved downwards in the test section. Then it was separated by the separator, and the liquid returned to the storage tank. The liquid temperature was maintained at 25 ± 0.2°C by a cooling coil and an automatic regulating system.

Experiments with laminar bubbly flow were performed on a similar flow loop. The test section was a 14.8 mm i.d. vertical pipe, 6.5 m long. Upward bubbly flow was realized in the test section.

To produce gas-liquid flow special mixers were used. The mixer used for downward flow studies had the following structure. Air was supplied to the liquid through 64 holes of diameter 0.15 mm drilled in the pipe wall. Air bubbles were injected into an annular slot. The liquid flow rate through this slot remained constant to maintain constant mean bubble size for various total liquid flow rates. To change the bubble size the flow rate through the slot was changed. The remainder of the liquid was supplied through the central tube. Air injectors used for upward bubbly flow studies will be described later.

Measuring Technique. The main technique for flow measurements was an electrodiffusional method (Nakoryakov et al., 1984, 1986). It is based on measurements of the rate of mass transfer from a microelectrode to the liquid to study liquid flow parameters. The test liquid was the solution of 0.005 N potassium ferri- and ferrocyanide and 0.25 M sodium hydroxide in distilled water. Wall shear stress measurements were made by electrodiffusional probes embedded into the wall. The sensing element of the probe was a platinum foil with the size of 30 μm in the flow direction and 0.2 mm in the transverse direction. The probes were polished flush to the wall. Two measuring units of shear stress probes were mounted in the test section (Fig. 1). Each of them contained 8 probes distributed uniformly across the pipe circumference to check the flow axial symmetry. Liquid velocity and local void fraction measurements were made by an electrodiffusional "blunt-nose" probe (Nakoryakov et al., 1984). It was a 20 μm platinum wire welded into the glass capillary. The total diameter of the probe at the measuring tip was 50 μm. The probe could be moved in transverse

1. Storage tank
2. Cooling coils
3. Centrifugal pump
4. Liquid flow regulating valve
5. Orifice flow meter (liquid)
6. Pressure line
7. Air flow regulating valve
8. Orifice flow meter (air)
9. Mixer
10. Test section
11. Shear stress probes
12. Velocity probe
13. Manometer
14. Regulating valve
15. Separator
16. Air vent
17. Returning line

Fig. 1 Experimental installation

direction by a traversing mechanism. The distance from the wall was measured to the accuracy of 0.02 mm.

Both velocity and wall shear stress probes were operating in diffusion-controlled regime. They were supplied by a d.c. voltage of about 0.5 V. The probe current was amplified and measured using a 10 bit A-D converter. All measuring quantities were averaged numerically for 50–100 s.

Pressure drop measurements were made in the test section. Two pressure taps of 0.5 mm diameter were separated by 1.3 m distance. The pressure drop was measured by a liquid U-manometer.

Pressure drops from liquid and gas orifice meters were measured by calibrated silicon diaphragm differential manometers with the accuracy of 0.5 percent.

Wall shear stress was calculated from the probe current I using the relation:

$$\tau_w = AI^n, \qquad (1)$$

where coefficient A and the exponent n were obtained from the probe calibration. The calibration was made in a single-phase fully developed turbulent flow in a pipe. Wall shear stress values were calculated from the liquid flow rate using the Blasius equation (Schlichting, 1969). The values of the exponent n for the probes varied in a range from 3 to 3.5.

Similar procedure was used for measuring liquid velocity. The velocity probe calibration was made in a single-phase turbulent flow at the pipe axis. The following relation between the probe current and liquid velocity was used:

$$I = a + bu^{1/2}, \qquad (2)$$

where coefficients a, b were obtained from the calibration.

Calibrations were made for a wide range of liquid flow rates just before the two-phase experiment. Just after two-phase experiment all the probes were recalibrated by the same procedure. Results of experiments were considered reliable if the difference in probe currents between these calibrations did not exceed 1 percent.

Uncertainty Analysis. The uncertainty was estimated using rms method (Kline, 1985). Liquid and gas orifice meters were calibrated against standard devices that established the precision uncertainty interval for the liquid and gas flow rates of 1 and 2.5 percent, respectively. Measuring equipment used for probe current measurements provided the accuracy of current of at least 0.5 percent. This establishes a precision uncertainty interval for the wall shear stress of 7 percent and velocity measurements of 4 percent at a probability level of 0.95 and negligible bias since we have calibrated the probes.

Local void fraction was determined from the measurements of the time of probe residence in the gas phase. The random uncertainty of time interval measurements was less than 0.1 percent so it could be neglected. The bias error of void fraction measurements was caused by the process of the probe interaction with the gas bubbles. To check the accuracy of local void fraction measurements, integrated values of local void fraction were compared to the liquid holdup φ obtained from pressure drop and wall shear stress measurements. The results of this comparison will be presented in the next sections. The estimated bias error of φ measurements was 20 percent (absolute error). This value was the same for all liquid velocities. Therefore, it can be assumed that the accuracy of local void fraction was the same independently on the position of the measuring point. So the bias uncertainty of local void fraction was also 20 percent.

The error of liquid fluctuations measurements consisted of the random error and bias error. The estimate of the random error was made from the scatter of measurements; it was about 10 percent. The bias error resulted from the effect of transverse velocity fluctuations in the probe readings. The estimate of the bias error for the value of turbulence intensity measured in the experiments was 12 percent. So the total uncertainty of rms liquid fluctuation measurements was 16 percent. Similar considerations gave the uncertainty of τ' measurements of 15 percent.

Downward Bubbly Flow

Wall Shear Stress. Experiments in downward bubbly flow were performed in a 42.3 mm diameter pipe. Superficial liquid velocity varied from 0.5 to 1 m/s. The axial symmetry of the flow was tested by simultaneous recording of 8 wall shear stress

---

Nomenclature

A = calibration coefficient, Eq. (1)
B = coefficient, Eq. (5)
I = probe current, A
R = pipe radius, mm
U_b = terminal speed of bubbles, m/s
V_l, V_g = superficial liquid and gas velocities, m/s
V_m = integrated cross-sectional liquid velocity, m/s
a, b = calibration coefficients, Eq. (2)

d_b = mean bubble diameter, mm
n = exponent, Eq. (1)
u = liquid velocity, m/s
u_τ = friction velocity, $(\tau_w/\rho)^{1/2}$, m/s
y = distance from the wall, mm
α = local void fraction
α_m = mean cross-sectional void fraction
β = gas flow rate ratio $V_g/(V_l + V_g)$
ϵ = calculated holdup, Eq. (5)
φ = holdup

ν = liquid viscosity, m²/s
τ_0 = single-phase wall shear stress, N/m²
τ_w = two-phase wall shear stress, N/m²
τ_c = calculated wall shear stress, Eq. (4), N/m²

Subscripts

$'$ = rms fluctuations

Table 1   Wall shear stress in a 42.3 mm pipe. (Uncertainty of data: $\tau_w \pm 7\%$, $\tau'_w \pm 15$ percent)

V_l	β	d_b	τ_w	τ_c	τ'_w/τ_w
0.50	0.000		0.857	0.830	0.388
0.50	0.037	0.80	1.000	0.993	0.291
0.50	0.038	1.70	1.303	1.070	0.311
0.50	0.075	1.50	1.548	1.290	0.273
0.50	0.077	0.90	1.353	1.210	0.231
0.50	0.155	1.50	2.153	1.890	0.247
0.50	0.156	0.96	1.978	1.710	0.226
0.75	0.000		1.733	1.690	0.392
0.75	0.025	0.80	1.790	1.860	0.369
0.75	0.026	1.70	1.935	1.950	0.359
0.75	0.038	1.70	2.130	2.080	0.365
0.75	0.052	0.90	2.090	2.100	0.367
0.75	0.052	1.50	2.245	2.200	0.353
0.75	0.109	1.50	2.835	2.840	0.333
0.75	0.112	0.96	2.830	2.670	0.342
1.00	0.000		2.880	2.790	0.390
1.00	0.019	0.80	2.998	2.990	0.380
1.00	0.019	1.70	2.955	3.070	0.375
1.00	0.039	0.90	3.098	3.240	0.387
1.00	0.039	1.70	3.295	3.360	0.379
1.00	0.040	1.50	3.243	3.350	0.362
1.00	0.084	0.96	3.835	3.830	0.353
1.00	0.084	1.50	3.968	4.030	0.352

Fig. 2   Liquid velocity profiles in a 42.3 mm pipe. (Uncertainty of data ± 4 percent)

Liquid Velocity Profiles.   Liquid velocity profiles measured in downward bubbly flow plotted in "universal" semilog coordinates are presented in Fig. 2. Here the friction velocity $u_\tau = (\tau_w/\rho)^{1/2}$, where τ_w is measured two-phase value of wall shear stress, ρ is liquid density. Solid lines represent the single-phase "law-of-the-wall" (Schlichting, 1969). A good agreement with these curves is seen up to the values of yu_τ/ν about 200. Velocity points closest to the wall correlate with the single-phase linear velocity distribution in the viscous sublayer. As β increases the deformation of the velocity profile is observed from a single-phase one ($\beta = 0$) to flattened profiles at β higher than 0.05.

To check the accuracy of liquid velocity measurements a standard procedure was used. Average liquid velocity V_m was calculated from measured liquid velocity and void fraction profiles using the relation:

$$V_m = \frac{2}{R^2} \int_0^R ru(1 - \alpha)dr. \tag{6}$$

This value was compared to the liquid flow rate. Integrated cross-sectional values of liquid velocity are presented in Table 2 as V_m. Their deviation from the superficial liquid velocity V_l did not exceed 5 percent.

Mean cross-sectional void fractions α_m obtained by integration of α over the pipe cross section are presented in Table 2. For comparison, the values of holdup φ calculated from pressure drop and wall shear stress measurements are also presented in the Table. The discrepancy between values of α_m and φ obtained by the two different methods does not exceed 20 percent.

Wall Shear Stress and Velocity Fluctuations.   Fluctuational characteristics of wall shear stress are also presented in Table 1. Here τ'_w/τ_w is relative intensity of wall shear stress fluctuations, where τ'_w is r.m.s. fluctuation value. Measurements in single-phase flow give τ'_w/τ_w of about 0.38. In downward

probes. It was shown that in all regimes the maximum difference of the probe readings did not exceed 10 percent. Comparison of the readings of both measuring units (shear stress probes 11 on Fig. 1) was made to check the flow stabilization along the pipe. Mean wall shear stress values for both units separated by 1.3 m differed no more than by 5 percent. Therefore, the downward flow may be considered as stabilized and axisymmetrical.

Results of wall shear stress measurements for different liquid and gas flow rates are presented in Table 1. Here, τ_w is the mean value of wall shear stress obtained by averaging the readings of 8 probes in the same regime. Gas flow rate ratio β is calculated as:

$$\beta = V_g/(V_l + V_g), \tag{3}$$

where V_g is taken at the test section pressure. The static pressure in the measuring unit 12 (Fig. 1) was maintained at 1.25 atm by diaphragming the outlet.

Single-phase wall shear stress values τ_0 taken at the same superficial liquid velocity V_l are also presented in Table 1 (regimes with $\beta = 0$). It can be seen that in all cases two-phase wall shear stress values are higher than single-phase values. The ratio τ_w/τ_0 for prescribed V_l and β depends on the mean bubble size d_b. When d_b increases this ratio becomes higher.
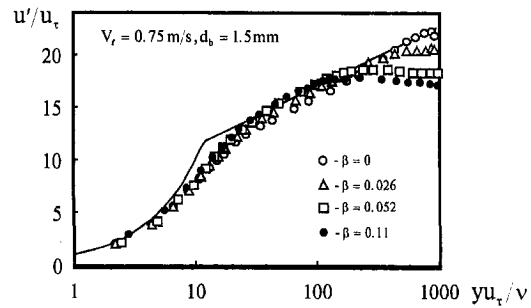
Clark and Flemmer (1985) suggested the technique for wall shear stress prediction in upward and downward bubbly flow. The model based on the generalization of "mixing length" hypothesis for two-phase flows gives the following relation for wall shear stress:

$$\tau_c = \tau_0(1 - \epsilon)^{-1}[(1 - \epsilon)^{-1} + BU_b\epsilon/V_l], \tag{4}$$

where the coefficient $B = 21.81$ for downflow, as recommended in Clark and Flemmer (1985), and

$$\epsilon = \beta/(1 + U_b(1 - \beta)/V_l), \tag{5}$$

the terminal speed of bubbles U_b was calculated by the formula presented in Wallis (1974). Calculations of wall shear stress by the above formula for experimental flow regimes are also presented in Table 1 as τ_c. The agreement of measured and calculated wall shear stress values is reasonably good; the maximum discrepancy does not exceed 15 percent.

Table 2   Average flow parameters in a 42.3 mm pipe. (Uncertainty of data ± 20 percent)

V_l	β	d_b	V_m	α_m	φ
0.75	0.025	0.80	0.761	0.0289	0.0249
0.75	0.026	1.73	0.752	0.0293	0.0283
0.75	0.038	1.69	0.768	0.0425	0.0455
0.75	0.052	0.92	0.745	0.0643	0.0541
0.75	0.052	1.46	0.780	0.0574	0.0576
0.75	0.109	1.47	0.787	0.1340	0.1164
0.75	0.112	0.96	0.791	0.1300	0.1155
1.00	0.019	0.80	0.986	0.0221	0.0179
1.00	0.019	1.73	0.996	0.0235	0.0205
1.00	0.039	1.71	1.000	0.0456	0.0403
1.00	0.040	1.46	1.020	0.0478	0.0394
1.00	0.084	1.47	1.010	0.1080	0.0855
1.00	0.084	0.96	0.979	0.1040	0.0829
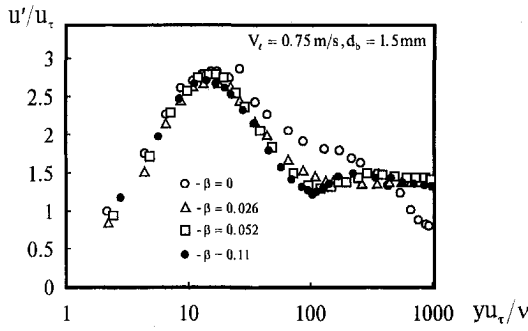
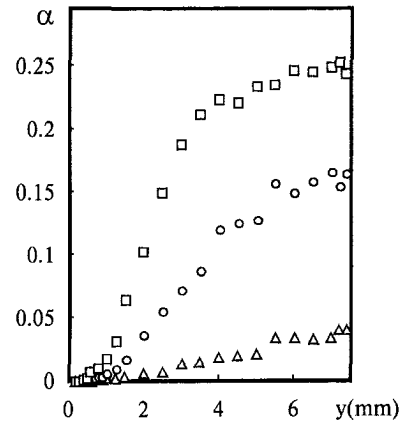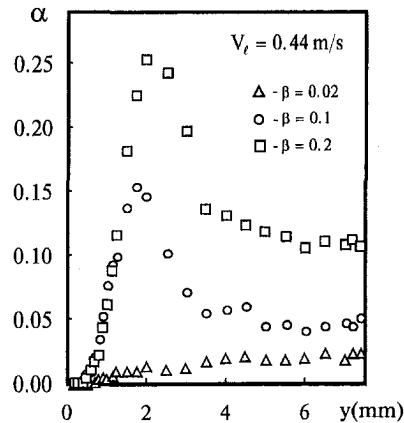Fig. 3 Liquid velocity fluctuations in a 42.3 mm pipe. (Uncertainty of data ± 16 percent)

Fig. 4(a)

Fig. 4(b)

Fig. 4 Void fraction profiles in a 14.8 mm pipe; (a) N-injector, (b) P-injector. (Uncertainty of data ± 20 percent)

gas-liquid flow values of τ'_w/τ_w become less and decrease with β increase. The smallest value of τ'_w/τ_w observed in the experiments is 0.23. Similar effect was observed in Wang et al. (1987) and Gorelik et al. (1987) for 15 mm diameter pipe where the intensity of fluctuations decrease was up to 5 times compared to a single-phase turbulent flow.

Liquid velocity fluctuations are presented in Fig. 3. In the central part of the pipe, the intensity of fluctuations is higher than in a single-phase flow, this increase becomes more pronounced with higher void fraction. Close to the wall values of u'/u_τ in gas-liquid flow become significantly less than in single-phase flow. This is well demonstrated for yu_τ/ν from 30 to 200. It is interesting to note that the reduction of velocity fluctuations occurs in the region of the flow that is free of bubbles ($yu_\tau/\nu < 50$). Close to the wall the values of u'/u_τ fall on the same curve independently of gas flow rate ratio.

Upward "Laminar" Bubbly Flow

Experimental Conditions. Experiments were performed in a 14.8 mm i.d. vertical pipe. To produce laminar single-phase flow at moderate liquid velocities a liquid of elevated viscosity was used in the experiments (glycerine was added to the solution). The value of kinematic liquid viscosity was maintained at $(3.5 \pm 0.1) \cdot 10^{-6}$ m²/s; the liquid density was 1127 kg/m³. The liquid temperature was 20 ± 0.2°C. Liquid flow rate was measured by rotameters calibrated with the test liquid at operating temperature. The liquid viscosity was kept constant and measured before each set of experiments.

Two types of gas-liquid mixers were used. The mixer body was a 90 mm i.d. cylindrical chamber 120 mm long. At the center of this chamber a plastic cylinder of 32 mm o.d. was placed. Gas was injected through holes drilled in the side surface of this cylinder. The first mixer (P injector) had 18 holes of 0.15 mm diameter drilled uniformly over the cylinder circumference. The second one (N injector) had 6 hypodermic needles with the inner diameter of 0.4 mm inserted into the wall flush

Table 3 Average flow parameters in a 14.8 mm pipe. (Uncertainty of data ± 20 percent)

V_l	Injector	β	d_b	V_m	α_m	φ
0.207	P	0.02	2.1	0.202	0.008	0.010
0.207	P	0.10	2.2	0.206	0.050	0.051
0.207	P	0.20	2.1	0.205	0.122	0.118
0.440	P	0.02	1.9	0.431	0.011	0.013
0.440	P	0.10	2.0	0.435	0.069	0.067
0.440	P	0.20	2.4	0.418	0.128	0.127
0.440	N	0.02	2.0	0.440	0.010	0.011
0.440	N	0.10	3.7	0.444	0.055	0.053
0.440	N	0.20	3.6	0.433	0.118	0.113

with it. Both injectors produced different structures of gas-liquid flow.

Experiments were made at two values of superficial liquid velocity 0.207 and 0.44 m/s. This corresponded to pipe Reynolds numbers (based on liquid parameters) of 875 and 1860, so the single-phase flow was laminar for both V_l.

Velocity and Void Fraction Profiles. The profiles were measured for liquid and gas flow rates listed in Table 3. Mean bubble diameters d_b measured in the experiments are also given. The P injector produced quite uniform bubbles of the diameter 2.2–2.4 mm. Bubbles produced by N injector had much higher diameter at $\beta \geq 0.1$, so the effect of bubble diameter on the flow could be studied. Integrated liquid velocity and void fraction are also presented in the Table 3 to check the accuracy of liquid velocity measurements. Also the results of gas holdup measurements from pressure drop and wall shear stress are given. The discrepancy between values of α_m and φ obtained by the two different methods does not exceed 10 percent.

Measured values of local void fraction α approached zero value near the wall. The closest to the wall measuring point was $y = 0.1$ mm. The value of α at the wall was zero, this could be concluded from the continuity of wall shear stress probe signal. Therefore, at all flow conditions there was a layer of liquid at the wall.

Void fraction profiles are shown in Fig. 4 for the superficial liquid velocity $V_l = 0.44$ m/s and different injectors. All the profiles for $\beta = 0.02$ are center-peaked; no void fraction increase near the wall is observed. At higher β for P injector wall-peaked profiles are developed. Quite different behaviour
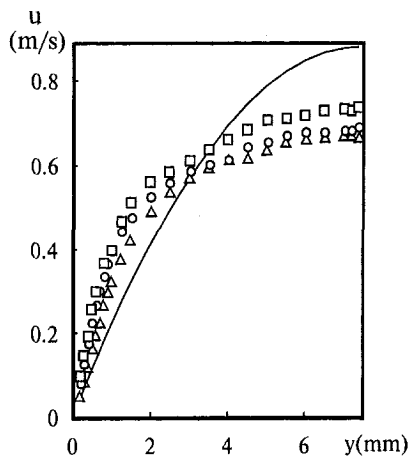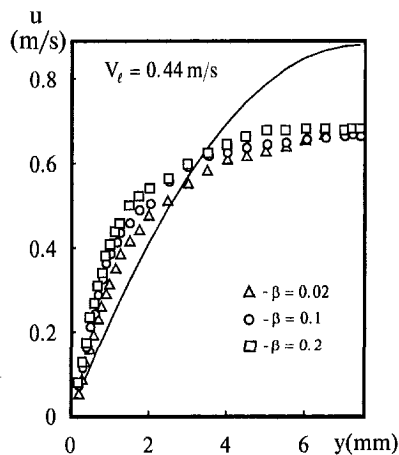
Fig. 5(a)

Fig. 5(b)

Fig. 5 Liquid velocity profiles in a 14.8 mm pipe; (a) N-injector, (b) P-injector. (Uncertainty of data ± 4 percent)

part of the pipe even for $\beta = 0.02$ as compared to higher β values. For $V_l = 0.207$ m/s velocity fluctuations in the pipe center practically do not depend on β values. However, this dependence becomes evident for center-peaked void profiles (N injector). Almost all u' profiles have peak near the wall. This can be easily understood for void profiles having maximum near the wall, but this profile is hardly to be expected, for example, for $\beta = 0.02$, N injector.

Therefore, generally no direct correlation exists between local void fraction and values of liquid velocity fluctuations. The development of fluctuations should be regarded as a collective effect even in laminar bubbly flow. Possibly, this development demonstrates the generation of bubble-induced turbulence at subcritical pipe Reynolds numbers whose distribution is qualitatively similar to that of wall-induced turbulence.

Discussion

Analysis of the void distributions obtained confirms the suggestion of Zun (1980) that the main reason for the bubble migration in the flow is the lateral force acting on the rising bubble in the flow with the velocity gradient. This force has opposite signs in upflow and downflow. Therefore, center-peaked profiles were obtained in downflow while in upflow wall-peaked profiles dominated. The character of void distribution does not depend too much on the pipe diameter and the regime of the flow (laminar or turbulent). In upflow the "wall force" exists which pushes the bubbles from the wall. One
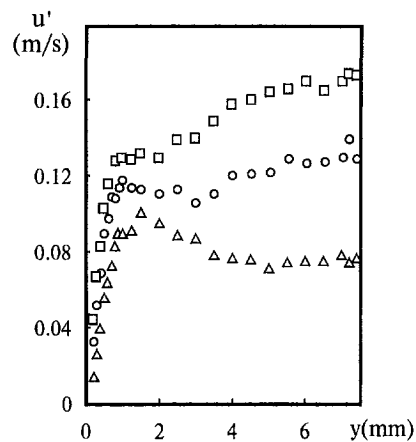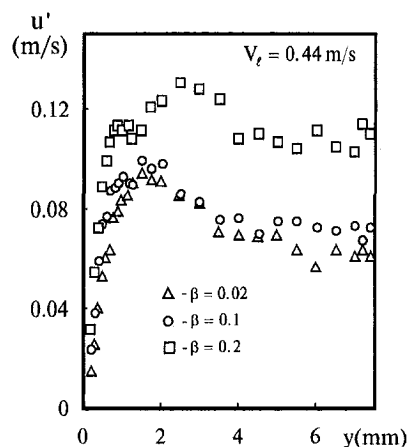

Fig. 6(a)

Fig. 6(b)

Fig. 6 Liquid velocity fluctuations in a 14.8 mm pipe; (a) N-injector, (b) P-injector. (Uncertainty of data ± 16 percent)

is observed for N injector. In this case bubbles have higher mean diameter (Table 3). The resulting void profiles have no peak near the wall. Comparison of data demonstrates that quite different void distributions may exist in the same flow conditions (defined by V_l and β) depending on the mean bubble size. This effect was first demonstrated by direct measurements in Valukina et al. (1979). Also the effect of bubble size on upward turbulent bubbly flow was studied by Zun (1980).

Liquid velocity profiles are shown in the Fig. 5. All the profiles are deformed as compared to a single-phase parabolic profile. A gradual development of velocity distributions with increasing β is observed. These results are quite similar to those reported in Kashinsky et al. (1993) for the liquid with the viscosity of $10 \cdot 10^{-6}$ m²/s. Experiments with water as the test liquid (Valukina et al., 1979) demonstrated almost uniform velocity distribution even at smallest gas flow rates $\beta = 0.01$. It is interesting to note in the present experiments that the profile with $\beta = 0.02$ for P injector is less deformed for $V_l = 0.207$ m/s than for 0.44 m/s. This may be caused by the approaching to the critical pipe Reynolds number. No significant effect of bubble injector on the shape of the velocity profiles was observed.

Liquid Velocity Fluctuations. Rms values of liquid velocity fluctuations u' measured in laminar bubbly flow are presented in Fig. 6. A rapid growth of fluctuations is observed near the wall even in the region where local void fraction is close to zero (N injector). Besides, high u' values exist in the central

possible explanation for this force is the "lubrication force" suggested by Antal et al. (1991). The combined action of both forces produces the void distribution with the maximum at some distance from the wall.

The strong effect of bubble size on void profiles in upflow (Fig. 4) may be explained as follows. Bubbles produced by P injector were almost spherical while those produced by N-injector were nonspherical. Therefore, their trajectory should be different even in the stagnant liquid. Spherical bubbles travel along the straight line while nonspherical bubbles go along the spiral line. When the bubbles are in the pipe flow this difference in their behaviour remains. In the given flow conditions the amplitude of large bubble oscillations in the transverse direction was enough to eliminate wall-peaked profiles.

Generally, the bubble size produces effect on the flow parameters even if the bubbles are spherical. The momentum exchange between liquid and gas depends on bubble diameter and its relative velocity. The relative velocity of bubbles increases with the increase of bubble size. So the momentum exchange increases strongly with the increase of bubble diameter. The effect of bubble size on flow parameters was observed both in upflow and downflow (Gorelik et al., 1987, Valukina et al., 1979).

Nonuniform void distribution of void fraction over the pipe section produces the conditions in the flow similar to combined thermal convection. This results in the redistribution of shear stress over the radius and in the change of other flow parameters. The effect of local slip velocity on the intensity of liquid velocity fluctuations was observed in the downflow. In this case the introduction of the gas phase in the liquid flow decreased the intensity of both wall shear stress and liquid velocity fluctuations. Experiments in the upflow were made in at subcritical pipe Reynolds numbers when the single-phase flow for the same liquid flow rate was laminar. In this case the addition of gas phase resulted in the production of bubble-driven liquid fluctuations.

Conclusions

The following main conclusions can be made from the experiments described:

- Measured wall shear stress values in a downward turbulent bubbly flow are higher than in a single-phase flow with the same superficial liquid velocity. A good agreement is found with the prediction of Clark and Flemmer (1985).
- The single-phase "law-of-the-wall" is valid for near-wall liquid velocity distribution in a downward bubbly flow up to the dimensionless distance from the wall of 200.
- Reduction of wall shear stress fluctuations and those of liquid velocity close to a wall is observed in downward bubbly flow.

- New experimental data on upward bubbly flow with subcritical liquid Reynolds numbers are presented. Both wall-peaked and center-peaked void profiles are shown to exist for the same liquid and gas flow rates depending on the type of gas-liquid mixer and, hence, on the mean bubble diameter.
- A high increase of liquid velocity fluctuations is observed in upward laminar bubbly flow at low gas flow rate ratios.

Data Bank Contribution

The data files for upward laminar bubbly flow provided on a disk contain information on radial profiles of local void fraction and on radial profiles of the Mean and rms of the axial component of the liquid velocity measured for different gas and liquid flow rates. Data files are presented in ASCII format. Data in the files are space separated.

References

Achard, J. L., and Cartellier, A., 1985, "Local Characteristics of Upward Laminar Bubbly Flows," *Physico-Chemical Hydrodynamics*, Vol. 6, No. 5/6, pp. 841–852.

Antal, S. P., Lahey, R. T., and Flaherty, J. E., 1991, "Analysis of Phase Distribution in Fully Developed Laminar Bubbly Two-Phase Flows," *International Journal of Multiphase Flow*, Vol. 17, No. 5, pp. 635–652.

Clark, N. N., and Flemmer, R. L. C., 1985, "Two-Phase Pressure Loss in Terms of Mixing Length Theory," *Industrial and Engineering Chemistry Fundamentals*, Vol. 24, No. 4, pp. 412–423.

Ganchev, B. G., and Peresadko, V. G., 1985, "Hydrodynamics and Heat Transfer Processes in Descending Bubble Flows," *Journal of Engineering Physics*, Vol. 49, No. 2, pp. 181–189.

Gorelik, R. S., Kashinsky, O. N., and Nakoryakov, V. E., 1987, "Study of Downward Bubbly Flow in a Vertical Pipe," *Journal of Applied Mechanics and Technical Physics*, No. 1, pp. 69–73.

Kashinsky, O. N., Timkin, L. S., and Cartellier, A., 1993, "Experimental Study of Laminar Bubbly Flow in a Vertical Pipe," *Experiments in Fluids*, Vol. 15, No. 4/5, pp. 308–314.

Kline, S. J., 1985, "The Purposes of Uncertainty Analysis," ASME JOURNAL OF FLUIDS ENGINEERING, Vol. 107, pp. 153–160.

Nakoryakov, V. E., Kashinsky, O. N., and Kozmenko, B. K., 1984, "Electrochemical Method for Measuring Turbulent Characteristics of Gas-Liquid Flows," *Measuring Techniques in Gas-Liquid Two-Phase Flows*, J. M. Delhaye and G. Cognet, eds., Springer, pp. 695–721.

Nakoryakov, V. E., Burdukov, A. P., Kashinsky, O. N., and Geshev, P. I., 1986, "Electrodiffusional Method for Studying Local Structure of Turbulent Flows," Novosibirsk, Institute of Thermophysics.

Oshinovo, T., and Charles, M. E., 1974, "Vertical Two-Phase Flow. Holdup and Pressure Drop," *Canadian Journal of Chemical Engineering*, No. 52, pp. 438–448.

Schlichting, G., 1969, "Boundary Layer Theory," McGraw Hill.

Valukina, N. V., Kozmenko, B. K., and Kashinsky, O. N., 1979, "Characteristics of a Flow of Monodisperse Gas-Liquid Mixture in a Vertical Pipe," *Journal of Engineering Physics*, Vol. 36, No. 4, pp. 695–699.

Wang, S. K., Lee, S. J., Jones, O. C., and Lahey, R. T., 1987, "3-D Turbulence Structure and Phase Distribution Measurements in Bubbly Two-Phase Flows," *International Journal of Multiphase Flow*, Vol. 13, No. 3, pp. 327–343.

Wallis, G. B., 1974, "The Terminal Speed of Drops and Bubbles in an Infinite Medium," *International Journal of Multiphase Flow*, Vol. 1, pp. 491–511.

Zun, I., 1980, "The Transverse Migration of Bubbles Influenced by Walls in Vertical Bubbly Flow," *International Journal of Multiphase Flow*, Vol. 6, No. 6, pp. 583–588.

Application of Chaos Theory in Identification of Two-Phase Flow Patterns and Transitions in a Small, Horizontal, Rectangular Channel[1]

Y. Cai
Mechanical Engineer.

M. W. Wambsganss
Senior Mechanical Engineer.

J. A. Jendrzejczyk
Mechanical Engineer.

Energy Technology Division,
Argonne National Laboratory,
Argonne, IL 60439

Various measurement tools that are used in chaos theory were applied to analyze two-phase pressure signals with the objective of identifying and interpreting flow pattern transitions for two-phase flows in a small, horizontal rectangular channel. These measurement tools included power spectral density function, autocorrelation function, pseudo-phase-plane trajectory, Lyapunov exponents, and fractal dimensions. It was demonstrated that the randomlike pressure fluctuations characteristic of two-phase flow in small rectangular channels are chaotic, and governed by a high-order deterministic system. The correlation dimension is potentially a new approach for identifying certain two-phase flow patterns and transitions.

1 Introduction

This study presents an application of chaos theory in identifying two-phase flow patterns and transitions in a small, horizontal, rectangular channel. The data analyzed in this study are from previous experiments (Wambsganss et al., 1991, 1992, 1994). In the experiments, horizontal two-phase flow was studied in a rectangular channel with a small cross-sectional area (19.05 × 3.18 mm). Adiabatic flows of air/water mixtures were tested over a large mass flux range (50–2000 kg/m²s). The full quality covered the experimentally achievable range. The two-phase flow patterns and transitions had been identified by dynamic pressure measurements, together with visual observations and photographic data; flow pattern maps were also developed (Wambsganss et al., 1992, 1994).

Usually, the flow pattern maps of two-phase flows are based on visual identification of phase distribution (Clarke and Blundell, 1989; Brauner and Maron, 1992; Galbiati and Andreini, 1992; Koizumi, 1992; Hibiki et al., 1992). Although identification of visual flow patterns may be adequate for some cases, in many situations these methods are not applicable or are too subjective. Several other methods have been developed to more objectively identify and interpret flow patterns and transitions of two-phase flow, e.g., pressure/time signals (Weisman et al., 1979), root mean square (RMS) of pressure/time series and friction pressure gradients (Wambsganss et al., 1991, 1992, 1994), rescaled range (R/S) analysis (Saether et al., 1990), the power spectral density function (PSD), and probability density function (PDF) (Hubbard and Dukler, 1966; Jones and Zuber, 1975; Matsui, 1984 and 1986; Tutu, 1982 and 1984; Vince and Lahey, 1982). These studies have contributed to our understanding of flow patterns and transitions of two-phase flows, but there is no accepted method for objectively distinguishing flow patterns.

The purpose of this study is to apply chaos theory to experimental data on dynamic pressure-to-time signals from two-phase flows in an attempt to identify and interpret flow pattern transitions. This new approach may present a promising way to identify flow patterns.
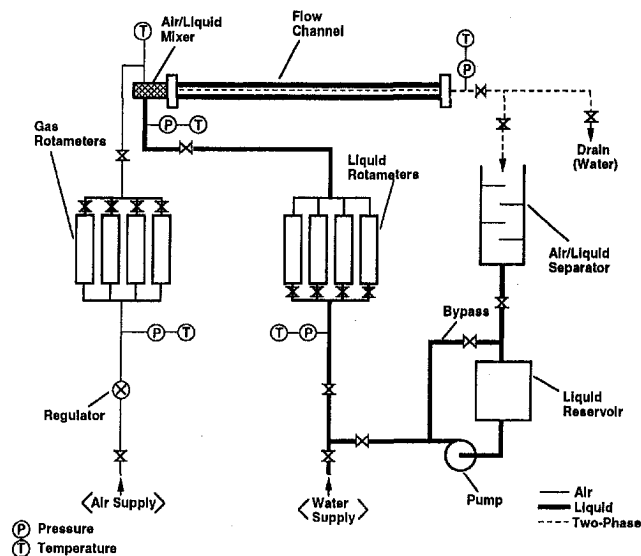
Chaotic oscillations mark the emergence of randomlike motions from completely deterministic systems. Such motions had been known in fluid mechanics, but they have only recently been observed in low-order mechanical and electrical systems. The recognition that chaotic vibrations can arise in low-order, nonlinear deterministic systems raises the hope of understanding the source of randomlike noise. The new discoveries in nonlinear dynamics bring with them new concepts and tools for detecting chaotic vibrations in physical systems and for quantifying this "deterministic noise" with new measures such as fractal dimensions and Lyapunov exponents (Moon, 1987).

Two-phase flows and their nonlinear dynamics are far more complicated than other physical systems. Only a few reports on the application of chaos theory can be found in the literature (Lahey, 1991). Some theoretical developments and "computer experiments" in chaotic dynamics of multiphase flows have been investigated recently (Dorning, 1989a, 1989b; Lahey et al., 1989; Rizwan-uddin and Dorning, 1986; Rizwan-uddin et al., 1988; Rizwan-uddin, 1989). Some experimental investigations of two-phase (gas/solid) flow were conducted, and while the two-phase flow was believed to be deterministic chaos, it could not be identified with a low-dimensional strange attractor (Tam and Davine, 1989 and 1992). Asymptotic power spectrum analysis and fractal dimension estimation have been employed to characterize chaotic behavior of two-phase flows in fluidized beds (Ding and Tam, 1994). The PSD, PDF, and calculation of correlation dimension were used by Franca et al. (1991) in an attempt to identify two-phase flow regimes in a 19-mm-inside diameter (i.d.) Plexiglas pipe.
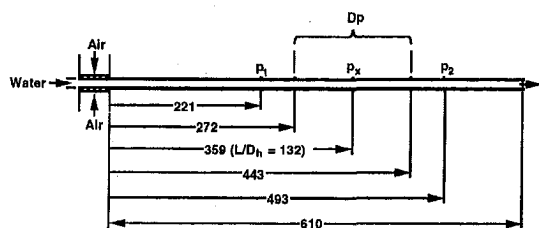
In this study, time history data of dynamic pressure p_1 from previous experiments (Wambsganss et al., 1991, 1992, 1994) were processed with various measuring tools, such as PSD, autocorrelation function, pseudo-phase-plane trajectory, Lyapunov exponents, and fractal dimensions. It was demonstrated that the randomlike pressure fluctuations characteristic of two-phase flow in small rectangular channels are chaotic, and governed by a high-order deterministic system. The correlation dimension,

(a) Schematic illustration of experimental apparatus

(b) Flow channel (length dimension is in mm). Dp is measured pressure drop, p_1 and p_2 are measured absolute pressures, and p_x is calculated

Fig. 1 Schematic illustration of adiabatic two-phase flow apparatus

channel was rectangular, 1.14 m in length, and had cross-sectional dimensions of 19.05 × 3.18 mm (aspect ratio, defined as the ratio of the height of the vertical side of the channel to the width of the horizontal side, was 6).

Both differential pressure, over a specified channel length, and dynamic pressures, at two locations, were measured. Differential pressure was measured with a strain-gage-type transducer (Viatran Model 209), and dynamic pressure was measured with piezoresistive type transducers (Endevco Model 8510B-50). All transducers were calibrated against a known standard. The frequency response of the differential pressure transducer is DC to ≈5 Hz, while the frequency response of the dynamic pressure transducers is from DC to >5000 Hz. Two small drilled ports are used to measure the differential pressure. The dynamic pressure transducers are very small and flush with the inner wall of the channel. Relative to the exit of the mixer, the pressure taps used with the dynamic-pressure-measuring transducers, p_1 and p_2, were located at L/D_h of 79 and 142, respectively (Fig. 1(b)). Background noise of the dynamic transducers and associated amplifiers is much less than 1 percent of the average pressure measurements. Typically, pressure measurement accuracies are < ±5 percent of their measured values.

The test procedure consisted of establishing total mass flux G and a mass quality x in the test section. As overall test channel pressure drop allowed, tests were performed over a range of quality (typically $10^{-4}-1$) for each mass flux used (50–2000 kg/m²s). At steady state, visual and photographic observations were made and pressures were measured.

Typical pressure/time history, root mean square (RMS) pressure, and frictional pressure gradient data in the form of two-phase frictional multipliers plotted as a function of both mass quality x and Martinelli parameter X, together with visual observations and photographic data, were summarized in previous work (Wambsganss et al., 1991, 1992, 1994). Such results were used to identify two-phase flow patterns and transitions and to develop flow pattern maps for two-phase flow in a small, horizontal, rectangular channel.

3 Measuring Chaos

In this study, data on dynamic pressure p_1 (see Fig. 1(b)) in flow regimes of plug, slug, and annular flows, with a fixed mass flux G = 500 kg/m²s, were investigated with various chaos measuring tools. (No stratified flow was found in this mass flux range (Wambsganss et al., 1991, 1992, 1994)). Typical pressure/time histories (with the "DC contribution" removed) from pressure transducer p_1, exhibiting different characteristics corresponding to the different flow patterns (plug, slug, and annular flows), are shown in Figs. 2(a–c). It is demonstrated that different flow patterns of two-phase flows in the small channel always exhibit randomlike pressure fluctuation characteristics, even though plug and slug flow are characterized by low frequency, and annular flow is characterized by high frequency.

Various measurement tools that are used in chaos theory were applied in this study to analyze dynamic pressure signals of two-phase flows with the objective of identifying and interpreting flow pattern transitions. These measurement tools included

which has been recently applied on two-phase flows, is potentially a new approach for identifying certain two-phase flow patterns and transitions.

2 Experiment

Experiments on two-phase flow in a small, horizontal, rectangular channel were conducted several years ago (Wambsganss et al., 1991, 1992, 1994). The flow apparatus (illustrated schematically in Fig. 1(a)) was designed to allow adiabatic flow experiments with air/liquid mixtures in channels of small cross-sectional area. Air was supplied from a compressed air storage tank, flowed through a pressure regulator and preselected rotameter to an air/liquid mixer. Laboratory water was the liquid in the experiments. The water flowed through a control valve and preselected rotameter to the mixer, where air was injected into the liquid stream through a porous medium in opposing walls of the flow channel. The two-phase mixture then flowed through a rectangular flow channel. The mixture exiting from the channel flowed through an expansion to a drain. The flow

---

Nomenclature

$C_{(r)}$ = correlation function
D_h = hydraulic diameter, m
D_p = measured pressure drop, kPa
d = a measure of the later time distance of two trajectories
d_c = correlation dimension
d_E = embedding dimension

G = total mass flux of two-phase mixture, kg/(m²s)
L = test section length, m
N = number of dimensional vectors
r = scaling range
p = absolute channel pressure defined in Fig. 1, kPa
t = time, s

X = Martinelli parameter
x = mass quality
x_i = dimensional vectors
ϵ = a measure of the initial distance between the two starting points of trajectories
λ = Lyapunov exponent
τ = delay time

power spectral density function (PSD), autocorrelation function, pseudo-phase-plane trajectory, Lyapunov exponents, and fractal dimensions.

The experimental pressure data were obtained from original recorded tapes at a sampling rate of 1000 digitizations per second with a Macintosh computer. The data length of 65,000 points for each test case was utilized to calculate various measures of chaos, especially for the algorithm for computing the fractal dimension.

3.1 Power Spectral Density.
Power spectral density (PSD) makes it possible to distinguish between periodic and chaotic responses. For a chaotic motion, the power spectrum is known to be continuous.

The PSD analysis can give a first indication of the dimensional behavior of a time series. The PSD analysis suggested by Gorman and Robbins (1992) can reveal information complementary to a conventional dimensional analysis or an estimation of Lyapunov exponents. Therefore, this approach should be considered before performing an expensive and time-consuming dimensional analysis like the correlation integral or the "nearest neighbor" approaches.

The characteristics of the power spectrum of chaotic-dynamic systems in the low-to-moderate-frequency regimes are reflected as broad-band structures without dominant peaks. However, at the high-frequency limit of the asymptotic regimes, power spectra decay toward a noise level. That noise level may be determined by instrumentation limits for data originating from measurements. The manner in which the spectrum decays toward the noise level contains useful information on the underlying dynamics. Some researchers have suggested that the asymptotic analysis of power spectra is very useful in distinguishing between high- and low-to-moderate dimensional chaos (Ding and Tam, 1994).

The PSD of plug, slug, and annular flows in a small channel are shown in Figs. 3(a-c) on a semi-log scale. All of the flow regimes exhibit a broad band of frequencies, which is a characteristic of chaotic behavior. At the high-frequency range for all of the flow regimes (see Figs. 3), the power spectra show a clear power-law falloff by visual inspection. As suggested by Sigeti and Horsthemke (1987), the power-law falloff of the power spectrum should indicate high-dimensional chaos rather than a stochastic process because the data were generated from a deterministic system (this is not universally accepted (Kennel and Isabelle, 1992)).

Therefore, the above analysis of the PSD for two-phase flows in the small channel indeed indicates the existence of high-dimensional chaotic behavior, and, as we will see later the high-dimensional attractors from correlation integral estimations.

However, it is not possible to distinguish the flow patterns and transitions of two-phase flows in the small rectangular channel from the analysis of PSD or probability density function (PDF), as other researchers have successfully conducted in their common flow channels (Hubbard and Dukler, 1966; Jones and Zuber, 1975; Matsui, 1984). In our experimental results, with specific small size channel, all of the flow regimes exhibit a broad-band signal characteristic, which can be observed from both time history records and PSD analysis.

3.2 Autocorrelation Function.
Autocorrelation function is another signal processing tool used to identify chaotic motion. When a signal is chaotic, information about its past origins is lost. This means that the signal is only correlated with its recent past.

The autocorrelation functions of the plug, slug, and annular flows are shown in Figs. 4(a-c). The autocorrelation functions for plug, slug, and annular flows have a peak at the origin delay time $\tau = 0$, and drop off rapidly with time, thus reflecting chaotic behavior.

It can be observed from Figs. 4 that the plug, slug, and annular flow have different periodic oscillations along the time
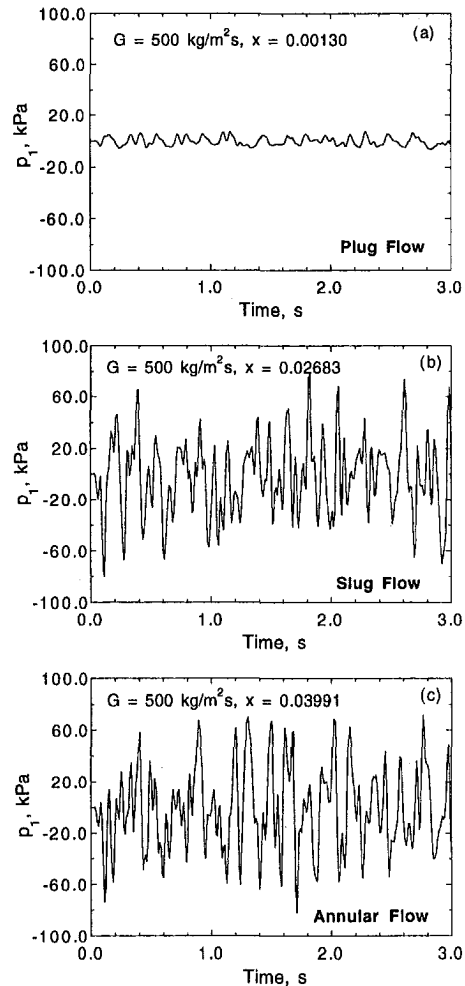
Fig. 2 Time histories of dynamic pressure $p_1(t)$ for (a) plug, (b) slug, and (c) annular flows (The estimated uncertainty in pressure measurements is < ±5 percent.)

delay axis, with the amplitude values of autocorrelation functions near zero. However, with limited analysis, we cannot claim that those differences can be used to identify flow patterns.

The importance and contribution of calculating the autocorrelation functions before performing other measurements of chaos is not only in that the autocorrelation function has provided a useful tool to distinguish chaotic behavior but also in that it can provide an optimum choice of time delay τ for other measurements of chaos. To estimate the attractor dimension, it is necessary to construct the phase space. The phase space may be reconstructed by using the time-delay embedding method, while the calculated values of the correlation dimension and Lyapunov exponents from reconstructed phase space are very sensitive to the time delay τ. Our experience has indicated that it is very useful and practical to choose an optimum time delay value from the calculated autocorrelation functions. This approach was originally suggested by Shaw (1985) and has since been extensively tested (Frazer and Swinney, 1986). As shown in Figs. 4, the optimum time delay is estimated to be the smallest value of τ at which the first minimum in the autocorrelation function occurs. This is the time delay used in subsequent measurements of chaos.

3.3 Pseudo-Phase-Planes.
To obtain the fractal dimension of a strange attractor, many methods assume that the dimension of the phase space wherein the attractor lies is known, or that all the stable variables can be measured. However, in our experiments, the time history of only one state variable is
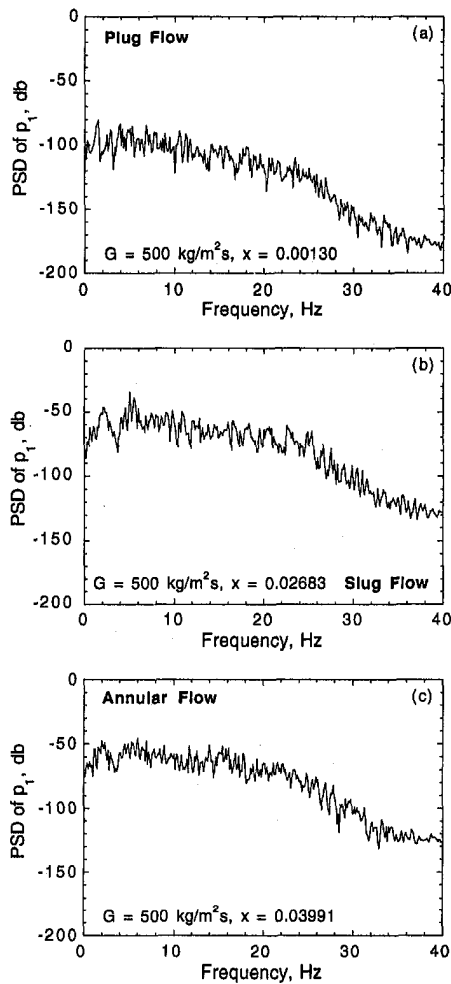
Fig. 3 PSD of dynamic pressure $p_1(t)$ for (a) plug, (b) slug, and (c) annular flows

available, i.e., dynamic pressure $p_1(t)$. Also, the number of degrees of freedom, or minimum number of significant modes contributing to the chaotic dynamics of two-phase flows, are not known a priori. In this case, pseudo-phase-space (embedding space) trajectories of the motion, or a strange attractor, can be reconstructed with the time delay embedding method (Packard et al., 1980). Given a scalar time series, one can reconstruct D-dimensional vectors from the following equation:

$$x_i = \{x(t_i), x(t_i + \tau), x(t_i + 2\tau), \ldots, x[t_i + (D - 1)\tau]\}$$

where D is the embedding dimension (the minimum dimension of the subspace), and τ is the time delay. The reconstructed geometrical structure has the same dimensional characteristics, for example, the correlation dimension of the attractor generated from the dynamics underlying the original scalar time series.

Figures $5(a-c)$ present pseudo-phase-plane plots of the measured dynamic pressure for plug, slug, and annular flows, respectively. It is obvious from these three flow patterns that the pseudo-phase-plane plots, indeed, indicate chaotic behavior. Franca et al. (1991) identified flow patterns from pseudo-phase-plane plots for two-phase flows in a horizontal round pipe of 19 mm i.d. However, the difference of pseudo-phase-plane signatures among the three flow patterns in Fig. 5 is not sufficiently clear to allow one to distinguish flow patterns in this small rectangular channel.

3.4 Lyapunov Exponents. Chaos in dynamics implies that the outcome of a dynamic process is sensitive to changes in initial conditions. If one imagines a set of initial conditions

within a sphere or radius ϵ in phase space, the chaotic motion trajectories originating in the sphere will map the sphere into an ellipsoid whose major axis grows as $d = \epsilon e^{\lambda t}$, where λ is known as a Lyapunov exponent. Lyapunov exponents, the average exponential rates of divergence or convergence of nearby orbits in phase space (Moon, 1987), have been shown to be the most useful dynamic diagnostic tool in quantifying chaotic systems.

Several investigators of chaotic dynamics have developed algorithms to calculate the Lyapunov exponent. For regular motion $\lambda \leq 0$; but for chaotic motion, $\lambda > 0$. Thus, the sign of λ is a criterion for chaos. Any system containing at least one positive Lyapunov exponent is defined as chaotic.

We used the algorithm proposed by Wolf et al. (1985) to determine the Lyapunov exponents from a time series of absolute pressure for different flow patterns. This algorithm is commonly used even though it is considered not to be a perfect and reliable one. Figures $6(a-c)$ show Lyapunov exponents for plug, slug, and annular flows. In the figures, evolution time refers to fractions of the "orbit time." This is the characteristic time scale for the average duration of a wiggle. In Fig. 6, the exponents are positive, which shows that the attractor had an expanding direction, constituting convincing evidence for chaotic behavior of plug, slug, and annular flows. The results provide further evidence of chaotic behavior in two-phase flows in small channels.

3.5 Correlation Dimensions. Another approach for predicting chaotic motion quantitatively is the use of fractal dimensions. A noninteger fractal dimension of the orbit in a phase
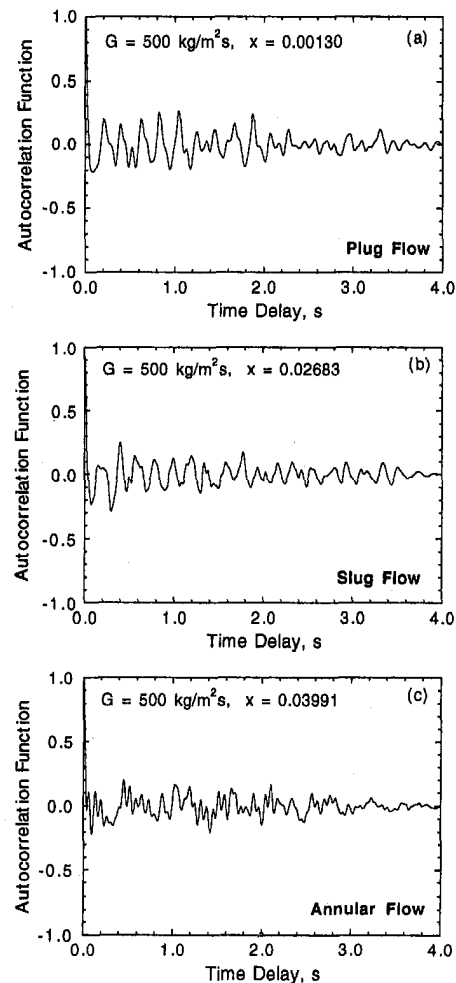

Fig. 4 Autocorrelation functions of dynamic pressure $p_1(t)$ for (a) plug, (b) slug, and (c) annular flows
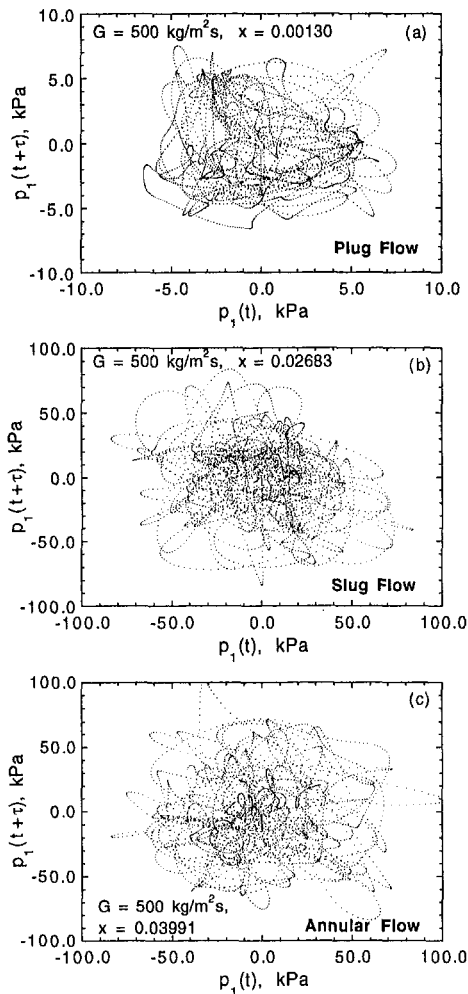
Fig. 5 Pseudo-phase planes of dynamic pressure $p_1(t)$ for (a) plug, (b) slug, and (c) annular flows

sions at different embedding dimensions are determined by the slopes of the least-squares fitted straight line of the correlation functions. The estimated correlation dimensions versus the embedding dimensions for plug, slug, and annular flows are plotted in Fig. 8, which shows that the correlation dimensions tend to saturate at values of $d_c \approx 6.6$ as the embedding dimension reaches 15 or greater for the plug flow, at values of $d_c \approx 5.4$ as the embedding dimension reaches 20 or greater for the slug flow, and at values of $d_c \approx 9.3$ as the embedding dimension reaches 20 or greater for the annular flow. The results from Figs. 7 and 8 provide evidence that two-phase flow in the small channel is deterministic chaotic motion, not a random oscillation (the dimension of random oscillation will increase as the embedding dimension increases). It appears that the correlation dimension may provide a new tool for the identification of two-phase flow patterns and transitions in a small, horizontal, rectangular channel.

4 Identifying Flow Patterns and Transitions

Correlation functions $C(r)$ with various mass quality x in the three regimes of plug, slug, and annular flows are shown in Figs. 9(a–c) (with embedding dimension $d_E = 20$). For plug flows, the correlation functions fall in the region of $\log_2 r = -5$ to 0, and with mass quality x increasing, the correlation function advances to the right (see Fig. 9(a)); for the slug flows, the correlation functions fall in the region of $\log_2 r = -1$ to 3, and with mass quality x increasing, the correlation function again shifts to the right (see Fig. 9(b)); for the annular

space implies the existence of a strange attractor. The basic idea is to characterize the "strangeness" of the chaotic attractor. Although practical use of fractal dimensions in measuring and characterizing chaotic motion has yet to be fully established, various definitions have been developed, including the capacity dimension, correlation dimension, and information dimension.

Of the several methods available to estimate the attractor dimensions, we used measurement of the correlation dimension, which has been used successfully by many investigators in other fields (Moon, 1987). In particular, we used Grassberger and Procaccia's method (1983) to calculate the correlation dimensions of measured pressure data of two-phase flow. This method is a commonly used dimension algorithm to date but with some limitations in the scaling of correlation dimension as pointed out by Kennel and Isabelle (1992).

The correlation function is defined as: $C(r) = \lim_{N \to \infty} (1/N^2)$ (number of pairs of points on the attractor whose distance is less than r). Here, N is the number of D-dimensional vectors constructed from the scalar time series. For some range r, called the scaling region, $C(r)$ scales as r^{d_c}, where d_c is the correlation dimension (Grassberger and Procaccia, 1983). A saturation of d_c as the embedding dimension D increases indicates that the time series has a nonrandom component.

Correlation integral analysis is applied to the experimental data of pressure in two-phase flows. Figures 7(a–c) show the correlation functions $C(r)$ versus $\log_2 r$ for plug, slug, and annular flows, respectively, with embedding dimensions increasing from 5 to 30 in intervals of 5. The correlation dimen-
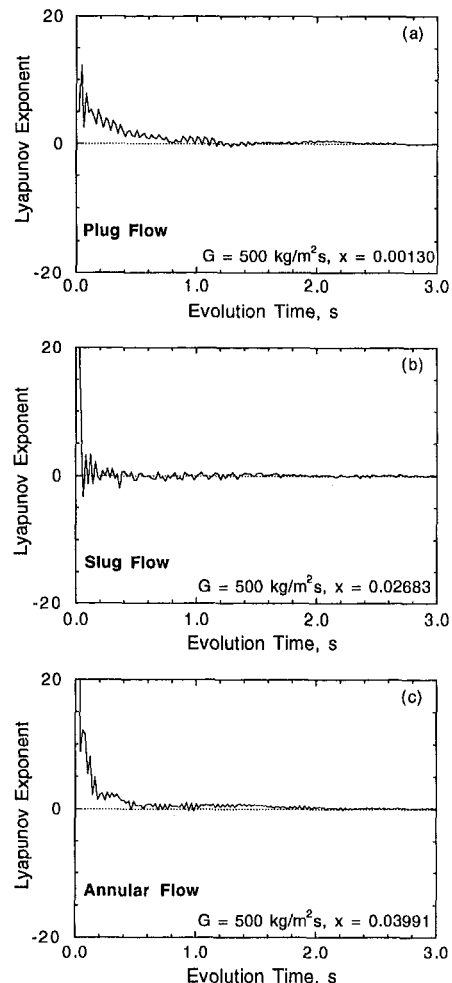

Fig. 6 Lyapunov exponents of dynamic pressure $p_1(t)$ for (a) plug, (b) slug, and (c) annular flows
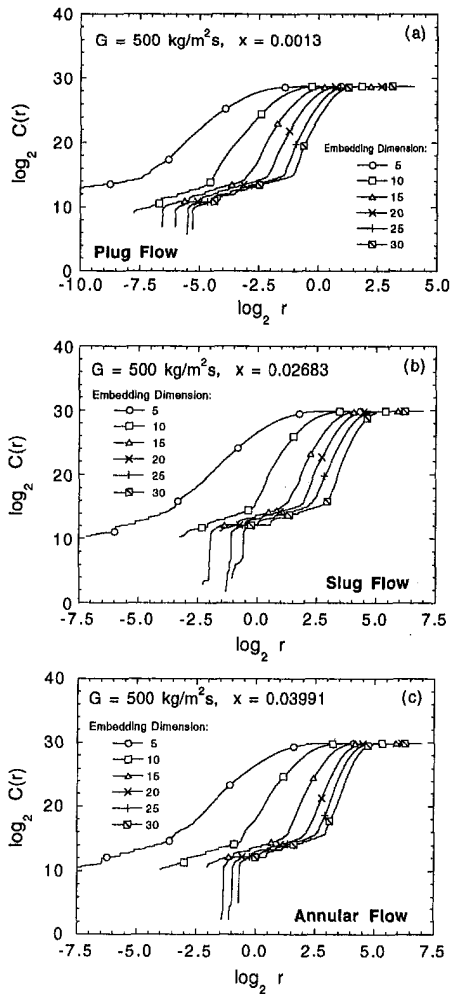
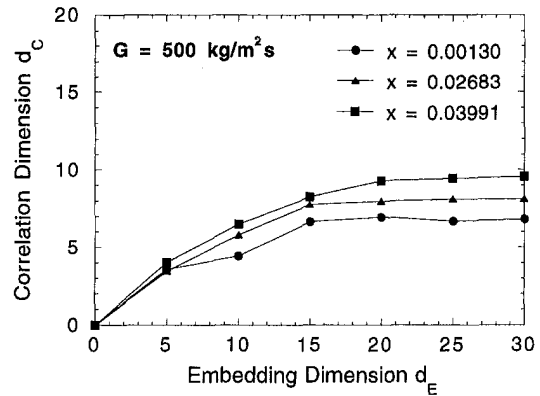Fig. 7 Correlation dimensions of dynamic pressure $p_1(t)$ for (a) plug, (b) slug, and (c) annular flows

Fig. 8 Correlation dimensions d_c versus embedding dimension d_E for plug, slug, and annular flows

tion dimension data. The result of the transition of plug to slug flow is in good agreement with the result of the RMS of dynamic pressure-time signals (Wambsganss et al., 1991, 1992, 1994).

Figures 9 and 10 show that changes apparently exist in the trend of the estimation of the fractal dimension that can be used to distinguish flow patterns and transitions, as these two-phase flows in small channels are, in fact, deterministic systems.
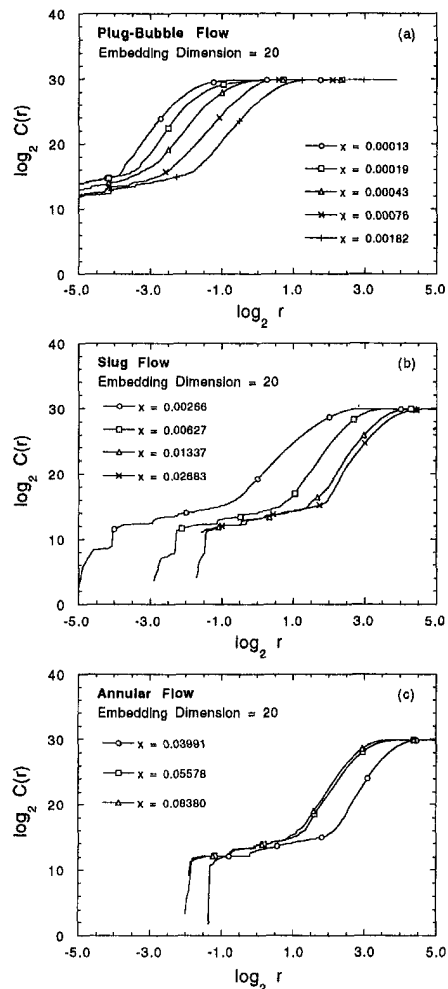
flows, the correlation functions fall in the region of $\log_2 r = 1$ to 3, and with mass quality x increasing, the correlation function shifts to the left (see Fig. 9(c)). Figures 9 show a tendency of the correlation function to distinguish flow patterns for two-phase flows in small channels.

For different flow patterns, the correlation functions fall in different regions. In the case of mass flux $G = 500$ kg/m²s, which is a relatively high mass flux value in the experiment (see Wambsganss et al., 1991, 1992, 1994), the range of values for the plug flow is different from that for the two other flow patterns. It is easy to distinguish the plug flow for it usually has low value of the correlation function. With a high mass flux, the values of the correlation function for the annular flow fall in the same region as that for the slug flow. While, with mass quality increasing, the curves of correlation functions shift to the left for the annular flow but shift to the right for the slug flow.

Correlation dimensions as a function of mass quality x are presented with root mean square (RMS) pressures in Fig. 10. We can identify a difference in fractal dimension levels for the various flow regimes, even though all would be defined as high-dimensional chaos. When plotted as a function of mass quality, a change in the trend of the correlation dimension could be identified with the transition of the plug to the slug flow pattern. With increasing mass quality, the correlation dimension decreases in the plug region and increases in the slug region. The correlation dimension was also lower in the plug region. The transition to annular flow could not be determined from correla-

Fig. 9 Correlation dimensions of dynamic pressure $p_1(t)$ for (a) plug, (b) slug, and (c) annular flows with embedding dimension $d_E = 20$
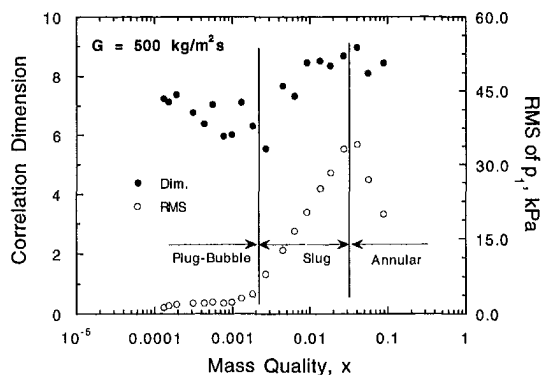
Fig. 10 Correlation dimension and RMS of pressure $p_1(t)$ versus mass quality x

5 Conclusions

Various measurement tools that are used in chaos theory were applied to analyze two-phase pressure signals with the objective of identifying and interpreting flow pattern transitions. These tools included power spectral density function (PSD), autocorrelation function, pseudo-phase-plane trajectory, Lyapunov exponents, and fractal dimensions.

Application of the pseudo-phase-plane trajectory, the PSD and autocorrelation functions, indeed, indicated the existence of chaotic behavior in the two-phase pressure measurement. In particular, the pseudo-phase-plane trajectory displayed complicated patterns, the PSD was continuous, and the autocorrelation function showed a peak at $\tau = 0$ and then dropped off rapidly. The Lyapunov exponents were shown to be >0 in quality ranges corresponding to the various flow patterns of interest. This provides the most convincing evidence for chaotic behavior and distinguishes two-phase flow in a small, horizontal, rectangular channel as a deterministic chaos rather than a random system. However, the results obtained with the various measurement tools of chaotic motion, such as the PSD function, autocorrelation function, pseudo-phase-plane trajectory, Lyapunov exponents, cannot be easily adopted as criteria for identifying flow pattern transition in very small, horizontal and rectangular channels.

The theory of fractal dimensions, in the form of correlation dimensions, was used to quantify the identified chaotic behavior. Embedding techniques and an approach to obtain optimum time delay were employed to calculate the correlation dimensions. In general, high dimensions were found for two-phase pressure signals in ranges corresponding to the various flow patterns of interest. When plotted as a function of mass quality, a change in trend of the correlation dimension could be identified with the transition of the plug to the slug flow pattern. The correlation dimension decreased as mass quality increased in the plug region, whereas the correlation dimension increased as the mass quality increased in the slug region. The correlation dimension in the plug region was lower.

It appears that fractal dimensions offer a promising way to objectively classify flow patterns. However, the time for data processing is such that it is not a practical tool for online analysis. The software we used for estimating dimensions is not well developed. Algorithms should be improved so that more data points can be involved and processing time can be reduced. Then, not only will the measurement of chaos be more accurate, but the method of estimating fractal dimension will be easily applied to broad practical purposes.

It was demonstrated that the randomlike pressure fluctuations characteristic of two-phase flow in small rectangular channels are chaotic, and governed by a high-order deterministic system. The correlation dimension is potentially a new approach to identifying certain two-phase flow patterns and transitions.

However, more work will be required before objective techniques are available for the identification and classification of two-phase flow patterns and transitions. We hope this study will stimulate future research relating to the application of chaos theory in this important area.

Acknowledgments

References

Brauner, N., and Maron, D. M., 1992, "Identification of the Range of 'Small Diameters' Conduits, Regarding Two-Phase Flow Pattern Transitions," *International Communications in Heat and Mass Transfer,* Vol. 19, pp. 29–39.

Clarke, R. H., and Blundell, N., 1989, "The Two-Phase Flow Patterns Occurring Inside a Plane-Fin Passage of a Plate-Fin Heat Exchanger," *Proceedings of AIChE Symposium Series, Heat Transfer - Philadelphia,* Vol. 85, pp. 287–292.

Ding, J., and Tam, S. W., 1994, "Asymptotic Power Spectrum Analysis of Chaotic Behavior in Fluidized Beds," *International Journal of Bifurcation and Chaos,* Vol. 4, No. 2, pp. 327–341.

Dorning, J., 1989a, "Nonlinear Dynamics and Chaos in Heat Transfer and Fluid Flow," *Proceedings of AIChE Symposium Series, Heat Transfer - Philadelphia,* Vol. 85, pp. 13–29.

Dorning, J., 1989b, "An Introduction to Chaotic Dynamics in Two-Phase Flow," *Proceedings of AIChE Symposium Series, Heat Transfer - Philadelphia,* Vol. 85, pp. 241–248.

Franca, F., Acikgoz, M., Lahey, R. T. Jr., and Clausse, A., 1991, "The Use of Techniques for Flow Regime Identification," *International Journal of Multiphase Flow,* Vol. 17, pp. 545–552.

Frazer, A. M., and Swinney, H. L., 1986, "Independent Coordinates for Strange Attractors from Mutual Information," *Physics Review A,* Vol. 33, p. 1135.

Galbiati, L., and Andreini, P., 1992, "Flow Pattern Transition for Vertical Downward Two-Phase Flow in Capillary Tubes. Inlet Mixing Effects," *International Communications in Heat and Mass Transfer,* Vol. 19, pp. 791–799.

Gorman, M., and Robbins, K. A., 1992, "Real-Time Identification of Flame Dynamics," *Applied Chaos,* Kim, J. H., and Stringer, J., eds., Wiley, New York, pp. 261–276.

Grassberger, P., and Procaccia, I., 1983, "Measuring the Strangeness of Strange Attractors," *Physica,* Vol. 9D, pp. 189–208.

Hibiki, T., Mishima, K., Yoneda, K., Fujine, S., Kanda, K., and Nishihara, H., 1992, "Visualization and Measurement of Gas-Liquid Two-Phase Flow in a Narrow Rectangular Duct with Use of the Neutron Radiography and Image Processing Technique," *ANS Proceedings, 1992 National Heat Transfer Conference,* Aug. 9–12, 1992, San Diego, CA., Vol. 6, pp. 101–108.

Hubbard, M. G., and Dukler, A. E., 1966, "The Characterization of Flow Regimes for Horizontal Two-Phase Flow," *Proceedings of Heat Transfer and Fluid Mechanics Institute,* Stanford Univ. Press, Stanford, CA.

Jones, O. C., and Zuber, N., 1975, "The Interrelation between Void Fraction Fluctuation and Flow Patterns in Two-Phase Flow," *International Journal of Multiphase Flow,* Vol. 2, pp. 273–306.

Kennel, M. B., and Isabelle, S., 1992, "Method to Distinguish Possible Chaos from Colored Noise and to Determine Embedding Parameters," *Physics Review A,* Vol. 46, p. 3111.

Koizumi, Y., 1992, "Air/Water Two-Phase Flow in a Horizontal Large-Diameter Pipe—Flow Regime and Pressure Drop—," *ANS Proceedings, 1992 National Heat Transfer Conference,* Aug. 9–12, 1992, San Diego, CA., Vol. 6, pp. 309–320.

Lahey, R. T., 1991, "An Application of Fractal and Chaos Theory in the Field of Two-Phase Flow and Heat Transfer," *Warmw- und Stoffubertragung,* Vol. 26, pp. 351–363.

Lahey, R. T., Clause, A., and DiMarco, P., 1989, "Chaos and Non-Linear Dynamics of Density-Wave Instabilities in a Boiling Channel," *Proceedings of AIChE Symposium Series, Heat Transfer - Philadelphia,* Vol. 85, pp. 256–261.

Matsui, G., 1984, "Identification of Flow Regimes in Vertical Gas Liquid Two-Phase Flow Using Differential Pressure Fluctuations," *International Journal of Multiphase Flow,* Vol. 10, pp. 711–720.

Matsui, G., 1986, "Automatic Identification of Flow Regimes in Vertical Two-Phase Flow Using Differential Pressure Fluctuations," *Nuclear Engineering and Design,* Vol. 95, pp. 221–231.

Moon, F. C., 1987, *Chaotic Vibration,* Wiley, New York.

Packard, N., Muench, J., Schwartz, C., Mees, A. I., and Rapp, P. E., 1980, "Geometry from a Time Series," *Physics Review Letters,* Vol. 45, p. 712.

Rizwan-uddin, 1989, "Strange Attractors in Forced Two-Phase Flow Heated Channels," *Proceedings of AIChE Symposium Series, Heat Transfer - Philadelphia,* Vol. 85, pp. 249–255.

Rizwan-uddin, and Dorning, J. J., 1986, "Some Nonlinear Dynamics of a Heated Channel," *Nuclear Science and Engineering,* Vol. 93, pp. 1–14.

Rizwan-uddin, and Dorning, J. J., 1988, "A Chaotic Attractor in a Periodically Forced Two-Phase Flow System," *Nuclear Science and Engineering,* Vol. 100, pp. 393–404.

Saether, S., Bendiksen, K., Müller, J., and Froland, E., 1990, "The Fractal Statistics of Liquid Slug Lengths," *International Journal of Multiphase Flow,* Vol. 16, pp. 1117–1126.

Shaw, R. S., 1985, *The Dripping Faucet as a Model Chaotical System,* Aerial Press, Santa Cruz, CA.

Sigeti, D., and Horsthemke, W., 1987, "High-Frequency Power Spectrum for Systems Subject to Noise," *Physics Review A,* Vol. 35, pp. 2276–2282.

Tam, S. W., and Davine, M., 1989, "Is There a Strange Attractor in a Fluidized Bed?" *Measures of Complexity and Chaos,* Abraham, N. B., et al., eds., Plenum Press, New York, pp. 193–197.

Tam, S. W., and Davine, M., 1992, "A Study of Fluidized-Bed Dynamical Behavior: A Chaos Perspective," *Applied Chaos,* Kim, J. H., and Stringer, J., eds., Wiley, New York, pp. 381–393.

Tutu, N. K., 1982, "Pressure Fluctuations and Flow Pattern Recognition in Vertical Two-Phase Gas-Liquid Flow," *International Journal of Multiphase Flow,* Vol. 8, pp. 443–447.

Tutu, N. K., 1984, "Pressure Drop Fluctuations and Bubble-Slug Transition in a Vertical Two-Phase Water Flow," *International Journal of Multiphase Flow,* Vol. 10, pp. 211–216.

Vince, M. A., and Lahey, R. T., 1982, "On the Development of an Objective Flow Regime Indicator," *International Journal of Multiphase Flow,* Vol. 8, pp. 93–124.

Wambsganss, M. W., Jendrzejczyk, J. A., and France, D. M., 1991, "Two-Phase Flow Patterns and Transitions in a Small, Horizontal, Rectangular Channel," *International Journal of Multiphase Flow,* Vol. 17, pp. 327–342.

Wambsganss, M. W., Jendrzejczyk, J. A., France, D. M., and Obot, N. T., 1992, "Frictional Pressure Gradients in Two-Phase Flow in a Small Horizontal Rectangular Channel," *Experimental Thermal Fluid Science,* Vol. 5, pp. 40–56.

Wambsganss, M. W., Jendrzejczyk, J. A., and France, D. M., 1994, "Determination and Characteristics of the Transition to Two-Phase Slug Flow in a Small Horizontal Channel," ASME JOURNAL OF FLUIDS ENGINEERING, Vol. 116, pp. 140–146.

Weisman, J., Duncan, O., Gibson, J., and Crawford, T., 1979, "Effects of Fluid Properties and Pipe Diameter in Two-Phase Flow Patterns in Horizontal Lines," *International Journal of Multiphase Flow,* Vol. 5, pp. 437–462.

Wolf, A., Swift, J. B., Swinney, H. L., and Vastano, J. A., 1985, "Determining Lyapunov Exponents from a Time Series," *Physica,* Vol. 16D, pp. 285–317.

A Review of Electrical Impedance Techniques for the Measurement of Multiphase Flows

S. L. Ceccio
Assistant Professor.

D. L. George
Graduate Student.

Department of Mechanical Engineering and
Applied Mechanics,
University of Michigan,
Ann Arbor, MI 48109-2121

Various developments in the use of electrical impedance methods in multiphase flow are reviewed. Because the components of a multiphase flow often exhibit different electrical properties, a variety of probes have been developed to study such flows by measuring impedance in the region of interest. Nonintrusive devices are used to measure spatially averaged flow properties, such as void fraction. Local probes have been developed to measure a variety of pointwise flow quantities, including film thickness in annular flow, local void fraction in dispersed flows, bubble and particle sizes, and flow velocities. Such impedance probes are usually easy to build and use, and can have a high frequency response. However, the spatial resolution of the probes may be limited, calibration may be difficult, and the accuracy of some probes may be limited to specific phase distributions. Researchers are now using electric fields to reconstruct the impedance distribution within a measurement volume via Electrical Impedance Tomography (EIT). EIT systems employ voltage and current measurements on the boundary of a domain to create a representation of the impedance distribution within the domain. EIT inversion algorithms are discussed, and the application of EIT to multiphase flows is reviewed. The benefits and limitations of EIT systems are also discussed.

Introduction

The study of multiphase flows has led to the development of various electrical impedance probes. In many multiphase flows, the phases have significantly different electrical impedances, and local or volume averaged measurement of these quantities can reveal information about the spatial and temporal distribution of the phases within the flow. Resistance, capacitance, inductance, or any combination of these quantities may be measured by probes of various designs. The scale on which information is gathered can vary also: the impedance of the flow may be measured in a small region with a local probe, or averaged over a large volume with an integrating probe. With a strategic selection of the probe geometry and appropriate calibration, impedance probes have been used to measure a variety of multiphase flow quantities, including mean and fluctuating void fraction in bubbly pipe flows, the dynamics of slug flows, film thickness in annular flows, void fraction in ocean waves, and bubble size and velocity distributions in fluidized beds. Impedance probes offer high frequency response, potentially low cost, and relative ease of construction.

Impedance techniques have been used since the late 1950s, and a number of authors have reviewed the use of electrical impedance probes in multiphase flows. Of particular note are the reviews by Bergles (1969), Jones and Delhaye (1976), Hewitt (1978), Banerjee and Lahey (1981), Cheremisinoff (1986), and Jones et al. (1992), all of whom describe a variety of measurement techniques. This paper will review past and current work in the use of impedance probes to measure multiphase flow properties, with emphasis placed on recent developments.

Bulk Void Fraction Meters

One of the earliest uses of impedance probes has been the measurement of the void fraction in a multiphase pipe flow. The bulk electrical properties of the multiphase flow depend upon the relative concentrations of the various phases, making measurement of the void fraction possible. For a uniformly disperse bubbly mixture Hewitt (1978) follows the analysis of Maxwell (1881) to determine the void fraction, α, from the electrical properties of the two phases:

$$\alpha = \left(\frac{A - A_L}{A + 2A_L} \right) \left(\frac{\epsilon_G + 2\epsilon_L}{\epsilon_G - \epsilon_L} \right). \qquad (1)$$

Here, A is the admittance (the reciprocal of the impedance, Z) of the mixture and A_L is the admittance of the liquid alone. ϵ_G and ϵ_L are either the conductivities or the dielectric constants of the gas and liquid phases, respectively, depending upon which electrical quantity dominates the admittance of the mixture. At the other extreme, the void fraction of a mixture of liquid droplets and air is given by:

$$\alpha = \left(\frac{A\epsilon_L - A_L\epsilon_G}{A\epsilon_L + 2A_L\epsilon_G} \right) \left(\frac{\epsilon_L + 2\epsilon_G}{\epsilon_L - \epsilon_G} \right). \qquad (2)$$

By placing electrodes at the perimeter of a pipe and measuring the bulk impedance across the electrodes, the void fraction of the pipe flow may be deduced. Figure 1 shows a typical void fraction meter based on this principle. Investigators have successfully used this technique since the late 1950s, and Hewitt (1978) provides an extensive review of its use. Polarization effects on the electrodes can be avoided in most void fraction meters by the use of alternating current. The frequency range selected for the current will determine which component of the total impedance will dominate the measurement (usually resistance or capacitance). As the applied frequency is in-
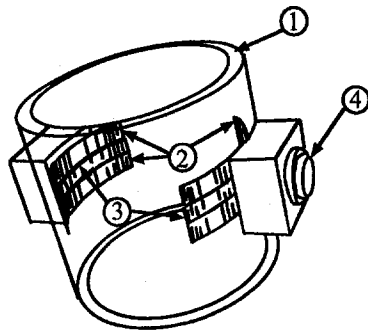
Fig. 1 An impedance void fraction meter with two shielded electrodes. (1) acrylic pipe; (2) stainless steel shielding electrodes; (3) stainless-steel measuring electrodes; (4) 3-pin connector. Adapted from Kytömaa and Brennen (1991).

electrode geometry

coaxial cable connector

acrylate tube   cement

cutaway view

| electrode 1 | shield electrode |
| electrode 2 | guard electrode |

Fig. 2 A void fraction meter design using a helical electrode geometry (adapted from Geraets and Borst, 1988)

creased, the capacitance of the phases will dominate the bulk admittance (Olsen, 1967). For air-water mixtures, the frequency of operation found in the literature by the authors ranges from 5 kHz to 5 MHz.

A serious limitation of the impedance void fraction meter is its sensitivity to the particular phase distribution across the electrodes. As shown by the above equations, the void fractions associated with a measured admittance value are markedly different for the cases of dispersed air and dispersed fluid. Bolman et al. (1974) calculated admittance ratios for a variety of pipe-flow regimes, and concluded that a simple two-electrode device must be recalibrated for each specific flow regime. Chang et al. (1984) experimented with a two-ring capacitance transducer, and they also determined that the transducer response is strongly related to the flow regime. Olsen (1967) first attempted to study permutations on the traditional two-electrode design to avoid this limitation, and other more recent investigations have continued to do so.

Kytömaa (1987) altered the impedance void meter of Bernier (1981) by introducing guard electrodes which bracket the two measuring electrodes (Fig. 1). In this arrangement, the measurement volume will more closely approximate a cross-sectional slice of the pipe. Xie et al. (1990) used finite-element analysis of the potential field in a two-electrode system to search for a design in which the system capacitance changes linearly with flow concentration. Their optimum design contained electrodes which subtended an angle of 125 deg each; they recommended that the pipe should be made of low-permittivity material, and should have an outer radius twice that of the inner radius. Along similar lines, a study by Lemonnier et al. (1991) explored the sensitivity of the two-electrode instrument to eccentricity of voids in annular flow. Their results suggest that in annular flows where the phases are not radially symmetric, each electrode should subtend an angle of 90 deg to properly measure void fractions. This differs from the angular criteria of Xie et al., but while the theoretical work of Lemonnier et al. applies only to annular flow, Xie et al. considered annular and core flow in their numerical studies.

Abouelwafa and Kendall (1980) experimented with a variety of electrode configurations for air-water, air-oil, and oil-water mixtures over a range of flow regimes. They concluded that a double helix electrode arrangement provided the best overall measurement of average void fraction. Geraets and Borst (1988) examined a helix electrode geometry analytically and experimentally by adding guard electrodes, as shown in Fig. 2. They determined that the system satisfactorily measured the average void fraction over a variety of flow regimes, since spatial averaging is automatically achieved for the helical geometry. The authors do point out, however, that impedance meters will become less effective as the void fraction of the flow increases, and suggest one solution may be the placement of a
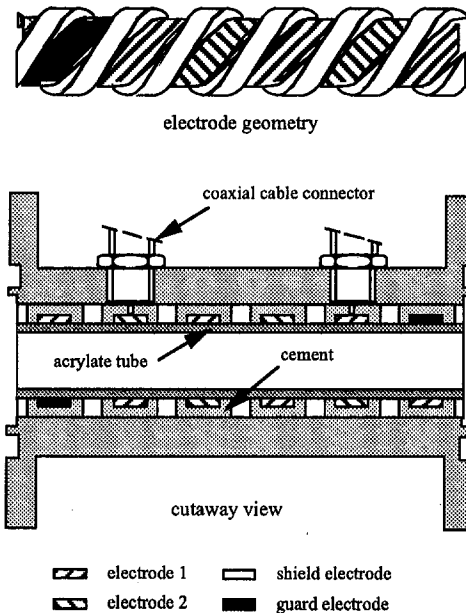
dielectric inner tube in the pipe to force the electric field lines to cross the middle of the pipe.

Merilo et al. (1977) introduced yet another design, meant to overcome the sensitivity of the impedance void fraction meter to the phase distribution. Their system used six electrodes flush-mounted around the pipe inner wall. A rotating electric field was then set up inside the pipe by applying a three-phase signal to the three pairs of opposing electrodes (Fig. 3). Calibrations of the initial design were compared to the theoretical results of Maxwell (1881) and Bruggeman (1935), and good agreement was found over a range of flow regimes. Snell et al. (1978) modified the system, turning the electrode assembly about a horizontal test section to find the best attitude for measuring stratified flows. With an electrode instead of an insulator at the top of the horizontal pipe, a linear calibration for horizontal flows was achieved with a standard deviation of only 2.3 percent. Their calibration for vertical flow was also linear, although the data scatter in this case was larger due to greater slugging in the flow. They found that the calibrations work well over the entire range of void fractions, 0 to 100 percent. Tournaire (1986) compared conventional and rotating impedance void meters and concluded that the rotating field device provided a better measure of void fraction.

sensor cross section   oscillator drive signals
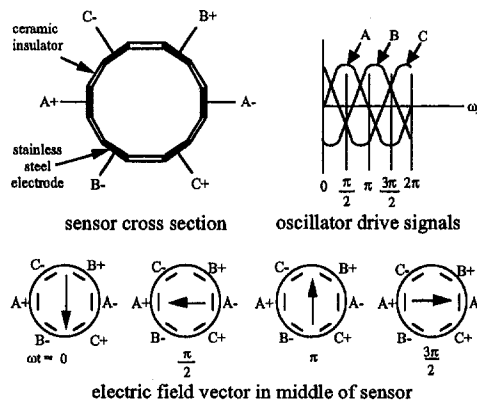
electric field vector in middle of sensor

Fig. 3 Schematic of a void fraction meter using a rotating electric field (adapted from Merilo et al., 1977)

The sensitivity of impedance void fraction meters to flow regime has been turned into an advantage by some investigators. Recently, Wang et al. (1991) reported an investigation in which a conventional void fraction sensor was used to indirectly identify two-phase flow regimes in dynamic vertical pipe flow, through Fourier analysis of the transient void fraction signal. Klug and Mayinger (1993) also report an indirect method of identifying the two-phase flow regime. In their impedance meter, eight surface plate electrodes are mounted on the inner side of the tube, and impedances are measured between combinations of electrodes excited in sequence. A total of 27 electrode combinations (and electric fields) is possible. The matrix of impedance measurements is compared against a reference matrix of impedances for flow regimes of interest. By interpolating the measurements within the reference matrix, the void fraction and flow regime are identified. Klug and Mayinger tested their instrument in oil/gas and water/gas flows, using only a subset of the electrode combinations for faster measurements. Results of the tests demonstrate that even with shorter measurement cycles, the void fraction can be measured with an uncertainty of ± 3 percent voids in stratified and bubbly flow, and an uncertainty of ± 9 percent voids in annular flows.

One distinct advantage of electrical impedance probes is their high frequency response, a feature which makes them useful for studying time-dependent flows. Investigators have used integrating void fraction meters to measure mean and fluctuating void fractions at a specific pipe cross section. By correlating the signals of two or more meters, disturbance velocities can be recorded. Recent examples of dynamic impedance void fraction measurements include the work of Kytömaa and Brennen (1991), who used two conventional impedance void fraction meters to examine the propagation and attenuation of small amplitude disturbance waves in vertical bubbly and particulate flows. Saiz-Jabardo and Boure (1989) used a series of conventional and rotating field void fraction meters to study the propagation of void fraction disturbances in vertical bubbly flows and in bubbly-slug flows. The system of Wang et al. (1991) described earlier in this section uses time-dependent measurements to identify flow regimes. Furthermore, Andreussi et al. (1988) and Andreussi and Bendiksen (1989) have used a multiple electrode ring system to study the dynamics of slug flows.

Local Void Fraction Probes

Electrical impedance probes have been devised which measure local void fractions of dispersed multiphase flows. Instruments of this kind use either wire electrodes stretched across the flow, or probes flush-mounted to the walls of the channel. In one example of the use of wire electrodes, Hardy and Hylton (1984) measured the average void fraction over a large area of a pipe flow using a dual wire string probe designed for harsh chemical environments. Lamarre and Melville (1992) developed an instrument using three parallel wire electrodes and employed it to accurately measure the void fraction of breaking surface waves, a phenomenon important in oceanic physics. Cheremisinoff (1986) reviews the use of flush-mounted probes to measure properties of multiphase fluidized beds. Again, these probes may be used in both resistive and capacitive modes. Ceccio and Brennen (1991 and 1992) have used flush-mounted impedance probes in the study of cavitation. Individual cavitation bubbles were detected and measured with pairs of point and local area probes, and the dynamics of attached cavities were examined with flush-mounted probes.

Barnea et al. (1980) combined flush-mounted and wire probes to study transition between flow patterns in gas-liquid flows. Kelessidis and Dukler (1989) and Das and Pattanayak (1993) adapted Barnea's instrument and method to identify two-phase flow transitions in the annuli between concentric and eccentric tubes by analyzing the probability density functions of the probe signal.

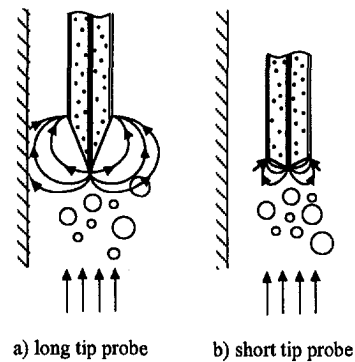a) long tip probe   b) short tip probe

Fig. 4 Conductivity probes used to measure local void fractions in bubbly flows, showing electric field lines (adapted from Teyssedou and Tapucu, 1988)

A series of electrical impedance probes have been developed to examine the interior behavior of multiphase pipe flows. The simplest devices consist of needle probes; a probe is placed with its tip in the center of a pipe, and a corresponding electrode is mounted flush to the wall. By examining the dynamics of the signal, one may infer the flow pattern in the pipe (Hewitt, 1978). Warrier and Nguyen (1993) used such a probe to measure bubble velocities in horizontal flow. This method can only provide an approximate indication of the internal flow, however. More common are local point probes with two or more electrodes. Bergles (1969) and Jones and Delhaye (1976) review the use of these local probes, which allow the void fraction to be inferred over a region close to the probe; guard electrodes may be used to alter the probe's measuring volume. Nasr-El-Din et al. (1987) give a detailed analysis of such a probe used in dispersed water-solids systems, and Teyssedou and Tapucu (1988) describe a system used to measure local void fraction in a bubbly flow (Fig. 4). Evaluation of the signals from impedance probes such as these is not straightforward, because the probe response is influenced by the entire electric field, not just the nearby field exemplified in Fig. 4. A void passing the probe but not intersecting the measuring volume can still produce a signal, for instance, and alter the signal from a bubble in the neighborhood of the probe.

More sophisticated probes have been developed to measure bubble size and velocity distributions in turbulent fluidized beds and bubbly flows. Calderbank et al. (1976) developed a five-electrode probe to determine bubble sizes and trajectory (see also Burgess and Calderbank, 1975). By analyzing the time delay between each electrode contact, bubble velocities, trajectories, shapes and size distributions could be determined, although this required complex data reduction and difficult probe calibration. Also, as with every intrusive measurement device, the probe may affect the flow field near the bubble, and the bubble may be deformed by the probe. Rowe and Masson (1980) calibrated an impedance probe similar to that of Werther and Molerus (1973) and found that the measurements of bubble size and velocity compared poorly to measurements made with X-ray photography. In a later study, Rowe and Masson (1981) compared the bubble probe results with photographic observations and noted that the probes significantly affect the motion and geometry of the bubble, concluding that single bubble data from impedance probes was suspect. In more recent studies, Gunn and Al-Doori (1985), van der Welle (1985), and Clark et al. (1992) have attempted to perform more detailed calibration of these probes using photographic calibration, gamma-ray attenuation data, and statistical analysis combined with photographic data, respectively.

Point resistivity probes which measure the density of interfacial areas between phases have been described by Kataoka et al. (1986) and Revankar and Ishii (1992 and 1993). Interfacial
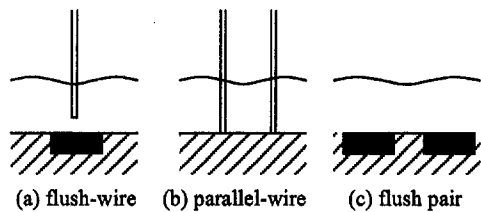
Fig. 5 Probes used to measure film thickness at a wall: (a) single wire and flush-mounted electrode; (b) parallel wires; (c) flush-mounted electrode pair (adapted from Kim and Kang, 1990, and Özgü et al., 1973)

area concentration can be related to bubble diameter and void fraction, and is particularly needed for accurate analysis of two-phase flows using the two-fluid model. Using correlation functions to describe the motion of the interface in directions other than the flow direction (Kataoka and Serizawa, 1990), measurements from a two-sensor probe were translated into local interfacial area concentrations, void fractions and bubble velocities. Probe measurements in vertical bubbly and slug flows compared very favorably with void fractions and bubble velocities from differential pressure and photographic measurements. A second probe design uses four point resistivity sensors along three orthogonal axes; here, the timing of voltage changes among the four probes provides a measurement of void fraction and interface velocity without the statistical assumptions required for the two-sensor probe. The four-sensor probe also measured void fractions and interface areas satisfactorily in bubbly and cap-bubbly vertical flows.

Similar to resistance and capacitance probes is the inductance probe developed by Cranfield (1972). Here, magnetic particles will induce small currents in a coil mounted in the probe. Consequently, individual components of a multiphase flow can be detected, if they can be magnetized. Abuaf et al. (1979) designed and tested a radio-frequency probe consisting of two parallel wires, one wire emitting a sinusoidal signal and the other acting as a receiver. With systematic study of the probe response to individual bubbles, the investigators were able to determine bubble sizes and velocities to within ± 10 percent. Yoshida et al. (1982) has developed an electrical discharge probe which can be used to detect particles or bubbles which have a significantly lower breakdown voltage than the continuous media in which they reside.

Film Thickness Probes

Wire electrode, needle, and flush-mounted probes have also been applied to the measurement of liquid film dynamics in annular and stratified flows. Bergles (1969) and Hewitt (1978) detail much of the early work on these devices. In many applications, a needle electrode is placed a fixed distance above a flush-mounted wall electrode to measure the distribution of local film thickness or wave height. Figure 5 shows such a probe developed by Kim and Kang (1990). When the liquid film contacts the needle, the circuit is completed, and a signal is generated. Contact with the needle is usually intermittent, and analysis of the number and duration of the probe contacts at different probe heights can be used to derive the local film-thickness probability distribution.

Film thickness may also be measured continuously by impedance probes. An example of a continuous measurement instrument is the dual wire electrode probe, also shown in Fig. 5. As the height of the fluid on the wires increases, the impedance across the wires decreases, although this relationship is not linear. The two wires may just pierce the liquid film and measure film thickness in several locations at a particular pipe position (e.g., Cheremisinoff, 1977), or the electrodes may span the entire cross section of the pipe. Miya et al. (1971) and Brown et al. (1978) discuss the theoretical basis for these probes and

present experimental calibration curves. Recent applications of the parallel wire probe include the studies of Lin and Hanratty (1987), Koskie et al. (1989), and Ruder et al. (1989). Wire probes of either kind (needle and flush-mounted, or dual wire probe) may only be used when their presence does not interfere with the flow itself. Also, wire and needle probes may be influenced by hysteresis effects which result from the finite time required for fluid to drain from the wire surface.

Pairs of electrodes mounted flush to the pipe wall can provide a nonintrusive measurement of film thickness, and this technique has been in use for some time. An example of this electrode geometry is also shown in Fig. 5. Coney (1978) reviewed the use of these probes to measure film thickness, and mentioned several limitations of these devices. As the electrodes are made smaller and are brought closer together, the area over which the probe averages its measurements will be reduced, but the maximum fluid height the probe can measure will also be reduced. Özgü et al. (1973) and more recently Delil (1987) discuss the theoretical and experimental response of a capacitance probe for measuring film thicknesses of a variety of conducting and nonconducting fluids. For thin films, the response of this probe is approximately linear for thicknesses on the order of the electrode dimension. Keska (1990) combined coplanar and transverse flush-mounted electrode probes to determine both film thickness and spatial concentration in annular flow.

One disadvantage of flush-mounted probes is the small currents that must be measured. Because current decreases as the electrode size is reduced, a compromise must be struck for a given instrument scale between fast response time and the elimination of stray signals. A successful and affordable compromise will depend on whether the fluid impedance is dominated by conductance or capacitance, and may not be possible in some cases. A drawback of all impedance methods, including bulk void fraction meters and local probes, is the need to compensate for changes in the electrical properties of the phases over time. Variations in the conductivity of phases with temperature can easily be corrected, but unforeseen changes in phase composition or ionic content after instrument calibration can only be compensated for under controlled laboratory conditions. For this reason, impedance probes and meters are not often found in industrial applications.

Electrical Impedance Tomography

The variety of probes and electrode geometries described above points to a dilemma in multiphase flow measurements: probes should be placed outside the domain of the flow, so as not to disturb the flow itself, yet phase distributions cannot easily be measured from the flow boundary. Tomography is a possible solution to this dilemma. With tomographic instruments, the spatial phase distribution can be determined without disturbing the flow. Most of the tomographic instruments available to study multiphase flow have been derived from devices for medical applications, such as X-ray, nuclear magnetic resonance (NMR), and positron emission tomography (PET) scanners. These instruments are often limited to the study of slowly changing systems, however, and can be difficult to use due to safety and cost considerations.

In recent years, the medical community has pioneered the use of electrical impedance tomography (EIT) as a low cost alternative relative to conventional medical tomographic systems. EIT uses measurements of the electrical impedance at the boundary of a test domain to reconstruct the impedance within the domain. A survey of the basics of the method and its application to medical diagnostics is found in the book *Electrical Impedance Tomography,* edited by J. G. Webster (1990). Researchers are now attempting to implement such systems for the study of multiphase flows.

In EIT, a number of electrodes are mounted to the surface of a domain of interest **D**. As with bulk void fraction meters,

alternating current (AC) is used to avoid polarization effects on the electrodes. For AC electrical conduction with field frequencies on the order of tens of megahertz or lower, the electric potential within a conducting domain is given by

$$\nabla \cdot \sigma \nabla V = 0 \qquad (3)$$

when no charge sources or sinks are present in $\mathbf{D}$. Here, σ is the complex conductivity and V is the electric potential. At the boundary of $\mathbf{D}$, the mixed boundary conditions are given by

$$\sigma(\nabla V \cdot \mathbf{n}) + q = 0, \qquad (4)$$

where $\mathbf{n}$ is the unit normal vector outward from the domain boundary, and q is a charge flux on the boundary. Multiple measurements of q and V at the boundary of $\mathbf{D}$ are used to reconstruct the conductivity distribution within $\mathbf{D}$. An iterative reconstruction process is required to arrive at a conductivity distribution which will yield the measured boundary conditions.

In practice, current injections and voltage measurements will be performed at a finite number of locations on the boundary, and these measurements may be averaged over a portion of the boundary surface. Consequently, the limited resolution of the reconstructed conductivity field will be strongly related to the number of locations used to probe the domain. If N electrodes are used, the domain can be modeled as an N-port impedance network. A current source and current sink of equal strength are placed on two of the ports, and the resulting voltage distribution around the "network" can be measured at $(N - 1)$ ports, with one port referenced to ground. The total number of linearly independent voltage measurements, R_N, is then given by

$$R_N = \frac{N(N - 1)}{2}. \qquad (5)$$

R_N is also the number of independent impedance elements which can be determined from these voltage "projections" and used to model the domain.

Several simplifying assumptions are generally employed in EIT, the validity of which should be noted. First, the domain is assumed to be two-dimensional, and the injection current is assumed to be confined to a two-dimensional plane. In practice, applied fields are three-dimensional, especially for small, unguarded electrodes; unless the test domain is carefully chosen to be uniform in the third dimension, the 2-D image which results will reflect the 3-D nature of the excitation field. (Full three-dimensional EIT is possible in principle, but would require state-of-the art computer equipment and impractical amounts of time and memory.) Another common assumption is that the conductivity within the domain may be assumed to be piecewise constant, although some works discussed later in this section model conductivity with continuous functions. A third simplification is that the voltage in the domain is easily represented by mathematical models. These assumptions make it possible to represent the domain by discrete finite elements during reconstruction. It is also assumed that the impedance distribution within the domain does not change significantly over time while voltage projections are acquired. As a result, EIT systems must acquire projections rapidly to image most multiphase flows, and can be severely limited in applications to dynamic flows.

To reconstruct the image of the domain, a "candidate" representation of the impedance distribution is first constructed. A set of voltage projections are then computed from the candidate distribution. The candidate projections are compared to voltages measured on the boundary during current injection, and their difference is characterized by some error criterion. Finally, the candidate distribution is modified based on the error, and a new set of candidate projections is computed. This process continues until some minimum error criterion is satisfied.

EIT reconstruction is an ill-posed problem. As such, the reconstructed impedance "solution" may not satisfy requirements of existence or continuous dependence on the problem
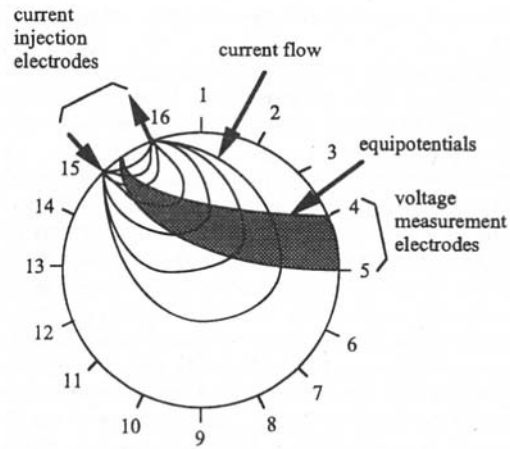

Fig. 6 Schematic of current injection and voltage measurements taken by an EIT system (adapted from Plaskowski et al., 1995). The shaded region indicates where impedances are to be computed from equipotential measurements.

data. Most importantly, as a consequence of the ill-conditioning of the problem, the solution is sensitive to noise in the projections. As the number of electrodes or the spatial resolution of the solution increases, the ill-conditioning and the sensitivity to noise increase also. A priori knowledge of the impedance distribution may be used to aid in restoration, but in most multiphase flows, such information may not be readily available.

Beck and co-workers at the University of Manchester Institute of Science and Technology (UMIST) are one of two teams developing an EIT system for multiphase flow diagnostics (Plaskowski et al., 1995). Xie et al. (1989a and b) discuss their algorithm for image reconstruction and identification of flow regimes. In their system, voltage projections are acquired by measuring the capacitance across pairs of electrodes. Linear backprojection between equipotential lines is then used to reconstruct the impedance distribution following the method of Barber and Brown (1984).

In this technique, the domain is first assumed to have a uniform impedance distribution equal to the measured bulk average impedance. A set of voltage projections is then computed for the uniform domain. The actual domain to be reconstructed is not uniform, so the measured projections will be different from these calculated ones. For each projection measurement, current is sourced at one port and sinked at another to impose a voltage gradient over the domain (Fig. 6). The result is a set of measured voltage differences between adjacent pairs of electrodes, which can be taken as the difference between the voltages of two equipotential lines extending from the ports at the boundary of the domain. The principal assumption of the backprojection method is that the voltage on the equipotentials of the measured, inhomogeneous domain differ from those of the uniform domain by only a small amount for all projections. Under this assumption, the difference in impedance $\Delta \sigma$ between pairs of equipotential lines in the calculated and measured domains can be calculated from

$$\frac{\sigma_H + \Delta \sigma}{\sigma_H} = \frac{\Delta V_H}{\Delta V_M}. \qquad (6)$$

Here, σ_H is the homogeneous impedance of the calculated projection set, and ΔV_M and ΔV_H are the potential differences between the equipotential lines (measured at the same positions on the boundary) in the measured and calculated projection sets, respectively. The region of the calculated domain between the two equipotential lines will enclose a number of discrete elements, or "pixels," and the impedance of those elements is perturbed by $\Delta \sigma$. This is repeated for all the projections to

Journal of Fluids Engineering

produce a new, non-uniform representation of the impedance distribution.

The backprojection method has limitations which will influence its accuracy. First, the impedance distribution in the measured domain will usually not be a small perturbation from the bulk average impedance. In air-water mixtures, for example, the electrical properties of the two phases differ by nearly two orders of magnitude. Second, it is also assumed in the backprojection method that small changes in conductivity do not significantly change the path of current within the domain (Seagar et al., 1987). In actual backprojection applications (and in EIT in general), this assumption is often violated, particularly in air-water mixtures. Backprojection is therefore of limited validity when small changes in conductivity significantly alter the current path through the domain. Third, several of the calculated equipotential lines will inevitably intersect some of the discrete elements which comprise the calculated domain, rather than follow pixel boundaries. Thus, the backprojection method will tend to "smooth out" the calculated impedance distribution.

Two additional steps may be taken to refine the computed impedance distribution. The UMIST group (Dickin et al., 1993) employs a ramp filter to reduce the blurring of the reconstructed distribution. However, the type and extent of filtering will significantly influence the final image, and filtering is often successful only when a priori assumptions are made about the actual phase distribution. Second, the backprojection process may be iterated to refine the solution. Iterative backprojection uses the last result of the domain calculation to derive new equipotential lines and impedance perturbations, and requires a much more refined analysis than once-through backprojection for successful results.

Jones and co-workers at Rensselaer Polytechnic Institute have also been developing an EIT system for the study of multiphase flows (Jones et al., 1992, 1993, and 1994; Lin et al., 1993). Their reconstruction algorithm is based on the method developed by Yorkey et al. (1987) and is referred to as the YWT method. In this method, the domain is modeled as a network of M impedances, σ_M, which can be real or complex. A finite element solution of the currents and voltages within the domain can be formulated using Kirchoff's law in matrix form:

$$\mathbf{Y}_{N \times N} \mathbf{V}_{N \times P} = \mathbf{C}_{N \times P}. \tag{7}$$

Here, $\mathbf{Y}$ is the matrix of admittances (the inverse of the impedance matrix), $\mathbf{V}$ is the nodal voltage matrix, $\mathbf{C}$ is the nodal current matrix, N is the number of nodes, and P is the number of current excitations. If E electrodes are employed at the domain boundary, a vector $\mathbf{f}_{E \times P}$ may be constructed from the calculated boundary voltages, and measured boundary voltages can form another vector $\mathbf{g}_{E \times P}$. The calculated and measured boundary voltages can be used to form an error criterion ϕ, where

$$\phi = \tfrac{1}{2} [\mathbf{f} - \mathbf{g}]^T [\mathbf{f} - \mathbf{g}] \tag{8}$$

is the squared error of the domain reconstruction.

An iterative procedure is used to minimize ϕ by modifying the elemental impedances σ_M. The error is minimized when the derivative of ϕ with respect to σ_M is zero, or

$$\phi' = \frac{d\phi}{d\sigma_M} = [\mathbf{f}']^T [\mathbf{f} - \mathbf{g}] = 0 \tag{9}$$

where the Jacobian $\mathbf{f}' = d\mathbf{f}/d\sigma_M$. ϕ' can be evaluated by expanding it in a Taylor series about a reference impedance distribution σ_{MO}, such that

$$\phi' \cong \phi'(\sigma_{MO}) + \phi''(\sigma_{MO}) \nabla \sigma_{MO} = 0. \tag{10}$$

The gradient of the impedance is then approximated by

$$\nabla \sigma_{MO} \cong - \frac{\phi'(\sigma_{MO})}{\phi''(\sigma_{MO})} \tag{11}$$

where

$$\phi'(\sigma_{MO}) = [\mathbf{f}'(\sigma_{MO})]^T [\mathbf{f}(\sigma_{MO}) - \mathbf{g}] \tag{12}$$

and the approximate Hessian matrix is

$$\phi''(\sigma_{MO}) \cong [\mathbf{f}'(\sigma_{MO})]^T [\mathbf{f}'(\sigma_{MO})]. \tag{13}$$

Consequently, the calculated distribution of the elemental impedances σ_M can be updated toward the actual distribution by adding the computed gradient of the reference impedance $\nabla \sigma_{MO}$. This process can be repeated until $\phi < \epsilon$, where ϵ is a stopping criterion.

Yorkey et al. (1987) compared the performance of several EIT reconstruction algorithms using ideal data. The single backprojection method and the YWT method were examined along with three others: the "perturbation method" of Kim et al. (1983), iterative backprojection, and the "double constraint method" of Wexler et al. (1985). The perturbation method uses an approximation of the Jacobian matrix in determining changes to the resistivity elements. The double constraint method employs a finite element method solution to calculate current density in the domain, using measured voltages and current source values as constraints, then determines the resistivity of each element in the domain. In the implementation of the backprojection method of Barber and Brown (1985), no correction was made for angular non-uniformity of the equipotentials, and no filtering was employed. A weighted correction was made to account for the fact that often a fraction of each elemental impedance was integrated between the equipotential lines. The results of this study indicated that the YWT method was the only method to converge to zero error, and was the method which converged to the minimum error most rapidly. It is expected that the YWT method will converge quadratically, and the computation time and ill-conditioning of the Hessian matrix may be reduced through judicious choice of the methods used to calculate the Jacobian matrix.

An implementation of the YWT algorithms by Jones and co-workers uses several improvements in both data acquisition and numerical techniques. Among the computational methods in their recent work is "preconditioned voltage conversion," a technique which maps measured voltages to the computational domain in such a way that geometric distortions and numerical errors can be corrected. A block decomposition method allows conductivity within each finite element of the domain to vary so that results are continuous between elements (Lin et al., 1993). Both bilinear and biquadratic exponentials are used as conductivity shape functions in this procedure (Jones et al., 1994, and Jones, 1995). They report that the resulting resolution is comparable to that of much finer discrete meshes, but the computational effort involved is greatly reduced. To increase measurement sensitivity, Jones and co-workers use plate electrodes instead of point electrodes to provide more uniform voltage gradients in the test object, and have increased the conductivity of water within the test object to reduce experimental error and improve image accuracy (Jones et al., 1994).

Recent results of this work are presented in Fig. 7, which compares the actual geometry of three square insulators in a test phantom to a reconstructed image created using preconditioned voltage conversion and bilinear exponential shape functions. The bilinear shape function produces constant conductivity along straight lines, leading to jagged edges in the resulting images. Biquadratic exponential shape functions are now being tested; these can potentially model circular, elliptic, parabolic or hyperbolic lines of constant conductivity, producing sharp but continuous variations in conductivity. Work is also progressing on a layer reduction method, in which layers above and
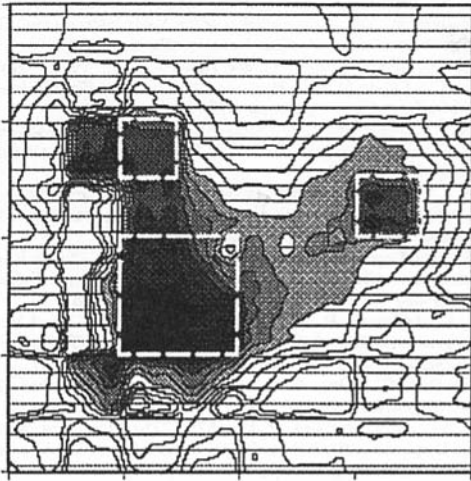
Fig. 7 Impedance image created using the technique of Jones et al. (1994). The dashed lines mark the actual positions of the electrical insulators in the water phantom.

below the electrically excited layer of interest are "folded" into the central layer, allowing the three-dimensional problem to be solved two-dimensionally. (Jones et al., 1994, and Jones, 1995).

Issues related to the accuracy of EIT methods in general have been considered by several authors. For instance, EIT algorithms which employ a finite element method will have spatial resolution strongly dependent on the number and type of elements used in the mesh. Since the impedance distribution is not known a priori, the element boundaries will generally not coincide with the interfaces between regions of different impedance. Thus, sharp discontinuities in impedance will be smeared out over the area of the intersecting element. It is this smoothing of impedance distributions that poses problems for most EIT algorithms when applied to multiphase flows, because conductivity always varies discontinuously in such flows. Jones and co-workers (Jones et al., 1994, and Jones, 1995) have minimized this effect by using the exponential shape functions discussed above.

In principle, the choice of electrode pairs used to determine the voltage projections is not important, since R_N projections are linearly independent, and all others are only linear combinations of the independent set. In practice, because of the ill-conditioning of the EIT problem and the resulting sensitivity to noise, the measurement pattern will influence the quality of the projection. For example, the backprojection method uses adjacent pairs of electrodes to inject the current and acquire the voltage projections (the "neighboring method"). Alternatively, current injection and voltage measurements can be performed using electrodes which are diametrically opposed. Many other collection schemes have been proposed (Webster, 1990); differences in the magnitude of the injected current arise between these collection methods. For example, the neighboring method may not inject significant amounts of current into the center of the domain when compared to the "opposite" method. As a result, the resolution in the interior of the domain may be compromised by "neighboring" measurements (Hua et al., 1987). Measurement patterns may be optimized for specific geometries: Isaacson and Cheney (1990) have demonstrated that an optimal application of current to a radially-symmetric system takes the forms $\sin k\theta$ and $\cos k\theta$, where $k = 1$ to K and K is half the number of circumferential electrodes around the test domain. This pattern excites all electrodes simultaneously, forcing current through the center of the domain as well as the edges, and the total current is the sum of currents at individual electrode-pairs. This approach was found to increase current

flow and sensitivity and decreases noise effects. Jones et al. (1995) have applied voltage patterns involving Walsh functions to a rectangular domain and have obtained similar improvements in imaging.

The total time required to both collect and process a set of EIT projections depends strongly on the inversion algorithm employed and the number of electrodes. The UMIST group (Dickin et al., 1993) reports that their low frequency 16-electrode system requires about 1 millisecond to acquire a set of projections, and Fasching and Smith (1991) report that their 16-electrode system acquires a set of projections in 10 ms. However, the time required for image reconstruction varies widely depending on the inversion algorithm used. Using a personal computer, the UMIST group reported that inversion using backprojection took 24 seconds. Alternatively, the YWT method took 2 minutes to proceed through three iterations (Dickin et al., 1993). Jones et al. (1994) reported that the time needed for the YWT method to reconstruct an image increases as the 3.3 power of the number of elements, making detailed imaging prohibitive. The exponential block decomposition method now used in their investigations increases computation speed over the YWT method by three orders of magnitude.

Finally, the experimental equipment necessary to acquire the projections for EIT imaging has been under development concurrent with the inversion algorithms. The UMIST group (Dickin et al., 1993) has been developing both high and low frequency excitation systems. The former may be used for liquid-gas systems where the liquid conductivity is high, and the latter may be used when the system impedance is low. Stray impedances must be limited in high frequency systems, and the signal to noise ratio for the projection set must be maximized. Care must also be taken in the design of the electrode geometry, and the effects of contact resistance between the electrodes and the fluid must be minimized and/or accounted for in the reconstruction. Implementing these requirements can yield dramatic improvements in image quality, but can be expensive as well. The group has presented results for a 16-electrode low frequency system (from 75 to 153 kHz excitation frequency) which has been tested on static phantoms and on a transient system of two mixing liquids. A high frequency system (1.25 MHz) has been implemented with 12 electrodes, with a noise level low enough to allow changes in void fraction of 2 percent to be detected (Huang et al., 1992).

Fasching and Smith (1991) have implemented a capacitive system (400 kHz excitation frequency) to reconstruct the impedance distribution in a fluidized bed. Their system uses 16 evenly spaced circumferential electrodes and measures displacement currents after a voltage field has been applied to the domain. Backprojection is used to reconstruct the impedance distribution. The researchers were able to detect transients in the fluidized bed which were consistent with the known phase distributions.

Conclusion

A variety of impedance probes have been devised for the study of multiphase flows. Probes have been developed to determine average or local void fractions, flow velocities, film thicknesses, and spatial phase distributions. Depending upon the properties of the various phases, changes in conductivity, capacitance, inductance, or a combination of these can be measured.

Maxwell (1881) performed the first mathematical analysis to find the void fraction of a flow from the electrical properties of the phases. From this, the average void fraction can be determined for a region of a multiphase flow by measuring the bulk average impedance of the region. Bulk void fraction meters can be quite sensitive to the phase distribution of the flow, and investigators have worked to overcome this limitation. Xie et al. (1990) have developed plate electrode configurations which respond linearly to changes in flow concentration, while Geraets

Journal of Fluids Engineering

and Borst (1988) determined that a helix electrode geometry with guard electrodes can measure void fraction in a pipe satisfactorily over a variety of flow regimes. Another useful design applies rotating electric fields to overcome sensitivity to phase distributions in a pipe. Void fraction meters such as these may be used readily in oil-gas or air-water flows, and provide a high-frequency response useful in studying time-dependent flows.

Flush-mounted electrical probes are nonintrusive, but can only provide average measurements over the flow domain or local measurements near the flow boundary. Detailed examination of the local phase distribution over the entire flow domain often requires the insertion of an electrode probe into the flow; local probes have been used in such diverse applications as studies of ocean waves, cavitation, and fluidized beds. Evaluation of the signals from local impedance probes is not straightforward, since analysis must include the influence of voids or particles in all areas of the electric field, and local probes may disturb the phase distribution and other flow properties. However, recent work by Revankar and Ishii (1992, 1993) with two-point and four-point sensors placed on orthogonal axes has provided satisfactory measurements of void fractions and bubble velocities and dimensions in several vertical flow regimes.

Electrical impedance tomography (EIT) may be thought of as a higher-order impedance method: a non-intrusive means to determine the local phase distribution throughout a region of the multiphase flow. EIT systems reconstruct the impedance distribution within a domain from voltage and current measurements at the domain boundary. Beck and co-workers are developing an EIT system using linear backprojection between equipotential lines (Plaskowski et al., 1995). While the method has limitations on accuracy, particularly in air-water mixtures, filtering and iteration have been used to refine the results of the method. Jones and co-workers (1994) are developing another EIT system and imaging algorithm based on the YWT method, but refined to correct geometric distortions and allow continuous properties between finite elements. Imaging tests have been performed with non-conducting objects in a water medium, and work on instrumentation and numerical methods continues in order to improve resolution. Present systems have limited spatial resolution, however, work to improve both the hardware and software of EIT systems continues.

In summary, while there is no single impedance probe that is universally applicable to measurements in multiphase flows, there are a number of well-developed techniques which do provide specific information in certain flows with low cost and reasonable accuracy. EIT systems now under development appear to offer particularly exciting possibilities for future non-intrusive, full-field measurements of multiphase flow properties.

Acknowledgments

References

Abouelwafa, M. S. A., and Kendall, E. J. M., 1980, "The Use of Capacitance Sensors for Phase Percentage Determination in Multiphase Pipelines," *IEEE Transactions on Instrumentation and Measurement,* Vol. IM-29, pp. 24–27.

Abuaf, N., Feierabend, T. P., Zimmer, G. A., and Jones, O. C., 1979, "Radio-frequency Probe for Bubble Size and Velocity Measurements," *Review of Scientific Instruments,* Vol. 50, pp. 1260–1263.

Andreussi, P., Di Donfrancesco, A., and Messia, M., 1988, "An Impedance Method for the Measurement of Liquid Hold-Up in Two-Phase Flow," *International Journal of Multiphase Flow,* Vol. 14, pp. 777–785.

Andreussi, P., and Bendiksen, K., 1989, "An Investigation of Void Fraction in Liquid Slugs for Horizontal and Inclined Gas-Liquid Pipe Flow," *International Journal of Multiphase Flow,* Vol. 15, pp. 937–946.

Banerjee, S., and Lahey, R. T., Jr., 1984, "Advances in Two-Phase Flow Instrumentation," *Advances in Nuclear Science and Technology,* Lewins, J., and Becker, M., eds., Plenum Press, New York, Vol. 13, pp. 227–414.

Barber, D. C., and Brown, B. H., 1984, "Applied Potential Tomography," *Journal of Physics E: Scientific Instruments,* Vol. 17, pp. 723–733.

Barber, D. C., and Brown, B. H., 1985, "Recent Developments in Applied Potential Tomography-APT," *Proceedings of the Ninth International Conference on Information Processing in Medical Imaging,* Washington, D.C.

Barnea, D., Shoham, O., Taitel, Y., and Duckler, A. E., 1980, "Flow Pattern Transition for Gas-Liquid Flow in Horizontal and Inclined Pipes," *International Journal of Multiphase Flow,* Vol. 6, pp. 217–225.

Bergles, A. E., 1969, "Electrical Probes for the Study of Two-Phase Flows," *Proceedings of the Eleventh National ASME/AIChE Heat Transfer Conference,* Minneapolis, pp. 70–81.

Bernier, R. J. N., 1981, "Unsteady Two-Phase Flow Instrumentation and Measurement," Report No. E200.4, Division of Engineering and Applied Science, California Institute of Technology, Pasadena, CA.

Bolman, H., van Koppen, C. W. J., and Raas, L. J., 1974, "Some Investigation on the Influence of the Heat Flux on Flow Patterns in Vertical Boiler Tubes," *European Two-Phase Flow Group Meeting,* Harwell, Paper A2.

Brown, R. C., Andreussi, P., and Zanelli, S., 1978, "The Use of Wire Probes for the Measurement of Liquid Film Thickness in Annular Gas-Liquid Flows," *Canadian Journal of Chemical Engineering,* Vol. 56, pp. 754–757.

Bruggeman, D. A. G., 1935, "Berechnung Verschiedener Physikalischer Konstanten von Heterogenen Substanze," *Annalen Physik,* Leipzig, Vol. 24, p. 363.

Burgess, J. M., and Calderbank, P. H., 1975, "The Measurement of Bubbles in Two-Phase Dispersions-III: Bubble Properties in a Freely Bubbling Fluidized-Bed," *Chemical Engineering Science,* Vol. 30, pp. 1511–1518.

Calderbank, P. H., Pereira, J., and Burgess, J. M., 1976, "The Physical and Mass Transfer Properties of Bubbles in Fluidized Beds of Electrically Conducting Particles," *Fluidization Technology,* Keairns, D. L., ed., Hemisphere Publishing, Washington, D. C., Vol. 1, pp. 115–167.

Ceccio, S. L., and Brennen, C. E., 1991, "Observations of the Dynamics and Acoustics of Traveling Bubble Cavitation," *Journal of Fluid Mechanics,* Vol. 233, pp. 633–660.

Ceccio, S. L., and Brennen, C. E., 1992, "Dynamics of Attached Cavities on Bodies of Revolution," ASME JOURNAL OF FLUIDS ENGINEERING, Vol. 114, pp. 93–99.

Chang, J. S., Girard, R., Raman, R., and Tran, F. B. P., 1984, "Measurement of Void Fraction in Vertical Gas-Liquid Two-Phase Flow by Ring Type Capacitance Transducers," *Mass Flow Measurements-1984,* Hedrick, T. R., and Reimer, R. M., eds., ASME, New Orleans, FED-Vol. 17, pp. 93–99.

Cheremisinoff, N. P., 1977, "An Experimental and Theoretical Investigation of Horizontal Stratified and Annular Two-Phase Flow with Heat Transfer," Ph.D. thesis, Clarkson College of Technology, Potsdam, NY.

Cheremisinoff, N. P., 1986, *Instrumentation for Complex Fluid Flows,* Technomic Publishing Inc., Lancaster, PA, pp. 73–103.

Clark, N. N., Seiss, R., and Turton, R., 1992, "Probe Measurements in Gas-Liquid Systems," *Flow Measurement and Instrumentation,* Vol. 3, pp. 17–23.

Coney, M. W. E., 1978, "The Theory and Application of Conductance Probes for the Measurement of Liquid Film Thickness in Annular Gas-Liquid Flows," *Canadian Journal of Chemistry,* Vol. 56, pp. 754–757.

Cranfield, R. R., 1972, "A Probe for Bubble Detection and Measurement in Large Particle Fluidised Beds," *Chemical Engineering Science,* Vol. 27, pp. 239–245.

Das, R. K., and Pattanayak, S., 1993, "Electrical Impedance Method for Flow Regime Identification in Vertical Upward Gas-Liquid Two-Phase Flow," *Measurement Science and Technology,* Vol. 4, pp. 1457–1463.

Delil, A. A. M., 1987, "Feasibility Demonstration of a Sensor for High-Quality Two-Phase Flow," Report No. NLR TR 87009 U, National Aerospace Laboratory, Amsterdam, the Netherlands, pp. 8–13.

Dickin, F. J., Williams, R. A., and Beck, M. S., 1993, "Determination of Composition and Motion of Multicomponent Mixtures in Process Vessels using Electrical Impedance Tomography-I. Principles and Process Engineering Applications," *Chemical Engineering Science,* Vol. 48, pp. 1883–1897.

Fasching, G. E., and Smith, N. S., Jr., 1991, "A Capacitive System for Three-Dimensional Imaging of Fluidized Beds," *Review of Scientific Instruments,* Vol. 62, pp. 2243–2251.

Geraets, J. J. M., and Borst, J. C., 1988, "A Capacitance Sensor for Two-Phase Void Fraction Measurement and Flow Pattern Identification," *International Journal of Multiphase Flow,* Vol. 14, pp. 305–320.

Gunn, D. J., and Al-Doori, H. H., 1985, "The Measurement of Bubble Flows in Fluidized Beds by Electrical Probes," *International Journal of Multiphase Flow,* Vol. 11, pp. 535–551.

Hardy, J. E., and Hylton, J. O., 1984, "Electrical Impedance String Probes for Two-Phase Void and Velocity Measurements," *International Journal of Multiphase Flow,* Vol. 10, pp. 541–556.

Hewitt, G. F., 1978, *Measurement of Two Phase Flow Parameters,* Academic Press, London, pp. 57–60, 182.

Hua, P., Webster, J. G., and Tompkins, W. J., 1987, "Effect of the Measurement Method on Noise Handling and Image Quality of EIT Imaging," *Proceedings of the Annual International Conference of the IEEE Engineering in Medicine and Biology Society,* IEEE, Boston, Vol. 3, pp. 1429–1430.

Huang, S. M., Xie, C. G., Thorn, R., Snowden, D., and Beck, M. S., 1992, "Design of Sensor Electronics for Electrical Capacitance Tomography," *IEE Proceedings: Part G,* Vol. 139, pp. 83–88.

Isaacson, D., and Cheney, M., 1990, "Current Problems in Impedance Imaging," *Inverse Problems in Partial Differential Equations,* Coliton, D., Ewing, R., and Rundell, W., eds., SIAM, Philadelphia, pp. 141–149.

Jones, O. C., and Delhaye, J., 1976, "Transient and Statistical Measurement Techniques for Two-Phase Flows: A Critical Review," *International Journal of Multiphase Flow,* Vol. 3, pp. 89–116.

Jones, O. C., Lin, J. T., and Ovacik, L., 1992, "Investigation of Electrical Impedance Imaging Relative to Two-Phase, Gas-Liquid Flows," *Chemical Engineering Communications,* Vol. 118, pp. 299–325.

Jones, O. C., Lin, J. T., Ovacik, L., and Shu, H., 1993, "Impedance Imaging Relative to Gas-Liquid Systems," *Nuclear Engineering and Design,* Vol. 141, pp. 159–176.

Jones, O. C., Lin, J. T., Shu, H., Ovacik, L., and He, Y., 1994, "Impedance Imaging Relative to Binary Mixtures," *Fifth International Symposium on Liquid-Solid Flows,* ASME, Lake Tahoe, NV.

Jones, O. C., 1995, private communication.

Kataoka, I., Ishii, M., and Serizawa, A., 1986, "Local Formulation and Measurements of Interfacial Area Concentration in Two-Phase Flow," *International Journal of Multiphase Flow,* Vol. 12, pp. 505–529.

Kataoka, I., and Serizawa, A., 1990, "Interfacial Area Concentration in Bubbly Flow," *Nuclear Engineering and Design,* Vol. 120, pp. 163–180.

Kelessidis, V. C., and Dukler, A. E., 1989, "Modeling Flow Pattern Transitions for Upward Gas-Liquid Flow in Vertical Concentric and Eccentric Annuli," *International Journal of Multiphase Flow,* Vol. 15, pp. 173–191.

Keska, J. K., 1990, "Some Methodical and Experimental Aspects of Measurement of a Void Fraction in Gas-Liquid Flows," *Advances in Gas Liquid Flows,* Kim, J. H., Rohatgi, U. S., and Hashemi, A., eds., ASME, Dallas, pp. 139–145.

Khan, S. H., and Abdullah, F., 1993, "Finite Element Modelling of Multielectrode Capacitive Systems for Flow Imaging," *IEE Proceedings: Part G,* Vol. 140, pp. 216–222.

Kim, Y., Webster, J. G., and Tompkins, W. J., 1983, "Electrical Impedance Imaging of the Thorax," *Journal of Microwave Power,* Vol. 18, pp. 245–257.

Kim, M., and Kang, H., 1990, "The Development of a Flush-Wire Probe and Calibration Technique for Measuring Liquid Film Thickness," *Advances in Gas Liquid Flows,* Kim, J. H., Rohatgi, U. S., and Hashemi, A., eds., ASME, Dallas, pp. 131–138.

Klug, F., and Mayinger, F., 1993, "Novel Impedance Measuring Technique for Flow Composition in Multi-phase Flows," *ANS Proceedings: 1993 National Heat Transfer Conference,* American Nuclear Society, Atlanta, pp. 76–83.

Koskie, J. E., Mudawar, I., and Tiederman, W. G., 1989, "Parallel-Wire Probes for the Measurement of Thick Liquid Films," *International Journal of Multiphase Flow,* Vol. 15, pp. 521–530.

Kytömaa, H. K., and Brennen, C. E., 1991, "Small Amplitude Kinematic Wave Propagation in Two-Component Media," *International Journal of Multiphase Flow,* Vol. 17, pp. 13–26.

Kytömaa, H. K., 1987, "Stability of the Structure in Multicomponent Flows," Report No. E200.24, Division of Engineering and Applied Science, California Institute of Technology, Pasadena, CA.

Lamarre, E., and Melville, W. K., 1992, "Instrumentation for the Measurement of Void-Fraction in Breaking Waves: Laboratory and Field Results," *IEEE Journal of Oceanic Engineering,* Vol. 17, pp. 204–215.

Lemonnier, H., Nakach, R., Favreau, C., and Selmer-Olsen, S., 1991, "Sensitivity Analysis of an Impedance Void Meter to the Void Distribution in Annular Flow: a Theoretical Study," *Nuclear Engineering and Design,* Vol. 126, pp. 105–112.

Lin, J.-T., Jones, O. C., Ovacik, L., and Shu, H.-J., 1993, "Advances in Impedance Imaging Relative to Two-Phase Flow," *ANS Proceedings: 1993 National Heat Transfer Conference,* American Nuclear Society, Atlanta, pp. 68–75.

Lin, P. Y., and Hanratty, T. J., 1987, "Detection of Slug Flow From Pressure Measurements," *International Journal of Multiphase Flow,* Vol. 13, pp. 13–21.

Maxwell, J., 1881, *A Treatise on Electricity and Magnetism,* Clarendon Press, Oxford, England.

Merilo, M., Dechene, R. L., and Cichowlas, W. M., 1977, "Void Fraction Measurement with a Rotating Electric Field Conductance Gauge," ASME *Journal of Heat Transfer,* Vol. 99, pp. 330–332.

Miya, M., Woodmansee, D. E., and Hanratty, T. J., 1971, "A Model for Roll Waves in Gas-Liquid Flow," *Chemical Engineering Science,* Vol. 26, pp. 1915–1931.

Nasr-El-Din, H., Shook, C. A., and Colwell, J., 1987, "A Conductivity Probe for Measuring Local Concentrations in Slurry Systems," *International Journal of Multiphase Flow,* Vol. 13, pp. 365–378.

Olsen, H. O., 1967, "Theoretical and Experimental Investigations of Impedance Void Meters," Report No. 118, Institutt for Atomenergi, Kjeller Research Establishment, Kjeller, Norway.

Özgü, M. R., Chen, J. C., and Eberhardt, N., 1973, "A Capacitance Method for Measurement of Film Thickness in Two-Phase Flow," *Review of Scientific Instruments,* Vol. 44, pp. 1714–1716.

Plaskowski, A., Beck, M. S., Thorn, R., and Dyakowski, T., 1995, *Imaging Industrial Flows: Applications of Electrical Process Tomography,* Institute of Physics Publishing, Bristol, England, pp. 127–141.

Revankar, S. T., and Ishii, M., 1992, "Local Interfacial Area Measurement in Bubbly Flow," *International Journal of Heat and Mass Transfer,* Vol. 35, pp. 913–925.

Revankar, S. T., and Ishii, M., 1993, "Theory and Measurement of Local Interfacial Area Using a Four Sensor Probe in Two-Phase Flow," *International Journal of Heat and Mass Transfer,* Vol. 36, pp. 2997–3007.

Rowe, P. N., and Masson, H., 1980, "Fluidised Bed Bubbles Observed Simultaneously by Probe and X-rays," *Chemical Engineering Science,* Vol. 35, pp. 1443–1447.

Rowe, P. N., and Masson, H., 1981, "Interaction of Bubble with Probes in Gas Fluidised Beds," *Transactions of the Institution of Chemical Engineers,* Vol. 59, pp. 177–185.

Ruder, Z., Hanratty, P. J., and Hanratty, T. J., 1989, "Necessary Condition for the Existence of Stable Slugs," *International Journal of Multiphase Flow,* Vol. 15, pp. 209–226.

Saiz-Jabardo, J. M., and Boure, J. A., 1989, "Experiments on Void Fraction Waves," *International Journal of Multiphase Flow,* Vol. 15, pp. 483–493.

Seagar, A. D., Barber, D. C., and Brown, B. H., 1987, "Electrical Impedance Imaging," *IEE Proceedings: Part A,* Vol. 134, pp. 201–210.

Snell, C. C., Dechene, R. L., and Newton, R. E., 1978, "Two-Phase Relative Volume Fraction Measurement with a Rotating Field Conductance Gauge," *Measurements in Polyphase Flows,* Stock, D. E., ed., ASME, San Francisco, pp. 21–24.

Teyssedou, A., and Tapucu, A., 1988, "Impedance Probe to Measure Local Void Fraction Profiles," *Review of Scientific Instruments,* Vol. 59, pp. 631–638.

Tournaire, A., 1986, "Dependence of the Instantaneous Response of Impedance Probes on the Local Disturbance of the Void Fraction in a Pipe," *International Journal of Multiphase Flow,* Vol. 12, pp. 1019–1024.

van der Welle, R., 1985, "Void Fraction, Bubble Velocity and Bubble Size in Two-Phase Flow," *International Journal of Multiphase Flow,* Vol. 11, pp. 317–345.

Wang, Y. W., Pei, B. S., and Lin, W. K., 1991, "Verification of Using a Single Void Fraction Sensor to Identify Two-Phase Flow Patterns," *Nuclear Technology,* Vol. 95, pp. 87–94.

Warrier, G. R., and Nguyen, T., 1993, "Void Fraction Investigation in Horizontal Gas-Liquid Two-Phase Flow," *Cavitation and Multiphase Flow Forum-1993,* Furuya, O., ed., ASME, Washington, D.C., FED-Vol. 153, pp. 53–62.

Webster, J. G., ed., 1990, *Electrical Impedance Tomography,* Adam Hilger, Bristol, England, pp. 1–20, 75–86, 175–200.

Werther, J., and Molerus, O., 1973, "The Local Structure of Gas Fluidized Beds-I. A Statistically Based Measuring System," *International Journal of Multiphase Flow,* Vol. 1, pp. 103–122.

Wexler, A., Fry, B., and Neuman, M. R., 1985, "Impedance-Computed Tomography Algorithm and System," *Applied Optics,* Vol. 24, pp. 3985–3992.

Xie, C. G., Plaskowski, A., and Beck, M. S., 1989, "8-Electrode Capacitance System for Two-Component Flow Identification-Part 1: Tomographic Flow Imaging," *IEE Proceedings: Part A,* Vol. 136, pp. 173–183.

Xie, C. G., Plaskowski, A., and Beck, M. S., 1989, "8-Electrode Capacitance System for Two-Component Flow Identification-Part 2: Flow Regime Identification," *IEE Proceedings: Part A,* Vol. 136, pp. 184–190.

Xie, C. G., Stott, A. L., Plaskowski, A., and Beck, M. S., 1990, "Design of Capacitance Electrodes for Concentration Measurement of Two-Phase Flow," *Measurement Science and Technology,* Vol. 1, pp. 65–78.

Yorkey, T. J., Webster, J. G., and Tompkins, W. J., 1987, "Comparing Reconstruction Methods for Electrical Impedance Tomography," *IEEE Transactions on Biomedical Engineering,* Vol. 11, pp. 843–852.

Yoshida, K., Sakane, J., and Shimizu, F., 1982, "A New Probe for Measuring Fluidized Bed Characteristics at High Temperatures," *Industrial Engineering Chemistry Fundamentals,* Vol. 21, pp. 83–85.

S. Otsuka
Graduate Student,
Osaka University,
Engineering Science,
Osaka, Japan

Y. Tsujimoto
Professor at Osaka University,
and
Visiting Researcher
at National Aerospace Laboratory,
Toyonaka, Osaka 560, Japan

K. Kamijo[1]
Director,
Rocket Propulsion Division,
National Aerospace Laboratory,
Kakuda Research Center,
Miyagi, Japan

O. Furuya
President,
OF TECHnologies, Inc.,
Pasadena, CA

Frequency Dependence of Mass Flow Gain Factor and Cavitation Compliance of Cavitating Inducers

Unsteady cavitation characteristics are analyzed based on a closed cavity model in which the length of the cavity is allowed to oscillate. It is shown that the present model blends smoothly into quasi-steady calculations at the low frequency limit, unlike fixed cavity length models. Effects of incidence angle and cavitation number on cavitation compliance and mass flow gain factor are shown as functions of reduced frequency. The cavity volume is evaluated by three methods and the results are used to confirm the accuracy and adequacy of the numerical calculations. By comparison with experimental data on inducers, it is shown that the present model can simulate the characteristics of unsteady-cavitation qualitatively.

Introduction

Unsteady characteristics of cavitating inducers were extensively studied in the 1970's in relation to "POGO" instability which is a hydraulic system instability in the liquid rocket propellant feed line coupled with structural vibration (Rubin, 1966). At an early stage, only cavitation compliance received attention. In the middle of the 1970's, however, it was realized that another characteristic of cavitation called "flow gain" or "mass flow gain factor" plays an important role (Young et al., 1972) in instability of the hydraulic system including cavitating pumps (cavitation surge), and efforts were made to evaluate this factor.

Recently, it was found that another type of cavitation instability can cause shaft vibration of rocket pumps, i.e., rotating cavitation (Kamijo et al., 1993), which was also found to be caused by the positive mass flow gain factor (Tsujimoto et al., 1993). For the prediction of rotating cavitation, we need information about cavitation compliance and mass flow gain factor at significantly higher frequencies. Studies to date, however, have been limited to low frequencies relevant to surge analysis.

Most analytical studies have been made under quasi-steady assumptions (Brennen and Acosta (1973), (1976)). The first study employing fully unsteady treatment was made by Kim and Acosta (1976) who established the mathematical formulation for this type of problem. It should be noted, however, that they and later Nishiyama and Nishiyama (1980) assumed a fixed cavity length. Acosta and Furuya (1979) have clearly shown that such assumption does not allow the flow to blend smoothly into quasi-steady calculations.

All of the above-cited studies deal with attached blade surface cavitations. Although it is clear that other forms of cavitation

(e.g., bubble cavitation, vortex cavitation, and tip clearance cavitation), can, in practice, contribute to the dynamic characteristics, the present paper treats only blade surface cavitation.

The fundamental mathematical formulation of the present study was made by Furuya (1982) to allow the cavity length to oscillate. Unfortunately, a low frequency assumption was made in his study and no numerical results were given. In the present study, therefore, an attempt has been made to remove the assumption of low frequency and numerical results are given up to high frequencies required for the analysis of rotating cavitation. We treat here partial cavitations in a two-dimensional semi-infinite cascade, assuming applications to inducers.

Outline of Mathematical Formulation

The purpose of the present calculations is to obtain the change of the blade surface cavity volume in a two-dimensional semi-infinite cascade flow, as shown in Fig. 1, in response to the inlet pressure and velocity fluctuations normal to the cascade axis. The velocity components in the (x, y) directions are linearized around the uniform steady flow U by writing

$$q = (U + u, v)$$
$$u = u_s + \tilde{u}e^{j\omega t}$$
$$v = v_s + \tilde{v}e^{j\omega t} \tag{1}$$

with assumptions of both steady (subscript s) and unsteady (superscript $\tilde{\ }$) disturbances being small. We map the complex conjugate velocity disturbance $w = u - iv$ around a blade onto the upper half of the $\zeta = \xi + i\eta$ plane by the following mapping function:

$$z = \frac{d}{2\pi} \left\{ e^{-i\gamma} \ln\left(1 - \frac{\zeta}{\zeta_1}\right) + e^{i\gamma} \ln\left(1 - \frac{\zeta}{\bar{\zeta}_1}\right) \right\} \tag{2}$$

The flow field in the ζ-plane is shown in Fig. 2 in which the respective points are shown by the same letters as in Fig. 1.
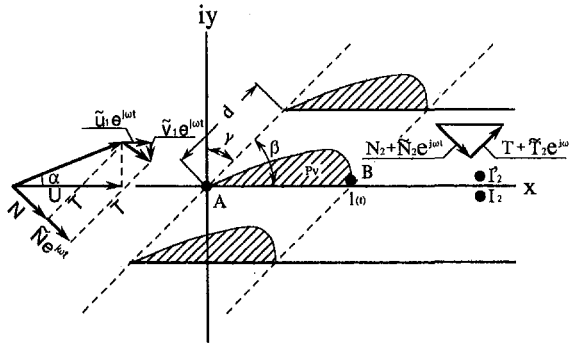
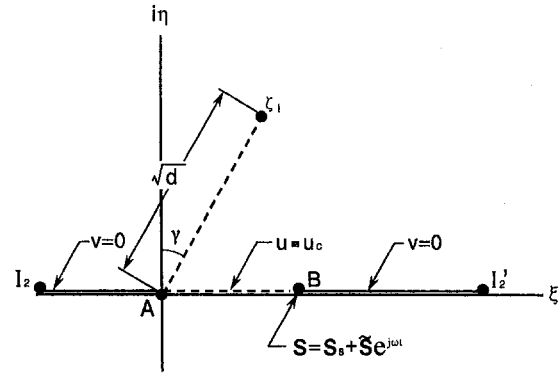**Fig. 1 Flow configuration at pulsating cavity in cascade**

Fig. 2 An auxillary plane, $\zeta = \xi + i\eta$, where the flow field is mapped onto the upper half plate

Complex Conjugate Velocity. Redefining u-velocity and pressure on the cavity surface as

$$u_c = u_{cs} + \tilde{u}_c e^{j\omega t}$$

$$p_c = p_v \tag{3}$$

and substituting these expressions into the x-component of the momentum equation, we find

$$j\omega\tilde{u}_c + U\frac{d\tilde{u}_c}{dx} = 0 \tag{4}$$

and thus

$$\tilde{u}_c = \tilde{g}e^{-jkx/l_s} \tag{5}$$

$$k = \frac{\omega l_s}{U} \tag{6}$$

where k is a reduced frequency and $\tilde{g}$ is an unknown constant. The cavity length l is allowed to oscillate around a steady-state value of l_s:

$$l = l_s + \tilde{l}e^{j\omega t}$$

The cavitation number is defined as

$$\sigma = \frac{p_{1s} - p_v}{1/2\rho U^2} \tag{7}$$

and the upstream infinity pressure is written as

$$p_1 = p_{1s} + \tilde{p}_1 e^{j\omega t}$$

The steady part of u_c in Eq. (3) is determined from the steady component of Bernoulli's equation:

$$u_{cs} = \frac{\sigma U}{2} \tag{8}$$

On the wetted part of the blade surface, we should apply the flow tangency condition:

$$v = 0 \tag{9}$$

By using an analytical continuation to the lower half of the ζ plane and Plemelj's formula, we find the complex conjugate velocity disturbance $w = u - iv$ with appropriate singularities at the leading edge and cavity terminus, satisfying the boundary conditions of Eqs. (5), (8), and (9) to be as follows:

$$w(\zeta, t) = \frac{1}{\sqrt{\zeta(\zeta - s(t))}} \left(\frac{\sigma U}{2\pi} \int_0^{s(t)} \frac{\sqrt{\xi'(s(t) - \xi')}}{\xi' - \zeta} d\xi' \right.$$

$$\left. + \frac{\tilde{g}e^{j\omega t}}{\pi} \int_0^{s(t)} \frac{\sqrt{\xi'(s(t) - \xi')}}{\xi' - \zeta} e^{-jkx(\xi')/l_s} d\xi' + A + B\zeta \right) \tag{10}$$

where A and B are unknown real constants with respect to i and represented by

$$A = A_s + \tilde{A}e^{j\omega t}$$

$$B = B_s + \tilde{B}e^{j\omega t} \tag{11}$$

which are determined in the following section. $s(t)$ is the time dependent cavity length in the mapping plane.

Nomenclature

d = cascade blade spacing
i = imaginary index in spatial domain
j = imaginary index in time domain
k = reduced frequency ($\omega l_s/U$)
K = cavitation compliance
l = cavity length
M = mass flow gain factor
N = flow velocity component normal to the axis of the cascade
p = pressure
$q = (U + u, v)$
s = the coordinate on the ξ-axis corresponding to the end point of the cavity
t = time
T = flow velocity component parallel to the axis of the cascade

U = upstream uniform velocity in the x direction
u = perturbed velocity component in the x direction
v = perturbed velocity component in the y direction
w = perturbed complex conjugate velocity ($u - iv$)
α = flow incidence angle with the x axis
β = vane angle = $(\pi/2) - \gamma$
γ = geometric stagger angle of the cascade
ζ = transform plane ($\xi + i\eta$)
ξ = horizontal coordinate in ζ-plane
η = vertical coordinate in the ζ-plane and cavity boundary coordinate in the z-plane

ρ = fluid density
σ = cavitation number
τ = transformed variable
ω = angular velocity of fluctuation

Superscript
$\sim$ = fluctuating quantities

Subscripts
c = cavity
s = steady state
1 = upstream infinity
2 = downstream infinity
v = vapor

Determination of Flow

We assume

$$s(t) = s_s + \tilde{s}e^{j\omega t} \tag{12}$$

in the mapping plane. Then we have the following unknowns.

- Steady components

$$-s_s, A_s \text{ and } B_s$$

- Unsteady components

$$-\tilde{s}, \tilde{A}, \tilde{B}, \text{ and } \tilde{g}$$

These constants are determined by the following:

- Velocity disturbances at upstream infinity (2 conditions, corresponding to u and v)
- Cavity closure

For unsteady components, we should use the following relation in addition to the above,

- The condition specifying the upstream pressure fluctuation.

For steady components, the condition of upstream pressure has already been incorporated through Eq. (8).

Upstream Velocity. We consider the velocity fluctuation $\tilde{N}_1$, which is normal to the cascade axis as shown in Fig. 1, and correspond to the flow rate fluctuation through the impeller. Then the velocity disturbances at $x = -\infty$ are $(u_{1s}, v_{1s}) = (0, T\cos\gamma - N_1\sin\gamma)$ and $(\tilde{u}_1, \tilde{v}_1) = (\tilde{N}_1\cos\gamma, -\tilde{N}_1\sin\gamma)$, with the nondisturbed flow $U = N_1\cos\gamma + T\sin\gamma$ and $\alpha = \tan^{-1}(v_{1s}/U)$. On the other hand, the velocity disturbance at $x = -\infty$ is given by $w(\zeta_1)$. To facilitate the integrations in Eq. (10), we employ

$$\xi = \frac{s(t)}{2}(\tau + 1) \tag{13}$$

Then the unsteady cavity surface $0 < \xi < s(t)$ comes to $-1 < \tau < 1$, which is no longer time dependent. This transformation allows us to treat cavities with fluctuating length. After this transformation, we separate steady and unsteady components under the assumption that the unsteady components are small. After all, the boundary conditions at upstream infinity can be represented as follows:

Steady Part

$$-i(T\cos\gamma - N_1\sin\gamma) = \frac{1}{\sqrt{\zeta_1(\zeta_1 - s_s)}}$$

$$\times \left(\frac{\sigma U}{8\pi}s_s^2 \int_{-1}^{1} \frac{\sqrt{1 - \tau'^2}}{-\zeta_1 + s_s(\tau' + 1)/2}d\tau' + A_s + B_s\zeta_1 \right) \tag{14}$$

Unsteady Part

$$\tilde{N}_1\cos\gamma + i\tilde{N}_1\sin\gamma = \frac{1}{\sqrt{\zeta_1(\zeta_1 - s_s)}}\left\{ \frac{1}{2}\frac{\tilde{s}}{\zeta_1 - s_s} \right.$$

$$\times \left(\frac{\sigma U}{8\pi}s_s^2 \int_{-1}^{1} \frac{\sqrt{1 - \tau'^2}}{-\zeta_1 + s_s(\tau' + 1)/2}d\tau' + A_s + B_s\zeta_1 \right)$$

$$+ \frac{\sigma U}{2\pi}\left(\frac{s_s}{2} \int_{-1}^{1} \frac{\sqrt{1 - \tau'^2}}{-\zeta_1 + s_s(\tau' + 1)/2}d\tau' \right.$$

$$\left. - \frac{s_s^2}{8} \int_{-1}^{1} \frac{\sqrt{1 - \tau'^2}(\tau' + 1)}{(-\zeta_1 + s_s(\tau' + 1)/2)^2}d\tau' \right)\tilde{s}$$

$$+ \frac{s_s^2}{4\pi}\tilde{g}\int_{-1}^{1} \frac{\sqrt{1 - \tau'^2}}{-\zeta_1 + s_s(\tau' + 1)/2}$$

$$\times e^{-jkx(\tau')/l_s}d\tau' + \tilde{A} + \tilde{B}\zeta_1 \right\} \tag{15}$$

Note that Eqs. (14) and (15) are both complex and we now have two conditions each, corresponding to u and v velocity components. Unlike Furuya's original formulation (1982), no expansion in terms of k was made in the present analysis so that it can be applied to higher frequency fluctuations.

Closure Condition. The kinematical boundary condition on the cavity surface $y = \eta(x, t)$ is

$$\frac{\partial\eta}{\partial t} + U\frac{\partial\eta}{\partial x} = v_c(x, t) \tag{16}$$

The solution to this equation is given by

$$\eta(x, t) = \frac{1}{U}\int_0^x v_c\left(\hat{x}, t - \frac{x - \hat{x}}{U} \right)d\hat{x}$$

$$= \eta_s(x(\tau, t)) + \tilde{\eta}(x(\tau, t))e^{j\omega t} \tag{17}$$

$$\xi(\hat{x}(t)) = \frac{s(t)}{2}(\hat{\tau} + 1)$$

$$\xi(x(t)) = \frac{s(t)}{2}(\tau + 1) \tag{18}$$

where $v_c(\hat{x}, t')$ with $t' = t - (x - \hat{x})/U$ is given by $-\text{Imag}(w(\xi(\hat{x}), t')$. The second expression of Eq. (17) is obtained by using the transformations of Eqs. (18) and evaluating the cavity thickness at a position with fixed τ. The cavity closure condition is

$$\eta(l(t), t) = 0 \tag{19}$$

Using the transformation $\xi' = s(t)(\tau' + 1)/2$ and noting that v_c should be evaluated at time $t' = t - (x - \hat{x})/U$, we obtain the following expressions of the closure condition after linearization:

Steady Part

$$0 = \left(A_s + \frac{B_s s_s}{2} \right)\int_{-1}^{1} \sqrt{\frac{1 + \hat{\tau}}{1 - \hat{\tau}}}\frac{1}{h}d\hat{\tau}$$

$$+ \frac{s_s}{2}\left(B_s - \frac{\sigma U}{2} \right)\int_{-1}^{1} \sqrt{\frac{1 + \hat{\tau}}{1 - \hat{\tau}}}\frac{\hat{\tau}}{h}d\hat{\tau} \tag{20}$$

Unsteady Part

$$0 = C_{31}\tilde{A} + C_{32}\tilde{B} + C_{33}\tilde{g} + C_{34}\tilde{s} \tag{21}$$

where $C_{31} - C_{34}$ and h are given in Appendix A.

For the steady components, the closure condition can also be represented through the continuity relation at upstream ($\zeta = \zeta_1$) and downstream ($\zeta = \infty$) infinity. This relation is represented by

$$B_s = \left(\frac{\sin^2\gamma}{\cos^2\gamma} - \sin\gamma\frac{\tan\alpha\cos\gamma + \sin\gamma}{\cos\gamma - \tan\alpha\sin\gamma} \right)N_1 \tag{22}$$

In the present study, Eq. (22) is used to determine the flow, and Eq. (20) is used to confirm the accuracy of numerical calculation. For the unsteady component, the continuity relation includes the change in cavity volume. Closure condition (21) is used for the determination of unknown parameters and the continuity relation is used for confirmation of accuracy as will be discussed later.

Pressure Condition. Through the integration of the x component of the linearized Euler's equation from $x = -\infty$ to $x = 0$, we obtain

$$\int_{-\infty}^{0} j\omega\tilde{u}e^{j\omega t}dx + U(u_s + \tilde{u}e^{j\omega t})|_{-\infty}^{0} = -\frac{1}{\rho}(p_v - p_1)$$

Applying partial integration and using the conditions at upstream infinity and on the cavity, the unsteady part of the above equation yields

$$-j\omega\int_{-\infty}^{0} x\frac{d\tilde{u}}{dx}dx + U(\tilde{g} - \cos\gamma\tilde{N}_1) = \frac{\tilde{p}_{1p}}{\rho} \quad (23)$$

where

$$\tilde{p}_{1p} = \tilde{p}_1 - \lim_{x\to\infty}(-j\omega\rho\tilde{u}x)$$

is the pressure fluctuation at the pump inlet, indicated by $\tilde{\sigma} = \tilde{p}_{1p}/\frac{1}{2}\rho U^2$ after linearization. For the steady part, Eqs. (7) and (8) correspond to this relation. Since $\tilde{u}$ can be represented in terms of $\tilde{A}$, $\tilde{B}$, $\tilde{g}$, and $\tilde{s}$, we can express Eq. (23) as follows:

$$-j\omega J_1\tilde{A} - j\omega J_2\tilde{B} + (U - j\omega J_3)\tilde{g} - j\omega J_4$$
$$= U\tilde{N}_1\cos\gamma + \frac{\tilde{p}_{1p}}{\rho} \quad (24)$$

where $J_1 - J_4$ are infinite integrals given in Appendix B. For the calculations of cavitation compliance or mass flow gain factor, conditions $\tilde{N}_1 = 0$ and $\tilde{p}_{1p} = 0$ are, respectively, used.

The unknowns and equations which can be used to determine them can be summarized as follows:

Steady components $(s_s, A_s$ and $B_s)$

• Real and imaginary parts of Eq. (14), Eq. (22)

Unsteady component $(\tilde{s}, \tilde{A}, \tilde{B}$ and $\tilde{g})$

• Real and imaginary parts of Eq. (15), Eqs. (21) and (24)

Cavitation Compliance and Mass Flow Gain Factor

By representing the cavity area V_c as

$$V_c = \int_0^{l(t)} \eta(x, t)dx = V_{cs} + \tilde{V}_c e^{j\omega t} \quad (25)$$

we can define cavitation compliance K and mass flow gain factor M as follows:

$$K = -\frac{\partial(V_c/d^2)}{\partial\sigma} = -\frac{(\tilde{V}_c/d^2)_{\tilde{N}_1=0}}{\tilde{p}_{1p}/\frac{1}{2}\rho U^2} \quad (26)$$

$$M = -\frac{\partial(V_c/d^2)}{\partial(N_1/U)} = -\frac{(\tilde{V}_c/d^2)_{\tilde{p}_{1p}=0}}{\tilde{N}_1/U} \quad (27)$$

Note that K and M are generally complex.

In some cases, K and M are defined using $\sqrt{N^2 + T^2}$ or T in place of the representative speed U of the present paper. However, for the practical cases with small α and β, the difference in the definition results in only a small difference in the results.

Evaluation of Cavity Volume Fluctuation. The cavity volume fluctuation $\tilde{V}_c$ was evaluated using the following three methods:

(a) Integration of cavity thickness. Direct integration of Eq. (17) gives the following expression of $\tilde{V}_c$

Journal of Fluids Engineering
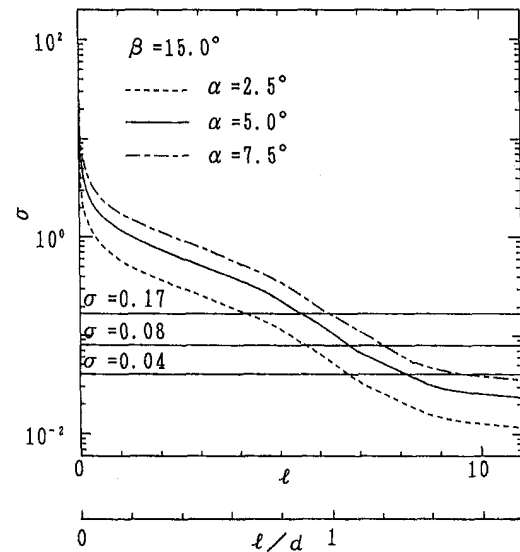
Fig. 3 The relation between steady cavity length l and cavitation number σ for incident angles α = 2.5, 5.0 and 7.5 degrees

$$\tilde{V}_{c1} = \frac{\cos\gamma}{4\pi}s_s^2\int_{-1}^{1}\tilde{\eta}(\hat{\tau})\frac{\hat{\tau}+1}{h}d\hat{\tau}$$
$$+ \frac{\cos\gamma}{4\pi}s_s\int_{-1}^{1}\left(\frac{h'}{h}+2\right)\eta_s(\hat{\tau})\frac{\hat{\tau}+1}{h}d\hat{\tau}\tilde{s} \quad (28)$$

The second term appears from $\eta_s(x(\tau, t))$ since we evaluated the velocity at $\tau = 2\xi(x)/s(t) - 1$ which is fixed on the cavity surface but moving in the physical plane in accord with the change in cavity length.

(b) Integration of Eq. (16). If we integrate Eq. (16), we obtain

$$\frac{\partial}{\partial t}\int_0^{l(t)}\eta(x, t)dx + U\int_0^{l(t)}\frac{\partial\eta}{\partial x}dx = \int_0^{l(t)}v_c(x, t)dx \quad (29)$$

Since $\eta = 0$ at $x = 0$ and $l(t)$, we obtain

$$\tilde{V}_{c2} = \frac{1}{j\omega}\int_0^{l(t)}\tilde{v}_c(x, t)dx$$

Note that this equation is satisfied only when the cavity is closed.

(c) Continuity relation. If we apply the continuity relation in the physical plane, we obtain

$$\tilde{V}_{c3} = \frac{d}{j\omega}(\tilde{N}_2 - \tilde{N}_1) \quad (30)$$

where $\tilde{N}_2$ and $\tilde{N}_1$ can be obtained from Eq. (10) with $\zeta = \infty$ and $\zeta = \zeta_1$, respectively.

K and M evaluated from $\tilde{V}_{c1}$, $\tilde{V}_{c2}$ and $\tilde{V}_{c3}$ are represented by K_1, K_2, K_3 and M_1, M_2, M_3 respectively. By comparison of these values, we confirm cavity closure conditions, continuity, and the accuracy of numerical integration.

Results and Discussions

Results are presented for an inducer with the vane angle $\beta = 15$ deg (stagger $\gamma = 75$ deg). The spacing d is set to be 2π.

Steady-State Characteristics. Figure 3 shows the relation between cavity length l and cavitation number σ. The cavity shapes are shown in Fig. 4. We find that $-dl/d\sigma$ is larger for cavities with $l > 8$ for which the maximum thickness occurs at the locations where $x > d = 2\pi$. It was confirmed that $\eta(l)$ is less than 10^{-3}, which means that the present numerical

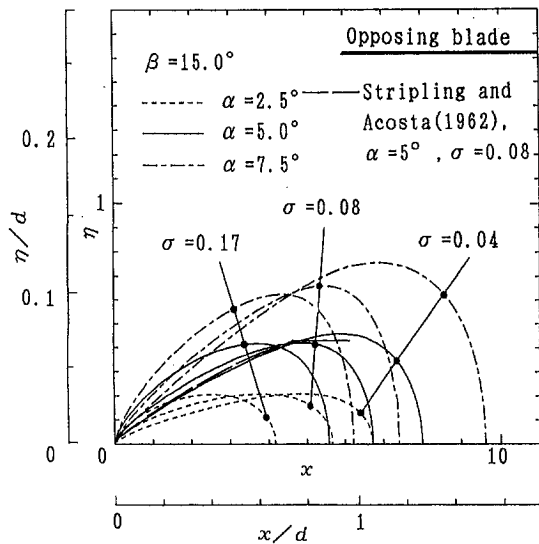Fig. 4 Steady cavity shapes under various conditions

Unsteady Cavitation Compliance. Figure 7(a) and (b) show the effects of incidence angle and mean cavitation number. Three values, K_1, K_2 and K_3 are plotted. There is reasonable agreement between them, showing that the accuracy of numerical integration is sufficient and that the cavity closure and the continuity relation are satisfied. We should note that they blend into the quasi-steady value at the limit of $k \to 0$. The phase is advanced slightly, near $k = 1$ for the cases with shorter cavities. This might be related to the shift of the cavity surface fluctuation from the standing wave type to the propagating wave type. This tendency becomes less significant for longer cavities. For $k \geq 2$, the phase is constantly delayed with the increase in k. With the increase of k, the amplitude or the absolute value of K increases for shorter cavities, and decreases for longer cavities in this frequency range. It is interesting to observe that K is nearly equal for the cases with ($\sigma = 0.08$, $\alpha = 2.5$ deg) and ($\sigma = 0.17$, $\alpha = 5$ deg) for which the steady cavity length is nearly equal but the thickness is quite

calculations have an accuracy such that the closure condition (20) is satisfied to this order. In Fig. 4, the cavity shape is compared with that of Stripling and Acosta (1962), in which an open cavity model was used. It is encouraging to find agreement in the shape of the front surface and general tendencies, irrespective of the difference of the models.

To check the validity of the present calculations, the shapes of the cavities from steady flow calculation and unsteady flow calculation with $\omega = 0$ are compared in Fig. 5 for the cases of fluctuations of incidence angle $\tilde{\alpha}$ and inlet pressure $\tilde{\sigma}$. The results of unsteady calculation are shown as the sum of η_s and $\tilde{\eta}e^{j\omega t}$. To obtain reasonable agreement, it is necessary to consider fluctuations of significantly small amplitude, especially for the case of inlet pressure fluctuation. Physically, this suggests the non-linear feature of the problem. However, it was confirmed that the steady calculations agree with the quasi-steady calculations if we reduce the amplitude of the fluctuation. Figure 5 also shows that the change in the cavity thickness at fixed x due to η_s is nicely and smoothly cancelled by that due to $\tilde{\eta}$. The present comparison assures the accuracy of the numerical integrations.

Unsteady Cavity Shape. Figure 6 shows the fluctuation of cavity shape. The upper figures show the instantaneous cavity shape for relatively large amplitude fluctuations of $\tilde{\sigma} = 0.025$ ((a), (b)) and of $\tilde{\alpha} = 0.5$ deg ((c), (d)). These values may be too large to be linear but were used to illustrate the characteristics of the cavity shape fluctuations. The lower figures show the fluctuation of cavity thickness $\Delta\eta$ at fixed chordwise location x. For this case, smaller amplitudes $\tilde{\sigma} = 0.0025$ and $\tilde{\alpha} = 0.1$ deg were used so as to preserve the linearity. (Nonlinearity appears in the present representation of linear calculation because of the curvature of cavity surface and $\eta_s(x(\tau, t))$.) Referring to Fig. 6(a) for inlet pressure fluctuation with $k = 0$, $\Delta\eta$ has the opposite sign depending on location x, either upstream or downstream of the location with maximum cavity thickness, just as in the case of a standing wave. This is because a change in inlet pressure results mainly in a change in cavity length, with a nearly constant maximum thickness as shown in Fig. 4. For the case of $k = 3$ (Fig. 6(b)), the cavity surface exhibits the propagating nature of waving motion downstream. For the case of incidence angle fluctuations with $k = 0$ (Fig. 6(c)), $\Delta\eta$ is almost linear with x and in phase, as can be understood from the steady cavity shape in Fig. 4. For $k = 3$, the cavity shape has some propagating characteristics but not as significant as for the case of inlet pressure fluctuation. Rather, the phase delay which is almost constant over the cavity is more significant.

Fig. 5(a) Change in incidence angle α (α = 5.0 deg, $\tilde{\alpha}$ = 0.1 deg)

Fig. 5(b) Change in cavitation number σ (σ = 0.17, $\tilde{\sigma}$ = 0.0025)

Fig. 5 Comparison of cavity shape from steady flow calculation and unsteady flow calculation with $\omega = 0$
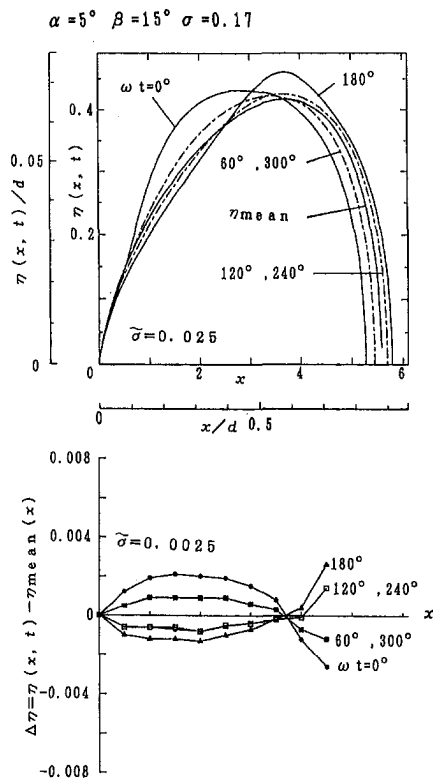
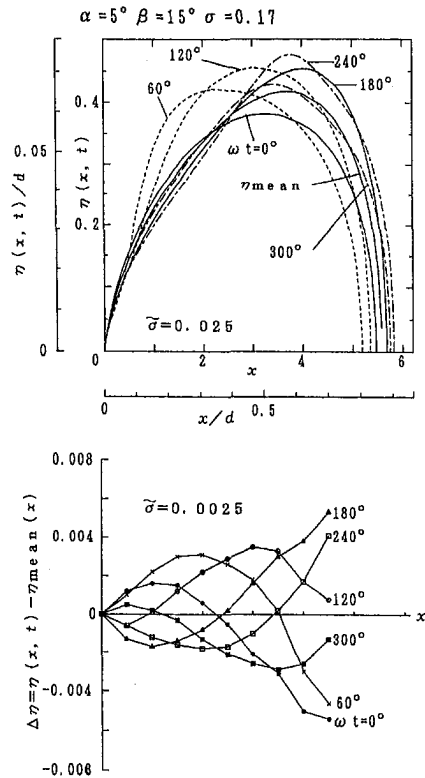Fig. 6(a) Inlet pressure fluctuation, $k = 0$

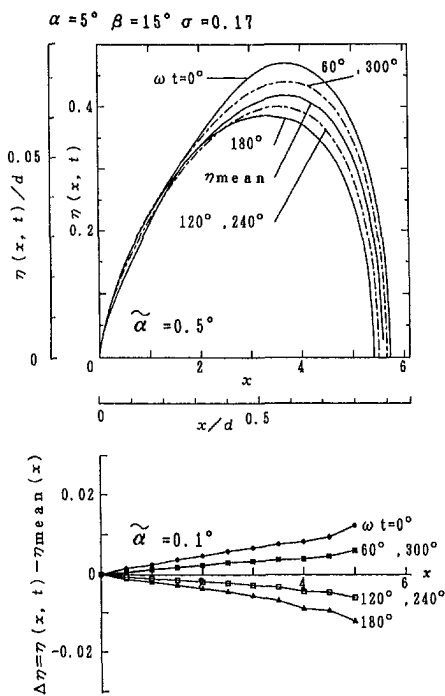Fig. 6(b) Inlet pressure fluctuation, $k = 3$

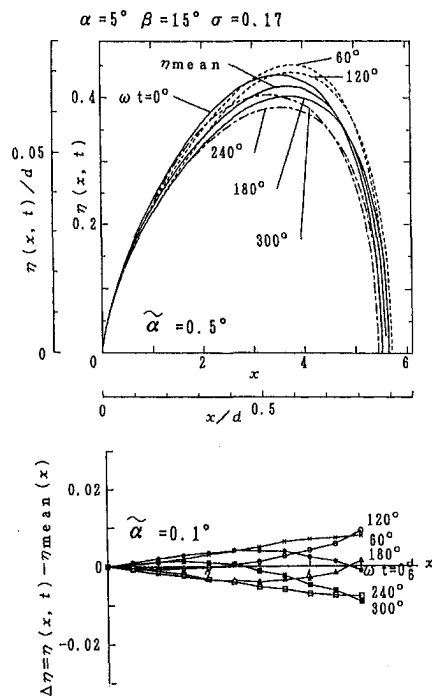Fig. 6(c) Incident angle fluctuation, $k = 0$

Fig. 6(d) Incident angle fluctuation, $k = 3$

Fig. 6 Unsteady cavity shape

different (see Fig. 4). Through further calculations, it was confirmed that $M(k)$ and $K(k)$ are dependent only on the steady cavity length l_s, rather than on σ and α.

Unsteady Mass Flow Gain Factor. We again observe agreement between the results of the three evaluation methods of cavity volume, as shown in Fig. 8. It smoothly blends into the quasi-steady value when $k \to 0$. Unlike cavitation compli-

ance, the phase is smoothly delayed with the increase in k. This corresponds to the smooth delay in cavity thickness as shown in Fig. 6(a) – (d). We observe a nearly identical M for the cases with ($\sigma = 0.08$, $\alpha = 2.5$ deg) and ($\sigma = 0.17$, $\alpha = 5$ deg) for which the steady cavity length is nearly the same.

Comparisons With Former Studies. Although not shown, it was confirmed that the present calculations agree with quasi-
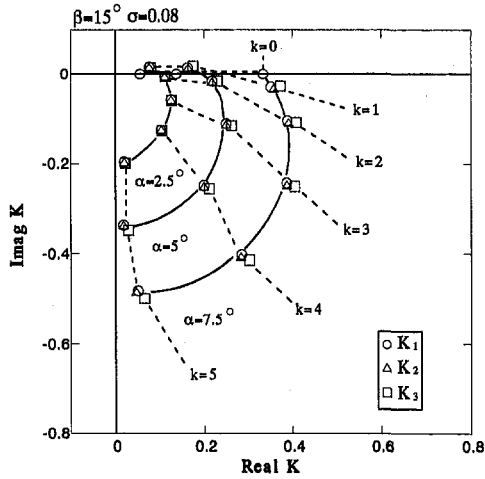
Fig. 7(a) Effects of incidence angle
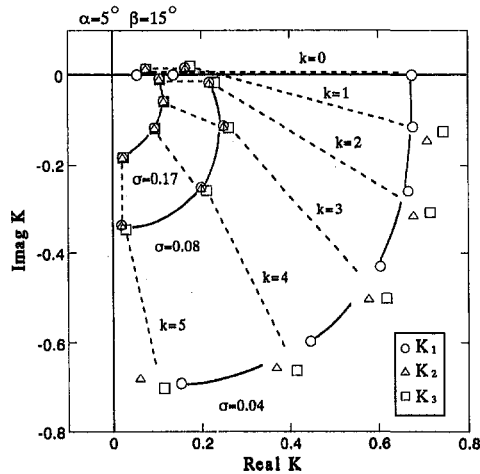
Fig. 7(b) Effects of cavitation number

Fig. 7 Unsteady cavitation compliance K

steady calculations by Brennen and Acosta (1973) at the limit of $k \to 0$. As to the comparison with unsteady calculations where the cavity length is fixed (Kim and Acosta, 1975, and Nishiyama and Nishiyama, 1980), they give different orders of magnitude. In particular, they do not have reasonable behavior at the limit of $k \to 0$ as shown by the present calculations.

In actual machines, the flow is highly three-dimensional, and such machines usually have large tip cavities with bubble cavitations. We cannot, therefore, expect quantitative agreement, but it is still interesting to compare general tendencies. This is done in Figs. 9(a) and (b). (Theoretical results are given for a cascade with $\beta = 10.27$ deg which is typical for modern inducers. Comparisons with Figs. 7 and 8 show the effects of β.) The data for the Space Shuttle Main Engine (SSME) low pressure oxidizer turbopump (LPOTP) are from the pioneering work of Brennen et al. (1982). They were obtained from independent sets of data on fluctuating pressure and flow rate at the inlet and outlet. The data for the 10.2 cm model in the literature are plotted here, although data for the 7.6 cm model have also been given. For the ARIANE V LOX inducer (Iacopozzi et al. 1993), a similar experimental method was applied, but only oscillating pressure measurements were utilized in order to avoid technical difficulties related to flow measurements. Although K and M are given as functions of reduced frequency $k^* = \omega d/U = k(d/l)$, there seems to be no systematic effect of k^*, and average values over k^* are plotted here. Both K and M are treated as real and are shown on the real axis. The data for the LE-7 LOX inducer (Shimura, 1993) were determined so that the peak frequency and the gain of a transfer

function of a linear model of the hydrauric system agrees with those from experiments. Quasi-steady assumptions were made and the results are shown on the real axis. Unfortunately experimental uncertainties are not given in all of the above-cited reports.

First let us consider K (Fig. 9(a)). Quasi-steady values for ARIANE V and LE-7 are significantly larger than the present calculations and the data of the SSME. The data for the 10.2 cm model of the SSME shown in the figure exhibit phase lag as the increase in k^*, while the 7.6 cm model (Brennen et al., 1982, not shown here) shows a decrease in the magnitude with a nearly constant phase.

The magnitudes of M (see Fig. 9(b)) are of the same order for all the cases. For the SSME, the phase lags at smaller σ but advances at larger σ. In the case of the 7.6 cm model (not shown here), the phase lags for all σ, and thus the phase lag in the present calculations is considered to be realistic.

Brennen (1978) proposed a bubbly flow model which predicts general tendencies of the transfer matrix fairly well. This model includes two empirical constants which are closely related to the magnitudes of the mass flow gain factor and cavitation compliance. A phase advance in K and a phase delay in M with the increase in k^* are predicted by the model.

The present theory predicts increases in the magnitudes of K and M with the decrease in σ, which is more significant with K. This tendency can be seen in the data of ARIANE V and LE-7.

Judging from the large discrepancies between the experiments, further experimental work appears to be needed to determine the frequency dependence and the relative importance of various kinds of cavitation. The authors hope that the present study can serve as a guideline for such studies.

Conclusion

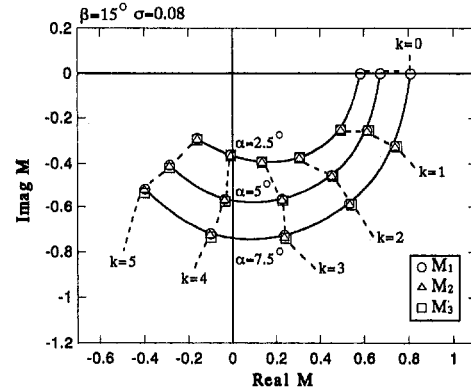Cavitation compliance and mass flow gain factor were obtained based on the closed cavity model in which the cavity

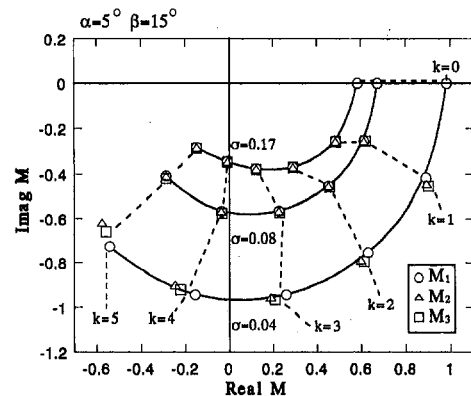
Fig. 8(a) Effects of incidence angle

Fig. 8(b) Effects of cavitation number
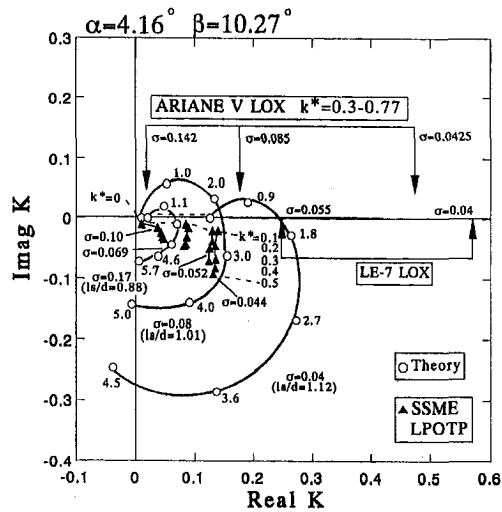
Fig. 8 Unsteady mass flow gain factor M
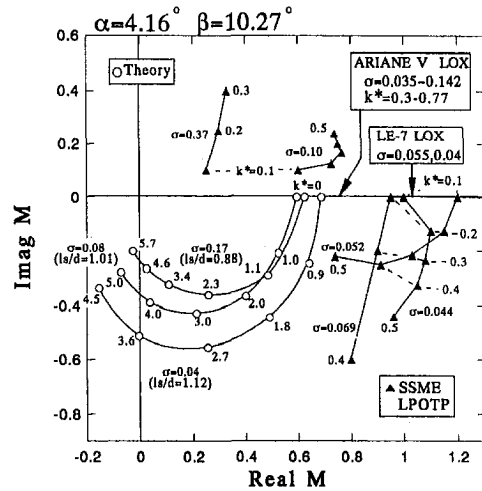
Fig. 9(a) Cavitation compliance K

Fig. 9(b) Mass flow gain factor M

Fig. 9 Comparison with experiments. (The data for SSME LPOTP are from Brennen et al. 1982, those for ARIANE V LOX are from Iacopozzi et al. 1993, and those for LE-7 LOX are from Shimura 1993.)

length was allowed to oscillate. Although more elaborate cavity models might be possible, the present simple model provides the baseline for analytical models and experiments.

This study was partly supported by a Grant-in-Aid for Scientific Research of the Ministry of Education.

References

Acosta, A. J., and Furuya, O., 1976, "A Brief Note on Linearized, Unsteady, Supercavitating Flows," *Journal of Ship Research,* Vol. 23, No. 2, pp. 85-88.

Brennen, C. E., and Acosta, A. J., 1973, "Theoretical Quasi-Static Analysis of Cavitation Compliance in Turbopumps," *J. Spacecraft,* Vol. 10, No. 3, pp. 175-180.

Brennen, C. E., and Acosta, A. J., 1976, "The Dynamic Transfer Function for a Cavitating Inducer," ASME JOURNAL OF FLUIDS ENGINEERING, Vol. 98, No. 2, pp. 182-191.

Brennen, C., 1978, "Bubbly Flow Model for the Dynamic Characteristic of Cavitating Pumps," *Journal of Fluid Mechanics,* Vol. 89, Part 2, pp. 223-240.

Brennen, C. E., Meissner, C., Lo, E. Y., and G. S. Hoffman, 1982, "Scale Effects in the Dynamic Transfer Functions for Cavitating Inducers," ASME JOURNAL OF FLUIDS ENGINEERING, Vol. 104, No. 4, pp. 428-433.

Furuya, O., 1982, "Dynamic Characteristics of Cavitating Pumps and Inducers," ASME paper, pp. 147-155.

Iacopozzi, M., Lignaporo, V., and Prevel, D., 1993, "POGO Characteristics of ARIANE V Turbopump LOX Pump with Hot Water," AIAA Paper 93-2124.

Kamijo, K., Yoshida, M., and Tsujimoto, Y., 1993, "Hydraulic and Mechanical Performance of the LE-7 LOX Pump Inducer," *AIAA Journal of Propulsion and Power,* Vol. 9, No. 6.

Kim, J. H., and Acosta, A. J., 1975, "Unsteady Flow in Cavitating Turbopumps," ASME JOURNAL OF FLUIDS ENGINEERING, Vol. 17, No. 4, pp. 412-418.

Nishiyama, H., and Nishiyama, T., 1980, "Dynamic Transfer Characteristics of Partially Cavitated Hydrofoil Cascade," *Proc, IAHR Symposium, Tokyo,* pp. 243-254.

Rubin, S., 1966, "Longitudinal Instability of Liquid Rockets Due to Propulsion Feed Back (POGO)," *Journal of Spacecraft and Rockets,* Vol. 3, No. 8, pp. 1188-1195.

Shimura, T., 1995, "The Effects of Geometry in the Dynamic Response of the Cavitating LE-7 LOX Pump," *AIAA Journal of Propulsion and Power,* Vol. 11, No. 2, pp. 330-336.

Stripling, L. B., and Acosta, A. J., 1962, "Cavitation in Turbopump-Part 1," ASME *Journal of Basic Engineering,* Vol. 84, pp. 326.

Tsujimoto, Y., Kamijo, K., and Yoshida, Y., 1993, "A Theoretical Analysis of Rotating Cavitation in Inducers," ASME JOURNAL OF FLUIDS ENGINEERING, Vol. 115, No. 1, pp. 135-141.

Young, Y. E. et al., 1972, "Study of Cavitating Inducer Instabilities, Final Report," NASA-CR-123939.

APPENDIX A

$$C_{31} = s_s \int_{-1}^{1} \sqrt{\frac{1+\hat{\tau}}{1-\hat{\tau}}} \, e^{-j\omega(l-x(\hat{\tau}))/U} \frac{1}{h} \, d\hat{\tau}$$

$$C_{32} = \frac{s_s^2}{2} \left(\int_{-1}^{1} \sqrt{\frac{1+\hat{\tau}}{1-\hat{\tau}}} \, e^{-j\omega(l-x(\hat{\tau}))/U} \frac{1}{h} \, d\hat{\tau} \right.$$

$$\left. + \int_{-1}^{1} \sqrt{\frac{1+\hat{\tau}}{1-\hat{\tau}}} \, e^{-j\omega(l-x(\hat{\tau}))/U} \, d\hat{\tau} \right)$$

$$C_{33} = \frac{s_s^2}{2\pi} \int_{-1}^{1} \sqrt{\frac{1+\hat{\tau}}{1-\hat{\tau}}} \, e^{-j\omega(l-x(\hat{\tau}))/U} \frac{1}{h}$$

$$\times \int_{-1}^{1} \frac{\sqrt{1-\tau^2}}{\tau - \hat{\tau}} \, e^{-jkx(\tau)/l}{}_s d\tau d\hat{\tau}$$

$$C_{34} = \left\{ A_s + \left(B_s - \frac{\sigma U}{4} \right) s_s \right\} \int_{-1}^{1} \sqrt{\frac{1+\hat{\tau}}{1-\hat{\tau}}} \frac{1}{h} \, d\hat{\tau} + \left(B_s - \frac{\sigma U}{2} \right) s_s \int_{-1}^{1} \sqrt{\frac{1+\hat{\tau}}{1-\hat{\tau}}} \frac{\hat{\tau}}{h} \, d\hat{\tau} + \left(A_s + \frac{B_s s_s}{2} \right) s_s \int_{-1}^{1} \sqrt{\frac{1+\hat{\tau}}{1-\hat{\tau}}} \frac{h'}{h^2} \, d\hat{\tau}$$

$$+ \frac{s_s^2}{2} \left(B_s - \frac{\sigma U}{.2} \right) \int_{-1}^{1} \sqrt{\frac{1+\hat{\tau}}{1-\hat{\tau}}} \hat{\tau} \frac{h'}{h^2} \, d\hat{\tau} + \frac{\sigma U}{4} s_s \int_{-1}^{1} \sqrt{\frac{1+\hat{\tau}}{1-\hat{\tau}}} \, e^{-j\omega(l-x(\hat{\tau}))/U} \frac{1}{h} \, d\hat{\tau} + \left(A_s + \frac{B_s s_s}{2} \right)$$

$$\times \int_{-1}^{1} \sqrt{\frac{1+\hat{\tau}}{1-\hat{\tau}}} \frac{1}{1-\hat{\tau}} \left(1 - e^{-j\omega(l-x(\hat{\tau}))/U} \right) \frac{1}{h} \, d\hat{\tau} + \frac{s_s}{2} \left(B_s - \frac{\sigma U}{2} \right) \int_{-1}^{1} \sqrt{\frac{1+\hat{\tau}}{1-\hat{\tau}}} \frac{\hat{\tau}}{1-\hat{\tau}} \left(1 - e^{-j\omega(l-x(\hat{\tau}))/U} \right) \frac{1}{h} \, d\hat{\tau}$$

$$h = \frac{s_s^2}{4d} \hat{\tau}^2 + s_s \left(\frac{s_s}{2d} - \frac{\sin \gamma}{\sqrt{d}} \right) \hat{\tau} + \frac{s_s^2}{4d} - s_s \frac{\sin \gamma}{\sqrt{d}} + 1$$

$$h' = - \frac{s_s}{2d} \hat{\tau}^2 + \left(\frac{\sin \gamma}{\sqrt{d}} - \frac{s_s}{d} \right) \hat{\tau} + \frac{\sin \gamma}{\sqrt{d}} - \frac{s_s}{2d}$$

APPENDIX B

$$J_1 = \int_{-\infty}^0 x(\zeta) dH_1(\zeta) \quad J_2 = \int_{-\infty}^0 x(\zeta) dH_2(\zeta)$$

$$J_3 = \int_{-\infty}^0 x(\zeta) dH_3(\zeta) \quad J_4 = \int_{-\infty}^0 x(\zeta) dH_4(\zeta)$$

$$H_1 = \mathrm{Re} \left(\frac{1}{\sqrt{\zeta(\zeta - s_s)}} \right) \quad H_2 = \mathrm{Re} \left(\frac{\zeta}{\sqrt{\zeta(\zeta - s_s)}} \right)$$

$$H_3 = \frac{s_s^2}{4\pi} \mathrm{Re} \left(\frac{1}{\sqrt{\zeta(\zeta - s_s)}} \int_{-1}^1 \frac{\sqrt{1 - \tau'^2}}{-\zeta + s_s(\tau' + 1)/2} e^{-jkx/l_s} d\tau' \right)$$

$$H_4 = \frac{1}{2} \mathrm{Re} \left\{ \frac{1}{\sqrt{\zeta}(\zeta - s_s)^{3/2}} \right.$$

$$\times \left(\frac{\sigma U}{8\pi} s_s^2 \int_{-1}^1 \frac{\sqrt{1 - \tau'^2}}{-\zeta + s_s(\tau' + 1)/2} d\tau' + A_s + B_s \zeta \right) \right\}$$

$$+ \frac{\sigma U}{4\pi} s_s \mathrm{Re} \left\{ \frac{1}{\sqrt{\zeta(\zeta - s_s)}} \left(\int_{-1}^1 \frac{\sqrt{1 - \tau'^2}}{-\zeta + s_s(\tau' + 1)/2} d\tau' \right. \right.$$

$$\left. \left. - \frac{s_s}{4} \int_{-1}^1 \frac{\sqrt{1 - \tau'^2}(\tau' + 1)}{(-\zeta + s_s(\tau' + 1)/2)^2} d\tau' \right) \right\}$$

Pressure Drop in Corrugated Pipes

D. M. Bernhard[1] and C. K. Hsieh[1]

Introduction

Corrugated pipes of thermoplastic composites surrounded by a protective polyester braid bonded to a straight-wall polyurethane casing are a durable alternative to many rigid piping systems. These pipes are highly flexible to the extent that they can be easily bent to facilitate installation and removal. They are ideally suited for use as underground piping, particularly in sinkhole and earthquake prone regions where localized ground movements have often been a concern for pipe failure. Using different inner wall materials makes these pipes compatible to a wide range of chemicals without corrosion problems.

While the use of the corrugated pipes in engineering cannot be claimed as a new idea, the pressure drop in these pipes has often been overlooked. Indeed, the smooth surface of the plastic material fabricated in the form of corrugated ripples provides a roughness reading of 0.55 ± 0.05 μm (22 ± 2 μ in) AA and surface contour that defies the use of the Moody diagram (Moody, 1944) to determine the pressure drop. The turbulent flow inside such pipes also precludes the development of a simple analysis for prediction of the head loss. An experiment must therefore be performed. This technical brief is offered for presentation of the experimental data for pressure loss inside the corrugated pipes of the geometries shown in Table 1. As will be shown, the final results are correlated in a dimensionless form to enhance their usefulness in design.

Experiment
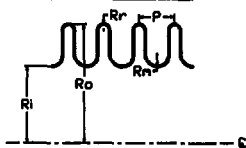
Two corrugated pipes of 0.0381 m ($1\frac{1}{2}$ in) and 0.0635 m ($2\frac{1}{2}$ in) ID were chosen for tests because of their popularity for use in industry. The specifications of these pipes are detailed in Table 1. To cover the broad range of the flow rates tested for each pipe, three venturi meters with overlapped operating ranges were used. Each test section of corrugated pipe was 9.14 m (30 ft) long with pressure taps located at each end of the section to measure the pressure drop. Before testing, the system was carefully vented to eliminate air pockets.

To test the reproducibility of the data reported in this paper, the 0.0635 m ID pipe was tested twice with two different specimens but of the same specification. Data were found repeatable

---

Table 1 Specifications of corrugated pipes

SIZE	Ri	Ro	Rr	Rn	P
0.0381	0.019	0.022	0.0009	0.0021	0.0063
0.0635	0.031	0.034	0.0012	0.0026	0.0076

ALL DIMENSIONS ARE IN METERS

to within 2 percent. A smooth-bore PVC pipe of 0.0508 m (2 in) ID was also tested in order to compare the test data with the empirical formula reported by Colebrook (1939)

$$\frac{1}{f^{1/2}} = -2 \log \left(\frac{e/d}{3.7} + \frac{2.51}{\mathrm{Re}_d f^{1/2}} \right) \qquad (1)$$

where f is the friction factor, e is the pipe roughness, d is the diameter of the pipe, and Re is the Reynolds number defined in terms of the mean velocity and the diameter of the pipe. The test data were in good agreement with Colebrook's formula at low flow rates but slightly higher at large flow rates (up to 5 percent at 1.58 E-2 m^3/s (250 gal/min)). The data reported in this paper have an error band of ± 3 percent.

Results and Discussion

Tests were carried out at a water temperature of 16°C (60°F). Both pipes were tested at a lower flow rate of 3.15 E-4 m^3/s (5 gal/min). The upper flow rate differs slightly. The small pipe was tested to 1.26 E-2 m^3/s (200 gal/min), whereas the large pipe was tested to 1.58 E-2 m^3/s (250 gal/min). These are the usual operating ranges for these pipe sizes. Test results indicated that the corrugated pipe has a much larger pressure drop than a smooth-bore pipe of the same roughness. For a smooth-bore pipe to have a comparable pressure drop as the corrugated pipes, the surface would have a roughness as large as 3.175 E-3 m (0.125 in), which corresponds to a riveted steel pipe (Moody, 1944). Yet, the pressure drop of the riveted pipe is slightly higher than the corrugated pipe at low flow rates but lower at high flow rates. Thus, if the pressure drop is expressed in terms of the friction factor, the friction factor of the smooth-bore pipe holds constant at large Reynolds numbers as is well known from the Moody diagram. However, in the case of the corrugated pipes, the friction factor behaves differently—it holds steady for Reynolds number in the range of 10^4 to $4 \times$
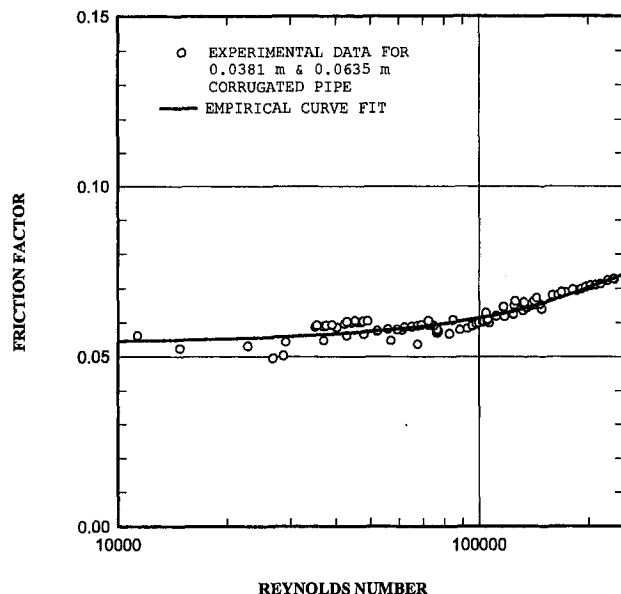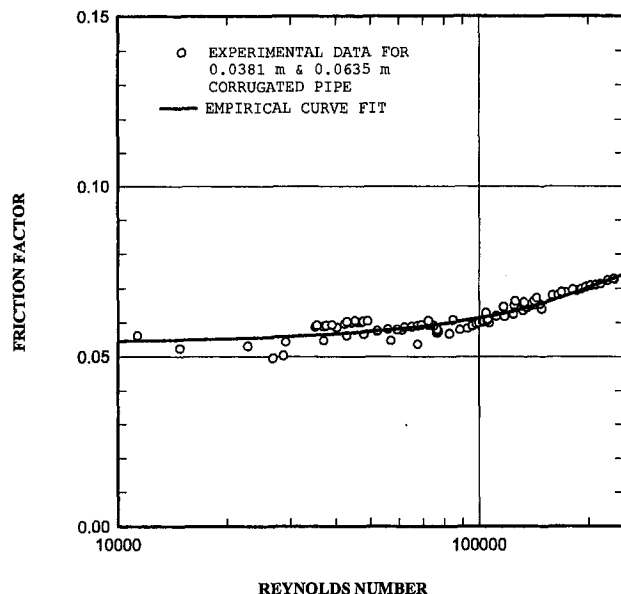
Fig. 1 Friction factor versus Reynolds number plot for corrugated pipes

10^4. Beyond this range, the friction factor rises steadily as shown in Fig. 1.

It is believed that the pressure drop in the corrugated pipes is caused by different mechanisms. Unlike the turbulent flow in a smooth-bore pipe in which the surface roughness displaces the logarithm-law velocity profile, the pressure drop in the corrugated pipes is the result of the combination of the head loss in the core region outside the wall ripples and the loss in the recirculation zone inside the corrugation recess. This flow pattern persists at the low Reynolds numbers in the turbulent region and as a result, the friction factor stays constant. However, at large Reynolds numbers this flow pattern is disrupted. At large Reynolds numbers, the flow in the core region is able to penetrate into the corrugation recess. This results in a smaller recirculation region. At the same time, the flow impinges on the downstream side of the corrugation wall thus resulting in an increase in the pressure loss. Notice that, irrespective of the variations in the pipe size corrugation, the friction factor data in Fig. 1 converge nicely. A single formula is thus correlated as

$$f = \ln \left(C_0 + C_1 \, \mathrm{Re}_d + C_2 \, \mathrm{Re}_d^2 \right)$$

where

$$C_0 = 1.05534 \quad C_1 = 0.72094E\text{-}7 \quad C_2 = 0.75129E\text{-}13$$

This empirical formula should enhance the usefulness of the results presented in this paper.

References

Colebrook, C. F., 1938–1939, "Turbulent Flow in Pipes, with Particular Reference to the Transition Between Smooth and Rough Pipe Laws," *Journal of Institute of Civil Engineers*, London, Vol. 11, pp. 133–156.

Moody, L. F., 1944, "Friction Factors for Pipe Flow," *Trans. ASME*, Vol. 66, pp. 671–684.

Effect of Laminar Flow Control by Suction on Separation

Jamal A. Masad[1] and Ridha Abid[2]

Laminar flow separation decreases lift and increases the pressure drag on aerodynamic surfaces, which results in a reduced efficiency of these surfaces (Schlichting, 1979). Furthermore, separation strongly enhances the onset of laminar-turbulent transition (Masad and Malik, 1994), and the skin-friction drag of turbulent flow is much larger than its counterpart in laminar flow. Application of surface suction allows the boundary layer to overcome stronger adverse pressure gradients before separation occurs, so that it can be used to remove the decelerating fluid particles and delay or prevent laminar separation.

Separation of the boundary layer on aerodynamic surfaces commonly occurs because of relatively long regions of adverse pressure gradient that result from the curvature of the surface. Moreover, on practical aerodynamic surfaces, separation can be caused by a strong, localized adverse pressure gradient that can result from an isolated roughness element. Isolated roughness elements are an unavoidable part of the design of an aerodynamic surface, including roughness elements such as flush screw-head slots or steps and gaps at the joints between the wing and the control surfaces on airplane flaps. Other roughness elements can result from manufacturing; these include surface waviness or incorrectly installed flush rivets. Furthermore, roughness on aerodynamic surfaces can result from material degradation (corrosion), rain erosion, insect impingement, and icing. Laminar flow control experimental (Hahn and Pfenninger, 1973) and computational (Masad and Iyer, 1994) studies showed clearly that suction delays the onset of transition in flow over a roughness element. These studies also showed that the optimal stabilizing location of a suction strip is downstream of the roughness element. In this study, we evaluate how does the suction which is used to laminarize the flow influence separation. Furthermore, we compare the optimal stabilizing location of a suction strip with its optimal location for preventing or delaying separation.

We consider a two-dimensional subsonic flow around a single smooth two-dimensional hump on a flat plate. We consider a two-parameter family of symmetric hump shapes given by

$$y = \frac{y^*}{L^*} = \frac{h^*}{L^*} f(z) = h f(z) \tag{1}$$

where

$$z = \frac{2(x^* - L^*)}{\lambda_h^*} = \frac{2(x - 1)}{\lambda_h} \tag{2}$$

and

$$f(z) = \begin{cases} 1 - 3z^2 + 2|z|^3, & \text{if } |z| \le 1 \\ 0, & \text{if } |z| > 1 \end{cases} \tag{3}$$

Here, h^* is the symmetric hump dimensional height, and λ_h^* is the dimensional length of the hump with the center located at $x^* = L^*$.

The roughness element under consideration could produce separation bubbles behind it. In such flows, both a strong viscous-inviscid interaction and an upstream influence exist. The conventional boundary-layer formulation fails to predict such flows; therefore, we use the interacting boundary-layer (IBL) theory to analyze them. The capability of the IBL to accurately

[1] Research Scientist, High Technology Corporation, 28 Research Drive, Hampton, VA 23666.

[2] Senior Research Scientist, High Technology Corporation, 28 Research Drive, Hampton, VA 23666.

Fig. 1 Friction factor versus Reynolds number plot for corrugated pipes

10^4. Beyond this range, the friction factor rises steadily as shown in Fig. 1.

It is believed that the pressure drop in the corrugated pipes is caused by different mechanisms. Unlike the turbulent flow in a smooth-bore pipe in which the surface roughness displaces the logarithm-law velocity profile, the pressure drop in the corrugated pipes is the result of the combination of the head loss in the core region outside the wall ripples and the loss in the recirculation zone inside the corrugation recess. This flow pattern persists at the low Reynolds numbers in the turbulent region and as a result, the friction factor stays constant. However, at large Reynolds numbers this flow pattern is disrupted. At large Reynolds numbers, the flow in the core region is able to penetrate into the corrugation recess. This results in a smaller recirculation region. At the same time, the flow impinges on the downstream side of the corrugation wall thus resulting in an increase in the pressure loss. Notice that, irrespective of the variations in the pipe size corrugation, the friction factor data in Fig. 1 converge nicely. A single formula is thus correlated as

$$f = \ln\left(C_0 + C_1 \, \mathrm{Re}_d + C_2 \, \mathrm{Re}_d^2\right)$$

where

$$C_0 = 1.05534 \quad C_1 = 0.72094E\text{-}7 \quad C_2 = 0.75129E\text{-}13$$

This empirical formula should enhance the usefulness of the results presented in this paper.

References

Colebrook, C. F., 1938–1939, "Turbulent Flow in Pipes, with Particular Reference to the Transition Between Smooth and Rough Pipe Laws," *Journal of Institute of Civil Engineers*, London, Vol. 11, pp. 133–156.

Moody, L. F., 1944, "Friction Factors for Pipe Flow," *Trans. ASME*, Vol. 66, pp. 671–684.

Effect of Laminar Flow Control by Suction on Separation

Jamal A. Masad[1] and Ridha Abid[2]

Laminar flow separation decreases lift and increases the pressure drag on aerodynamic surfaces, which results in a reduced efficiency of these surfaces (Schlichting, 1979). Furthermore, separation strongly enhances the onset of laminar-turbulent transition (Masad and Malik, 1994), and the skin-friction drag of turbulent flow is much larger than its counterpart in laminar flow. Application of surface suction allows the boundary layer to overcome stronger adverse pressure gradients before separation occurs, so that it can be used to remove the decelerating fluid particles and delay or prevent laminar separation.

Separation of the boundary layer on aerodynamic surfaces commonly occurs because of relatively long regions of adverse pressure gradient that result from the curvature of the surface. Moreover, on practical aerodynamic surfaces, separation can be caused by a strong, localized adverse pressure gradient that can result from an isolated roughness element. Isolated roughness elements are an unavoidable part of the design of an aerodynamic surface, including roughness elements such as flush screw-head slots or steps and gaps at the joints between the wing and the control surfaces on airplane flaps. Other roughness elements can result from manufacturing; these include surface waviness or incorrectly installed flush rivets. Furthermore, roughness on aerodynamic surfaces can result from material degradation (corrosion), rain erosion, insect impingement, and icing. Laminar flow control experimental (Hahn and Pfenninger, 1973) and computational (Masad and Iyer, 1994) studies showed clearly that suction delays the onset of transition in flow over a roughness element. These studies also showed that the optimal stabilizing location of a suction strip is downstream of the roughness element. In this study, we evaluate how does the suction which is used to laminarize the flow influence separation. Furthermore, we compare the optimal stabilizing location of a suction strip with its optimal location for preventing or delaying separation.

We consider a two-dimensional subsonic flow around a single smooth two-dimensional hump on a flat plate. We consider a two-parameter family of symmetric hump shapes given by

$$y = \frac{y^*}{L^*} = \frac{h^*}{L^*} f(z) = h f(z) \tag{1}$$

where

$$z = \frac{2(x^* - L^*)}{\lambda_h^*} = \frac{2(x - 1)}{\lambda_h} \tag{2}$$

and

$$f(z) = \begin{cases} 1 - 3z^2 + 2|z|^3, & \text{if } |z| \le 1 \\ 0, & \text{if } |z| > 1 \end{cases} \tag{3}$$

Here, h^* is the symmetric hump dimensional height, and λ_h^* is the dimensional length of the hump with the center located at $x^* = L^*$.

The roughness element under consideration could produce separation bubbles behind it. In such flows, both a strong viscous-inviscid interaction and an upstream influence exist. The conventional boundary-layer formulation fails to predict such flows; therefore, we use the interacting boundary-layer (IBL) theory to analyze them. The capability of the IBL to accurately

[1] Research Scientist, High Technology Corporation, 28 Research Drive, Hampton, VA 23666.

[2] Senior Research Scientist, High Technology Corporation, 28 Research Drive, Hampton, VA 23666.
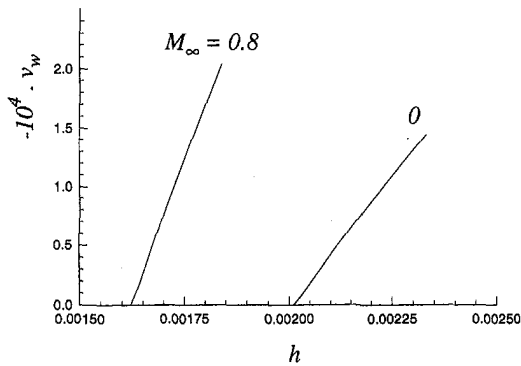
Fig. 1 Variation of uniform suction level needed to prevent separation with various hump heights

predict the flow field under consideration was established by comparing its results with the results of Navier-Stokes (NS) solvers (e.g., Ragab et al., 1990). Details of the IBL formulation for the compressible subsonic flow under consideration are available in many references.

In the results presented in this work, the surface suction velocity v_w is made nondimensional with respect to the free-stream streamwise velocity U_∞^*; therefore, $v_w = v_w^*/U_\infty^*$, where v_w^* is the dimensional surface suction velocity which is negative for suction. The free-stream Reynolds number Re is defined as

$$\text{Re} = \frac{U_\infty^* L^*}{\nu_\infty^*} \qquad (4)$$

where ν_∞^* is the free-stream dimensional kinematic viscosity. We emphasize here that L^* is the dimensional distance from the leading edge of the flat plate to the center of the hump and x is made nondimensional with respect to L^*; therefore, $x = x^*/L^*$. As a result, the hump is centered at $x = 1$. In the computations in this work, the nondimensional length of the hump $\lambda_h = \lambda_h^*/L^*$ is 0.2, so that the hump is located between $x = 0.9$ and 1.1. In the case of suction through a strip, the nondimensional length of the strip is denoted by λ_s and is made nondimensional with respect to L^*; therefore, $\lambda_s = \lambda_s^*/L^*$. The nondimensional distance x between the leading edge of the flat plate and the center of the suction strip is denoted by x_c. For the compressible flow calculations, the free-stream temperature is 300 K, the Prandtl number is constant and equal to 0.72, and the variation of viscosity with temperature is governed by the Sutherland formula.

We first examine the effect of continuous uniform suction on preventing flow separation. With IBL, we compute the subsonic flow field over a flat plate with a hump of height h, which causes the flow to separate. Low-level uniform suction v_w is applied over the entire plate, and the flow field is recomputed. The uniform suction level v_w is then increased, and the flow field is recomputed again. This procedure is continued until the value of v_w at the point where separation is prevented (incipient separation) is determined. The determined suction level v_w is then plotted against the hump height h. Various heights that cause separation are considered; for each height, the minimum value of v_w that prevents separation (the incipient separation point) is determined. The combinations of h and v_w are plotted for two free-stream Mach numbers $M_\infty = 0$ and 0.8; these results are shown in Fig. 1. As the hump height h increases, the suction level v_w needed to prevent separation increases, and the variation of v_w with h is almost linear at both Mach numbers. Note in figure 1 that compressibility enhances separation. For example, at $v_w = 0$, the hump height that causes incipient separation at $M_\infty = 0$ is $h = 0.00201$, whereas at $M_\infty = 0.8$, it is $h = 0.00162$.

The suction used in computing the results in Fig. 1 is uniform and is applied everywhere on the flat plate. Nonuniform suction is more efficient for delaying transition in laminar flow control applications. For this reason, we consider the possibility of localized surface suction through a strip. To explore this possibility, we considered incompressible flow over a hump with height $h = 0.0021$. At this height and with no suction, the flow separates at $x = 1.07$ and reattaches at $x = 1.1$ with a maximum flow reversal of 0.04 percent. A suction strip of length $\lambda_s = 0.2$ is placed at various locations. The suction level needed to prevent separation is determined for each suction-strip location. The variation of the suction level v_w with the location of the center of the suction strip x_c is shown in Fig. 2. The circles indicate the points at which the actual computations were made, and the circles are connected. Recall here that the hump is located between $x = 0.9$ and 1.1. Figure 2 shows clearly that the optimal location of the suction strip for preventing separation (the location with minimum v_w) is within the hump. However, on laminar flow control surfaces it is most unlikely to have suction within the roughness element, then it follows from Fig. 2 that the optimal practical location of the suction strip for preventing separation is upstream of the hump. Suction strips located downstream of the roughness element require the most suction. The further the suction strip is placed in either the upstream or downstream directions, the more suction is required to prevent separation. The large levels of suction needed to prevent separation when the suction strip is placed in a downstream location are due to the relatively weak upstream influence the suction has on the flow field. Upstream, the suction has a much greater influence on the flow field. Figure 2 also shows the results for $h = 0.0022$. At this height with no suction, the maximum flow reversal is 0.14 percent and the suction level needed to prevent separation is obviously larger than that needed at $h = 0.0021$ at all suction-strip locations. The general features of the variation of v_w with x_c at $h = 0.0022$ are similar to those at $h = 0.0021$.

In the results shown in Fig. 2, we assume that the flow is laminar. Linear stability calculations, coupled with the empirical e^N method ($N = 9$), predict the transition onset location for the conditions shown in Fig. 2 with no suction to be at $x = x_t = 1.9$ for $h = 0.0022$. Both a reduction in the height to $h = 0.0021$ and the application of suction increase the value of x_t.

In Fig. 2, the length of the suction strip λ_s is 0.2. To investigate the effect of varying the suction-strip length on the occurrence of separation, we consider incompressible flow over a hump of height $h = 0.0021$ and suction strips of three different lengths λ_s of 0.2, 0.1, and 0.05. At various locations, the suction level needed to prevent separation for each of the three strips is determined. The results of these computations are shown in Fig. 3 in which the product $\lambda_s \cdot v_w$ (proportional to the total mass flux) is plotted against the location of the center of the suction strip. Figure 3 clearly shows that the optimal practical location
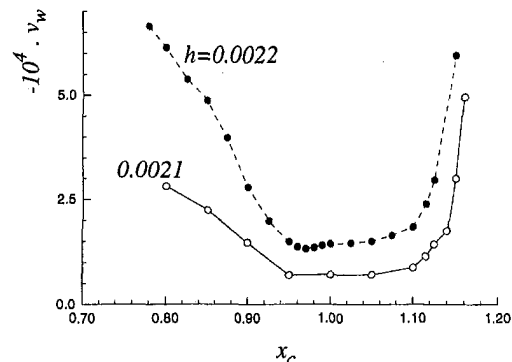

Fig. 2 Variation of discrete suction level needed to prevent separation with location of center of suction strip ($\lambda_s = 0.2$) at $M_\infty = 0$
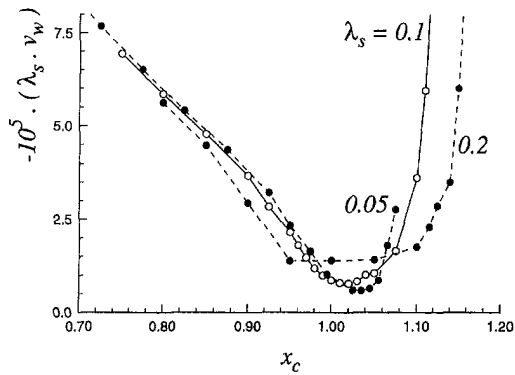
Fig. 3 Variation of the total mass flux needed to prevent separation with various locations of suction-strip center at $M_\infty = 0$

for a suction strip to prevent separation is upstream of the hump. A reduction in the suction-strip length results in a more efficient (less total mass flux) application of suction. The results in Figs. 1–3 are for Re = 10^6, and it is known that flow separation phenomenon depends on the Reynolds number. Additional calculations at Re = 0.2×10^6 and 0.6×10^6 show all the reached conclusions to hold at these Reynolds numbers as well. The hump's height needed to cause separation increases as Re decreases.

In summary, it is found that although the optimal stabilizing location of a suction strip on a laminar flow control surface with a roughness element is downstream of the roughness element, the optimal practical location of the suction strip for preventing separation is upstream of the roughness element. A relatively long suction strip is found to be more optimal in delaying or preventing separation than a short strip.

References

Hahn, M., and Pfenninger, W., 1973, "Prevention of Transition Over a Backward Step by Suction," *Journal of Aircraft*, Vol. 10, pp. 618–622.

Masad, J. A., and Iyer, V., 1994, "Transition Prediction and Control in Subsonic Flow over a Hump," *Phys. Fluids*, Vol. 6, No. 1, pp. 313–327.

Masad, J. A., and Malik, M. R., 1994, "On the Link Between Flow Separation and Transition Onset," AIAA Paper No. 94-2370.

Ragab, S. A., Nayfeh, A. H., and Krishna, R. C., 1990, "Stability of Compressible Boundary Layers over a Smooth Backward-Facing Step," AIAA Paper No. 90-1449.

Schlichting, H., 1979, *Boundary-Layer Theory*, 7th ed., McGraw-Hill, New York.

Structural Modeling of the Wall Effects of Lorentz Force

P. R. Bandyopadhyay[1] and R. Balasubramanian[2]

1 Introduction

Due to its salinity, sea water is electrically conducting. This opens up the possibility of controlling turbulent boundary layers

[1] Naval Undersea Warfare Center, Newport, RI. Fellow ASME.

[2] Spectrex Inc, Gloucester, VA.

in ocean going vehicles by means of electro-magneto hydrodynamic forces (also called MHD, EMHD, or Lorentz forces), which can be generated by crossing magnetic and electric fields within the liquid boundary layer (Branover, 1978). Recent experiments on the subject have been reported by Nosenchuck (1994) and Henoch and Stace (1995). Nosenchuck attempted to control the production of turbulence in a turbulent boundary layer by inhibiting the well-known near-wall ejections attributed to the bursting process of turbulence production. He injected an electrolytic solution in the near-wall region of a turbulent boundary layer developing in a medium of fresh water. The orientation of the electro-magnetic field was such that the resulting Lorentz force was directed toward the wall. The force was confined to where the electrolyte was concentrated. A significant reduction of turbulence and drag was reported. On the other hand, Henoch and Stace (1995) experimented with salt water and they applied Lorentz force to the near-wall region in the streamwise direction.

It is desirable to apply the minimal amount of Lorentz force localizing it where required. Since the constituent vortices in a turbulent boundary layer have a preferred orientation, an inclined force field could minimize the amplitude requirement. Because of measurement difficulties, the data base of the effects of Lorentz force in sea water turbulent boundary layer is limited. An understanding of the interaction process of Lorentz force with the vortices, which are the building blocks of turbulence, would be beneficial. Here, this interaction process is studied through a structural model of the turbulent boundary layer, developed earlier by Bandyopadhyay and Balasubramanian (1995a; henceforth called B&B 1995a). The structural model of the canonical flat plate turbulent boundary layer is subjected to a Lorentz force, and a full numerical simulation of the effects has been carried out. The objective is to get insight and to determine the most beneficial direction of Lorentz force.

2 Structural Modeling of the Interaction of Lorentz Force With a Vortex in a Shear Flow

The components of the structural model are shown in Fig. 1. There are two sub-models, one is of the basic canonical flat plate turbulent boundary layer, and the other is of the Lorentz force. Put simply, the former has three essential elements within a computational domain that represents a unit volume of turbulence production: a flat wall, a (Blasius) mean shear (Ω_Z) and a coherent vortex in the transverse plane that is inclined at 45 degrees to the flow direction (ω_Z). This is reminiscent of Reynolds decomposition of Navier-Stokes equations for turbulent flows into mean (Ω_Z) and fluctuating components (ω_Z). The details of the structural model of the turbulent boundary layer, of numerical computations and of the comparison of the statistics of turbulence obtained from the model to those from measurements and other numerical simulations, are given in B&B (1995a). For a lack of space, these details will not be repeated here.
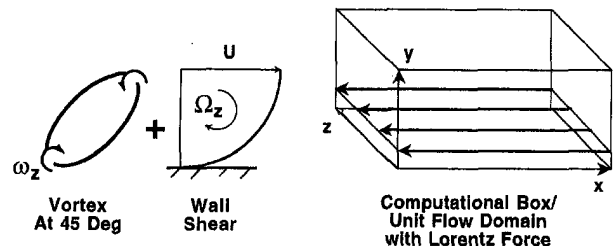

Fig. 1 A schematic representation of the structural model of the canonical flow and Lorentz force. The vortex lies in the inclined cross-stream plane.
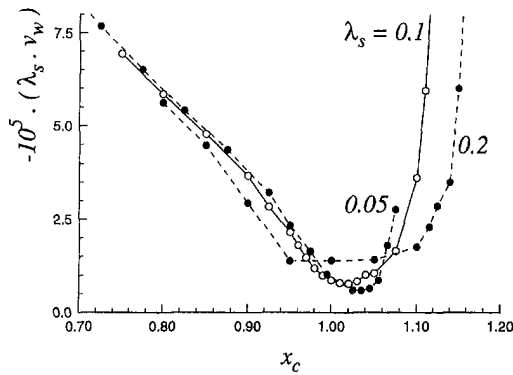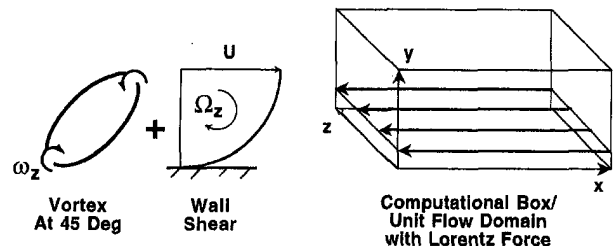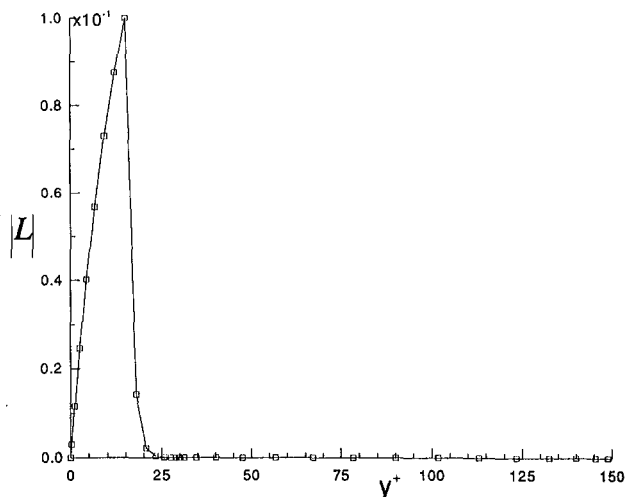
Fig. 3 Variation of the total mass flux needed to prevent separation with various locations of suction-strip center at $M_\infty = 0$

for a suction strip to prevent separation is upstream of the hump. A reduction in the suction-strip length results in a more efficient (less total mass flux) application of suction. The results in Figs. 1–3 are for Re $= 10^6$, and it is known that flow separation phenomenon depends on the Reynolds number. Additional calculations at Re $= 0.2 \times 10^6$ and 0.6×10^6 show all the reached conclusions to hold at these Reynolds numbers as well. The hump's height needed to cause separation increases as Re decreases.

In summary, it is found that although the optimal stabilizing location of a suction strip on a laminar flow control surface with a roughness element is downstream of the roughness element, the optimal practical location of the suction strip for preventing separation is upstream of the roughness element. A relatively long suction strip is found to be more optimal in delaying or preventing separation than a short strip.

References

Hahn, M., and Pfenninger, W., 1973, "Prevention of Transition Over a Backward Step by Suction," *Journal of Aircraft*, Vol. 10, pp. 618–622.

Masad, J. A., and Iyer, V., 1994, "Transition Prediction and Control in Subsonic Flow over a Hump," *Phys. Fluids*, Vol. 6, No. 1, pp. 313–327.

Masad, J. A., and Malik, M. R., 1994, "On the Link Between Flow Separation and Transition Onset," AIAA Paper No. 94-2370.

Ragab, S. A., Nayfeh, A. H., and Krishna, R. C., 1990, "Stability of Compressible Boundary Layers over a Smooth Backward-Facing Step," AIAA Paper No. 90-1449.

Schlichting, H., 1979, *Boundary-Layer Theory*, 7th ed., McGraw-Hill, New York.

Structural Modeling of the Wall Effects of Lorentz Force

P. R. Bandyopadhyay[1] and R. Balasubramanian[2]

1 Introduction

Due to its salinity, sea water is electrically conducting. This opens up the possibility of controlling turbulent boundary layers

[1] Naval Undersea Warfare Center, Newport, RI. Fellow ASME.
[2] Spectrex Inc, Gloucester, VA.

in ocean going vehicles by means of electro-magneto hydrodynamic forces (also called MHD, EMHD, or Lorentz forces), which can be generated by crossing magnetic and electric fields within the liquid boundary layer (Branover, 1978). Recent experiments on the subject have been reported by Nosenchuck (1994) and Henoch and Stace (1995). Nosenchuck attempted to control the production of turbulence in a turbulent boundary layer by inhibiting the well-known near-wall ejections attributed to the bursting process of turbulence production. He injected an electrolytic solution in the near-wall region of a turbulent boundary layer developing in a medium of fresh water. The orientation of the electro-magnetic field was such that the resulting Lorentz force was directed toward the wall. The force was confined to where the electrolyte was concentrated. A significant reduction of turbulence and drag was reported. On the other hand, Henoch and Stace (1995) experimented with salt water and they applied Lorentz force to the near-wall region in the streamwise direction.

It is desirable to apply the minimal amount of Lorentz force localizing it where required. Since the constituent vortices in a turbulent boundary layer have a preferred orientation, an inclined force field could minimize the amplitude requirement. Because of measurement difficulties, the data base of the effects of Lorentz force in sea water turbulent boundary layer is limited. An understanding of the interaction process of Lorentz force with the vortices, which are the building blocks of turbulence, would be beneficial. Here, this interaction process is studied through a structural model of the turbulent boundary layer, developed earlier by Bandyopadhyay and Balasubramanian (1995a; henceforth called B&B 1995a). The structural model of the canonical flat plate turbulent boundary layer is subjected to a Lorentz force, and a full numerical simulation of the effects has been carried out. The objective is to get insight and to determine the most beneficial direction of Lorentz force.

2 Structural Modeling of the Interaction of Lorentz Force With a Vortex in a Shear Flow

The components of the structural model are shown in Fig. 1. There are two sub-models, one is of the basic canonical flat plate turbulent boundary layer, and the other is of the Lorentz force. Put simply, the former has three essential elements within a computational domain that represents a unit volume of turbulence production: a flat wall, a (Blasius) mean shear (Ω_z) and a coherent vortex in the transverse plane that is inclined at 45 degrees to the flow direction (ω_z). This is reminiscent of Reynolds decomposition of Navier-Stokes equations for turbulent flows into mean (Ω_z) and fluctuating components (ω_z). The details of the structural model of the turbulent boundary layer, of numerical computations and of the comparison of the statistics of turbulence obtained from the model to those from measurements and other numerical simulations, are given in B&B (1995a). For a lack of space, these details will not be repeated here.

Fig. 1 A schematic representation of the structural model of the canonical flow and Lorentz force. The vortex lies in the inclined cross-stream plane.

Fig. 2 Lorentz force distribution across the boundary layer used in present modeling

Table 1 Results of structural modeling of the effects of Lorentz force on the root-mean-square of wall pressure fluctuations

	Lorentz force Off	Lorentz force: On		
		Case 1:	Case 2:	Case 5:
Lorentz force	$L_x = 0$ $L_y = 0$	$L_x < 0$ $L_y = 0$	$L_x > 0$ $L_y = 0$	$L_x = 0$ $L_y < 0$
$\dfrac{p_w}{U_\tau^2}$	3.25	2.67	3.83	2.77

2.1 Modeling of Lorentz Force.

The present numerical study examines a sea water like flow medium where Hartmann number is very low. Here, Lorentz force appears primarily by the crossing of electric and magnetic fields near the wall. The indirect effects of the flow back on the electromagnetic field can be neglected in this case, and the primary effect which needs to be modeled is that of the directly applied Lorentz force only. The Lorentz force considered has a distribution as shown in Fig. 2. Here, y^+ represents vertical distances from the wall in wall units yU_τ/v, where U_τ is friction velocity and v is kinematic viscosity. The distribution is held constant in both the streamwise and spanwise directions within the computational box (Fig. 1). The force peaks at $y^+ = 15$, which is known to be the location where turbulence production reaches a maximum value. It drops off exponentially above that height. In other words, the force field is practically confined to a thin layer above the wall. A parametric study has been conducted where the force (L) is allowed to lie in the planes and act in the directions, as given in the following five cases:

in the pointing upstream ($L_x < 0$, $L_y = 0$: Case 1), or pointing downstream ($L_x > 0$, $L_y = 0$: Case 2) direction, in a wall-parallel plane,

outward ($L_x = L_y > 0$: Case 3), or wallward ($L_x = L_y < 0$: Case 4), in a cross-stream plane inclined downstream at 45° to the flow direction, and

wallward ($L_x = 0$, $L_y < 0$: Case 5), in a wall-normal cross-stream plane.

In Fig. 1, the depicted force acts in a wall-parallel plane. It can be expected that Case 1 will lead to a drag reduction and Case 2, to a drag increase.

The force field has been modeled as a nondimensional peak pressure gradient term $|L| = (J \times B)/(q_\infty/X_0)$. Here, J is current, B is magnetic field strength, q_∞ is dynamic head and X_0 is a length scale. The non-dimensionalizing velocity scale is freestream velocity U_∞ and the length scale is the inflow development length of the Blasius base flow. L_x and L_y are components of L in the x and y directions, respectively. In the experiments of Nosenchuck (1994), the peak value of L was 0.1–0.2 (0.1 in Fig. 2). This range was deduced from a magnetic field strength $B = 0.03$ W/m^2, an applied current J of 100–200 C/m^2/s, and a freestream velocity of 0.15 m/s. The meaning of an applied Lorentz force of peak amplitude 0.1 can be understood by noting the following. In the upstream pointing direction, it causes a perturbation in skin friction by a maximum of only 2%, whereas a 100% perturbation is required to separate the boundary layer locally.

2.2 Wall-Pressure.

Full numerical solution of the convecting vortex and the base flow within the computational box (Fig. 1), under the influence of the Lorentz force (Fig. 2), has been carried out in the manner given in B&B (1995a and b). The distributions of the root-mean-square (rms) of the local pressure fluctuations across the boundary layer show that the effect of the Lorentz force shown in Fig. 2 remains confined to a small near-wall region of the shear layer (B&B 1995b), as desired. The calculated wall-pressure values are summarized in Table 1. In Table 2, the measurements of rms wall-pressure in unforced turbulent boundary layers, in laboratory and flight, are summarized. The symbols are as follows: p_w is root-mean-square of wall-pressure fluctuations, U_τ is friction velocity, Re_θ is Reynolds number based on momentum thickness, Re_x, which pertains to flight data, is Reynolds number based on streamwise distance from the nose of the aircraft, and M is flight Mach number. As a basic validation of the modeling, Tables 1 and 2 show that wall pressure in the unforced case, obtained from the present structural model, is in the range of measurements.

Table 1 shows that, an EMHD forcing which gives rise to a wall-jet like near-wall acceleration (Case 2), enhances wall pressure rms by 17.8 percent. In contrast, an EMHD forcing applied in the upstream direction (Case 1), that is similar to a near-wall deceleration, leads to a suppression of wall pressure rms also by 17.8%. Furthermore, a wallward EMHD forcing, similar to that of Nosenchuck (1994), leads to a suppression of wall pressure rms by 14.8%.

2.3 Skin Friction.

The strategy for turbulence control depends on whether a mean flow or a perturbation variable is the objective. In many engineering applications, while it is necessary to suppress the wall pressure fluctuations, in order to reduce the attendant turbulence induced noise, when it comes to skin friction, the reduction of the mean flow drag is what is more important. Furthermore, it is useful to separate the effects of Lorentz force on the vortex and those on the base flow. The latter is a "brute" force method of drag reduction, while the former offers the potential for benefit by "subtle" application. In the "time-averaged" sense of an experiment, these two effects get smeared. The effects of Lorentz force on skin friction are, therefore, presented by showing the detailed streamwise distribution within the computational box. This allows the two effects to be distinguished in space.

The effects of the EMHD forces on skin friction are shown in Fig. 3, nondimensionalizing the results by base flow skin friction and boundary layer thickness. Again, roughly two sepa-

Table 2 Measurements of RMS of wall pressure fluctuations in the absence of Lorentz force

Source/variable	Laboratory: (Willmarth, 1975)	Flight: Boeing 737 Forward (Bhatt, 1971)
Reynolds number	$Re_\theta \leq 4 \times 10^4$	$Re_x \sim 10^8$, $M \leq 0.6$
$\dfrac{p_w}{U_\tau^2}$	2.3–3.6	3.4

rate regimes of EMHD effect can be discerned: a short region of effect on the vortex followed by a long region of effect primarily on the base shear flow. In cases 1 and 4, where the EMHD force or a component of it acts in the upstream pointing direction, in the first region where the vortex resides, skin friction is increased in the upstream half of the vortex, and it is reduced in the downstream half, compared to the reference case of non-EMHD base flow with vortex. In contrast, the skin friction trend is reversed when the EMHD force acts in the downstream pointing direction (cases 2 and 3): in the upstream half of the vortex, skin friction is reduced, while it is increased in the downstream half; skin friction is increased in the remaining base flow as well.

The effects of the Lorentz force on the near-wall organized "turbulent" motion, with reference to the non-EMHD vortex-cum-base flow case are depicted schematically in Fig. 4. The motions considered are the streamwise perturbation velocities. Note that these are not the complete perturbation velocities over the Blasius base flow, but are those due to the Lorentz force only, and are in addition to the perturbation due to the vortex over the Blasius base flow. The streamwise perturbation velocities are derived from Fig. 3. A mean velocity profile made fuller by a downstream pointing perturbation vector leads to higher skin friction, and an upstream pointing perturbation vector has the opposite effect. The perturbation pattern due to the EMHD force is simple: the perturbations are converging toward the vortex over the entire unit domain of turbulence production when the MHD force is upstream pointing, and they are diverging from the vortex when the force is pointing downstream.

Figures 3 and 4 offer several control strategies for the reduction of skin friction. First, a continuous application of EMHD force derives benefit largely by affecting the base flow. Second, a maximum drag reduction is achievable by phase-matching the applied force to the passage of the vortex, as well as by varying the direction of the applied force: applying a downstream pointing force in the upstream-half of the vortex, followed by an upstream pointing force in the remaining half of the vortex, as well as in the base flow. Here also the force is applied over the entire surface. However, in the third strategy, the force can be applied only selectively to the vortex and not to the base flow. After the arrival of the vortex is sensed at a station, in the downstream half, the force can be applied in the upstream pointing direction, which could be subsequently reversed to the downstream pointing direction in the upstream half of the vortex. Because the direction of Lorentz force can be reversed by simply switching the polarity of the applied DC field, implementing these seemingly complicated selective control schemes may not be difficult (Bandyopadhyay and Castano, 1996). Figure 4 leads to the conclusion that, phase-matching and pulsing the applied Lorentz force to the quasi-periodically convecting constituting hairpin vortices in a turbulent boundary layer, could lead to a drag reduction.
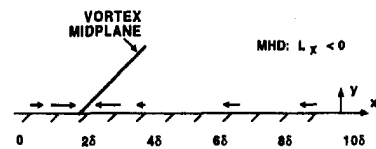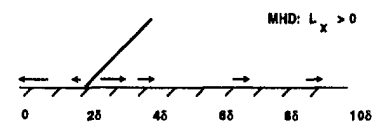

Fig. 4 Streamwise perturbation velocities near the wall due to Lorentz force. Lorentz force: upstream-pointing (a), and downstream-pointing (b).

References

Bandyopadhyay, P. R., and Balasubramanian, R., 1995a, "Vortex Reynolds Number in Turbulent Boundary Layers," *Journal of Theoretical and Computational Fluid Dynamics*, Vol. 7(2) 101–118.

Bandyopadhyay, P. R., and Balasubramanian, R., 1995b, "Structural Modeling of the Wall Effects of Lorentz Force in Turbulent Wall-Bounded Flows," *Paper No. AIAA-95-0858*.

Bandyopadhyay, P. R., and Castano, J. M., 1996, "Microtiles for Electromagnetic Turbulence Control in Saltwater—Preliminary Investigations," *Proc. ASME Sympo. on Turbulence Modeling and Drag Reduction*, July 7–11, 1996, San Diego, Ca.

Bhatt, W. V., 1971, "Flight Test Measurement of Exterior Turbulent Boundary Layer Pressure Fluctuations on Boeing Model 737 Airplane," *Journal of Sound and Vibrations*, Vol. 14(4), 439–457.

Branover, H., 1978, *Magnetohydrodynamic Flow in Ducts*, John Wiley, New York.

Henoch, C., and Stace, J., 1995, "Experimental Investigation of a Salt Water Turbulent Boundary Layer Modified by an Applied Streamwise Magnetohydrodynamic Body Force," *Physics of Fluids*, Vol. 7, No. 6, pp. 1371–1383.

Nosenchuck, D., 1994, "Electromagnetic Turbulent Boundary-Layer Control," *Bulletin of American Physics Society*, Vol. 39(9), p. 1938.

Willmarth, W. W., 1975, "Pressure Fluctuations Beneath Turbulent Boundary Layers," *Annual Review of Fluid Mech*, Vol. 7, pp. 13–38.

Sources of Error in Eigenvalue Spectra for Pipe-Poiseuille Flows

A. H. Abbot[1] and E. A. Moss[1]

An operational Chebyshev Tau approach was used to establish temporal eigenvalue stability spectra for pipe-Poiseuille flows, using the Sexl equation which was transformed to remove the singularity at the origin. Substantial deviations were noted between the long-standing results of Davey and Drazin (1969) which are scattered and display branching patterns, and those

[1] Graduate Student and Associate Professor, respectively, School of Mechanical Engineering, University of the Witwatersrand, Johannesburg, Johannesburg, South Africa.

Fig. 3 Effects of Lorentz force on detailed skin friction in the unit flow domain

rate regimes of EMHD effect can be discerned: a short region of effect on the vortex followed by a long region of effect primarily on the base shear flow. In cases 1 and 4, where the EMHD force or a component of it acts in the upstream pointing direction, in the first region where the vortex resides, skin friction is increased in the upstream half of the vortex, and it is reduced in the downstream half, compared to the reference case of non-EMHD base flow with vortex. In contrast, the skin friction trend is reversed when the EMHD force acts in the downstream pointing direction (cases 2 and 3): in the upstream half of the vortex, skin friction is reduced, while it is increased in the downstream half; skin friction is increased in the remaining base flow as well.

The effects of the Lorentz force on the near-wall organized "turbulent" motion, with reference to the non-EMHD vortex-cum-base flow case are depicted schematically in Fig. 4. The motions considered are the streamwise perturbation velocities. Note that these are not the complete perturbation velocities over the Blasius base flow, but are those due to the Lorentz force only, and are in addition to the perturbation due to the vortex over the Blasius base flow. The streamwise perturbation velocities are derived from Fig. 3. A mean velocity profile made fuller by a downstream pointing perturbation vector leads to higher skin friction, and an upstream pointing perturbation vector has the opposite effect. The perturbation pattern due to the EMHD force is simple: the perturbations are converging toward the vortex over the entire unit domain of turbulence production when the MHD force is upstream pointing, and they are diverging from the vortex when the force is pointing downstream.

Figures 3 and 4 offer several control strategies for the reduction of skin friction. First, a continuous application of EMHD force derives benefit largely by affecting the base flow. Second, a maximum drag reduction is achievable by phase-matching the applied force to the passage of the vortex, as well as by varying the direction of the applied force: applying a downstream pointing force in the upstream-half of the vortex, followed by an upstream pointing force in the remaining half of the vortex, as well as in the base flow. Here also the force is applied over the entire surface. However, in the third strategy, the force can be applied only selectively to the vortex and not to the base flow. After the arrival of the vortex is sensed at a station, in the downstream half, the force can be applied in the upstream pointing direction, which could be subsequently reversed to the downstream pointing direction in the upstream half of the vortex. Because the direction of Lorentz force can be reversed by simply switching the polarity of the applied DC field, implementing these seemingly complicated selective control schemes may not be difficult (Bandyopadhyay and Castano, 1996). Figure 4 leads to the conclusion that, phase-matching and pulsing the applied Lorentz force to the quasi-periodically convecting constituting hairpin vortices in a turbulent boundary layer, could lead to a drag reduction.
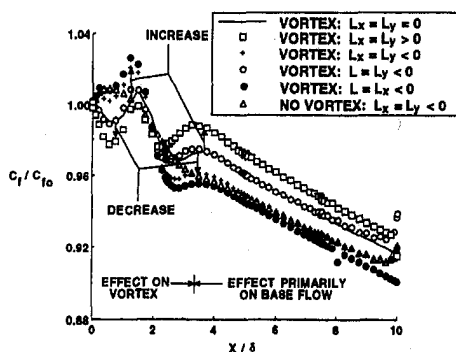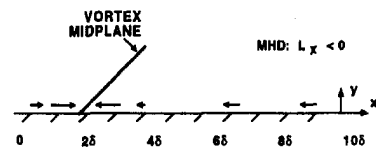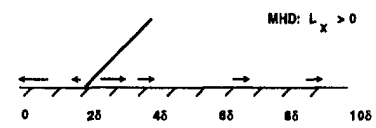

Fig. 4 Streamwise perturbation velocities near the wall due to Lorentz force. Lorentz force: upstream-pointing (a), and downstream-pointing (b).

References

Bandyopadhyay, P. R., and Balasubramanian, R., 1995a, "Vortex Reynolds Number in Turbulent Boundary Layers, *Journal of Theoretical and Computational Fluid Dynamics*, Vol. 7(2) 101–118.

Bandyopadhyay, P. R., and Balasubramanian, R., 1995b, "Structural Modeling of the Wall Effects of Lorentz Force in Turbulent Wall-Bounded Flows," *Paper No. AIAA-95-0858.*

Bandyopadhyay, P. R., and Castano, J. M., 1996, "Microtiles for Electromagnetic Turbulence Control in Saltwater—Preliminary Investigations," *Proc. ASME Sympo. on Turbulence Modeling and Drag Reduction*, July 7–11, 1996, San Diego, Ca.

Bhatt, W. V., 1971, "Flight Test Measurement of Exterior Turbulent Boundary Layer Pressure Fluctuations on Boeing Model 737 Airplane," *Journal of Sound and Vibrations*, Vol. 14(4), 439–457.

Branover, H., 1978, *Magnetohydrodynamic Flow in Ducts*, John Wiley, New York.

Henoch, C., and Stace, J., 1995, "Experimental Investigation of a Salt Water Turbulent Boundary Layer Modified by an Applied Streamwise Magnetohydrodynamic Body Force," *Physics of Fluids*, Vol. 7, No. 6, pp. 1371–1383.

Nosenchuck, D., 1994, "Electromagnetic Turbulent Boundary-Layer Control," *Bulletin of American Physics Society*, Vol. 39(9), p. 1938.

Willmarth, W. W., 1975, "Pressure Fluctuations Beneath Turbulent Boundary Layers," *Annual Review of Fluid Mech*, Vol. 7, pp. 13–38.

Sources of Error in Eigenvalue Spectra for Pipe-Poiseuille Flows

A. H. Abbot[1] and E. A. Moss[1]

An operational Chebyshev Tau approach was used to establish temporal eigenvalue stability spectra for pipe-Poiseuille flows, using the Sexl equation which was transformed to remove the singularity at the origin. Substantial deviations were noted between the long-standing results of Davey and Drazin (1969) which are scattered and display branching patterns, and those

[1] Graduate Student and Associate Professor, respectively, School of Mechanical Engineering, University of the Witwatersrand, Johannesburg, Johannesburg, South Africa.

Fig. 3 Effects of Lorentz force on detailed skin friction in the unit flow domain

of the present work which manifest a more orderly progression of the stable high-order eigenvalues. Formal distinctions are made between errors arising from round-off, basis truncation, and poor choice of basis function: the inaccuracies in Davey and Drazin's data are thought to have arisen from the latter two effects.

1 Introduction

It is generally accepted in the literature that Poiseuille-pipe flows do not possess a neutral stability curve and that such flows are unconditionally stable to infinitesimal axisymmetric and nonaxisymmetric disturbances (see for example Davey and Drazin, 1969; Salwen et al., 1980). Two papers that have presented comprehensive distributions of eigenvalues are those by Davey and Drazin (1969) and Schmid and Henningson (1994). The latter authors attributed the scatter in Davey and Drazin's spectra to the effect of roundoff and the characteristic splitting of their mean mode branch to truncation errors. The aim of the present research was to employ an operational Chebyshev Tau spectral approach (Ortiz and Samara, 1983) to establish eigenvalue spectra for Hagen-Poiseuille flows, in order to (i) further formalize the effect of truncation on the position of the lower fork, and (ii) highlight another source of error in such systems, beyond those discussed by Schmid and Henningson.

2 Formulation and Solution

The well-established Sexl equation governing the stability of pipe flows (see for example Drazin and Reid, 1981) is

$$\frac{-i}{\alpha \, \mathrm{Re_R}} [(L - \alpha^2)^2]\phi = (u - c)[L - \alpha^2]\phi - [Lu]\phi \quad (1)$$

with $L \equiv d^2/dr^2 - (1/r)d/dr$; u = axial velocity; r = radial co-ordinate; ϕ = amplitude function; $\mathrm{Re_R}$ = Reynolds number; α = wave number; c = phase velocity. The quantities have been scaled with respect to the cross-sectional mean velocity

U and pipe radius R. The boundary conditions at the pipe wall are given by $\phi(1) = \phi'(1) = 0$, and the constraints at the origin $\phi(0)/r = \phi'(0)/r = 0$ ensure boundedness at this singular point.

Initial attempts to solve Eq. (1), along with its auxiliary conditions, using the pipe Poiseuille velocity profile $u = 1 - r^2$, led to only algebraic (rather than spectral) convergent behaviour. This was ascribed to the existence of the singularity at the origin which was subsequently removed by the transformation $\phi(r) = r^2\hat{\phi}(r)$. When incorporated into Eq. (1) this led to the system below in which the pipe centreline constraints are implicitly satisfied and only wall conditions need be applied:

$$\frac{-i}{\alpha \, \mathrm{Re_R}} [P - 2\alpha^2 Q + \alpha^4 r^2]\hat{\phi}$$

$$= (u - c)[Q - \alpha^2 r^2]\hat{\phi} - [Su]\hat{\phi} \quad (2)$$

where

$$P \equiv r^2 D^4 + 6rD^3 + 3D^2 - 3\frac{1}{r}D,$$

$$Q \equiv r^2 D^2 + 3rD, \quad S \equiv r^2 D^2 - rD \quad \text{and} \quad D \equiv \frac{d}{dr}.$$

The transformed system is a complex eigenvalue problem of the form $\mathcal{F}(\alpha, c, \mathrm{Re_R}) = 0$ with $\alpha = \alpha_r + i\alpha_i$ and $c = c_r + ic_i$. The temporal stability formulation was adopted, in which the wavenumber α is real and a linear eigenvalue problem results with complex eigenvalues c. Thus, for a fixed α and $\mathrm{Re_R}$, temporal instability is implied by $c_i > 0$ in the context of an equation possessing the form $(Ac - B)\hat{\phi} = 0$. This was solved using a modified operational-Tau approach, together with expansions in Chebyschev polynomials. Construction and solution of the complex linear matrix-eigenvalue problem was conducted in Matlab using the Q-Z algorithm with double-precision arithmetic.

3 Results and Discussion

Figure 1 shows eigenvalues ($\alpha = 1$; $\mathrm{Re_R} = 5{,}000$) generated by the current method for orders of solution $N = 46$; 80, together with those of Davey and Drazin (1969) for $N = 27$. The present eigenvalue spectrum for $N = 46$ has about the same position of the lower branching point as Davey and Drazin's spectrum, but with none of the scatter displayed by their results. In view of Schmid and Henningson's (1994) work, it was tempting to attribute the scatter to roundoff errors: however Davey and Drazin performed double precision calculations, rendering this an unlikely factor. It is important to note that they used eigenfunctions (a Bessel function series) from a system similar to the Sexl equation as basis functions. While this was a superficially logical choice, it is flawed because such functions do not share the property of infinite differentiability with the ostensibly simpler Chebyshev or Legendre polynomials. Hence, poor choice of basis functions appears to have been the most likely reason for the scatter. This highlights the fact that for a given set of scattered results calculated at sufficient order of solution it is not easy to distinguish between the adverse contributions of roundoff and poor choice of basis function. Further, Drazin and Reid comment that the spectrum given by Davey and Drazin for $\mathrm{Re_R} = 5000$ shows two families of modes unexplained by the asymptotic theory—the two lower branches which diverge below $c_i \simeq -1$. As may be seen in Fig. 1 the data set corresponding to $N = 46$ yields a lower fork similar to that of Davey and Drazin: however the feature disappears on this scale of axes when the order is increased to $N = 80$. Arising from this the superimposed eigenvalue spectra at several different values of
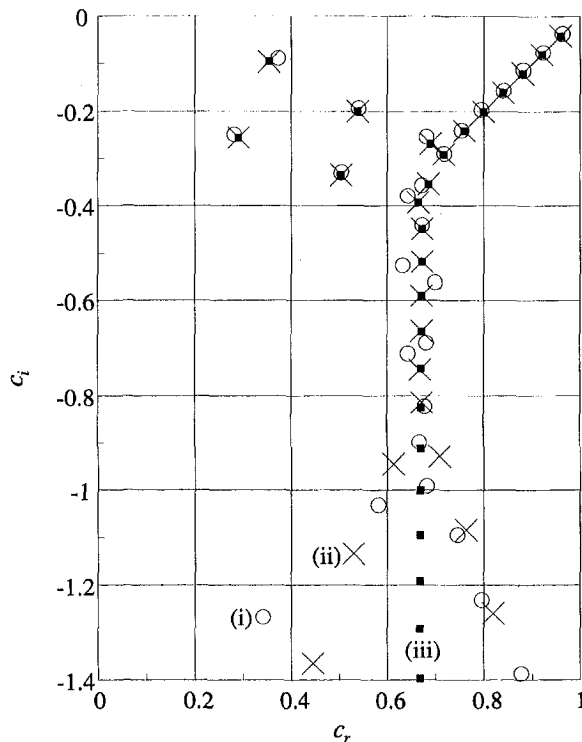

Fig. 1 Eigenvalue spectra for $\alpha = 1$, $\mathrm{Re_R} = 5{,}000$: (i), Davey and Drazin (1969); (ii), present data for $N = 46$; (iii), present data for $N = 80$

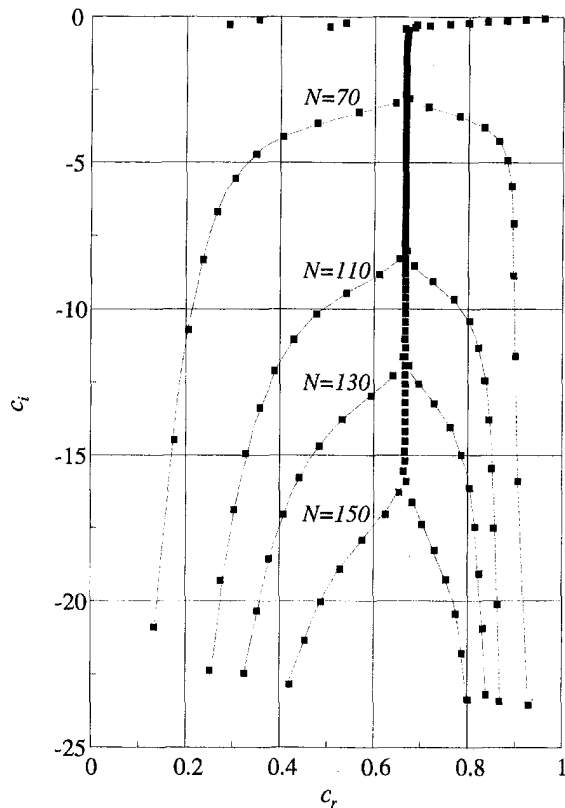**Fig. 2 The present eigenvalue spectrum for $\alpha = 1$, $Re_R = 5,000$, with varying N to show the order-dependent nature of the lower fork**

solution increases. Therefore, as corroborated by Schmid and Henningson (1994), this feature has been clearly introduced by the finite order discretisation (basis truncation), and is spurious to the continuum system. Furthermore, eigenvalues that were previously ill-determined in the basis truncated at a lower order, retain their identity and become convergent to the line $c_r = 2/3$ as the order increases. For the sake of clarity the ordinate has been limited to the range $0 \leq c_i \leq -25$: however the most negative value of c_i diminishes rapidly with increasing order ($c_i \simeq -6 \times 10^4$ for $N = 150$). The left and right-hand forks are bounded in that they asymptote to $c_r = 0$ and $c_r = 1$, respectively, while the number of "bad" eigenvalues they contain is virtually invariant with N.

4 Conclusions

While this study essentially confirms the results of of Schmid and Henningson (1994), it draws a more precise distinction between various sources of error in the calculations of eigenvalues. To summarize: basis truncation affects the number of properly converged eigenvalues as indicated by the position of the lower fork, while decimal precision affects scatter; however an inappropriate choice of basis function exacerbates both convergence and scatter.

References

Davey, A., and Drazin, P. G., 1969, "The Stability of Poiseuille Flow in a Pipe," *Journal of Fluid Mechanics*, Vol. 36, pp. 209–218.

Drazin, P. G., and Reid, W. H., 1981, *Hydrodynamic Stability*, Cambridge Univ. Press.

Ortiz, E. L., and Samara, H., 1983, "Numerical Solution of Differential Eigenvalue Problems with an Operational Approach to the Tau Method," *Computing*, Vol. 31, pp. 95–103.

Salwen, H., Cotton, F. W., and Grosch, C. E., 1980, "Linear Stability of Poiseuille Flow in a Circular Pipe," *Journal of Fluid Mechanics*, Vol. 98, pp. 273–284.

Schmid, P. J., and Henningson, D. S., 1994, "Optimal Energy Density Growth in Hagen-Poiseuille Flow," *Journal of Fluid Mechanics*, Vol. 277, pp. 197–225.

N and plotted at a much larger scale in Fig. 2 show that the fork occurs at diminishing values of c_i As the order of the

---

An Experimental Study of a Three-Dimensional Pressure-Driven Turbulent Boundary Layer

(Data Bank Contribution*)

M. S. Ölçmen[1] and R. L. Simpson[1]

The Laser-Doppler velocimeter data presented by Ölçmen and Simpson (1992) for the Ölçmen flow at 8 measurement stations in a three-dimensional turbulent boundary layer have been remeasured using the five component laser-Doppler velocimeter (5CLDV) probe apparatus of Ölçmen and Simpson (1995a). Further details of the new data set are presented by Ölçmen and Simpson (1995b). The purposes of this brief note are to report on the discrepancies between the Ölçmen and Simpson (1992) and the Ölçmen and Simpson (1995b) data, to provide an explanation, and to present the new set of data to be deposited in the *Journal of Fluids Engineering* Data Bank.

Table 1 Uncertainties in measured quantities with 20:1 odds

	New data set	Old data set
U/U_{ref}	±0.0031	±0.023
V/U_{ref}	±0.0011	±0.015
W/U_{ref}	±0.0025	±0.018
$\overline{u}^2/U_{ref}^2$	±0.00014	±0.0007
$\overline{v^2}/U_{ref}^2$	±0.00005	±0.0003
$\overline{w^2}/U_{ref}^2$	±0.00007	±0.0004
$-\overline{uv}/U_{ref}^2$	±0.00008	±0.0004
$-\overline{uw}/U_{ref}^2$	±0.00004	±0.0004
$-\overline{vw}/U_{ref}^2$	±0.00002	±0.0003

Both sets of measurements were made in air at $U_{ref} \approx 27.5$ m/s in a wing-body junction flow ($Re_\Theta \approx 6000$ at 0.75 chord upstream of the wing). Details of the old LDV system are described by Ölçmen (1990).

One reason for these discrepancies is believed to be due to the complicated LDV setup for the old data. The old data were obtained with three discrete optical component systems located along the side and under the wind tunnel. In order to determine the shear stresses, mean velocity and normal stress components were measured from two of these optical systems. Mean velocity and normal stress components were measured four times and the shear stresses were measured twice, using two different frequency domain analyzers, the swept spectrum analyzer, and the DANTEC Burst Spectrum Analyzer. The two separate data sets obtained using these two signal processors showed good agreement between mean velocities and normal stresses but large differences between the shear stress components, especially for $\overline{vw}$.
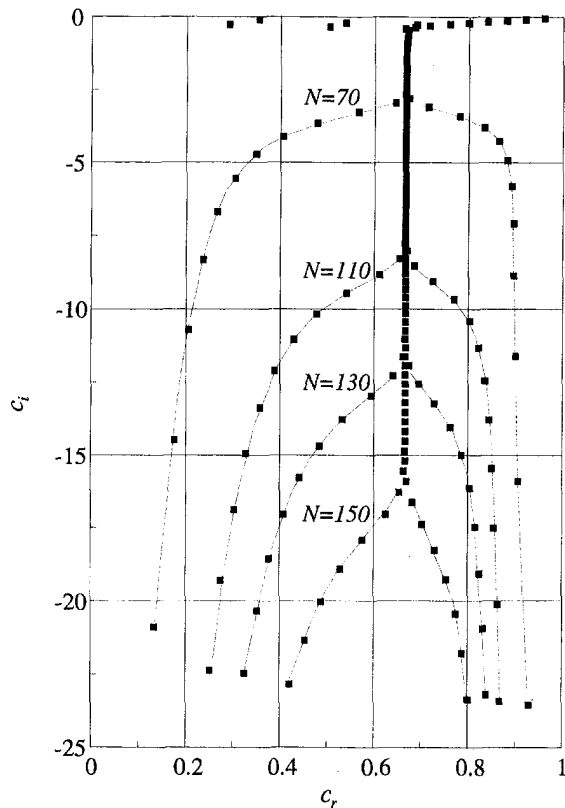
Fig. 2 The present eigenvalue spectrum for $\alpha = 1$, $Re_R = 5,000$, with varying N to show the order-dependent nature of the lower fork

N and plotted at a much larger scale in Fig. 2 show that the fork occurs at diminishing values of c_i As the order of the

solution increases. Therefore, as corroborated by Schmid and Henningson (1994), this feature has been clearly introduced by the finite order discretisation (basis truncation), and is spurious to the continuum system. Furthermore, eigenvalues that were previously ill-determined in the basis truncated at a lower order, retain their identity and become convergent to the line $c_r = 2/3$ as the order increases. For the sake of clarity the ordinate has been limited to the range $0 \leq c_i \leq -25$: however the most negative value of c_i diminishes rapidly with increasing order ($c_i \simeq -6 \times 10^4$ for $N = 150$). The left and right-hand forks are bounded in that they asymptote to $c_r = 0$ and $c_r = 1$, respectively, while the number of "bad" eigenvalues they contain is virtually invariant with N.

4 Conclusions

While this study essentially confirms the results of of Schmid and Henningson (1994), it draws a more precise distinction between various sources of error in the calculations of eigenvalues. To summarize: basis truncation affects the number of properly converged eigenvalues as indicated by the position of the lower fork, while decimal precision affects scatter; however an inappropriate choice of basis function exacerbates both convergence and scatter.

References

Davey, A., and Drazin, P. G., 1969, "The Stability of Poiseuille Flow in a Pipe," *Journal of Fluid Mechanics*, Vol. 36, pp. 209–218.

Drazin, P. G., and Reid, W. H., 1981, *Hydrodynamic Stability*, Cambridge Univ. Press.

Ortiz, E. L., and Samara, H., 1983, "Numerical Solution of Differential Eigenvalue Problems with an Operational Approach to the Tau Method," *Computing*, Vol. 31, pp. 95–103.

Salwen, H., Cotton, F. W., and Grosch, C. E., 1980, "Linear Stability of Poiseuille Flow in a Circular Pipe," *Journal of Fluid Mechanics*, Vol. 98, pp. 273–284.

Schmid, P. J., and Henningson, D. S., 1994, "Optimal Energy Density Growth in Hagen-Poiseuille Flow," *Journal of Fluid Mechanics*, Vol. 277, pp. 197–225.

An Experimental Study of a Three-Dimensional Pressure-Driven Turbulent Boundary Layer

(Data Bank Contribution*)

M. S. Ölçmen[1] and R. L. Simpson[1]

The Laser-Doppler velocimeter data presented by Ölçmen and Simpson (1992) for the Ölçmen flow at 8 measurement stations in a three-dimensional turbulent boundary layer have been remeasured using the five component laser-Doppler velocimeter (5CLDV) probe apparatus of Ölçmen and Simpson (1995a). Further details of the new data set are presented by Ölçmen and Simpson (1995b). The purposes of this brief note are to report on the discrepancies between the Ölçmen and Simpson (1992) and the Ölçmen and Simpson (1995b) data, to provide an explanation, and to present the new set of data to be deposited in the *Journal of Fluids Engineering* Data Bank.

Table 1 Uncertainties in measured quantities with 20:1 odds

	New data set	Old data set
U/U_{ref}	±0.0031	±0.023
V/U_{ref}	±0.0011	±0.015
W/U_{ref}	±0.0025	±0.018
$\overline{u^2}/U_{ref}^2$	±0.00014	±0.0007
$\overline{v^2}/U_{ref}^2$	±0.00005	±0.0003
$\overline{w^2}/U_{ref}^2$	±0.00007	±0.0004
$-\overline{uv}/U_{ref}^2$	±0.00008	±0.0004
$-\overline{uw}/U_{ref}^2$	±0.00004	±0.0004
$-\overline{vw}/U_{ref}^2$	±0.00002	±0.0003

Both sets of measurements were made in air at $U_{ref} \approx 27.5$ m/s in a wing-body junction flow ($Re_\Theta \approx 6000$ at 0.75 chord upstream of the wing). Details of the old LDV system are described by Ölçmen (1990).

One reason for these discrepancies is believed to be due to the complicated LDV setup for the old data. The old data were obtained with three discrete optical component systems located along the side and under the wind tunnel. In order to determine the shear stresses, mean velocity and normal stress components were measured from two of these optical systems. Mean velocity and normal stress components were measured four times and the shear stresses were measured twice, using two different frequency domain analyzers, the swept spectrum analyzer, and the DANTEC Burst Spectrum Analyzer. The two separate data sets obtained using these two signal processors showed good agreement between mean velocities and normal stresses but large differences between the shear stress components, especially for $\overline{vw}$.
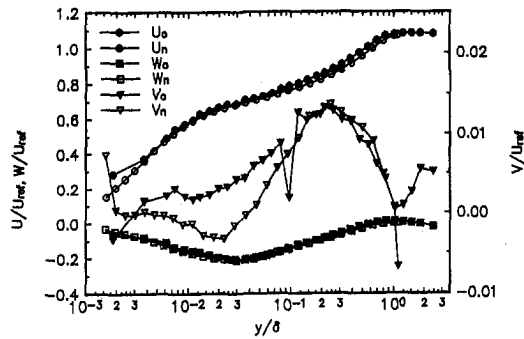
Fig. 1 Mean velocities measured at Station 5. ( )$_o$ and ( )$_n$ denote "old" and "new" data, respectively
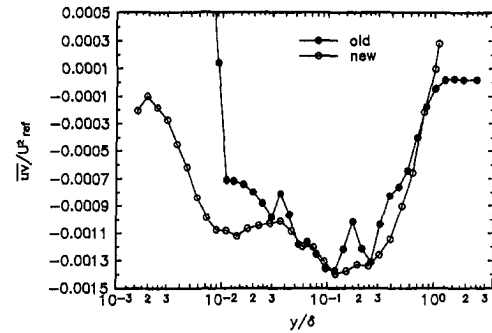

Fig. 5 $\overline{uv}/U_{ref}^2$ shear stress measured at Station 5
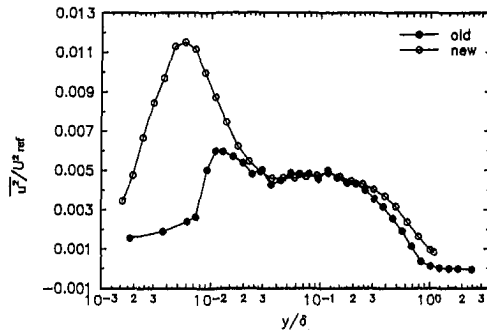

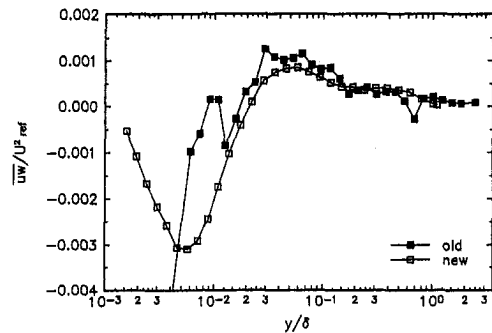Fig. 2 $\overline{u^2}/U_{ref}^2$ normal stress measured at Station 5

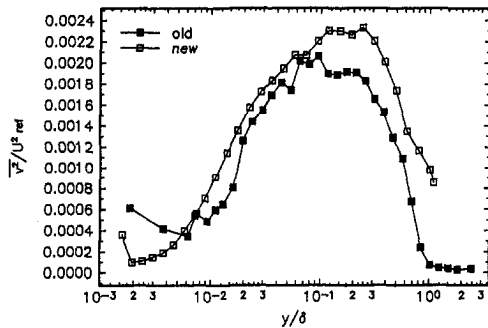Fig. 6 $\overline{uw}/U_{ref}^2$ shear stress measured at Station 5

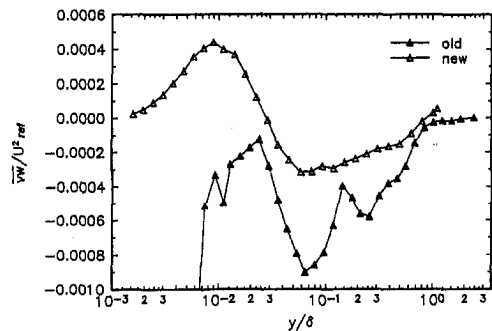Fig. 3 $\overline{v^2}/U_{ref}^2$ normal stress measured at Station 5

Fig. 7 $\overline{vw}/U_{ref}^2$ shear stress measured at Station 5
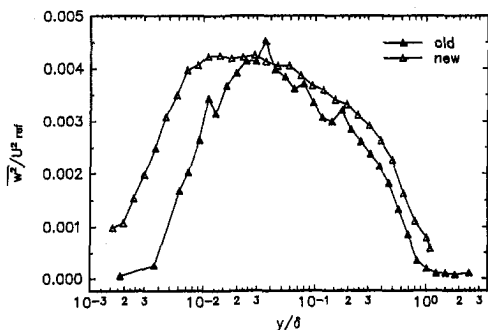

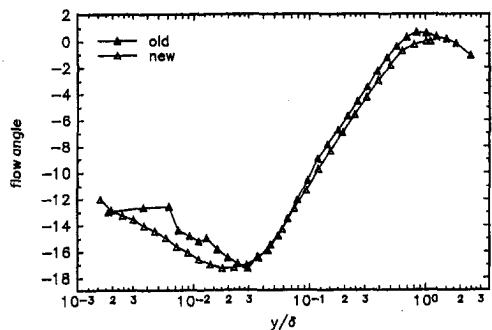Fig. 4 $\overline{w^2}/U_{ref}^2$ normal stress measured at Station 5

Fig. 8 Flow angle calculated at Station 5

The new LDV setup is a fiber-optic, two color system allowing measurements at $y^+ \approx 3$ and above at high Reynolds numbers. The system is located in close proximity to the measurement location. Probe volume size is ≈ 30 μm in diameter. This results in increased spatial resolution of the system, and less velocity gradient broadening in the probe volume. New data were obtained with three MACRODYNE model FDP3100 frequency domain processors in coincidence mode. The 20:1 odds uncertainties of the old and the new data are given in Table 1. The uncertainties of the data sets clearly indicate that the new data set is more reliable.
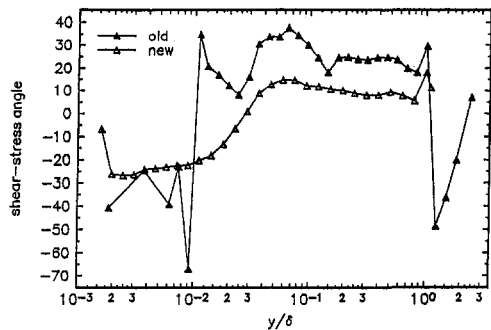
Fig. 9

The figures show the old and new data obtained at the Station 5 with two different LDV techniques in local freestream coordinates. The data clearly show that the mean velocities are in good agreement with each other. However, there is less agreement between the two data sets for the normal stresses and $\overline{uv}$ and $\overline{uw}$ shear stress data. The two data sets are much different for the $\overline{vw}$ data. Especially below $y/\delta \approx 0.03$, these differences are believed to be due to the large gradient-broadening corrections (Durst et al., 1981) applied to the old data set near the wall, which affected only the normal and shear stresses. Quoted uncertainties on the old data set do not reflect uncertainties due to the gradient-broadening corrections. For example, Fig. 2 and

Fig. 4 show low values near the wall due to lack of spatial resolution and gradient-broadening effects. Near the wall the shear stresses are much more scattered in the old data set (Figs. 5, 6, and 7). Outer layer differences for the stresses are believed to be due to the finite-transit-time broadening (Durst et al., 1981) applied to the old data. The new data set was not corrected for these broadening effects.

Data Bank Contribution

The new data set have been deposited to the JFE data bank. These include profiles of all quantities shown in Figs. 1–9 for stations 1–7 that are discussed by Ölçmen and Simpson (1995b).

References

Durst, F., Melling, A., and Whitelaw, J. H., 1981, *Principles and Practice of Laser-Doppler Anemometry*, Second Edition, Academic Press, London, New York, Toronto, Sydney.

Ölçmen, M. S., 1990, "An Experimental Study of a Three-Dimensional Pressure-Driven Turbulent Boundary Layer," Ph.D. dissertation, VPI&SU, AOE Dept., Blacksburg, VA.

Ölçmen, M. S., and Simpson, R. L., 1992, "Perspective: On the Near-Wall Similarity of Three-Dimensional Turbulent Boundary Layers," JOURNAL OF FLUIDS ENGINEERING, Vol. 114, pp. 487–495.

Ölçmen, M. S., and Simpson, R. L., 1995a, "A Five-Velocity-Component Laser-Doppler Velocimeter for Measurements of a Three-Dimensional Turbulent Boundary Layer," *Measurement Science and Technology*, Vol. 6, pp. 702–716.

Ölçmen, M. S., and Simpson, R. L., 1995b, "An Experimental Study of a Three-Dimensional Pressure-Driven Turbulent Boundary Layer," *Journal of Fluid Mech.*, Vol. 290, pp. 225–262.